

https://dspace.org/

Antimicrobial surface coatings via cold spray and 3D printing technologies

Lucas, Michael David Ian

2020
https://hdl.handle.net/10539/31283

Downloaded from a DSpace repository. https://dspace.org/

Antimicrobial Surface Coatings via Cold Spray and 3D Printing Technologies

Michael David Ian Lucas

A thesis submitted to the Faculty of Engineering and the Built Environment, University of the Witwatersrand, Johannesburg, in fulfilment of the requirements for the degree of Doctor of Philosophy.

Johannesburg, July 2020

Declaration

I declare that this thesis is my own, unaided work, except where otherwise acknowledged. It is being submitted for the degree of Doctor of Philosophy in the University of the Witwatersrand, Johannesburg. It has not been submitted before for any degree or examination at any other university.

Signed this 28th day of July 2020



Michael David Ian Lucas

For Prof

Acknowledgements

"'If ever you are passing my way', said Bilbo, 'don't wait to knock! Tea is at four; but any of you are welcome at any time!"

Bilbo Baggins, The Hobbit

It is with heartfelt thanks that I recognise the support, encouragement and expertise of the following people who were instrumental in this academic journey. The following people provided assistance, support and ideas throughout the course of my research and I would like to thank them for their time and assistance, without which the completion of this research would have been that much harder.

To my supervisors Professor Ionel Botef and Professor Sandy van Vuuren, for your dedicated support and unwavering interest, thank you for everything. Your enthusiasm and ideas took this research further than I thought possible. You both deserve rewards no thanks alone can bring. Thank you for being more than just supervisors. Thank you for being true mentors.

I have been so fortunate with academic supervisors. Professor Robert Reid and Professor Craig Law, during the difficult and emotionally challenging time following the passing of Prof. Botef, you took on the role of stand-in supervisors. Thank you for your support, time and expertise. Your commitment to my research, in taking on that role, is much appreciated.

Thank you, also, to Mr Francesco Pietra for reviewing my thesis and assisting in identifying Prof Reid and Prof Law for this unconventional role.

To Prof. Kienhöfer and Prof. Polese for your additional support and encouragement throughout my studies. Thank you for the suggested conferences and symposia and for granting me access to the relevant laboratories and equipment.

Prof. Sacks and Dr van der Merwe thank you for granting me access to the laboratories within the School of Chemical and Metallurgical Engineering and providing advice on related procedures.

I would like to thank you, Mr Riekert and Mr Heydendrych for your assistance within the North West Engineering laboratories, from maintenance on the cold spray unit, to access and support within the workshop. My thanks also goes to you, Mr Chipoyera, for your advice regarding statistical analyses; to you, Brayner, for training me on the roughness tester and helping with SEM analyses and to you, Shadrack, for your practical expertise in metallurgical preparation including mounting, grinding and polishing of test samples.

A special thanks goes to the team at the Pharmacy and Pharmacology Department at Wits Medical School, lead by Prof. van Vuuren. Thank you for making me feel so welcome and included in your team for the better part of a year. A massive thanks to Prof. van Vuuren and Phumzile Moerane for the most efficient and well organised lab I've ever worked in.

A big thank you to Professor David Chandler. Thank you for the independent review and the assistance in editing my thesis.

To all other staff, support staff and peers at the University of the Witwatersrand who had an impact and influence on my research - Thank you.

The financial assistance of the National Research Foundation (NRF), the DST-NRF Centre of Excellence in Strong Materials (CoE-SM) and SITA Information Networking and Computing UK Limited (SITA) towards this research is hereby acknowledged. Opinions expressed and conclusions arrived at, are those of the author and are not necessarily to be attributed to the NRF, CoE-SM or SITA.

It is not always the people in the spotlight, those that influence the academic material of such an undertaking, that need to be acknowledged. As such I wish to thank my parents Dave and Margie, my sister Michelle and the rest of my family and friends for their constant support, encouragement and understanding throughout my studies. Thank you for everything!

A final acknowledgement goes to a person who played a paradoxically small, yet significantly pertinent, role in this research; someone who would otherwise go unacknowledged. I first approached Prof. Demitri Constantinou in July 2015 for assistance in identifying a colleague who would possibly be able to assist with a related undergraduate research project. It was from his suggestion and later introduction to Prof. Sandy van Vuuren that, five years down the line, this research was ultimately possible. So, thank you Demitri. In his own words, he definitely is, "a good matchmaker".

Abstract

Surface contamination and subsequent microbial transmission is a persistent problem in healthcare facilities, contributing to the global pervasion of nosocomial infections and the aggressive prevalence of resistant strains. Touch-contact surfaces, as effective intermediaries for pathogenic transmission, are priority targets for solution development.

Polymer metallisation of ABS, PEEK and PC polymers with antimicrobially active copper, silver and zinc metals, via multi-step and multi-material additive manufacturing, for antimicrobial surface coating production, was investigated. Cold spray and polymer 3D printing technologies were, for the first time, integrated for the application of self-sanitising surface coatings. Theoretical modelling, in conjunction with a targeted particle depth-of-penetration model and adapted Taguchi optimisation method, aided cold spray parameter selection. Successful coatings were achieved using a novel independent parameter effects and variation decision framework and a tailored experimental optimisation procedure. Antimicrobial efficacy was evaluated using two, independent, *in vitro* assays: a diffusion assay and an adapted time-kill assay simulating touch-contact pathogenic exposure. Preliminary prototype trials were also conducted, which included a 3D printed smartphone cover.

Enhanced antimicrobial efficacy under both wet and dry contact conditions was observed. In a touch-contact environment, cold spray coatings were found to be five times more biocidal than their respective base metals. A 50% w/w copper-zinc coating on a 3D printed ABS substrate exhibited synergistic bacteriostatic activity: found to be 43% more effective than the combined average activity of copper and zinc coatings against *Staphylococcus aureus*, *Pseudomonas aeruginosa* and *Klebsiella pneumoniae*. Additional test pathogens included *Enterococcus faecalis* and *Candida albicans*. A combination of factors is believed to be responsible for this activity, including the known mechanisms of action of oligodynamic metals, enhanced diffusion of ions and surface topography supporting direct microbial contact, made possible by the novel coating process employed. Antimicrobial activity was not significantly impaired by resistant pathogens: gentamicin-methicillin-resistant *S. aureus*, azlocillin-carbenicillin-resistant *P. aeruginosa* and a fluconazole-resistant *C. albicans*. Against these resistant pathogens - under dry, touch-contact conditions - the cold spray coatings achieved complete microbial elimination within 12 min for a copper coating on 3D printed ABS and within 5 min for a copper coating with a 5 wt% silver additive on a copper metal substrate. In response to the global need for alternative solutions to infection control and prevention, these effective antimicrobial surface coatings are proposed.

Research Outputs

"As we acquire knowledge, things do not become more comprehensible, but more mysterious."

Albert Schweitzer, Theologian

The following section records the various research outputs related to this current work, including: journal papers submitted, conferences and symposia participated in, presentations given and competitions attended, along with the relevant awards received. Details of a filed and published international patent application are also included.

Journal Papers

Infection Control and Hospital Epidemiology

A research article, submitted to the journal of Infection Control and Hospital Epidemiology, under the title *Laboratory-based study of novel antimicrobial cold spray coatings to combat surface microbial contamination*, has been accepted for publication as of 2nd July 2020. The paper's authors are Michael David Ian Lucas, Ionel Botef*, Robert Reid and Sandy van Vuuren.

*Deceased

Conferences

18th Annual RAPDASA Conference - 2017

A presentation with the title *Integration of Cold Spray and 3D Printing for Antimicrobial Surfaces* was given at the annual Rapid Product Development Association of South Africa (RAPDASA) international conference during November 2017. The conference was hosted by Rapid 3D at the Durban International Conference Centre. The conference theme was: Game Changing Thinking: 3D Printing, Additive Manufacturing, Internet of Things.

Published Extended Abstract

Lucas, M.D.I., Botef*, I., van Vuuren, S., (2017), Integration of Cold Spray and 3D Printing for Antimicrobial Surface Coatings, 18th Annual RAPDASA Conference, Durban, South Africa, 7-10 November.

(RAPDASA 2017 Conference Proceedings - ISBN: 978-0-620-77329-4)
*Deceased

SAIMechE Postgraduate Student Conference - 2017

The South African Institution of Mechanical Engineering (SAIMechE) is the senior body for Mechanical Engineering in South Africa. Their postgraduate student conference was attended on the 17th of November 2017, which covered engineering research into: heat transfer, refrigeration, coatings, welding, solar systems and biomedical applications.

SAIMechE Postgraduate Student Conference - 2018

Participating in the 2018 SAIMechE Postgraduate Student Conference, held at the Resolution Circle Towers, Milpark, Johannesburg, South Africa on the 23rd of November, a presentation was delivered titled: *Cold Spray Metallisation of Polymers for Antimicrobial Applications*. This presentation was voted the Most Interesting Conference Presentation, by those in attendance.

ICPIC conference - 2019

The 5th International Conference on Prevention & Infection Control (ICPIC) was hosted in Geneva, Switzerland from the 10th to the 13th of September 2019. A submitted abstract titled *Polymer metallisation via cold spray and 3D printing for the mitigation of nosocomial infection transmission* was selected to be presented as part of the ICPIC Innovation Academy Pitch, including both an oral and poster presentation. Judged by the expert international jury of the Academy the innovation was selected to present at the Innovation Academy Finals. As the top Innovation Award of Excellence the Prix Hubert Tuor Innovation Award was received for the most innovative approach of tomorrow's infection prevention and control. The abstract was published in the supplement of ARIC (Antimicrobial Resistance & Infection Control) Journal.

Published Abstract
M.D.I. Lucas, I. Botef*, S. van Vuuren, 2019, Polymer Metallisation via Cold Spray and 3D Printing for the Mitigation of Nosocomial Infection Transmission, Abstracts from the 5th International Conference on Prevention & Infection Control (ICPIC 2019), Antimicrobial Resistance & Infection Control, Volume 8, Supplement 1, DOI: 10.1186/s13756-019-0567-6.
*Deceased

Symposia

Faculty of Health Sciences' Research Day and Postgraduate Expo - 2018

A presentation, titled: *Self-Sanitising Surfaces to Combat Nosocomial Infections*, was presented at the University of the Witwatersrand's Health Sciences research day and postgraduate expo on the 6th of September 2018.

9th Cross Faculty Postgraduate Symposium - 2018

Participating in the 9th Annual Cross Faculty Postgraduate Symposium at the University of the Witwatersrand the presentation titled: *Developing Antimicrobial Surface Coatings via Cold Spray and 3D Printing* was awarded Best Oral Presentation in the Faculty of Engineering and the Built Environment, as well as the Best Overall Cross-Faculty Oral Presentation. These were the top two respective awards for both intra- and inter-faculty research at the university.

Presentations

SAIMechE Student Award - 2015

The SAIMechE Student Award for the Best Presentation in the Mechanical Engineering programme at the University of the Witwatersrand was presented for the presentation titled: *Biomaterials via cold spray on 3D-printed polymers*, which was presented at the 2015 Mechanical, Industrial and Aeronautical Engineering Valediction.

SAIMechE Techno Dinner - 2018

The SAIMechE hosted a Techno Dinner on the 29th of August 2018, titled: The Power of Additive Manufacturing. The presentation and dinner was attended, which was presented by Baker Baynes (Technology partners in association with Autodesk computer aided design (CAD) software).

DST-NRF CoE-SM Student Presentation Workshop - 2018

On the 4th of April 2018 a poster was presented at the Student Presentation Workshop as part of the Centre of Excellence in Strong Materials (CoE-SM) set up by the Department of Science and Technology (DST) and National Research Foundation (NRF). The poster was titled: *Antimicrobial Surface Coatings via Cold Spray and 3D Printing Technologies.*

SAIMechE Techno Dinner - 2019

Upon invitation by the South African Institution for Mechanical Engineers (SAIMechE) part of this research was presented at the SAIMechE Techno Dinner on the 17th of April 2019. The presentation was titled: *Handling the Hospital Staph.*

Competitions

International FameLab Competition - NRF - SAASTA - 2019

This research was nominated for the Wits Science Communication Workshop and Wits Heat of the FameLab competition held at the University over the 3rd and 4th of April 2019 which was subsequently attended. As an initiative of the Cheltenham Science Festivals, FameLab is an international science communication competition promoting engagement with science,

technology, engineering, mathematics and innovation. FameLab South Africa was implemented in partnership with the British Council, the South African Agency for Science and Technology Advancement (SAASTA) and Jive Media Africa.

Patents

International Patent Application Filed

Based on the novel and inventive aspects of this research an international patent application has been filed, under the title: *Method of Applying an Antimicrobial Surface Coating to a Substrate*. The inventors are: Michael David Ian Lucas, Ionel Botef and Sandy van Vuuren. The patent applicant is the University of the Witwatersrand, Johannesburg. The International application number is: PCT/IB2018/057488. The International Publication Number is: WO 2019/064216 AI. The filed patent currently holds jurisdiction in the following countries/regions: South Africa (Ref: 2020/01762), United States of America (Ref: 16/652,389), China (Reference pending) and Europe (Reference pending).

Contents

Declaration i

Acknowledgements iii

Abstract v

Research Outputs vi

Contents x

List of Figures xiv

List of Tables xxiii

List of Symbols xxxiii

List of Acronyms xxxiv

1 Introduction 1

1.1 Background and motivation 1

1.2 Research hypotheses 4

1.3 Research objectives 5

1.4 Scope delimitation 6

1.5 Thesis overview 7

2 Literature Survey **9**

2.1 Impact of nosocomial infections 9

2.2 Hospital acquired infections 12

2.3 Antimicrobial surfaces 20

2.4 Polymer metallisation 32

2.5 Conclusion - Literature Survey 76

3 Research Methodology **78**

3.1 Research approach 78

3.2 Theoretical cold spray modelling 79

3.3 Cold spray and 3D printing analysis 93

3.4 Antimicrobial susceptibility testing 107

4 Theoretical Cold Spray Modelling **115**

4.1 Mathematical cold spray algorithm 115

4.2 Targeted particle depth-of-penetration 144

4.3 Taguchi Method 146

4.4 Theoretical cold spray parameter sets 152

5 Cold Spray and 3D Printing Analysis **155**

5.1 The IPEV Decision Framework 155

5.2 Independent cold spray parameter effects 174

5.3 Experimental optimisation 177

5.4 Experimental cold spray parameter sets 181

5.5 Coating characterisation 184

6 Antimicrobial Susceptibility Testing **199**

6.1 Standard pathogens 200

6.2 Resistant pathogens 231

6.3 Prototype testing 240

7 Research Consolidation **248**

7.1 Antimicrobial inferences and mechanisms of action 248

7.2 Surface topography effects on antimicrobial activity 255

7.3 Surface wear and topography correlation analysis 262

7.4 Substrate topography effects on particle penetration 269

7.5 Cold spray polymer metallisation 270

8 Conclusions and Recommendations **281**

8.1 Research conclusions 281

8.2 Future recommendations 286

Glossary **290**

References **294**

Appendices **315**

A Theoretical Cold Spray Model **316**

B Taguchi Optimisation Procedure **371**

C Experimental Cold Spray **373**

D Antimicrobial Susceptibility Test Data **418**

E Coating Combinations **454**

F Research Consolidation **456**

List of Figures

1.1 Proposed investigative steps in the development of an antimicrobial surface coating process, as a means of addressing the problem of surface contamination and pathogenic touch-contact transmission. 4

1.2 Thesis overview and research approach. 7

2.1 Gram stain of Gram-positive *Staphylococcus aureus*, courtesy of the CDC and Dr Richard Facklam [43]. 14

2.2 Gram stain of Gram-negative *Pseudomonas aeruginosa*, courtesy of Dr Kenneth Todar [42]. 15

2.3 Modes of copper's antimicrobial activity against bacterial cells, courtesy of the American Society for Microbiology [66]. 23

2.4 Mechanisms of microbial resistance to metal toxicity, courtesy of Springer Nature [71]. 25

2.5 Surface structure biomimicry: patterned surface structures of shark skin (a) and synthetic micro-patterned surfaces for the prevention of microbial attachment (b), courtesy of Sharklet Technologies, Inc [89]. 29

2.6 Interpretation of current research technologies, processes and consumables (based on the additive manufacturing distribution schematic in Figure 2 of [96]). 35

2.7 Schematic cold spray nozzle with powder feeder and gas pre-heater. 38

2.8 Variation in particle impact velocities (a) and temperatures (b) based on 1D isentropic calculations for different operating temperature and pressure levels in a theoretical copper cold spray system, courtesy of Dr Frank Gaertner [116]. 40

2.9 Cold spray nozzle cross-section for particle impingement angle. 45

2.10 Cold spray window of deposition, illustrated by representative ballistics of large 20 mm copper balls impinging onto a low carbon steel substrate, courtesy of Dr Frank Gaertner [116]. 46

2.11 Theoretical windows of deposition for various cold sprayed materials, assuming a particle size of 25 μm and an impact temperature of 20°C, courtesy of Dr Frank Gaertner [116]. The shaded region represents typically attainable velocities using commercial cold spray equipment. For each material the data bar depicts the viable window of deposition from the minimum, critical (V_{crit}) and maximum, erosive ($V_{erosion}$) particle velocities. 47

2.12 The fused deposition modelling (FDM) process for 3D printing, courtesy of John Wiley and Sons [97]. 49

2.13 Flow regimes through a converging-diverging nozzle, with detailed analysis of nozzle exit over-expanded (G) and under-expanded flow (H) (derived from [147, 148]). 54

2.14 CFD results of temperature (T) and velocity (v) development for both the spray gas (g) and particles ($p15$) along a converging-diverging cold spray nozzle axis, under over-expanded flow conditions, courtesy of Dr Horst Richter, Prof Heinrich Kreye and Springer Nature [127]. 57

2.15 Bow shock formation ahead of a target substrate during cold spraying. 60

2.16 Taguchi Method product array. 70

2.17 Mean and S/N response plot format with a superimposed targeted response line. 72

2.18 Variation of coating thickness (raw data and S/N ratio) with process parameters: (a) feed arrangement, (b) substrate material, (c) air pressure [Psi], (d) air temperature [°C] and (e) nozzle standoff distance [mm], courtesy of Taylor & Francis publishers [122]. 74

2.19 Decision table template for cold spray parameter variation. 76

3.1 Theoretical cold spray system layout for theoretical modelling. 80

3.2 Five key depositional effects for cold spray polymer metallisation based on experimental trials: (b) lack of deposition, (c) lack of depositional consistency, (d) lack of densification, (e) thermal effects and (f) erosive features. Figure (a) represents an ideal cold spray coating of copper onto 3D printed ABS. . . 94

3.3 Scanning electron micrographs of cold spray powders: A - Copper (C5003), B - Zinc (Z5001), C - Silver (327107) and D - a copper-aluminium-alumina blend (C0075). 98

3.4 Cold spray optimisation procedural flow chart. 100

3.5 High-low parameter variation matrix for Level B of the experimental optimisation, where SOD is the nozzle standoff distance, TS is the nozzle traverse speed and PFR is the powder feed rate. 101

3.6 Horizontal and vertical part orientations for FDM polymer 3D printed components. 103

3.7 Diffusion assay procedural flow chart (*1 [185] *2 [186]). 110

3.8 Annotated graphical representation of the dry contact test procedure. 111

3.9 Antimicrobial cold spray coating prototypes with 3D printed substrate designs (a) pen, (b) security access cards, (c) smartphone cover. 112

3.10 Design and manufacturing process for an antimicrobial 3D printed smartphone cover, employing effective polymer metallisation via cold spray. 114

4.1 High order flow chart of the theoretical cold spray model algorithm. 117

4.2 Cold spray theoretical model initialisation steps. 118

4.3 Flow chart of nozzle calculations for the theoretical cold spray model. 120

4.4 Implications of high and low Biot numbers with regards to internal thermal diffusivity of spray particles. 125

4.5 Flow chart of spray gap calculations between the nozzle exit and the target substrate for the theoretical model. 131

4.6 Nozzle exit flow regimes and the consequent free jet characterisation. 132

4.7 Flow geometry through an oblique shock. 133

4.8 Empirical trends between cold spray particle depth-of-penetration and the associated particle and substrate material properties (A = density, B = Young's Modulus and C = ultimate tensile strength). 145

4.9 Taguchi Method Part 1: Effect of controllable factors and S/N ratio analysis: (A) operating pressure, (B) operating temperature, (C) nozzle standoff distance, (D) nozzle traverse speed, with respect to particle depth-of-penetration. 148

4.10 Taguchi Method Part 2: Mean response plots of (A) operating pressure, (B) operating temperature, (C) nozzle standoff distance, (D) nozzle traverse speed, with respect to predicted particle depth of penetration (X) and particle impact velocity (V_{pi}). 151

5.1 Theoretical independent parameter effects for cold spray of copper on copper substrates: A = stagnation pressure, B = stagnation temperature, C = nozzle standoff distance and D = nozzle traverse speed. 156

5.2 Theoretical independent parameter effects for cold spray of copper on ABS polymer substrates: A = stagnation pressure, B = stagnation temperature, C = nozzle standoff distance and D = nozzle traverse speed. 156

5.3 Visual discrimination analysis: independent variation in operating pressure. . 160

5.4 Visual discrimination analysis: independent variation in operating temperature. 161

5.5 Visual discrimination analysis: independent variation in nozzle standoff distance. 162

5.6 Visual discrimination analysis: independent variation in nozzle traverse speed. 163

5.7 Visual discrimination analysis: independent variation in powder feed rate. . . 164

5.8 Independent parameter effects: copper-aluminium-aluminium oxide cold spray onto a solid polymer ABS substrate. 165

5.9 Scatter plot matrix of independent cold spray parameter effects on surface topography (single pass coating). 175

5.10 Scatter plot matrix of independent cold spray parameter effects on surface topography (multi-pass coating). 176

5.11 Micrograph of copper cold sprayed PEEK during Level A of the experimental optimisation procedure, using the theoretically optimum parameter set. . . . 177

5.12 IPEV parameter selections for Level B of the experimental optimisation of copper coated PEEK (truncated selection table). 178

5.13 Micrographs of copper cold sprayed PEEK during Level B of the experimental optimisation procedure, using the theoretically optimum parameter set. . . . 179

5.14 Micrographs and parameter sets of the theoretically and experimentally optimum cold spray copper coatings on a PEEK thermoplastic substrate. 179

5.15 Experimental optimisation process for the unsuccessful experimental optimisation of copper cold spray coating of polycarbonate. 180

5.16 Surface topography analysis of copper coatings on various ABS substrates. . . 192

5.17 Binary micrographs of copper cold spray coating cross-sections with different substrate types: (a) solid ABS, (b) horizontally oriented 3D printed ABS and (c) vertically oriented 3D printed ABS, isolating the coating material. 193

5.18 Development and physical variation investigation of a 50:50 copper-zinc cold spray coated 3D printed ABS pen case, used as such for over a year (January 2018 - March 2019). 195

5.19 Detail view of the coated pen case after a year of active use. 196

5.20 Changes in uncoated 3D printed ABS over a year of use as a keyring. 197

5.21 Changes in copper coated 3D printed ABS over a year of use as a keyring. . . 197

5.22 Changes in uncoated solid ABS over a year of use as a keyring. 197

5.23 Changes in zinc coated ABS over a year of use as a keyring. 197

6.1 Average zones of inhibition for standard coatings against the standard bacterial and fungal pathogens. 203

6.2 Synergistic diffusive activity from copper-zinc blended coatings against the standard pathogens. 204

6.3 Touch-contact antimicrobial efficacy of copper coatings against *S. aureus* (ATCC 25923). 207

6.4 Touch-contact antimicrobial efficacy of copper-aluminium-alumina coatings against *S. aureus* (ATCC 25923). 207

6.5 Touch-contact antimicrobial efficacy of zinc coatings against *S. aureus* (ATCC 25923). 208

6.6 Touch-contact antimicrobial efficacy of copper-zinc blended coatings against *S. aureus* (ATCC 25923). 208

6.7 Touch-contact antimicrobial efficacy of copper coatings against *P.aeruginosa* (ATCC 27853). 209

6.8 Touch-contact antimicrobial efficacy of copper-aluminium-alumina coatings against *P.aeruginosa* (ATCC 27853. 209

6.9 Touch-contact antimicrobial efficacy of zinc coatings against *P.aeruginosa* (ATCC 27853. 210

6.10 Touch-contact antimicrobial efficacy of copper-zinc blended coatings against *P.aeruginosa* (ATCC 27853. 210

6.11 Touch-contact antimicrobial efficacy of copper coatings against *C.albicans* (ATCC 10231). 211

6.12 Touch-contact antimicrobial efficacy of copper-aluminium-alumina coatings against *C.albicans* (ATCC 10231). 211

6.13 Touch-contact antimicrobial efficacy of zinc coatings against *C.albicans* (ATCC 10231). 212

6.14 Touch-contact antimicrobial efficacy of copper-zinc blended coatings against *C.albicans* (ATCC 10231). 212

6.15 Viable CFU/ml per sampling period for a cold spray copper coating on vertically oriented 3D printed ABS against *Staphylococcus aureus*. 217

6.16 Viable CFU/ml per sampling period for a cold spray copper coating on solid ABS against *Pseudomonas aeruginosa*. 217

6.17 Viable CFU/ml per sampling period for a cold spray copper coating on 3D printed ABS against *Candida albicans*. 218

6.18 Average zones of inhibition for special, silver additive, coatings against the standard bacterial and fungal pathogens. 220

6.19 Graphical comparison between diffusive antimicrobial activity from coatings with and without a 5wt% silver additive. 221

6.20 Touch-contact antimicrobial efficacy of cold spray coatings, with a 5 wt% silver additive, against *S. aureus* (ATCC 25923). 225

6.21 Touch-contact antimicrobial efficacy of cold spray coatings, with a 5 wt% silver additive, against *P. aeruginosa* (ATCC 27853). 226

6.22 Touch-contact antimicrobial efficacy of cold spray coatings, with a 5 wt% silver additive, against *C. albicans* (ATCC 10231). 226

6.23 Average microbial inhibition for cold spray coatings against resistant pathogens GMRSA, *P. aeruginosa* and a clinically resistant *C. albicans*. 232

6.24 Touch-contact antimicrobial efficacy of cold spray coatings against Gentamicin-methicillin-resistant *Staphylococcus aureus* (ATCC 33592). 234

6.25 Touch-contact antimicrobial efficacy of cold spray coatings against Reference *Pseudomonas aeruginosa* (DSM 46316). 235

6.26 Touch-contact antimicrobial efficacy of cold spray coatings against Clinically Resistant *Candida albicans* (Ref. No. 4122). 235

6.27 Viable CFU/ml per sampling period for copper coatings against the multi-resistant gentamicin methicillin resistant *S. aureus* (ATCC 33592). 238

6.28 Viable CFU/ml per sampling period for copper coatings against resistant reference *P. aeruginosa* (DSM 46316). 238

6.29 Viable CFU/ml per sampling period for copper coatings against clinically resistant *C. albicans* (4122). 239

6.30 Visual comparison between original test samples and autoclaved samples for solid ABS, copper-aluminium-alumina coated ABS and zinc coated ABS. . . 241

6.31 Copper and zinc coated 3D printed smartphone cover. 244

6.32 Average viable bacterial colony forming units isolated daily from the smartphone and antimicrobial 3D printed cover. 245

6.33 Average viable fungal colony forming units isolated daily from the smartphone and antimicrobial 3D printed cover. 246

7.1 Antimicrobial diffusive activity against surface profile features for copper cold spray coatings. 257

7.2 Antimicrobial diffusive activity against surface profile features for zinc cold spray coatings. 258

7.3 Antimicrobial touch-contact activity against surface profile features for copper cold spray coatings. 259

7.4 Antimicrobial touch-contact activity against surface profile features for zinc cold spray coatings. 259

7.5 Coefficient of friction (μ) trends for copper, zinc and 50:50 copper-zinc cold spray coatings on solid ABS and 3D printed ABS (hor.) substrates. 263

7.6 Wear coefficient (k) trends for copper, zinc and 50:50 copper-zinc cold spray coatings on solid ABS and 3D printed ABS (hor.) substrates. 263

7.7 Coefficient of friction (μ) trends for various polymer substrates with copper and zinc cold spray coatings. 264

7.8 Wear coefficient (k) trends for various polymer substrates with copper and zinc cold spray coatings. 264

7.9 Correlations between surface topographical features of copper coatings on various ABS substrates against friction (μ) and wear (k) coefficients. 265

7.10 Surface topographical effects on wear properties. 267

7.11 Graphical illustration of skewness of profile (Rsk) surface topography parameter. 268

7.12 Substrate surface topographical effects on particle depth-of-penetration for different copper and zinc coated polymer substrate combinations. 269

7.13 Comparison between both the targeted and theoretically predicted depths-of-penetration and the experimental depths-of-penetration for a range of cold spray polymer metallised coatings, using the originally developed theoretical model and target penetration equation. 272

7.14 Comparison between both the targeted and predicted depths-of-penetration and the experimental depths-of-penetration for a range of cold spray polymer metallised coatings, using the re-derived theoretical model and penetration equation as well as the experimentally optimum parameter sets. 276

A.1 Impinging cold spray jet regions 330

A.2 Theoretical independent parameter effects on particle depth-of-penetration, using the developed theoretical model and a copper cold spray on a copper substrate scenario. 367

A.3 Theoretical independent parameter effects on particle depth-of-penetration, using the developed theoretical model and a copper cold spray on an ABS polymer substrate scenario. 368

C.1 Screening wear test parameter variations of friction and wear. 416

D.1 Zone-of-inhibition measurement method. 432

F.1 Trends between cold spray particle depth-of-penetration and the associated system property of (A) surface roughness and the particle and substrate material properties of (B) Young's Modulus and (C) ultimate tensile strength. . 460

F.2 Piecewise graph of powder-substrate density ratio vs target scaling factor for optimum particle depth of penetration of cold spray polymer metallisation. . 461

List of Tables

2.1 An L9 orthogonal array for the Taguchi Method's fractional factorial optimisation approach. 71

3.1 Adapted Taguchi Method for cold spray parameter selection. 87

3.2 Taguchi Method part 1: Product orthogonal array (L_9 & L_4). 90

3.3 Taguchi Method part 2: L9 orthogonal array. 90

3.4 Selected cold spray powders and powder blends with respective properties and research usage designations. 97

4.1 Method scores for the selection of a theoretical particle depth-of-penetration model, based on the predictive accuracy, resistance to system noise and strategic measures of central tendency. 144

4.2 Source data for targeted particle depth-of-penetration model development. . . 145

4.3 Taguchi analysis Part 1: Product array - copper cold spray onto an ABS substrate. 147

4.4 Taguchi analysis Part 1: Separation of signal and control factors. 147

4.5 Taguchi analysis Part 2: Orthogonal array - copper cold spray onto an ABS substrate. 149

4.6 Theoretical cold spray parameter sets - Copper coatings. 152

4.7 Theoretical cold spray parameter sets - Zinc coatings. 153

4.8 Theoretical cold spray parameter sets - Nickel coatings. 153

4.9 Theoretical cold spray parameter sets - Tin coatings. 154

4.10 Theoretical cold spray parameter sets - Aluminium coatings. 154

5.1 The cold spray parameter selection and variation decision table. 173

5.2 Experimentally optimum cold spray parameter sets. 182

5.3 Cold spray coating naming convention for theoretical, experimental and antimicrobial susceptibility tests. 183

5.4 Coating profile trends based on the effects of substrate surface roughness for copper cold spray coatings on polymer substrates. 194

6.1 Inhibition zones for diffusion assay of cold spray feedstock powders. 201

6.2 Overall efficacy ranking based on average zone of inhibition from diffusion assays of standard coatings against standard pathogens. 205

6.3 Ranked dry contact antimicrobial test results for standard coatings against the *S. aureus* (ATCC 25923). 214

6.4 Ranked dry contact antimicrobial test for standard coatings against the *P. aeruginosa* (ATCC 27853). 215

6.5 Ranked dry contact antimicrobial test for standard coatings against the *C. albicans* (ATCC10231). 216

6.6 Overall efficacy ranking for standard coatings tested via the dry contact test procedure against the standard pathogens. 219

6.7 Comparison between diffusive antimicrobial activity from coatings with and without a silver additive against Gram-positive bacteria (*S. aureus* and *E. faecalis*). 222

6.8 Comparison between diffusive antimicrobial activity from coatings with and without a silver additive against Gram-negative bacteria (*P.aeruginosa* and *K. pneumoniae*). 223

6.9 Comparison between diffusive antimicrobial activity from coatings with and without a silver additive against all standard test pathogens. 224

6.10 Overall efficacy ranking based on average zone of inhibition from diffusion assays of special, silver additive, coatings against standard pathogens. 225

6.11 Summary results for dry contact antimicrobial test for silver additive coatings against *S. aureus*. 227

6.12 Summary results for dry contact antimicrobial test for silver additive coatings against *P. aeruginosa*. 228

6.13 Summary results for dry contact antimicrobial test for silver additive coatings against *C. albicans*. 228

6.14 Overall efficacy ranking for special coatings tested via the dry contact test procedure against the standard pathogens. 229

6.15 Silver additive effects - cold spray coatings against *S. aureus*. 229

6.16 Silver additive effects - cold spray coatings against *P. aeruginosa*. 230

6.17 Silver additive effects - cold spray coatings against *C. albicans*. 230

6.18 Diffusion assay efficacy ranking per culture and resistant pathogen type. . . . 233

6.19 Efficacy ranking for selected cold spray coatings against resistant pathogenic strains in a diffusive test environment. 233

6.20 Summary results for dry contact antimicrobial test for developed coatings against gentamicin methicillin resistant *S. aureus* (ATCC 33592). 236

6.21 Summary results for dry contact antimicrobial test for developed coatings against resistant reference *P. aeruginosa* (DSM 46316). 236

6.22 Summary results for dry contact antimicrobial test for developed coatings against the clinically resistant *C. albicans* (4122). 237

6.23 Overall efficacy ranking for developed coatings tested via the dry contact test procedure against the resistant pathogens. 240

6.24 Comparison between alcohol dip and autoclave sterilisation effects on diffusive antimicrobial activity. 242

6.25 Comparison between alcohol dip and autoclave sterilisation effects on touch-contact antimicrobial activity. 243

6.26 Microbial contamination of cold spray coated and uncoated security access cards after seven days exposure to various high-contact and high-risk surfaces and environments. 244

7.1 Comparison between copper and zinc coatings and their metal counterparts with regards to the average rate of microbial reduction (m_{ar}) [$\log_{10}$(CFU/ml)/min]. 250

7.2 Comparison between copper and zinc coatings and their metal counterparts with regards to the percentage reduction in viable CFUs over a 15 min exposure period. 250

7.3 Comparison between diffusive antimicrobial efficacy of coatings against standard and resistant pathogenic strains of *S. aureus* and *P. aeruginosa*. 251

7.4 Comparison between touch-contact antimicrobial efficacy of coatings against standard and resistant pathogenic strains of *S. aureus*, *P. aeruginosa* and *C. albicans*. 252

7.5 Percentage difference in wear properties comparing cold spray coated samples to their corresponding polymer substrates. 266

7.6 Normalised depth of particle penetration (X/D) data for theoretical and experimentally optimum parameter sets together with their theoretically targeted and predicted values for various copper and zinc coatings on polymer substrates. 271

7.7 Normalised particle depth-of-penetration data for theoretical and experimental cold spray of polymer substrates, comparing the predictive accuracy of the modified theoretical cold spray model for experimentally optimum parameter sets. 276

7.8 Theoretical and experimental cold spray parameter set comparisons and results for copper coated 3D printed ABS. 278

7.9 Theoretical and experimental cold spray parameter set comparisons and results for zinc coated 3D printed ABS. 279

7.10 Theoretical cold spray parameter set comparisons and results for tin coated solid ABS. 280

A.1 Cold spray gas properties. 320

A.2 Cold spray feedstock powder properties. 321

A.3 Cold spray substrate properties. 322

A.4 Model function nomenclature for theoretical cold spray model 324

A.6 Historical cold spray trials. 364

A.7 Equivalent theoretical cold spray parameter sets (see Table A.6). 365

A.8 Independent parameter variation on a copper-copper theoretical coating. . . . 366

A.9 Independent parameter variation on a copper-ABS theoretical coating. 366

A.10 Combined average coefficient of variation values for each depth-of-penetration method with respect to each process parameter. 367

A.11 Number of time each particle penetrative model achieved a predicted response closest to the mean predicted penetration from all five penetration models, based on 1000 random cold spray parameter sets. 369

A.12 Number of time each particle penetrative model achieved a median response with respect to all five penetration models, based on 1000 random cold spray parameter sets. 369

A.13 Combined variability analysis table for theoretical particle depth-of-penetration model selection. 370

B.1 Initial parameter levels for all theoretical cold spray powder-substrate combinations. 371

B.2 Initial noise factor levels. 372

C.1 Cold spray run card template. 387

C.2 Experimental parameter effects for high-low parameter variation. 388

C.3 Surface topographical effects from independent cold spray parameter variation (single pass coatings). 389

C.4 Pearson correlation coefficient (R) for surface topographical effects from independent cold spray parameter variation (single pass coatings). 389

C.5 Surface topographical effects from independent cold spray parameter variation (multi-pass coatings). 389

C.6 Pearson correlation coefficient (R) for surface topographical effects from independent cold spray parameter variation (multi-pass coatings). 389

C.7 Cold spray parameter sets for experimental optimisation procedure 391

C.8 Experimental cold spray optimisation: List of all cold spray runs for all levels. 392

C.9 Sampling lengths for measurement of the parameters of periodic roughness profiles and for measurement of the RSm of periodic/non-periodic profile curves [218]. 395

C.10 Roughness sampling lengths for the measurement of Ra, Rq, Rsk and R$\triangle$q of non-periodic profiles [218]. 396

C.11 Roughness sampling lengths for the measurement of Rz, Rv, Rp, Rc and Rt of non-periodic profiles [218]. 396

C.12 Published literature surface wear test parameter sets. 401

C.13 Coating characterisation of theoretically optimum parameter sets - particle size and shape analysis. 402

C.14 Coating characterisation of theoretically optimum parameter sets - particle depth-of-penetration analysis. 403

C.15 Coating characterisation of experimentally optimum parameter sets - particle size and shape analysis. 404

C.16 Coating characterisation of experimentally optimum parameter sets - particle depth-of-penetration analysis. 405

C.17 Arithmetic mean profile deviations (Ra) [μm] for single and multi-pass cold spray coatings and their uncoated substrates made according to ISO 4288 for theoretically optimum cold spray coatings. 406

C.18 Arithmetic mean profile deviations (Ra) [μm] for single and multi-pass cold spray coatings and their uncoated substrates made according to ISO 4288 in two orthogonal sampling orientations for experimentally optimum cold spray coatings. 407

C.19 Maximal profile height (Rz) [μm] measurements for single and multi-pass cold spray coatings and their uncoated substrates made according to ISO 4288 in two orthogonal sampling orientations for experimentally optimum cold spray coatings. 408

C.20 Mean roughness profile spacing (Rsm) [mm] for single and multi-pass cold spray coatings and their uncoated substrates made according to ISO 4288 in two orthogonal sampling orientations for experimentally optimum cold spray coatings. 409

C.21 Mean profile peak spacing (Rs) [mm] for single and multi-pass cold spray coatings and their uncoated substrates made according to the ISO 4288 standard in two orthogonal sampling orientations for experimentally optimum cold spray coatings. 410

C.22 Profile skewness (Rsk) for single and multi-pass cold spray coatings and their uncoated substrates made according to ISO 4288 in two orthogonal sampling orientations for experimentally optimum cold spray coatings. 411

C.23 Pin-on-disc screening wear test results for copper coated solid ABS test samples - Distance variation. 413

C.24 Pin-on-disc screening wear test results for copper coated solid ABS test samples - Load variation. 414

C.25 Pin-on-disc screening wear test results for copper coated solid ABS test samples - Parametric combinations. 415

C.26 Combined surface wear test results for cold spray coatings and associated substrates. 416

C.27 Summary of wear test validation data using copper coated 3D printed ABS and uncoated 3D printed ABS as reference test samples. 417

D.1 Standard cold spray coatings and their controls. 429

D.2 Special cold spray coatings with a 5 wt% silver additive. 430

D.3 Microsoft Excel dry contact test data processing template for a single time period (30 sec). 435

D.4 Average zone of inhibition results from diffusion assays of standard coatings against standard pathogens. 438

D.5 Diffusion assay efficacy ranking per culture and pathogen type - standard coatings. 439

D.6 Dry contact test results of standard coatings against *Staphylococcus aureus* (ATCC 25923). 441

D.7 Dry contact test results of standard coatings against *Pseudomonas aeruginosa* (ATCC 27853). 442

D.8 Dry contact test results of standard coatings against *Candida albicans* (ATCC 10231). 443

D.9 Average zone of inhibition results from diffusion assays of special, silver additive, coatings against standard pathogens. 445

D.10 Efficacy ranking of culture and pathogen type for silver additive diffusion assay. 445

D.11 Dry contact test results of special coatings against *Staphylococcus aureus* (ATCC 25923). 447

D.12 Dry contact test results of special coatings against *Pseudomonas aeruginosa* (ATCC 27853). 447

D.13 Dry contact test results of special coatings against *Candida albicans* (ATCC 10231). 448

D.14 Dry contact test results against Gentamicin-methicillin-resistant *S. aureus* (GMRSA) (ATCC 33592). 450

D.15 Dry contact test results against reference *P. aeruginosa* (RPA)(DSM 46316). 450

D.16 Dry contact test results against clinically resistant *C. albicans* (CRCA) (Ref. No. 4122). 451

D.17 Average zone of inhibition sizes for cold spray coatings undergoing two sterilisation techniques: alcohol dip and autoclave sterilisation. 452

D.18 Autoclave sterilisation effects on touch-contact antimicrobial activity for cold spray coated 3D printed ABS polymers. (CFU/ml). 452

D.19 Quantified viable bacterial and fungal colony forming units over a three week longitudinal study of a copper and zinc coated 3D printed ABS smartphone cover, used in a microbiology laboratory environment. 453

E.1 Cold spray coating naming convention for theoretical, experimental and antimicrobial susceptibility tests. 455

F.1 Surface topography effects of ABS polymer substrates against wear properties for cold spray zinc coatings. 457

F.2 Surface topography effects on wear properties from polished and unpolished copper cold spray coatings on PEEK substrates. 457

F.3 Overall data for surface wear and topographical effects correlation. 457

F.4 Pearson correlation coefficients (R) for surface wear and topographical effects correlation analysis. 458

F.5 Pearson correlation analysis for identifying linear trends between substrate surface topographical effects and particle depth-of-penetration using copper coatings on various ABS polymer substrates as a test case. 458

F.6 Pearson correlation analysis for identifying linear trends between substrate surface topographical effects and particle depth-of-penetration for copper coated polymer substrates. 459

F.7 Pearson correlation analysis for identifying linear trends between substrate surface topographical effects and particle depth-of-penetration for zinc coated polymer substrates. 459

F.8 Depth of penetration, substrate surface roughness and coating-substrate ratios of density, Young's Modulus and ultimate tensile strength for the optimum cold spray coatings. 460

F.9 Cold spray particle and substrate material density ratios and target scaling factors for normalised particle depth-of-penetration for various copper and zinc polymer metallised coatings. 461

List of Symbols

Only the main symbols, Greek letters and important subscripts and superscripts are quoted here. Any additional nomenclature made use of in-text referencing.

Symbols

$\boldsymbol{A}$	Area
$\boldsymbol{B}$	Brinell hardness
$\boldsymbol{C}$	Heat capacity
$\boldsymbol{D}$	Diameter
$\boldsymbol{d}$	Diameter
$\boldsymbol{E}$	Young's Modulus
$\boldsymbol{F}$	Force
$\boldsymbol{H}$	Shape factor
$\boldsymbol{k}$	Wear coefficient
$\boldsymbol{L}$	Characteristic length
$\boldsymbol{M}$	Mach number
$\boldsymbol{m}$	Microbial reduction rate
$\boldsymbol{N}$	Normal load
$\boldsymbol{P}$	Pressure
$\boldsymbol{R}$	Specific gas constant
$\overline{R}$	Universal gas constant
$\boldsymbol{T}$	Temperature
$\boldsymbol{V}$	Velocity
$\boldsymbol{X}$	Depth-of-penetration

Greek Letters

γ	Specific heat ratio
θ	Angle
σ	Temperature dependent flow stress
ρ	Density
χ	Extent of plastic zone
μ_k	Coefficient of friction

Subscripts

$\boldsymbol{0}$	Stagnation or initial state
$\boldsymbol{2}$	State immediately before the bow shock
$\boldsymbol{3}$	State immediately after the bow shock
$\boldsymbol{e}$	State at nozzle exit
$\boldsymbol{g}$	Gas property
$\boldsymbol{i}$	State at cold spray jet impingement
$\boldsymbol{p}$	Particle property
$\boldsymbol{s}$	Substrate property

Superscripts

$\boldsymbol{*}$	State at choked flow conditions i.e. at the nozzle throat

List of Acronyms

ABS	Acrylonitrile Butadiene Styrene
AFM	Atomic Force Microscopy
ASTM	American Society for Testing and Materials
ATCC	American Type Culture Collection
CAD	Computer Aided Design
CDC	Centers for Disease Prevention and Control
CFU	Colony Forming Unit
CI	Confidence Interval
CoE-SM	Centre of Excellence in Strong Materials
CRCA	Clinically Resistant *Candida albicans*
CSIR	Council for Scientific and Industrial Research
CV	Coefficient of Variation
DARPA	Defense Advanced Research Projects Agency
DNA	Deoxyribonucleic Acid
ECDC	European Centers for Disease Control and Prevention
EPA	Environmental Protection Agency
ESKAPE	*Enterococcus faecium*, *Staphylococcus aureus*, *Klebsiella pneumoniae*, *Acinetobacter baumanni*, *Pseudomonas aeruginosa* and *Enterobacter* species
FDM	Fused Deposition Modelling
GMRSA	Gentamicin-methicillin-resistant *Staphylococcus aureus*
HAI	Hospital Acquired Infection
HDPE	High Density Polyethylene
HPCS	High Pressure Cold Spray
ICP-MS	Inductively Coupled Plasma Mass Spectrometer
ICU	Intensive Care Unit
IPEV	Independent Parameter Effects and Variation
ISO	International Organisation for Standardization
JIS	Japanese Industrial Standards

LPCS	Low Pressure Cold Spray
MRSA	Methicillin Resistant *Staphylococcus aureus*
MSSA	Methicillin Sensitive *Staphylococcus aureus*
PC	Polycarbonate
PEEK	Polyetheretherkeytone
PIDAC-IPC	Provincial Infectious Diseases Advisory Committee on Infection Prevention and Control
PLC	Programmable Logic Controller
PFR	Powder Feed Rate
PVC	Polyvinyl Chloride
RAPDASA	Rapid Product Development Association of South Africa
REDOX	Reduction and Oxidation
RH	Relative Humidity
RNA	Ribonucleic Acid
ROS	Reactive Oxygen Species
RPA	Reference *Pseudomonas aeruginosa*
SAIMechE	The South African Institution for Mechanical Engineers
SOD	Standoff Distance
SST	Supersonic Spray Technology
USCDC	United States Centers for Disease Control and Prevention
UTS	Ultimate Tensile Strength
WHO	World Health Organisation

Chapter 1 Introduction

"'Begin at the beginning,' the King said, very gravely, 'and go on till you come to the end: then stop.'"

Lewis Carroll, Alice's Adventures in Wonderland

1.1 Background and motivation

Surface contamination and subsequent microbial transmission within hospitals is a major concern that requires critical assessment, solution development and targeted implementation. This research, based on such an assessment, details the development and validation of a solution for implementation.

Nosocomial infections are a global concern. The persistence of hospital acquired infections (HAIs) and the intensifying rates of antibiotic resistance pose a serious threat to healthcare services; including staff, patients and visitors [1,2]. Surface contamination is a major contributing cause with many infections - including resistant microbial strains - transmissible via contact sites [3,4]. Common hospital surfaces including stainless steel and plastic polymers are known to harbour micro-organisms for extended periods of time. Methicillin-resistant *Staphylococcus aureus* (MRSA), for example, has been reported to survive on such surfaces for over half a year [1]. It is these surfaces that provide an intermediary for infection transmission, via recurrent contact with various surfaces, including: handrails, doorknobs, medical equipment and even portable electronic devices (tablets, smartphones, smartwatches).

Hand hygiene and surface cleaning protocols have been the predominant solution to mitigate infection transmission; however, studies have shown that many hospital surfaces fail to comply with regulated contamination standards; with a range of non-compliance between 50 and 90% [5,6].

There is, therefore, an urgent need to develop innovative means of mitigating the spread of infections, especially within hospitals. Of the four core actions suggested by the Centers for

Disease Control and Prevention (a collaborator with the South African National Department of Health [7]) that aim to fight aggressive resistant infections, the first action involves preventing infections and their transmission [8]. This approach to infection control pre-empts the need for additional antibiotic use and consequently disrupts antimicrobial resistance cycles.

Antimicrobials are agents that kill or significantly inhibit the growth of micro-organisms. The mechanism of action dictates the means by which this activity is achieved. Certain metals possess oligodynamic, biocidal properties; expressed as effective antimicrobial efficacy in small quantities [9]. The term *contact killing* is often used to describe the activity of copper metal, and denotes the rapid and effective antimicrobial activity exhibited by this metal, particularly in a dry environment. Alternatively, the term *self-sanitising* may be used to describe the activity of such metals.

Copper has recorded medical use from as early as 2600 BC for the sterilization of wounds and drinking water [9, 10]. Zinc, while being an essential element in cellular operation, has exhibited antimicrobial tendencies, even at low concentrations [5]. Zinc has also proved a capable anti-fungal agent and an effective growth inhibitor for bacteria [10]. Silver is another metal with known antimicrobial properties [1]. Silver metal has been applied to many environments requiring sterile conditions, including water treatment systems [10] and even in communion chalices in Christian churches.

Surface coating technology was suggested as a means of developing active antimicrobial coatings, using these oligodynamic metals as the primary antimicrobial agents. Various techniques were evaluated based on their suitability for polymer metallisation. Physical vapour deposition and chemical vapour deposition techniques have high equipment and processing costs, as well as work-piece size limitations [11]. Electroplating, as an alternative, encounters limitations and concerns regarding coating adhesion and environmentally harmful waste products [13]. The thermal effects of thermal spray techniques become a concern when coating temperature-sensitive polymers [14], as was proposed for this research.

Cold spray - as a low temperature, versatile coating technique - proved a viable coating technology. The cold spray process utilizes a supersonic, converging-diverging (de Laval type) nozzle to accelerate powder particles which, with careful parameter selection, may be used to create a desired surface coating, even between dissimilar materials.

Plastics are common hospital surfaces, easily contaminated by persistent pathogens, and therefore, the decision to use polymer substrates was based on their frequent use in a large proportion of hospital surfaces as well as the versatile nature of these materials. The use of such materials introduced the potential for functional surface design via additive manufacturing techniques. It was, therefore, proposed that the challenge of polymer metallisation

be considered; applying the principles of additive manufacturing and surface coating design. If successful, design-for-function, as opposed to design-for-manufacture, could be achieved. A shift away from conventional metal-on-metal cold spray to include polymer metallisation sets this research apart. Introducing design versatility and retrofitting capabilities through the use of polymer 3D printing extends the application potential, while introducing tailored surface topographical modifications.

Parameter selection, however, is a problematic area in cold spray research. The inability to know, before cold spraying, the effect such a parameter set will have on coating quality introduces inefficiencies and design uncertainty. Addressing this required the incorporation of theoretical approaches with the aim of reducing uncertainty in parameter selection and improving production efficiency in the cold spray process, especially for coating/substrate combinations of dissimilar materials.

This research, therefore, encompassed the development of a cold spray polymer metallisation protocol, together with essential 3D printing involvement; investigating the relationships between substrate and coating topography and their effects on coating generation and ultimately antimicrobial efficacy. Antimicrobial susceptibility testing investigated the inhibitory and biocidal activity of the developed coating materials, comparing activity in a wet, diffusive environment with that in a dry, touch-contact environment.

1.1.1 Purpose of study

The research set out to disrupt the chain of infection transmission within the hospital environment through the development of antimicrobial surface coatings via cold spray surface coating technology with antimicrobially active metals (copper, zinc and silver) and polymer 3D printing. Figure 1.1 depicts a flow chart of the proposed research steps: from the identified need, to strategies for technology implementation, based on effective, multi-component solution development. In particular the integration of cold spray and 3D printing was investigated and a novel surface coating for healthcare related applications was developed. A theoretical approach to polymer metallisation was suggested as a means of assisting parameter selection, a known area of uncertainty in the cold spray process, making use of mathematical algorithm development, software development and various optimisation strategies. Cold spray powder combinations and surface coating effects were investigated while antimicrobial susceptibility testing characterised the efficacy of the developed coatings against known pathogenic micro-organisms.

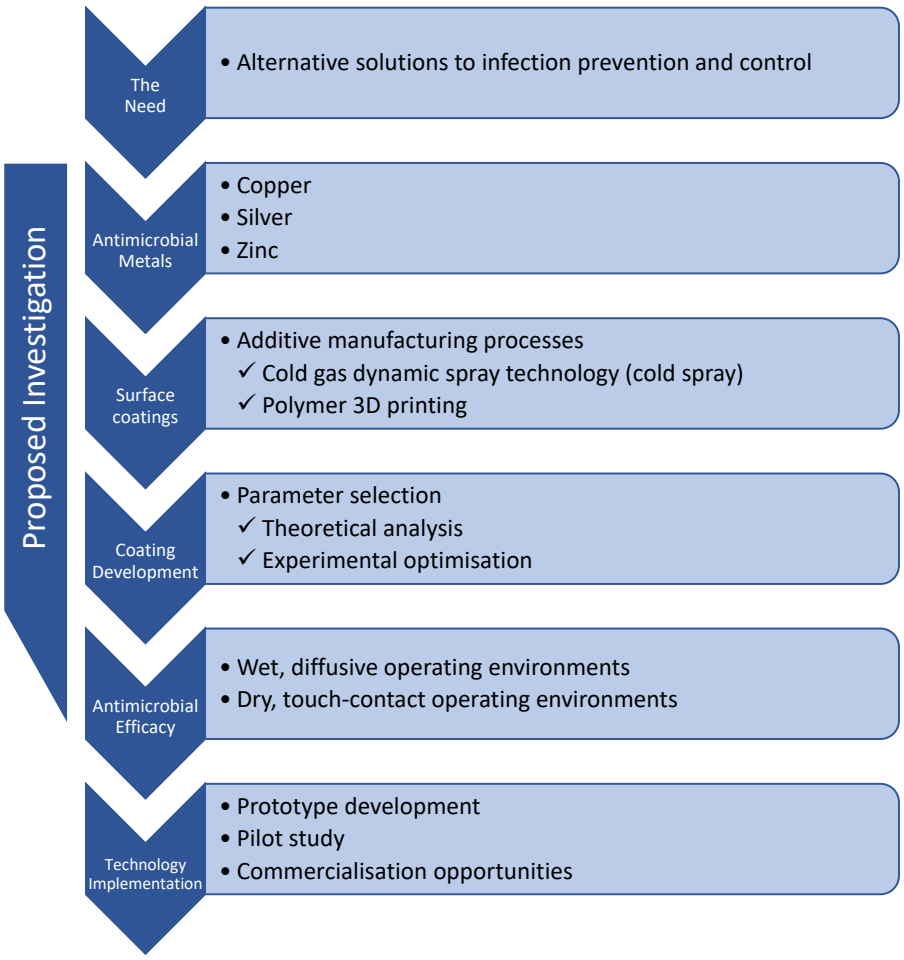


Figure 1.1: Proposed investigative steps in the development of an antimicrobial surface coating process, as a means of addressing the problem of surface contamination and pathogenic touch-contact transmission.

1.2 Research hypotheses

1. Mathematical modelling, using spray particle depth-of-penetration as the key discriminating criterion, is able to accurately predict cold spray parameter set effects.
2. The Taguchi Method is a suitable tool for cold spray parameter set selection.
3. An empirical model, based on the properties of the relevant cold spray powders and target substrate materials, is able to effectively determine a target particle depth-of-penetration for ideal coating quality.
4. Theoretical cold spray modelling is able to suitably represent and make accurate prediction of cold spray coating effects as well as aid rapid selection of process parameters.

5. Polymer metallisation via cold spray is possible, across a range of thermoplastic polymers, including metallisation of 3D printed Acrylonitrile Butadiene Styrene (ABS).

6. Cold spray surface coatings on polymer substrates, using antimicrobially active metals, mitigates nosocomial infection transmission.

7. Antimicrobial efficacy is enhanced by a corresponding increase in surface contact area observed in an increase in arithmetic mean surface roughness.

1.3 Research objectives

1. To develop a mathematical algorithm to calculate spray particle depth-of-penetration for a specified cold spray parameter set, specifically tailored to polymer metallisation.

2. To assess the suitability of the Taguchi Method for theoretical cold spray parameter set selection, based on a targeted response characteristic in the form of particle depth-of-penetration (X).

3. To develop an empirical model for targeted particle depth-of-penetration for suitable cold spray deposition, within the scope of polymer metallisation, based on literature review findings and experimental tests.

4. To develop a comprehensive and modular theoretical cold spray model for polymer metallisation, integrating trial run testing and optimisation methods for targeted parameter selection.

    - To use the particle depth-of-penetration empirical model to define a target response for the optimisation procedure.

5. To isolate ideal cold spray parameter sets[i] for various cold spray powder-substrate (metal-thermoplastic) combinations, including polymer 3D printed ABS substrates, for the implicit application of touch-contact antimicrobial surfaces.

    - To develop an independent parameter effects and variation decision framework for polymer metallisation, to be used in experimental cold spray parameter selection, evaluation and optimisation.

6. To investigate and prove the viability of the manufactured cold sprayed coatings as antimicrobial surfaces.

    - To investigate the antimicrobial ability of the developed surface coatings against standard, resistant and multi-resistant microbial strains.

[i] Critical and controllable cold spray system parameters include: operating temperature and pressure, nozzle standoff distance, nozzle traverse speed and powder feed rate (PFR) as the key variable parameters.

7. To investigate the mechanical and antimicrobial effects of surface topography and coating composition.

   - To compare and correlate the results of surface profile, wear testing and antimicrobial analysis as a means of defining the key requirements for effective antimicrobial surface coatings, using additive manufacturing techniques as a means of achieving unique surface profiles.

1.4 Scope delimitation

Cold spray process

Cold spray equipment constraints were subject to the custom built low pressure cold spray (LPCS) system from Centerline Supersonic Spray Technology (SST) Cold Spray Systems (The LPCS unit was based on the SST Series P cold spray system [15]), which was used throughout the course of this research. Process parameters were subsequently limited by the operating range of the cold spray unit [16]. Cold spray coating was primarily focused on single pass coatings, whereby a coating or deposition layer is successfully achieved after only a single pass of the cold spray nozzle.

3D Printing

Polymer substrate 3D printing was carried out on a Stratasys uPrint SE 3D printer, using Acrylonitrile Butadiene Styrene (ABS) from Stratasys. This printer uses fused deposition modelling (FDM) as the 3D printing build process, thus limiting substrate generation to this method. Build orientation was the primary design variable, with layer thickness, extrusion speed and other associated variables kept constant.

Antimicrobial susceptibility testing

Test pathogens for the antimicrobial susceptibility tests covered the structural and phylogenetic classification range of micro-organisms. They were selected based on their prevalence as nosocomial infections, including three resistant strains. While those selected pathogens provided a suitable representation of possible pathogenic contamination, they represent only a small fraction of possible contagions.

1.5 Thesis overview

Figure 1.2 depicts a flow chart defining and outlining the research scope. A chapter-by-chapter breakdown provides an overview of the thesis.

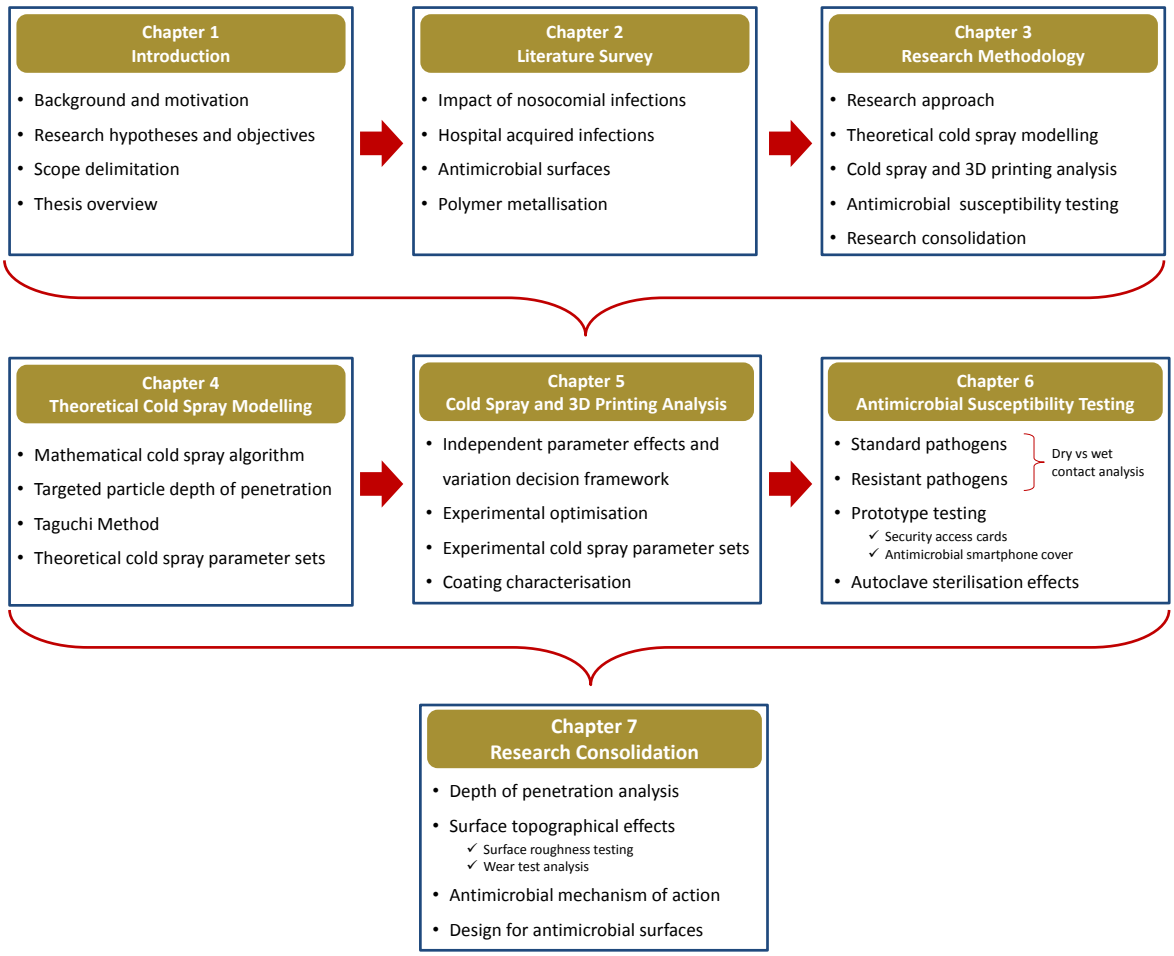


Figure 1.2: Thesis overview and research approach.

Chapter 2 - Literature Survey

This chapter provides a summary of knowledge, history and present status of the research field; including critical reviews of the associated published literature. Each section begins with a background to the major research topics and techniques, followed by an evaluation of previous investigations. A key part of this chapter is the identification of critical knowledge gaps within the current literature. Prior to the commencement of this research an extensive Topic Analysis was carried out, which informed the purpose of study statement and the development of the principle research objectives previously stated. A concurrent gap analysis is, therefore, incorporated into this chapter.

Chapter 3 - Research Methodology

Details of the experimental designs and procedures are presented in this chapter. The three core areas of research were that of: theoretical cold spray modelling, experimental cold spray optimisation and antimicrobial analysis. The research methodology inevitably involved cycles of development and therefore no section stands independent of another.

Chapter 4 - Theoretical Cold Spray Modelling

This chapter documents the development of a theoretical cold spray algorithm, together with a Taguchi optimisation procedure which made use of a targeted particle depth-of-penetration model. The chapter concludes with the theoretically derived cold spray parameter sets for various powder-substrate combinations for polymer metallisation.

Chapter 5 - Cold Spray and 3D Printing Analysis

Drawing on the results of the previous chapter, Chapter 5 details the experimental cold spray of selected powder-substrate combinations. The independent parameter effects of the cold spray process parameters are evaluated and consolidated into an independent parameter effects and variation decision framework as a decision table, based on published literature as well as theoretical and experimental findings. The experimentally optimum parameter sets are defined and the associated surface coatings characterised.

Chapter 6 - Antimicrobial Susceptibility Testing

Antimicrobial susceptibility testing assessed the extent of antimicrobial activity evident from the developed surface coatings. Two main forms of analysis were employed: that of a diffusive test and that of a dry, touch contact scenario. Samples were tested against both standard and resistant pathogenic strains. Three prototype trials were conducted, simulating the conditions of the intended technology's application.

Chapter 7 - Research Consolidation

As a means of consolidating the various research elements this chapter investigates the relationships between theoretical predictions and experimental observations. Comparisons and correlations are drawn between surface topographical effects and antimicrobial ability. Statements regarding surface design for antimicrobial applications are discussed and a re-evaluation of the suitability of the particle depth-of-penetration criterion and the developed targeted particle depth-of-penetration model was carried out.

Chapter 8 - Conclusions and Recommendations

The key research findings, encompassing all research elements are stated here. A list of further research prospects and areas that may yet yield additional and valuable contribution to knowledge conclude this chapter.

Chapter 2 Literature Survey

"There are known knowns. There are things we know that we know. There are known unknowns. That is to say, there are things that we now know we don't know. But there are also unknown unknowns. There are things we do not know we don't know."

Donald Rumsfeld, 2002, US Secretary of State for Defence

2.1 Impact of nosocomial infections

2.1.1 Prevalence statistics

Surveillance of hospital acquired infections provides a quantified, regional view of the state of nosocomial infections. Such studies are costly and research intensive; with few studies in developing countries, and even fewer with implemented response strategies. The data obtained from successful studies generally includes the quantification of those affected, the subsequent cost to healthcare facilities and patients with regards to extra days in hospital, the financial implications and the resulting mortality statistics. The implications of unbridled nosocomial infections when revealed, provide the necessary motivation for aggressive and alternative approaches to infection prevention and control.

Based on a European Centre for Disease Prevention and Control (ECDC) study between 2011 - 2012, 3.2 million patients presented with at least one HAI in acute care hospitals across Europe and 2.6 million from long term care facilities [1, 4, 17]. For acute care hospitals this works out to 81 089 cases per day (95% CI 64 624 - 105 895) [17]; which equates to 16 million additional hospital days, 37 000 deaths and associated costs reaching €7 billion annually, within European facilities alone [4, 18]. The daily prevalence of nosocomial infections in Europe, based on a pre-BREXIT study, was reported to be 5.7% (95% confidence interval 4.5% - 7.4%) [17].

According to the US Department of Health and Human Services Centre for Disease Prevention (USCDC) in their 2013 study on antibiotic resistance threats in the United States, two million

people are infected with antibiotic-resistant infections in the United States and 23 000 die each year as a result [8]. The USCDC believe these figures to be minimum estimates only. Insufficient surveillance may lead many other studies to underestimate the true burden of HAIs. In a recent paper (2016) the authors refer to previous studies which report that there are between 648 000 and 1.7 million patients affected by HAIs in the United States annually [19]. The cost of antibiotic resistance in the United States was estimated at $20 billion (2008 dollars) in excess costs and $35 billion from productivity loss [8].

According to the World Health Organisation (WHO) the prevalence of HAIs in high-income countries is 7.6%, while in low to middle-income countries it is 10.1% [18, 21].

South Africa is a developing country; which, when coupled with a lack of standardized nosocomial infection surveillance [22, 23], puts the country at high risk when it comes to the prevalence of hospital acquired infections. From limited data it was, however, estimated that the HAI prevalence in South African hospitals lies between 10% and 20% [23], with one study suggesting that one in seven patients entering a South African hospital are at high risk of contracting a hospital acquired infection [24].

While the prevalence of these infections, taking into account all areas of a hospital, are high, the intensive care units (ICUs) are seen to incur the highest reported cases of HAI infections. In high income, developed countries approximately 30% of patients present with at least one HAI in ICUs [18]. Considering healthcare system limitations in developing countries this percentage rises to 50% of ICU patients acquiring such an infection [22].

The prevalence of HAIs involving urinary tract infections, surgical site infections, blood stream infections and pneumonia in six South African hospitals (four in the public sector and two in the private sector) in 2005 was 9.7% [22]. The results of an HAI surveillance study, which was conducted at the Tygerberg Childrens Hospital in Cape Town, South Africa in 2015, showed that out of 72 Gram-negative incidences, 35 were from *Klebsiella pneumoniae* and six from *Pseudomonas aeruginosa*. Out of 25 Gram-positive incidences, 13 were from *Staphylococcus aureus* of which three were MRSA, and two were from *Enterococcus faecalis*. Out of 18 fungal infections, 10 were derived from *Candida albicans* [25].

The term "ESKAPE" encompasses six such pathogens with growing multi-drug resistance and virulence, namely: *Enterococcus faecium*, *Staphylococcus aureus*, *Klebsiella pneumoniae*, *Acinetobacter baumanni*, *Pseudomonas aeruginosa* and *Enterobacter* species [20, 26]. It is noted that while *Enterococcus faecium* is more prevelent as a nosocomial infection, *Enterococcus faecalis* is considered more virulent [27].

From a patient-centric perspective the burden of hospital acquired infections is realised as a significant health risk. Patients subsequently incur exacerbated medical costs and lengthy hospital stays. A study into the costs attributed to HAIs in hospitalised adults, found that in a sample group of 1 253 high-risk adults, the length of stay increased by 62.7%, with an attributed mortality rate of 6.1% [28].

2.1.2 Social implications

In response to the prevalence statistics presented above and the intimate effects nosocomial infections have on human health; the social implications of hospital acquired infections are considered. In addition to the financial and logistical costs incurred from a rise in reported nosocomial infections, these social costs are also important.

Hospital avoidance is a suggested unintended consequence of the rise in infection awareness from healthcare facilities. Increasing awareness to the issue of hospital acquired infections also increases patient concern, unintentionally instilling a mentality of hospital avoidance. Patients, and prospective patients, are faced with very real concerns when seeking healthcare services, thus exacerbating these effects.

While hospitals offer mitigation strategies for both practitioners and patients, these are often ineffective, or at least flawed. Hand hygiene protocols, for example, are at the forefront of awareness programmes, encouraging the use of sanitiser stations within hospitals. The World Health Organisation, however, reported that compliance with hand hygiene protocols for healthcare providers was sitting at 38.7% as of 2009 [33]. More recently, the Centers for Disease Control and Prevention (CDC) stated that, "On average, healthcare providers clean their hands less than half of the times they should" [29]. A 2019 survey, based on the WHO Hand Hygiene Self-Assessment Framework, which received responses from 198 infection preventionists from 71 countries, reported that only 47% of hospitals perform direct hand hygiene compliance monitoring, with a further 27% restricting surveillance to specific wards only [30].

Looking at healthcare worker hand hygiene practices in more detail an interesting and worrying trend emerges. It has been observed from a number of studies that hand hygiene compliance from healthcare workers increases after direct contact with a patient [31, 32]. A study assessing hand hygiene compliance among healthcare workers in six intensive care units found that, on average, hand hygiene compliance before patient contact was 38.4%, which then increased to a 55.1% compliance directly after patient contact [32]. This same study suggests that this rise in hand hygiene compliance after patient contact is a consequence of an attitude which, at its fundamental level, maintains that hand hygiene practices are primarily

in place to protect healthcare workers and not their patients. This subconscious practice, carried out by healthcare workers, maintains the high levels of patient risk, with regards to contracting a communicable disease.

2.2 Hospital acquired infections

Hospital acquired infections are those infections with a point of transmission linked physically and temporally with a patient's stay in hospital (or another related healthcare facility). Various definitions and requirements for an active infection to be deemed a hospital acquired infection have been used in various studies [4, 17, 34, 35], yet the key element is the hospital/healthcare facility being the root cause or source of the infection. The initial reason for hospital admittance by a patient is therefore something other than the later acquired HAI. The reason for hospital admittance may, however, be indirectly linked to healthcare providers, by way of healthcare associated infections [34], such that the root cause of the patients affliction may be traced to previous healthcare services. The line between a strictly hospital acquired infection and a healthcare associated infection may be blurred, yet the underlying concern is the persistence of these infectious agents and the development of resistant pathogenic strains.

2.2.1 Modes of pathogenic transmission

Infection occurs as a consequence of continuous transmission paths between an infectious source (person, object or environment) and a susceptible host. The transmission path is the link between the source of infection and the receptive host [1]. Exogenous infectious agents are transmitted in three ways: (1) contact spread, (2) droplet spread and (3) airborne spread [24].

Contact spread may be attributed to direct contact paths from skin-to-skin contact, or via indirect means, including contact with contaminated surfaces. Peter Teska, a global infection prevention expert at Diversey Inc., stated at a satellite symposium during the 5th International Conference on Infection Prevention and Control in 2019 that there is a 'bidirectional exchange of microorganisms between hands and the touched object.' Thus transmission paths from contact include the interaction of all those who come into contact with a hospital space.

In addition, the frequency at which high contact surfaces within a patient's room are touched far exceed the number of times hand hygiene takes place. Commenting on the findings from a hospital study, Peter Teska illustrated the frequency at which healthcare workers, patients and visitors contact surfaces within the patient and environmental domains in a hospital.

The results showed that during active patient care surfaces are contacted on average once every 4.2 seconds for healthcare workers alone. Including the actions of patients and visitors, bedrails for example are touched between 16 and 20 times an hour. Knowing that there is only, on average, a 50% compliance with environmental cleaning within hospitals (according to the studies Teska reported on), the risk of infection transmission by way of these contact paths is unreservedly high.

It is known that micro-organisms are able to colonize plastic and stainless steel surfaces commonly found in hospitals and persist for weeks [1], thereby enabling effective acquisition and transmission of the harboured infectious agents.

Droplet and airborne transmission is realised through dissemination via coughing and sneezing. These two transmission modes (droplet and airborne) are differentiated by droplet characteristics, with airborne spread having suspended droplets smaller than 5 μm which expand the potential radius of infection [24]. Droplet and airborne spread may in turn contaminate surfaces, thereby prioritising surface contamination and contact spread mechanisms as the transmission mode of interest.

2.2.2 Common infections

The ECDC's point prevalence survey of healthcare-associated infections conducted between 2011 and 2012 [17] consolidated data from over 230 000 patients in 947 hospitals, ensuring statistically significant results. From this study the micro-organisms most frequently isolated from nosocomial infections were: *Escherichia coli* (15.9%), *Staphylococcus aureus* (12.3%), *Enterococcus* spp. (9.6%), *Pseudomonas aeruginosa* (8.9%), *Klebsiella* spp. (8.7%), Coagulase-negative *staphylococci* (7.5%), *Candida* spp. (6.1%), *Clostridium difficile* (5.4%), *Enterobacter* spp. (4.2%), *Proteus* spp. (3.8%) and *Acinetobacter* spp. (3.6%).

A recent surveillance of ESKAPE pathogens within the four largest, private-sector pathology laboratories in South Africa was undertaken [36]. The study revealed that of the 9029 ESKAPE isolates from all blood cultures submitted to these laboratories during the 2016 year: 11.6% were from *Enterococci* species (*E. faecalis* and *E. faecium*), 16.8% from *S. aureus*, 27.3% from *K. pneumoniae*, 3.4% from *A. baumannii*, 10.1% from *P. aeruginosa* and 30.8% from *E. coli*. A similar number of ESKAPE pathogens were reported from the public sector within the same year.

It was from this pool of infectious micro-organisms that this current study selected its test pathogens. Further evaluation of the distinguishing features and prevalence trends from these pathogens are hereunder detailed, aiding pathogen selection. One such distinguishing feature

is that of the structural make-up of bacteria; specifically the differences between Gram-positive and Gram-negative bacteria. Refer to microbiologyinfo.com [37] for a diagrammatic representation of such structural differences.

Gram-positive bacteria

Figure 2.1 depicts a Gram stain of *Staphylococcus aureus*. Gram-positive bacteria have a thick peptidoglycan cell wall [37, 39], which retains the crystal violet dye in a characterising Gram stain test [38]. Therefore, since these cells have retained the blue/purple colour, *S. aureus* is classified as a Gram-positive bacteria.

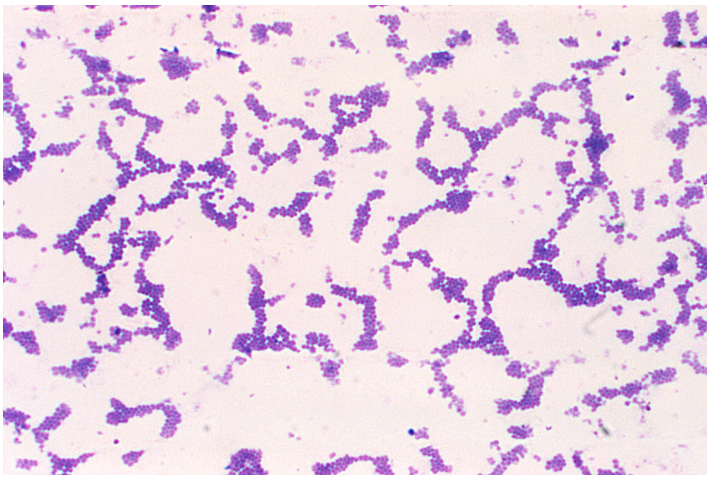


Figure 2.1: Gram stain of Gram-positive *Staphylococcus aureus*, courtesy of the CDC and Dr Richard Facklam [43].

Peptidoglycan is a macromolecule which protects cells and defines their shape [39]. In addition Gram-positive bacteria lack an outer membrane [38], which historically meant they were characterised as less pathogenic than Gram-negative bacteria [39], which do contain an outer membrane. This is not always the case, however, with *Staphylococcus aureus* being a virulent source of infection [38].

Two prevalent Gram-positive pathogens were selected for inclusion in this research, that of *Staphylococcus aureus* and *Enterococcus faecalis*.

Staphylococcus aureus

The CDC state that *Staphylococcus* species are a leading cause of HAIs [8]. *S. aureus* is known to be effective in its role in causing nosocomial bacteraemia, hospital-acquired pneumonia, and surgical site infections [40]. For the year 2011, the CDC reported over 80 000 invasive methicillin-resistant *Staphylococcus aureus* (MRSA) infections in the United States, with over 11 000 consequent deaths [8].

While MRSA infections are reported to be on the decline, with numbers down by 31% between 2005 and 2011, this is still an area of serious concern considering its effects on skin and wound infections as well as causing pneumonia and bloodstream complications [8].

Enterococcus faecalis

The CDC reports that an estimated 66 000 nosocomial *Enterococcus* infections occur in the United States each year, related to bloodstream, surgical site and urinary tract infections [8]. Patients with compromised immune systems are particularly susceptible to *Enterococci* infections [41], making this bacteria particularly harmful in a hospital environment. In addition, surface contact spread is a viable means of infection transmission via high contact surfaces, including telephones, doorknobs, towels and even soap [41].

Vancomycin-resistant *Enterococci* (VRE) infections are a growing concern, with a VRE emergence within South African hospitals reported [47]. VREs are known to cause a number of infections, from urinary tract to deep tissue infections [47]. A haematology/oncology unit at the Red Cross War Memorial Children's Hospital's tertiary paediatric unit in South Africa observed the emergence of VRE infections in 2013 [48]. 14.5% of patients were found to be infected with VRE. These infections were determined to be transmitted via patient-to-patient contact and microbial persistence within the unit, thus measures to mitigate transmission is an ongoing priority.

Gram-negative bacteria

Figure 2.2 depicts a gram stain of *Pseudomonas aeruginosa*, a Gram-negative bacteria. Gram-negative bacteria present with a red colour after Gram staining, due to the leaching of dye from the thin, single layered peptidoglycan layer of the bacterium [38].



Figure 2.2: Gram stain of Gram-negative *Pseudomonas aeruginosa*, courtesy of Dr Kenneth Todar [42].

Gram-negative bacteria, in contrast to Gram-positive bacteria, have a protective outer membrane, which helps to exclude toxic molecules [39]. Gram negative bacteria are observed, however, to have a lower resistance to physical disruption and dry environments [37]. A significant concern for these bacteria is the lack of drugs to combat resistant pathogenic strains [8].

Two prevalent Gram-negative pathogens were selected for inclusion in this research, that of *Pseudomonas aeruginosa* and *Klebsiella pneumoniae*.

Pseudomonas aeruginosa

The CDC report that every year in the United States 51 000 cases of nosocomial *Pseudomonas aeruginosa* infections occur, with 13% being multi-drug resistant infections with around 400 attributable deaths [8, 44]. Thus approximately 8% of all reported nosocomial infections for the United States are caused by this pathogen alone [8]. Related infections include pneumonia, bloodstream infections, urinary tract infections and surgical site infections [8].

P. aeruginosa is an opportunistic pathogen, targeting compromised host environments [42]; making this Gram-negative bacteria particularly effective as a nosocomial infection. Antibiotic resistance is common, due to the impermeability of the outer membrane [42]. Contamination and transmission of this HAI may occur between hosts via contaminated reservoirs (touch-contact surfaces and ingested food) [42, 44], with pathogenic persistance of several months from these reservoirs observed, particularly in a moist environment [45].

Klebsiella pneumoniae

Historically (prior to 1998) *Klebsiella* species were ranked in the top eight most virulent nosocomial infections and were second only to *Escherichia coli* as a nosocomial Gram-negative bacteria, causing an estimated 8% of all nosocomial bacterial infections in the United States and Europe [46]. Its relevance today as a significant nosocomial infection is supported by the 2011 - 2012 study conducted by the ECDC, which reported that *Klebsiella* species are now the fifth most frequently isolated pathogen from HAIs, with a European prevalence of approximately 8.7% [17]. This pathogen is known to cause pneumonia, bloodstream infections, meningitis and wound or surgical site infections [44]. Infection mostly occurs through person-to-person transmission, but environmental contamination and touch-contact transmission is possible [44].

Yeast

Candida albicans

Candida albicans is regarded as an opportunistic fungal pathogen and is reportedly the most prevalent source of fungal infections [49, 50]. Targeting those with a compromised immune system, *C. albicans* is typically regarded as an endogenous infectious agent [49]. This affects

patients who already harbour the pathogen, yet asymptomatically, until the conditions are suitable for auto-infection. Every year, however, an estimated 46 000 nosocomial *Candida* infections occur in the United States alone [8]. The CDC state that *Candida* is the fourth most common cause of healthcare-associated bloodstream infections in the United States and is showing increased resistance to previously effective drugs [8].

Touch-contact transmission of *C. albicans*, as an exogenous means of infection, is not a typical mode of transmission for candidiasis and yet was previously identified and investigated [51,52] and more recently proved via a transmission model [53], albeit at sub-infectious levels. Non-compliance with hand hygiene protocols, however, increases the risk and rate of transmission and subsequent infection. Therefore, *C. albicans*, as the 'model fungal pathogen' [54], provides a good test specimen for the subsequent antimicrobial susceptibility testing.

Microbial surface contamination and subsequent persistence on common hospital surfaces is a major source of infection transmission across Gram-positive and Gram-negative bacteria as well as many fungi [55]. Subsequent touch-contact transmission, therefore, becomes a prominent pathogenic mode of transmission. The following case studies provide further evidence for surface contamination, prolonged survival and pathogenic transmission.

2.2.3 Nosocomial infection: contamination and transmission studies

Hospital surveillance, as previously discussed, is not always conducted and where such studies are conducted there is little to no evidence of a feedback loop to initiate change. A number of studies from the past ten years have, however, provided a glimpse into this global problem. The driving message from these studies is that of the serious nature of contamination and infection transmission from high contact surfaces.

A study investigating the contamination of mobile phones in the healthcare environment was conducted at the medical college in Pune, India over a period of three months [56]. The results showed that 90% of healthcare worker's phones (27 out of 30) and 100% of their hands were contaminated with *Staphylococcus aureus*. The study also investigated the prevalence of resistant strains. They found that 36.7% of hands were contaminated with methicillin-sensitive *Staphylococcus aureus* (MSSA) and 80% of phones had were contaminated with MRSA.

Another study investigated the contamination of access cards from 39 doctors at the Queen Elizabeth Hospital in the United Kingdom [60]. All cards were found to be contaminated with environmental bacteria, with 20.5% contaminated with potentially pathogenic bacteria,

including *S. aureus*. Interestingly the study also found that higher levels of contamination were associated with cards that were used infrequently and stored in wallets or pockets.

Two independent studies, with similar protocols, investigated contamination of elevator buttons. The first included a comparative study within three teaching hospitals in Toronto, Ontario, comparing the contamination of elevator buttons to that of toilet surfaces [3]. The study collected samples from 120 elevator buttons and 96 toilet surfaces. Coagulase-negative *Staphylococci*, frequently associated with nosocomial infections [62], were the most abundant pathogens cultured. A noteworthy observation was a 61% colonisation prevalence for elevator buttons compared with only a 41% prevalence from toilet seats. Depending on the bacterial types found on these surfaces, these results may suggest that elevator buttons observe higher levels of pathogenic contamination than toilet seats. A possible cause stemming from limited or neglected cleaning protocols on these secondary surfaces may be inferred.

The second study supports these observations, where 100% prevalence of Gram-positive and Gram-negative bacteria, including *Staphylococci* and *Enterobacter* species, was recorded from seven elevator button panels in the schools of Isfahan University of Medical Science, in Iran [63]. The identified cultures were primarily non-pathogenic, but as with the previous study conclusive evidence is maintained for contamination of these often overlooked surfaces.

In addition to the aforementioned surfaces, which may be considered 'overlooked' surfaces for infection transmission, computer keyboards, telephone handsets and even stethoscopes may be included. An Italian study investigated the contamination of these frequently handled objects [4]. The study observed a 28.6% MRSA prevalence on stethoscopes, 18.9% on telephone handsets and 22.2% on computer keyboards; in addition to other species of *Staphylococcus*, moulds, *Enterococcus*, *Pseudomonas*, *Acinetobacter* species as well as *E. coli* and *Clostridium difficile*. A noteworthy result was observed when comparing the percentage of contaminated objects and the total colony forming unit (CFU) counts on those objects for each of the three items. Considering only MRSA contaminants, the stethoscopes had an average total of 130 CFUs, the telephone handsets had 23 CFUs and the computer keyboards had 27 CFUs. This suggests that stethoscopes, which come into direct contact with patients, pose a greater threat of pathogenic transmission.

From these studies commonly encountered pathogen strains were from the *Staphylococci* genus. A 14 month study into the transmission of *S. aureus* within a hospital environment was carried out in the ICU and high dependency units of the Royal Sussex County Hospital in Brighton, England [61]. The sample group consisted of 198 healthcare workers, 40 environmental locations and 1 854 patients. Over the course of the study 605 genetically distinct *S. aureus* subtypes were identified. There were 25 instances of transmission to patients, of

which only seven were transmitted directly from healthcare worker-to-patient contact, two were from environmental contaminants and 16 from other patients.

The authors concluded that there was a continuous ingress of distinct pathogen subtypes, rather than healthcare workers being the significant source of infection. What this means for environmental contamination is that hospital environments are continuously exposed to new pathogens, increasing the burden of cleaning and disinfection protocols. The extensive variety and pervasive prevalence of pathogen subtypes justifies the need for broad-based counter measures to mitigate the prevailing nosocomial infections.

2.2.4 Prevention and protection strategies

Many nosocomial infections are able to survive and be transmitted from inanimate, touch-contact surfaces. Environmental contamination accounts for 20 to 40% of all nosocomial infections, with surface cleaning protocols effective less than 50% of the time [6]. The aforementioned nosocomial infections have the ability to persist on these surfaces for extended periods of time. These surfaces include, but are not limited to: surgical equipment, clothing, mobile devices, medical devices (e.g. stethoscopes, thermometers), computers, elevator buttons, doorknobs, hand rails, table tops and other surfaces in and around healthcare facilities [3, 4].

As a reasonable standard for disinfection compliance on non-critical hospital surfaces it was suggested that microbial contamination of surfaces should not exceed five CFU per square centimetre [1]. This deterministic criterion, may find a suitable place in future surveillance protocols and infection control practices.

Based on evidence from a point prevalence survey of healthcare-associated infections and antimicrobial use in Euorpean acute care hospitals (2011 - 2012) [17] at least 20% of nosocomial infections are preventable. This is most likely through targeted approaches against 'device-associated infections' or contact and surgical infection sites. A study conducted through the University of Pensylvania concluded that 46% of nosocomial infections reported in the United States for the year 2002 were preventable and of those resulting in patient death 49% were preventable [64]. The retrospective study collated data from 15 previous studies related to HAI and mitigation intervention strategies.

2.3 Antimicrobial surfaces

Metallic biocidal activity against micro-organisms is a phenomenon known and exploited throughout history. Its use and application within the field of healthcare has fluctuated, with subsequent medical advances. The emergence of resistant strains and the persistence of nosocomial infections, however, has put pressure on the healthcare industry to incorporate novel technologies and techniques to combat the spread of infectious diseases through the reconsideration of historical biocidal agents.

2.3.1 Oligodynamic metals

Copper, silver and zinc metals are known to possess innate antimicrobial properties [5, 65]. Oligodynamic action refers to the ability of small amounts of these metals to exert a lethal effect on microbial cells [9]. The term *contact killing* or *contact mediated killing* is often applied to these metals, particularly copper, due to its effective and efficient antimicrobial activity in a dry, touch-contact environment [66].

Copper is a typical and widely used antimicrobial metal and is suggested to be one of the most promising metals for biomedical applications. Its historical use dates back over 4000 years [10]. Over this time it has been used to treat wounds, skin infections, sterilize drinking water and treat other infections [66]. Copper was used to treat a number of medical conditions including neurological, immunological and metabolic deficiencies before the advent of antibiotics [66]. Studies have confirmed bacteriocidal properties of solid copper and copper alloys against both Gram-positive and Gram-negative bacteria [10].

Silver is often used in the medical and health related industries. From water and air purification, within food preparation processes and many household products, to the healthcare sector where it is used to prevent infection and treat wounds, silver has a broad, yet effective application scope [1, 10]. The range of silver metal application extends beyond bacteria, to include fungi, algae and even viruses [1].

Zinc also possesses antimicrobial properties, even at low concentrations [10]. Zinc differs slightly from that of silver and copper and is reported to be primarily an anti-fungal agent, possessing only bacterial inhibitory properties [1]. The term bacteriostatic is used to describe these properties, which refers to an agent with growth inhibiting properties, mitigating bacterial reproduction without, necessarily, exhibiting lethal biocidal activity [1].

All three of these metals are effective antimicrobial metals, with a study stating that, in the case of silver, the metal is effective at mitigating infection at concentrations 1000 times below

the toxic level to mammalian life [9]. The oxides of copper, silver and zinc are also known to be antimicrobially active, yet possibly with lowered efficacies, prompted by the reduced activity observed by copper oxides [5].

How these metals achieve this antimicrobial activity depends on their independent and, in special cases, synergistic mechanisms of action.

2.3.2 Mechanisms of action

These antimicrobial metals each have specific mechanisms of action and yet our understanding of metal ion toxicity remains incomplete. Working together in conjunction with other metals a multi-faceted mechanism of action arises [10]. This may even result in synergistic antimicrobial activity. It is generally accepted that the generation and diffusion of metal ions plays a fundamental role in the antimicrobial mechanism of action [5,10]; yet direct microbial contact, through surface contact, is additionally an important factor of consideration [70]. A review of the antimicrobial activity of metals suggests the following five key mechanisms of action [71]:

1. **Impaired membrane function**

   • This is achieved either through loss of membrane potential (e.g. silver activity) or physical membrane damage (e.g. copper activity).

2. **Interference with nutrient uptake**

   • This is the prevention of normal cell transport of ions, by essentially taking over or inhibiting those operational sites and mechanisms.

3. **Production of reactive oxygen species**

   • Through the cycling of reduction and oxidation (REDOX) reactions the generation of reactive oxygen species (ROS) is observed. These ROS entities include: oxygen (O_2), superoxide anion ($O_2^{\cdot}-$), peroxide (O_2^{-2}), hydrogen peroxide (H_2O_2), hydroxyl radical ($OH^{\cdot}$) and hydroxyl ion (OH^-) [75]. They are seen to impart damage to biomolecules including DNA, proteins and lipids [76].

   • Copper is believed to catalyse the reactions generating reactive oxygen species. These are described by Fenton-like reactions which demonstrate the copper-catalysed Haber-Weiss reaction [71,76]. These reactions are described by the following equations, where Equation 2.1 represents the net Haber-Weiss reaction, Equation 2.2

and Equation 2.3 represent the catalysed Fenton-like reactions. The cycling of copper between its cupric (Cu^{2+}) and cuprous (Cu^{+}) states generates the reactive oxygen species which target the bacterial cells causing significant damage, leading to cell death [1, 76].

$$H_2O_2 + O_2^{\cdot -} \rightarrow O_2 + OH^- + OH^{\cdot} \tag{2.1}$$

$$Cu^{2+} + O_2^{\cdot -} \rightarrow Cu^{+} + O_2 \tag{2.2}$$

$$Cu^{+} + H_2O_2 \rightarrow Cu^{2+} + O_2 + OH^- + OH^{\cdot} \tag{2.3}$$

4. **Protein dysfunction**

    • The generation of reactive oxygen species may play a part in inactivating proteins. Additionally it is suggested that copper ions may compete with other metals, such as zinc, for important binding sites on proteins, therefore depleting the concentration of such required ions within the cell itself [66].

5. **Genotoxicity**

    • Lethal DNA damage is proposed under certain circumstances, including interference with DNA replication by silver ions and degradation of plasmid and chromosomal DNA via copper-catalysed ROS generation [10].

In a review of antibacterial metallic touch surfaces the formation of metal oxides and their effect on antimicrobial activity was discussed [5]. For copper, a reduced antimicrobial activity was suggested to be associated with the formation of copper oxides; whereas for silver it was suggested that the efficacy observed is in fact a consequence of oxide formation. The review comments on a study that investigated the diffusive antimicrobial activity of silver and silver oxide thin films. The study found that against *Staphylococcus epidermidis* - an opportunistic pathogen - within the context of a disc diffusion assay, the oxide samples observed effective zones of inhibition, indicative of antimicrobial activity; yet no activity was observed for the silver metal.

Zinc oxides have also been reported to exhibit antimicrobial activity, even observing a synergistic relationship with incident light, subsequently enhancing antimicrobial activity [5].

Based on this general evaluation of metal mechanism of action, each metal is seen to work in different ways, with specific strengths and weaknesses.

Copper

A similar process was suggested specifically for copper, where the efficacy of copper, as a biocidal agent, is dependent on the copper ion concentration [5, 10, 77].

The four modes or stages of copper's antimicrobial activity against bacteria are depicted in Figure 2.3 [66]. These antimicrobial events are: (A) cellular damage, (B) cell lysis, (C) generation of reactive oxygen species and (D) DNA degradation. It was further suggested that DNA degradation is a secondary event to cell membrane damage, such that the activity of copper may proceed sequentially through these events, initiated by membrane damage, ionic copper influx, oxidative damage inducing cell death and eventual DNA degradation [66].

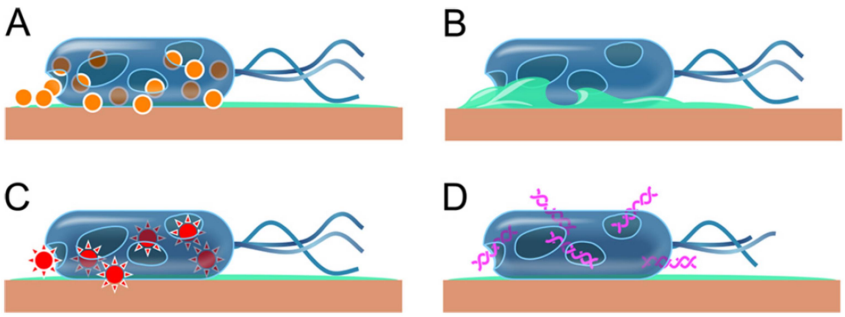


Figure 2.3: Modes of copper's antimicrobial activity against bacterial cells, courtesy of the American Society for Microbiology [66].

In response to the five key antimicrobial mechanisms of action [71] (referring particularly to the production of reactive oxygen species) the production of hydrogen peroxide was suggested to cause severe damage to the cytoplasmic membrane of microbial cells [77, 78]. These destructive hydroxyl radicals are generated via Fenton-like reactions [79, 80].

As discussed previously, in the section on hospital acquired infections, bacterial cell walls are made up of the macromolecule peptidoglycan. Peptidoglycan provides the necessary structure and rigidity for a cell. This macromolecule maintains an overall negative charge, thereby attracting the positively charged copper ions [77]. From this a heightened antimicrobial efficacy may be inferred, yet additionally this provides another claim for the safety of copper in touch contact surfaces for human exposure, due to the fact that peptidoglycan is absent from eukaryotic cells. It was, therefore, postulated that the activity of copper is more pronounced in bacteria than in human eukaryotic cells, thereby making the use of copper as an antimicrobial agent that much safer.

Copper is well suited to dry contact action and is seen to perform better in such environments [66,80]. This response may be related to the oxidation of copper, where Cu_2O is observed to be nearly as effective as pure copper, while CuO - the predominant oxide in a humid environment - is less effective [80]. Studies have shown that in a dry environment the accumulation of

copper ions in bacterial cells is significantly greater than in wet contact environments, leading to increased rates of antimicrobial activity [79].

Silver

The antimicrobial activity of silver metal is suggested to occur via multiple paths, with similar processes to that of the five general mechanisms of action previously stated [1]. As with copper, silver's activity is dependent on the release of ions [1]. Silver is reported to perform better in a wet/humid environment [80]. Interestingly silver is reported to exhibit antimicrobial activity when used in conjunction with copper, in a possible synergistic relationship.

Metal interactions and synergy

It was reported that copper is effective at targeting the bacterial cell wall, thereby allowing silver ions access to the interior of bacterial cells [9]. Silver ions are then able to bind with and damage DNA, RNA, enzymes and proteins within the target bacterial cell. This combination of copper and silver was reported to successfully result in cell death. The interaction of copper and silver in combination has, however, been reported to result in both synergistic and antagonistic behaviour, depending on the opposing bacterial species [65]. Selective use of such combinations is therefore advised.

Microbial metal resistance

Pathogens are hardy and adaptive. This brings with it concerns of metal resistance, which limits the effectiveness of antimicrobial metals. Fortunately this is seen to be limited to specific bacterial types and, in the case of copper, suggested to be highly unlikely [81].

Figure 2.4[i] depicts seven general ways, suggested in a review of the antimicrobial activity of metals [71], in which micro-organisms resist metal toxicity, namely: reduced uptake, efflux, extracellular sequestration, intracellular sequestration, repair, metabolic by-pass and chemical modification.

Considering the potential for copper resistance from micro-organisms it was found that Gram-positive bacteria are more likely than Gram-negative bacteria to develop copper resistance [1]. This resistance relates to varying the permeability of the outer and inner cellular membranes and initiating active copper efflux [66]. These mechanisms of resistance do not, however, prevent elimination by contact killing, but merely afford prolonged survival. In high concentrations the copper ion influx, a key mechanism of antimicrobial action, overpowers resistive measures, such that increased ion concentration increases the rate of antimicrobial activity [66].

[i] Licence agreement for use in PhD thesis provided by the Copyright Clearance Center (Licence No. 4872951234754), on behalf of Springer Nature and the paper's authors.

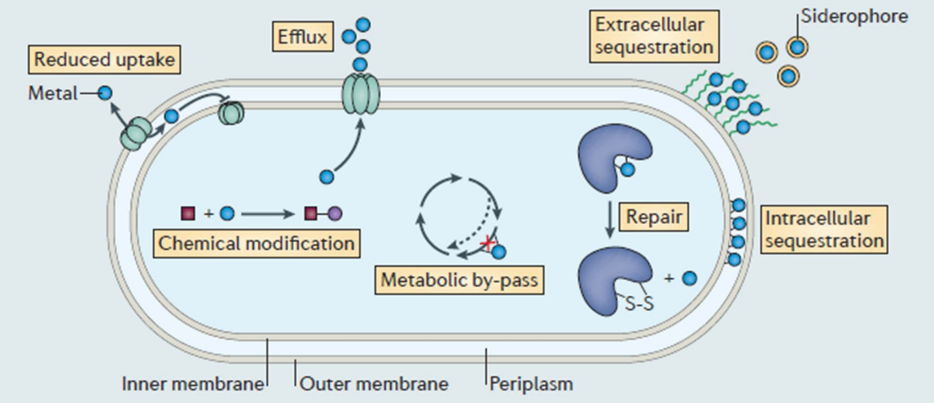


Figure 2.4: Mechanisms of microbial resistance to metal toxicity, courtesy of Springer Nature [71].

In the case of silver, acquired resistance is more likely from Gram-negative bacteria; by means of three processes: reduced cellular influx, increased active efflux and ionic reduction [1]. In this way the bacterial cells attempt to prevent ionic silver from penetrating the cell, while actively expelling and reducing accumulated ions to a less active metallic form.

Microbial resistance to antimicrobial metals relates to a tolerance, such that above a certain level this resistance is mitigated and these metals once again are seen to exhibit antimicrobial properties. Another consideration is the multi-faceted approach many of these metals have with regards to the way they exert their antimicrobial activity. This range of activity includes: 'damage to proteins, DNA and biological membranes, interference in enzyme function and cellular processes, and oxidative stress' [10]. In addition, environmental and operating conditions are important factors of consideration. A study compared the antimicrobial activity of copper surfaces in a wet contact environment against standard *Staphylococci* strains as well as viable strains isolated from copper coins (resistant strains) [1]. They found that some isolates were as sensitive to copper as standard, non-resistant *Staphylococci* strains. Antimicrobial mechanism of action from these metals is, therefore, found to be a complex process, with inter-related factors contributing to the expression of efficacy.

2.3.3 Alternative approaches to surface sterilisation

As the preceding literature illustrates, the metals of copper, silver and zinc all exhibit known antimicrobial properties. There has been a recent rise in the use of alternative approaches to surface sterilisation. Copper, as an effective antimicrobial agent, is often investigated for its antimicrobial properties and sanitising applications.

Before these metals are tested within hospital based pilot studies, extensive laboratory based tests are usually conducted.

A review, by Schettler (2016) [1] discussed the results of a study which investigated the antimicrobial properties of a 14% zinc zeolite material with a 2.5% silver additive [1]. Zeolites are framework structures of 'hydrated aluminosilicate minerals' [84], providing an ideal matrix for embedded metal ions where applications of ion diffusivity are desired. This material was applied as a coating to stainless steel test samples, which were tested via diffusive, wet contact antimicrobial susceptibility test methodologies. Test cultures included *E. coli*, *P. aeruginosa*, *S. aureus* and *Listeria monocytogenes*. From broth cultures, a 5 $\log_{10}$ microbial reduction of *S. aureus*, 3.6 $\log_{10}$ reduction of *E. coli* and a 4-5 $\log_{10}$ reduction for all other test pathogens within six hours was reported. The study did not, however, indicate the specific advantage of the silver additive, nor whether this combination exhibits potential synergistic activity.

Another study, though, investigated the antimicrobial and toxicity effects of combined silver and transition metals [65]. Minimum inhibitory concentration and broth time-kill tests were used to evaluate the antimicrobial efficacy of the metals. A cytotoxicity assay in mammalian cells was similarly conducted. Synergistic activity was observed in the context of this study. The activity of these metals, while effective against *E. coli* and *Bacillus subtilis*, was seen to be below toxic levels for human keratinocyte cells. Keratinocyte cells make up the majority of skin cells and provide a first line of defence against toxins and pathogens [85]. The use of these cells was appropriate, considering touch-contact applications.

This study also investigated the possible mechanisms of action for these metals. It was found that prokaryotic cell permeability was increased, thereby affording increased ion diffusion and cellular uptake; after which intracellular biocidal processes may be initiated.

A dry contact antimicrobial test evaluated the antimicrobial activity of pure copper against copper-sensitive and copper-resistant *Escherichia coli* [76]. Using a sterile cotton swab a 40 μl volume of *Escherichia coli* culture, containing approximately 2.8 x 10^{10} cells, was spread over the surface of a 25 x 25 mm copper test piece[ii]. It was noted that all samples dried within five seconds. The inoculated test samples were then incubated for different times at 23°C. Following this the samples were vortexed mixed in phosphate-buffered saline, diluted, agar plated and incubated for 16 h at 37°C.

The results from this study reveal complete microbial elimination of *E. coli* cells, regardless of the extent of copper resistivity expressed by the micro-organism. Plating stress, which results in a 1 $\log_{10}$ reduction in colony forming units (CFU) for the stainless steel sample, was seen to be a factor of consideration, yet not a reflection of the bacterial elimination exhibited by the copper metal. Dessication stress, due to the dry plating approach, is not the

[ii] By this method the equivalent volume of culture retained by the test samples was determined to be 7% of the total volume, with 4.3% of the initial cells.

underlying mechanism for the observed antimicrobial activity since the stainless steel samples retain CFU levels in excess of 10^7 even after 14 minutes.

What is proved in the laboratory, is validated in the hospital. A ten week trial in a UK hospital involving copper surfaces placed strategically within a ward (toilet seats, tap handles, ward entrance door push plate), observed between 90 and 100% reduction in bacterial colonies, compared to chrome plated plastic and aluminium control surfaces [82]. The test was conducted in a busy acute care medical ward. In order to eliminate bias and ensure accurate real-world conditions, the surfaces were installed six months prior to test commencement.

A review of metallic copper used as antimicrobial surfaces documents a six month study conducted in a walk-in primary healthcare centre in Grabouw, rural Western Cape, South Africa [66, 83]. In this study copper surfaces were installed in strategic locations (trolleys, desks, windowsills) and the bacterial contamination investigated over time. A 71% reduction in bacterial colonies was observed when compared with non-copper (control) surfaces. A similar 32 week study conducted in a Hamburg hospital, in Germany, using brass retrofitted surfaces observed an average 63% reduction in bacterial load [66].

These in-situ, hospital based studies confirm the efficacy of this contact killing metal against a diverse range of hospital based pathogens. Laboratory based trials have, however, tried to enhance this innate activity through various techniques and novel approaches.

A study investigated the use of laser cladding technology for the development of antimicrobial copper-silver alloyed coatings, with a 10 wt% silver additive, on stainless steel substrates [80]. Under wet plating conditions - that is inoculation with a microbial culture (*Escherichia coli*) where the inoculated surface remains in a humid environment preventing evaporation, laser clad coatings were found to outperform pure copper samples, by two orders of magnitude. A pure copper, non-laser clad coating observed a 4 $\log_{10}$ reduction in viable *E. coli* colonies over a three hour period. The copper-silver laser cladded coating, however, observed a 6 $\log_{10}$ reduction over the same time period. According to conclusions drawn by the authors, this observation was suggestive of synergistic activity between the coating constituents. A noteworthy result was that pure silver metal exhibited no antimicrobial activity, as did the stainless steel.

An alternative interpretation, not considered by the paper's authors, involves the influence the coating method had with regards to antimicrobial activity. Surface topographical effects and the expression of the oligodynamic metals induced by the surface coating technique, the enlargement of the effective surface/contact area and increased diffusivity of metallic ions subsequently may, in this study, have lead to a heightened antimicrobial activity. This

would imply that the activity was not due to synergistic activity, but rather due to surface topographical effects. This, however, remains to be confirmed.

Wire arc spraying was used to develop a copper coating on stainless steel [86]. The antimicrobial efficacy of the coatings were assessed via a wet contact test procedure based on the JIS Z 2801:2000 test protocol. 20 ml of 10^5 CFU/ml bacterial suspensions of *E. coli* and *S. aureus* were spread onto 10 x 10 mm samples, under humid environmental conditions. Test samples were transferred to 10 ml of neutralising phosphate-buffer saline solution every hour for six hours. Serial dilutions were made and 100 μl aliquots were spread onto Tryptone Soya agar (TSA) plates and then incubated at 37°C for 24 hrs.

The results showed a 97% reduction in *E. coli* colonies within 6 hrs. *S. aureus* required a longer exposure time to achieve this level of activity. Comparing this result to a stainless steel control, which observed a 60% microbial reduction over 6 hrs, was indicative of significant and effective antimicrobial activity from the copper coatings. Plating stress and environmental conditions may explain the reduction in bacterial load on the stainless steel control samples. Therefore, the additional activity observed by the copper coatings may be attributed to the innate antimicrobial, contact killing activity of the metal.

Based on the ISO 22196:2011 and JIS Z 2801:2010 standards, an adapted time-kill assay was conducted evaluating the antimicrobial activity of copper magnetron sputtered coatings against *S. aureus* [5]. An aliquot of culture was placed on the coating and then sampled at various time periods (every 5 min for 1 hr). Agar plating and incubation was followed by a quantification of the viable colony forming units (CFUs). Zero bacterial CFUs were observed after a 50 min exposure, from an initial bacterial CFU concentration of 4.6 x 10^7.

This study exemplified the antimicobial activity of copper metal and subsequently validates the use of thin film coating technology for the development of antimicrobial surface coatings. The idea is to maximise efficacy, while minimising the quantity of active materials used, inevitably keeping costs down.

Antimicrobial susceptibility testing investigated the efficacy of three copper coated aluminium substrates, using three different coating techniques, namely: plasma spray, wire arc spray and cold spray [87]. Test samples were inoculated with methicillin-resistant *S. aureus* under dry contact test conditions dictated by the US EPA protocol: Test method for efficacy of copper alloy surfaces as a sanitizer. After a two hour exposure period the cold spray coatings were seen to be the most effective method. This activity was related to the hardness of the cold spray coatings, improving the diffusivity of copper ions.

The study therefore demonstrates the advantage gained by the use of cold spray technology for the development of antimicrobial surface coatings. The extent to which the cold spray coatings were more effective than both plasma and wire arc spray suggests that the unique deposition technique plays a significant role.

Alternative approaches to surface sanitisation have also been proposed, from embedded antimicrobials to hydrophobic surfaces which limit microbial adhesion. A few of which have become successful commercialised products.

Palram, a manufacturer of extruded thermoplastic sheets and panel systems, has developed a commercial polyvinyl chloride (PVC) wall cladding with embedded silver ions (PALCLAD Pro HYG) [88]. According to antimicrobial susceptibility tests these materials exhibit effective antimicrobial activity. Against ten common pathogens, including MRSA, the materials observed an average microbial reduction of 96.2% over a 24 hr period. Test conditions were fixed at an exposure temperature of 37°C and greater than 90% humidity.

The commercial Sharklet micro-patterned surface is a material which uses micro-surface features to prevent microbial attachment [89]. In this way the technology maintains 'clean' surfaces. The technology draws its inspiration from nature, imitating the natural surface patterns of shark skin, which have shown to be effective in preventing biofouling by algae. Figure 2.5 depicts the surface structure of shark skin (a) and the similar synthetic, micro-patterned surface manufactured by Sharklet Technologies (b).

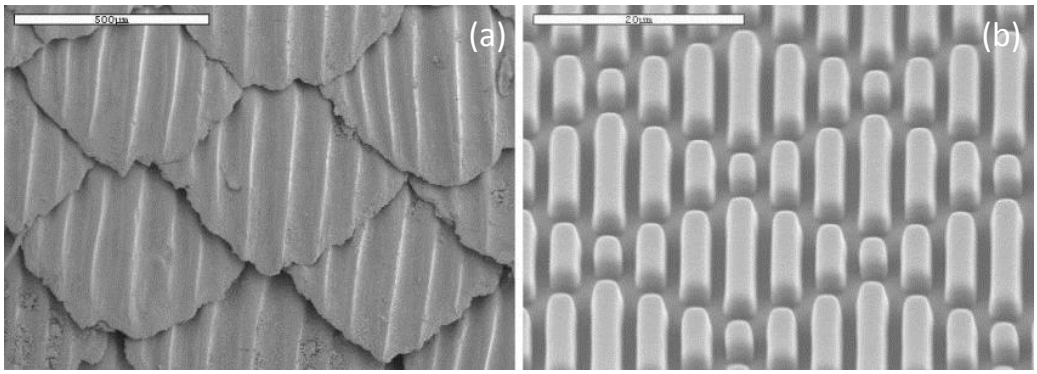


Figure 2.5: Surface structure biomimicry: patterned surface structures of shark skin (a) and synthetic micro-patterned surfaces for the prevention of microbial attachment (b), courtesy of Sharklet Technologies, Inc [89].

A simulated clinical scenario, involving a simulated patient (mannequin) contaminated with *S. aureus* on the lower leg, and hospital equipment covered in the micro-patterned material was investigated [6]. A simulated medical procedure was conducted to replicate an *in-situ* scenario. Thereafter, the control and micro-patterned surfaces were sampled and evaluated

for microbial contamination. There was, on average, five times fewer bacteria attached to the micro-patterned surfaces than the uncoated surfaces.

It was hypothesised that this ability to prevent microbial transmission is most effective from a dry contact context and would be ineffective in a moist/wet contact perspective where a contaminated droplet may persist, unaffected, on such a surface. Thus, while this material may limit adhesion and thereby reduce transmission levels, it does nothing to stop any mico-organisms that are able to reside on the surface from both replicating and being subsequently transmitted.

This is where bacteriostatic and biocidal agents are effective in terminating the transmission path of an infectious pathogen. Further research is required to investigate whether a designed surface structure and combined active biocidal coatings could maximise the anti-microbial effectiveness against such prevalent nosocomial infections. Additive manufacturing may provide the means to achieve such a result.

Biofouling is the accumulation of micro-organisms, plant matter and algae on surfaces in an aquatic environment. It causes a major problem for surfaces in these environments, limiting functional capabilities. A study investigated the use of cold spray technology for the development of antifouling thermoplastic surfaces [91]. Two polymer materials: a hard nylon and a softer high-density polyethylene (HDPE), together with a copper metal control were considered. Dissolution rates and subsequent biofouling efficacy were correlated against particle depth-of-penetration, where the deeper the particle embedment the longer the material performed as a biofouling agent as a consequence of a lowered dissolution rate. The study was conducted over 250 days, with the HDPE copper coated material and the copper metal control exhibiting sustained anti-biofouling activity over that time.

Based on a 2013 study conducted by the Defence Advanced Research Projects Agency (DARPA), which investigated the antimicrobial properties of silver embedded ABS 3D printed surgical devices, a follow-up study was carried out by Stratasys, Ltd. in 2014 [92,93]. In the original DARPA study the materials were reported to achieve only a 60% reduction in bacterial growth, when compared to standard ABS 3D printed parts [93].

The Stratasys team had since developed an antimicrobial coating to test on these materials. Under wet contact test conditions and based on the ASTM E2190 standard testing method for determining antimicrobial activity in polymeric or hydrophobic materials, the antimicrobial efficacy of a water-based coating with 10 wt% silver sulfodiazine[iii] was conducted.

[iii] The coating tested is a commercial product from Surface Solutions Laboratories.

In the Stratasys study triplicate samples were exposed to both *S. aureus* and *E. coli* cultures, independently, for 24 hrs at 36°C in a 78% - 80% relative humidity environment [92]. The results demonstrated significant antimicrobial activity. Against *S. aureus*, without the coating, the silver incorporated 3D printed components achieved only a 57.4% bacterial reduction, yet with the coating, greater than 99.999% reduction was reported. Against *E. coli* the results were even more noteworthy, with less than 10.9% bacterial reduction without the coating and greater than 6 $\log_{10}$ (99.9999%) bacterial reduction over 24 hrs with the coating observed.

The association between antimicrobial surfaces and additive manufacturing is important in looking towards future solutions to meet current infection problems. The versatility in design, from part customisation to retrofitting ability, is a strong motivation for integrated additive manufacturing technology.

2.3.4 Antimicrobial surface requirements

The development of antimicrobial surfaces, as a means of addressing the persistent problem of nosocomial infections, was motivated by the growing awareness with regards to the impact of hospital acquired infections and the need for alternative and implementable solutions.

An important aspect for antimicrobial surfaces should be the aim to supplement and not replace current infection control practices. In this way, such surfaces will offer an additional line of defence against these virulent infections.

There are three primary test standards for the critical evaluation of antimicrobial products, specifically related to antimicrobial surface performance [5]. These are: JIS Z2801:2010[iv], ISO 22196:2011[v] and US EPA:2016[vi]. In addition there is a further ASTM devised protocol: ASTM E2180:2018[vii]. These standards propose certain requirements from antimicrobial surfaces, for example the US EPA:2016 states that, 'An effective product is expected to achieve a 3 $\log_{10}$ reduction in viable bacteria, compared to the stainless steel control, for each microbe (*Staphylococcus aureus* and *Pseudomonas aeruginosa*) within a 1 hr contact period.' Under compliance with this requirement a material is considered a sanitiser.

[iv] JIS Z2801:2010 - Antibacterial products: Test for antibacterial activity and efficacy.

[v] ISO 22196:2011 - Measurement of antibacterial activity on plastics and other non-porous surfaces.

[vi] US EPA:2016 - Protocol for the evaluation of bactericidal activity of hard, non-porous copper containing products.

[vii] ASTM E2180:2018 - Standard test method for determining the activity of incorporated antimicrobial agent(s) in polymeric or hydrophobic materials.

Based on the findings of a 2016 review of antimicrobial metallic touch surfaces within the healthcare environment it was proposed that 'an authentic time course' for antimicrobial susceptibility testing be included in such susceptibility tests [5]. This was prompted by studies estimating the average time between someone touching a surface and that very same surface being touched again within a hospital environment. This critical time is reportedly only five minutes [5]. Therefore the ultimate target for microbial elimination from antimicrobial touch-contact surfaces, based on these studies, is under five minutes from the time of initial contamination.

An understanding of the medically related requirements must be complemented with an understanding of the surfaces themselves, from a generation or manufacturing point of view. An economic consideration was proposed, promoting the consideration of techniques, technologies and processes for the development of effective and sustainable coatings, avoiding profligate use of materials [5].

Surface topography, related specifically to surface roughness, was a further consideration affecting antimicrobial activity of surfaces. Rougher surfaces are seen to promote bacterial adhesion, whereas smooth surfaces prevent such adhesion [5, 94]. However, a rougher surface incurs a greater surface area, thereby potentially increasing the effective area for surfaces to exert antimicrobial action [78].

Antimicrobial wire arc coatings exhibited a microbial reduction of 92% with a surface roughness of approximately 100 μm, while a similar magnetron coating, with a roughness of 1 nm produced a 5 log_{10} microbial reduction (i.e. 99.999% reduction) [5]. Surface topographical effects were therefore investigated with regards to possible correlations between surface and coating roughness, effective surface area, profile properties and antimicrobial activity.

It was suggested that the use of embedded antimicrobials, specifically silver, in polymers could be used as an antimicrobial agent, with sustained efficacy, due to slow ion release [1].

2.4 Polymer metallisation

2.4.1 Additive manufacturing

Additive manufacturing (AM), as an independent design and manufacturing approach, typically involves a layer-by-layer approach to part generation [95, 96] and yet may also include multi-axis manufacturing processes, in-line with the methodologies of rapid manufacturing [97]. Considering conventional layer-by-layer generation, additive manufacturing builds up physical designs based on digital models guiding successive layer generation. This

may be achieved through precise material deposition or via binding agents, with intra- and inter-lamina bonding of both solid and liquid materials.

The characteristic processes of additive manufacturing differ from conventional subtractive or formative manufacturing. The idea to *Think Generatively* is a key shift of mindset, which affords additive manufacturing its place as a separate manufacturing approach [101]. Additive manufacturing is seen to be a 'versatile, flexible and highly customisable' [96] manufacturing process. This customisation and design freedom has been likened to software based services, where design evolution undergoes successive development producing functional upgrades [101].

The field of additive manufacturing is rapidly developing, from its initial introduction in the 1980's [102] to the multi-billion dollar industry it is today [96]. An important step has been taken away from the 3D printing hype that clouds additive manufacturing media to a structured, cost-effective and realisable manufacturing approach [96,101]. Additive manufacturing has previously been associated, and therefore defined, in terms of rapid prototyping, thus limiting its growth [97]. This definition has changed and the process is beginning to be appreciated for its ability to transform the design, manufacturing and assembly industries for the creation of economic end use products. Even early discussions on additive manufacturing observed its unique implications for the design and manufacturing industries [97]. Novel engineering solutions stem from the diverse and expansive range of applicability - by way of design freedom - and the potential for low volume production viability, with a high level of customer input for tailored solutions. Additive manufacturing is ultimately an effective, disruptive technology with significant market value.

From prototyping applications to final part creation, additive manufacturing has the potential to improve design and manufacturing efficiency through reduced equipment, material and tooling costs while actively evolving design mentality from design-for-manufacture to design-for-function [97]. Functional design development is a philosophy aimed at enhancing properties and functionality through every aspect of a design, and is believed to be the fastest growing aspect of additive manufacturing [102]. Additive manufacturing is ultimately an important and integral part of the future of design and manufacture [96].

As the concept of functional design expands, the need for unique guidelines to the design for additive manufacturing becomes more important. According to a presentation on the power of additive manufacturing presented by Baker Baynes[viii] at a Techno Dinner hosted by the South African Institution of Mechanical Engineering (SAIMechE) in August 2018, design for additive manufacturing involves three key elements:

[viii] The Baker Baynes company are technology partners, backed by global technology brands, who assist with efficiency management.

1. Generative design

    • This approach to design involves the iterative optimisation of the actual form of the component. The design takes on a form suited to its function, while minimising superfluous material. Generative manufacturing for additive manufacturing may be considered a 'form-finding process', describing the evolutionary nature of such a design approach [103]. Successive iterations result in an optimal design, based on key performance specifications.

2. Topology optimisation

    • A design optimisation approach minimising material consumption, component weight and reducing associated costs by isolating key structures of a design (e.g. those elements bearing the active component loads) and removing redundant or even unnecessary elements.

3. Latticing

    • Similarly, in the pursuit of weight and cost saving an effective design approach is the incorporation of internal lattice structures. This design approach also imparts strength to developed components, as well as other performance enhancing properties, including thermal properties related to enhanced heat-dissipation.

Design for additive manufacturing is ultimately about tailoring the design's structure to its function. Where conventional manufacturing techniques could achieve such a design they would require high tooling costs with extended manufacturing times; which additive manufacturing avoids [96, 102].

A joint international standard between ISO and ASTM International (ISO/ASTM 52900:2015) defines seven process categories for additive manufacturing [104]. The first two (material extrusion and material jetting) are of particular relevance to this research.

- **Material extrusion**

    ◦ Build and support material are selectively extruded through a nozzle based on the requirements of an individual layer of a design.

    Example - Fused deposition modelling (FDM).

- **Material jetting**

    ◦ Selective deposition of material droplets. (In the context of this research a droplet is extended to include solid material particles, in addition to the conventional liquid particles.)

    Example - Cold spray.

- Binder jetting
    - An additive manufacturing process employing a two part (powder-liquid) application. Selective deposition of a liquid binder onto a powder layer bonds the powder material. This process is repeated for successive layers.
- Directed energy deposition
    - Bonding of melted material via thermal energy (laser, electron beam or plasma arc) during material deposition.
- Powder bed fusion
    - Fusion of powders targeted by thermal energy (laser, electron beam) onto a powder bed. A common example includes selective laser sintering.
- Sheet lamination
    - An additive manufacturing process involving the bonding of layered material sheets [96].
- Vat photopolymerisation
    - Photopolymer component layers are light-cured within a liquid container where a movable build platform exposes a fresh liquid layer to the selective light source upon layer completion.

Based on these categories and the process characterisation [96], an interpretation of the current research technologies, processes and consumables (FDM 3D printing and cold spray) is depicted in Figure 2.6.

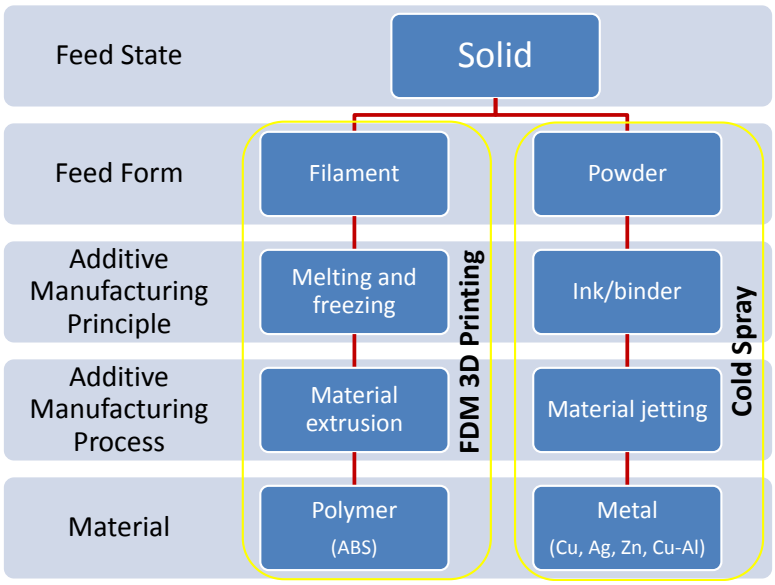


Figure 2.6: Interpretation of current research technologies, processes and consumables (based on the additive manufacturing distribution schematic in Figure 2 of [96]).

While cold spray is not a typical material jetting process, as described by the standard, it is a recognised emerging additive manufacturing technique and is best aligned with the processes of this category. Many studies do not include cold spray as an additive manufacturing technique, yet the inclusion within this field is suitable. There is a growing interest in cold spray as an additive manufacturing technique. A recent publication investigated and summarised the use and application of cold spray additive manufacturing (CSAM) [105]. A 2017 review paper also includes cold spray within the scope of additive manufacturing and suggests cold spray's advanced potential for surface functionalisation [106].

Current and future prospects

According to predictions made in a Delphi study[ix] looking at the future of additive manufacturing, the emergence and use of multi-material additive manufacturing is expected by the year 2030 [101]. Based on structured interviews with experts and systematic analysis, technical developments of additive manufacturing and the corresponding trends were consolidated. Multi-material additive manufacturing refers to the integration of two or more materials during a print job [102]. This may be extended to multi-step processes; which, according to the ISO/ASTM 52900:2015 standard, is defined as the implementation of multiple additive manufacturing operations or processes for component fabrication. The standard extends the definition to suggest that the first process usually defines the basic geometric shape, whereas the following operations are applied to further enhance functional properties.

The findings from this study (R. Jiang, R. Kleer & F.T. Piller, 2017 [101]) point to multi-material manufacture as a key developmental outcome for additive manufacturing. In this way, additive manufacturing is seen to have a unique and influential role in integrated systems and is no longer considered a standalone process [107]. An industry expert, quoted in the Delphi Study, suggested that this development is still only a future prospect for additive manufacturing, possible only within the next twenty years.

It is believed, however, that the technology is in place now for such development and that the material and process combinations presented in this current research are well suited to the application of antimicrobial surface coatings. Under this framework of multi-material and multi-process additive manufacturing, polymer metallisation via FDM 3D printing and metal cold spray technologies (see Figure 2.6), may be aptly integrated for effective functional surface design. An embedded metal coating via cold spray which integrates with the final layer of the 3D printed polymer substrate, effectively makes use of the innate antimicrobial properties of the metal; thereby enhancing functional properties.

[ix] A forecasting methodology involving expert responses to structured questionnaires.

2.4.2 Cold spray surface coating technology

Cold spray, as a surface coating technology, was developed during the 1980's at the institute of Theoretical and Applied Mechanics of the Siberian division of the Russian Academy of Science in Novosibirsk [108]. The technology was then patented in 1994 [109]. The technology is also known by other names, including: cold gas dynamic spray method, kinetic energy metallisation, kinetic spraying, high-velocity powder deposition, supersonic particle deposition, high-velocity consolidation and kinetic spray [123]. While occasionally classified as a sub-set of thermal spray processes [110], its unique features, particularly with regards to the use of high velocity (kinetic energy) rather than high temperature (thermal energy) to generate coatings, suggests that it is better suited to a separate surface coating field of its own [111–113].

The range of applicability of the cold spray system is far reaching. Its capabilities as a repair and restorative process, to its application in precise surface coatings, exemplifies the diverse applications in which cold spray may be found and effectively applied. It may be used as both a surface coating technology - including thin films - and as an additive manufacturing technique - implementing the stratified, layer-by-layer material deposition-development process of 3D printing. Additionally cold spray is able to join chemically dissimilar materials [111]. In this way advanced component manufacture and novel repair processes may be realised. Cold spray is therefore considered and characterised as a specialised deposition technique, offering a high level of process control for the generation of depositionally and energy efficient, surface coatings [114].

The cold spray system works on the principle of a supersonic nozzle; employing high pressure to drive a gas-powder mixture through a converging-diverging nozzle as depicted in Figure 2.7, such that the flow velocity transitions from subsonic flow - prior to the nozzle throat - to supersonic flow thereafter. This supersonic jet of gas and entrained powder particles exits the nozzle, travels the short predefined standoff distance (SOD) and subsequently impinges on the substrate surface. Parameter selection plays a critical role in determining particle impact conditions and subsequently with regards to surface coating creation.

The cold spray process may be divided into two classes: That of low pressure cold spray (LPCS), as used in this research, and high pressure cold spray (HPCS). The operating pressure range for LPCS is usually between 0.5 MPa and 1.0 MPa; which corresponds to a particle velocity range of 300 - 600 m/s [112].

Parameter effects

The cold spray process is controlled and subsequently optimised by the careful selection of various operating parameters. Cold spray parameters may be divided into three groups: (1)

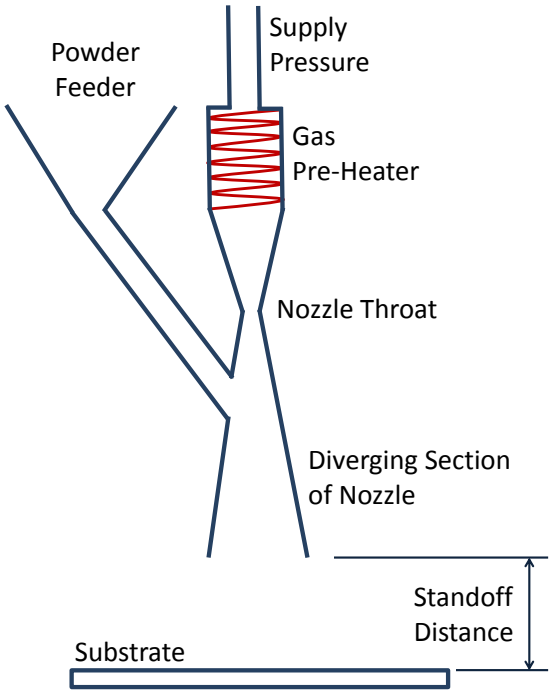


Figure 2.7: Schematic cold spray nozzle with powder feeder and gas pre-heater.

process parameters, (2) spray powder properties and (3) substrate properties [113]. Considering parameter selection and the proposed development of a theoretical predictive cold spray model, this classification becomes important. Coating quality is based on carefully selected parameter levels, which are in turn critically dependent on the understanding of known parameter effects. This categorization was therefore maintained for the parameter effect analysis.

1. **Process parameters**

   Cold spray process parameter sub-classifications include (i) gas conditions, (ii) nozzle design and (iii) spray kinematics.

   (i) Gas conditions

   Operating pressure and temperature, along with the cold spray carrier gas, are the factors controlling the gas condition. Operating pressure and temperature, particularly, have been suggested to be the key influential cold spray process parameters [116].

   Operating pressure - the stagnation pressure from gas dynamic analysis - is the driving force behind nozzle operation. Pressure adjustment not only affects flow velocity, but the type of flow and expected flow phenomena, including the generation of shock waves. Thus, this high priority process parameter needs to be carefully controlled to ensure desired flow fields are set up and maintained.

In general, higher gas pressures correspond to higher gas densities and could therefore lead to associated higher velocities [116, 119]. Higher gas velocities correspond to higher particle velocities, which have been reported to have the following effects on coating properties: increased coating micro-hardness [120], coating densification [121], coating layer thickening [122], increased particle depth of penetration [123] and improved depositional efficiency [120, 124]. The effects of cold spray operating pressure on impact particle velocity and temperature from a 1D gas dynamic analysis, assuming isentropic flow, is dipicted in Figure 2.8 [116].

This trend is not continuous. Increased gas pressure does not continually translate to further coating improvements. A parameter selection window is therefore introduced, which corresponds to a range of parameter values affording acceptable coating qualities. Parameter optimisation strategies aim to narrow this parameter window, isolating the ideal parameter set for a specific coating-substrate combination, within the context of an intended application. This is one of the reasons why parameter control and selection require careful and systematic attention for cold spray coating development.

Operating temperature - the stagnation temperature from gas dynamic analysis - controls gas pre-heating. Control of the pre-heat temperature facilitates bonding due to its influence on particle kinetic energy, via thermal-to-kinetic energy conversion, and provides a degree of thermal softening to both the spray particles and the substrate material [108, 113, 116, 125]. A study by Stoltenhoff, et al. [127] through a CFD analysis of the cold spray system showed that the particle temperature, which is influenced by the set operating temperature, does influence particle impact behaviour and subsequent bonding.

In general, and within the boundaries of acceptable coating quality and the parameter selection window, a higher operating temperature has been reported to produce improved spray quality, with favourable surface coatings. A higher operating temperature is seen to be associated with lower levels of coating porosity and therefore improved coating density [121, 126]. Additionally higher temperatures have been associated with thicker coating build-up [120, 122]. From an efficiency standpoint, however, this parameter is often designed to be minimised [122].

Considering gas dynamics, flow through a choked converging-diverging nozzle has a fixed mass flow rate dependent on the speed of sound, which itself is a function of temperature [116]. Therefore as the operating temperature is increased so does the associated gas and particle velocities and particle impact temperatures (See Figure 2.8 [116]).

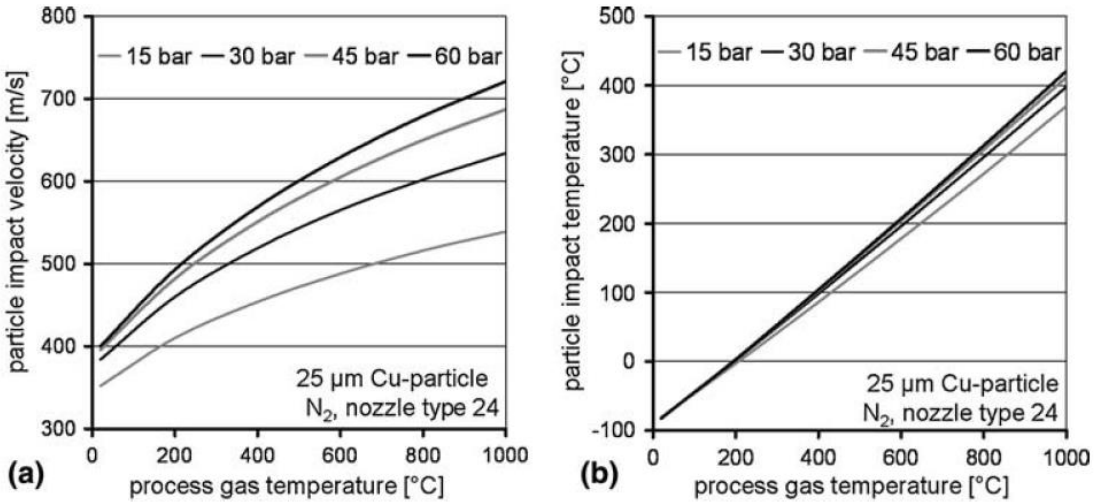


Figure 2.8: Variation in particle impact velocities (a) and temperatures (b) based on 1D isentropic calculations for different operating temperature and pressure levels in a theoretical copper cold spray system, courtesy of Dr Frank Gaertner [116].

Spray gas - the selection of the specific spray gas used has a significant impact on parameter selection and resultant coating quality. The main gas properties affecting spray characteristics are: molecular weight, specific heat, specific heat ratio and viscosity [113]. Equation 2.4 governs the gas velocity at the nozzle exit (V_e), based on a 1D gas dynamic analysis.

$$V_e = M_e \sqrt{\gamma R T_e} \tag{2.4}$$

where M_e is the Mach number at the nozzle exit, γ is the specific heat ratio and T_e is the gas temperature at the nozzle exit.

Considering the use of helium vs air, Equation 2.4 indicates that due to the lower molecular weight and thus larger specific gas constant (R) of helium and since it is a monoatomic gas with a specific heat ratio ($\gamma = 1.6$) greater than that of diatomic air ($\gamma = 1.4$), helium is a more efficient carrier gas than air. Helium, however, is far more expensive, requiring pressurised gas cylinders as opposed to a compressor for the use of air. In the current research the use of air as the carrier gas was sufficient, since lower gas velocities and subsequently lower particle velocities were required.

(ii) Nozzle design

The nozzle length (L), from throat to exit (Figure 2.7), as well as the area ratio, that is the ratio of nozzle exit area (A_e) to throat area (A_t), plays a significant role in the flow dynamics and performance of the cold spray nozzle system.

(iii) Spray kinematics

Besides the operating temperature and pressure, the following process parameters are of high importance when considering spray kinematics: nozzle standoff distance (SOD), nozzle traverse speed (V_n) and the powder feed rate (PFR).

Nozzle standoff distance - is defined as the distance from the nozzle exit plane to the surface of the target substrate (Figure 2.7). This parameter is seen to influence coating quality. A large standoff distance (>50 mm) is reported to limit deposition quality [127], while a small standoff distance (<10 mm) has the potential to induce detrimental thermal effects to the coating and substrate [128]. Detrimental thermal effects are of particular concern for this research considering the use of thermally sensitive, polymer substrates.

At larger standoff distances, an increase in the resulting particle impact velocities has been observed [122]. This relates to the acceleration of particles within the spray gap, even if gas velocity is decreasing, since particle velocities may be lower than gas velocity at nozzle exit. Depending on the materials and intended coating application this may improve coating depositional characteristics.

Additional effects of higher-than-nominal standoff distance include a reduction in coating density [121] and increased run width [129], based on geometrical relationships between the angle of the diverging section of the nozzle, flow trajectory and the nozzle standoff distance (Figure 2.7).

Nozzle traverse speed - is the velocity the cold spray nozzle moves relative to the substrate. Ideally this parameter should be maximised, based on desired production efficiency. However, nozzle traverse speed influences the duration of jet interaction with the substrate, thus affecting coating quality. An extended contact time, associated with a lower traverse speed, results in a greater impingement volume potentially leading to thicker coatings [120], yet risking detrimental thermal and erosive effects, depending on the impinging jet conditions. When working with thermally and mechanically sensitive materials, as in this research, it is imperative that all thermal and erosive effects are considered and suitably mitigated.

Powder feed rate - controls the rate at which powder enters the cold spray nozzle. The Centerline cold spray system used in this research defines powder feed rate as a percentage, representative of the quantity of powder delivered to the spray nozzle system

in a defined interval[x]. Experimental measurements and calibration procedures may, if necessary, be undertaken to determine the corresponding mass flow rate (g/min), for a specific spray task. Additionally, there is an association between nozzle traverse speed and powder feed rate, based on their independent and combined effect on the rate of powder deposition. While both parameters have a direct effect on deposition, their associated effects on coating quality and coating features vary. According to a study investigating the preparation of aluminium coatings on Lexan (polycarbonate thermoplastic) via cold spray, increased powder feed rate was seen to improve coating continuity, coating thickness and coating density [114]. Another consequent effect observed from an increased powder feed rate is that of increased coating adhesion.

Comparing the variation of powder feed rate to that of nozzle traverse speed it was observed that with powder feed rate variation there is low risk of inducing detrimental thermal effects. From an operational perspective, however, an increased powder feed rate increases the risk of clogging the powder feed pipes. If the spray powder has an elevated moisture content the risk of powder agglomeration and subsequent clogging is further elevated.

The current research restricted the variable parameters controlling the cold spray process to the following five parameters: operating pressure, operating temperature, nozzle standoff distance, nozzle traverse speed and the powder feed rate. Parameter selection was to be based on theoretical and experimental approaches dependent on the spray gas, spray powder, substrate and the desired surface coating.

2. **Spray powder properties**
   Observations regarding particle size distribution have indicated that with an increased particle size a commensurate decrease in both particle velocity and the target critical velocity is observed [113]. The critical velocity is a deterministic criterion for deposition and suitable bonding, understood as the average particle velocity necessary for particle deposition and subsequent bonding [113].

   Smaller particles were found to diverge more readily from a cold spray nozzle's axis of symmetry, than larger particles which tend to remain within the core jet region [146]. The effects of particle dispersion relate to diminished particle acceleration [146], as well as possible disperse particle impacts on the substrate.

[x] According to the SST Centerline Series P Portable Spray Machine's user manual the powder feed rate may be varied from 0%, which indicates that there will be no powder through-flow to the nozzle system, through to 100%, which indicates that a maximum amount of feedstock powder will be introduced to the nozzle system.

Particle morphology is a further consideration. Whether spray powder particles are spherical or of irregular morphology their influence on flow characteristics and particle-substrate interactions during jet impingement must be considered. It has been noted that irregular particles tend to align their largest cross sectional area normal to the flow direction, thereby inducing higher drag coefficients [124]. It has also been suggested that irregular particles may improve coating density [113].

3. **Substrate properties**

   The last group of cold spray parameters encompasses the properties of the substrate. This is an area of cold spray research requiring greater attention. Parameter selection, based on critical velocity, for example, typically assumes the feedstock powder and the substrate are the same material, or the effects of such substrate properties are simply neglected. The acknowledgement that this latter approach to parameter selection is a considerable limitation [134], provides motivation for a wider view of material effects for successful cold spray deposition and coating development. An article which set out to provide an overview of cold spray from a materials perspective suggested that further work, with regards to the inclusion of substrate material property effects, was required for the prediction of critical particle velocity [113]. A significant advantage, afforded by the use of cold spray, is coating of dissimilar materials and so this gap in cold spray knowledge was a key aspect addressed in this current research. The interaction between impacting particles and the target substrate, was therefore accounted for, suitably incorporating the substrate properties.

Mechanical properties of the substrate

Surface roughness, defined as small surface asperities and deviations from the nominal surface, is related to both material characteristics and manufacturing processes [111]. A higher surface roughness, in cold spray deposition, has been shown to improve first layer deposition [124, 130]. The manual for the Centerline cold spray equipment, however, proposes a caveat, suggesting that pronounced surface roughness may limit depositional efficiency [115]; while another study found that a grit blasted substrate, with higher surface roughness (Ra = 2.66 μm) compared to a polished (Ra = 0.046 μm) or ground (Ra = 0.21 μm) substrate, led to a lower bond strength for cold spray of coarse titanium powder (min 99% Ti) [124]. Thus a lack of consensus prevails.

The hardness ratio between the impacting spray particles and the target substrate is seen to influence bonding and coating formation. The following behavioural interactions are suggested [126]:

- A *soft-soft* interaction (that is a soft spray particle impacting a soft target substrate) as well as a *hard-hard* interaction may lead to suitable particle penetration

and subsequent bonding; provided suitable cold spray process parameters have been selected.

- A *hard-soft* interaction - as is the arrangement for polymer metallisation - has the potential to result in deep particle penetration and a bonding mechanism associated with embedment, that is mechanical interlock. To achieve a successful deposition under this powder-substrate combination careful parameter selection is required, since this type of interaction involves concerns of substrate deformation and erosion. This issue is discussed further in the next section.
- A *soft-hard* interaction may either lead to a surface abradment, particle deflection or, under carefully controlled parameters, limited surface bonding associated with intense particle flattening.

Thermal properties of the substrate

The gas temperature at the substrate, for a cold spray scenario, was found to be close to the operating temperature due to a temperature rise observed during deceleration of the impinging gas [90]. This temperature rise needs to be taken into account, when considering cold spray of metals onto thermally sensitive polymer substrates. Selection of operating temperature should therefore be influenced by the substrate properties.

Bonding mechanisms

The cold spray process relies on the transfer of kinetic energy and not thermal energy to achieve deposition and subsequent bonding. The bonding mechanism may therefore be comparable to that of explosive cladding or shock wave powder compaction [131]. Thus bonding is associated with the overall particle energy [116]. The bonding mechanism of explosive cladding is dependent on the impacting angle, impact velocity and the interacting material properties [131]. These same properties are important when considering cold spray bonding mechanisms.

With regards to impacting angle there are two factors to consider in cold spray. The first is the nozzle orientation. Any deviation from a perpendicular nozzle orientation to the substrate leads to a reduced depositional efficiency. Centerline, manufacturers of cold spray equipment, suggest a maximum deviation of 10° from the perpendicular, to avoid significant loss of coating quality [115]. The second consideration is the maximum particle impacting angle (θ). Figure 2.9 depicts a cross section of a converging-diverging cold spray nozzle, used to calculated the particle impingement angle.

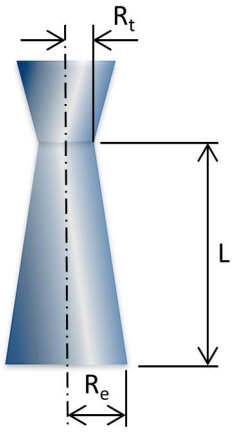


Figure 2.9: Cold spray nozzle cross-section for particle impingement angle.

The particle impingement angle (θ) is defined by the nozzle geometry, with respect to the diverging length (L), the nozzle throat radius (R_t) and the nozzle exit radius (R_e). Equation 2.5 defines this angle, which is suggested to maximise deposition efficiency in the range $\theta > 87°$ [119].

$$\theta = tan^{-1}\left(\frac{L}{R_e - R_t}\right) \tag{2.5}$$

Particle impact velocity, as previously mentioned, is a widely used criterion for cold spray parameter selection [116, 119, 125, 127, 132–136]. Deposition and bonding criteria are often based on the attainment of a particle impact velocity equal to a theoretical critical velocity [108, 113]. As a means of quantifying the critical velocity, as previously defined, one may consider the particle velocity required to achieve a depositional efficiency of 50% [116]. At particle velocities greater than this critical velocity cold spray deposition enters the *window of deposition*, bounded by the critical velocity on the lower end and the erosion velocity at the other extreme. This system and subsequent correlation between particle impact velocity and deposition efficiency is depicted in Figure 2.10.

A window of deposition may be determined for unique coating-substrate combinations, from which an ideal parameter set may be extracted. Such an analysis may be made in the pursuit of deposition optimisation, where the parameters required to achieve a specific coating are to be known. For example, in a study investigating the aspects of particle acceleration, impact and bonding; a theoretical analysis was used to calculate a critical particle velocity, assuming cold spray of like material (that is the same coating and substrate material), a particle size of 25 μm and an impact temperature of 20°C [116]. Thus the critical velocity may, for such investigations, be considered a useful deterministic criterion.

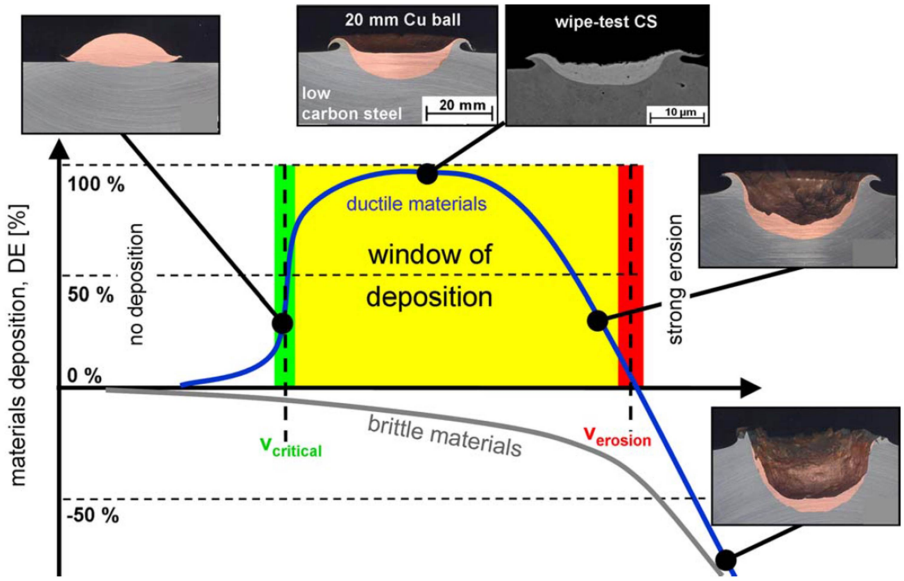


Figure 2.10: Cold spray window of deposition, illustrated by representative ballistics of large 20 mm copper balls impinging onto a low carbon steel substrate, courtesy of Dr Frank Gaertner [116].

The critical velocity, expressed as a function of material properties and temperature, may be given by Equation 2.6 [116]. Where σ is the temperature dependent flow stress given by Equation 2.7, ρ_p is the density of the spray particle, C_p is the heat capacity, T_m is the melting temperature of the material, T is the mean temperature of the particle upon impact and A and B are fitting constants ($A = 4$, $B = 0.25$). From Equation 2.7 T_r is the temperature at which the ultimate tensile strength was determined and σ_{ult} is the ultimate tensile strength.

$$V_{cr} = \sqrt{\frac{A\sigma}{\rho_p} + BC_p(T_m - T)} \tag{2.6}$$

$$\sigma = \sigma_{ult}\left[1 - \frac{T - T_r}{T_m - T_r}\right] \tag{2.7}$$

The windows of deposition for cold spray of like materials are depicted in Figure 2.11 [116]. The shaded grey region contains the typically attainable particle velocities, using conventional cold spray equipment. The upper limit for the particle velocity corresponds to the erosion velocity, which may be defined as the velocity at which impacting particles no longer adhere or bond to the substrate surface but begin to erode the substrate [116]. At this velocity the deposition efficiency approaches zero. It was suggested that the erosion velocity may be as high as three times the critical velocity [116]. This, however, suggests quite a large range of leniency in parameter selection, yet in practice and especially for polymer metallisation this is seen not to be the case. Small parameter variations were found, during preliminary

experimental trials, to incur significant depositional changes which subsequently influence the resultant coating quality.

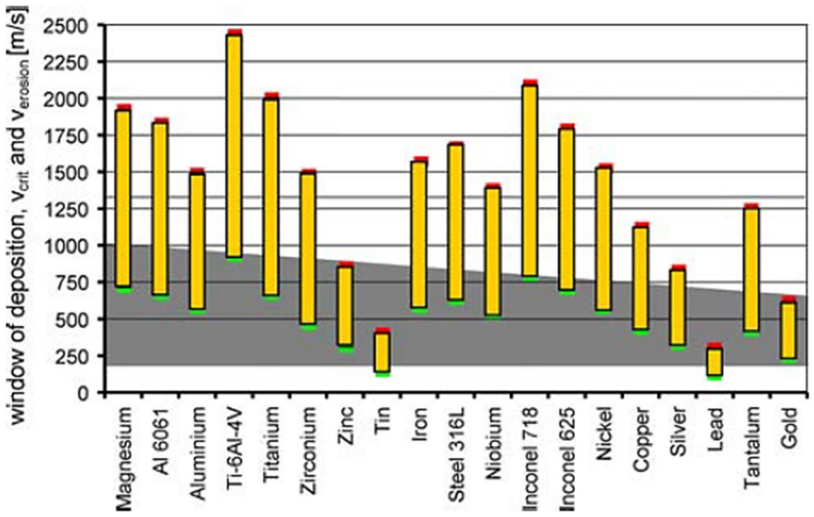


Figure 2.11: Theoretical windows of deposition for various cold sprayed materials, assuming a particle size of 25 μm and an impact temperature of 20°C, courtesy of Dr Frank Gaertner [116]. The shaded region represents typically attainable velocities using commercial cold spray equipment. For each material the data bar depicts the viable window of deposition from the minimum, critical (V_{crit}) and maximum, erosive ($V_{erosion}$) particle velocities.

Critical velocity is therefore an important criterion. Yet its application has previously been limited. Most calculations, including the theoretical analysis discussed herein, neglect the independent substrate properties; thereby limiting the analysis to cold spray of *like* materials. Although substrate effects are often neglected it is known that critical velocity is influenced by the substrate material as well as the spray material [128]. The particle impact velocity is known to be a function of nozzle geometry, operating temperature and pressure, particle and gas materials, particle size as well as the standoff distance from the substrate [145].

In addition to the use of particle impact velocity, alternative deterministic tools should be developed and subsequently used. Particle penetration phenomena is one such area of research which is believed to yield a refined understanding of cold spray bonding criteria, specifically for the case of cold spray polymer metallisation. Foundational research into this hypothesis arose from particle penetration and an observed 'rivet-like shape' for cold spray of copper onto an aluminium substrate at the particle/substrate interface [117]. A subsequent study investigated this mechanical interlocked bonding mechanism with the consideration of particle penetration as a condition for adhesion [118].

In the current research, which deals primarily with cold spray of dissimilar materials, the influence of the substrate and its material properties needs to be considered with regards to parameter selection and coating generation.

Thus, a consideration of interacting material properties needs to be made. From the perspective of traditional cold spray, that being metal-on-metal, adiabatic shear instability is a common feature in the bonding mechanism [126]. Shear loading and thermal softening, during a particle-substrate impact event, causes material to be ejected as an interfacial jet[xi] from the collision zone, landing on the surrounding surface and forming a metallurgical bond [112, 113, 123, 131].

Impact of spray particles onto a softer, less dense substrate precludes adiabatic shear instability from occurring, yet material jetting may occur from the substrate, thereby facilitating bonding [113]. Particle embedment was believed to be the cause of the suppressed adiabatic shear instability, since the impacting particle dissipates energy over an extended period of time and space (substrate contact surface area) during its deceleration and embedment. Particle embedment does, however, set the conditions for bonding via mechanical interlock.

Mechanical interlock explains bonding in terms of an interlocked particle in a substrate matrix due to overlapping material ejecta and embedded particles [137]. A study investigated the embedment of copper particles into polymers via the cold spray process [1]. In this analysis particle embedment was associated with mechanical interlocked bonding. Impinging spray particles were observed to deform the substrate, leading to embedment and subsequent adhesion. Particle depth-of-penetration was defined as the vertical distance from the substrate surface to the deepest point of embedment. The study achieved average embedment depths of up to 60 μm $\pm$ 2 μm into high density polyethylene. Physical bonding via van der Waals forces was suggested to be associated with mechanical interlocking [138].

It is this bonding mechanism, of mechanical interlocked particles in a substrate matrix, which may be a likely system of bonding for successful cold spray polymer metallisation. This current study should provide clarity on this.

2.4.3 Polymer 3D printing - fused deposition modelling

Fused deposition modelling (FDM) is a 3D printing process, depicted in Figure 2.12[xii], seen to effectively remove obstacles to design realisation [97]. Sequential layering of material, based

[xi] An interfacial jet refers to a jet of material originating from the contact area between the impacting particle and the substrate.

[xii] Licence agreement for use in PhD thesis provided by the Copyright Clearance Center (Licence No. 4872530446603), on behalf of John Wiley and Sons and the paper's authors.

on a predefined computer aided design (CAD) model and relevant configuration software builds up a scaled three dimensional replica of the given design. In the FDM process, filament material is heated to temperatures exceeding the Vicat softening temperature[xiii] and extruded through an extrusion head at a carefully controlled feed rate [96]. Support material, often water soluble, is occasionally used to support complex design construction. The system makes use of a dynamic base, which is lowered upon each successful layer completion, a dynamic extrusion head which adjusts its positioning accordingly, or a combination of the two. A temperature controlled print environment is often required to ensure effective intra- and inter-layer bonding, especially when printing certain polymers, such as ABS.

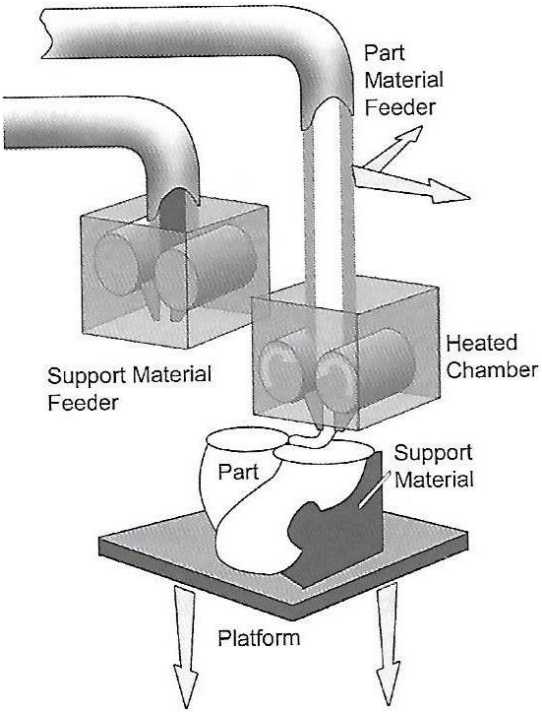


Figure 2.12: The fused deposition modelling (FDM) process for 3D printing, courtesy of John Wiley and Sons [97].

The FDM process parameters include: polymer melt rheology (how a material deforms and flows), process temperature, build speed, geometrical and layer design [102].

The use of 3D printed polymer substrates provides, not only a versatile manufacturing technique, but the ability to control design factors and component quality. Plastic polymers, while commonly found in hospital surfaces, are known to be a diverse group of materials

[xiii]The Vicat softening temperature defined by ASTM D1525 and ISO 306 as the 'temperature at which a flat-ended needle of 1 mm^2 circular cross section will penetrate a thermoplastic specimen to a depth of 1 mm under a specified load using a selected uniform rate of temperature rise'. The use of such a temperature criterion aids identification of a critical softening point for materials that have no set melting point.

with a wide range of applications [112]. Acrylonitrile butadiene styrene (ABS) is a commonly used and versatile thermoplastic for 3D printing applications [140, 141]. Design for functional surfaces is a means to enhance properties of the constituent materials or substrate surface, thereby extending their application. The Stratasys uPrint SE 3D printer has a layer resolution of 0.254 mm and offers three interior fill styles, offering further options for freedom of design [139]. These interior fills are: (i) solid (for high strength parts), (ii) sparse high density (solid boundaries with an internal structural lattice) and (iii) sparse low density (honeycombed interior).

Primary 3D printing factors include part orientation and the layer resolution of the printer, that is the minimum thickness of a single layer. Layer thickness is typically in the range of 15 to 500 μm [102]. Layer resolution has a direct effect on surface topography, together with the print orientation. Since layer resolution in many cases is more limited than print orientation, print orientation may be used to influence surface profile, based on the structural and functional requirements of a design. Part orientation influences, not only surface finish, but build speed and part strength [139].

The FDM process, when compared to other 3D printing processes, has a few limitations. These include spatial resolution [96, 102, 140], slow build speed [102] and compromised mechanical strength [140]. These limitations are managed during the design phase - mitigating possible hindering effects - and are outweighed by the advantages, of which some have previously been mentioned, but also include the broad range of model materials as well as low machinery and tooling costs [140].

Surface quality effects are considered opportunities and not limitations in the design for 3D printing, especially considering the development of functional surfaces. Surface roughness effects have been reported to influence functional properties in support of certain applications [102]. In this research, surface topography effects were investigated with regards to their effects on cold spray coating deposition and antimicrobial activity.

2.4.4 Theoretical cold spray modelling

Parameter selection plays a vital role in cold spray optimisation, especially when considering cold spray of dissimilar materials. In addition to the other cold spray parameters, the control and adjustment of the operating pressure and temperature requires careful selection and fine tuning, and according to a study by Schmidt, et al. [116] this requires the consideration of spray materials, powders sizes and the type of nozzle used.

As a means of evaluating and resolving some of the uncertainty inherent in cold spray, particularly for coating of dissimilar materials, theoretical modelling is an effective approach. In this section an investigation into various cold spray processes and the way they are modelled is undertaken. In cold spray modelling there are generally three regions of interest: the nozzle, the gap between the nozzle exit and the substrate, and finally the substrate interactions. While the design may be simple, the flow principles involved are fairly complex, including transitional flow velocities (subsonic to supersonic) and handling of multiphase flows.

Multiphase flow analysis

The typical criterion used to differentiate between low and high particle loadings, in a multiphase flow system, is that of the disperse phase volume fraction (or particle volume concentration) [127, 142, 143, 145, 146, 149], given by the volume ratio between the disperse phase and the complete multiphase flow [149]. While this criterion is widely used, both within the field of cold spraying and throughout multiphase flow analyses, there does not appear to be a consensus regarding the critical deciding value. The range in value of this criterion in literature extends from an optimistic estimate for the deciding volume fraction at 0.1 [143, 146], through to 0.001 [145], and finally to a conservative estimate of 0.0001 [142, 149].

Based on the system under analysis, the accuracy desired and the computational complexity allowed, a suitable critical volume fraction may be selected. Considering the niche study of cold spray flows a typical volume fraction usually lies below 10^{-4} [116, 127], unless specifically evaluating high particle loading scenarios [145]. Under these typical cold spray operating conditions and with regards to the conservative critical volume fraction criterion, the multiphase flows dealt with for such systems may be considered sufficiently dilute, therefore justifying the use of one-way coupling analysis methods. The spray powder can, therefore, be assumed to have negligible effect on the carrier gas and analysis of the continuous bulk flow may be carried out independently. Additionally particle-particle interactions may also be neglected [116, 127].

When the interactions between the neighbouring disperse phase particles[xiv] is negligible and their cumulative effect on the continuous phase flow is sufficiently low, which is the case for dilute multiphase flows, it becomes acceptable to solve for the continuous phase flow properties independent of the disperse phase [142]. The resultant flow properties may then be applied to the analysis of the disperse phase particles, via one-way coupling.

The analysis becomes significantly more complex when evaluating dense, disperse, multiphase flows. High particle loading in such flows has been observed to have a direct impact on

[xiv] In this instance *particles* refers to any of the common disperse phase constituents, including particles, bubbles and drops

flow turbulence (either dampening or augmenting those effects) [142, 145] and consequently altering the 'shape, strength and location' [145] of the compression and expansion waves outside of the nozzle, provided the presence of these particles doesn't trigger a transition to subsonic flow [145]. A rise in observed momentum transfer between two or more disperse flow phases leads to a reduction in the overall flow velocity [144, 145], which for a cold spray system may prevent the attainment of the critical particle impact velocity required for effective coating deposition. Notably, however, for small spray particles in a cold spray system a higher particle loading yields improved deposition efficiencies, due to improved penetration of the now weaker bow shock which develops ahead of the substrate [145]. A final consequence of a high particle loading was reported to be that of increased particle dispersion, radially from the cold spray nozzle centreline, consequently reducing deposition consistency [144].

Based on the justified assumption of discrete particle behaviour in low particle loading cold spray applications, the modelling of the disperse flow component may be achieved by way of trajectory modelling [142, 143], taking into account particle acceleration, drag and confined thermal history of the particles. The continuous phase flow is modelled independent of the disperse phase and the resulting flow conditions applied as required to the particle dynamics. The accuracy of such one-way coupling solutions is reasonably high, particularly for very dilute multiphase flows [143].

Under conditions where it is inadvisable to employ one-way coupling for a flow system consisting of two concentrated flow phases, the use of phase coupling via two-fluid models becomes a means to model such multiphase flows [142, 144, 145]. These models consider particle-particle and particle-gas interactions. This approach treats the disperse phase as a second continuous phase, approximating the interrelated effects of the interacting flow phases [142].

A notable phenomenon, which is seen to occur in particle-dense multiphase flows, involves the interaction of particles in the wake of other leading particles. A concentration or agglomeration of disperse phase particles within a continuous phase flow may arise through successive particle drafting, collision and pairing [142]. This may lead to disproportionate particle distribution throughout a flow field, which in the case of cold spray may induce irrregular and even erosive depositions on a target substrate.

Based on the understanding of multiphase flows and the requirements for a conservative approach to a validated one-way coupling analysis, the cold spray system may be modelled as a dilute multiphase flow provided the powder volume fraction is less than 10^{-4}. Based on calculated experimental trials, with an average powder feed rate of 10 g/min, an average volume fraction of 10^{-5} was reported for this current study. Accordingly, a one-way coupling method should be sufficient to accurately represent the complex flow system that is cold spray.

Compressibility effects become significant for Mach numbers exceeding M = 0.3. For the flow conditions involved in the cold spray process, which involves supersonic velocities and therefore high Mach numbers, compressibility effects are undoubtedly present. The details of a converging-diverging nozzle, as presented below, explain how such flows are taken into account, especially for cold spray modelling.

Converging-diverging nozzle operation

The cold spray process makes use of a converging-diverging supersonic nozzle. To model the behaviour of flow through such a nozzle it is important to understand the operation and allowable running conditions. Based on the justified use of one-way coupled analysis of the multiphase flow in a cold spray nozzle the independent nozzle gas flow conditions may be assumed ideal, isentropic and one-dimensional flows. Accounting for the DeLaval type converging-diverging nozzle used in the cold spray process, variable area flow is considered and discussed below based on the relevant background theory detailed in the textbooks *Fluid Mechanics* [147] and *Mechanics of Fluids* [148]. Additional supplementary literature is cited where necessary.

Under subsonic flow conditions, where the Mach number is less than one ($M < 1$), a reduction in area - via a converging nozzle - leads to a rise in gas velocity and a corresponding decrease in pressure. Any flow containing geometry that leads to a rise in gas velocity is known as a nozzle. For the case of subsonic flow an increasing area geometry observes a reduction in gas velocity and a corresponding rise in pressure. Any flow geometry that leads to a reduction in gas velocity is known as a diffuser. With regards to geometrical design, in general the opposite is true for supersonic flow; whereby an increasing area geometry functions as a nozzle and a reducing area geometry as a diffuser.

The effects observed in accelerated subsonic and supersonic flow may be combined, provided that critical flow is achieved at the section of minimum area. Critical flow refers to the condition where flow becomes sonic, $M^* = 1$ (denoted by a star). At this condition the flow is considered choked and the mass flow rate is fixed. Due to the choked condition regardless of what happens downstream of the throat the mass flow rate remains unchanged. Incorporating these effects allows supersonic flow to be achieved with the use of a converging-diverging nozzle. The converging section of the nozzle accelerates subsonic flow to sonic conditions at the throat. The flow then enters a diverging geometry whereby the flow Mach number increases into the supersonic flow regime. Choked flow is the maximum possible mass flow rate through a converging-diverging duct.

An important consideration is the control of the mass flow rate based on initial (system operating) process parameters. Assuming a fixed nozzle geometry - with a throat area designed for choked flow - and a specified carrier gas, the mass flow rate may be changed by variation

of the selected operating temperature, according to Equation 2.8 [147], due to the effects of the speed of sound, which is a function of temperature.

$$\dot{m}_{max} = \gamma^{1/2} \left(\frac{2}{\gamma + 1} \right)^{1/2(\gamma+1)/(\gamma-1)} \cdot A^* \cdot \rho_0 (RT_0)^{1/2} \tag{2.8}$$

It is noted that for choked, isentropic flow (reversible adiabatic flow) through a converging-diverging nozzle; pressure, density and temperature follow the same trends depending on area changes of constraining geometry or by way of velocity changes. The gas temperature in the diverging section of the nozzle may even drop below ambient temperature due to the expansion of the gas flow [127].

Figure 2.13 depicts the possible flow conditions through a converging-diverging nozzle, dependent on the prevailing operating pressure (derived from [147, 148]). The following observations are made with reference to the eight depicted flow regimes (A - H). While typical cold spraying processes operate with overexpanded nozzle exit conditions [108], a consideration of a broader range of flow regimes was deemed important in understanding the flow system towards the development of an inclusive theoretical cold spray model.

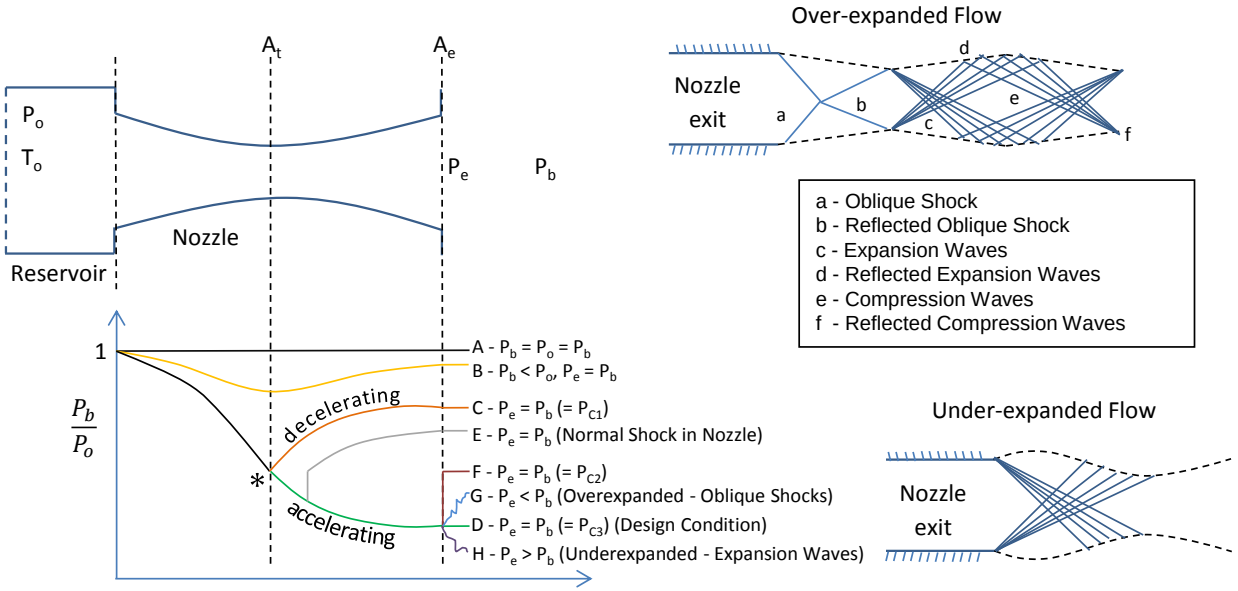


Figure 2.13: Flow regimes through a converging-diverging nozzle, with detailed analysis of nozzle exit over-expanded (G) and under-expanded flow (H) (derived from [147, 148]).

A No pressure difference, therefore no flow.

B The stagnation pressure rises above the back pressure. Subsonic flow exists throughout the nozzle, with a minimum pressure and maximum velocity at the throat.

C With increased stagnation pressure (operating pressure) a situation is reached where the Mach number at the throat is unity, i.e. sonic flow at throat. The flow, however, remains isentropic and subsonic throughout. The nozzle exit pressure is equal to the system back pressure and is termed - the First Critical Pressure (PC1).

D At a much higher stagnation pressure a situation is reached where the flow is sonic at the throat and accelerating supersonically through the diverging section, with a supersonic exit maintaining isentropic flow conditions. This pressure, under these design conditions, is known as the Third Critical Pressure (PC3).

E When the stagnation pressure is raised above the condition for the first critical pressure a weak[xv] shock is seen to develop near the throat of the nozzle, which moves along the nozzle, gaining strength, with increased stagnation pressure.

F At a pressure somewhere between PC1 and PC3 lies a system flow condition whereby a shock develops at the nozzle exit. This comes as a result of increasing the stagnation pressure such that the shock is moved to the exit plane of the nozzle. The shock is strongest at this point and the exit pressure is known as the Second Critical Pressure (PC2).

G As the stagnation pressure is increased beyond that required to achieve a shock at the nozzle exit a two dimensional flow condition develops outside the nozzle - oblique shock waves. The pressure in the exit plane of the nozzle is lower than the back pressure. The gas at the nozzle exit is therefore said to be overexpanded and an irreversible pressure rise is observed in the form of these oblique shocks. A deceleration of the gas flow is observed under this condition, along with a rise in temperature [145, 148].

H When the stagnation pressure is raised above the level required to achieve design flow conditions the pressure in the exit plane is higher than the system back pressure, such that the gas leaving the nozzle is said to be underexpanded. The flow adjusts to this pressure difference by way of expansion waves. The flow undergoes acceleration and cooling under this condition [148].

A previous analytical model of the cold spray process, assuming isentropic, one-dimensional flow through the converging-diverging nozzle, neglected boundary layer effects and considered flow primarily within the cold spray nozzle [108]. Many similar models often neglect the interaction between the spray gas on the nozzle wall, as well as flow in the free jet [116]. With reference to Figure 2.13 the study conducted by Dykhuizen and Smith [108] considered an operating condition of overexpanded flow, such that the gas pressure at nozzle exit is below that of the ambient pressure. Spray particle velocity was determined via a drag force

[xv] The strength of a shock relates to the rise in the static pressure ratio across the shock.

relationship, assuming a constant drag coefficient. The following dependencies were concluded for particle velocity: particle size, particle density, operating pressure, operating temperature, gas molecular weight and the nozzle shape. An increase in operating pressure corresponds with an increased gas velocity, which when applied to the drag force relationship in a one-way coupling the particle velocity was correspondingly seen to increase. Particle velocity is also increased by reducing the mean feedstock powder particle size [113] and lengthening the cold spray diverging section of the nozzle.

The assumption and use of a fixed drag coefficient may lead to potential inaccuracies and yet this is dependent on the extent of variation. The flow conditions within the diverging section of a cold spray nozzle change along its length based on gas temperature and relative velocity variations, and may consequently result in significant changes to the calculated drag coefficient at different points along the nozzle by as much as 50% [108]. Particle drag coefficient is a function of the flow Reynolds number and so is expected to change, unless the Reynolds number exceeds 10^8 [148]. The extent of variation was investigated as part of a study conducted by Grujicic, DeRosset and Helfritch [13]. In their study a variable drag coefficient, based on local flow conditions and correlating equations devised by Henderson [12], was found to result in negligible variations in gas and particle velocity. Such analyses, while effective in providing a suitable understanding of the system dynamics, are sometimes found to over-predict particle velocities by 5 to 10% [116].

A recent review paper [125] considered cold spray gas flow, particle acceleration and heat transfer effects, based on previous studies. This review highlighted a number of shortcomings inherent in the basic one dimensional, isentropic models. The following are noted to be omitted from these analyses: dissipation effects, nozzle geometry variations, spray gap and jet impingement considerations as well as bow shock formation ahead of the target substrate. A caveat to the development of advanced analytical models, as have previously been developed, relates to the complexity and abstruse design of such models.

Boundary layer phenomena, that is flow conditions influenced by friction and turbulence effects, within a converging-diverging cold spray nozzle have been investigated [149]. The volume fraction of particles entrained in the cold spray gas flow is considerably low (less than 10^{-4}), thereby affording an analysis based on gas flow parameters without the influence of particle loading [149], as previously discussed.

An additional consideration, which is often justifiably neglected, is that of gravitational effects on the disperse phase of spray particles in a cold spray system. Due to the short traverse time experienced by the particles in the nozzle and spray gap the effects of gravity are negligibly small and therefore suitably omitted from such cold spray models [146].

Free jet effects in the spray gap

Another study recognised the complexities of the cold spray process, suggesting the additional evaluation of flow turbulence effects and gap flow phenomena [127]. The CFD results from this study supported this premise, observing significant flow variation in the gap between the nozzle exit and the substrate; which is depicted in Figure 2.14[xvi].

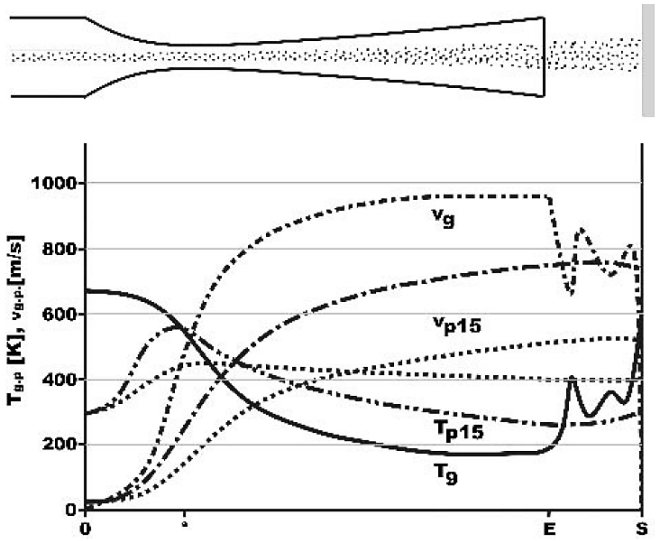


Figure 2.14: CFD results of temperature (T) and velocity (v) development for both the spray gas (g) and particles ($p15$) along a converging-diverging cold spray nozzle axis, under over-expanded flow conditions, courtesy of Dr Horst Richter, Prof Heinrich Kreye and Springer Nature [127].

Particle velocity was seen to increase in the later stages of the nozzle and within the nozzle gap [127]. Nitrogen was used as the process gas (g) and 15 μm copper powder particles were used as the feedstock powder. This study employed computational fluid dynamic simulation, therefore requiring higher computing power than, say, a simplified analytical model with predictive capabilities. Such a model would be highly beneficial with regards to practical on-the-job parameter set selection and optimisation.

Referring to Figure 2.14 from the study by Stoltenhoff, et al. [127] and a later study by Schmidt, et al. [116], the location of particle injection (or introduction) into the cold spray system plays a significant role in the thermal effects on the spray particles. Assuming no specific pre-injection particle heating, a particle introduced before the nozzle throat will undergo heating in the converging section and subsequent cooling in the diverging section of the nozzle. This cooling would also be experienced by a particle introduced to the system

[xvi] Licence agreement for use in PhD thesis provided by the Copyright Clearance Center (Licence No. 4874640299245), on behalf of Springer Nature and the paper's authors.

downstream of the throat. Particle heating, in both cases, may still occur within the spray gap, between the nozzle exit and the substrate.

In a study which involved numerical modelling with experimental characterisation of cold spray deposits, both heat transfer effects and variable drag coefficients were included in the analyses [124]. It was noted in the study that the drag coefficient depends on the flow Mach number, when compressibility effects are significant, as well as the Reynolds number. The study, however, did not account for the spray gap, assuming no decrease in particle velocity between the nozzle exit and the substrate.

Additionally, while heat transfer between the spray gas and particles was included, it was assumed that all particles, regardless of size and distribution, would have a uniform temperature, throughout its body, at every instant in time. This was based on the assertion that the Biot number (Bi), defined as the ratio of internal to external thermal resistance of a solid body [150], would be sufficiently small thereby ensuring a uniform temperature throughout each spray particle at every instant in time. Such a lumped capacity method relies on the assumption that particle internal conduction is sufficiently large to ensure the uniform temperature criterion [150]. The test criterion is given by $\mathrm{Bi} < 0.1$ [150]. Under this condition a maximum error of 5% may be induced if internal thermal effects are neglected [150]. This is seen to be justified as it was reported that from typical cold spray conditions with particles with a diameter less than 100 μm, the Biot number is usually below 0.1 [116]. Additionally for cold spray of copper, where the copper has a high heat conduction coefficient this assumption holds true [127]. The particle impact temperature, which plays an important role in coating deposition, depends on a number of system factors, including operating temperature, nozzle design as well as the aforementioned particle heat capacity (with the calculation dependent on the value of the Biot number) [116].

Gap effects and particularly jet impingement effects are important factors for consideration. The occurrence of supersonic free jets, originating at the nozzle exit plane and extending out towards the target substrate presents a further area of analysis. The pressure ratio between the nozzle exit plane pressure and the ambient pressure dictates the flow effects outside of a converging-diverging supersonic nozzle [151]. Where the exit pressure is below the ambient pressure, the exit flow is overexpanded, which produces a series of oblique shocks and expansion fans [145]. The jet passes through these shocks to re-align with the existing (higher) ambient pressure [152]. This flow phenomenon is depicted in Figure 2.13. Additionally, with overexpanded nozzle exit conditions and because of the presence of oblique shocks, flow changes will include a gas Mach reduction, a pressure and temperature rise in the spray gap [145]. This temperature rise, incidentally, may contribute to heat transfer effects and ultimately particle heating.

Where the nozzle exit plane pressure exceeds the ambient pressure underexpanded jets develop. This flow regime is characterised by expansion waves originating at the nozzle exit [151].

It is to be noted that the effect of overexpanded and underexpanded supersonic jets on the spray particles varies, based on a number of factors, including the particle size [144]. Larger particles are seen to be affected less by the shock patterns which develop outside the cold spray nozzle, due to high particle inertia [144]. Particle acceleration may still occur in the spray gap if the gas velocity exceeds the particle velocity.

When the supersonic jet nears the substrate a gas velocity reduction and flow turning takes place [149]. The transition from supersonic gas flow to subsonic gas flow is achieved by the formation of a standing shock wave, known as a bow shock, which appears in front of the substrate [126,149]. This bow shock is seen to develop regardless of flow regime at the nozzle exit, provided the flow is supersonic; whether the flow is under-expanded (Figure 2.13 H), over-expanded (Figure 2.13 G) or at the design condition (Figure 2.13 D). Gas deceleration is consequently observed, with a reported zero axial gas velocity approximately 1 mm ahead of the substrate accompanied by a radially orientated flow component [133]. In addition to the flow deceleration an accompanying rise in static pressure and temperature, as well as density rise is observed, with an associated loss in stagnation temperature and pressure [147, 148].

As particle size increases the bow shock is reported to have less effect on the spray particles, due to increased particle momentum [119, 133]. Particles greater than 10 μm have been reported, for conventional cold spray operation, to be negligibly affected by the presence of the bow shock [145]. Smaller particles may, however, be deflected by this standing shock wave [126, 145], with particles smaller than 5 μm reported to be easily swept away with the impinging gas flow, without being deposited onto the target substrate [116, 145].

Figure 2.15 depicts a cold spray nozzle-gap-substrate system with a developed bow shock. The bow shock develops at a standoff distance (Z_w) defined by Billig's approximation in Equation 2.9 [153], given in terms of Mach number (M_e) and the diameter of the nozzle (d_e) at the nozzle exit.

$$Z_w = 0.143 \cdot d_e \left[e^{\frac{3.24}{M_e^2}} \right] \tag{2.9}$$

Using the normal shock relationship, given by Equation 2.10, the Mach number behind the shock may be calculated and a linear reduction to zero at the substrate surface assumed, as was done by Alkhimov [149].

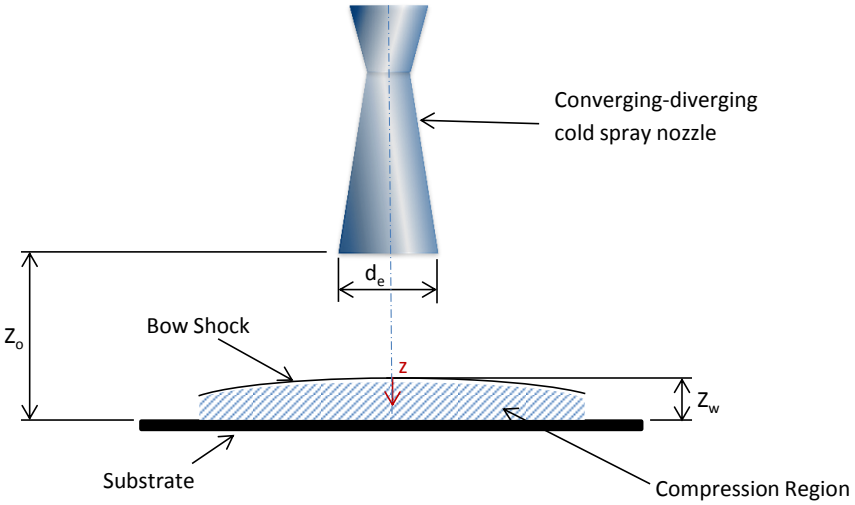


Figure 2.15: Bow shock formation ahead of a target substrate during cold spraying.

$$M^2 = \frac{{M_e}^2 + \dfrac{2}{\gamma - 1}}{\left(\dfrac{2\gamma}{\gamma - 1}\right){M_e}^2 - 1} \tag{2.10}$$

where γ is the specific heat ratio.

Computer simulation via CFD allows accurate investigation of real systems, incorporating these flow phenomena, but does so at a higher computational cost than analytical models and requires sufficient simulation time. Nozzle gap effects, including bow shock phenomena, have a significant influence on cold spray flow considerations and should, therefore, be taken into account [149]. An efficient analytical model may rapidly evaluate a cold spray system, yet be supplemented with the inclusion of complex flow phenomena. A combined analytical model may, therefore, be a possible contribution to knowledge. This gap in the current literature presents an opportunity for development in this current study.

Particle-substrate effects

By considering the particle depth-of-penetration as the key discriminating criterion, the powder-substrate properties and interactions may be included in determining a suitable cold spray parameter set. Theoretical analysis provides a means of applying the concept of particle impact velocity in calculating an associated particle embedment. In this way, both the particle and substrate materials, which may be dissimilar, are involved in theoretically evaluating a cold spray scenario.

Five particle depth-of-penetration models are considered here. The equations given below have been re-written using the equivalent parameters and names as used in this research. The

models were considered potential candidates for the cold spray particle depth-of-penetration analysis conducted in this research.

Model 1 - Frank and Zook
Based on the original Frank and Zook model [154], the following assumptions were made [118]:

- Particles act as rigid bodies, without deforming.
- The force acting on an impacting particle is given by the observed axial stress multiplied by the projected contact area of that particle.
- The substrate's resistance to deformation is assumed proportional to the substrate flow stress, which is the instantaneous stress required for continued plastic deformation.

Under these assumptions the following model was constructed. The relative penetration depth, given by the ratio of penetration depth (X) and average particle diameter (D) is given by Equation 2.11 [154].

$$\frac{X}{D} = \left[\frac{\left(\frac{L_c}{D}\frac{\rho_p}{\rho_s} + K_1\right)}{2K_t}\right] \cdot \left(1 + \frac{K_t \rho_p V_{pi}^2}{R_s}\right) \tag{2.11}$$

The ratio L_c/D, which relates the length (L_c) to the diameter (D) of the penetrator is taken to be 2/3 assuming a sphere is the mass equivalent of a cylinder with $L_c/D = 1$. The feedstock powder density is given by ρ_p, while ρ_s is the target (or substrate material) density. K_1 (= 0.557 [118]) and K_t (= 1.046 [118]) are fitting parameters and R_s is the substrate resistance, which may be calculated based on the flow stress of the substrate material (σ_s) multiplied by a coefficient of proportionality (ζ) related to the extent of plastic zone in the substrate.

The calculation steps to compute these factors (σ_s, ζ and R_s) are given below, detailing the evaluation of the normalised substrate temperature ($\theta_s{}'$) and the extent of plastic zone in the substrate (χ) in the process.

• Normalised substrate temperature ($\theta_s{}'$)

$$\theta_s{}' = \frac{T_{si} - T_{ref-s}}{T_{m-s} - T_{ref-s}} \tag{2.12}$$

where:
T_{si} = Substrate temperature immediately preceding particle impact.

T_{ref-s} = Reference temperature of the substrate.
T_{m-s} = Melting temperature of the substrate.

• Temperature dependent substrate flow stress (σ_s)

$$\sigma_s = |UTS_s(1 - \theta_s')| \tag{2.13}$$

where:
UTS_s = Ultimate tensile strength of the substrate material.

• Extent of plastic zone in the substrate (χ)

$$\chi = \left(\frac{2E_s}{3\sigma_s}\right)^{\frac{1}{3}} \tag{2.14}$$

where:
E_s = Elastic modulus of the substrate material [Pa].

• Coefficient of proportionality of the substrate (ζ)

$$\zeta = \frac{7}{3}ln(\chi) \tag{2.15}$$

• Substrate resistance (R_s)

$$R_s = \zeta \cdot \sigma_s \tag{2.16}$$

The next three penetration models (models 2, 3 and 4) were discussed by C.E. Anderson at the International Ballistics Society Conference (May 2016) [155] and are based on previous studies in the field of penetration mechanics.

Model 2 - Poncelet Equation
The Poncelet Equation, named after the French engineer and mathematician Jean-Victor Poncelet, describes rigid-body penetration and is expressed by Equation 2.17 [155].

$$\frac{X}{L_c} = \frac{\rho_p V_{pi}}{2R_s} \tag{2.17}$$

where a similar calculation as for Model 1 was used for the substrate resistance (R_s). Here the absolute value of the temperature dependent substrate flow stress (σ_s) is used.

The model relates penetrator velocity (V_{pi}), together with penetrator density (ρ_p) and the substrate static resistance (R_s) to the normalised penetration (X/L_c), where X is the depth of penetration and L_c is the characteristic length of the penetrator.

Model 3 - Eichelberger
Based on hydrodynamic theory of penetration and accounting for the substrate material strength, a penetration model is given by Equation 2.18 [155] where u is the time rate of change of penetration and t is the penetration time.

$$X = u \cdot t \tag{2.18}$$

This model assumes steady state behaviour and incompressible impacting bodies. Based on a form of Bernoulli's equation, a simplified and modified expression was developed [156]. This modified expression is given by Equation 2.19; where σ is the resistance to plastic deformation, given by the difference between the substrate and particle resistance.

$$\frac{1}{2}\rho_p(V_{pi} - u)^2 = \frac{1}{2}\rho_s u^2 + \sigma \tag{2.19}$$

From this the following expressions for the time rate of change of penetration were proposed. The expressions are dependent on the relative densities between the substrate and impacting particle materials [155].

If $\rho_p \neq \rho_s$:

$$u = \frac{V_{pi} - \mu\sqrt{({V_{pi}}^2 + 2(1-\mu^2)\frac{\sigma}{\rho_s})}}{1-\mu^2} \tag{2.20}$$

where $\mu = \sqrt{\frac{\rho_s}{\rho_p}}$.

If $\rho_p = \rho_s$:

$$u = \frac{V_{pi}}{2} - \frac{\sigma}{\rho V_{pi}} \tag{2.21}$$

Equation 2.22 was used to calculate the duration of particle penetration (t).

$$t = \frac{L_c}{V_{pi} - u} \tag{2.22}$$

From which Equation 2.18 may be used to evaluate the depth of particle penetration.

Model 4 - Christman and Gehring

An empirical model for predicting penetration from impacting projectiles was developed by Christman and Gehring [157]. Equation 2.23 expresses penetration as a two part process: a primary and a secondary penetration.

$$X = (L_c - D)\sqrt{\frac{\rho_p}{\rho_s}} + 0.13\left(\frac{\rho_p}{\rho_s}\right)^{\frac{1}{3}} \cdot \left(\frac{\frac{1}{2}m_p V_{pi}^2}{B_{max}}\right)^{\frac{1}{3}} \tag{2.23}$$

The primary penetration (Equation 2.24) represents a force and energy transfer phase, which has negligible contribution for low-aspect-ratio projectiles, such as essentially spherical imparting particles [157].

$$X_{Primary} = \left((L_C - D)\sqrt{\frac{\rho_p}{\rho_s}}\right) \tag{2.24}$$

The secondary phase (Equation 2.25), however, is dominated by projectile embedment and cavitation [157]. In this model the secondary component was based on empirical observations from impacting spheres and cylinders, with $L_c/D = 1$. Where L_c is the projectile's characteristic length, D is its diameter, m_p is the projectile's mass and B_{max} is the Brinell hardness of the substrate material [kg/mm^2].

$$X_{Secondary} = \left(0.13\left(\frac{\rho_p}{\rho_s}\right)^{\frac{1}{3}} \cdot \left(\frac{\frac{1}{2}m_p V_{pi}^2}{B_{max}}\right)^{\frac{1}{3}}\right) \tag{2.25}$$

Model 5 - Tate

An additional variation of the Bernoulli model was proposed by Clayton [158]. This was based on an extended Bernoulli equation [159]. Where projectile deceleration was neglected, Equation 2.26 estimates the depth-of-penetration of a projectile. L_c, in the context of a particle impacting a substrate, represents the average particle size, i.e. its mean diameter.

$$X = \frac{L_c}{\mu}\left(\frac{\mu\sqrt{V_{pi}^2 + A} - V_{pi}}{\mu V_{pi} - \sqrt{V_{pi}^2 + A}}\right) \tag{2.26}$$

where as with Model 3, $\mu = (\rho_s/\rho_p)^{1/2}$. The term A is given by Equation 2.36 or Equation 2.37, where R_s is the substrate resistance and Y_p the projectile strength. The additional related terms are calculated as follows:

- Normalised particle temperature ($\theta_p{}'$)

$$\theta_p{}' = \frac{T_{pi} - T_{ref-p}}{T_{m-p} - T_{ref-p}} \tag{2.27}$$

- Temperature dependent particle flow stress (σ_p)

$$\sigma_p = |UTS_p(1 - \theta_p{}')| \tag{2.28}$$

- Projectile strength (Y_p)

$$Y_p = \sigma_p \times 1.7 \tag{2.29}$$

- Normalised substrate temperature ($\theta_s{}'$)

$$\theta_s{}' = \frac{T_{si} - T_{ref-s}}{T_{m-s} - T_{ref-s}} \tag{2.30}$$

- Temperature dependent substrate flow stress (σ_s)

$$\sigma_s = |UTS_s(1 - \theta_s{}')| \tag{2.31}$$

- Substrate strength (Y_s)

$$Y_s = \sigma_s \tag{2.32}$$

- Extent of plastic zone in the substrate (χ)

$$\chi = \left(\frac{2E_s}{3Y_s}\right)^{\frac{1}{3}} \tag{2.33}$$

- Coefficient of proportionality of the substrate (ζ)

$$\zeta = \frac{7}{3} ln(\chi) \tag{2.34}$$

- Substrate resistance (R_s)

$$R_s = \zeta \cdot Y_s \tag{2.35}$$

If $Y_p < R_s$: Equation 2.36
If $Y_p > R_s$: Equation 2.37

$$A = 2(1-\mu^2)\frac{(R_s - Y_p)}{\rho_s} \tag{2.36}$$

$$A = 2(1-\mu^2)\frac{(Y_p - R_s)}{\rho_p} \tag{2.37}$$

In addition to the above conditions, according to Clayton [158], the following condition must be met, otherwise the model becomes invalid: $({V_{pi}}^2 + A) \geq 0$.

In the following chapters these models will be assessed for their ability to accurately and efficiently predict particle depth-of-penetration.

2.4.5 Cold spray process parameter optimisation

In the case of cold spray, for application as a surface coating technique, optimisation refers to the ideal set of process parameters to achieve a desired surface coating. It has been suggested that due to the numerable complexities with regards to the effects of cold spray process parameters, that 'identification of optimum spraying parameters for different materials continues to be a challenging aspect of cold spraying' [134].

This is particularly evident with regards to conflicting response characteristics in terms of opposing parameter variations [160]. The response characteristic refers to a specific outcome.

For example, a response characteristic of importance for the cold spray process may be coating thickness, or particle depth-of-penetration for embedded coatings.

An example of conflicting response characteristics are those of deposition density and thermal effects. Where depositional density is desired to be increased, thermal effects, including thermal warping of the substrate, are to be avoided. Considering the cold spray process parameter of nozzle traverse speed, when this is low the rate of particle impacts per unit area increases which leads to a potential increase in depositional density. This low traverse speed may, however, negatively impact on thermal energy transfer. A longer dwell time increases heat input which, for a thermally sensitive substrate, could lead to deleterious thermal effects. Careful parameter selection is therefore required to achieve an ideal coating based on the requirements of a specific application.

Concepts of optimisation

System optimisation, and not part optimisation, is a general guiding principle that should be followed when attempting any optimisation procedure [161]. The guiding principles and key optimisation concepts for this section were sourced from the textbook *Optimisation Methods for Engineering Design* (2013) [161].

To conduct an effective optimisation procedure, a clear and well defined objective is required. This is the *response characteristic*. A quantified model must exist for theoretical modelling, with variable inputs and the response characteristic(s) as its output(s). The variable inputs are termed *design variables*, with the collective group of design variables comprising the *design space*. System constraints, which limit the system, should be defined and incorporated into the model analysis. In certain instances, the introduction of noise factors may be necessary to better represent the system under scrutiny.

Using a typical design approach, the following six step optimisation process is suggested:

1. Define the design variables.
2. Define system requirements.
3. Define the system constraints.
4. Compile the model algorithm.
5. Run the algorithm.
6. Apply an optimisation strategy.

Feasibility space

The feasible space may be defined as the region where design variables result in system responses that are within the boundaries of the pre-defined constraints [161]. The optimum

design variables lie within this feasibility space. Or, more specifically, the local and a global optima lie within this space. A local optimum defines a point with the best response characteristic of any other feasible point in its vicinity. The global optimum is the best design point over the presented design space.

Types of system noise

Uncontrollable system variation is a consequence of noise factors. A robust design mitigates the influence these noise factors have on a system response. Noise factors may be categorised as one of three types [162].

1. Unit-to-unit
    - Random variations infiltrating a product or process during production.
2. Internal
    - Inherent system factors which cause variability in system functions.
3. External
    - External factors causing unintentional system variation.

Based on the concepts of optimisation a suitable design approach for the cold spray process was identified - the Taguchi Method.

Key Optimisation Approach: The Taguchi Method

The Taguchi Method is a design approach, previously used to good effect in cold spray parameter optimisation as discussed below.

T. Goyal, et al. published a set of three papers between 2012 and 2014 investigating the use of the Taguchi Method for the evaluation and optimisation of cold spray process parameters; based on the response characteristics of coating thickness [122], coating density [121] and a combined, multi-response optimisation of low pressure cold spray process parameters considering both previous coating characteristics [160].

The process parameters of nozzle stand-off distance, operating pressure and temperature, substrate material and the powder feed arrangement were investigated. The studies used an identical investigation framework, which involved cold spray of copper powder (Centerline C5001) onto aluminium alloy (ASTM B221), nickel alloy (ASTM B435) and brass (ASTM B36) rolled metal substrates. Nozzle design, carrier gas (compressed air) and particle size distribution (<45 μm) were set as fixed parameters. Their approach was successful in isolating an ideal parameter set for their intended applications. Details of the Taguchi Method are discussed below.

The Taguchi Method is an experimental optimisation design approach used to isolate system parameters that produce an ideal desired output, while preferentially selecting parameters that reduce system noise [163, 164]. The Taguchi approach is therefore an optimisation approach to produce robust systems. Its approach to noise variance is such that the inevitable presence of noise is accepted and instead of trying to actively eliminate the causes of noise the method aims to mitigate its effects [164].

Where a factorial design considers all possible combinations of parameter levels, a fractional factorial design, as is evident in the Taguchi Method, examines only a selected part of the full design in an attempt to make comments on the full design response [165]. The Taguchi Method actively reduces experimental time and cost [165]. This is achieved through selective experimental run choice. Results are subsequently analysed with regards to independent parameter effects. In this way parameter selection targets a *desired* system response, while being minimally constrained by noise.

For example, a system with four process parameters each identifying with three parameter levels will have $3^4 = 81$ possible test combinations in a full factorial design, whereas an L9 Taguchi approach requires only nine test combinations to achieve a similar understanding of parameter performance and association.

A caveat, with any fractional factorial design, is a consideration regarding the location of the best or *critical* design point. Measures need to be put in place to ensure that the best design point falls within the boundaries of the selected parameter levels. Accidental exclusion, due to parameter selection bias, must be avoided. A wide, initial parameter selection window should ensure the best design point is accounted for.

A typical Taguchi design approach comprises the following steps [166, 171].

1. Selection of independent process parameters.
    - These are the parameters used to define and control the system behaviour.
2. Selection of parameter levels.
    - Parameter levels should cover the effective range of viable process parameters.
3. Selection and level assignment of a suitable orthogonal array.
    - The Taguchi Method defines a number of orthogonal arrays, which accommodate various experimental designs. An orthogonal array, within the context of Taguchi optimisations, has been likened to a distillation mechanism [165]. Within this analogy, system parameters enter at various, randomly assigned combinations and emerge with traceable, independent parameter effects on both the mean response and system variation.

• An orthogonal array is a tabular environment consisting of structured experimental runs (rows) and process parameter allocations (columns). Intersection points define unique parameter sets based on collective independent process parameter levels [166]. Every column contains an equal number of parameter levels for that parameter [165].

• Orthogonal arrays are divided into three types: an inner array, containing control factors; an outer array (selectively applied), containing noise factors; and a product array, a combined inner and outer array matrix constituting the complete parameter design layout [165,170]. The layout of a Taguchi product array is given in Figure 2.16.

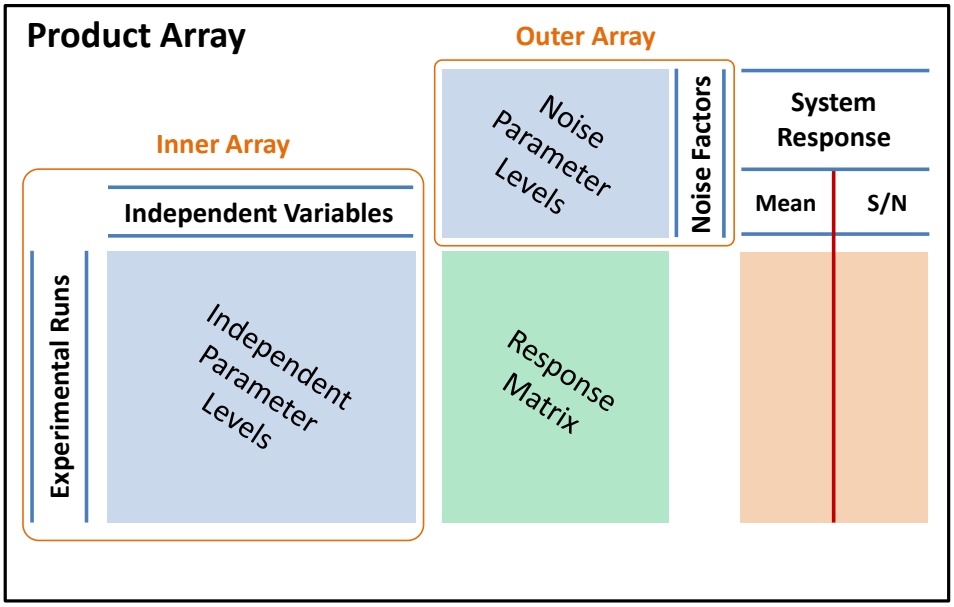


Figure 2.16: Taguchi Method product array.

An L9 (3^4) orthogonal inner array is depicted in Table 2.1. The system variables are defined as follows: A, B, C and D are the four independent variables, L denotes the specific parameter level (1,2,3), while the P's correspond to the system responses for each of the nine experimental runs. The order of the independent parameter levels is important as it ensures pairwise balancing [164,170,171]. Pairwise balancing guarantees that every level of a parameter occurs with every other level of the other parameters, the same number of times [166].

Table 2.1: An L9 orthogonal array for the Taguchi Method's fractional factorial optimisation approach.

L_9	Independent Variables				System Response
Run Number	Variable A	Variable B	Variable C	Variable D	
1	A_{L1}	B_{L1}	C_{L1}	D_{L1}	P1
2	A_{L1}	B_{L2}	C_{L2}	D_{L2}	P2
3	A_{L1}	B_{L3}	C_{L3}	D_{L3}	P3
4	A_{L2}	B_{L1}	C_{L2}	D_{L3}	P4
5	A_{L2}	B_{L2}	C_{L3}	D_{L1}	P5
6	A_{L2}	B_{L3}	C_{L1}	D_{L2}	P6
7	A_{L3}	B_{L1}	C_{L3}	D_{L2}	P7
8	A_{L3}	B_{L2}	C_{L1}	D_{L3}	P8
9	A_{L3}	B_{L3}	C_{L2}	D_{L1}	P9

- Randomisation is a key technique employed to safeguard against biased analysis. To mitigate any possible deleterious effects of parameter interaction, the columns of the orthogonal array should be randomly assigned parameters [166]. Experimental run assignment should strictly follow the Taguchi design of the orthogonal arrays.

4. Running of model.

   - Using the assigned parameter levels from the experimental run rows of the orthogonal array, model trials are conducted, recording the key system response.

5. Graphing independent parameter mean and S/N response plots.

   - The mean response for each independent parameter at each respective parameter level is calculated along with the signal-to-noise ratio (S/N). The Taguchi Method works to target a desired response, while minimising response variation.

   - The S/N ratio, measured in decibels (dB), is calculated using formulae that are based on a targeted response characteristic. A design may aim to maximise a response (Equation 2.41) - for example maximising coating thickness - or to minimise a response (Equation 2.42) - for example minimising coating porosity - or to target a desired response (Equation 2.38) - for example targeting an optimal particle depth-of-penetration for embedment and coating deposition [163](examples excluded).

$$S/N_N = 10 \cdot log_{10} \left[\frac{\frac{1}{n}(S_m - V_e)}{V_e} \right] \tag{2.38}$$

$$V_e = \frac{\sum y_i^2 - \frac{(\sum y_i)^2}{n}}{n-1} \tag{2.39}$$

$$S_m = \frac{(\sum y_i)^2}{n} \tag{2.40}$$

$$S/N = -10 \cdot log_{10}\left(\frac{1}{n}\sum \frac{1}{{y_i}^2}\right) \tag{2.41}$$

$$S/N = -10 \cdot log_{10}\left(\frac{1}{n}\sum y_i\right) \tag{2.42}$$

where n is the number of experimental runs for that particular experiment, y_i is the value of a specific response, V_e is the calculated variance and S_m is the sum of squares due to the mean [166]. It is noted that these formulae have been designed such that in order to minimise the effects of noise the factor levels maximising the S/N ratio should be selected [166].

• The mean and S/N response plots may take the form given by Figure 2.17 adapted from [164].

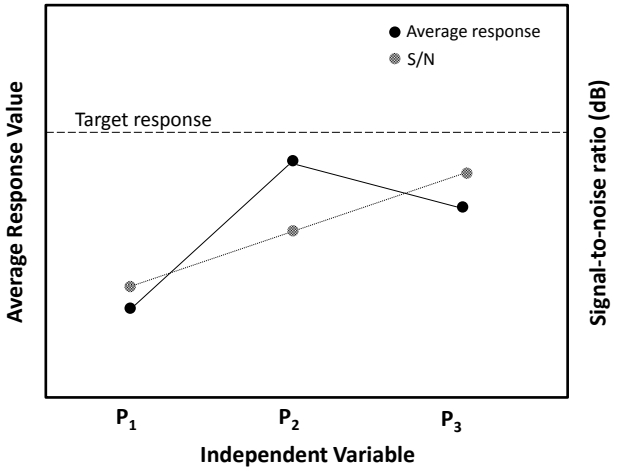


Figure 2.17: Mean and S/N response plot format with a superimposed targeted response line.

• The signal-to-noise ratio is therefore used to identify parameters which reduce variability caused by noise (refer to the section above on noise - Page 68), as well as to identify those parameters which have a significant influence on the mean response [163]. The former are termed control factors, while the latter are signal factors.

• Control factors are parameters that have a significant effect on the S/N ratio and thus affect response variation [166]. These are parameters that should be chosen to mitigate the effects of noise, by maximising the S/N ratio [164, 166]. Parameter

selection for robust design, based on the Taguchi methodology, should be made to maximise the S/N ratio, thereby mitigating response variation caused by noise factors [163, 164, 166, 170].

• Signal factors are parameters which are seen to affect the mean response, without influencing response variability [166]. These parameters should be selected based on a target response. It has been suggested that a linear relationship should exist between the levels of signal factors and the associated mean response and that identified signal factors should be easily controllable during production and/or operation [166]. A true signal factor is deemed to have no effect on system variation [172]; while in practice the determination of a statistically significant factor is required.

6. Identification of signal and control factors.

• Statistical analysis techniques are often used to identify control and signal factors. This need not always be the case, however. Where a parameter has a clear and obvious influence on the S/N ratio, it may be assigned to the control factors. Where there is doubt, the use of a statistical approach may be beneficial. Analysis of Variance is one such method often applied [164, 166]. Alternatively the Coefficient of Variation (CV) may be used.

• The coefficient of variation (CV) - expressed as the quotient of standard deviation and the mean response - is a useful test statistic used to compare system variability to a given input [164, 166]. It is often given as a percentage, i.e. %CV as in Equation 2.43.

$$\%CV = \frac{\sigma}{\overline{x}} \times 100 \tag{2.43}$$

The standard deviation is given by Equation 2.44.

$$\sigma = \frac{\sum(x - \overline{x})}{n - 1} \tag{2.44}$$

where σ is the standard deviation, $\overline{x}$ is the mean response and x is the value of a response. The level of the coefficient of variation signifying a response with high variability is dependent on the specific test case and the conditions of a specific design. It is, however, independent of system units [166] and may therefore be used to evaluate variation between different quantities. Any values of the percentage coefficient of variation exceeding a certain value represent control factors.

7. Selection of optimum process parameters.

• Besides evaluating independent parameter effects, optimum parameter levels may be identified accounting for both a targeted response and noise effects. For control

factors the parameter levels are selected to maximise S/N ratio. Signal factor parameter levels are selected to target a desired response (maximise, target or minimise a response). This process of parameter level selection forms part of parameter design [166].

- In addition to control and signal factors, and under rare experimental circumstances, there may arise a parameter which does not significantly effect the mean response nor the system variation [166]. In this case the parameter level is selected based on economical and efficiency considerations.

In the aforementioned T. Goyal, et al. papers [121, 122, 160] L18 orthogonal arrays were employed and each experimental run was conducted in triplicate, as a means of observing system variation due to noise. A higher-the-better approach was used since the response criteria were that of coating thickness [122] and coating density [121]. In the analysis they employed analysis of variance to study the relative contributions each process parameter had on the targeted response value.

Considering their study of coating thickness [122], the independent effect of the process parameters may be seen in Figure 2.18. From this, parameter percentage contributions to the mean response were calculated and an optimum parameter set defined.

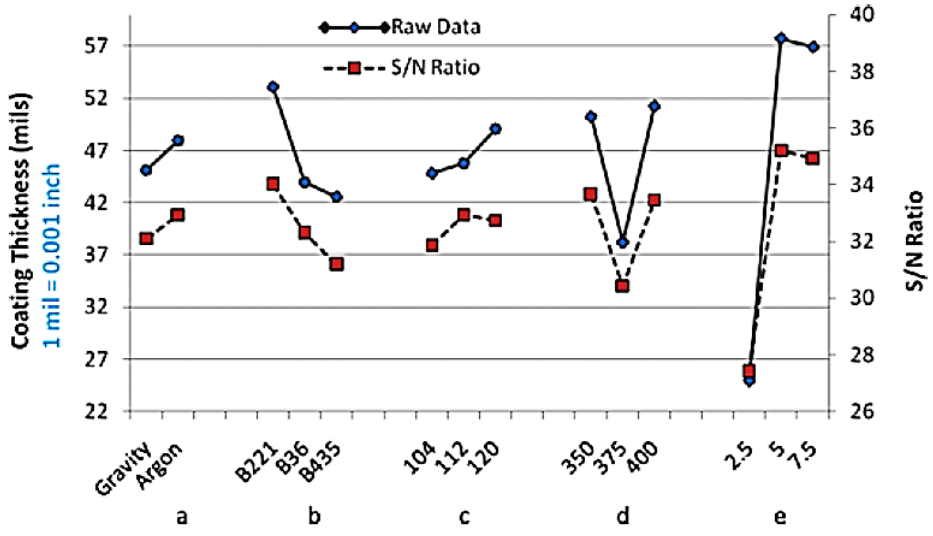


Figure 2.18: Variation of coating thickness (raw data and S/N ratio) with process parameters: (a) feed arrangement, (b) substrate material, (c) air pressure [Psi], (d) air temperature [°C] and (e) nozzle standoff distance [mm], courtesy of Taylor & Francis publishers [122].

Figure 2.18 depicts the key results from a Taguchi Method analysis [122]. The response of independent parameters may be evaluated with regards to the coating thickness, via the mean response, as well as by system variation, via the S/N ratio. From a purely graphical standpoint all parameters are seen to significantly affect both the mean and variation.

A noteworthy observation, however, was that of pressure and temperature effects. For these two parameters the maximum mean response and maximum S/N ratio occur at different parameter levels. The parameters maximising the mean response were preferentially selected over that of the S/N ratio. The mean response was observed to be more sensitive to variation than the S/N ratio. It could, however, be argued that temperature level should have been selected based on noise effect mitigation. A critical transition point for Taguchi control and signal factors may be given as 3%, such that any value exceeding this identifies the associated parameter as a control factor [166]. The percentage coefficient of variation for temperature was greater than 5% in this study. Another consideration involves possible deleterious effects that may be observed from high operating temperatures. Temperature is a cold spray parameter which should be minimised to avoid potential thermal effects, while maintaining acceptable coating quality. Identification of signal and control factors were therefore carefully considered in the current work, to ensure accurate and effective noise mitigation and critical response targeting.

Decision Theory

In addition to the Taguchi Method, which in this current study was applied to theoretical parameter set selection, additional approaches for experimental optimisation were considered. Decision Theory, as a means to control quality improvement, involves the development of a framework to characterise a decision problem [167]. This framework, which may take a number of forms, provides a structured methodology for system variation.

A common and useful approach to structured system variation makes use of decision tables, as a means of providing concise representation of implementable actions, based on identifiable system conditions or faults [168, 169]. For the cold spray system, with its critical process parameters and parameter effect complexities, the use of such a tool may provide the necessary structure for constructive analysis. A link between visual coating concerns and the relevant process parameters, coupled with actionable steps to *correct* the system, may suitably be contained in a decision table.

A decision table may take on various forms, tailored to the system and desired response [168]. Considering the cold spray polymer metallisation approach investigated in this current study a suitable decision table may take a similar form to that given by Figure 2.19.

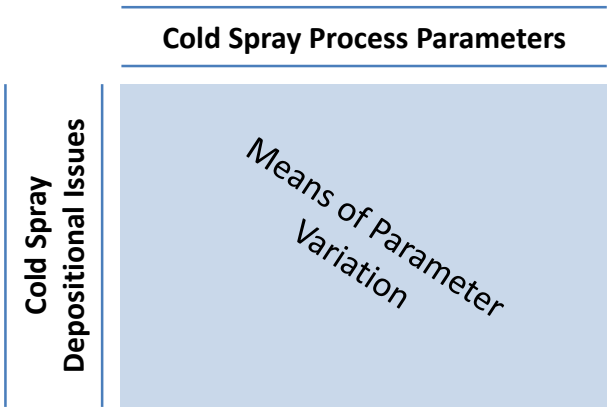


Figure 2.19: Decision table template for cold spray parameter variation.

The details of how this approach to experimental optimisation was carried out is discussed in the study methodology, detailing the extraction of key independent parameter effects and identification of associated visual cold spray depositional issues.

2.5 Conclusion - Literature Survey

This chapter set out to explore the knowledge space of antimicrobial surface coatings via polymer metallisation. In consolidating the *knowns* and *unknowns* of the related fields of engineering and health sciences, the scope and boundaries of the current research were defined. Key knowledge gaps were identified; which were later addressed.

The problem of nosocomial infections was identified, previous attempts at mitigating the impact of these infections were explored and the appropriate technologies of cold spray and 3D printing were investigated as a viable, integrated response. Theoretical modelling of the cold spray process and optimisation techniques for parameter selection were reviewed; with a comprehensive, yet efficient, analytical model proposed as a desired tool for mitigating the inherent uncertainties in cold spray parameter selection.

The literature survey - by exploring the impact of nosocomial infections and the characteristics of the responsible pathogens, as well as considering antimicrobial surfaces and the possibility of polymer metallisation as a means to address this issue - has identified the key gaps and challenging issues which provided the motivation for this research. This motivation originates with a need for alternative and innovative solutions to current infection control and prevention strategies, particularly within South Africa and other developing countries.

Surface coating technology was subsequently identified as a means to a solution. A lack of public awareness regarding the risks imposed by surface contamination previously provided

a barrier to entry for such technology, yet in light of the current coronavirus pandemic the necessary attention has been received. Looking at the prevalent and persistent problem of hospital acquired infections a critical concern relates to infection transmission pathways. Surface contamination is therefore a high priority. Cleaning protocols, where correctly implemented, are unable to control contamination. The ideal solution is to have the surface itself actively and continuously eliminating such contamination and preventing further pathogenic transmission.

The use of functional surface coatings within a hospital environment is therefore seen to be an opportunity. Plastic surfaces are common within a hospital environment and would benefit from such self-sanitising surface coatings. An opportunity arises out of the requirement of long lasting surfaces and the prevailing challenge of polymer metallisation, which if successful, would be a suitable means of coating. This gap provided the scope for a shift away from conventional metal-on-metal cold spray to a multi-step and multi-material polymer metallisation approach, based on additive manufacturing techniques. Thus a shift towards functional surface development, using 3D printing techniques, was identified.

Subsequently the need for theoretical analysis, specifically tailored to cold spray polymer metallisation, has been identified as a gap in the current literature, particularly with regards to the uncertainty in key cold spray parameter selection.

Finally, as identified by Villapún, et al. [5], there is a need for a realistic recording time period when evaluating the antimicrobial efficacy of touch-contact surfaces. The current test standards, such as the previously mentioned ASTM E2180:2018, JIS Z2801:2010 and the ISO 22196:2011 test methods consider biocidal activity after 24 hrs and even the US EPA:2016 test method only evaluates activity from 1 hr onwards; thus they inadvertently neglect more realistic contact time effects within the space of minutes and not hours.

The key findings from the literature review concern the highly prevalent pathogens (*Staphylococcus aureus*, *Enterococcus faecalis*, *Pseudomonas aeruginosa*, *Klebsiella pneumoniae* and *Candida albicans*), the oligodynamic metals (copper, silver and zinc), the cold spray process parameters (operating pressure, operating temperature, nozzle standoff distance, nozzle traverse speed and powder feed rate) and the critical elements of cold spray theoretical modelling (1D gas dynamics, heat transfer effects, nozzle gap effects and particle depth-of-penetration). Finally the use of the Taguchi Method was explored for its relevance as a suitable optimisation strategy for the cold spray system.

Chapter 3 Research Methodology

"We put together an elaborate plan for escape, involving a whaling ship to Russia, a barge to Cuba and a small, dirty canoe to Miami. We all knew it would be dangerous."

Edward Bloom, Big Fish (2003)

3.1 Research approach

This research involved various cycles of development; whereby refinement of the proposed antimicrobial surface coatings took place. The scope was such that four core research areas were defined: (1) theoretical cold spray modelling, (2) cold spray and 3D printing analysis, (3) antimicrobial susceptibility testing and (4) research consolidation.

Each core area, while being a self-contained research element, is also linked with other areas. This connection sets up a cycle of development both between and within these research elements. Theoretical cold spray modelling, as detailed in Chapter 4, will detail the development of a mathematical cold spray algorithm and use of the Taguchi Method, with a targeted particle depth-of-penetration function, for the isolation of theoretical cold spray parameter sets.

These parameter sets were then used as the initial parameter selection for cold spray and 3D printing analysis detailed in Chapter 5. This chapter details the development of an independent parameter effects and variation decision framework and an experimental optimisation procedure, resulting in ideal surface coatings via polymer metallisation techniques. Coating characterisation included average particle depth-of-penetration data and surface topography effects.

This culminates in the antimicrobial susceptibility testing, covered in Chapter 6, which set out to evaluate the antimicrobial efficacy of the developed coatings against both standard and resistant pathogenic strains. Tests were conducted in both a wet and dry contact environment,

thereby covering a broad range of operating environments. Prototype testing was undertaken as initial pilot studies to prove coating viability.

Research consolidation, detailed in Chapter 7, compares and correlates the results from the preceding chapters; evaluating the accuracy and subsequent suitability of the depth of particle penetration criterion, as well as evaluating surface topographical effects - via surface roughness and wear test analyses - and the subsequent effects this has on antimicrobial activity. Additionally the design for antimicrobial surfaces was re-evaluated; thereby proposing future recommendations, continuing the cycle of development outlined in this chapter.

3.2 Theoretical cold spray modelling

A user friendly, quick-check reference system providing predictive information regarding theoretical cold spray analysis was the aim of this research element. System functionality and predictive accuracy are design priorities. The use of high level programming software (Python) was important in developing a compact, modular program; based on a comprehensive mathematical model and Taguchi optimisation methodology. The cold spray model was used to target a desired particle depth-of-penetration, based on an investigation and consolidation of the factors influencing coating deposition.

The process of developing the mathematical algorithm, isolating a targeted particle depth-of-penetration and incorporating the Taguchi Method is detailed below.

3.2.1 Algorithm development

As a means of addressing the prevailing uncertainty in cold spray parameter selection, specifically with regards to polymer metallisation, a new and adapted theoretical model was developed.

Particle depth-of-penetration was used as the key discriminating criterion, thereby taking into account the material and system properties of both the cold spray feedstock powders and the target substrate. Mechanical entanglement as the expected principal bonding mechanism, informed the decision to use a ballistic analysis approach. A mathematical algorithm for accurately determining the depth-of-penetration of cold spray particles, given a set of process parameters and design variables, was the salient aspect of the algorithm. Figure 3.1 depicts the theoretical cold spray system layout.

Figure 3.1 provides a framework for model development. The five system regions, namely: flow gas conditioning, subsonic nozzle effects, supersonic nozzle effects, gap effects and substrate effects, provide the necessary stages of system evaluation. The model calculations are grouped into the following: (1) nozzle calculations, (2) gap calculations and (3) particle-substrate interactions. Gas flow (g) and particle (p) conditions are evaluated at the critical locations throughout the cold spray system including the nozzle exit (e), bow shock (2,3) and the particle-substrate interface (i).

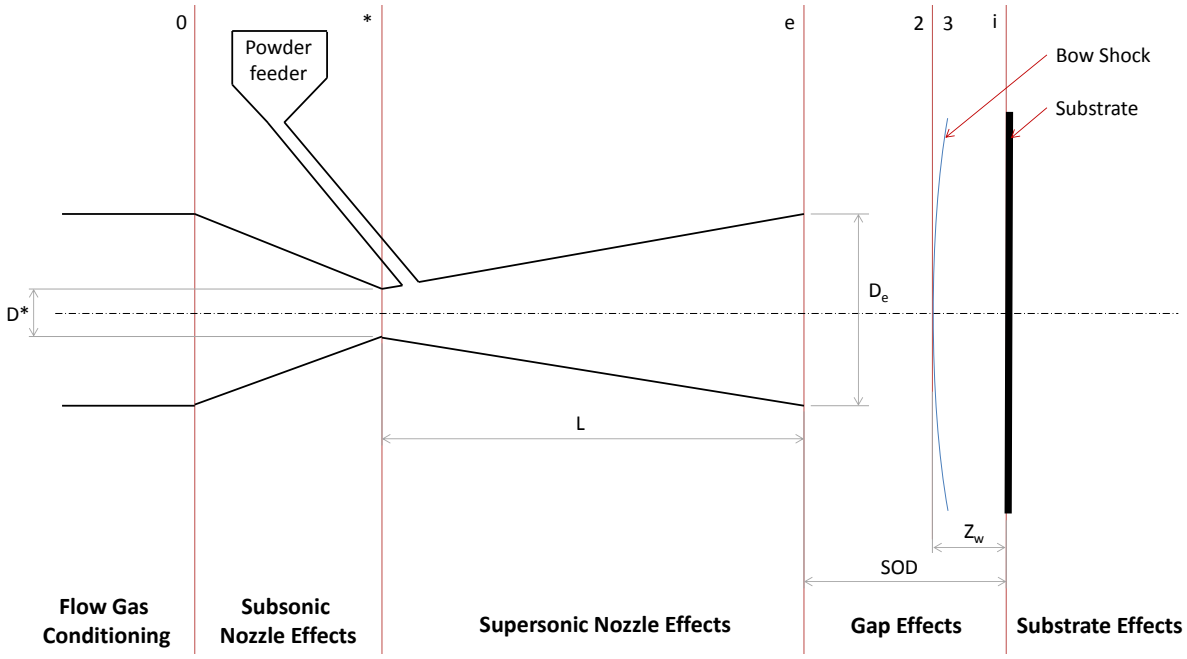


Figure 3.1: Theoretical cold spray system layout for theoretical modelling.

(1) Nozzle calculations

Nozzle calculations comprise gas and particle modelling. The nozzle calculation was based on a one dimensional gas dynamic analysis. This defines the gas condition within the nozzle, with regards to: pressure, temperature, density, mass flow rate and subsequent flow velocity. The nozzle exit was the primary cross-section of interest.

Particle modelling

- Heat transfer effects make use of the Biot number to confirm the validity of a lumped capacity model. That is, where the Biot number is below 0.1, the temperature throughout each spray particle is considered uniform at any instant in time. Where this criterion does not hold transient heat conduction charts are used to evaluate transient particle temperatures and heat flow mechanisms [150].

- Drag force analysis, incorporating a Mach-number-dependent drag coefficient based on the prevailing relative flow Reynolds number, was used to calculate particle velocities.

(2) Gap calculations

The flow effects in the gap between the nozzle exit and the substrate surface are often neglected, yet referring to Figure 2.15 in Chapter 2, temperature and velocity effects are significant and should be incorporated. The nozzle standoff distance (SOD) typically ranges from 5 mm to 15 mm and yet may extend beyond this limit, yet the powder consumption will often increase due to reduced fractional powder deposition and other factors affecting powder loss (e.g. powder deflection) [16]. A larger nozzle standoff distance may, however, be necessary for polymer metallisation so as to mitigate destructive thermal effects.

- The substrate temperature, as a consequence of the impinging jet, was estimated based on submerged jet heat transfer correlations [150].
- Observations made in the literature survey regarding theoretical cold spray modelling show that the gas flow conditions at nozzle exit may be at the design condition, over-expanded or under-expanded (Figure 2.14 in Chapter 2) and need to be suitably considered.

  - Where the flow is at the design condition, flow conditions are assumed constant leading up the the bow shock and set at the nozzle exit flow conditions.

  - A non-linear, basic, fixed point root finding method was used to evaluate oblique shocks, in the case of over-expanded flow.

  - The Prandtl-Meyer function was used to account for under-expanded flow and the associated expansion waves [147].

- The bow shock, which develops ahead of the target substrate, was treated as a normal shock wave.
- Heat transfer analysis was used to evaluate the particle impact temperature. The method employed was dependent on the value of the particle centric Biot number. Where Bi < 0.1, a combined heat transfer analysis was derived and employed. In the unlikely event that the Biot number exceeds 0.1 reference was made to a transient heat conduction analysis, using calibrated charts [150].
- Based on the location of the bow shock, given by the bow shock standoff distance (Z_w), the particle impact velocity was evaluated [113, 132, 173]. This particle velocity was then used in the evaluation of the particle-substrate interactions.

(3) Particle-substrate interface

With the previously calculated particle impact velocity and the particle impact temperature, the final critical calculation concerns the particle depth-of-penetration. The resultant value of maximum penetrative depth was used as the design criterion, defining theoretical coating quality.

Model setup is an important aspect in the design of such an algorithm and in the subsequent software development. Details of the system constants and boundary conditions are included in Appendix A. The Python programme was designed to be a self contained, yet modular system; whereby all required data may be found and edited within the code. This accommodates straightforward and efficient software updates and modifications, which may include modifications to the model algorithm or the addition of new test material properties for novel cold spray powder-substrate combinations.

Selection methodology for the depth-of-penetration theoretical model

In evaluating the suitability of the respective penetration models, a combined variability analysis was employed which considered predictive accuracy against published theoretical and experimental cold spray penetrative analyses, together with an associated coefficient of variation for missing process parameters from published literature case studies. Finally, using measures of central tendency, the models were ranked based on how effective each was in producing a mean response.

Each of the following three comparative analyses (predictive accuracy, coefficient of variation and measures of central tendency) resulted in a weighted method score (MS_i) for each respective particle penetration model. Using Equation 3.1, an overall Method Score (MS) was calculated such that the penetration model with the **lowest** Method Score was deemed the best suited model with the least response variability.

$$\begin{aligned} MS &= \sum WF_i \times MS_i \\ &= (WF_1 \cdot MS_1) + (WF_2 \cdot MS_2) + (WF_3 \cdot MS_3) \end{aligned} \tag{3.1}$$

Each of the three comparative analyses was assigned a weighting factor (WF), based on the relative importance that component has to method selection. Predictive accuracy was assigned $\mathrm{WF}_1 = 0.5$, coefficient of variation $\mathrm{WF}_2 = 0.3$ and measures of central tendency $\mathrm{WF}_3 = 0.2$.

The three elements, which comprise the evaluation of the effectiveness and appropriateness of the considered theoretical penetrative models, were that of predictive accuracy, coefficient of variation and measures of central tendency. Each of these elements targeted a specific desired aspect of the proposed theoretical particle penetration model. Predictive accuracy was used as a tool to see how close each model was to a target, which was the highest priority characteristic. Coefficient of variation was used to discern model robustness, in response to unintentional parameter deviation. Measures of central tendency provided a means of identifying a conservative model. This last characteristic, while important, was of lesser

importance than the previous two discriminating factors. The relative importance of these elements thus informed the associated weighting factors.

Predictive accuracy (MS_1)

Based on published data and preliminary theoretical and experimental cold spray trials, a collection of independent cold spray parameter scenarios with known process parameters and system response characteristics (particle depth-of-penetration) were defined. Equivalent theoretical cold spray runs were conducted using the developed theoretical model and the five penetration models previously discussed on pages 61 - 66. Where parameter values were missing, values were assumed and later evaluated for variability effects via the coefficient of variation sub-procedure.

Equation 3.2 was used to calculate the percentage difference between the respective *given* (X_{given}) and *theoretical* ($X_{theoretical}$) responses, where X is the particle depth-of-penetration value. These percentage differences were the first set of Method Scores (MS_1).

$$MS_1 = \%Diff = \left(\frac{X_{given} - X_{theoretical}}{X_{given}} \right) \times 100 \tag{3.2}$$

Coefficient of variation (MS_2)

When selecting a theoretical model one desires a model of high predictive accuracy, while being insensitive to system noise. As a means of mitigating the detrimental effects of assumed parameter values, where there was a lack of fully defined parameter sets from published literature, the following analysis was proposed.

Two fully defined random cold spray parameter sets were selected; that of cold spray of copper onto a copper and ABS substrate, respectively. The parameters in question included: nozzle throat diameter, nozzle exit diameter, nozzle divergent length, ambient pressure, ambient temperature, operating pressure, operating temperature, initial particle temperature, nozzle standoff distance, nozzle traverse speed and the initial substrate temperature. Each parameter, from both parameter sets, was independently varied by defining a *high* and *low* value, which was to be evaluated independently.

The theoretical model was then applied to each respective parameter set, varying each parameter value based on the respective 'high' and 'low' value. Each independent penetration model was applied to the theoretical model for these trials.

The mean system responses (particle depth-of-penetration) were tabulated, including the standard deviation (std. dev.) and coefficient of variation (CV) for each penetration model

for each process parameter. For each process parameter (e.g. nozzle throat diameter) the average CV values, per penetration model, were tabulated.

For each of the published data and preliminary theoretical and experimental cold spray trials the parameter sets that were originally missing parameter values or had questionable values were identified. The average, collective CV value for all the missing parameters, per penetration model, were calculated.

From this, the average %CV per particle penetrative model, which defines the second set of Method Scores (MS_2) (See Equation 3.3), were tabulated. In this way penetrative models with smaller CV values represent robust models with higher confidence in parameter sets.

$$MS_2 = \%CV \tag{3.3}$$

Measures of central tendency (MS_3)

Making the assumption that a mean response, from various theoretical models, is likely to lie near the actual, ideal system response, the measures of central tendency targeted a model whose response was closest to that of a mean and median response.

A thousand random cold spray parameter sets were run through each of the five respective penetration models. The key parameters of variation and their respective parameter ranges are given by: operating pressure (P_0) [0.6,1.0] MPa, operating temperature (T_0) [100,300] °C, spray powder (copper or zinc), substrate material (3D printed ABS, PEEK, PC), nozzle standoff distance [5,20] mm, nozzle traverse speed [5,30] mm/s. The number of times each model was closest to the mean response and the number times each model was the median response was collated and converted into a percentage value. This combined percentage value was defined as the Method Achievement Score (MAS). The corresponding Method Score was calculated via Equation 3.4.

$$MS_3 = 100 - MAS \tag{3.4}$$

Measures of central tendency provide a conservative approach, employing elements of *crowd wisdom* to theoretical model selection. With this approach the theory that the 'aggregate of a set of proposed solutions from a group of individuals performs better than the majority of individual solutions' was applied [174].

The final Method Score was calculated using Equation 3.1. The penetration model with the lowest overall method score was thereafter selected as the best suited model for future theoretical analysis.

3.2.2 Targeted particle depth-of-penetration

A target particle depth-of-penetration model was developed for a theoretical cold spray deposition. This model would be used to identify the ideal particle depth-of-penetration; which the theoretical cold spray model would then use as a target response.

In developing such a model, the relationship between depth-of-penetration and material properties was investigated. Published data on ideal relative particle penetration were investigated. The survey scope was limited to cold spray of copper powder onto known substrates including stainless steel, aluminium, aluminium alloys and polymers (polyethylene and high density polyethylene). Thereby a wide range of material substrates was incorporated, with differing material properties. The data collected included average particle size, average particle depth-of-penetration (or simply the relative penetration X/R) and the material properties of both the powder and the substrate materials (density, Young's Modulus and ultimate tensile strength).

In this research the ultimate tensile strength (UTS) of the feedstock cold spray powders was inferred from the bulk material properties. While possible inaccuracies were incurred as a consequence of this assumption, as indicated by Assadi et al. [113, 175], data for the mechanical properties of cold spray powders is hard to come by and often unavailable. There is both a lack of readily available mechanical property data for these cold spray powders, even from the leading suppliers, and a lack of standardised methods for such characterisation [175]. Assadi and Gärtner have just recently (May 2020) proposed a method to calculate the ultimate tensile strength of these powders directly from measured force-displacement data, based on a modified nanoindentor compression test [175]. In their study they suggest that microstructural differences, specific processing conditions, impurity content and even oxygen content can lead to differences in these properties. Their results reveal that the UTS of powder particles is a function of the particle size, such that smaller particles exhibit higher ultimate tensile strengths. Future work would benefit from including such new findings.

From the data obtained, graphical analyses of penetration and material property relationships were investigated. A combined, equal-weighted correlation expression was compiled as a tentative target particle depth-of-penetration model. The suitability of this model was later re-assessed based on experimental cold spray trials and successfully optimised surface coatings. This assessment is included in Chapter 7.

3.2.3 Taguchi Method

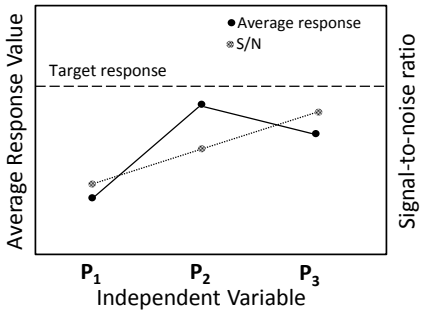
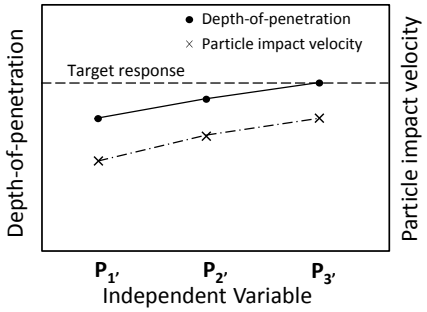
The Taguchi Method offers a systematic and efficient approach to optimisation, based on the principles of partial factorial experimental design. In this way a minimum number of experiments are performed to identify a potential optimum system. The Taguchi Method affords critical analysis of a system's controlled and limiting factors, with regards to a selected performance criterion. In this case the Taguchi Method was used to identify an initial cold spray parameter set for the development of effective coating deposition on polymer substrates, based on a targeted, ideal particle depth-of-penetration.

While the experimental design may be applied to any number of particle-substrate combinations, for the purposes of this research the theoretical combinations of metals (copper, nickel, zinc, tin and aluminium) and polymer substrates (ABS, PC, PEEK) were considered.

In setting up for a Taguchi Method analysis the general procedure, as detailed in the literature survey, was tailored to the requirements of this design. A two part optimisation approach to the Taguchi Method was devised. As was previously discussed in the literature survey on page 69, the orthogonal array approach to optimisation works on the principle of a distillation mechanism, sifting through a range of parametric combinations in search of an ideal combination. The decision to perform this procedure twice (once with the inclusion of noise factors) gives rise to a *double distillation* of suitable process parameter combinations. The first part (Part 1) employed a product array with the addition of noise factors. Part 2 used another orthogonal array to further refine parameter selection, deriving input process parameters from the results of Part 1. Table 3.1 summarises this adapted Taguchi Method. Details of the seven procedural steps are thereafter discussed.

Table 3.1: Adapted Taguchi Method for cold spray parameter selection.

Adapted Taguchi Method

	Part 1 **Noise mitigation**	**Part 2** **Parameter level refinement**
Step 1	**PARAMETER SELECTION**	
	Noise factors Ambient pressure Ambient temperature Spray powder particle size	**Design factors** Operating pressure Operating temperature Nozzle standoff distance Nozzle traverse speed Noise factors
Step 2	**PARAMETER LEVEL ASSIGNMENT**	
	• Level assignment encompasses the full, effective working range of each parameter. • Noise parameter levels are set at standard and extreme levels.	• A narrowed effective parameter range, about an optimum level, was derived from part 1.
Step 3	**ORTHOGONAL ARRAY SELECTION**	
	L_9 & L_4 → Product array	L_9
Step 4	**EXPERIMENTAL EXECUTION**	
	Coupled Taguchi Method and mathematical model.	
Step 5	**GRAPHICAL ANALYSIS**	
		
Step 6	**SEPERATION OF SIGNAL AND CONTROL FACTORS**	
	Control Factor if %CV > 3% Signal Factor if %CV ≤ 3%	N/A
Step 7	**IDEAL PARAMETER LEVEL SELECTION**	
	Identifying and testing a combined ideal cold spray parameter set	
	• Selection dependent on factor type	• Priority given to depth-of-penetration

1. **Parameter selection**

Selection of independent process parameters and noise factors

- The four process parameters of operating pressure and temperature, nozzle standoff distance and nozzle traverse speed, were used as the variable and independent parameters for the developed theoretical model.
- Ambient pressure, ambient temperature and the spray powder particle size were selected as the system noise factors for the first pass through the experimental procedure (Part 1).
- With regards to the theoretical model, the following are regarded as selectable, fixed parameters: nozzle throat diameter, nozzle exit diameter, nozzle diverging length, cold spray carrier gas, spray powder material and substrate material. These parameters are user defined, yet remain fixed throughout the analysis.

2. **Parameter level assignment**

Defining system boundaries

- To ensure that the working range of the process parameters was included in the experimental design, three variable parameter levels were selected, which covered the effective working range of the cold spray system. In selecting the specific parameter levels, the unique powder and substrate material combinations were considered, thereby tailoring parameter levels to suit each coating combination. This choice was based on equipment limitations, suggested parameter ranges given by Centerline SST [176–180] as well as experimental familiarity with parameter effects. The assigned parameter levels for the product array's independent variables is given in Table B.1 of Appendix B.
- A similar approach was undertaken for the noise factors in Part 1 of the adapted Taguchi Method. Two parameter levels for each noise factor were selected. In general this involved a lower value set at the standard operating level, and a higher value set at sea level conditions or a worst case scenario. An exception was made for the spray powder particle size, where the lower level was set at a value 20% below average. It is known that larger particles will embed deeper, due to higher momentum, and therefore to maximise depositional efficiency a conservative parameter set targeting smaller-than-average particle embedment will, by reasoning given above, result in an improved depositional efficiency. Table B.2, in Appendix B, contains the noise factor levels for each cold spray test powder.

3. **Orthogonal array selection**

Selection and level assignment of a suitable orthogonal array

- The minimum number of experimental runs required to conduct an effective Taguchi analysis (N_T) may be calculated using Equation 3.5 [171], based on the number of degrees of freedom (L) for each independent parameter (i). For this calculation, and the subsequent Taguchi analysis, a clearly defined number of independent system factors (N_v) to be varied is required. It is noted that the minimum number of experiments required for a Taguchi Method experimental design will be a multiple of two and three, such that pairwise balancing is enforced [171].

$$N_T = 1 + \sum_{i-1}^{N_v} (L_i - 1) \tag{3.5}$$

- Given four independent system factors, each expressed at three, well distributed parameter levels, an L9 orthogonal array as defined in Table 2.1 was used as the template inner array for this analysis. An L9 array, as defined in the literature review, is a description of an orthogonal array used in the Taguchi analysis where each parameter in a four parameter system identifies at three known levels. In a full factorial analysis this involves 81 possible test combinations, yet with the Taguchi analysis only nine are required to achieve a similar outcome.
- A coupled L_9 and L_4 Taguchi template was used for the first part of the theoretical optimisation procedure. The orthogonal arrays are depicted in Table 3.2. This made up the analysis structure for the first pass parameter distillation and noise mitigation scheme (Part 1). The second part of the theoretical optimisation employed an L_9 orthogonal array framework, as depicted in Table 3.3
- Parameter level entry followed that given by [164, 166] which is graphically illustrated in Table 3.2 and Table 3.3.

4. **Experimental execution**

Running the model

- Part 1 (Table 3.2) of the analysis was first conducted. Then using the refined parameter set, Part 2 (Table 3.3) was conducted.
- The Taguchi Method was coupled with the developed theoretical cold spray model. Successive model runs at the defined parameter sets were required. The Taguchi analysis was designed within a Microsoft Excel framework. The test run parameter sets were parsed to the Python model, which then initiated the mathematical algorithm. The model output gave the resultant particle depth-of-penetration as well as other important flow, particle and system characteristics.

Table 3.2: Taguchi Method part 1: Product orthogonal array (L_9 & L_4).

Powder-Substrate					L2	L2	L1	L1	**Ambient Pressure (Pa)**	**Noise Factors**	
L9 & L4 Orthogonal Array	**Independent Variables**				L2	L1	L2	L1	**Ambient Temperatures (°C)**		**Particle Depth of Penetration**
Cold Spray Run	**Stagnation Pressure (P_0)**	**Stagnation Temperature (T_0)**	**Nozzle Standoff Distance (SOD)**	**Nozzle Traverse Speed (V_n)**	L1	L2	L2	L1	**Spray Powder Particle Size (μm)**		$\bar{X}$	$S/\bar{N}_N$
1	L1	L1	L1	L1	X_{14}	X_{13}	X_{12}	X_{11}			$\bar{x}_1$	$S/\bar{N}_{\bar{x}1}$
2	L1	L2	L2	L2	X_{24}	X_{23}	X_{22}	X_{21}			$\bar{x}_2$	$S/\bar{N}_{\bar{x}2}$
3	L1	L3	L3	L3	X_{34}	X_{33}	X_{32}	X_{31}			$\bar{x}_3$	$S/\bar{N}_{\bar{x}3}$
4	L2	L1	L2	L3	X_{44}	X_{43}	X_{42}	X_{41}			$\bar{x}_4$	$S/\bar{N}_{\bar{x}4}$
5	L2	L2	L3	L1	X_{54}	X_{53}	X_{52}	X_{51}			$\bar{x}_5$	$S/\bar{N}_{\bar{x}5}$
6	L2	L3	L1	L2	X_{64}	X_{63}	X_{62}	X_{61}			$\bar{x}_6$	$S/\bar{N}_{\bar{x}6}$
7	L3	L1	L3	L2	X_{74}	X_{73}	X_{72}	X_{71}			$\bar{x}_7$	$S/\bar{N}_{\bar{x}7}$
8	L3	L2	L1	L3	X_{84}	X_{83}	X_{82}	X_{81}			$\bar{x}_8$	$S/\bar{N}_{\bar{x}8}$
9	L3	L3	L2	L1	X_{94}	X_{93}	X_{92}	X_{91}			$\bar{x}_9$	$S/\bar{N}_{\bar{x}9}$

Table 3.3: Taguchi Method part 2: L9 orthogonal array.

Powder-Substrate							
L9 Orthogonal Array	**Independent Variables**				**Performance Parameter Value**		**Critical particle velocity (V_{crit}) [m/s]**
Cold Spray Run	**Stagnation Pressure (P_0)**	**Stagnation Temperature (T_0)**	**Nozzle Standoff Distance (SOD)**	**Nozzle Traverse Speed (V_n)**	**Particle Depth of Penetration**	**Particle impact velocity (V_{pi}) [m/s]**	
1	L1	L1	L1	L1	$\bar{x}_1$	$\bar{V}_{pi1}$	$\bar{V}_{crit1}$
2	L1	L2	L2	L2	$\bar{x}_2$	$\bar{V}_{pi2}$	$\bar{V}_{crit2}$
3	L1	L3	L3	L3	$\bar{x}_3$	$\bar{V}_{pi3}$	$\bar{V}_{crit3}$
4	L2	L1	L2	L3	$\bar{x}_4$	$\bar{V}_{pi4}$	$\bar{V}_{crit4}$
5	L2	L2	L3	L1	$\bar{x}_5$	$\bar{V}_{pi5}$	$\bar{V}_{crit5}$
6	L2	L3	L1	L2	$\bar{x}_6$	$\bar{V}_{pi6}$	$\bar{V}_{crit6}$
7	L3	L1	L3	L2	$\bar{x}_7$	$\bar{V}_{pi7}$	$\bar{V}_{crit7}$
8	L3	L2	L1	L3	$\bar{x}_8$	$\bar{V}_{pi8}$	$\bar{V}_{crit8}$
9	L3	L3	L2	L1	$\bar{x}_9$	$\bar{V}_{pi9}$	$\bar{V}_{crit9}$

5. Graphical analysis

Graphing independent parameter mean and S/N response plots

- The mean response for each parameter - at each respective test level - was independently isolated and plotted. For Part 1 particle depth-of-penetration was the key mean response, while for Part 2 particle impact velocity as an additional system response was included. Equation 2.6 [113, 132] was used to calculate this velocity, where σ_p is the flow stress of the cold spray particle on impact with the substrate, ρ_p is the density of the particle, C_{p-p} is the specific heat (at constant pressure) of the particle [J/kg·K] and T_{pm} is the melting temperature of the

particle and T_{pi} is the particle impact temperature. With reference to Table 3.1 the parameter levels are plotted on the horizontal (abscissa) axis, while the depth-of-penetration and particle impact velocity responses are plotted on the vertical (ordinate) axis.

$$V_{crit} = \sqrt{\frac{4\sigma_p}{\rho_p} + 0.25C_{p\text{-}p}(T_{pm} - T_{pi})} \qquad \text{(2.6 revisited)}$$

- Onto these graphs the target (nominal response) was superimposed, based on the specific system conditions for that powder-substrate combination. This target response was calculated using the empirical penetration model that was developed and subsequently plotted as a target line on these graphs.
- Additionally the signal-to-noise ratios, as detailed in the literature survey on page 71, were calculated based on a Nominal-the-Better approach, which aims at targeting a desired response, as given by Equation 3.6, Equation 3.7 and Equation 3.8. The signal-to-noise analysis is only applicable for Part 1. These results were plotted on the aforementioned axes.

$$S/N_N = 10log_{10}\left[\frac{\frac{1}{n}(S_m - V_e)}{V_e}\right] \tag{3.6}$$

$$V_e = \frac{\sum y_i^2 - \frac{(\sum y_i)^2}{n}}{n-1} \tag{3.7}$$

$$S_m = \frac{(\sum y_i)^2}{n} \tag{3.8}$$

- An example of this method is given in Table 3.1.

6. **Separation of signal and control factors**

Targeting the mean response and mitigating noise variability

- Recalling that signal factors influence the system mean response, while control factors affect the S/N ratio; it was imperative that these factors be suitably separated. To distinguish between signal and control factors, the coefficient of variation was employed[i]. The ratio of standard deviation to the mean response for each parameter across all three tested levels comprised the coefficient of variation.
- Based on the trends observed with regards to the system response a percentage coefficient of variation of 3% was selected as the design criterion; such that a

[i] Graphical analysis may have been employed, yet it was desired to accurately target each factor, which the coefficient of variation allows while ensuring an unbiased section process.

parameter was deemed a control factor if its percentage coefficient of variation (%CV) was greater than 3% and a signal factor if it was less than or to equal to 3%.

7. **Ideal parameter level selection**

Theoretical parameter selection and validation

- Based on the identified signal and control factors the corresponding ideal parameter levels were selected from Part 1. Signal factor level selection targeted the nominal response, by selecting a parameter level with a response that was closest to the nominal response. Control factor levels were selected to maximise the S/N ratio. This parameter set was run through the theoretical model and then prepared for Part 2's analysis. This involved identifying a parameter value higher than the ideal parameter value from Part 1 and similarly selecting a parameter value lower than the ideal parameter value. These three levels (low, Part 1 ideal, high) were then transferred to the orthogonal array in Part 2.
- For Part 2, only the mean response was considered, since noise factors were not incorporated and therefore ideal parameters targeted the nominal particle depth-of-penetration (priority) and the critical particle impact velocity.
- The final, compiled parameter set was run through the theoretical algorithm and the particle depth-of-penetration response compared directly to the empirically calculated target particle depth-of-penetration (see page 85). Slight modifications to the theoretical parameter set may be made as necessary. These final parameter sets represent the initial theoretically optimum cold spray parameter sets for cold spray metallisation of specific polymers. Under the design approach taken for this research, that of cycles of development, these parameter sets may be subject to further refinement, based on alterations to the theoretical model itself.
- Using the newly optimised parameter sets, reference coatings for both single- and multi-pass (3 - 5 cold spray passes) coatings were cold sprayed for every theoretically viable powder-substrate combination. These would later be used to evaluate the theoretical model's predictive accuracy and subsequently lead to suggested, and in some cases, implemented solutions.

The novel approach in developing a comprehensive, analytical theoretical cold spray model by incorporating a predictive and optimisation methodology, using the Taguchi Method framework, affords rapid and accurate parameter selection and theoretical coating evaluation. In streamlining the cold spray process in this way significant progress may be made into effective polymer metallisation.

Where the Taguchi Method has previously been used as part of experimental optimisation [121, 122, 160], this approach has used the model for theoretical analysis. Thus theoretical modelling through this methodology affords both coating evaluation and, critically, the predictive optimisation and selection of process parameters.

The approach taken for the identification and use of the ideal cold spray parameters for various polymer metallised surface coatings, required cycles of development. As such the inputs required for the previously detailed targeted particle depth-of-penetration, while initially informed by published data, were later refined based on experimental findings from this study itself. This change propagates through to the Taguchi Method, where further parameter refinement may be achieved.

3.3 Cold spray and 3D printing analysis

Integrated cold spray and 3D printing analysis, through polymer metallisation, made use of the theoretically optimum parameter sets derived from theoretical cold spray modelling. This section, therefore, details the experimental procedures required to achieve experimentally optimum cold spray parameter sets for various metal coated polymer combinations.

3.3.1 Independent parameter effects

An independent parameter effects and variation decision framework was developed as a means of evaluating surface coating quality for cold spray onto polymer substrates. The development of such a framework was based on the literature covered on Decision Theory on page 75. Priority was given to the analysis, and subsequent design, of single pass coatings as a means of investigating the primary interaction between impacting cold spray powder particles and the target substrate, as well as to avoid profligate use of the antimicrobial metals.

Cold spray is reported to offer many advantages over other surface coating techniques including thermal spray processes [111]. Even so, coating characteristics related to depositional efficiency, coating porosity, thermal effects - particularly for cold spray of thermally sensitive materials - and erosive features dictate parameter selection and are the subject of much research [111, 113, 124, 128, 135]. When considering its application to polymer metallisation there were found to be five key coating depositional effects detrimental to the effective deposition of spray material (lack of deposition, lack of depositional consistency, lack of coating densification, thermal effects and erosive features).

Based on the experimental trials, examples of each of these depositional effects are depicted in Figure 3.2 along with an acceptable surface coating for copper cold spray of 3D printed ABS. It is noted that the striations observed on the coated surface are a consequence of the 3D printing process and comprise individual extrusion runs. Incidentally it is this patterned surface that was investigated with regards to the effects of the surface topography on coating formation and subsequent antimicrobial activity. This micro-pattern is hypothesised to not only aid coating deposition, but improve the antimicrobial performance of these novel materials.

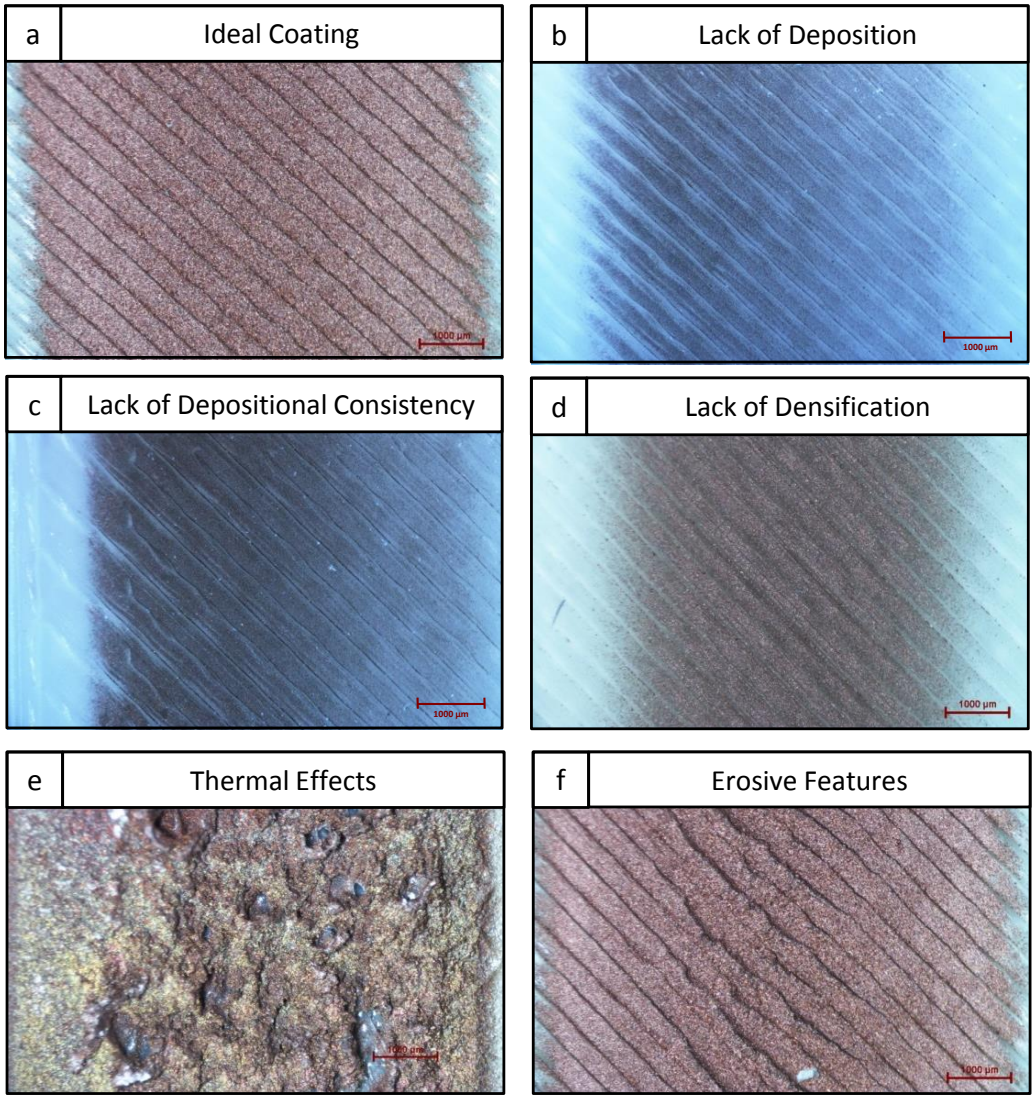


Figure 3.2: Five key depositional effects for cold spray polymer metallisation based on experimental trials: (b) lack of deposition, (c) lack of depositional consistency, (d) lack of densification, (e) thermal effects and (f) erosive features. Figure (a) represents an ideal cold spray coating of copper onto 3D printed ABS.

The independent parameter selection decision framework was developed to prevent adverse coating effects. The model drew on (1) theoretical and (2) experimental cold spray analyses as well as (3) published literature findings, with regards to the five key cold spray process parameters, namely: operating pressure, operating temperature, nozzle standoff distance, nozzle traverse speed and the powder feed rate.

(1) Theoretical approach

Two independent theoretical procedures were carried out. The first considered a theoretical cold spray copper coating on a copper substrate. The second considered theoretical cold spray copper onto an ABS substrate. Referring to the literature survey section on mechanical properties of the substrate (Page 43), it was observed that the bonding mechanism, in general, shifts from a mechanical-metallurgical bond as a result of adiabatic shear instability for metal-on-metal deposition, to a purely mechanical bond characteristic of mechanical entanglement for those materials of differing properties (metal embedment onto a polymer substrate) [137].

The independent effects of stagnation pressure, stagnation temperature, nozzle standoff distance and nozzle traverse speed on particle depth-of-penetration were evaluated. The powder feed rate was not included as a process parameter in the theoretical model, since the model specifically evaluated single particle impacts. Each parameter was independently varied from a nominal value to that of a higher and lower value respectively. Thereafter parameter sensitivity and observed trends were considered.

(2) Experimental approach

Using solid ABS as the test substrate and a copper blend, with constituent aluminium and alumina powder blends, as the feedstock powder, sample coatings were cold sprayed based on varied process parameter sets. The theoretically optimum parameter set was used as the baseline parameter set. Each parameter was independently varied according to the following: operating pressure was varied by 25%, operating temperature (degrees Celsius) by 50%, nozzle standoff distance by 50%, nozzle traverse speed by 50% and the powder feed rate by 25%.

The coatings were subsequently evaluated according to particle depth-of-penetration, average impacting particle size, surface area coverage and the general appearance, using the procedures detailed in Appendix C. A Leica DM6000M microscope with a Leica DFC490 camera mount, a stereoscopic Nikon SMZ 745T microscope with a Nicon DS-Fi2 camera mount and image processing software ImageJ were used in making these measurements on both surface and cross-sectional profiles. The latter profiles were analysed from suitably sectioned, cold mounted and polished test samples.

The findings were documented in cold spray run cards. The run card template is depicted in Table C1 in Appendix C. All relevant data was recorded and used within the relevant analyses.

(3) Published literature findings

Finally, published data for cold spray onto polymer substrates was examined and the key parameter effect trends extracted.

From these three sources of information an independent parameter effects and variation decision framework was developed, providing an effective decision making tool for cold spray applications. For each critical cold spray process parameter (operating pressure, operating temperature, nozzle standoff distance, nozzle traverse speed and powder feed rate) the key effects of parameter variation were summarised. The subsequent decision making tool, realised as a decision table, was to be able to guide the identification of cold spray coating issues, while providing the means to correct or mitigate their impact, through a range of independent parameter variations.

Independent parameter effects on surface topography

In addition to the independent parameter effects analysis, which was used to develop the cold spray parameter effects selection decision framework, a separate analysis was carried out to investigate the effect parameter variation has on surface topography[ii].

Analysis was carried out on both single pass coatings (the primary focus of this research) as well as multi-pass coatings. Each investigated process parameter (operating pressure, operating temperature, nozzle standoff distance, nozzle traverse speed and powder feed rate) was varied according to the design given in the development of the independent parameter effects and variation decision framework.

The correlation analysis between independent parameter levels and surface topography made use of the Pearson correlation coefficient (R_{xy} or R) as given by Equation 3.9 [167]. Where x and y are the relevant data points corresponding to the cold spray parameters and resultant roughness parameters respectively.

$$R_{xy} = \frac{\sum_{i=1}^{n} y_i(x_i - \overline{x})}{[\sum_{i=1}^{n} y_i(y_i - \overline{y})^2 \sum_{i=1}^{n}(x_i - \overline{x})^2]^{0.5}} \tag{3.9}$$

[ii]This analysis was not, however, included in the development of the cold spray parameter variation selection model since the desired surface roughness and topographical features are not known for the target application. It was suspected that an increasing surface roughness would correspond to an increased antimicrobial efficacy, due to an increased surface contact area. This, however, was to be confirmed at the time of testing.

The magnitude of the resulting coefficient dictates the appropriateness of a linear regression model [167].

- $R_{xy} < |0.5| \Rightarrow$ Weak correlation
- $|0.5| < R_{xy} < |0.8| \Rightarrow$ Moderate correlation
- $R_{xy} > |0.8| \Rightarrow$ Strong correlation

The coefficient of determination (R^2), equivalent to the square of the Pearson correlation coefficient, was then used in the correlation analysis. This term is generally used to evaluate the applicability of a regression model, by representing the degree of variability in data [167]. Since the the coefficient of determination has a value which lies between zero and one, when it is presented as a percentage it represents the percentage of the data that supports a specific regression model [167].

3.3.2 Experimental optimisation procedure

The starting point for experimental optimisation were the theoretically optimum parameter sets, which were refined for effective coating generation.

Cold spray powders were carefully selected from reputable sources and limited to the following types as given in Table 3.4. All feedstock powders, except for the silver powder, were sourced through SST Centerline, Canada. The silver powder was obtained through Sigma-Aldrich. Figure 3.3 depicts the scanning electron micrographs of the four core feedstock powders used. The silver powder comprised fine particles with scattered coarse particles interspersed. The copper-aluminium-alumina powder blend had a mixed morphology, including the irregular agglomerates of copper and the irregular globules of the aluminium and alumina particles.

Table 3.4: Selected cold spray powders and powder blends with respective properties and research usage designations.

Powder	**Purity**	**Morphology**	**Research usage**[iii]
Cu	> 99.7%	Irregular agglomerates	Theoretical and experimental
Zn	> 99.7%	Irregular globules	Theoretical and experimental
Ag	> 99.99%	Irregular	Experimental
Cu-Al-Al_2O_3	99.7 - 99.5 - 92%	Irregular	Experimental
Al	> 99.5%	Irregular globules	Theoretical
Sn	> 99.7%	Spherical	Theoretical
Ni	> 99.7%	Irregular agglomerates	Theoretical

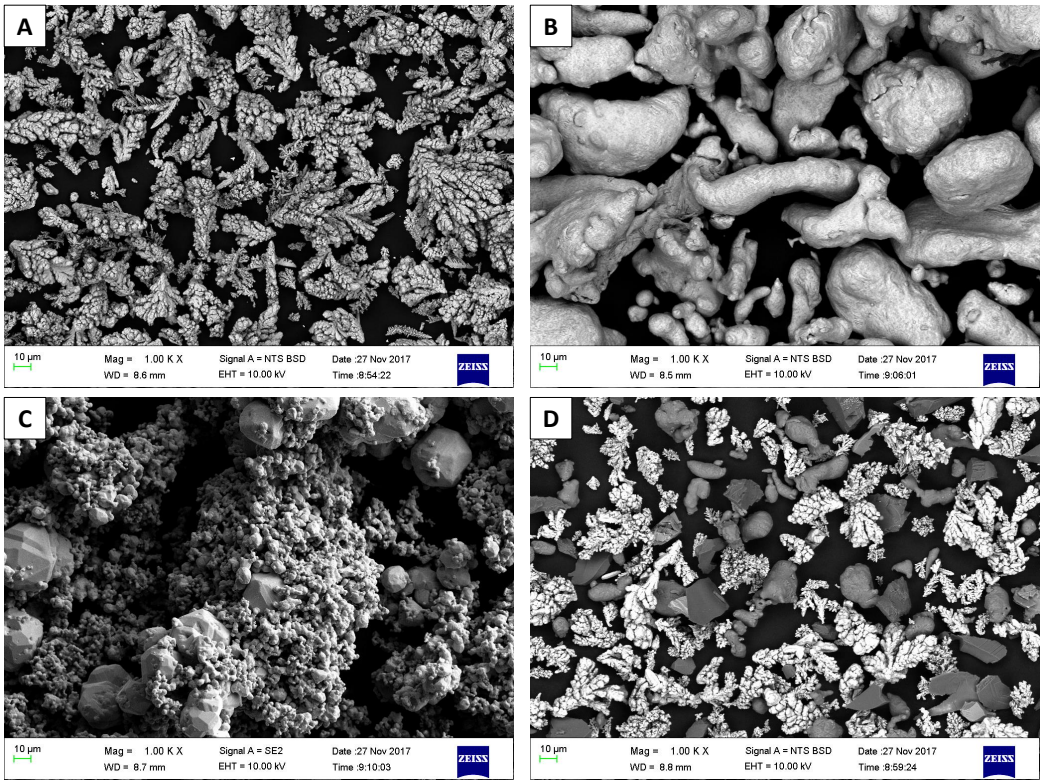


Figure 3.3: Scanning electron micrographs of cold spray powders: A - Copper (C5003), B - Zinc (Z5001), C - Silver (327107) and D - a copper-aluminium-alumina blend (C0075).

In addition to the standard/stock powders, specially blended powder combinations were devised. These blended coatings were developed to evaluate potential synergistic relationships between the various powders for enhanced antimicrobial activity. Powder blends, defined according to weight composition, included a 50:50, a 75:25 and a 25:75 copper-zinc blend and a 5 weight percent (wt%) silver additive to a high purity copper powder base.

The substrates for these cold spray coatings included various 3D printed ABS substrates as well as solid polymer substrates sourced through RS Components, namely: white ABS (Part No. 681-615), clear polycarbonate (Part No. 769-8720 and 681-643) and beige polyetherether-erkeytone (Part No. 514-300). The research focused primarily on polymer metallisation but for antimicrobial susceptibility testing a copper sheet was used as an additional substrate as a point of comparison. Copper, as a proven antimicrobial metal, was selected for this special addition so as to directly evaluate the effect a cold spray coating has in comparison to an uncoated metal surface. The copper sheet was sourced from Metals Centre cc, as were the stainless steel and galvanised (zinc coated) steel control samples.

[iii]Theoretical usage relates to the use of the cold spray theoretical model and therefore applying the properties of the respective powders to that model. Experimental usage, however, designates the physical use of the powder as the feed powder for a cold spray coating.

The custom built low pressure cold spray unit from Centerline Supersonic Spray Technology was used to coat the various substrates with the selected metal powders. All cold spray coating combinations are defined in Appendix E.

Unless otherwise stated, the geometry of the substrate materials were 25 mm × 30 mm[iv], allowing for three cold spray run types: line 1 - wipe test, line 2 - single pass coating, line 3 - five pass coating. The wipe test procedure evaluates single particle impacts, by accelerating the cold spray nozzle arm to 0.5 m/s and traversing a defined spray path over the target substrate.

A detailed Standard Operating Procedure (SOP) was drawn up for the cold spray system, which may be found in Appendix C.

Optimisation procedure

An optimisation procedure, as illustrated by the flow chart in Figure 3.4, was devised based on the need for a structured experimental parameter selection procedure. The specific design of experiments (DOE) presented here, was designed to efficiently isolate local, and possibly global, optimum parameter sets for the various polymer metallised coating types under investigation. The optimisation procedure involves four core procedural elements: (Level A) theoretical parameter set effects, (Level B) high-low parameter variations, (Level C) independent parameter variations and (Level D) combined parameter effects. These procedural elements made up the four levels of the optimisation, which were governed by specific parameter sets as defined in Table C.3 in Appendix C.

[iv]The test samples for the antimicrobial susceptibility tests were 12 × 12 mm.

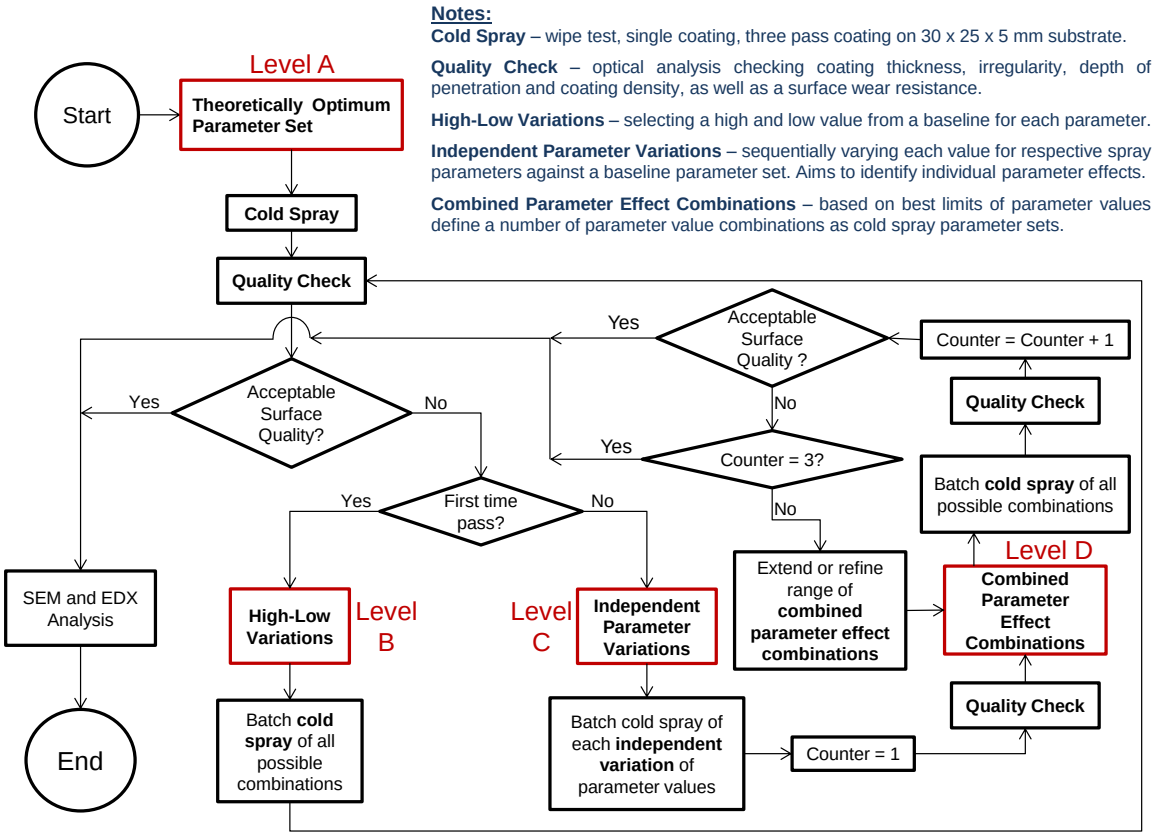


Figure 3.4: Cold spray optimisation procedural flow chart.

Between each experimental level a coating quality check sub-procedure was performed. This quality check, detailed in Appendix C, was used to evaluate and subsequently target desired surface coating qualities. Each cold spray coating sprayed was documented in a run card, as illustrated in Table C.1 in Appendix C. Coating quality was defined based on the intended application - that of antimicrobial touch contact surfaces - related to a coating which exhibits uniform and dense powder dispersion, with minimal substrate distortion. Thus the key criteria were based on the identification, and subsequent correction, of: coating deposition paucity, insufficient densification, the absence of depositional consistency and the presence of erosive and/or thermal effects.

The details of this experimental optimisation procedure, based on Figure 3.4, are given as follows. Once an ideal coating had been generated the procedure was terminated, thereby saving experimental time and costs. This process also allows additional novel coatings to be developed quickly and effectively.

Level A The optimisation procedure starts with the evaluation of the theoretically optimum parameter sets. Each relevant powder-substrate combination was cold sprayed in triplicate and evaluated based on the cold spray quality checks detailed in Appendix C.

Level B

Figure 3.5 depicts all possible parameter combinations for Level B - High-Low parameter variation. As a factorial design 32 unique parameter sets and associated experimental runs are defined. To reduce the number of runs conducted, independent parameter levels that are likely to yield unsatisfactory coatings are eliminated using the independent parameter effects and variation decision framework.

If, for example, the independent parameter effects and variation decision framework suggests that an increased operating temperature may lead to detrimental thermal effects, then for all subsequent Level B runs only lowered temperature levels are included. This alone halves the effective number of experimental runs required.

Out of the remaining cold spray runs, and after the necessary quality checks have been performed, the best performing parameter set is isolated. If this parameter set represents neither a local nor a global parameter set and would therefore not be acceptable for touch-contact surface applications, then Level C is conducted. Whether successful coatings were deemed global or local optimums was not of critical importance in this study. The goal was to develop a tool for effective parameter selection for cold spray polymer metallisation.

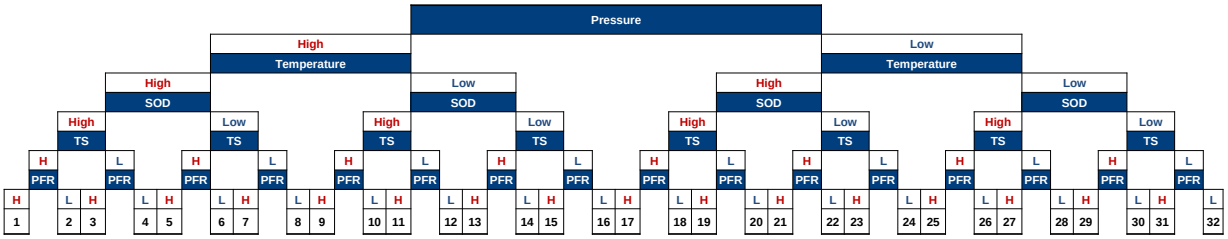


Figure 3.5: High-low parameter variation matrix for Level B of the experimental optimisation, where SOD is the nozzle standoff distance, TS is the nozzle traverse speed and PFR is the powder feed rate.

Level C

This protocol represents a selective, independent parameter variation process. Cold spray runs are conducted based on independent parameter variations of the best performing parameter set from Level B. Refer to Table C.7 in Appendix C for the specific parameter variations. Level C is linked with Level D, such that once Level C is completed Level D commences.

Level D	The best variations from Level C are combined and tested under various parameter combinations, as given in Table C.7 in Appendix C. The best combination is assessed for coating suitability. If acceptable, the optimisation is complete and that parameter set is defined as the optimum parameter set for that specific coating-substrate combination. In the event that the best combination does not achieve the required coating quality Level D is repeated once more with this parameter set. After the second cycle through Level D if no coating is acceptable that combination is deemed ill suited to cold spray coating and thereafter abandoned.

Cold spray powder combinations

Cold spray powder combinations were investigated, including bulk combinations of copper and zinc, as well as coatings with a 5 wt% silver powder additive. The bulk powder combinations followed the same previously detailed experimental optimisation procedure.

These powder combinations were intended to provide insight into the antimicrobial mechanism of action, related specifically to synergistic relationships and surface topographical effects. It has been suggested that copper acts as an effective cell wall breaching agent, while silver ions are reported to attack cell proteins, from within a microbial cell [80]. The intended powder combinations and subsequent susceptibility tests would therefore be able to comment on related mechanisms of action.

Substrate design and investigation via 3D printing

A uPrint SE, Stratasys 3D printer was used for all 3D printing operations. CatalystEX software was used to processes substrate designs. The two main process parameters of interest were those of the interior fill style and the build orientation.

Three interior fill styles were available: solid, sparse high density and sparse low density. The solid interior fill was selected to ensure adequate part strength and sufficient thermal capacity. Erosive damage to the substrate surface, caused by the abrasive impact of cold spray particles, is a concern faced when attempting cold spray of hard powder particles onto relatively soft polymer substrates. In addition to erosive features another concern was that of thermal effects. Substrate design has a direct influence on thermal capacity. Target substrates with intricate surface profiles or with internal latticing have lower thermal capacities and are therefore more susceptible to melting or surface warping as a result of the cold spray jet impingement temperatures.

In a similar way, part orientation is an important and crucial process parameter for Fused Deposition Modelling (FDM) 3D printing design. Part orientation during 3D printing influences not only component build speed, but also component strength and surface finish [139].

Of particular interest was the surface finish. Topographical effects were the primary focus, provided the designed substrates withstood the cold spray impacts. Surface roughness is dictated by the print orientation, the set layer resolution and layer deposition paths.

Two print orientations were therefore selected. The first was a horizontal orientation, inducing the highest surface homogeneity, with low surface roughness. A vertical orientation, at the opposite extreme, was the other print orientation. These two substrate designs are illustrated in Figure 3.6. The cold spray coatings were applied to the top surface of the horizontally orientated substrate and to the side (long side) of the vertically orientated substrate. The cross-sectional views of these 3D print orientations illustrate the layered structure and composition for the orthogonal views.

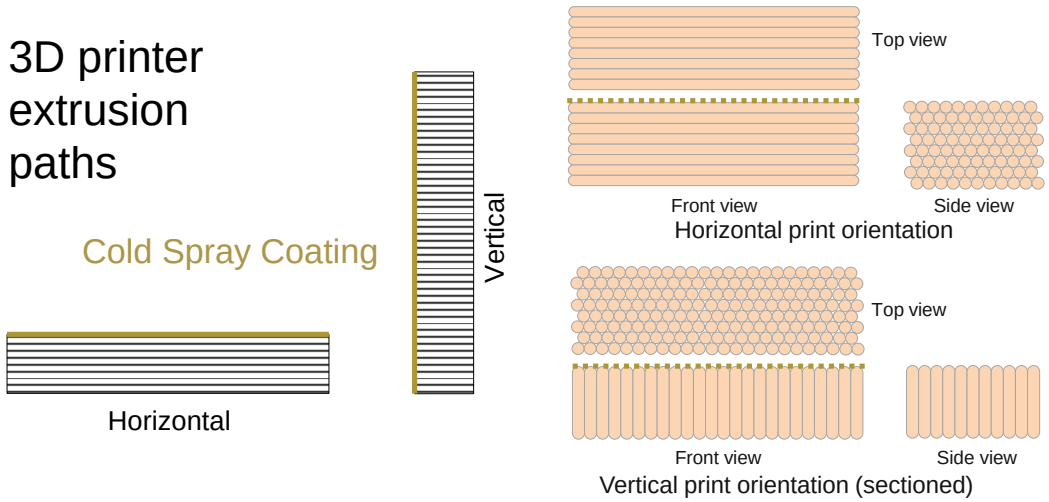


Figure 3.6: Horizontal and vertical part orientations for FDM polymer 3D printed components.

List of all coating combinations

A number of powder-substrate combinations were considered for antimicrobial surface coatings. Table E.1 in Appendix E includes all the investigated coating combinations, from all aspects of the study (theoretical, experimental and those used in the antimicrobial susceptibility tests).

The decision to carry forward coatings from one stage of research to the next was based on scope delimitation and coating viability and/or effectiveness. Scope delimitation applied specifically to the theoretical analysis, where additional coating types (nickel, tin and aluminium) were included for completeness, yet were not carried forward on the basis of sample size and time constraints.

3.3.3 Coating characterisation

Cold spray coatings were sprayed for all successful theoretically and experimentally optimised parameter sets. These physical coatings were characterised according to their general appearance, particle impacts, surface topography and surface wear properties. The results of these analyses were used in both material characterisation found in Chapter 5 as well for comparative analyses found in Chapter 7. The experimental designs and associated procedures for these four criteria are detailed below.

General appearance

The general appearance of a coating is made based on observations from both single and multi-pass cold spray coatings. Coatings are deposited via cold spray using the associated parameter set. Features of interest include: penetrative deposition thickness[v], deposition continuity and surface finish. Comments were made regarding the effect of jet impingement on the target substrate, related to thermal and mechanical effects (erosion and abrasion). In addition the extent of deposition and depositional consistency are also made.

A desired coating was that of a uniform, dense powder deposition with minimal substrate distortion. The surface coating should exhibit a consistent profile with negligible variation in appearance. Microscopy analysis was used to qualitatively assess this property.

Average particle size, shape and depth-of-penetration

Characterisation of particle impacts gains insight into bonding mechanisms and coating formation, related to the properties of the interacting materials. A wipe test was, therefore, conducted; which aimed to evaluate single particle impacts by rapidly accelerating the nozzle across the target substrate when spraying. All cold spray parameters, barring the nozzle traverse speed, are set to the required values, with the nozzle traverse speed set at a sufficient speed (500 mm/s) to achieve single particle impacts. These samples were thereafter sectioned, cold mounted and then ground and polished in preparation for microscopy analysis. The specific SOPs and supplementary procedures are detailed in Appendix C.

The single particle impacts were then analysed, considering particle size, shape and depth-of-penetration in particular. Stereoscopic, optical and scanning electron microscopy was used for this analysis. The relevant SOPs may be found in Appendix C. Image processing was carried out using Image J computer software[vi], which allows analysis and post-processing of multidimensional images and was ideal for accurate measurements of particle size, shape and depth-of-penetration.

[v] Recall that a coating, for the purposes of this research, is defined as a dense deposition and embedment of cold spray powder particles into a target substrate.

[vi] Image J is an open source, scientific image analysis software.

Surface topography

Surface topography was evaluated for the purpose of material and coating characterisation as well as for trend analysis with respect to wear resistance and antimicrobial efficacy. Substrate surface topography was also investigated with regards to coating development, to determine whether surface roughness has an influence on cold spray polymer metallisation and subsequently what that effect is and how to capitalise on that knowledge to optimise surface coating design.

The geometrical product specification defining the rules and procedures for the assessment of surface texture (ISO4288), was used as the framework for surface topography analysis. The derived experimental procedure may be found in Appendix C. Microscopy analysis (Leica DM6000M with a Leica DFC490 camera mount) and surface profilometry (TR220 surface roughness tester) were used to evaluate surface profiles and coating structure.

Where applicable the following roughness parameters were measured, recorded and integrated into the relevant analyses [181].

- Ra - Arithmetic mean deviation of the profile [μm].
- Rq - Root mean square deviation of the profile [μm].
- Rz - Maximal height of the profile (in sample length) [μm].
- Ry - Maximal height of the profile (in evaluation length) [μm].
- Rt - Total height from peak to valley within a profile [μm].
- Rp - Maximum peak height of the profile [μm].
- Rv - Maximum valley depth of the profile [μm].
- Rsm - Mean spacing for the microscopic roughness of the profile [mm].
- Rs - Mean spacing between individual profile peaks [mm].
- Rsk - Profile skewness.

Wear testing

The application of the coatings developed through this research are intended for touch-contact surfaces within hospitals. This may include table tops, hand rails, electronic device covers and even medical equipment and surgical instruments. As such the resistance to wear and the subsequent longevity of the surface coatings was considered.

Two wear criteria were used to quantify wear resistance and behaviour of the developed coatings. The first, the coefficient of friction (μ_k), represents the constant of proportionality

between kinetic force (F_k) and the resultant normal force (N). R.C. Hibbler (2010) [183] defines frictional force as a force which 'acts tangent to the contacting surfaces in a direction opposed to the motion or tendency for motion of one surface relative to another'. The coefficient of friction is given by Equation 3.10.

$$\mu_k = \frac{F_k}{N} \tag{3.10}$$

The coefficient of friction is a system property dependent on: materials, coating, lubricants, contact area, geometry, observed stress, surface topography, relative motion, sliding mode (unidirectional, reciprocating, multi-directional), contact type and period (continuous vs intermittent) as well as the environmental conditions (temperature and humidity) [182].

The second criterion is that of the wear coefficient (k), defined as the volume of material removed per unit load and sliding distance, with units $mm^3/N{\cdot}m$ [182]. The wear coefficient provides a means of comparing component durability. As with the coefficient of friction the wear coefficient is a system property and not a material property. As such comparisons must be made for materials tested under identical conditions.

As a means of providing a comparative analysis, and not to replicate operational conditions, the Pin-on-Disc wear test procedure was identified as a suitable test due to its widespread use and suitable handling of thin film coatings [184]. The developed coatings, while not strictly thin film coatings, are similar and therefore required commensurate handling.

The ASTM G99 standard test method for wear testing with a pin-on-disc apparatus, was selected as the standard to which this analysis would be based. This test method evaluates wear properties for sliding contact between a reference ball/pin and the test substrate, without the addition of an abrasive. From this procedure coating types may be compared and ranked based on wear resistance. Test parameters critical to a Pin-on-Disc test include: applied load (N), relative sliding speed (m/s), sliding distance (m), environmental test temperature ($°C$) and humidity (RH).

The test procedure devised, based on the ASTM G99 standard, is given in Appendix C.

Using this test procedure the follow stages of investigation were carried out.

Stage 1: Screening tests

In order to conduct a valid surface wear analysis the test parameters were required to remain constant, varying the coating type only. Therefore, a set of screening tests were devised as a means of isolating a suitable test parameter set. An initial screening parameter set was based

on data from seven relevant literature sources. The raw data is tabulated in Table C.12 in Appendix C.

A cold spray copper coating on solid ABS substrates was used as the reference material. The screening tests were based on three categories: sliding distance variation, load variation and a combined analysis. The test parameter sets, based on the published literature findings, were comprised of the following:

- Applied load [N]: 2, 5, 7
- Sliding distance [m]: 15, 50, 100, 150

The following fixed parameters were set:

- Linear speed [cm/s]: 12.57
- Temperature [°C]: Room temperature
- Humidity [%]: Atmospheric environmental conditions
- Static partner (ball): Stainless steel (6 mm diameter)
- Test sample surface dimensions: 12 x 12 mm
- Test sample disc dimensions: ϕ30, 10-20 mm thickness

In addition to the average coefficient of friction and wear coefficient, each wear profile of the test samples was analysed based on the effect on the coating (e.g. worn through), wear track appearance (e.g. consistency of track width, wear and debris formation) and static stainless steel ball. Microscopy analysis was used to inspect the wear tracks and relevant micrographs. A wear test parameter set was thereafter identified and used for the following wear tests (Stage 2).

Stage 2: Wear tests
The identified parameter set was then fixed for all further wear tests. The aim of which was to compare the wear resistance of the various developed coatings. Wear test data analysis was used as a means of characterising the coatings as well as investigating various wear and surface topographical relationships. The results are included in both Chapter 5 and Chapter 7.

3.4 Antimicrobial susceptibility testing

As discussed in the literature survey regarding the modes of pathogenic transmission, there are three modes of exogenous infection transmission, namely: contact spread, droplet spread

and airborne spread. To investigate the antimicrobial efficacy of the developed coatings against potential nosocomial infections two environmental conditions were used. These were contaminated wet and dry contact environments, encompassing all three modes of infection transmission from the perspective of surface contamination. For example droplet spread may be realised as a wet sneeze or cough with respiratory droplets landing on surrounding surfaces or via contaminated droplets indirectly transferred to surfaces from used tissues or from a hand that was sneezed into. These subsequent surfaces are then termed *wet contact surfaces*. Similarly contaminated *dry contact surfaces* may be a consequence of dried wet surfaces, the settling of airborne contaminants or simply from contact with an infected object or body (touch-contact transmission, from someone touching a door handle, for example).

Based on the findings of the European Centre for Disease Prevention and Control's study, conducted over 2011 and 2012 [17] and the list of highly prevalent nosocomial infections termed the ESKAPE pathogens, the following pathogens, from the American Type Culture Collection (ATCC), were selected and used as the standard test pathogens throughout this research.

Gram-positive strains

1. *Staphylococcus aureus* (ATCC 25923)
2. *Enterococcus faecalis* (ATCC 29212)

Gram-negative strains

3. *Pseudomonas aeruginosa* (ATCC 27853)
4. *Klebsiella pneumoniae* (ATCC 13887)

Yeast

5. *Candida albicans* (ATCC 10231)

The research also set out to investigate antimicrobial efficacy against resistant strains. Of the five standard pathogens one of each pathogen type was selected and a resistant strain sourced. The following resistant strains were subsequently used.

1. Gentamicin-methicillin-resistant *Staphylococcus aureus* (ATCC 33592).
2. Azlocillin-carbenicillin-resistant *Pseudomonas aeruginosa* from the German collection of micro-organisms and cell cultures at the Leibniz Institute (DSM 46316) - Also referred to as the reference *Pseudomonas aeruginosa* strain.

3. Fluconazole-resistant *Candida albicans* from the University of the Witwatersrand, Faculty of Health Sciences, Department of Clinical Microbiology and Infectious Diseases (Wits *C. albicans* 4122) - Also referred to as the clinically resistant *Candida albicans*.

As part of the experimental design both positive and negative controls were included. Positive controls, being those test samples which exhibit a known and expected *positive* antimicrobial response, were comprised of the antimicrobial metals, copper and zinc[vii] and the following antimicrobial agents: Ciprofloxacin (5 μg), Nystatin (100 μg) and Amphotericin B (0.1 mg/ml). Ciprofloxacin is an antibiotic, while Nystatin and Amphotericin B are anti-fungal agents. The negative controls, in which no response is the expected outcome (besides the influence of noise factors), were made up of uncoated substrates of the polymeric materials and stainless steel. The use of stainless steel was two-fold: firstly as a negative control, due to its innate inert properties, and secondly because stainless steel is a common and widely used material within the hospital environment and would provide an ideal point of comparison. The specific list of equipment and consumables may be found in Appendix D.

The following sections detail the experimental procedures conducted for effective antimicrobial susceptibility testing of the developed surface coatings.

3.4.1 Diffusion assay

A diffusion assay, based on the principles of a Kirby-Bauer antibiotic test as given in the *Manual of Antimicrobial Susceptibility Testing* [185], was developed to evaluate the antimicrobial efficacy of the coatings, quantified by the extent of inhibition surrounding such a coating when in contact with a culture-seeded agar plate. The extent of inhibition is proportional to the diffusive efficacy of the antimicrobial agent against the test pathogen, such that the larger the zone of inhibition, the greater the diffusive antimicrobial efficacy.

The procedure was based on the six key procedural steps depicted in Figure 3.7, from agar plating through to the measurement of zones of inhibition. Agar plates and the culture inoculates were prepared according to the standard disc diffusion test procedure. McFarland's standard suspension was spread evenly over the agar plates and test samples were placed coating side down onto the agar, ensuring adequate separation avoiding overlapping zones of inhibition. Following incubation the zones of inhibition were measured from the edge of the test samples to the extent of inhibition.

[vii] The zinc positive controls took the form of galvanised steel.

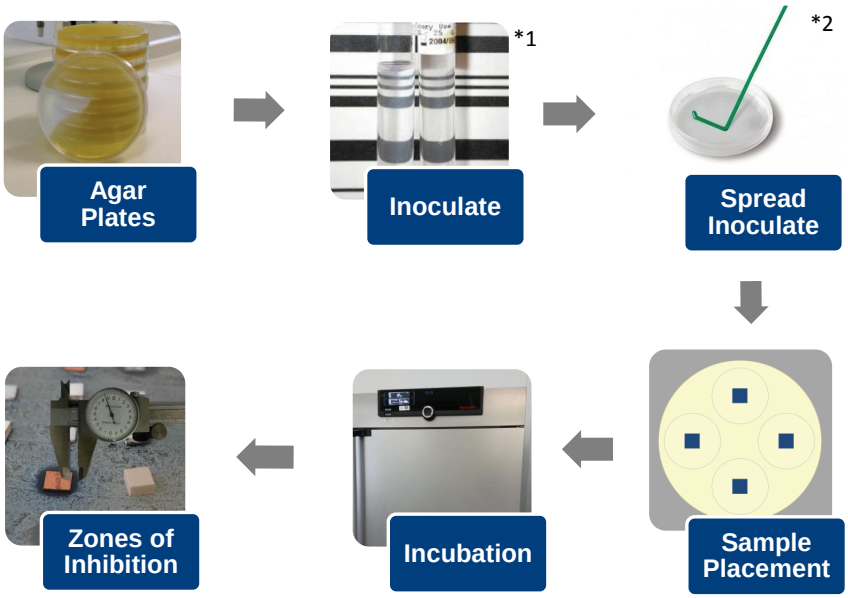


Figure 3.7: Diffusion assay procedural flow chart (*1 [185] *2 [186]).

The collated results were analysed as a means of evaluating the efficacy against the various pathogens (both powders and coatings), investigating possible synergistic activity and potential pathogenic susceptibility to developing resistance.

3.4.2 Dry contact test

A dry contact time-kill assay was designed to simulate touch-contact activity. The procedure was based on the Environmental Protection Agency's *Protocol for the Evaluation of Bactericidal Activity of Hard, Non-porous Copper Containing Surface Products* (2016) [187]. A culture suspension of approximately a million colony forming units was spread onto a test sample surface, incubated at room temperature, then neutralised in a saline solution after a pre-determined contact period (0.5, 5, 10, 15, 20, 60 and 180 minutes). Serial dilutions, agar plating, incubation and viable colony counts followed. Each test sample had an identical surface of 12 x 12 mm.

Figure 3.8 depicts an annotated graphical representation of the test method employed. Pre-trials showed two, consecutive serial dilutions to be sufficient for an effective colony count. OpenCFU, as an open source colony counting software, was employed as a means of ensuring accurate and consistent colony counts were achieved. The colony counts were, however, validated through manual counts. The final quantified data was then presented as the geometric mean CFU/ml present at each respective time period.

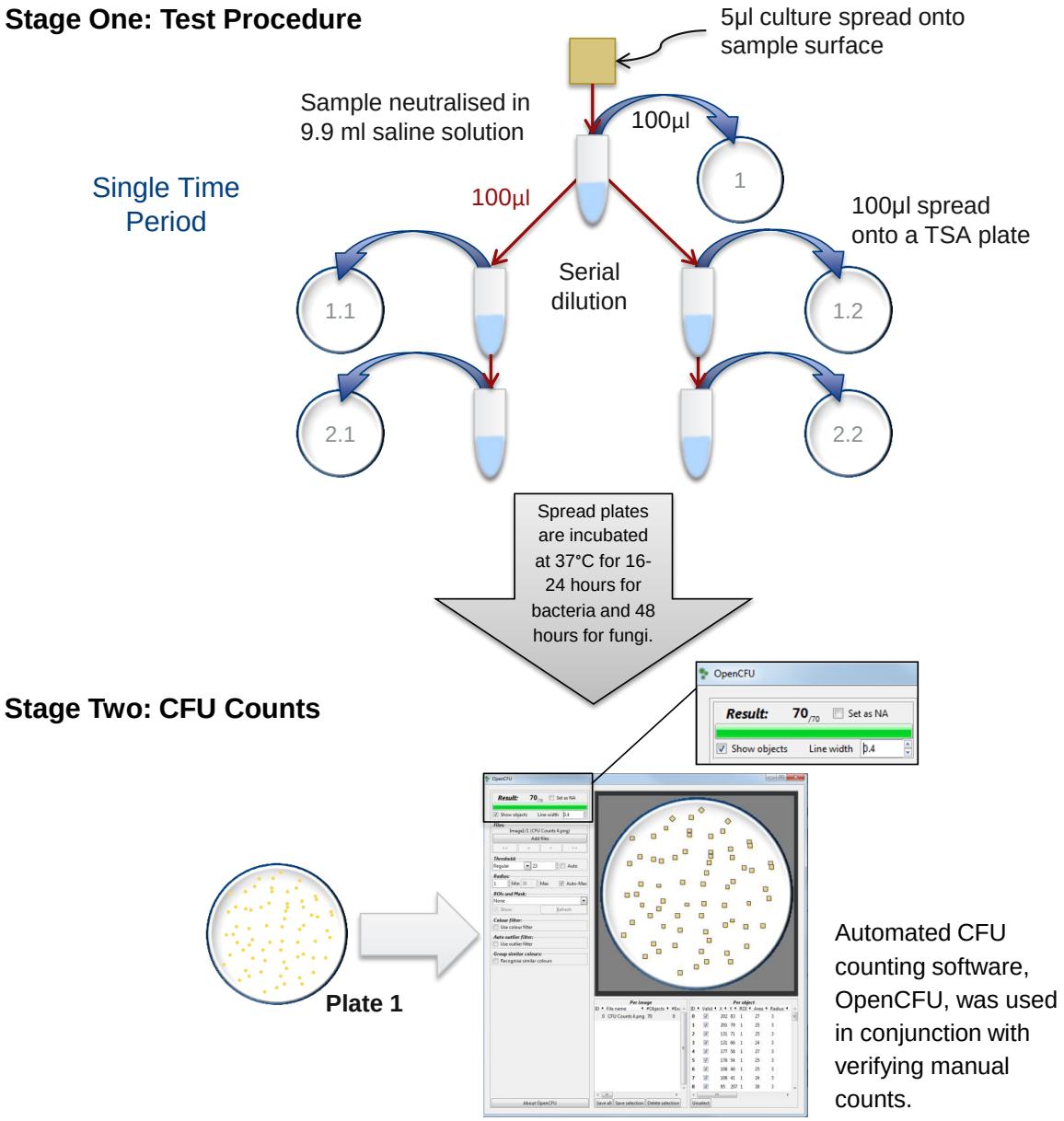


Figure 3.8: Annotated graphical representation of the dry contact test procedure.

Linear regression modelling was used to evaluate the dry contact test results. The antimicrobial reduction rate (m_{ar}), given by Equation 3.11 and with units $\log_{10}$(CFU/ml)/min, was defined as the relative antimicrobial rate of a coating material (m_{ts}) compared to the response of a stainless steel control (m_{ss}). The larger the antimicrobial rate, the faster microbial reduction takes place; which, therefore, represents a sample of higher antimicrobial efficacy.

$$m_{ar} = m_{ts} - m_{ss} \tag{3.11}$$

The antimicrobial rate of the stainless steel samples, while not indicative of active antimicrobial ability from the metal, is representative of system noise, which subsequently affects the antimicrobial rate. These noise factors include, but are not limited, to: plating stress, environmental conditions and volume loss during sample inoculation. The suitability of a regression model may be assessed by determining the coefficient of determination (R^2).

3.4.3 Prototype testing

As a means of drawing all research elements together and to provide a tangible example of a specific niche of application, antimicrobial mobile device covers (cell phones, tablets, slates) were considered as a means to showcase this material coating method. In addition antimicrobial pens and security access cards were included in the prototype trials. These prototypes are depicted in Figure 3.9[viii]. All three were manufactured via 3D printing and coated with one, or a combination, of the developed cold spray coatings. Test controls of uncoated 3D printed ABS test pieces, were included in the prototype experimental designs.

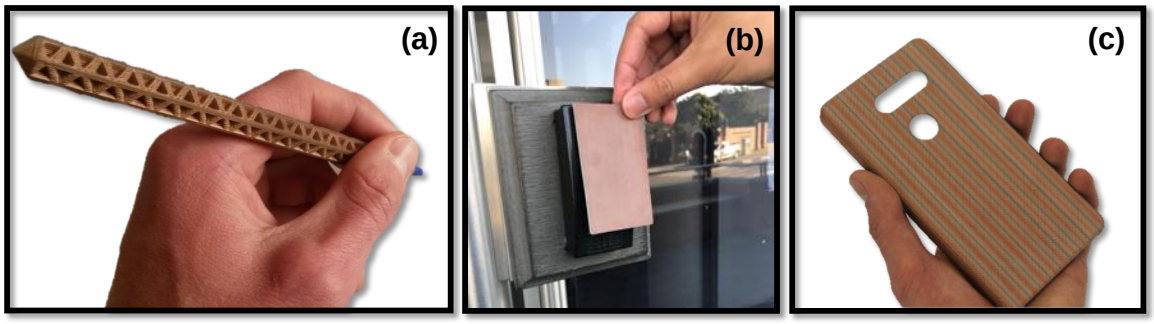


Figure 3.9: Antimicrobial cold spray coating prototypes with 3D printed substrate designs (a) pen, (b) security access cards, (c) smartphone cover.

Prototype 1 - 3D printed antimicrobial cold spray coated pen casing
The first prototype, that of a 3D printed and cold spray coated pen casing was used in a longitudinal cohort study, along with cold spray coated keyrings, investigating the long term durability of the developed coatings. This involved using the pen in daily writing tasks, in different environments and situations and then commenting on any observed changes over a period of at least a year (min. 12 months). The results represent a qualitative assessment of the combination of cold spray metal coatings on 3D printed ABS substrates.

Prototype 2 - 3D printed antimicrobial cold spray coated security access cards
An investigation into the efficacy of the antimicrobial security access cards was carried out. The tests were performed as part of the requirements for a Bachelor of Pharmacy by a team

[viii] The CAD designs for the pen housing and smartphone cover were obtained from Thingiverse.com

of final year Honours students at the University of the Witwatersrand's Medical School[ix]. Assistance and research coordination was provided by Professor Sandy van Vuuren and Michael Lucas.

Over a seven day period these coated cards, along with the necessary controls, were exposed to a number of healthcare related environments, including: the Charlotte Maxeke Johannesburg Academic Hospital (patient bedside tables, patient bathrooms), primary healthcare clinics, pharmacies, public spaces within the University of the Witwatersrand (cafeteria, lecture theatres, bathrooms and computer labs) as well as the card scanners in and around the medical school campus of the university.

Three coating types were tested - covering the broad range of developed materials. These coatings were all applied to 3D printed security access cards. The coatings were: a copper coating, a zinc coating and a 50:50 wt% copper-zinc blended coating.

Following the seven day exposure period swabs of the cards were taken and streaked onto blood agar plates. One batch was incubated for 24 hrs at 37°C to check for bacterial contamination, while a second batch were incubated for 48 hrs at 25°C to test for fungal contamination. The viable CFUs were quantified following incubation.

Prototype 3 - 3D printed antimicrobial cold spray coated smartphone cover
As a more rigorous test of coating efficacy in a practical environment a longitudinal contamination pilot study was conducted within the context of determining contamination in an active microbiology laboratory.

A specially designed copper and zinc cold spray patterned smartphone cover was devised. Design began with an idea, realised as a drawing and CAD model. The CAD model was then translated into an STL file format and layer slicing carried out. The 3D printer builds layer by layer and so the software sliced the CAD model into individual build layers. Each layer was set at a quarter of a millimetre thick. The 3D printing software (CatalystEX 4.4) creates tool paths for both the model material and the water soluble support material. The design was then ready for 3D printing. The 3D printer starts by laying down a support raft for the model to be built on and easily removed later. The subsequent layers are built, alternating between model and support material. In less than two hours a unique 3D printed smartphone cover emerges. The cold spray process was then conducted for the key polymer metallisation step. The process of developing the antimicrobial smartphone cover is depicted in Figure 3.10.

[ix]The team members were: Previn Ramiah, Nibha Ramkelwan, Eemaan Cohen, Usamah Dhaddabai, Maheela Moosa, Azraa Majid, Abu Bakr Nana.

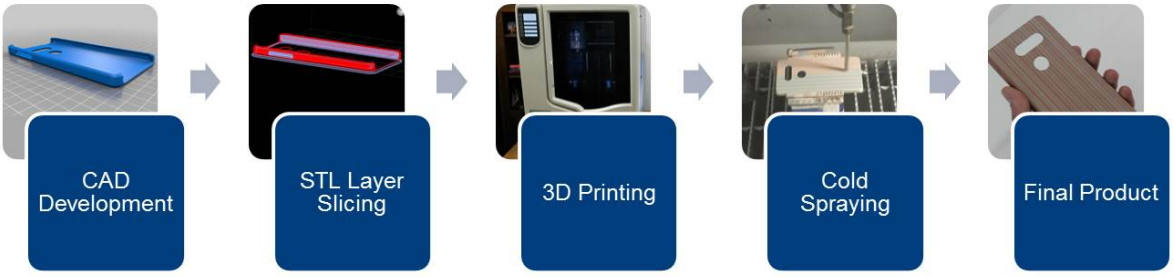


Figure 3.10: Design and manufacturing process for an antimicrobial 3D printed smartphone cover, employing effective polymer metallisation via cold spray.

A lab technician working in the department of Pharmacy and Pharmacology at the University of the Witwatersrand, was asked to use this 3D printed and cold spray coated smartphone cover on her smartphone over the course of three weeks. Over this time the smartphone was used as normal, with no additional washing or sterilisation.

For five days every week (Monday to Friday) the phone was sampled for microbial contamination. Samples were swabbed at the same time every day from the coated side of the cover as well as from the following three control sites: the smartphone screen, the inside surface of the cover and the back of the smartphone. The swabs were then spread over sterile agar plates and incubated. Sampling was conducted in duplicate, for both bacterial and fungal contamination analysis. Incubation set out to target both bacterial growth, by incubating at 37°C for 24 hrs; and fungal contamination, by incubating at 25°C for 48 hrs.

The results were analysed according to: (1) Overall microbial contamination on coated and control surfaces respectively, (2) Contamination trends over the course of a week, commenting on contamination levels on specific days, (3) Smartphone surfaces, as a means of the identifying the surfaces of a smartphone (screen, phone casing and phone protective casing) most prone to contamination. This data would then be used to propose design modifications for enhanced antimicrobial protection.

The results of the prototype tests would not only offer a means of technology validation, but would be used to aid future designs and potentially prompt further clinical trials, taking the technology forwards toward commercial viability.

Chapter 4 Theoretical Cold Spray Modelling

"*Bumba* - the act of moulding, shaping and creating"

From *Melusi's Everyday Zulu*, Melusi Tshabalala (2018)

As a means of understanding and fully utilising a piece of technology, such as cold spray, theoretical modelling becomes a useful tool. The structure of a theoretical framework, provided by successful interpretation and translation of a phenomenon or process using fundamental principles, affords traceable analysis and optimisation capabilities for that process. In pursuit of addressing and subsequently reducing the uncertainty in cold spray parameter selection, theoretical modelling was identified as an applicable means to instil experimental confidence. This was particularly relevant for cold spray polymer metallisation - a growing branch of cold spray technology - and a fundamental component of this research.

Therefore, the theoretical modelling of the cold spray system, as a means of achieving successful polymer metallisation, required the simplification of the complex system it represents into known theoretical terms. The model was to represent the conditions during the cold spray process as well as predict the physical outcome, with regards to coating deposition. The theoretical model was therefore designed as an optimisation tool for the cold spray process. The model itself is an algorithm for predicting the depth-of-penetration of cold spray particles into a polymer substrate, which was coupled with a Taguchi optimisation methodology.

4.1 Mathematical cold spray algorithm

The mathematical cold spray model was divided into six modular components. A distinction needs to be made with regards the theoretical cold spray modelling methods and the developmental process. Chapter 3 provides the general method employed for the design of a theoretical cold spray model. This chapter applies this method to a developmental process, which aimed to produce an efficient and effective cold spray algorithm and eventual Python programmed model. Model refinement was made throughout the research process and so the

final version presented here drew on the results from all aspects of the research. Previous model versions were therefore used to achieve the later detailed cold spray coatings, which in turn helped inform this final mathematical algorithm presented here.

① **Model initialisation and setup**
This section of code includes any mathematics that needed to be imported and any additional software packages that were required.

② **Model nomenclature**
A list of all variable names was included within this part of the code. The nomenclature was divided into two parts: those called within model functions and those used within the main algorithm.

③ **System constants**
Definitions of all system constants was defined in this section including the definition of material properties of the spray gas, spray powder and substrate materials.

④ **Parameter limitations**
Parameter limitations were enforced, including: cold spray equipment limitations, cold spray powder and substrate material limitations, as well as other system limitations.

⑤ **Called functions**
A modular program was devised therefore requiring clear definition of independent functions. The creation of standalone functions afforded an efficient algorithm structure and sufficient model verification, while aiding model adaptability.

⑥ **Model algorithm**
All main procedural steps were coded into this section. It was from this platform that the independent functions were selectively called.

The model algorithm is presented in detail below, yet additional information and modular components (for example the called functions) may be found in Appendix A.

4.1.1 Algorithm flow diagram

The model algorithm covered the three key sections of: nozzle calculations, gap calculations and particle-substrate interactions. Refer to Figure 4.1 which depicts a high order flow chart representing the model breakdown.

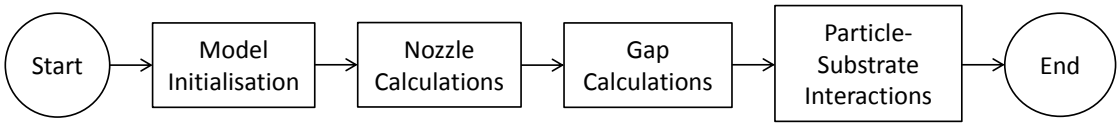


Figure 4.1: High order flow chart of the theoretical cold spray model algorithm.

4.1.2 Cold spray model algorithm

What follows is a mathematical model developed in response to the hypothesis: *Mathematical modelling, using spray particle depth-of-penetration as the key discriminating criterion, is able to accurately predict cold spray parameter set effects.*

The mathematical and conceptual elements of the algorithm are based on the findings from the literature survey, specifically the section dealing with theoretical cold spray modelling. Nozzle calculations were based on an isentropic, ideal, 1D gas dynamic model, assuming a one-way coupling scenario comprised of dilute particle entrained flow, whereby the particles themselves have negligible effect on the gas flow as well as maintaining sufficient particle spacing thus preventing any particle-particle interactions. This assumption was justified based on the low experimentally calculated particle volume fraction of 10^{-5}, which is well below the conservative threshold criterion of 10^{-4} [142, 149]. Particle flow dynamics, as part of the one-way coupling analysis, made use of drag analyses. Gap effects took into account supersonic nozzle exit flow phenomena and bow shock formation, and finally substrate effects were considered with regards to impinging particle depth-of-penetration.

Steps 1 to 5 of the model, given in Figure 4.2, relate to model initialisation. It is from this point in the model that initial estimates for the process parameters are introduced, either by means of the later discussed Taguchi Method or selected by the model user as a specific test case. All other properties, conditions and constants are defined here as well.

Step 1: Define fixed parameters and initial parameter estimates
While certain process parameters are defined at this step, their precise value may change. This model was developed to act as both a quick check system as well as a sub-procedure for parameter set optimisation. The model, therefore, enforced design and system constraints aimed at ensuring viable and ultimately effective cold spray deposition.

Fixed parameters
The spray gas and nozzle geometry (including the specification of: throat diameter (D^*), exit diameter (D_e) and diverging length (L)) remain fixed throughout a specific theoretical coating operation. It is to be noted that while the theoretical model has no restrictions with regards to physical geometry, thus extending its scope of use, for this current study the

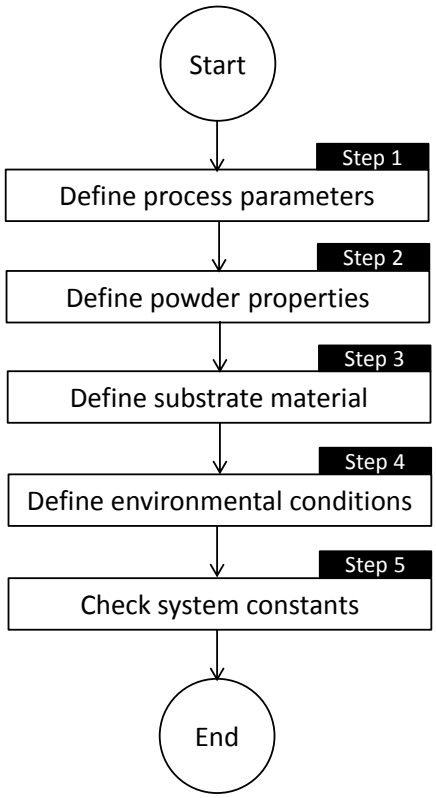


Figure 4.2: Cold spray theoretical model initialisation steps.

coupled experimental methods did restrict geometry to a specific cold spray nozzle design ($D^* = 2.5$ mm, $D_e = 6.5$ mm and L = 120 mm).

Initial (variable) parameters
Operating pressure (P_0), operating temperature (T_0), nozzle standoff distance (SOD) and the nozzle traverse speed (V_n) are subject to change, as dictated by the model algorithm and associated optimisation procedure.

Step 2: Define powder parameters
The feedstock cold spray powders were defined according to the material (e.g. copper), the fixed average particle size, regarded as the average diameter of a spherical body (d_p), and the initial particle temperature (T_p).

Step 3: Define substrate material
In a similar way to the powder properties, the substrate properties were defined according to the substrate material (e.g. ABS) and initial temperature (T_s).

Step 4: Define environmental conditions
The model was designed to incorporate and account for the environmental conditions of ambient temperature (T_{amb}) and ambient pressure (P_{amb})

Step 5: Check system constants

The typical cold spray working fluids include air, nitrogen and helium. For the purpose of this current study the model was built around a system with air as the working fluid. The relevant properties for the working fluid, spray powders and target substrates are defined according to the following.

- Ratio of specific heat (γ)
- Universal gas constant ($\overline{R}$)
- Molar mass of gas (M_m)
- Viscosity at reference temperature (μ_{ref})
- Reference temperature (T_{ref})
- Sutherland's Law constant (S')
- Non-dimensionalised impactor length (L/D)
- Substrate material Young's Modulus (E)
- Ultimate tensile strength (σ_{UTS})[i]
- Brinell hardness (B)[ii]
- Thermal conductivity of the gas (k_g)
- Spray powder thermal conductivity (k_p)

The model was designed to be used in conjunction with experimental analysis, both before and after cold spraying. The accuracy of model constants and properties may, therefore, be subject to that of the experimental methods used.

Nozzle calculations

Developmental steps 6 to 11 are concerned with evaluating and monitoring the flow and particle conditions within the cold spray nozzle system. The determination and compliance with the operating pressure threshold as well as the 1D gas dynamics and particle dynamics are the key techniques of analysis in this section. Figure 4.3 depicts the flow chart used for the nozzle calculation analysis in the model algorithm.

With reference to Figure 4.3 and based on the cold spray equipment limits for operating pressure there exists a global minimum (P_{0-min}) and global maximum (P_{0-max}). In order to ensure safe and viable running of the cold spray equipment, these limits must be adhered to. Additionally, based on the requirement of supersonic exit flow the system specific threshold stagnation pressure ($P_{0-threshold}$) must be exceeded.

[i] The UTS of both the spray powders and substrate materials were collated.

[ii] The Brinell hardness of both the spray powders and the substrate materials were collated.

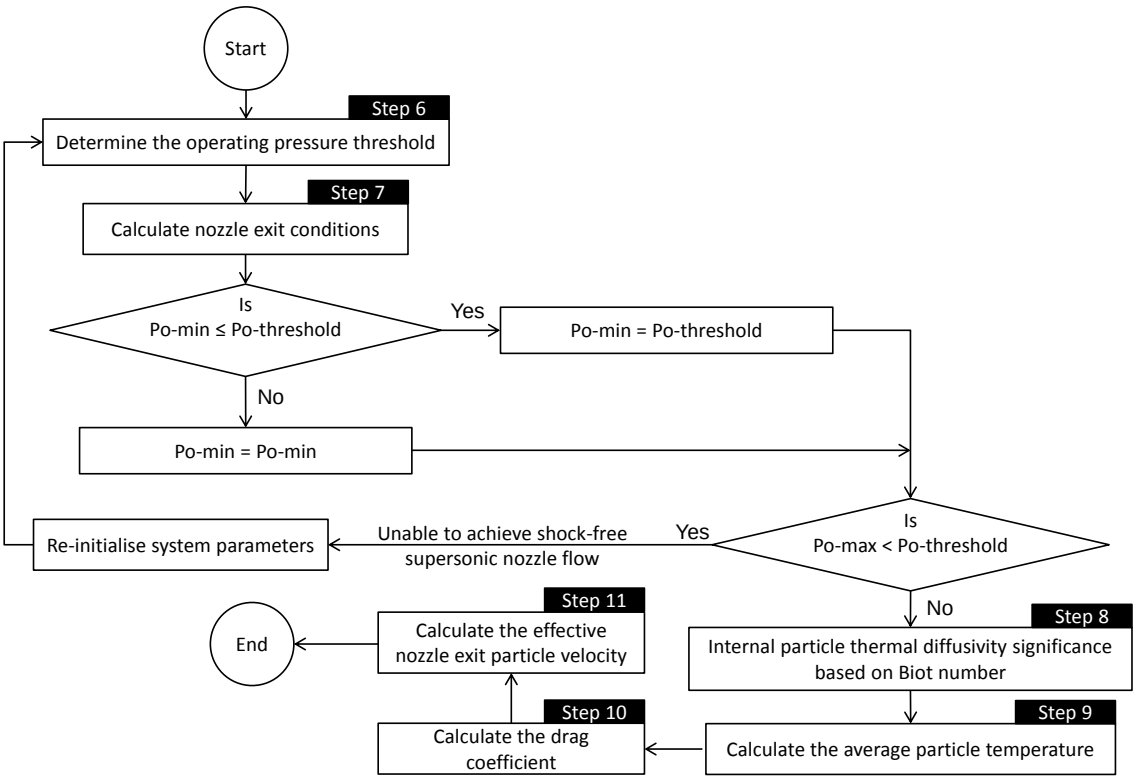


Figure 4.3: Flow chart of nozzle calculations for the theoretical cold spray model.

Step 6: Determine the operating pressure threshold

The stagnation pressure threshold ($P_{0-threshold}$) for a converging-diverging nozzle system is based on the limiting case of a normal shock wave at the nozzle exit. The operating pressure (P_0) for effective cold spraying must exceed that pressure which induces a shock at the nozzle exit; such that purely supersonic flow is present in the diverging section of the nozzle. The operating pressure threshold is not, however, a target or desired pressure. It merely provides a preliminary system check for viable cold spray operation, based on a pre-selected operating pressure.

6.1 Calculate the nozzle throat area (A*).

Called Function[iii]: *#1 - Circular Area*
Parsed Variable: Nozzle throat diameter (D*)
Returned Value: A*

6.2 Calculate the nozzle exit area (A_e).

[iii]The designation *Called Function* refers to the modular elements of the programmed algorithm. The called functions may be found in Appendix A under Called functions.

Called Function: *#1 - Circular Area*
Parsed Variable: Nozzle exit diameter (D_e)
Returned Value: A_e

6.3 Calculate the bulk averaged supersonic nozzle exit Mach number (M_e).

In order to calculate the supersonic nozzle exit Mach number an iterative approach was employed using Newton's fixed point root finding method[iv]. The gas flow Mach number, as a function of the nozzle area ratio, is given by Equation 4.1 assuming a perfect gas and isentropic flow conditions [147].

$$M_e = \frac{A*}{A_e}\left[\left(\frac{2}{\gamma+1}\right)\left(1+\frac{\gamma-1}{2}M_e^2\right)\right]^{\frac{(\gamma+1)}{(2\gamma-2)}} \tag{4.1}$$

An initial estimate of the exit Mach number is made using Equation 4.2 [189], where k_1 and k_2 are dependent on the ratio of specific heat and may be expressed by Equation 4.3 and Equation 4.4 [189], respectively[v].

$$M_{e-approx} = \left(k_1 \times \frac{A_e}{A*} + (1-k_1)\right)^{k_2} \tag{4.2}$$

$$k_1 = 218.0629 - 243.5764\gamma + 71.7925\gamma^2 \tag{4.3}$$

$$k_2 = -0.122450 + 0.2813\gamma \tag{4.4}$$

Called Function: *#22 - Newton's root finding method*
Parsed Variables: $M_{e-approx}$, $f(M_e)$, $f'(M_e)$
An initial guess for the value of the nozzle centreline exit Mach number ($M_{e-approx}$), an expression for nozzle centreline exit Mach number ($f(M_e)$), where $f(M_e) = 0$, and the first derivative ($f'(M_e)$).
Returned Value: (M_e)

Stepwise Method Derivation

Newton's fixed point root finding method is used a number of times in this algorithm and so as a means of clarifying its use a sample derivation for the calculation of the nozzle exit Mach number (M_e) is presented.

[iv] Alternative approaches to evaluating the nozzle exit Mach number include a trial-and-error approach or with the use of isentropic flow tables [148]. Neither method is appropriate for the Python algorithm and so a structured iterative approach was employed.

[v] Analysis is kept to three significant figures

Referring to the called function in Appendix A on page 327, Equation 4.5 represents Newton's fixed point root finding method.

$$x_{i+1} = x_i - \frac{f(x_i)}{f'(x_i)} \tag{4.5}$$

Here the variable x represents the nozzle exit Mach number M_e, such that the initial $f(x_i) = f(M_{e-approx})$. Therefore, in order to get the function in the form $f(M_e) = 0$, based on the expression for M_e given by Equation 4.1, requires the following:

$$0 = \frac{A*}{A_e}\left[\left(\frac{2}{\gamma+1}\right)\left(1+\frac{\gamma-1}{2}M_e^2\right)\right]^{\frac{(\gamma+1)}{(2\gamma-2)}} - M_e$$

$$0 = \left[\left(\frac{2}{\gamma+1}\right)\left(1+\frac{\gamma-1}{2}M_e^2\right)\right]^{\frac{(\gamma+1)}{(2\gamma-2)}} - \frac{A_e}{A*}M_e$$

This is of the form $(a + bM_e{}^2)^c - dM_e = 0$ such that $f(M_e) = (a + bM_e{}^2)^c - dM_e$
$\therefore f'(M_e) = 2bc(a + bM_e{}^2)^{c-1} \cdot M_e - d$

Therefore based on the expression for Newton's fixed point root finding method given above:

$$f(x_i) = \left[\left(\frac{2}{\gamma+1}\right)\left(1+\frac{\gamma-1}{2}x_i^2\right)\right]^{\frac{(\gamma+1)}{(2\gamma-2)}} - \frac{A_e}{A*}x_i$$

$$f'(x_i) = \left(\frac{2}{\gamma+1}\right)\left(1+\frac{\gamma-1}{2}x_i^2\right)^{\frac{-\gamma+3}{2\gamma-2}} \cdot x_i - \frac{A_e}{A*}$$

These expressions are now ready to be applied to Equation 4.5, using $M_{e-approx}$ as the initial guess, x_i. The resulting x_{i+1} is fed back into Equation 4.5 until the difference between x_i and x_{i+1} is negligibly small ($\approx 10^{-3}$[vi]). The last value for x_{i+1} then becomes the value for the nozzle exit Mach number (M_e) for the given system parameters.

6.4 Assume a normal shock is present at the nozzle exit with a back pressure (P_y), equal to the ambient pressure (P_{amb}), and with a Mach number upstream of the shock (M_x), equal to the previously calculated nozzle exit Mach number (M_e).

6.5 Calculate the gas pressure (P_x) upstream of the normal shock at the nozzle exit.

[vi] Maintaining three significant figures in the calculation steps.

$$P_x = \frac{P_y}{1 + \frac{2\gamma}{(\gamma+1)}({M_x}^2 - 1)} \tag{4.6}$$

6.6 Calculate the threshold stagnation pressure ($P_{0-threshold}$).

$$P_{0-threshold} = P_x \left[1 + \frac{(\gamma-1)}{2}{M_x}^2\right]^{\frac{\gamma}{(\gamma-1)}} \tag{4.7}$$

This threshold pressure is not a target pressure by any means, merely a system viability check. In reality the operating pressure needs to exceed this theoretical value by such a degree so as to account for friction losses in the pipe, which are not fully incorporated in the theoretical analysis presented here.

Step 7: Calculate nozzle exit conditions

Once the boundary conditions of stagnation pressure have been fully defined the nozzle exit gas conditions may be calculated, assuming 1D gas flow [147, 148]. This involves calculating the temperature, pressure, density and velocity at the nozzle exit.

7.1 Defining the allowable operating pressure range.

The parameter limitations (found in Appendix A - Page 323) include a set global minimum (P_{0-min}) and maximum (P_{0-max}) operating pressure. These are based on the performance of the cold spray equipment. These global parameter limitations are compared with the threshold stagnation pressure $P_{0-threshold}$ previously calculated. The following is enforced:

- If $P_{0-min} \leq P_{0-threshold} \Rightarrow P_{0-min} = P_{0-threshold}$
- If $P_{0-min} > P_{0-threshold} \Rightarrow P_{0-min} = P_{0-min}$
- If $P_{0-max} < P_{0-threshold} \Rightarrow$ Unable to achieve supersonic flow.

7.2 Ensure the selected operating pressure complies with the allowable operating range, based on the aforementioned re-allocations:

$$P_{0-min} < \mathbf{P}_0 < P_{0-max}$$

7.3 Ensure the user selected operating temperature[vii] lies within the allowable operating range as defined by the cold spray equipment parameter limitations and feedstock powder limitations.

[vii] For the case of a user specific cold spray parameter set, as opposed to the Taguchi Method optimisation add-on made available for this Python program, which is designed to optimise the selection of the key cold spray process parameters.

$$T_{0-min} < \mathbf{T}_0 < T_{0-max}$$

7.4 Calculate the specific gas constant (R)[viii].

Called Function: *#3 - Specific Gas Constant*
Parsed Variables: $\overline{R}$, M_m
Returned Value: R

7.5 Calculate the nozzle bulk averaged stagnation density (ρ_0).

Called Function: *#4 - Ideal Gas Law*
Parsed Variables: P_0, T_0, R
Returned Value: ρ_0

7.6 Calculate the nozzle bulk averaged exit pressure (P_e).

$$P_e = \frac{P_0}{\left[1 + \frac{(\gamma - 1)}{2} {M_e}^2\right]^{\frac{\gamma}{(\gamma - 1)}}} \tag{4.8}$$

7.7 Calculate the nozzle bulk averaged exit temperature (T_e).

$$T_e = \frac{T_0}{1 + \frac{(\gamma - 1)}{2} {M_e}^2} \tag{4.9}$$

7.8 Calculate the nozzle bulk averaged exit density (ρ_e).

$$\rho_e = \frac{\rho_0}{\left[1 + \left(\frac{(\gamma - 1)}{2}\right) {M_e}^2\right]^{\frac{1}{(\gamma - 1)}}} \tag{4.10}$$

7.9 Calculate the nozzle bulk averaged exit velocity (V_e).

Called Function: *#5 - Mach Number*
Parsed Variables: M_e, γ, R, T_e
Returned Value: V_e

[viii] This constant may be looked in an appropriate table to the required precision, yet for the purposes of a computer algorithm a calculation is appropriate.

Step 8: Internal particle thermal diffusivity significance based on Biot number
Using the Biot number, a decision regarding the influence thermal diffusivity has on a single spray particle was made. The Biot number is a measure of the relative importance of the thermal resistance within a solid body, expressed as the ratio of the internal to external thermal resistance [150]. The implications of high and low Biot numbers is depicted in Figure 4.4.

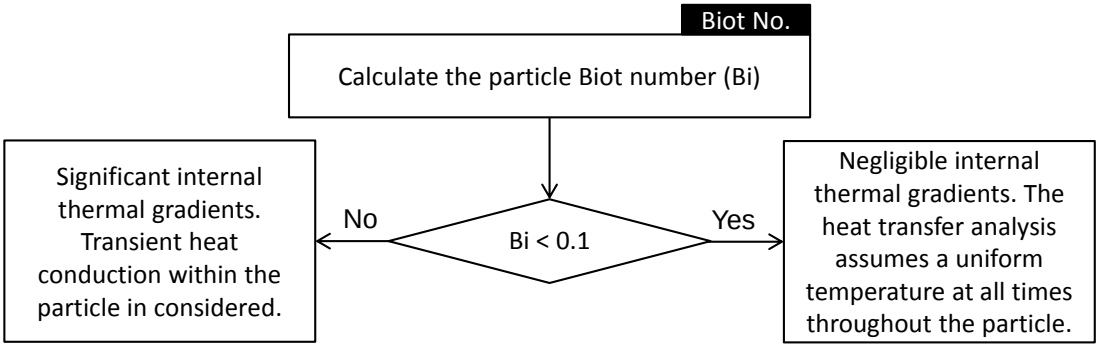


Figure 4.4: Implications of high and low Biot numbers with regards to internal thermal diffusivity of spray particles.

8.1 Determine the average convective heat transfer coefficient of an average spray particle (hc).

Considering a single, average spray particle the following was derived. An approximate value for the particle velocity ($V_{pe}{}'$) at the cold spray nozzle exit is given by Equation 4.11 [119,149].

$$V_{pe}{}' = \frac{V_{ge}}{1 + 0.85\sqrt{\frac{d_p}{L}}\sqrt{\frac{\rho_p {V_{ge}}^2}{P_0}}} \tag{4.11}$$

An approximate value for the relative Reynolds number is calculated based on a relative gas flow velocity ($\Delta V = |V_{ge} - V_{pe}{}'|$) and the average particle diameter (d_p), assuming a spherical spray particle.

Called Function: *#7 - Reynolds Number*
Parsed Variables: ΔV, d_p, ν_{ge}
Returned Value: Re_{dp}

The following condition was required to be met: $25 < \mathrm{Re}_{dp} < 10^5$[ix] [150]. Following which, the Nusselt number for the flow around the particle was calculated according to Equation 4.12 [150].

$$Nus_{dp} = 0.37 {Re_{dp}}^{0.6} \tag{4.12}$$

The heat transfer coefficient (hc) of the particle was thereafter determined.

Called Function: *#17 - Heat Transfer Coefficient for the Particle*
Parsed Variables: Nus_{dp}, k_p, d_p
Returned Value: hc

8.2 Calculate the powder particle Biot number (Bi).

Based on the average powder particle size (d_p) and the powder thermal conductivity (k_p) the associated particle Biot number was calculated. The characteristic length (L_c) required by Equation 4.13, is defined as the ratio of particle volume to its surface area. The characteristic length (L_c) is therefore equal to a sixth of the particle diameter.

$$\left(Bi = \frac{hc \cdot Lc}{k} \right) \tag{4.13}$$

Called Function: *#18 - Biot Number*
Parsed Variables: hc, L_c, k_p
Returned Value: Bi

8.3 Calculate the surface area of an average spray particle (As).

Called Function: *#19 - Surface Area of a Sphere*
Parsed Variables: d_p
Returned Value: As

8.4 Calculate the specific heat capacity at constant pressure (Cp).

Called Function: *#8 - Specific Heat Capacity at Constant Pressure*
Parsed Variables: γ, R
Returned Value: Cp

[ix] If Re_{dp} lies outside this range a suitable alternative expression for the Nusselt number may be used. Alternative expressions for the calculation of the Nusselt number may be found in the book *Principles of Heat Transfer*, by F. Kreith and M. Bohn [150]. This substitution approach is applicable to all similar equations limited by a given parameter range, unless otherwise stated.

The specific heat ratio γ is assumed constant, in agreement with the Perfect Gas Law. When air is used as the carrier gas for cold spray, as is the case in this current study, a constant value of $\gamma = 1.4$ is maintained.

8.5 Determine the significance of the thermal diffusivity of the spray particle [150].

- If Bi $< 0.1 \Rightarrow$ Negligible temperature variation within a spray particle.
- If Bi $\gg 0.1 \Rightarrow$ Significant temperature variation within a spray particle.

Step 9: Calculate the average particle temperature.

9.1 Calculate the surface temperature of an average spray particle at the nozzle exit (T_{pe}).

9.1 A - If Bi < 0.1

When the Biot number is less than 0.1 the spray particle experiences no internal thermal gradients and therefore has a uniform temperature throughout at any instant. [150]. A combined heat transfer equation was derived. The full derivation of the combined heat transfer equation may be found in Appendix A.

If the gas temperature at the nozzle exit (T_{ge}) is higher than the initial powder temperature (T_{p0}) - approximated by the ambient temperature (T_{amb}) - then the particle temperature is calculated via Equation 4.14, otherwise using Equation 4.15.

$$T_{pe} = T_{ge} - e^{\left(\frac{\overline{h_c} A_s L}{M_p C p V_{pe}{}'} + ln|T_{ge} - T_{p0}|\right)} \tag{4.14}$$

$$T_{pe} = T_{ge} + e^{\left(\frac{\overline{h_c} A_s L}{M_p C p V_{pe}{}'} + ln|T_{ge} - T_{p0}|\right)} \tag{4.15}$$

9.1 B - If Bi $\gg 0.1$

When the Biot number is greater than 0.1 the thermal diffusivity of the spray particle material needs to be taken into account. This was achieved by employing a transient heat transfer method using calibrated charts for a sphere. These charts, which represent the dimensionless transient temperatures and heat flow for a sphere, may be found on page 139 and 140 of the textbook *Principles of Heat Transfer* (6th Edition) by Frank Kreith and Mark Bohn. Under typical cold spray operating conditions the Biot number lies well below 0.1 and so a lumped capacity model is usually sufficient, yet this is included for completeness.

Step 10: Calculate the drag coefficient

The calculations for drag coefficient at the nozzle exit (C_{De}) were based on both the relative flow Reynolds number and the relative Mach number. Separate formulas exist for subsonic, *definite* supersonic and *just* supersonic relative flow.

10.1 Calculate the relative Mach number (M_{re}).

The relative velocity between the carrier gas and the spray particles, calculated using Equation 4.16, was used to evaluate the relative flow Mach number at the nozzle exit.

$$V_{e-rel} = |V_{ge} - V_{pe}{}'| \tag{4.16}$$

Called Function: *#5 - Mach Number*
Parsed Variables: V_{e-rel}, γ, T, T_{ge}
Returned Value: M_{re}

10.2 Calculate the kinematic viscosity (ν_e).

Called Function: *#6 - Sutherland's Law*
Parsed Variables: μ_{ref}, T_{ge}, $T_{ref-sutherland}$, S′
Returned Value: μ_e

$$\nu_e = \frac{\mu_e}{\rho_{ge}} \tag{4.17}$$

10.3 Calculate the relative flow Reynolds number (Re_{dp}).

Called Function: *#7 - Reynolds Number*
Parsed Variables: V_{e-rel}, d_p, ν_e
Returned Value: Re_{dp}

10.4 Evaluate the particle drag coefficient dependent on the prevailing flow regime, according to the value of the relative Mach number [13].

- Subsonic flow ($M_{re} < 1$) ⇒ Equation 4.19.
- Low supersonic flow ($1 < M_{re} < 1.75$) ⇒ Equation 4.20
- High supersonic flow ($M_{re} > 1.75$) ⇒ Equation 4.21.

where S is the molecular speed ratio, given by Equation 4.18 [13].

$$S = M_{re}\sqrt{\frac{\gamma}{2}} \tag{4.18}$$

$$\begin{aligned} C_{De} =& 24\left\{ Re_{dp} + S\left[4.33 + \left(\frac{3.65 - \frac{1.3T_{pe}}{T_{ge}}}{1 + \frac{0.353T_{pe}}{T_{ge}}}\right) \times e^{\left(-0.247\frac{Re_{dp}}{S}\right)}\right]\right\}^{-1} \\ &+ e^{\left(-\frac{0.5M_{re}}{\sqrt{Re_{dp}}}\right)}\left[\frac{4.5 + 0.38\left(0.03Re_{dp} + 0.48\sqrt{Re_{dp}}\right)}{1 + 0.03Re_{dp} + 0.48\sqrt{Re_{dp}}} + 0.1{M_{re}}^2 + 0.2{M_{re}}^8\right] \\ &+ \left[1 - e^{\left(-\frac{M_{re}}{Re_{dp}}\right)}\right] 0.6S \end{aligned} \tag{4.19}$$

$$\begin{aligned} C_{De}(M_\infty, R_{e\infty}) =& C_D(1.0, Re_{dp}) \\ &+ \frac{4}{3}(M_\infty - 1.0)\left[C_D(1.75, Re_\infty) - C_D(1.0, Re_\infty)\right] \end{aligned} \tag{4.20}$$

where:
$C_D(1.0,Re_{dp})$ ⇒ Drag coefficient for subsonic flow (Equation 4.19) [13].
$C_D(1.75,R_{e\infty})$ ⇒ Drag coefficient for high supersonic flow (Equation 4.21) [13].

$$C_{De} = \frac{0.9 + \frac{0.34}{{M_\infty}^2 + 1.86\left(\frac{M_\infty}{R_{e\infty}}\right)^{0.5}}\left[2 + \frac{2}{S^2} + \frac{1.058}{S}\left(\frac{T_{pe}}{T_{ge}}\right)^{0.5} - \frac{1}{S^4}\right]}{1 + 1.86\left(\frac{M_\infty}{R_{e\infty}}\right)^{0.5}} \tag{4.21}$$

where:
M_{ge} is the gas Mach number at the nozzle exit and Re_{ge} is the gas Reynolds number at the nozzle exit [13].

10.5 Apply the Cunningham Correction Factor (C_c).

The Cunningham correction factor was applied to the drag coefficient to account for minute spray particles that are of the order of magnitude of the gas mean free path length [190]. The applicability of the Cunningham correction factor is based upon the value of the Knudsen number, where a value exceeding 0.1 necessitates the use of the correction factor [190]. A

constant drag coefficient was assumed for this calculation[x], based on the nozzle exit conditions.

The mean free path length (λ), which describes the average distance between colliding molecules [147], was calculated. This term was then used in the calculation of the Knudsen number [190].

Called Function: *#11 - Mean Free Path Length*
Parsed Variables: μ_{ge}, ρ_{ge}, R, T_{ge}
Returned Value: λ

Called Function: *#12 - Knudsen Number*
Parsed Variables: λ, d_p
Returned Value: Kn

- If Kn $>$ 0.1 $\Rightarrow$ The Cunningham Correction factor is applied to the determination of the average drag coefficient.

Called Function: *#13 - Cunningham Correction Factor*
Parsed Variables: λ, d_p, C_{De}
Returned Value: C_{De}

Step 11: Calculate the effective nozzle exit particle velocity (V_{pe})
Based on the calculated particle temperature (T_{pe}) and the drag coefficient (C_D) at the nozzle exit plane, the effective nozzle exit particle velocity (V_{pe}) may be calculated. The effective particle velocity was derived by equating particle acceleration to drag force, as suggested by R.C. Dykhuizen and M.F. Smith [108]. The full derivation may be found in Appendix A. A root finding method was required to solve the resultant non-linear particle velocity equation. Newton's root finding method was selected.

The governing equation is given by Equation 4.22.

$$V_{pe} = \frac{V_{ge}}{ln\left|\frac{V_{ge} - V_{pe}}{V_{ge}}\right| - 1 - \frac{C_D A_p \rho_p L}{2 m_p}} + V_{ge} \tag{4.22}$$

Using the called function Newton's Root Finding Method and an initial guess ($V_{pe}{}'$) given by Equation 4.11 the effective nozzle exit particle velocity (V_{pe}) was determined.

[x] In reality the drag coefficient varies throughout the nozzle, dependent on Reynolds number and particle mass fraction.

Called Function: *#22 - Newton's Root Finding Method*
Parsed Variables: $V_{pe}{}'$, f(V_{pe}), f′(V_{pe})
Returned Value: V_{pe}

Where:

$$f(V_{pe}) = 0 = ln\left|\frac{V_{ge} - V_{pe}}{V_{ge}}\right| + \frac{V_{ge}}{V_{ge} - V_{pe}} - 1 - \frac{C_D A_p \rho_p L}{2m_p}$$

$$f'(V_{pe}) = \frac{V_{pe}}{(V_{ge} - V_{pe})^2}$$

Gap Calculations

Developmental steps 12 to 18, depicted in Figure 4.5, set out to evaluate the flow and particle dynamics within the spray gap. That is, critically analysing the conditions between the nozzle exit and the target substrate. Included is an evaluation of the bow shock effects. As part of the developmental process a submerged jet analysis was constructed, yet was unsuitable for the current model and so has been omitted here. A detailed background, model development and exclusionary explanation is included in Appendix A.

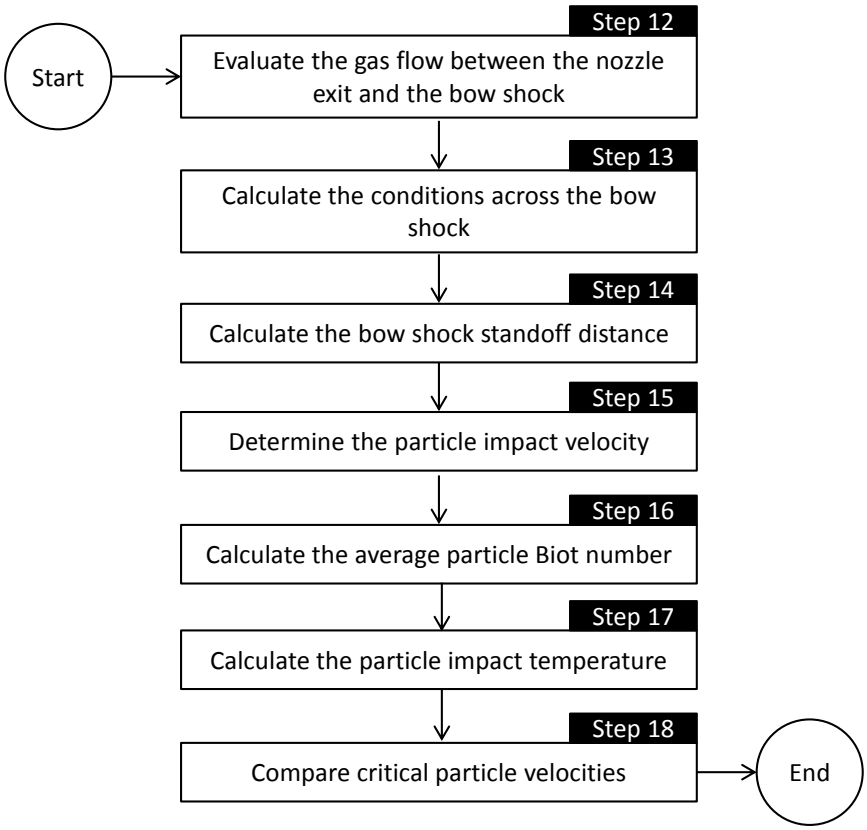


Figure 4.5: Flow chart of spray gap calculations between the nozzle exit and the target substrate for the theoretical model.

Step 12: Evaluate the gas flow between the nozzle exit and the bow shock

The gas flow conditions in the nozzle gap needed to be evaluated in order to be in a position to evaluate the particle impact conditions. Of importance was the determination of the flow conditions outside the nozzle. Depending on the relative operating pressure and the nozzle geometry the flow leaving the cold spray nozzle may be *overexpanded*, that is the nozzle exit pressure is below the ambient pressure and oblique shock waves result, or the flow may be at the *design condition*, where the nozzle exit pressure and the ambient pressure are equal and isentropic supersonic flow results, or the nozzle exit pressure may be greater than the ambient pressure leading to expansion waves from the nozzle exit, due to *underexpanded* flow conditions.

A bow shock develops in front of the substrate provided the jet remains supersonic. This is independent of the flow regime at the nozzle exit (underexpanded, overexpanded or at the design condition) [125] [90].

12.1 Evaluate the flow condition outside of the cold spray nozzle.

With reference to Figure 2.14 from the literature survey and Figure 4.6, the three possible flow conditions occurring outside of the cold spray nozzle may be (1) isentropic, shock-free supersonic flow, (2) an overexpanded jet with oblique shocks or (3) an underexpanded jet with resulting expansion waves.

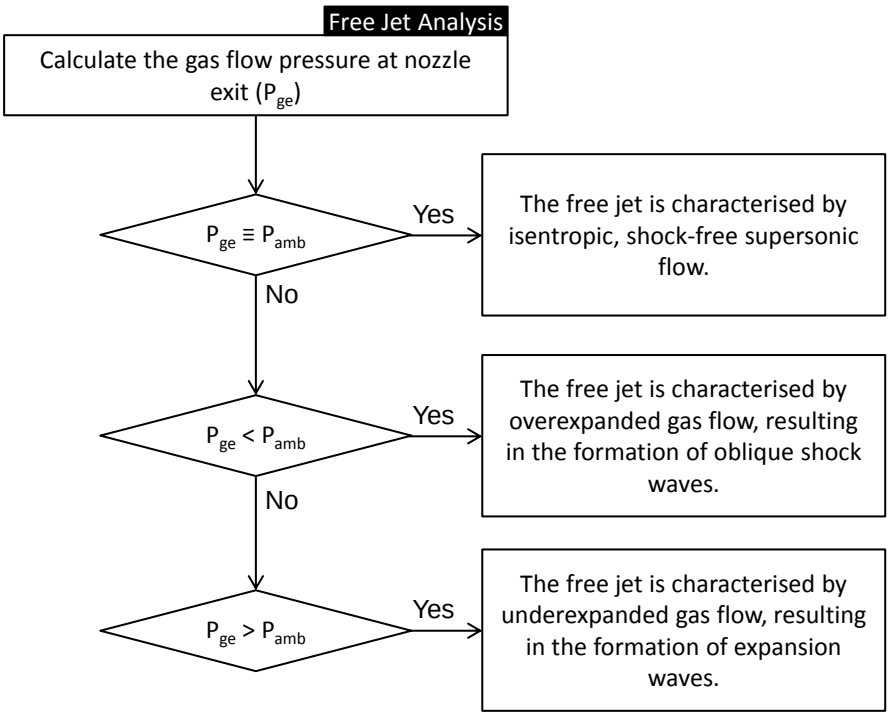


Figure 4.6: Nozzle exit flow regimes and the consequent free jet characterisation.

Once the flow regime outside the nozzle exit has been identified the specific flow conditions upstream of the bow shock may be calculated.

12.2 A - If $\mathbf{P_{ge} \equiv P_{amb}}$

It was assumed that under these conditions and with the relatively short nozzle standoff distance that all flow properties remain constant from the nozzle exit to the bow shock [13] (refer to Figure 3.1 for the theoretical cold spray system layout).

12.2 B - If $\mathbf{P_{ge} < P_{amb}}$

If the nozzle exit pressure (P_{ge}) lies below that of the ambient pressure (P_{amb}) the flow is overexpanded. An oblique shock deflection angle (θ) of four degrees was assumed present at the nozzle exit [147]. Figure 4.7 depicts the geometry of the flow through an oblique shock wave, adapted from [147]. Equation 4.23 is the governing equation for the oblique shock angle [147].

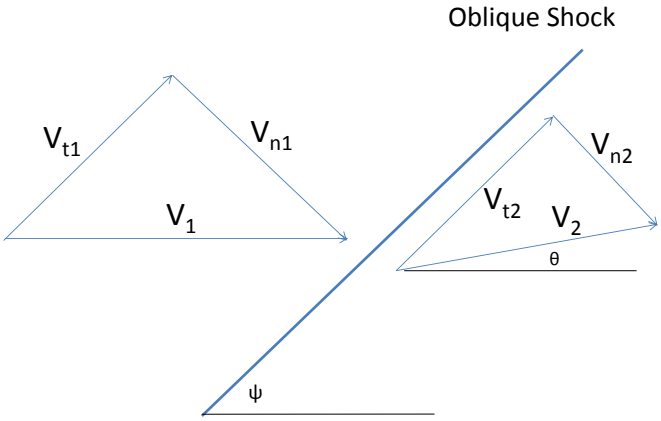


Figure 4.7: Flow geometry through an oblique shock.

$$\psi = tan^{-1}\left\{\frac{2cot\theta\left(M_{ge}{}^{2}\left((sin\psi)^{2}\right)-1\right)}{M_{ge}{}^{2}\left(\gamma+cos\psi^{2}\right)+2}\right\} \tag{4.23}$$

The oblique shock angle (ψ), used in the calculation of all other flow properties, was seen to be a function of the assumed deflection angle and the nozzle exit gas Mach number (M_{ge}). This relationship is non-linear and therefore required a non-linear solver. A basic fixed point root finding method was used, with an assumed initial trial value between five and ten degrees.

Called Function: *#2 - Basic Root Finding Method*
Parsed Variables: θ, f(ψ)
Returned Value: ψ

The flow properties downstream of the oblique shocks are then calculated. Based on equations from [147], these include:

1. Pressure (P_{g2})

$$P_{g2} = P_{ge}\left(\frac{1}{\gamma+1}\right)\left[2\gamma(M_{ge})^2(sin\psi)^2 - (\gamma-1)\right] \tag{4.24}$$

2. Density (ρ_{g2})

$$\rho_{g2} = \rho_{ge}\frac{tan(\psi)}{tan(\psi-\theta)} \tag{4.25}$$

3. Temperature (T_{g2})

$$T_{g2} = T_{ge}\left[2+(\gamma-1)(M_{ge})^2(sin\psi)^2\right]\left(\frac{\left[2\gamma(M_{ge})^2(sin\psi)^2-(\gamma-1)\right]}{(\gamma+1)^2}(M_{ge})^2(sin\psi)^2\right) \tag{4.26}$$

4. Stagnation pressure (P_{02})

$$P_{02} = P_0\left[\frac{(\gamma+1)^2(M_{ge})^2(sin\psi)^2}{2+(\gamma-1)(M_{ge})^2(sin\psi)^2}\right]^{\frac{\gamma}{\gamma-1}}\left[\frac{\gamma+1}{2\gamma(M_{ge})^2(sin\psi)^2-(\gamma-1)}\right]^{\frac{1}{\gamma-1}} \tag{4.27}$$

5. Stagnation temperature (T_{02})

$$T_{02} = T_0 \tag{4.28}$$

6. Mach number normal to oblique shock (entering) (M_{an1})

$$M_{an1} = M_{ge}{\cdot}sin(\psi) \tag{4.29}$$

7. Mach number normal to oblique shock (exiting) (M_{an2})

$$M_{an2} = \sqrt{\frac{(\gamma-1)(M_{an1})^2+2}{2\gamma(M_{an1})^2-(\gamma-1)}} \tag{4.30}$$

8. Mach number downstream of the shock

$$M_{g2} = \frac{M_{an2}}{sin(\psi-\theta)} \tag{4.31}$$

9. Gas velocity ahead of bow shock

$$V_{g2} = M_{g2}\sqrt{\gamma R T_{g2}} \tag{4.32}$$

12.2 C - If Pge > P_{amb}

If, however, the nozzle exit pressure (P_{ge}) lies above the ambient pressure (P_{amb}) the flow is underexpanded. The flow adjusts to this condition through expansion waves. Using the Prandtl-Meyer function [147, 148] and the assumption that the flow may be considered isentropic, the flow conditions upstream of the bow shock are calculated.

In evaluating the flow across expansion waves the following is conducted:

1. Calculate the ratio of stagnation pressure (P_0) to exit pressure (P_{ge}).

$$\frac{P_0}{P_{ge}} = \left(1 + \frac{\gamma - 1}{2}(M_{ge})^2\right)^{\frac{-\gamma}{\gamma - 1}} \tag{4.33}$$

2. Calculate the ratio of ambient pressure (P_{amb}) to the stagnation pressure downstream of expansion waves (P_{02}).

$$\frac{P_{amb}}{P_{02}} = \frac{P_{amb}}{P_{ge}} \cdot \frac{P_0}{P_{ge}} \tag{4.34}$$

3. Calculate the Mach number behind the expansion waves (M_{g2}).

$$M_{g2} = \sqrt{\frac{\left(\frac{P_{g2}}{P_{02}}\right)^{\frac{\gamma}{\gamma - 1}} - 1}{\frac{\gamma - 1}{2}}} \tag{4.35}$$

4. Calculate the ratio of the nozzle exit temperature (T_{ge}) to stagnation temperature (T_0).

$$\frac{T_{ge}}{T_0} = \left(1 + \frac{\gamma - 1}{2}(M_{ge})^2\right)^{-1} \tag{4.36}$$

5. Calculate the ratio of temperature behind the expansion waves (T_{g2}) to the corresponding stagnation temperature (T_{02}).

$$\frac{T_{g2}}{T_{02}} = \left(1 + \frac{\gamma - 1}{2}(M_{g2})^2\right)^{-1} \tag{4.37}$$

6. Calculate the temperature behind the expansion waves (T_{g2}).
   Since the flow was assumed adiabatic $T_{02} = T_0$ the temperature behind the expansion waves is given by Equation 4.38.

$$T_{g2} = T_{02}\left(1 + \frac{\gamma - 1}{2}(M_{g2})^2\right)^{-1} \tag{4.38}$$

7. Calculate the downstream density (ρ_{g2}).

$$\rho_{g2} = \frac{P_{amb}}{R \cdot T_{g2}} \tag{4.39}$$

8. Calculate the downstream velocity (V_{g2}).

$$V_{g2} = M_{g2}\sqrt{\gamma \cdot R \cdot T_{g2}} \tag{4.40}$$

9. Calculate the flow deflection angle w.r.t. the upstream flow Mach number ($\theta_1{}'$).

$$\theta_1{}' = \left(\frac{\gamma+1}{\gamma-1}\right)^{\frac{1}{2}} \left(tan^{-1}\left(\left(\frac{\gamma-1}{\gamma+1}\right)\left({M_{ge}}^2-1\right)\right)\right)^{\frac{1}{2}} - \left(tan^{-1}\left({M_{ge}}^2-1\right)\right)^{\frac{1}{2}} \tag{4.41}$$

10. Calculate the flow deflection angle w.r.t. the downstream flow Mach number ($\theta_2{}'$).

$$\theta_2{}' = \left(\frac{\gamma+1}{\gamma-1}\right)^{\frac{1}{2}} \left(tan^{-1}\left(\left(\frac{\gamma-1}{\gamma+1}\right)\left({M_{g2}}^2-1\right)\right)\right)^{\frac{1}{2}} - \left(tan^{-1}\left({M_{g2}}^2-1\right)\right)^{\frac{1}{2}} \tag{4.42}$$

11. Determine the overall system flow deflection angle ($\Delta\theta'$).

$$\Delta\theta' = \theta_2{}' - \theta_1{}' \tag{4.43}$$

This constraint for the deflection angle is then used to solve for the flow properties as above.

Step 13: Calculate the flow conditions across the bow shock

The bow shock was treated as a normal shock wave and analysed as such. The relevant analysis for evaluating the immediate downstream flow conditions was derived from *Mechanics of Fluids* 4th Ed. and *Fluid Mechanics* 7th Ed. [147, 148]. Ultimately for this analysis the particle velocity was the priority factor, which was assumed to remain constant over the short standoff distance between the bow shock and the substrate. The other flow properties will vary, such that while the gas flow velocity decelerates the pressure, temperature and density are expected to rise.

13.1 Calculate the downstream Mach number (M_{g3}).

$$M_{g3} = \sqrt{\frac{{M_{g2}}^2 + \left(\frac{2}{\gamma-1}\right)^2}{\left(\frac{2\gamma}{\gamma-1}\right)M_{g2}} - 1} \tag{4.44}$$

13.2 Calculate the downstream flow temperature (T_{g3}).

$$T_{g3} = T_{g2}\left[\frac{\left(1+\left(\frac{\gamma-1}{2}\right){M_{g2}}^2\right)\left(\left(\frac{2\gamma}{\gamma-1}\right){M_{g2}}^2-1\right)}{\left(\frac{(\gamma+1)^2}{2(\gamma-1)}\right){M_{g2}}^2}\right] \tag{4.45}$$

13.3 Calculate the downstream flow pressure (P_{g3}).

$$P_{g3} = P_{g2}\left[1 + \left(\frac{2\gamma}{\gamma+1}\right)\left({M_{g2}}^2 - 1\right)\right] \tag{4.46}$$

13.4 Calculate the downstream gas density (ρ_{g3}).

$$\rho_{g3} = \rho_{g2}\left[\frac{\left(\frac{\gamma+1}{2}\right){M_{g2}}^2}{1 + \left(\frac{\gamma-1}{2}\right){M_{g2}}^2}\right] \tag{4.47}$$

13.5 Calculate the downstream flow velocity (V_{g3}).

$$V_{g3} = V_{g2}\left[\frac{\left(\frac{\gamma+1}{2}\right){M_{g2}}^2}{1 + \left(\frac{\gamma-1}{2}\right){M_{g2}}^2}\right]^{-1} \tag{4.48}$$

Step 14: Calculate the bow shock standoff distance

The position of the bow shock, defined as a standoff distance from the substrate to the bow shock (Z_w), was calculated using Equation 2.9 [132].

$$Z_w = 0.143 D_e\left[e^{\frac{3.24}{{M_{ge}}^2}}\right] \tag{2.9 revisited}$$

Step 15: Determine the particle impact velocity

The particle impact velocity (V_{pi}) may now be calculated. This involved determining the relative flow velocity in front of the bow shock (V_{rel-2}). Reference is made to Figure 3.1 which depicts the annotated theoretical cold spray system. The flow viscosity (μ_{g2}), Reynolds number (Re_{g2}) and drag coefficient (C_{D2}) - which itself is influenced by the approaching substrate [190] - are also evaluated. The impact velocity was assumed to be suitably represented by the particle velocity at the bow shock (V_{p2}). This assumption relates to the physical observation discussed in the literature survey related to the effect of the bow shock on particles of different size. According to literature the momentum of larger particles mitigates some of the disruptive effects induced by the presence of the bow shock [119, 133]. Therefore, by assuming a particle impact velocity equal to the particle velocity at the bow shock, the use of sufficiently large powder particles is inferred ($d_p > 5\ \mu m$).

The non-linear expression of the particle impact velocity was based on Derivation 2 in Appendix A (Page 329) and is given by Equation 4.49. Due to the above assumptions, this approach to the estimation of particle impact velocity relies on the effects of particle drag as a primary influencing factor.

$$V_{pi} = V_{p2} = V_{g2} - \frac{V_{g2}}{A - B + C + D - E} \tag{4.49}$$

$$\begin{aligned}
\text{A} &= \left(\frac{C_{D2} A_p \rho_{g2} (SOD - \Delta_{bow} + L)}{2m_p}\right) \\
\text{B} &= \left(\frac{C_{D2} A_p \rho_{g2} L}{2m_p}\right) \\
\text{C} &= \frac{V_{g2}}{V_{g2} - V_{pe}} \\
\text{D} &= ln|V_{g2} - V_{pe}| \\
\text{E} &= ln|V_{g2} - V_{p2}|
\end{aligned}$$

The following steps were required to be followed before solving the non-linear Equation 4.49. These are given as follows:

15.1 Calculate the relative flow velocity (V_{rel-2}).

$$V_{rel-2} = |V_{g2} - V_{pe}| \tag{4.50}$$

15.2 Calculate the flow viscosity in front of the bow shock (μ_{g2}).

Called Function: *#6 - Sutherland's Law*
Parsed Variables: μ_{ref}, T_{g2}, $\text{T}_{ref-sutherland}$, S'
Returned Value: μ_{g2}

15.3 Calculate the relative Reynolds number (Re_{g2}).

$$\nu_{g2} = \frac{\mu_{g2}}{\rho_{g2}} \tag{4.51}$$

Called Function: *#7 - Reynolds Number*
Parsed Variables: V_{rel-2}, d_p, ν_{g2}
Returned Value: Re_{g2}

15.4 Calculate the average drag coefficient (C_{D2}), based on wall effects with body motion normal to a wall [190].

$$C_{D2} = \frac{24}{Re_{g2}} \left(1 + \frac{d_p}{2{\cdot}SOD}\right) \tag{4.52}$$

15.5 The particle impact velocity (V_{pi}) was then evaluated accordingly using a basic root finding method of the form $x = f(x)$ based on Equation 4.49, with the particle velocity at the nozzle exit as an initial estimated response.

Called Function: *#2 - Basic Root Finding Method*
Parsed Variables: V_{pe}, $f(V_{pi})$
Returned Value: V_{pi}

Step 16: Calculate the average particle Biot number

Again the Biot number was calculated with respect to the average spray particle to determine whether or not thermal diffusivity of the spray powder was required to be taken into account. The Reynolds number, Nusselt number and associated average convective heat transfer coefficient for the relative flow in front of the bow shock are also calculated.

16.1 Calculate the impact Reynolds number (Re_i) [150].

$$V_{rel-i} = |V_{g2} - V_{pi}| \tag{4.53}$$

Called Function: *#7 - Reynolds Number*
Parsed Variables: V_{rel-i}, d_p, ν_{g2}
Returned Value: Re_i

The heat transfer analysis employed requires a Reynolds number within the range:
$25 < Re_i < 10^5$ [150].

16.2 Calculate the associated Nusselt number (Nus_i).

$$Nus_i = 0.37 {Re_i}^{0.6} \tag{4.54}$$

16.3 Calculate the average heat transfer coefficient of the spray particle upon impact (hc).

$$hc = \frac{Nus_i{\cdot}k_p}{d_p} \tag{4.55}$$

16.4 Calculate the relevant Biot number (Bi).

$$Bi = \frac{(hc \cdot d_p)}{k_p} \tag{4.56}$$

Step 17: Calculate the particle impact temperature

The corresponding particle impact temperature (T_{pi}) is calculated, making use of the heat transfer relation derived in Derivation 1 (Page 328) and Derivation 3 (Page 331) from Appendix A. The evaluation of the particle impact temperature is dependent on the effect of thermal diffusivity and, therefore, the Biot number calculated in Step 16. Figure 4.4 provides an overview of the effects that the Biot number has, with regards to its value.

17 A - If Bi $<$ 0.1

If Bi $<$ 0.1 the temperature of the reference spray particle may be considered constant. A further consideration, however, was the gas temperature in front of the bow shock (T_{g2}).

- If $T_{g2} > T_{pe}$:

$$T_{pi} = T_{g2} - e^{\left[-\left(\frac{hcA_s(SOD - Z_w + L)}{m_p CpV_{pi}} - \frac{hcA_s L}{m_p CpV_{pi}}\right) + ln|T_{g2} - T_{pe}|\right]} \tag{4.57}$$

  where:
  hc = Average heat transfer coefficient of the spray particle (Equation 4.55).
  A_s = Surface area of an average spray particle (*#19 - Surface Area of a Sphere*).
  SOD = Nozzle standoff distance from the nozzle exit plane to the target substrate.
  Z_w = Bow shock standoff distance from the substrate (Equation 4.70).
  L = Nozzle diverging section length.
  m_p = Average mass of a spray particle.
  Cp = Specific heat at constant pressure.
  V_{pi} = Average particle impact velocity (Step 17).
  T_{g2} = Gas temperature in front of the bow shock (Step 14).
  T_{pe} = Particle temperature exiting the cold spray nozzle (Step 10.9).

- If $T_{g2} < T_{pe}$:

$$T_{pi} = T_{g2} + e^{\left[-\left(\frac{hcA_s(SOD - Z_w + L)}{m_p CpV_{pi}} - \frac{hcA_s L}{m_p CpV_{pi}}\right) + ln|T_{g2} - T_{pe}|\right]} \tag{4.58}$$

17 B - If Bi > 0.1

In evaluating the particle impact temperature (T_{pi}) where internal thermal diffusivity effects are required to be taken into account a transient heat transfer method using the calibrated charts as used in Step 9 on page **??** for the same scenario.

Step 18: Compare critical particle velocities

According to many studies [116,119,125,127,132–136], as previously discussed in the literature survey, particle deposition and subsequent bonding criteria are based on the particle impact velocity. The value is generally required to exceed a critical particle velocity [108,113], which is used as a deterministic criterion for deposition and suitable bonding.

A caveat to the use of such a criterion is the fact that calculations usually omit independent powder and substrate material properties, thereby precluding analysis of unique powder-substrate cold spray combinations. Therefore particle velocity was incorporated into a further analysis of particle-substrate interactions via a particle depth-of-penetration model.

For completeness two models of critical particle velocity were included. The first was given as suggested by Assadi, et al. [113] based on the work by Schmidt, et al. [132]; while the second and earlier model, the Tate Model, was as presented by Walker and Anderson [173].

Model 1

This model employs a normalised temperature ($\theta_p{}'$) and a flow stress value (σ_p) for the spray particle calculation as given by Equation 4.59 and Equation 4.60 [113], respectively.

$$\theta_p{}' = \frac{T_{pi} - T_{ref-p}}{T_{pm} - T_{ref-p}} \tag{4.59}$$

$$\sigma_p = \sigma_{UTS-p}(1 - \theta_p{}') \tag{4.60}$$

where:
T_{ref-p} = Reference temperature for the powder material.
σ_{UTS-p} = Ultimate tensile strength of the powder material.

The critical impact velocity was then given by Equation 4.61.

$$V_{cr} = \sqrt{\frac{4\sigma_{UTS-p}}{\rho_p} + 0.25Cp(T_{pm} - T_{pi})} \tag{4.61}$$

Model 2 - Tate Model [173]

Using the same approach as Model 1 for the calculation of a normalised temperature and a flow stress value the Tate model further includes substrate properties based on a calculated substrate resistance (R_s).

The strength of the projectile (Y_p) is given by Equation 4.62.

$$Y_p = 1.7 \times \sigma_p \tag{4.62}$$

The normalised substrate temperature (θ_s') is given by Equation 4.63.

$$\theta_s{}' = \frac{T_{si} - T_{ref-s}}{T_{sm} - T_{ref-s}} \tag{4.63}$$

The substrate flow stress (σ_s) is given by Equation 4.64.

$$\sigma_s = \sigma_{UTS-s}(1 - \theta_s{}') \tag{4.64}$$

The strength of the substrate (Y_s) is given by Equation 4.65.

$$Y_p = |\sigma_s| \tag{4.65}$$

The extent of plastic flow of the substrate (α_s) is given by Equation 4.66. Where E_s is the Young's Modulus of the substrate material.

$$\alpha_s = \frac{2 \cdot E_s}{3 \cdot Y_s}^{(1/3)} \tag{4.66}$$

The substrate resistance is then given by Equation 4.67.

$$R_s = \frac{7}{3} log(\alpha_s) Y_s \tag{4.67}$$

Depending on the relative magnitudes of the particle strength (Y_p) and substrate resistance (R_s), the critical velocity is determined accordingly.

If $Y_p < R_s$:

$$V_{crit} = \left(2\left[\frac{R_s - Y_p}{\rho_p}\right]\right)^{0.5} \tag{4.68}$$

If $Y_p > R_s$:

$$V_{crit} = \left(2\left[\frac{Y_p - R_s}{\rho_s}\right]\right)^{0.5} \tag{4.69}$$

Particle-substrate interactions

The developmental process has been preparing for this step, in which the particle-substrate interactions are considered. Particular focus is made to the determination of particle depth-of-penetration. It is this parameter that was to be used as the key theoretical discriminating criterion.

Step 19: Calculate the particle depth-of-penetration

Five penetration models were included in the model algorithm. The Python model, for the complete algorithm, is reproduced in Appendix A (Page 334).

Particle depth-of-penetration model selection

While all five of the penetration models aim to predict the depth-of-penetration of cold spray particles, only one was used in the following theoretical optimisation. In order to select the best suited model for this purpose, reference is made to the selection methodology for the depth-of-penetration theoretical model detailed in Chapter 3 (Page 82). The combined variability analysis was subsequently applied, from which a suitable penetration model was selected. The details of this selection process may be found in Appendix A.

Model 1

$$\frac{X}{D} = \left[\frac{\left(\frac{L_c}{D}\frac{\rho_p}{\rho_s} + K_1\right)}{2K_t}\right] \cdot \left(1 + \frac{K_t \rho_p V_{pi}^2}{R_s}\right) \qquad \text{(2.11 revisited)}$$

Model 2

$$\frac{X}{L_c} = \frac{\rho_p V_{pi}}{2R_s} \qquad \text{(2.17 revisited)}$$

Model 3

$$X = u \cdot t \qquad \text{(2.18 revisited)}$$

Model 4

$$X = (L_c - D)\sqrt{\frac{\rho_p}{\rho_s}} + 0.13\left(\frac{\rho_p}{\rho_s}\right)^{\frac{1}{3}} \cdot \left(\frac{\frac{1}{2}m_p V_{pi}^2}{B_{max}}\right)^{\frac{1}{3}} \qquad \text{(2.23 revisited)}$$

Model 5

$$X = \frac{L_c}{\mu}\left(\frac{\mu\sqrt{V_{pi}^2 + A} - V_{pi}}{\mu V_{pi} - \sqrt{V_{pi}^2 + A}}\right) \qquad \text{(2.26 revisited)}$$

Table 4.1 contains the independent predictive accuracy, coefficient of variation and measures of central tendency method scores for the selection of a suitable and robust theoretical particle

penetration model. The overall combined method score incorporates the three weighting factors ($WF_1 = 0.5$, $WF_2 = 0.3$, $WF_3 = 0.2$) for each method score respectively. The penetration model with the lowest combined method score is indicative of the best theoretical model and, therefore, Model 1 was subsequently found to be the most suitable penetration model for the purposes of polymer metallisation.

Table 4.1: Method scores for the selection of a theoretical particle depth-of-penetration model, based on the predictive accuracy, resistance to system noise and strategic measures of central tendency.

	Model 1	Model 2	Model 3	Model 4	Model 5
Predictive accuracy (MS_1)	69.9	130.5	95.2	62.2	95.6
Coefficient of variation (MS_2)	13.6	16.6	15.4	3.5	7.0
Measures of central tendency (MS_3)	40.2	78.5	88.7	100	92.7
Combined Method Score (MS_1)	**47**	86	70	52	68

4.2 Targeted particle depth-of-penetration

The cold spray theoretical model algorithm predicts the resultant particle depth-of-penetration given a fixed input parameter set. Yet to identify the parameter set that will subsequently achieve an ideal coating deposition a known target value is required. This target or desired particle penetration would thereby represent the attainment of a suitable coating deposition. A method of determining this desired or target particle depth-of-penetration, for a given powder-substrate combination, was based on the empirical model developed.

The relationships and observable trends between cold spray particle depth-of-penetration and the interacting material properties (density, Young's Modulus, ultimate tensile strength) were investigated. Table 4.2 contains source data for deriving an initial, tentative targeted particle depth-of-penetration model. This table includes: the penetration type, materials, relevant material property ratios between the cold spray particle material (p) and the substrate material (s) and the observed non-dimensionalised particle depth-of-penetration - given as the ratio between the penetrative depth (X) and the average (or observed) impacting particle size (d_p), for each published data set.

Table 4.2: Source data for targeted particle depth-of-penetration model development.

Penetration type	Particle	Substrate	Reference	$\frac{\rho_p}{\rho_s}$	$\frac{E_p}{E_s}$	$\frac{UTS_p}{UTS_s}$	$\frac{X}{d_p}$
Hard-on-hard	Copper	Stainless steel	[118, 191]	1.120	0.519	0.408	0.15
Hard-on-medium	Copper	Al7050	[192]	3.170	1.534	0.401	0.60
Hard-on-medium	Copper	Al	[192]	3.320	1.594	1.909	1.15
Hard-on-soft	Copper	HDPE	[90]	9.240	137.500	10.345	2.23
Hard-on-soft	Copper	LDPE	[112]	9.240	392.857	30.000	2.00
Hard-on-soft	Copper	3D Printed ABS	Trial	8.620	50.000	6.364	2.07

Figure 4.8 depicts the trends observed between cold spray particle depth-of-penetration and the associated particle and substrate material properties. Using Microsoft Excel's integrated trendline analysis, tentative empirical expressions with which to model these relationships were derived. The method of least squares ensured variance between the empirical trend and the actual data points were adequately minimised. The coefficient of determination (R^2) was used to identify the best possible function type for the regression analysis. The trendline type with a coefficient of determination closest to unity was therefore selected as the closest representation of that particular data set. A second order polynomial curve (Equation 4.70) best represented the density relationships[xi], while the Young's Modulus and ultimate tensile strength were expressed by logarithmic expressions (Equation 4.71 and Equation 4.72 respectively).

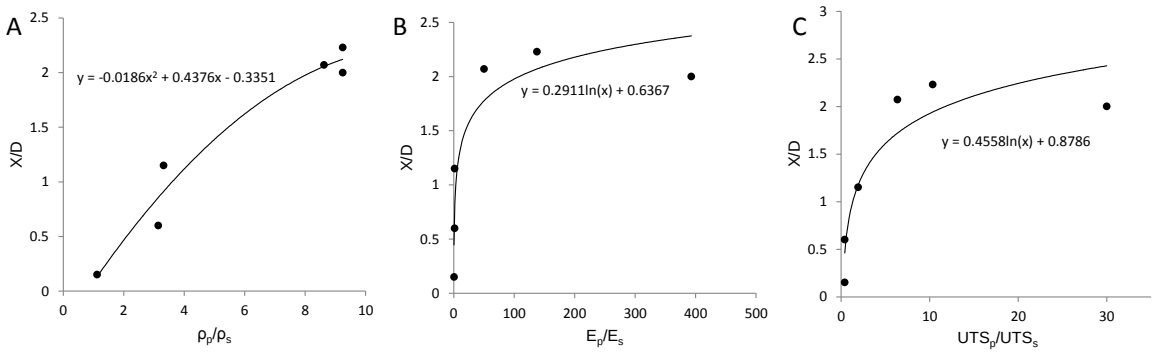


Figure 4.8: Empirical trends between cold spray particle depth-of-penetration and the associated particle and substrate material properties (A = density, B = Young's Modulus and C = ultimate tensile strength).

$$\left(\frac{X}{d_p}\right)_\rho = -0.0186\left(\frac{\rho_p}{\rho_s}\right)^2 + 0.4376\left(\frac{\rho_p}{\rho_s}\right) - 0.3351 \tag{4.70}$$

[xi] While a linear regression line may have been suitable, a comparison between the respective R^2 values indicated that with $R^2 = 0.9604$ the second order polynomial, without significant additional complexity, did a better job of mitigating variance than a linear expression with an R^2 value equal to 0.9463.

$$\frac{X}{d_p}_E = 0.2911ln\left(\frac{E_p}{E_s}\right) + 0.6367 \tag{4.71}$$

$$\frac{X}{d_p}_{UTS} = 0.4558ln\left(\frac{UTS_p}{UTS_s}\right) + 0.8786 \tag{4.72}$$

These expressions were amalgamated as an initial and tentative, equal weighted expression of the targeted particle depth-of-penetration for cold spray polymer metallisation[xii]. This expression, given by Equation 4.73, was later re-evaluated based on data produced from this study and subsequently refined.

$$\begin{aligned}\frac{X}{d_p}_{TARGET} = 0.3934 &- 0.0062\left(\frac{\rho_p}{\rho_s}\right)^2 + 0.1459\left(\frac{\rho_p}{\rho_s}\right) \\ &+ 0.097ln\left(\frac{E_p}{E_s}\right) \\ &+ 0.1519ln\left(\frac{UTS_p}{UTS_s}\right)\end{aligned} \tag{4.73}$$

This empirical model was subsequently used as part of the Taguchi Method to define a nominal targeting value for the particle depth-of-penetration. The resultant value obtained through the use of this expression was to be representative of an *ideal* scenario, according to published and experimental findings.

4.3 Taguchi Method

The execution of the Taguchi Method required integrated access to the programmed theoretical model[xiii]. To achieve this, a Microsoft Excel file containing all the initial parameter level values was imported into the Python programme using Python's csv.reader function. The theoretical cold spray model would then run, parsing (interpreting) those pre-defined parameter sets, and the particle depth-of-penetration output would be exported to the required Microsoft Excel file, in which the Taguchi Method was developed. The theoretical selection and optimisation of an ideal parameter set for a copper cold sprayed coating onto a polymer ABS substrate is demonstrated by the following sample analysis. All other material combinations underwent the same process.

[xii] For completeness, the limiting cases for this expression must be considered. For example as a theoretical limiting case as the substrate material's Young's Modulus tends to infinity the depth-of-penetration (X) approaches zero. Analysis, for all three property types, was therefore maintained for realistic particle/substrate ratios greater than zero.

[xiii] It is to be noted that the theoretical model underwent continuous development based on the input of these theoretical optimisations as well as the later experimental findings, as such the model version used for these calculations, while being the most up to date version at the time, has since undergone modifications.

Taguchi Method Sample Analysis - Part 1

Using the initial parameter values and the product array template (Appendix B), the product array for Part 1 of the analysis is given by Table 4.3

Table 4.3: Taguchi analysis Part 1: Product array - copper cold spray onto an ABS substrate.

Cu-ABS					101325	101325	83060	83060	Ambient Pressure (Pa)	Noise Factors		
	Independent Variables				25	15	25	15	Ambient Temperatures (°C)		Particle Depth of Penetration	
Cold Spray Run	Stagnation Pressure - P [MPa]	Stagnation Temperature - T [°C]	Nozzle Standoff Distance - SOD [mm]	Nozzle Traverse Speed - NTS [mm/s]	25	20	20	25	Spray Powder Particle Size (µm)		$\bar{X}$ µm	S/N_N
1	0.6	0	10	10	35.52	19.91	21.37	33.21			27.5025	10.630
2	0.6	125	20	25	36.92	20.04	21.51	34.54			28.2525	10.116
3	0.6	250	30	40	37.17	19.64	21.09	34.77			28.1675	9.7169
4	0.8	0	20	40	42.03	24.32	26.04	39.39			32.945	11.132
5	0.8	125	30	10	44.49	25.04	26.81	41.74			34.52	10.656
6	0.8	250	10	25	45.29	24.91	26.67	42.5			34.8425	10.285
7	1	0	30	25	47.32	28.06	29.99	44.44			37.4525	11.539
8	1	125	10	40	50.39	29.12	31.11	47.38			39.5	11.070
9	1	250	20	10	52.12	29.52	31.53	49.03			40.55	10.725

The results were then processed, calculating the S/N ratio and the percentage coefficient of variation (%CV). From which, the distinction between control and signal factors was made. Table 4.4 summarises the separation of signal and control factors.

Table 4.4: Taguchi analysis Part 1: Separation of signal and control factors.

S/N Ratio of Parameter Levels		Coefficient of Variation (%)	Control or Signal Factors
$S\bar{N}_{P1}$	10.155	4.5	Stagnation Pressure – Control Factor
$S\bar{N}_{P2}$	10.692		
$S\bar{N}_{P3}$	11.112		
$S\bar{N}_{T1}$	11.101	4.04	Stagnation Temperature - Control Factor
$S\bar{N}_{T2}$	10.615		
$S\bar{N}_{T3}$	10.242		
$S\bar{N}_{SOD1}$	10.662	0.12	SOD - Signal Factor
$S\bar{N}_{SOD2}$	10.658		
$S\bar{N}_{SOD3}$	10.638		
$S\bar{N}_{NTS1}$	10.671	0.15	Nozzle Traverse Speed - Signal Factor
$S\bar{N}_{NTS2}$	10.647		
$S\bar{N}_{NTS3}$	10.640		

Graphical analysis and ideal parameter level selection for Part 1 of the Taguchi optimisation was then conducted. The mean response plots for particle depth-of-penetration and S/N ratio, with respect to each variable process parameter, are depicted in Figure 4.9.

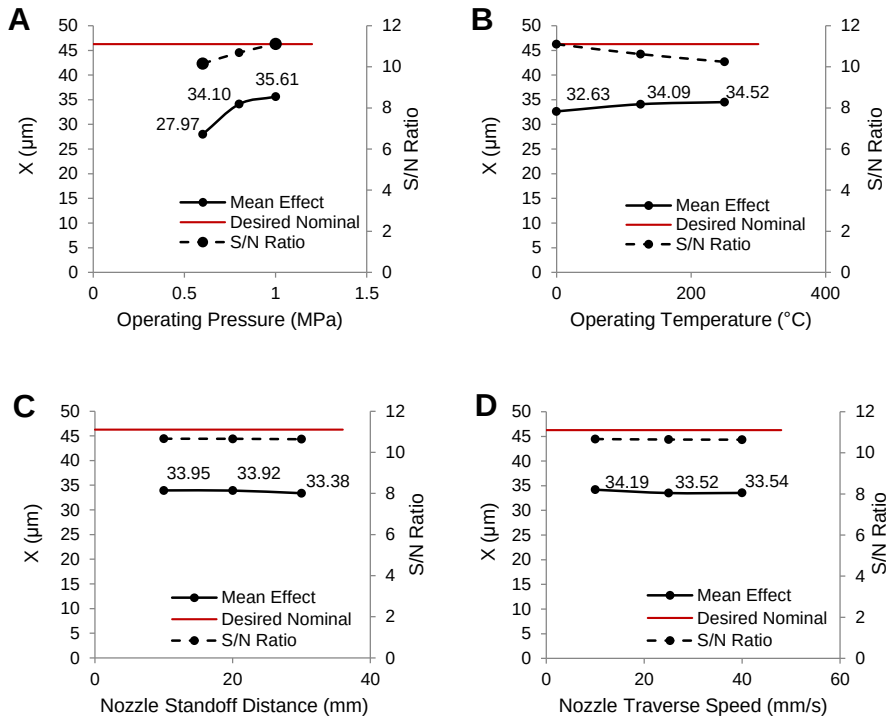


Figure 4.9: Taguchi Method Part 1: Effect of controllable factors and S/N ratio analysis: (A) operating pressure, (B) operating temperature, (C) nozzle standoff distance, (D) nozzle traverse speed, with respect to particle depth-of-penetration.

Based on Table 4.4, it was concluded that the operating pressure and temperature were control factors, which therefore have a significant effect on system variance. As such the value of these control factors were selected so as to maximise the S/N ratio and thereby mitigate the effects of noise and system variance.

In addition, the nozzle standoff distance and nozzle traverse speed were classified as signal factors, which influence the mean response. These two parameters were selected to target the desired response, which itself was defined by the developed targeted particle depth-of-penetration empirical model as 46.27 μm (or $X/d_p = 1.85$).

Based on this, the Part 1 theoretical parameter set was defined as: an operating pressure of 1 MPa, an operating temperature at $0°C$), a nozzle standoff distance of 10 mm and a nozzle traverse speed of 10 mm/s.

Taguchi Method Sample Analysis - Part 2

The L9 orthogonal array for Part 2 of the Taguchi optimisation is depicted in Table 4.5 and includes the evaluation of the critical particle velocity. While theoretically an operating temperature of $0°C$ is possible, in practice this is not the case[xiv]. Therefore, as a means of aligning the theoretical analysis with real world capabilities, without dismissing any theoretical inferences gained from Part 1 of the analysis, the operating temperature values for the analysis in Part 2 were spread across the lower two temperature settings starting at an average ambient temperature of $15°C$ and rising to $100°C$.

The theoretical cold spray model parses the associated trial parameter sets after being imported, thereby interpreting the variable values. The theoretical model is then run, from which the predicted particle depth-of-penetration (X), particle impact velocity (V_{pi}) and the theoretical critical particle velocity (V_{crit}) are exported to the programmed Taguchi analysis.

Table 4.5: Taguchi analysis Part 2: Orthogonal array - copper cold spray onto an ABS substrate.

Cu-ABS							
L9 Orthogonal Array	Independent Variables				Performance Parameter Value		Critical Particle Velocity (Vcrit) [m/s]
Cold Spray Run	Stagnation Pressure - P [Mpa]	Stagnation Temperature - T [°C]	Nozzle Standoff Distance - SOD [mm]	Nozzle Traverse Speed - NTS [mm/s]	Particle Depth of Penetration - X [µm]	Particle Impact Velocity (Vpi) [m/s]	
1	0.9	15	7	5	42.3	264.96	455.54
2	0.9	50	10	10	43.23	268.75	450.06
3	0.9	100	13	15	44.25	272.9	442.13
4	1	15	10	15	44.73	274.89	455.47
5	1	50	13	5	45.79	279.2	449.97
6	1	100	7	10	46.88	283.62	442.03
7	1.1	15	13	10	46.96	283.95	455.41
8	1.1	50	7	15	48.04	288.33	449.9
9	1.1	100	10	5	49.38	293.77	441.94
						Ave	449.16

[xiv] Freezing and sub-zero operating temperatures may be possible, yet would require the use of a refrigeration or blast freezing system. Subsequent experimental analysis showed this not to be a necessary implementation, due to desirable deposition properties achieved with higher operating temperatures.

The cumulative average response for each process parameter was plotted in Figure 4.10. It was evident that the parameter selection had been significantly refined. For all four process parameters the predicted depth-of-penetration response closely matches the targeted response. Therefore a localised optimum parameter set was successfully achieved.

For the case of stagnation temperature it may appear that a drastic improvement has been made with little parameter variation, when comparing the mean responses between Part 1 and Part 2. This, however, is not the case. While the lowest applied stagnation temperature has only gone up from $0°C$ to $15°C$ the average response has gone from only 33 μm to nearly 45 μm (just below the target response); yet a direct comparison between Part 1 and Part 2 should not be made. Each *part* in this adapted Taguchi Method is regarded as a separate step in parameter refinement and is subsequently comprised of different parameter values. The cumulative average response values plotted for each process parameter are not derived in isolation from the other parameters and so the responses represent inferred trends and not independent effects of that specific parameter.

Referring again to Figure 4.10 the predicted particle impact velocity, lies significantly below the predicted critical particle velocity for all parameters. This provides an initial observation regarding the suitability of particle velocity as a cold spray criterion for polymer metallisation applications. Based on the theoretical analysis this criterion was seen to be ineffective in handling cold spray of differing materials, particularly the aforementioned hard-on-soft penetration type. Experimental analysis, conducted in the following chapter, would further investigate and potentially validate this observation.

Based on the targeted response and theoretical particle depth-of-penetration a theoretical parameter set for a copper cold spray coating onto an ABS polymer substrate was defined: operating pressure (P_0): 1 MPa, operating temperature (T_0) = 90°C, nozzle standoff distance (SOD) = 10 mm and nozzle traverse speed (V_n) = 10 mm/s.

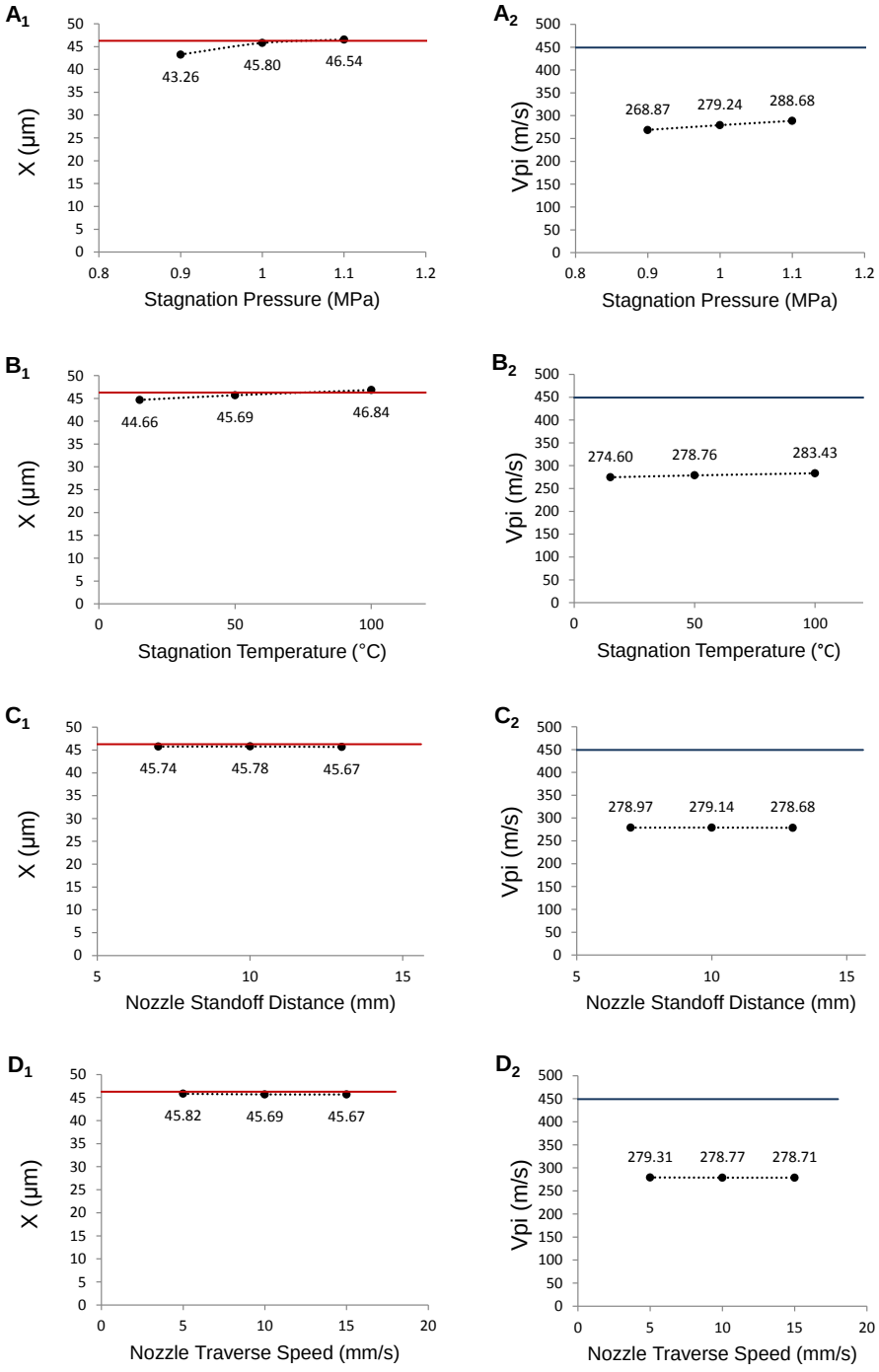


Figure 4.10: Taguchi Method Part 2: Mean response plots of (A) operating pressure, (B) operating temperature, (C) nozzle standoff distance, (D) nozzle traverse speed, with respect to predicted particle depth of penetration (X) and particle impact velocity (V_{pi}).

4.4 Theoretical cold spray parameter sets

Using the aforementioned approach, theoretical cold spray parameter sets were successfully identified for polymer metallised coatings on ABS, PC and PEEK substrates (Table 4.6 to Table 4.10).

Table 4.6: Theoretical cold spray parameter sets - Copper coatings.

	Copper coatings		
	ABS	PC	PEEK
Throat Diameter (mm)	2.5	2.5	2.5
Exit Diameter (mm)	6.5	6.5	6.5
Divergent Length (mm)	120	120	120
Spray Gas	Air	Air	Air
Ambient Pressure (Pa)	83060	83060	83060
Ambient Temperature (C)	15	15	15
Spray Powder	Copper	Copper	Copper
Stagnation Pressure (MPa)	1	1.4	1.55
Stagnation Temperature (°C)	90	250	300
Initial Particle Temperature (°C)	15	15	15
Nozzle Standoff Distance (mm)	10	10	7
Nozzle Traverse Speed (mm/s)	10	7	7
Substrate Material	ABS	PC	PEEK
Initial Substrate Temperature (°C)	15	15	15
Powder Mean Diameter (μm)	25	25	25
Target X (μm)	46.27	42.22	38.50
Predicted Penetration X (μm)	46.71	39.96	30.89
Critical Velocity Info (V_{pi}/V_{crit})	0.64	0.8	0.86

Table 4.7: Theoretical cold spray parameter sets - Zinc coatings.

	Zinc coatings		
	ABS	PC	PEEK
Throat Diameter (mm)	2.5	2.5	2.5
Exit Diameter (mm)	6.5	6.5	6.5
Divergent Length (mm)	120	120	120
Spray Gas	Air	Air	Air
Ambient Pressure (Pa)	83060	83060	83060
Ambient Temperature (°C)	15	15	15
Spray Powder	Zinc	Zinc	Zinc
Stagnation Pressure (MPa)	1.05	1.45	1.55
Stagnation Temperature (°C)	100	275	350
Initial Particle Temperature (°C)	15	15	15
Nozzle Standoff Distance (mm)	20	10	10
Nozzle Traverse Speed (mm/s)	10	5	5
Substrate Material	ABS	PC	PEEK
Initial Substrate Temperature (°C)	15	15	15
Powder Mean Diameter (μm)	27.5	27.5	27.5
Target X (μm)	45.88	41.22	37.07
Predicted Penetration X (μm)	46.08	39.39	30.27
Critical Velocity Info (V_{pi}/V_{crit})	0.92	1.33	1.57

Table 4.8: Theoretical cold spray parameter sets - Nickel coatings.

	Nickel coatings		
	ABS	PC	PEEK
Throat Diameter (mm)	2.5	2.5	2.5
Exit Diameter (mm)	6.5	6.5	6.5
Divergent Length (mm)	120	120	120
Spray Gas	Air	Air	Air
Ambient Pressure (Pa)	83060	83060	83060
Ambient Temperature (°C)	15	15	15
Spray Powder	Nickel	Nickel	Nickel
Stagnation Pressure (MPa)	1.1	1.4	1.6
Stagnation Temperature (°C)	100	250	300
Initial Particle Temperature (°C)	15	15	15
Nozzle Standoff Distance (mm)	10	10	7
Nozzle Traverse Speed (mm/s)	5	7	7
Substrate Material	ABS	PC	PEEK
Initial Substrate Temperature (°C)	15	15	15
Powder Mean Diameter (μm)	25	25	25
Target X (μm)	49.29	45.23	41.50
Predicted Penetration X (μm)	49.18	39.81	31.35
Critical Velocity Info (V_{pi}/V_{crit})	0.54	0.63	0.68

Table 4.9: Theoretical cold spray parameter sets - Tin coatings.

	Tin coatings		
	ABS	PC	PEEK
Throat Diameter (mm)	2.5	2.5	2.5
Exit Diameter (mm)	6.5	6.5	6.5
Divergent Length (mm)	120	120	120
Spray Gas	Air	Air	Air
Ambient Pressure (Pa)	83060	83060	83060
Ambient Temperature (°C)	15	15	15
Spray Powder	Tin	Tin	Tin
Stagnation Pressure (MPa)	0.95	1.05	1.55
Stagnation Temperature (°C)	150	210	200
Initial Particle Temperature (°C)	15	15	15
Nozzle Standoff Distance (mm)	15	15	10
Nozzle Traverse Speed (mm/s)	10	10	5
Substrate Material	ABS	PC	PEEK
Initial Substrate Temperature (°C)	15	15	15
Powder Mean Diameter (μm)	25	25	25
Target X (μm)	42.08	37.86	34.08
Predicted Penetration X (μm)	42.43	30.75	27.33
Critical Velocity Info (V_{pi}/V_{crit})	0.91	1.12	1.26

Table 4.10: Theoretical cold spray parameter sets - Aluminium coatings.

	Aluminium coatings		
	ABS	PC	PEEK
Throat Diameter (mm)	2.5	2.5	2.5
Exit Diameter (mm)	6.5	6.5	6.5
Divergent Length (mm)	120	120	120
Spray Gas	Air	Air	Air
Ambient Pressure (Pa)	83060	83060	83060
Ambient Temperature (°C)	15	15	15
Spray Powder	Aluminium	Aluminium	Aluminium
Stagnation Pressure (MPa)	1.2	1.4	1.5
Stagnation Temperature (°C)	275	350	350
Initial Particle Temperature (°C)	15	15	15
Nozzle Standoff Distance (mm)	30	15	15
Nozzle Traverse Speed (mm/s)	40	25	15
Substrate Material	ABS	PC	PEEK
Initial Substrate Temperature (°C)	15	15	15
Powder Mean Diameter (μm)	25	25	25
Target X (μm)	31.43	27.66	24.31
Predicted Penetration X (μm)	31.50	24.40	18.69
Critical Velocity Info (V_{pi}/V_{crit})	0.9	1.02	1.03

Chapter 5 Cold Spray and 3D Printing Analysis

"Technology in any field takes a few versions to optimise before reaching a mass market."

Elon Musk, Technology Entrepreneur, Engineer, Founder of SpaceX and Tesla.

This chapter sets out to achieve three main objectives; firstly, to investigate independent cold spray parameter effects; secondly, to carry out effective cold spray parameter set optimisation for polymer metallisation with the intended application of antimicrobial surface coatings; and finally, to characterise the successful polymer metallised coatings, for both the theoretically[i] and experimentally optimum parameter sets.

5.1 The IPEV Decision Framework

The Independent Parameter Effects and Variation (IPEV) decision framework developed in this current study was designed to aid experimental cold spray parameter selection, evaluation and optimisation. The framework was to be used during practical cold spray applications and should therefore inherently be based on visual inspections made in real time, during the cold spraying process, thus allowing for constructive and timeous variation to process parameters to be made.

According to the design methodology detailed in Chapter 3, development was based on three design elements: theoretical effects, experimental effects and historical studies.

5.1.1 Theoretical effects

The independent theoretical parameter effects analysis made use of the observations made during the particle depth-of-penetration model selection in Chapter 4, specifically with regards to the coefficient of variation analysis. Under this theoretical analysis, independent

[i]The theoretical parameter sets, used as the starting point for experimental optimisation, are referred to as the theoretically optimum parameter sets, since they have undergone the Taguchi optimisation process and therefore represent the best case scenario from the preceding theoretical analysis.

parameter variations were investigated for both copper-on-copper and copper-on-ABS cold spray coatings.

The results for the first case (Cu-on-Cu) may be found in Appendix A for Model 1 and are plotted below in Figure 5.1.

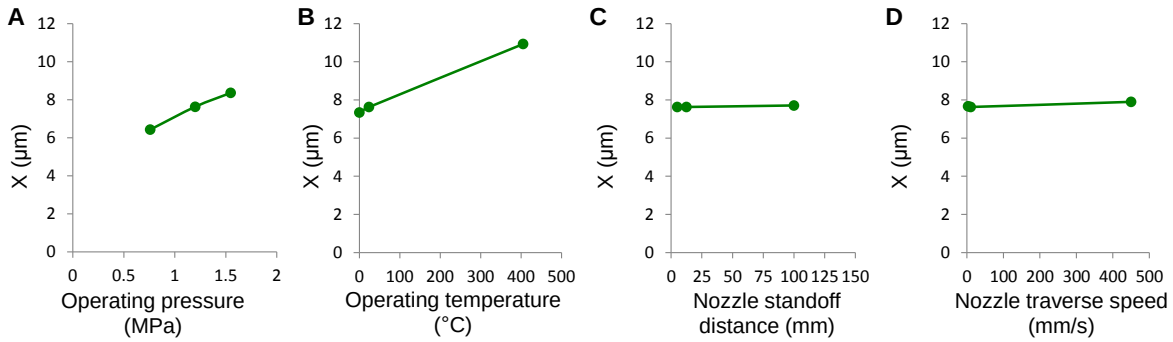


Figure 5.1: Theoretical independent parameter effects for cold spray of copper on copper substrates: A = stagnation pressure, B = stagnation temperature, C = nozzle standoff distance and D = nozzle traverse speed.

The results for the second case (Cu-on-ABS) may be found in Appendix A for Model 1 and are plotted below in Figure 5.2.

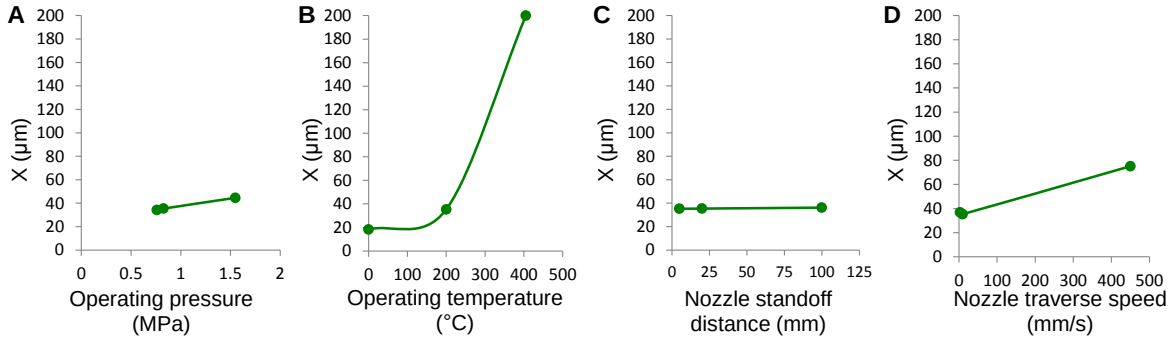


Figure 5.2: Theoretical independent parameter effects for cold spray of copper on ABS polymer substrates: A = stagnation pressure, B = stagnation temperature, C = nozzle standoff distance and D = nozzle traverse speed.

Trend analysis for theoretical effects

Based on the theoretical data it was observed that moderately consistent trends exist for the two independent test cases. Parameter sensitivity, however, varied significantly between cold spray of similar materials (e.g. Cu - Cu) and dissimilar materials (e.g. Cu - ABS). Cold spray of dissimilar powder and substrate materials was seen to yield vastly greater variations in the design characteristic - particle depth-of-penetration.

Trend analysis considered both the general and material specific trends. With respect to the ultimate impact on coating quality, the effects for copper cold spray onto an ABS substrate were given higher priority, considering the focal area of the research, regarding polymer metallisation.

It was noted that the required particle depth-of-penetration of a specific powder-substrate combination is material specific. The extent of variation was an indication of this. While a small penetration variation in cold spray of like materials (Cu-Cu) may be significant, the same may not be true for that of dissimilar material cold spray (Cu-ABS). This was related to material sensitivity and therefore for dissimilar material cold spraying it was concluded that parameter selection exhibits heightened sensitivity. Parameter selection therefore becomes increasingly important in such cold spray applications.

With regards to coating quality the following may be deduced: an increasing particle depth-of-penetration increases the potential risk of substrate erosion or in general the inability to develop a surface layer coating. Fully embedded particles are less likely to offer a surface area for touch-contact applications, therefore reducing their antimicrobial efficacy.

This is not to say that such embedment does not offer antimicrobial activity for other applications. Vucko et al. (2012) observed that copper embedded thermoplastic polymers behaved differently with different depths of particle embedment for biofouling applications [91]. Samples with deeper embedments observed sustained anti-biofouling, a consequence of a lower dissolution rate.

The following trends in independent parameter effects were observed:

1. **Operating pressure**

   An increase in operating pressure resulted in an essentially linear increase in particle depth-of-penetration. Over a 789 KPa pressure range, including a suitable nominal value of 0.827 MPa, the penetration varied by 10.39 μm, for cold spray polymer metallisation.

   Inferences:

   - Low coating deposition may be caused by insufficient pressure.
   - Correspondingly, substrate erosion may be related to excessive pressure.

2. **Operating temperature**

   An increase in operating temperature resulted in an associated increase in particle depth-of-penetration. The trend and extent of variation was dependent on the constituent materials. Similar materials observe an essentially linear increase in penetration,

while dissimilar material combinations observe an almost exponential rise in penetration. Over a 400°C temperature range, including a suitable nominal value of 200°C, the particle penetration varied by 181.54 μm for cold spray polymer metallisation. Particle depth-of-penetration was therefore seen to be highly sensitive to the operating temperature.

Inferences:

- No significant coating variations at low temperatures (0 - 150°C).
- As temperature exceeds 200°C (roughly 100°C above the Vicat softening temperature of the substrate material) the depth-of-penetration increases considerably.

3. **Nozzle standoff distance**

   A marginal increase in particle depth-of-penetration was observed from an increase in nozzle standoff distance. Over a 95 mm range, including a suitable nominal value of 20 mm, the penetration varied by only 0.98 μm, for cold spray polymer metallisation.

   Inferences:

   - No significant effects on particle depth-of-penetration observed for varied nozzle standoff distance.

4. **Nozzle traverse speed**

   An increase in the nozzle traverse speed corresponded with an increase in particle depth-of-penetration. Parameter sensitivity was significantly higher for dissimilar cold spray powder-substrate combinations. Over a 447 mm/s range, with a suitably nominal value of 10 mm/s, the penetration varied by 38.35 μm for copper cold spray onto ABS substrates.

   This result was ill founded. There should be little to no correlation between nozzle traverse speed and the particle depth-of-penetration for the theoretical analysis. This trend will therefore be carefully considered, based on the experimental and published data observations.

   It is to be noted that dwell time, that is the time the cold spray jet is in continuous contact with a portion of the substrate may, from an experimental perspective, have a contributing influence on particle depth-of-penetration, due to heat input and subsequent substrate softening. Dwell time is directly related to the nozzle traverse speed: the slower the nozzle traverse speed, the longer the dwell time and therefore the substrate receives a greater heat input.

   Inferences:

   - No inferences are made, due to suspected erroneous theoretical data trend.

5. **Powder feed rate**

   No theoretical data was possible for powder feed rate, since powder volumetric effects are not inferable from the singular particle analysis at the core of the theoretical analysis.

5.1.2 Experimental effects

The experimental investigation made use of a copper-aluminium-alumina blended powder (C0075 Centerline SST) and a solid ABS polymer substrate. The theoretically optimum parameter set was used as the baseline. As such the operating pressure was set at 1 MPa, the operating temperature at 90°C, the nozzle standoff distance at 10 mm and the nozzle traverse speed was set at 10 mm/s. The powder feed rate was set at a nominal value of 20%.

As detailed in the methodology for this analysis, this nominal parameter set was varied based on pre-defined independent parameter modifications. The variation of each parameter was not made in an attempt to test the extreme parameter cases, but to observe the effects of reasonable parameter variations within the viable parameter ranges. The extreme limits were, however, investigated separately. Examples of which are depicted in Figure 3.2 in the Research Methodology.

Visual discrimination

The following figures (Figure 5.3 to Figure 5.7) record all cold spray trials associated with the experimental analysis of independent process parameter effects.

Figures in row A correspond with naked eye observations of the three cold spray run types tested. These run types are (from left to right): a wipe test, evaluating single particle impacts; a multi-pass coating, consisting of 5 cold spray passes; and finally a single pass deposition as the target deposition type for optimisation. The micrographs in row B corresponds with stereoscopic microscopy analysis[ii], undertaken using a Nikon SMZ 745T microscope and Nikon DS-Fi2 camera. The micrographs in C and D were taken with a Leica DM6000M microscope, with Leica DFC490 camera mount and represent top views and cross-sectional views, respectively. Gold stars were assigned to the stereoscopic micrographs which, at first appearance, represented desirable coating profiles.

[ii] All stereoscopic images were taken with an image scale of 3.058 μm/px.

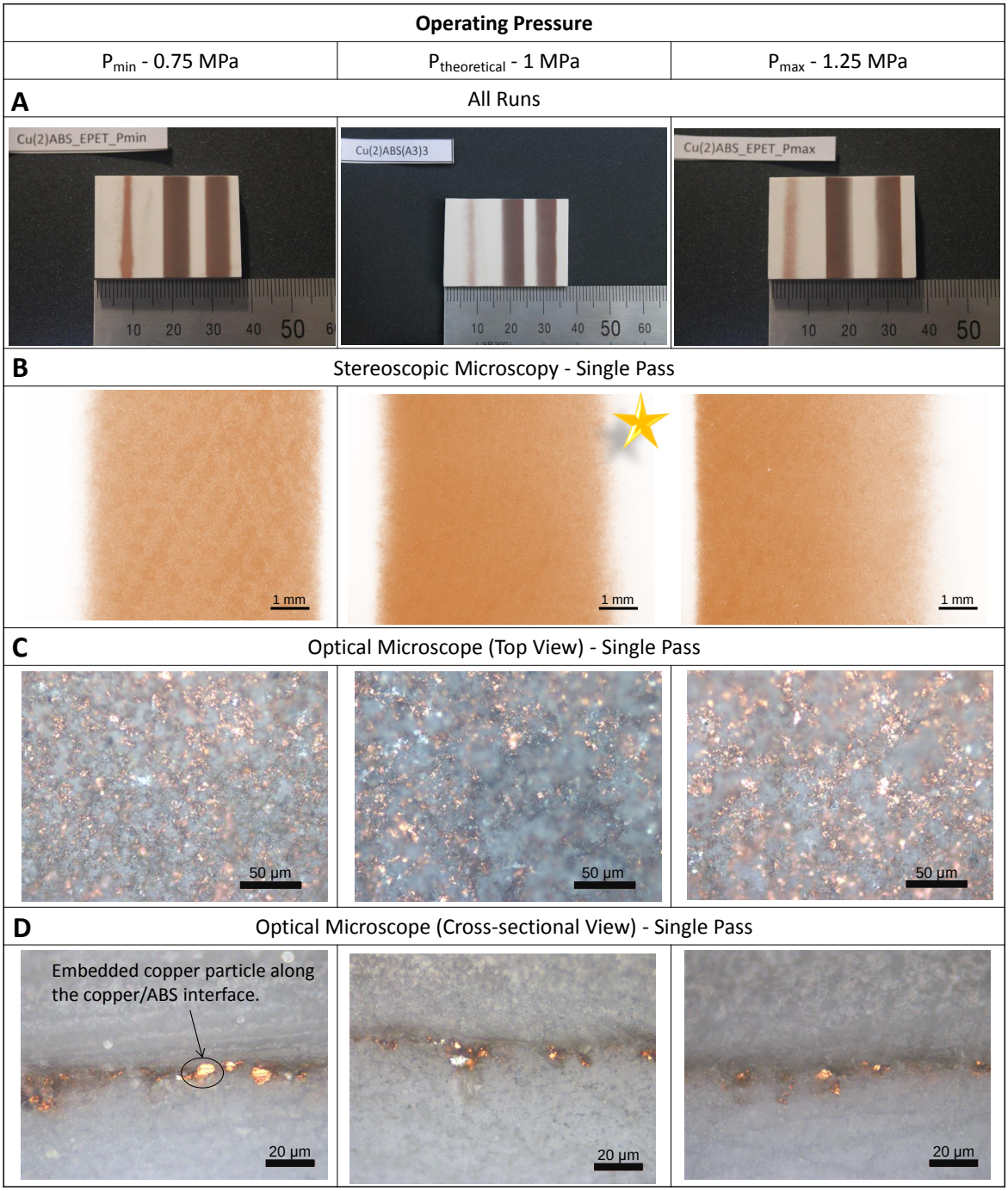


Figure 5.3: Visual discrimination analysis: independent variation in operating pressure.

The variation of operating pressure was carried out over a 500 kPa range. No significant difference was observed via optical microscopy at higher magnifications; yet based on naked eye and stereoscopic observations the median parameter value was deemed the most uniform and dense coating deposition (Micrograph marked with a star). This suggested that the parametric variation - both above and below theoretically optimum - for pressure, may result in lower quality coatings. Three of the five depositional issues, namely: lack of deposition, lack of densification and a lack of depositional consistency, are seen to be factors influenced by the cold spray operating pressure.

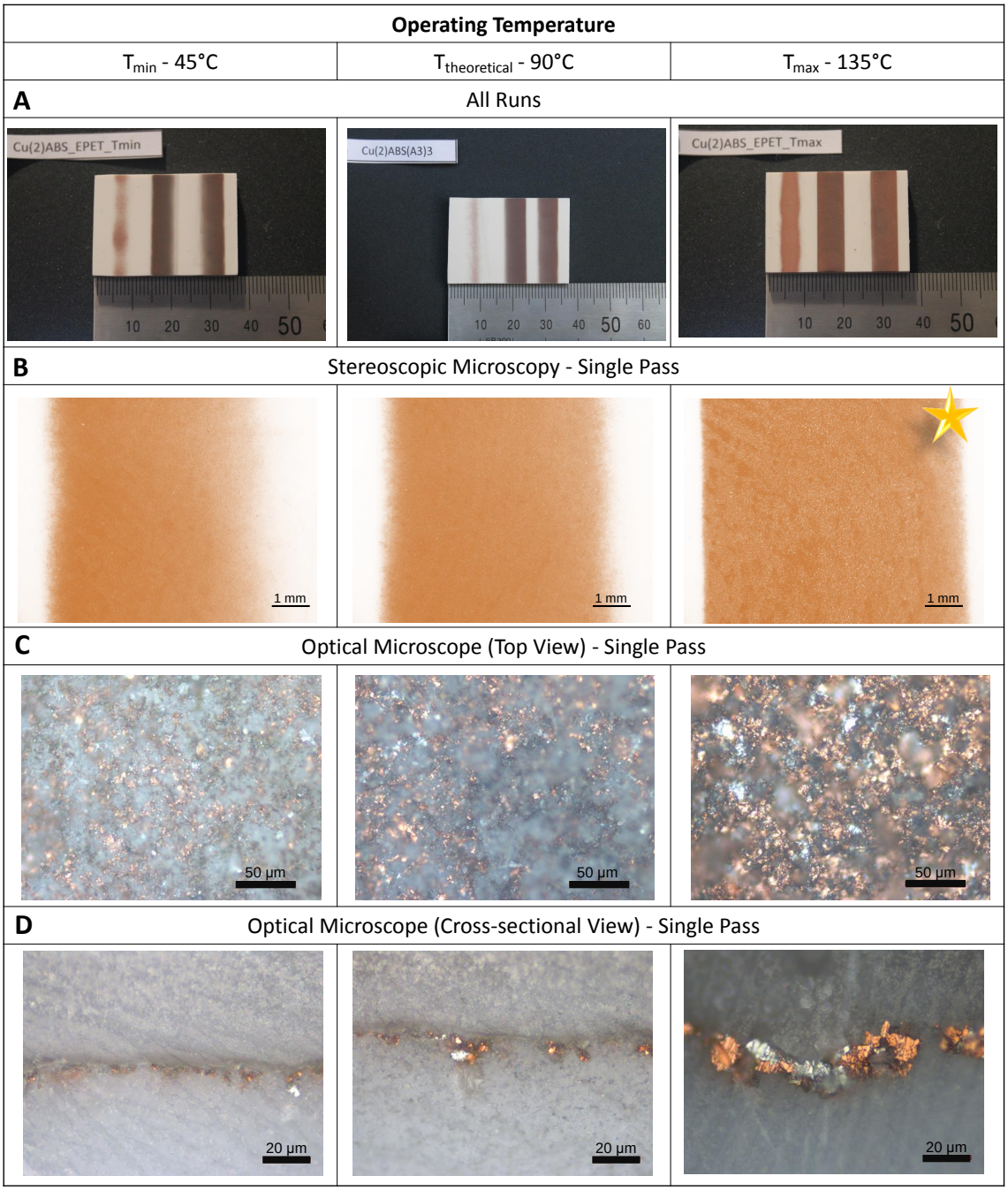


Figure 5.4: Visual discrimination analysis: independent variation in operating temperature.

The variation of operating temperature was carried out over a 90°C range. Significant effects on deposition were observed across the entire parameter range, at both low and high magnification. Deposition quality based on coverage, densification and consistency were seen to improve as the operating temperature was increased. Deposition thickness observed clear and evident thickening as observed in the optical microscopy cross-sectional images over this thermal range. The size of embedded particles was also seen to increase, particularly for the highest test temperature of 135°C.

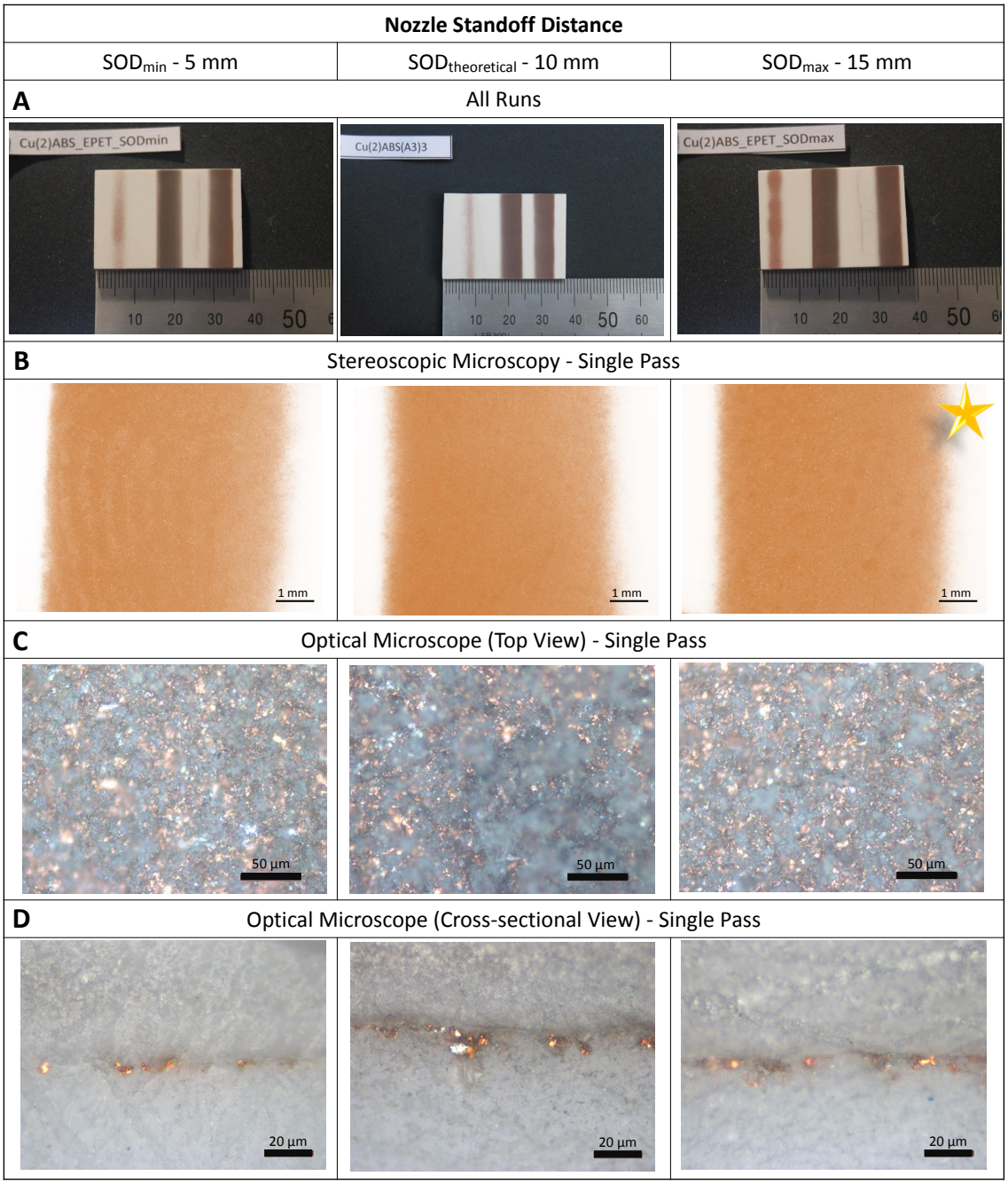


Figure 5.5: Visual discrimination analysis: independent variation in nozzle standoff distance.

The variation of the nozzle standoff distance was carried out over a 10 mm range. An increase in nozzle standoff distance was seen to produce a more uniform and densely deposited coating. Powder acceleration was identified as the cause; producing higher average particle impact sizes and therefore achieving deposition for a wider range of particle sizes. This was particularly evident from the wipe test runs, where a wipe test with a nozzle standoff distance of 15 mm was observed to achieve a higher deposition volume than with lower standoff distances.

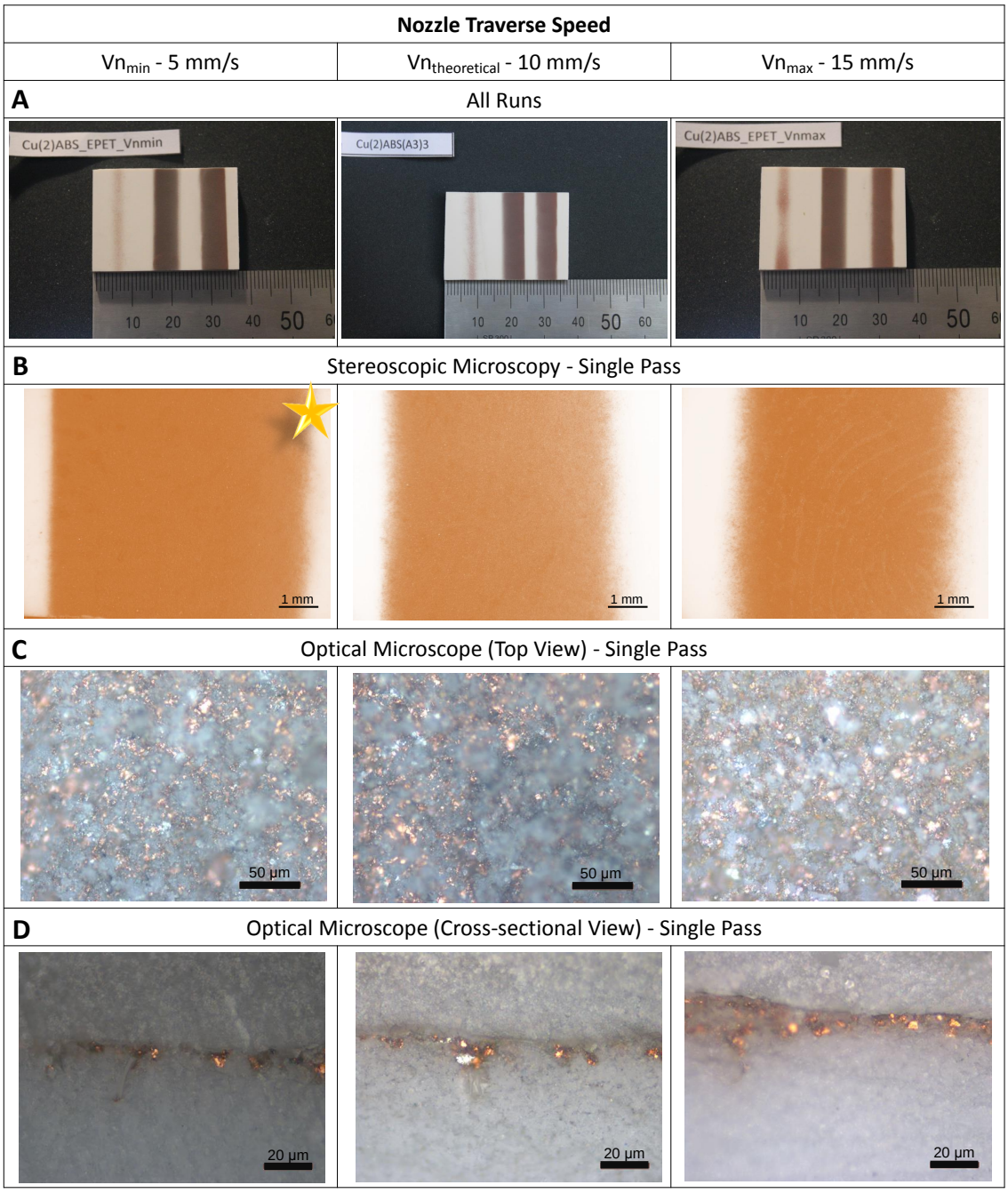


Figure 5.6: Visual discrimination analysis: independent variation in nozzle traverse speed.

The variation of the nozzle traverse speed was carried out over a 10 mm/s range. From a stereoscopic analysis the coating deposition, densification and consistency were seen to improve with a decrease in nozzle traverse speed. This was such that noticeable imperfections in deposition, including surface area coverage and deposition consistency, were eliminated as the nozzle traverse speed was decreased to 5 mm/s. Inconsistent results were observed for the wipe test, which under this test case should be identical since the nozzle traverse speed for a wipe test is fixed at 500 mm/s. The wipe test results for this test case are in any case ignored since they have no bearing on the effects of nozzle traverse speed variation.

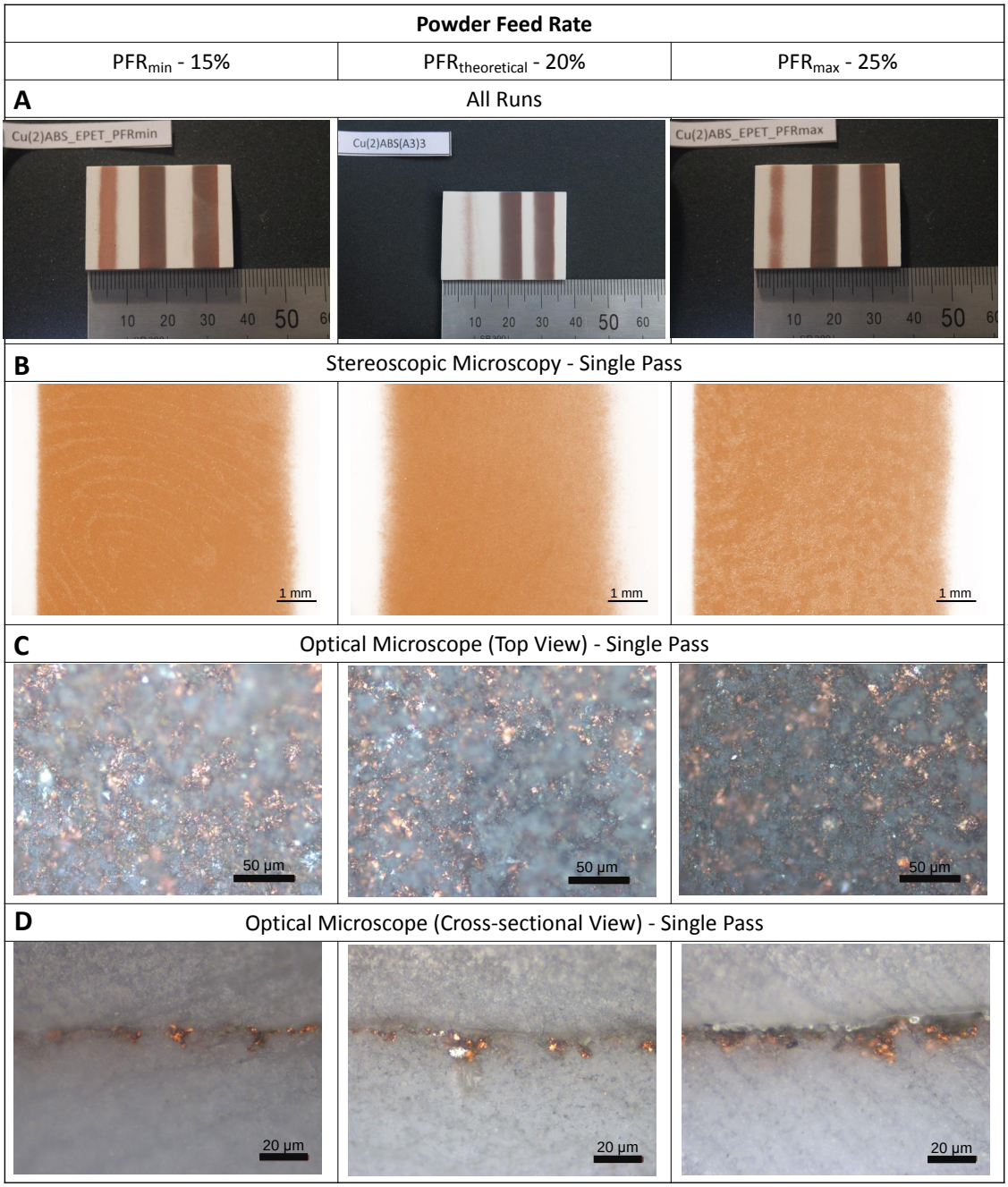


Figure 5.7: Visual discrimination analysis: independent variation in powder feed rate.

A 10% variation in the powder feed rate was investigated. The experimental results were inconclusive from a purely visual analysis. At both high and low powder feed rate levels deposition was seen to increase, when compared to the baseline level. This was most noticeable from the wipe test data.

Experimental quantification

Refer to Appendix C for the tabulated experimental parameter effects for high-low parameter variation. The results, however, are graphed in Figure 5.8.

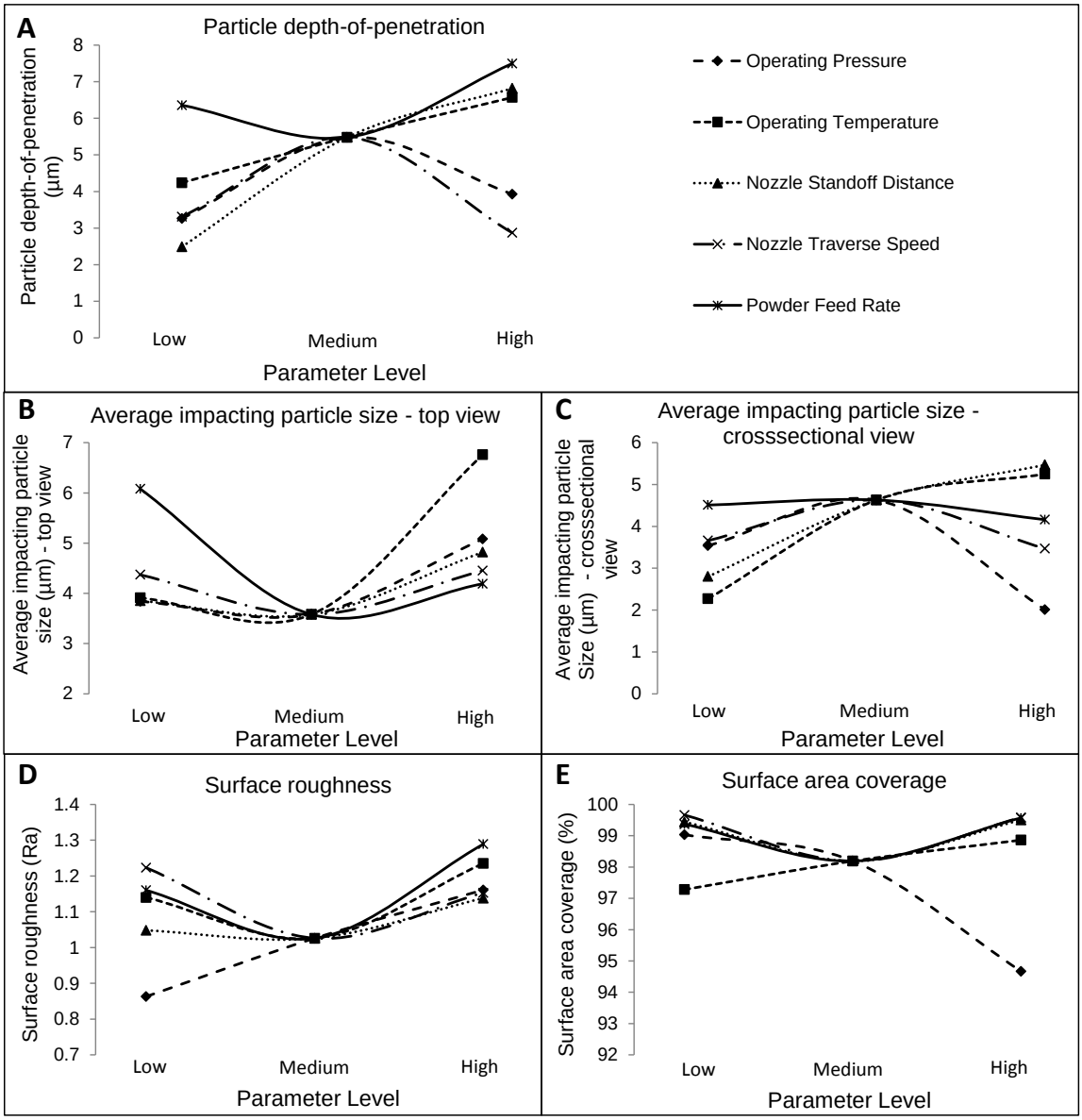


Figure 5.8: Independent parameter effects: copper-aluminium-aluminium oxide cold spray onto a solid polymer ABS substrate.

Trend analysis for experimental effects

The following independent parameter effect trends were observed:

1. **Operating pressure**

   High operating pressures may lead to an increase in surface roughness and a reduction in surface area coverage as is evident in Figure 5.8 D and E, respectively. Based on the

qualitative observations made in Figure 5.3 operating pressure is seen to have an affect on deposition, densification and depositional consistency.

Inferences:

- Operating pressure at both high and low extremes may have detrimental effects on coating quality.

2. **Operating temperature**

   Operating temperature was observed to be the most influential cold spray parameters for cold spray onto polymer substrates. An increase in operating temperature was observed to significantly increase the average particle depth-of-penetration, surface area coverage and depositional density, from both a qualitative (Figure 5.4) and quantitative perspective (Figure 5.8). Taken to the extreme this manifests as unwanted erosive and thermal effects (see Figure 3.2 e and f from the Research Methodology - Page 94). An increased operating temperature was seen to lead to the deposition of larger spray particles at greater penetrative depths.

   Inferences:

   - Increasing operating temperature increases particle deposition as well as particle depth-of-penetration.
   - Erosive and thermal effects are a consequence of high operating temperatures, far exceeding the Vicat and melting temperatures of the polymer substrates. These effects are demonstrated in Figure 3.2.

3. **Nozzle standoff distance**

   An increase in particle depth-of-penetration was observed at larger standoff distances. This was attributed to the acceleration of spray particles within the nozzle gap; since the gas velocity, although decelerating, is still greater than the average particle velocity. This presumed relationship would, however, have to be confirmed by experimental analysis. In general an increasing standoff distance corresponds to an increase in average impacting particle size. From Figure 5.5 coating uniformity and densification were attributed to an increased nozzle standoff distance.

   Inferences:

   - Particles acquire increased kinetic energy at larger nozzle standoff distances.
   - Increased powder deposition observed at higher standoff distances.

4. **Nozzle traverse speed**

   Nozzle traverse speed is a cold spray process parameter seen to influence coating quality across a range of parameter levels. From Figure 5.6 coating uniformity, densification

and consistency were seen to improve at lower traverse speeds. A caveat, however, relates to possible thermal and erosive effects arising due to a longer jet impingement dwell time. (This, however, was not evident from the visual qualitative analysis conducted here, which avoided extreme parameter values. Subsequent trials demonstrating the detrimental coating effects depicted in Figure 3.2 were able to reveal these effects).

Inferences:

- Substrate erosion may be mitigated by increasing the nozzle traverse speed.

5. **Powder feed rate**

   Within the parameter range covered by the powder feed rate variation analysis, coating quality remained fairly consistent, with no specific discernible detrimental coating conditions observed.

   Inferences:

   - Powder feed rate is not a highly sensitive parameter for low pressure cold spray for the purpose of polymer metallisation. Two caveats, however, must be mentioned. Firstly, at sufficiently high powder feed rates substrate erosion may arise, due to substrate abrasion. Secondly, higher powder feed rates may induce feeder tube clogging, due to powder agglomeration. This is exacerbated when using powders with a significant moisture content.

5.1.3 Historical studies

Previous studies into cold spray parameter effects were consulted and parameter trends and sensitivities extracted. Amongst other criteria, the key discriminating criteria for an investigation into published cold spray studies included: particle depth-of-penetrations, coating thickness, depositional efficiency, surface roughness, surface hardness and general appearance. The focus was on physically observable effects; allowing for rapid coating assessment and subsequent parameter variation for effective coating improvement. These features of interest included: substrate erosion, thermal effects, deposition, coating uniformity and perceived deposition/coating density.

Trend analysis for historical studies
The following independent parameter effect trends were observed:

1. **Operating pressure**

   Higher operating pressures have been known to:

   - Increase particle velocity [108, 193],

- Higher impacting velocities [120],

- Increase depositional efficiency [120, 124],
- Increase gas velocity [116],
- Increase coating density [121],
- Increase coating thickness [122] and
- Increase particle depth-of-penetration [123].

Inferences:

- An increase in operating pressure may lead to increased deposition and densification.

2. **Operating temperature**

Higher operating temperatures have been observed to:

- Increase coating density [121],
- Increase thermal softening of both the powder particles and the substrate, thus aiding bonding and coating development [91, 113, 193],
- Increase particle velocity [91, 108, 113, 116, 119, 120, 125, 193],
- Decrease coating porosity [126],
- Increase coating thickness [120, 122],
- Produce better spray quality in general, leading to more favourable surface coatings [122] and
- Decrease coating micro-hardness [120].

Inferences:

- Increasing operating temperature may increase deposition, reduce porosity and, to an extent, lead to a more uniform deposition.

3. **Nozzle standoff distance**

Larger nozzle standoff distances have been known to:

- Reduce coating density [121],
- Increase run width [129],
- Decrease depositional efficiency [128] and
- Increase particle impact velocity [122].

Inferences:

- Avoiding thermal effects, while increasing particle velocity, is possible with an increased nozzle standoff distance.

4. **Nozzle traverse speed**

   Nozzle traverse speed may be selectively comparable to the powder feed rate, since both influence the quantity of powders exposed to the substrate per unit area.

   Lower nozzle traverse speeds have been shown to:

   - Increase the risk and severity of thermal effects, via prolonged jet exposure time,
   - Increase coating thickness since the quantity of powder per unit time is being spread over a smaller area [120] and
   - Have little effect on micro-hardness [120].

   Inferences:

   - While increasing the risk of thermal effects, a decrease in traverse speed may increase powder deposition.

5. **Powder feed rate**

   Higher powder feed rates have been shown to:

   - Improve coating continuity [114],
   - Increase coating density [114, 120],
   - Increase coating thickness [114],
   - Decrease coating porosity [120] and
   - Increase coating adhesion to the substrate [120].

   Inferences:

   - Depositional density may be improved via a powder feed rate increase.

5.1.4 Combined parameter set effects

Based on the combined observations, trends and inferences from the theoretical model, experimental analysis and published literature findings; the Independent Parameter Effects and Variation (IPEV) decision framework was derived. For each critical cold spray parameter - operating pressure, operating temperature, nozzle standoff distance, nozzle traverse speed and powder feed rate - the key effects of parameter variation were collated. This, in turn, lead to the development of a cold spray parameter selection and variation decision framework.

The following analysis was based on general trends and is not specific to a spray gas, feedstock powder or substrate material, but is specifically applicable to cold spray polymer metallisation.

Collated trend analysis

The following independent parameter effect trends were observed:

1. **Operating pressure**

   A low pressure may cause:

   - Insufficient gas and particle velocities, and
   - Limited deposition.

   Higher pressure may:

   - Increase gas and particle velocities, and
   - Increase particle deposition and depth-of-penetration.
     - Thereby improving depositional efficiencies, improving coating density for potential coating build-up.

   Excessive pressure may:

   - Reduce powder deposition due to substrate abrasion, particle dislodgement and other erosive effects.
     - Thereby limiting surface area coverage and producing inconsistent deposition, which may subsequently introduce erosive surface features.

2. **Operating temperature**

   A low temperature may:

   - Limit deposition.
   - Reduce surface roughness at the cost of deposition.

   Higher temperatures may:

   - Increase particle impact velocities.
   - Result in the deposition of larger particles, as well as smaller.
   - Increase particle deposition and depth-of-penetration.
     - Thereby improving depositional efficiencies, reducing coating porosity, increasing surface area coverage and facilitating bonding and coating development, via thermal softening of both the spray particles and the substrate material.
   - Lead to improved spray quality and a more uniform deposition.

- Reduce coating micro-hardness.

Excessive temperatures may:

- Introduce erosive surface effects.
    - Thereby increasing surface irregularities and surface roughness.
- Induce unwanted thermal effects.
    - Including substrate melting and erosive features and ultimately prevent suitable deposition.

3. **Nozzle standoff distance**

A low standoff distance may:

- Induce thermal and erosive effects.
- Cause insufficient powder deposition.
- Cause a reduction in the average embedding particle size.
- Reduce the run width, which in turn improves cold spray run definition along the edges.
- Improve coating density.

Higher standoff distances may:

- Increase average particle impact velocity.
- Increase particle depth-of-penetration.
- Improve powder deposition through an increase in the average embedding spray particle size.
- Introduce increased surface roughness.
- Increase the average run width.
- Mitigate thermal effects.

Extreme standoff distances may:

- Significantly reduce coating deposition, density and run consistency.

4. **Nozzle traverse speed**

A low nozzle traverse speed may:

- Increase potential powder deposition.
    - Thereby improving depositional efficiencies.
- Increase the risk of thermal and erosive effects.
    - These effects manifest as severe surface roughness and surface irregularity.

Higher nozzle traverse speeds may:

- Reduce potential substrate erosion.
    - Thereby reducing undesired surface irregularity.
- Mitigate destructive thermal effects.

Extreme nozzle traverse speeds may:

- Significantly limit powder deposition.
- Result in depositional inconsistencies.

5. **Powder feed rate**

   Low feed rates may result in:

   - Insufficient powder deposition.
   - Inconsistent deposition.

   Higher feed rates may:

   - Improve powder deposition.
       - Thereby improving coating continuity and depositional densification.

   Excessive feed rates may cause:

   - Erosive surface features.
   - Clogging of the cold spray units powder feeder tubes.
   - Introduce inconsistencies in powder deposition.

Cold spray parameter selection and variation decision framework

These collated and consolidated parameter effects were then used to develop a tool for cold spray parameter selection and refinement, based on the five detrimental coating depositional effects (lack of deposition, lack of depositional consistency, lack of coating densification, thermal effects and erosive features). The final decision table, based on the structure suggested by Figure 2.19 in the literature survey, is depicted here in Table 5.1.

The strength of the decision table lies in the quantitative data informing variation, from which parameter selection is inferred from real-time, qualitative, visual observations. This decision table, as a critical research outcome, has significant application potential for novel cold spray polymer metallisation. While this parameter selection and variation decision framework was derived as a means of assisting cold spray polymer metallisation for the generation of antimicrobially active surface coatings; its *big picture* use extends into a much broader feasibility space within the various branches of cold spray technology. From thin film applications,

through to advanced multi-material and multi-step additive manufacturing processes, benefit may be gained from such a practical experimental tool. One such application example is that of thermal protection layers for polymer moulds as a novel, cost effective idea for injection moulding applications.

For the current application, this tool was coupled with the system constraints, which function as overall limiting factors. Parameter selection and subsequent variations, requires an initial constraint check so as to ensure all selected parameter values fall within acceptable levels. These system constraints are given by:

Operating pressure: 0.55 MPa $< P_0 <$ 1 MPa
Operating temperature: $T_0 < 550°C$
Nozzle standoff distance: SOD > 5 mm
Nozzle traverse speed: $V_n < 500$ mm/s
Powder feed rate: (Percentage value i.e. 0 - 100%)

Table 5.1: The cold spray parameter selection and variation decision table.

	Parameter Variations				
Cold Spray Deposition Issues	**Operating Pressure**	**Operating Temperature**	**Nozzle Standoff Distance**	**Nozzle Traverse Speed**	**Powder Feed Rate**
Lack of Deposition	Increase if previously low. Decrease if previously high.	Increase	Increase if previously low. Decrease if previously high.	Decrease	Increase
Lack of Densification	Increase if previously low. Decrease if previously high.	Increase	Decrease	Decrease	Increase
Lack of Depositional Consistency	Increase if previously low. Decrease if previously high.	Increase	Increase if previously low. Decrease if previously high.	Decrease	Increase if previously low. Decrease if previously high.
Erosive Features	Decrease	Decrease	Increase	Increase	Decrease
Thermal Effects	N/A	Decrease	Increase	Increase	N/A

5.2 Independent cold spray parameter effects

The effects of independent parameter levels were related to the surface topographical effects of: arithmetic mean deviation of the profile (Ra), the maximal height of the profile (Rz), the mean spacing for the microscopic roughness profile (Rsm), the mean spacing between individual profile peeks (Rs), the root mean square deviation of the profile (Rq) and finally the skewness of the profile (Rsk), which is a measurement of the asymmetry of amplitude distribution.

Figure 5.9 and Figure 5.10 depict scatter plot matrices for the independent cold spray parameter effects on surface topography for single and multi-pass coatings respectively. Based on the Pearson correlation analysis the associated coefficient of determination (R^2) values are included for all graphs. The Pearson correlation (R) represents the extent of a linear relationship between two sets of data [167]. The strongly correlated trends are highlighted **dark orange** (dark grey if viewed in greyscale), while the moderate correlations are **light orange** (light grey if viewed in greyscale) coloured. Data was collected from trials involving the independent variation of cold spray process parameters, maintaining all other parameters at a central (medium) level. The corresponding data tables are given in Appendix C, which include the raw roughness measurements and the Pearson correlation coefficient analysis.

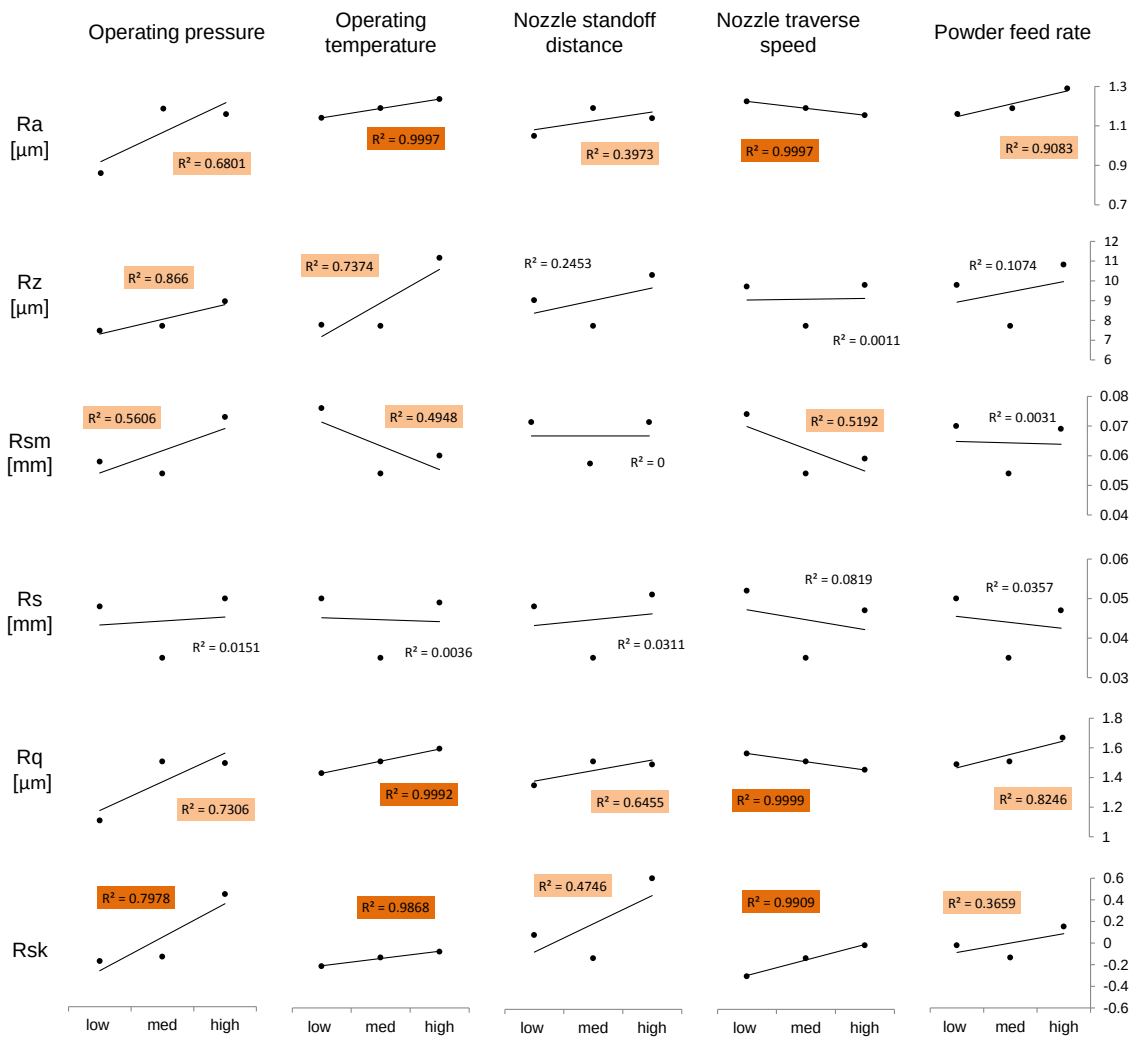


Figure 5.9: Scatter plot matrix of independent cold spray parameter effects on surface topography (single pass coating).

Operating temperature and nozzle traverse speed were seen to have the greatest effect on surface topographical effects for a single pass coating, while operating pressure, operating temperature and nozzle standoff distance have the greatest influence on surface profile for a multi-pass coating. This was, however, based on a linear trend analysis.

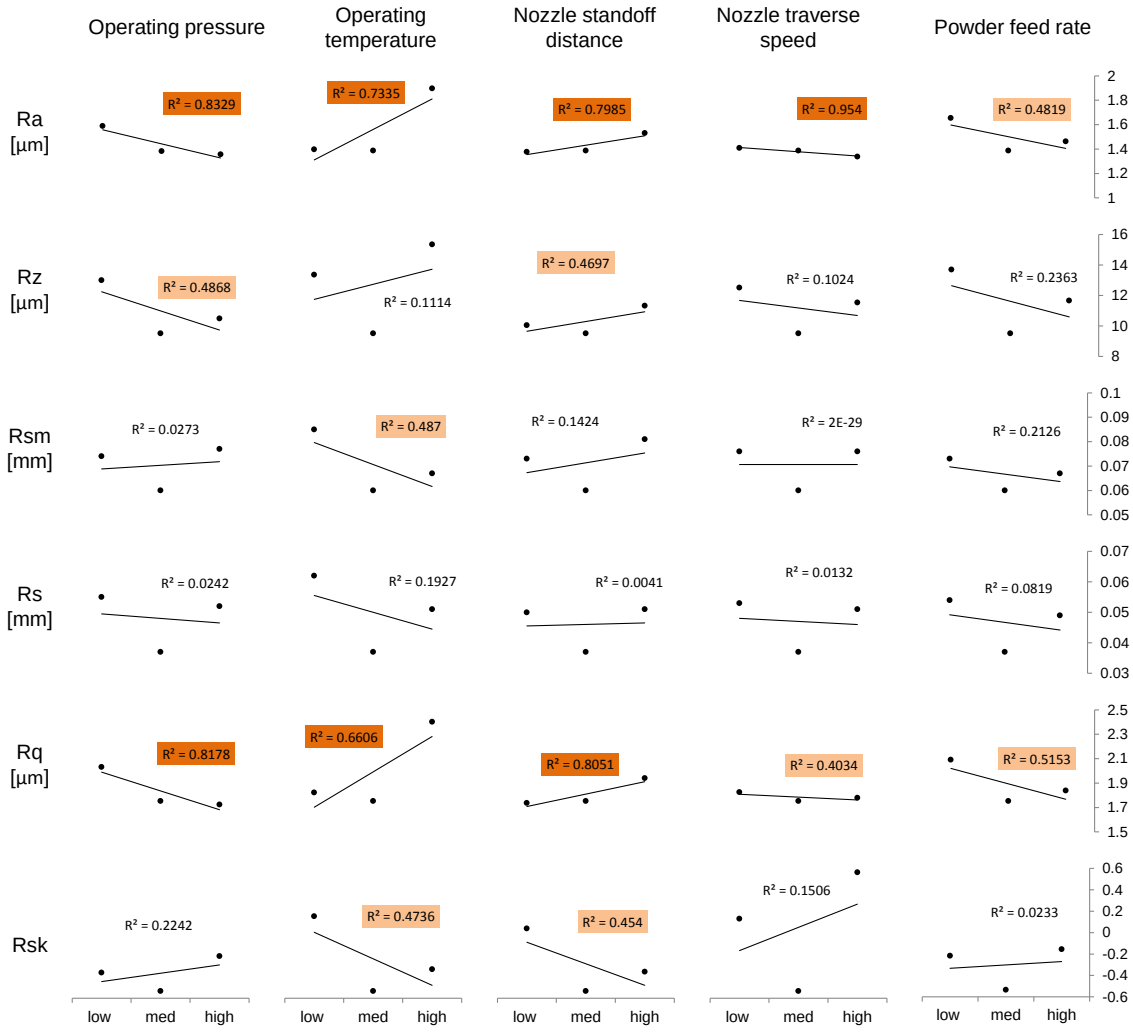


Figure 5.10: Scatter plot matrix of independent cold spray parameter effects on surface topography (multi-pass coating).

In general the overall effect of an increase in each cold spray process parameter on surface topography, for a single pass coating, may be summarised according to the following:

1. **Operating pressure** ⇒ An increase in coating roughness.
2. **Operating temperature** ⇒ An increase in coating roughness.
3. **Nozzle standoff distance** ⇒ A marginal increase in coating roughness.
4. **Nozzle traverse speed** ⇒ A decrease in coating roughness.
5. **Powder feed rate** ⇒ A marginal increase in coating roughness.

The desired response regarding surface topography was to be based on the later evaluated antimicrobial ability of the respective coatings, documented in Chapter 6.

5.3 Experimental optimisation

Experimental optimisation was carried out, based on thirteen successful theoretically optimised coating types. The Independent Parameter Effects and Variation (IPEV) decision table for cold spray polymer metallisation was successfully applied, thereby reducing the number of cold spray runs required and avoiding profligate use of time and cold spray consumables.

5.3.1 Sample Analyses

As a means of demonstrating the experimental procedure two coating types were selected. The first represents the successful optimisation of a copper cold spray coating on a PEEK substrate; while the second demonstrates the attempted, yet unsuccessful, optimisation of a copper coating on a polycarbonate substrate. Each test run had an associated reference number. The reference prefix for the copper-PEEK combination is *Cu(1)PEEK*, while *Cu(1)PC* represents the copper-PC combination.

Sample analysis 1 - Copper-PEEK
Level A
The first stage of experimental optimisation evaluated the quality of the theoretically optimum parameter sets. Of the five depositional issues that are prevalent with cold spray of polymer substrates only one was evident for cold spray of copper onto PEEK substrates, that of a lack of densification (See Figure 5.11). The developed IPEV decision table was then used to make recommendations as to strategic parameter variations. Based on this analysis it was determined that a decrease in operating pressure, an increase in operating temperature and an increase in powder feed rate may yield higher deposition density.

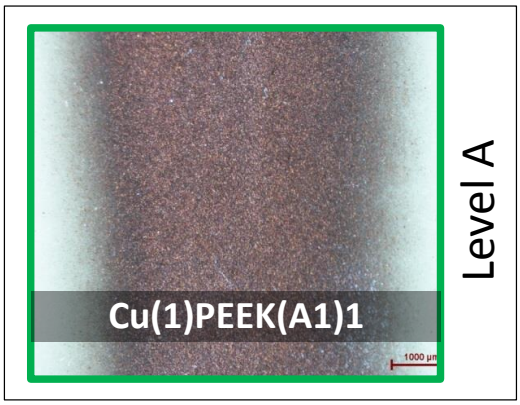


Figure 5.11: Micrograph of copper cold sprayed PEEK during Level A of the experimental optimisation procedure, using the theoretically optimum parameter set.

Level B

Applying these parameter variations, as part of the process of Level B, Figure 5.12 depicts the selection of experimental runs 17, 19, 21 and 23 according to Table C.7.

The naming convention for test samples in his section relates to a two part designation. The first part denotes the coating and substrate. For example given Cu(1)PEEK, the Cu(1) represents the high purity copper powder coating and PEEK is the abbreviation for the thermoplastic substrate polyetheretherkeytone. The second part of the nomenclature denotes the specific test conducted, related to the optimisation level (A,B,C or D), the specification of the test parameter levels and any special test modifications, such as an additional temperature variation. Again as an example, Cu(1)PEEK**(B21 - T)24** refers to a copper cold spray coated polyetheretherkeytone test sample undergoing the Level B optimisation procedure (see page 101) with the 21st parameter variation (see Table C.7 in Appendix C for details) and modified by a special temperature variation (using a reduced operating temperature indicated by the -T). The 24 indicates that this is the 24th possible parameter set combination for the optimisation of a copper-PEEK cold spray coating.

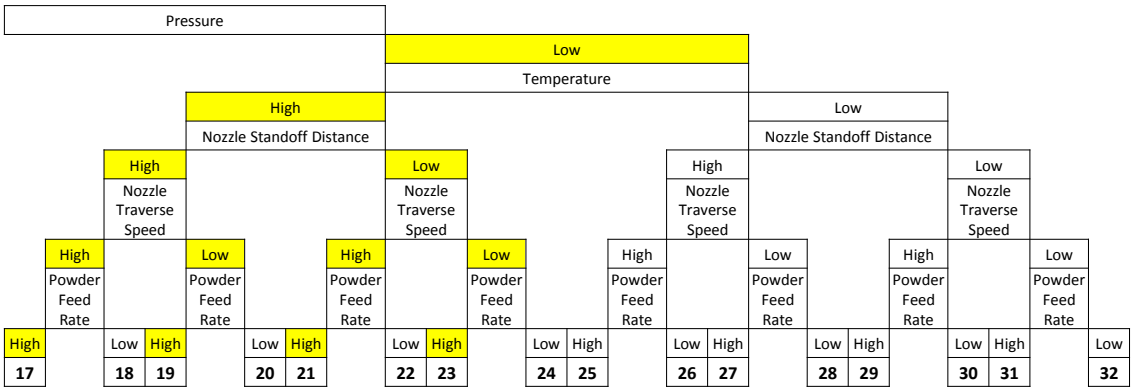


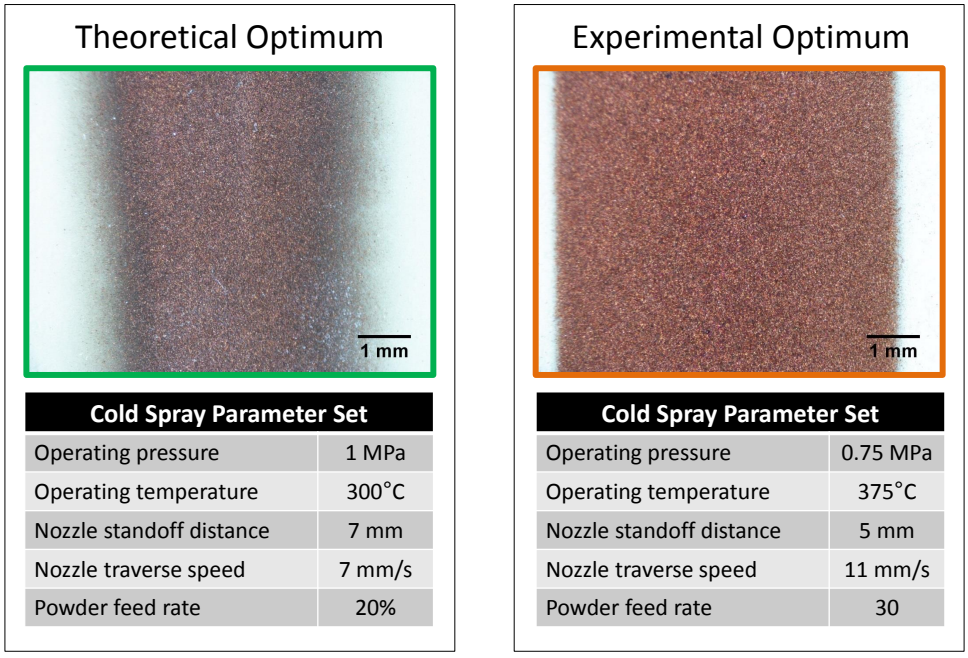
Figure 5.12: IPEV parameter selections for Level B of the experimental optimisation of copper coated PEEK (truncated selection table).

For each of the four cold spray runs independent variations of temperature (decrease) and pressure (increase) were included, such that 12 unique cold spray runs were carried out. Figure 5.13 depicts the stereoscopic microscopy results for the optimisation of a copper coating of PEEK substrates. These coatings were evaluated and coating Cu(1)PEEK(B21-T)24 (See Figure 5.13) was identified as a local optimum. This parameter set achieved a good, uniform deposition, without the occurrence of any of the five detrimental depositional issues.



Figure 5.13: Micrographs of copper cold sprayed PEEK during Level B of the experimental optimisation procedure, using the theoretically optimum parameter set.

Figure 5.14 depicts the micrographs and parameter sets for both the theoretically and experimentally optimum parameter sets for the optimisation of a copper cold spray coating on a PEEK substrate.



Cold Spray Parameter Set	
Operating pressure	1 MPa
Operating temperature	300°C
Nozzle standoff distance	7 mm
Nozzle traverse speed	7 mm/s
Powder feed rate	20%

Cold Spray Parameter Set	
Operating pressure	0.75 MPa
Operating temperature	375°C
Nozzle standoff distance	5 mm
Nozzle traverse speed	11 mm/s
Powder feed rate	30

Figure 5.14: Micrographs and parameter sets of the theoretically and experimentally optimum cold spray copper coatings on a PEEK thermoplastic substrate.

Sample analysis 2 - Copper-PC

Figure 5.15 depicts the optimisation process for a copper coating on a polycarbonate substrate. Micrographs with a coloured outline represent the best result for each level and/or process parameter. This specific coating was unsuccessful for the intended touch contact antimicrobial application, due to the persistence of at least one of the critical depositional issues; even though successive parameter refinement was observed.

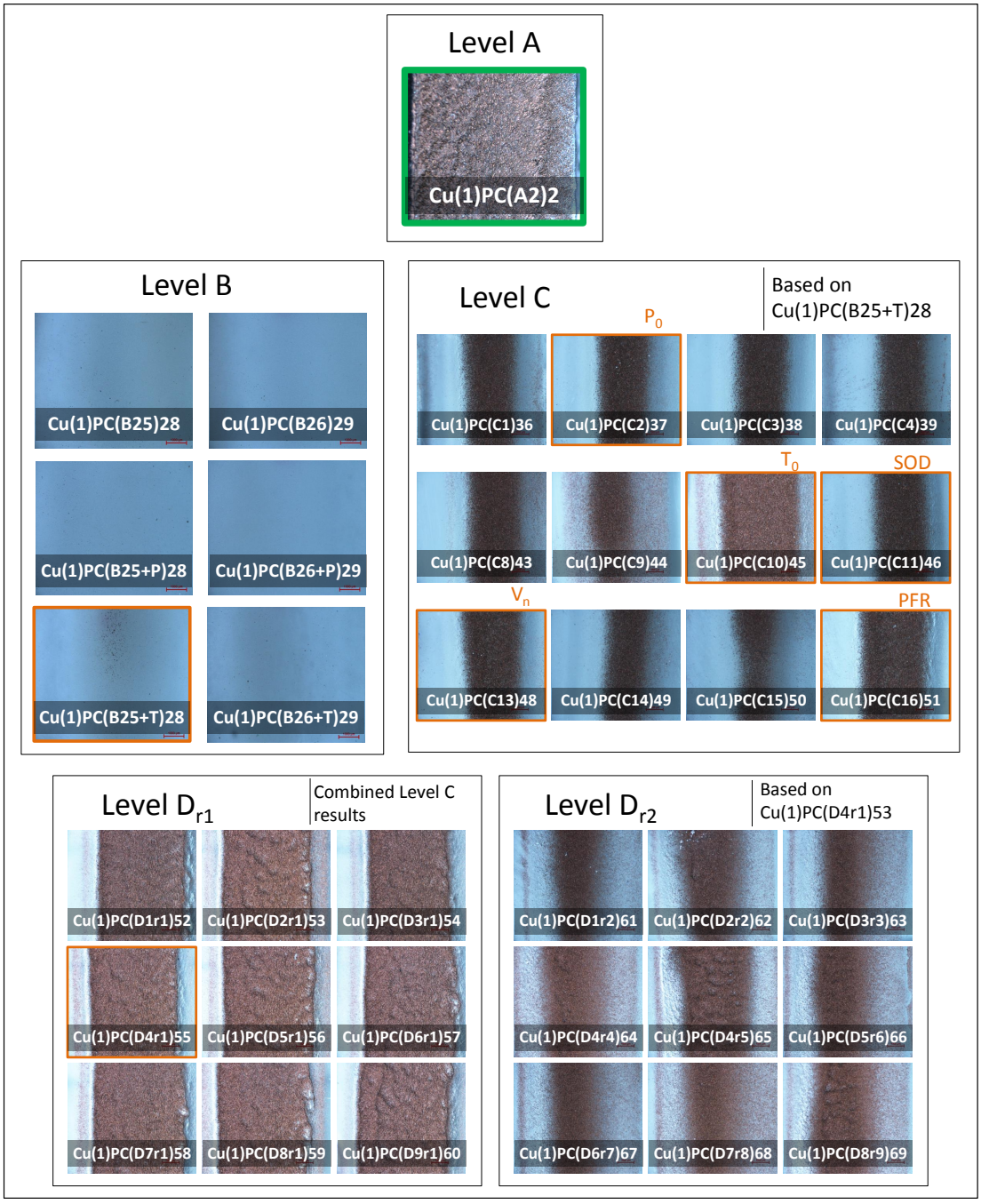


Figure 5.15: Experimental optimisation process for the unsuccessful experimental optimisation of copper cold spray coating of polycarbonate.

This experimental procedure was repeated for all coating types (Cu, $CuAlAl_2O_3$ and Zn) and their respective substrates (3D Printed ABS, ABS, PC and PEEK). A list of all cold spray runs conducted is given in Appendix C, Table C.8. The optimum coatings are highlighted yellow.

5.4 Experimental cold spray parameter sets

The optimised cold spray parameter sets, while uniquely tailored to each powder coating type, rely on additional set system parameters. These parameters relate to the nozzle design, spray gas, powder properties and ambient conditions. Their specifications are given as follows:

Nozzle design
Throat diameter ⇒ 2.5 mm
Exit diameter ⇒ 6.5 mm
Nozzle divergent length ⇒ 120 mm

Spray gas
Air

Powder properties
Dessicated powder with average particle size in the range 20 - 30 μm.

Ambient conditions
Atmospheric conditions

Table 5.2 contains the experimentally optimised cold spray parameter sets. The key parameters are: operating pressure, operating temperature, nozzle standoff distance, nozzle traverse speed, powder feed rate and the run step distance (i.e. the set distance between adjacent cold spray runs). Appendix E contains a table (Table E.1) which defines the test samples used in all three aspects of this current study, from theoretical optimisation to the coatings used in the next chapter covering the antimicrobial susceptibility testing. This table is reproduced here (Table 5.3) specifically to aid interpretation of the material naming convention.

Table 5.2: Experimentally optimum cold spray parameter sets.

Powder – Substrate Combination	Operating Pressure (MPa)	Operating Temperature (°C)	Nozzle Standoff Distance (mm)	Nozzle Traverse Speed (mm/s)	Powder Feed Rate (%)	Step Distance (mm)
Copper – 3D Printed ABS (hor.)	0.75 (109 Psi)	190	5	15	30	4
Copper – ABS	0.75 (109 Psi)	190	5	15	30	5
Copper – PEEK	0.75 (109)Psi	375	5	11	30	5
Copper – PEEK (polished coating)	0.75 (109)Psi	375	5	11	30	5
Copper – 3D Printed ABS (vert.)	0.75 (109 Psi)	190	5	15	30	4
(Cu-Al-Al_2O_3) – 3D Printed ABS (hor.)	0.75 (109 Psi)	190	15	15	30	4
(Cu-Al-Al_2O_3) – ABS	0.75 (109 Psi)	190	5	15	30	5
Zinc – 3D Printed ABS (hor.)	0.8 (116 Psi)	200	10	15	30	5
Zinc – ABS	0.8 (116 Psi)	200	10	5	30	5
Zinc – PC	0.9 (116 Psi)	300	15	10	20	5
75 wt% Cu - 25 wt% Zn – 3D Printed ABS (hor.)	0.85 (102 Psi)	210	15	12	30	6
50% (w/w) Cu - Zn – 3D Printed ABS (hor.)	0.85 (102 Psi)	200	15	10	30	6
75 wt% Zn - 25 wt% Cu – 3D Printed ABS (hor.)	0.7 (102 Psi)	180	15	10	30	6
Copper – Copper*	0.89(130 Psi)	420	15	15	20	5
5 wt% Ag - 95 wt% Cu – Copper*	0.89(130 Psi)	420	15	15	20	5
5 wt% Ag – 95 wt% Cu - ABS	0.75 (109 Psi)	190	5	15	30	5
5 wt% Ag - 95 wt% Cu – 3D Printed ABS (vert.)	0.75 (109 Psi)	190	5	15	30	4
5 wt% Ag - 95 wt% Cu – 3D Printed ABS (hor.)	0.75 (109 Psi)	190	5	15	30	4
5 wt% Ag - 47.5 wt% Cu-Zn – 3D Printed ABS (hor.)	0.85 (102 Psi)	200	15	10	30	6
5 wt% Ag - 95 wt% Zn – 3D Printed ABS (hor.)	0.8 (116 Psi)	200	10	15	30	5
*Requires grit blasting with Aluminium Oxide (G0002)	0.41(60 Psi)	room temp.	20	25	15	5

Table 5.3: Cold spray coating naming convention for theoretical, experimental and antimicrobial susceptibility tests.

Theoretical Coatings		Experimental Optimisation Coatings		Antimicrobial Susceptibility Test Coatings	
Coating	Substrate	Coating	Substrate	Coating	Substrate
Copper	ABS	Copper	3D Printed ABS (hor.* and vert.*)	Copper	3D Printed ABS (hor. and vert.)
	Polycarbonate		ABS		ABS
	PEEK		Polycarbonate		PEEK
Nickel	ABS		PEEK		PEEK (polished coatings)
	Polycarbonate	Cu-Al-Al_2O_3	3D Printed ABS (hor.)		Copper
	PEEK		ABS	Cu-Al-Al_2O_3	3D Printed ABS (hor.)
Zinc	ABS		Polycarbonate		ABS
	Polycarbonate	75 wt% Cu - 25 wt% Zn	3D Printed ABS (hor.)	Zinc	3D Printed ABS (hor.)
	PEEK	50% (w/w) Cu-Zn	3D Printed ABS (hor.)		ABS
Tin	ABS	75 wt% Zn - 25 wt% Cu	3D Printed ABS (hor.)		Polycarbonate
	Polycarbonate	Zinc	3D Printed ABS (hor.)	75 wt% Cu - 25 wt% Zn	3D Printed ABS (hor.)
	PEEK		ABS	50% (w/w) Cu-Zn	3D Printed ABS (hor.)
Aluminium	ABS		Polycarbonate	75 wt% Zn - 25 wt% Cu	3D Printed ABS (hor.)
	Polycarbonate			5 wt% Ag - 95 wt% Cu	Copper
	PEEK				3D Printed ABS (hor. And vert.)
					ABS
				5 wt% Ag - 47.5% (w/w) Cu-Zn	3D Printed ABS (hor.)
				5 wt% Ag - 95 wt% Zn	3D Printed ABS (hor.)

* hor. = horizontal print orientation, vert. = vertical print orientation

5.5 Coating characterisation

5.5.1 Theoretical and experimental coating characterisation

Characterisation of both the theoretical and experimental coatings was made on a comparative analysis basis. The key points of characterisation included: a general appearance description; defining the average impacting particle size, shape and depth-of-penetration; followed by surface topography and wear resistance specifications. For the theoretical coatings, which were not deemed local optima, an additional classification of surface area coverage was included. The three critical areas of coating characterisation include: particle depth-of-penetration, surface topography analysis and coating wear resistance.

Particle depth-of-penetration

The analysis of particle depth-of-penetration encompasses impacting particle area (A), particle perimeter (P), circularity (C), equivalent diameter (D), the area of the partially embedded particle above the substrate surface and the area below the substrate surface. These data and the determined maximum depth-of-penetration and normalised particle depth-of-penetration may be found in Appendix C, for both the theoretical and experimentally optimum cold spray parameter sets.

Surface topography analysis

Surface topography analysis was carried out for both theoretically and experimentally optimum cold spray coatings, along with the respective substrates. The theoretically optimum coatings were cold sprayed both as single pass coatings and multi-pass (5 layer) coatings and their arithmetic mean profile deviations (Ra) measured in accordance with ISO4288. The results for these tests are given in Appendix C, Table C.17.

The experimentally optimum coatings and their relevant substrates were evaluated in terms of the following parameters: arithmetic mean profile deviation (Ra), maximal profile height (Rz), mean roughness profile spacing (Rsm), mean peak spacing (Rs) and profile skewness (Rsk). The comprehensive results for these parameters with measurements made in two orthogonal orientations for both single pass coatings (the primary focus of this research) and multi-pass (5 layers) coatings may be found in the relevant tables in Appendix C, Tables C.18 - C.22 (All units of the parameters are given by the standard units defined on page 105).

Coating wear resistance

Wear resistance is a property which was ultimately desired to be maximised as a means of prolonging operational durability. The primary objective of the present research, however, was with regards to the development of effective antimicrobial surface coatings. Therefore,

instead of being used as a developmental step, the ASTM G99 standard test method provided the required steps for effective wear resistance characterisation. Chapter 7, provides for a diverse and interrelated evaluation of coating properties and characteristics towards the goal of effective design for antimicrobial surface coatings.

The wear resistance screening tests, which were used to isolated a suitable wear test parameter set for effective analysis of cold spray polymer metallised coatings, are documented in Table C.23 and Figure C.1 of Appendix C.

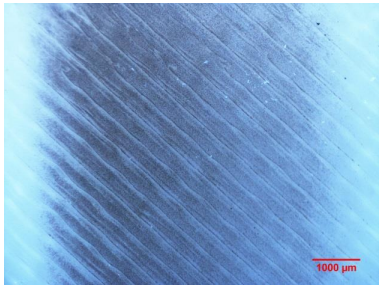
The combined results for the surface wear tests may be found in Table C.24 of Appendix C, while the key results are included in the coating characterisation.

The average quantified features of both the theoretical and experimentally optimum cold spray coatings, which include the three key parameters of: particle depth-of-penetration, surface topography and coating wear resistance, are summarised in the coating characterisation. As an initial strategy and tool for coating development, the theoretical coatings were seen to be effective in isolating a good first pass parameter set for novel powder-substrate combinations. The experimental optimisation procedure effectively modified these initial parameter sets to those which produced successful cold spray polymer metallised coatings.

Theoretically optimum coating characterisation focused on depositional quality, with regards to successful powder deposition. Thus the priority parameters included surface area coverage. Experimentally optimum coating characterisation, on the other hand, prioritised qualities of coating application. Thus wear resistance and detailed surface topography analyses replaced surface area coverage. General coating appearance and the particle impact analysis were, however, consistent points of analysis across both coating types.

Copper – 3D Printed ABS (hor.)

Theoretically optimum



General appearance

Low and variable spray deposition such that of the five key depositional effects this coating exhibits three.

1. Lack of deposition.
2. Lack of depositional consistency.
3. Lack of densification.

Impacting particle analysis

Particle size (D):	13.57 µm
Particle circularity:	0.54
Depth-of-penetration (X):	8.25 µm
X/D:	0.61

Surface topography

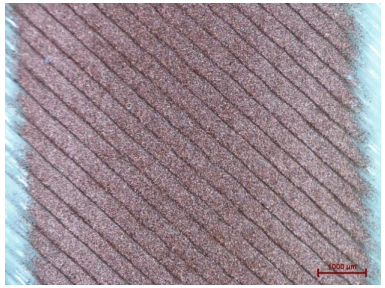
Ra = 8.935 µm (SD = 0.98)

Surface area coverage

84.37 %

Copper – 3D Printed ABS (hor.)

Experimentally optimum



General appearance

Uniform, dense powder deposition without substrate distortion. 3D printer tracks still visible, contributing to the unique surface profile.

Impacting particle analysis

Particle size (D):	9.25 µm
Particle circularity:	0.68
Depth-of-penetration (X):	4.34 µm
X/D:	0.57

Surface topography

Ra = 3.61 µm Rz = 11.36 µm

Rsm =0.08 mm Rs = 0.05 mm

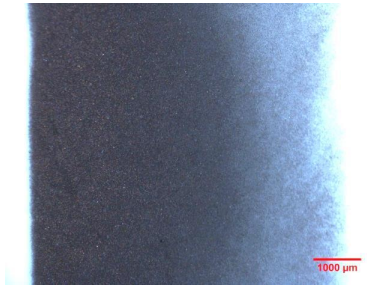
Rsk = 0.33

Wear resistance

µ = 0.509 | k = 1.3 x 10^{-3} mm^3/N·m

Copper – ABS

Theoretically optimum



General appearance

Deposition achieved, yet lacking coating thickening and continuity. Two out of five depositional effects present.

1. Lack of depositional consistency.
2. Lack of densification.

Impacting particle analysis

Particle size (D):	9.58 µm
Particle circularity:	0.59
Depth-of-penetration (X):	6.59 µm
X/D:	0.93

Surface topography

Ra = 0.875 µm (SD = 0.1)

Surface area coverage

95.97 %

Copper – ABS

Experimentally optimum



General appearance

Uniform, dense powder deposition without substrate distortion. Consistent deposition across length and width of a cold spray run.

Impacting particle analysis

Particle size (D):	9.16 µm
Particle circularity:	0.53
Depth-of-penetration (X):	7.41 µm
X/D:	0.81

Surface topography

Ra = 1.04 µm Rz = 7.85 µm

Rsm = 0.05 mm Rs = 0.03 mm

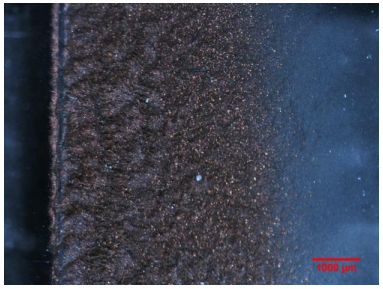
Rsk = 0.04

Wear resistance

µ = 0.442 | k = 4.40 x 10^{-4} mm^3/N·m

Copper - PC

Theoretically optimum



General appearance

Clear evidence of thermal and erosive features, with uneven spray deposition. Three of the five depositional effects evident.

1. Lack of depositional consistency.
2. Erosive features.
3. Thermal effects.

Impacting particle analysis

Particle size (D):	/
Particle circularity:	/
Depth-of-penetration (X):	/
X/D:	/

Surface topography

Ra = 12.55 µm

Surface area coverage

86.39 %

Copper - PC

Experimentally optimum

No optimum coating achieved

Impacting particle analysis

Particle size (D):	N/A
Particle circularity:	N/A
Depth-of-penetration (X):	N/A
X/D:	N/A

Surface topography

Ra = N/A Rz = N/A

Rsm = N/A Rs = N/A

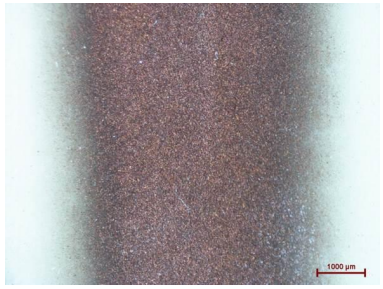
Rsk = N/A

Wear resistance

µ = N/A | k = N/A

Copper - PEEK

Theoretically optimum



General appearance

Narrow deposition run, yet exhibiting consistent deposition with no thermal or erosive features . One out of the five depositional effects present.

1. Lack of densification.

Impacting particle analysis

Particle size (D):	4.38 µm
Particle circularity:	0.71
Depth-of-penetration (X):	0.95 µm
X/D:	0.26

Surface topography

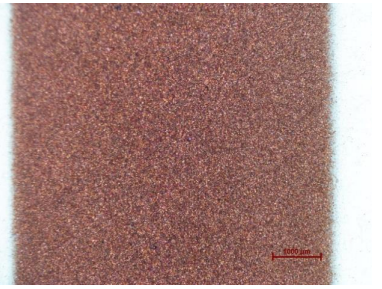
Ra = 3.167 µm (SD = 0.3)

Surface area coverage

/

Copper - PEEK

Experimentally optimum



General appearance

Good, uniform deposition of acceptable quality. Bright copper colouring with a uniform surface finish, consistent profile with negligible variation.

Impacting particle analysis

Particle size (D):	3.27 µm
Particle circularity:	0.65
Depth-of-penetration (X):	0.93 µm
X/D:	0.28

Surface topography

Ra = 3.93 µm Rz = 29.82 µm

Rsm = 0.09 mm Rs = 0.06 mm

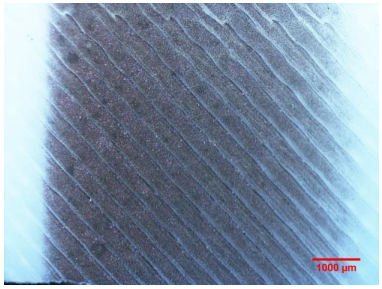
Rsk = 0.28

Wear resistance

µ = 0.481 | k = 5.20×10^{-4} $mm^3/N \cdot m$

Cu-Al-Al_2O_3 – 3D Printed ABS (hor.)

Theoretically optimum



General appearance

Uniform, yet light deposition, with the 3D surface profile clearly visible. Consistent spray deposition with fairly well defined run edges. One of the five depositional effects present.

1. Lack of densification.

Impacting particle analysis

Particle size (D):	7.10 µm
Particle circularity:	0.57
Depth-of-penetration (X):	5.19 µm
X/D:	0.76

Surface topography

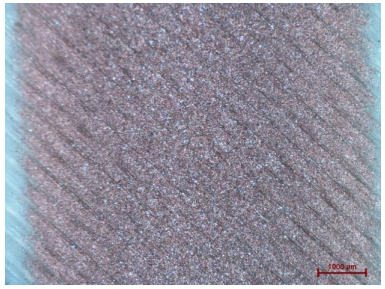
Ra = 22.57 µm (SD = 3.25)

Surface area coverage

89.68 %

Cu-Al-Al_2O_3 – 3D Printed ABS (hor.)

Experimentally optimum



General appearance

Very good deposition – uniform and consistent. Well defined run edges and perceived thick deposition layer. No discernible substrate deformation.

Impacting particle analysis

Particle size (D):	6.81 µm
Particle circularity:	0.75
Depth-of-penetration (X):	4.26 µm
X/D:	0.63

Surface topography

Ra = 4.4 µm Rz = 9.68 µm

Rsm = 0.05 mm Rs = 0.03 mm

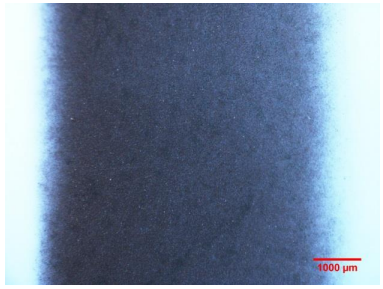
Rsk = 0.64

Wear resistance

µ = / | k = /

Cu-Al-Al_2O_3 – ABS

Theoretically optimum



General appearance

Uniform coating with acceptable consistency. Multi-pass coatings improved densification significantly, yet for a single pass coating one of the five depositional issues was present.

1. Lack of densification.

Impacting particle analysis

Particle size (D):	9.31 µm
Particle circularity:	0.68
Depth-of-penetration (X):	5.21 µm
X/D:	0.56

Surface topography

Ra = 1.03 µm (SD = 0.11)

Surface area coverage

98.18 %

Cu-Al-Al_2O_3 – ABS

Experimentally optimum



General appearance

Excellent coating quality from a single pass coating. Uniform and dense cold spray deposition with smooth surface finish.

Impacting particle analysis

Particle size (D):	10.25 µm
Particle circularity:	0.62
Depth-of-penetration (X):	4.89 µm
X/D:	0.47

Surface topography

Ra = 1.25 µm Rz = 9.95 µm

Rsm = 0.04 mm Rs = 0.03 mm

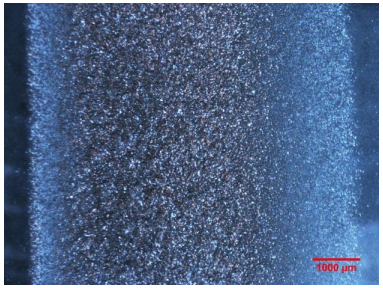
Rsk = 0.67

Wear resistance

µ = / | k = /

Cu-Al-Al_2O_3 – PC

Theoretically optimum



General appearance

Clear jet impingement effects and a lack of depositional consistency. Three out of five depositional effects present.

1. Lack of depositional consistency.
2. Erosive features.
3. Thermal effects.

Impacting particle analysis

Particle size (D):	N/A
Particle circularity:	N/A
Depth-of-penetration (X):	N/A
X/D:	N/A

Surface topography

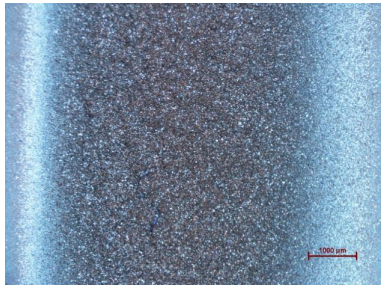
Ra = 8.32 µm

Surface area coverage

93.33 %

Cu-Al-Al_2O_3 – PC

Experimentally optimum



General appearance

Coating exhibited none of the five depositional effects to an extent to warrant its notification. However, the coating wasn't deemed good enough to take through further analysis.

Impacting particle analysis

Particle size (D):	N/A
Particle circularity:	N/A
Depth-of-penetration (X):	N/A
X/D:	N/A

Surface topography

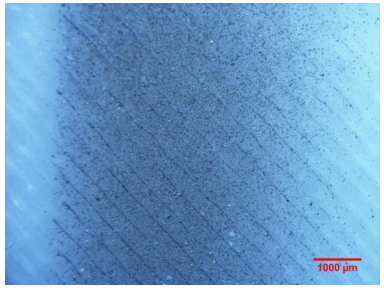
Ra = N/A	Rz = N/A
Rsm = N/A	Rs = N/A
Rsk = N/A	

Wear resistance

µ = / | k = /

Zinc – 3D Printed ABS (hor.)

Theoretically optimum



General appearance

Uniform deposition, yet lacking densification for coating thickening. Two out of five depositional issues present.

1. Lack of deposition.
2. Lack of densification.

Impacting particle analysis

Particle size (D):	14.20 µm
Particle circularity:	0.75
Depth-of-penetration (X):	18.92 µm
X/D:	1.28

Surface topography

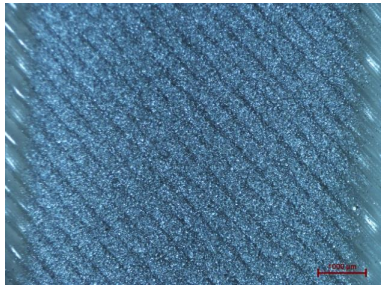
Ra = 7.38 µm (SD = 0.48)

Surface area coverage

48.18 %

Zinc – 3D Printed ABS (hor.)

Experimentally optimum



General appearance

Uniform and dense cold spray deposition. Consistent deposition without damaging the substrate surface.

Impacting particle analysis

Particle size (D):	11.87 µm
Particle circularity:	0.77
Depth-of-penetration (X):	13.21 µm
X/D:	1.29

Surface topography

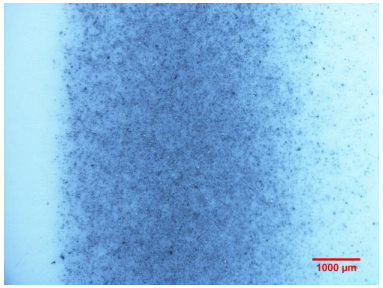
Ra = 4.98 µm	Rz = 18.02 µm
Rsm = 0.07 mm	Rs = 0.05 mm
Rsk = -0.1	

Wear resistance

µ = 0.544 | k = 2.87 x 10^{-3} mm^3/N·m

Zinc – ABS

Theoretically optimum



General appearance

Uniform deposition, lacking sufficient coating densification. Multi-pass coatings were, however, suitable. Single pass coatings exhibited two out of five depositional effects.

1. Lack of deposition.
2. Lack of densification.

Impacting particle analysis

Particle size (D):	21.23 µm
Particle circularity:	0.52
Depth-of-penetration (X):	10.16 µm
X/D:	0.42

Surface topography

Ra = 1.91µm (SD = 0.33)

Surface area coverage

57.02 %

Zinc – ABS

Experimentally optimum



General appearance

High density deposition with high consistency and uniformity in cold spray deposition. No thermal or erosive effects. Desirable surface finish achieved.

Impacting particle analysis

Particle size (D):	19.48 µm
Particle circularity:	0.61
Depth-of-penetration (X):	19.96 µm
X/D:	0.92

Surface topography

Ra = 6.27 µm Rz = 43.43 µm

Rsm = 0.11 mm Rs = 0.07 mm

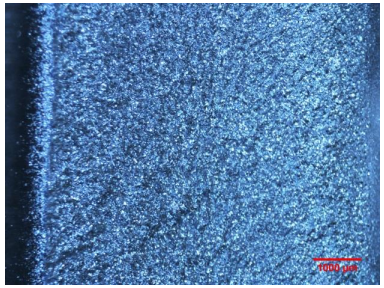
Rsk = 0.5

Wear resistance

µ = 0.413 | k = 1.69 x 10^{-3} m^3/N·m

Zinc – PC

Theoretically optimum



General appearance

High deposition with a thick coating, yet exhibiting clear thermal and erosive features. Two out of five depositional issues present.

1. Erosive features.
2. Thermal effects.

Impacting particle analysis

Particle size (D):	4.55 µm
Particle circularity:	0.75
Depth-of-penetration (X):	/
X/D:	/

Surface topography

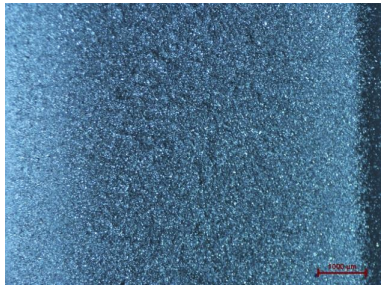
Ra = 13.37 µm (SD = 3.1)

Surface area coverage

100 %

Zinc – PC

Experimentally optimum



General appearance

Good deposition, with a coating of acceptable quality. Skewed deposition, with higher concentration of particle deposition along a cold spray centreline.

Impacting particle analysis

Particle size (D):	2.35 µm
Particle circularity:	0.85
Depth-of-penetration (X):	2.27 µm
X/D:	0.96

Surface topography

Ra = 7.01 µm Rz = 46.71 µm

Rsm = 0.13 mm Rs = 0.07 mm

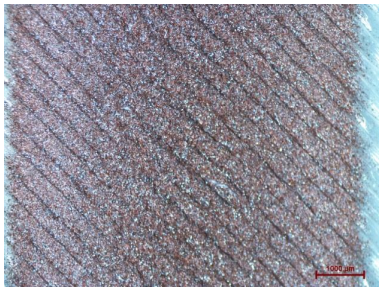
Rsk = 0.24

Wear resistance

µ = 0.505 | k = 1.81 x 10^{-3} mm^3/N·m

75 wt% Cu – 25wt% Zn – 3D Printed ABS (hor.)

Experimentally optimum



General appearance

Good coating, with a slight higher concentration of deposited spray particles along the cold spray run centreline.

Impacting particle analysis

Particle size (D):	/
Particle circularity:	/
Depth-of-penetration (X):	/
X/D:	/

Surface topography

Ra = 5.21 µm	Rz = 12.52 µm
Rsm = 0.06 mm	Rs = 0.03 mm
Rsk = 0.33	

Wear resistance

µ = /	k = /

50% (w/w) Cu-Zn – 3D Printed ABS (hor.)

Experimentally optimum



General appearance

Visually the most consistent, uniform and dense coating out of the three copper-zinc blended coatings.

Impacting particle analysis

Particle size (D):	9.37 µm
Particle circularity:	0.64
Depth-of-penetration (X):	5.89 µm
X/D:	0.81

Surface topography

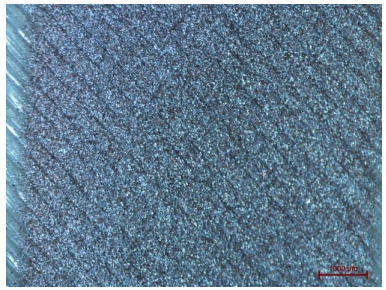
Ra = 5.16 µm	Rz = 14.78 µm
Rsm = 0.07 mm	Rs = 0.03 mm
Rsk = 0.14	

Wear resistance

µ = 0.475	k = 2.29 x 10^{-3} $mm^3/N{\cdot}m$

75 wt% Zn – 25wt% Cu – 3D Printed ABS (hor.)

Experimentally optimum



General appearance

Uniform and dense deposition. Good surface finish with no thermal or erosive effects.

Impacting particle analysis

Particle size (D):	/
Particle circularity:	/
Depth-of-penetration (X):	/
X/D:	/

Surface topography

Ra = 5.49 µm	Rz = 16.18 µm
Rsm = 0.09 mm	Rs = 0.04 mm
Rsk = 0.12	

Wear resistance

µ = /	k = /

5.5.2 3D Printing design for effective coating development

With reference to the research objective: *To investigate the mechanical and antimicrobial effects of surface topography and coating composition*, an important point of investigation was that of the effect substrate surface structure and profile has on coating development. Figure 5.16 depicts the results of a surface topography analysis using a copper cold spray coating on solid ABS and 3D printed ABS with two print orientations (horizontal and vertical - see Figure 3.6 on page 103).

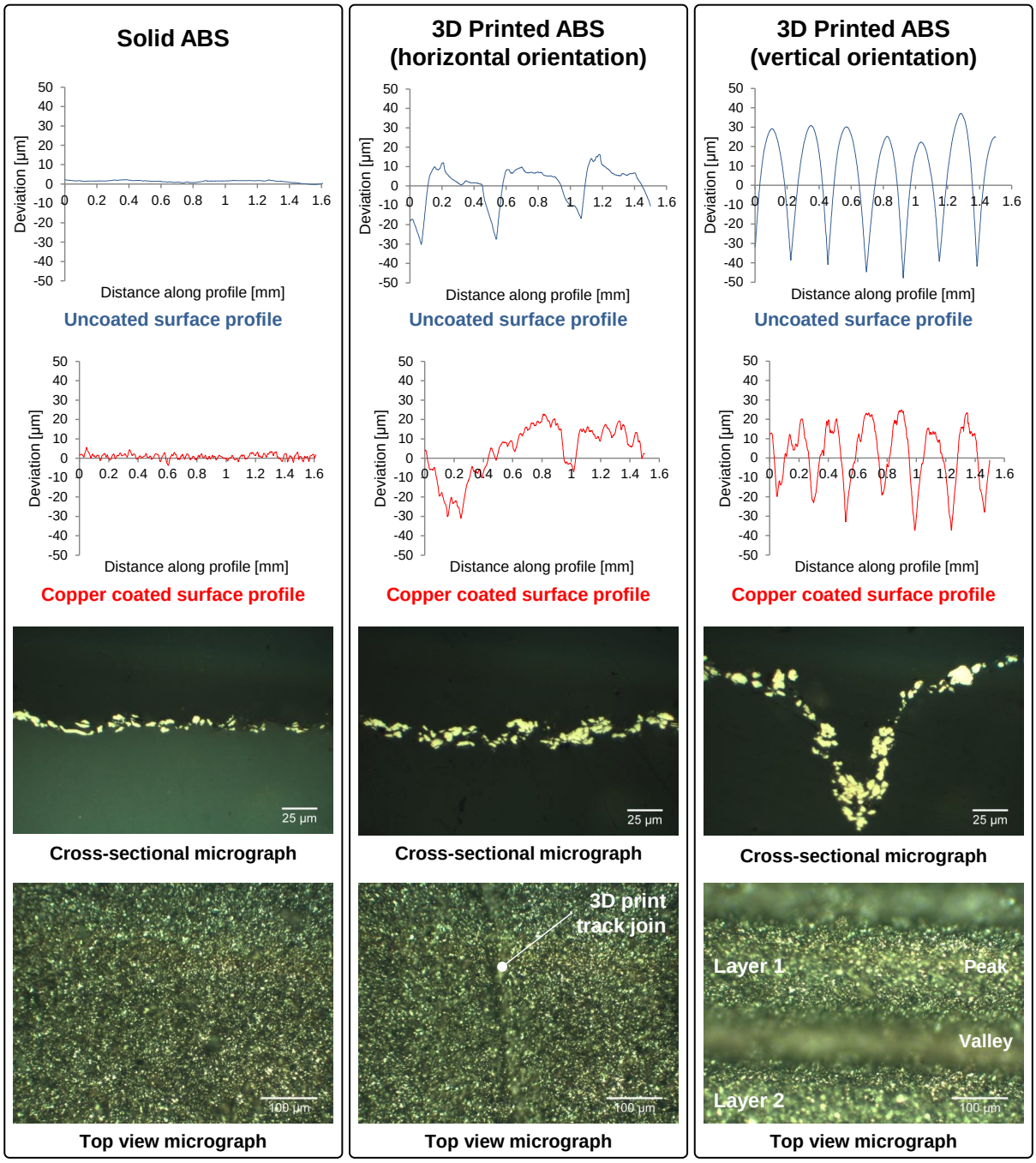


Figure 5.16: Surface topography analysis of copper coatings on various ABS substrates.

In this analysis the uncoated surface profile, measured using stylus profilometry, along with the coated surface profile were plotted for each substrate surface geometry type. In addition both cross-sectional and top view micrograph were taken of each coating, supporting the profilometry data.

Based on Figure 5.16 it was evident that the solid ABS substrate, when coated with a cold spray copper coating, produced a uniform, smooth coating. The horizontally orientated 3D printed substrate observed a rough, yet repeating coated profile. The vertically orientated substrates have a distinct wavy profile, which suggests that 3D printer layer bonding between layers is not as close and tight as within a layer, leaving pockets for subsequent copper deposition. This was evident in the agglomerated deposition in the substrate valleys.

The cross-sectional micrographs were used to evaluate the coating profiles. Using the image processing software, ImageJ, the cold spray depositions were isolated from the surrounding substrate material for independent analysis. Figure 5.17 depicts binary micrographs of the three coating types. The valley in Figure 5.18 (c) is typical of the 3D printer layering when printing in the vertical orientation and provides supporting evidence for minimal substrate distortion during cold spraying.

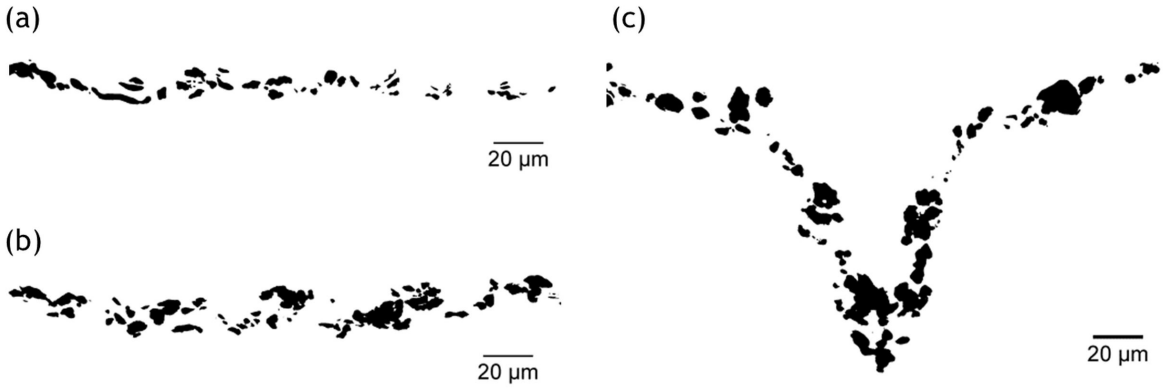


Figure 5.17: Binary micrographs of copper cold spray coating cross-sections with different substrate types: (a) solid ABS, (b) horizontally oriented 3D printed ABS and (c) vertically oriented 3D printed ABS, isolating the coating material.

Substrate surface roughness has been shown, in specific cases, to achieve higher deposition efficiencies, especially with the first coating layer [66, 87]. This observed effect of roughness was a suggested consequence of the increased surface area, improving deposition efficiency [87]. The degree of roughness induced by the 3D printing process played a critical role in cold spray coating quality. With reference to Figure 5.17 the substrate for coating (a) had an average arithmetic mean surface roughness (Ra) of 0.4 μm, while the substrates for coatings (b) and (c) observed Ra values of 4.3 μm and 7.4 μm respectively. An increased substrate roughness set the conditions for a thicker coating build up (70% thicker for the case

of a copper coating on vertically orientated 3D printed ABS, than for solid ABS), increased percent metallisation and even resulted in the deposition of larger particles for both the first layer and subsequent coating layers. This may possibly be a result of particle trapping; a response to the steep valley sides which prevent particles which deposit in the valley bottom from being dislodged by subsequent particle impacts. Subsequent impinging particles may then concentrate in the valleys, resulting in the distinctive thicker coating along the 3D print valleys.

One element favouring coating longevity is the composition of the developed coatings. The coating itself consists of embedded metal particles mechanically interlocked via a surrounding polymer matrix, conferring durability and eliminating concerns of *coat peeling*. Diffusion, mechanical erosion and general surface wear are the primary loss mechanisms.

Table 5.4 contains the trends observed as a consequence of increased substrate roughness, induced by substrate design and polymer FDM 3D printing. The standard deviations (SD) are given for each respective coating criterion. Substrate surface roughness was, therefore, seen to have a significant effect on coating development, increasing deposition and subsequent coating thickness.

Table 5.4: Coating profile trends based on the effects of substrate surface roughness for copper cold spray coatings on polymer substrates.

Substrate surface roughness (Ra) [μm] SD = 0.4	Average particle size in first layer [μm] SD = 4.5	Average particle size in coating layers [μm] SD = 0.8	Coating roughness (Ra) [μm] SD = 0.5	Average coating thickness [μm] SD = 6.0	Percentage metallisation [%] SD = 7
0.4	9.2	7.1	1	11.4	22
4.3	9.3	8.8	3.6	14.6	29
7.4	12.1	10.4	6.1	19.4	36

5.5.3 Prototype testing

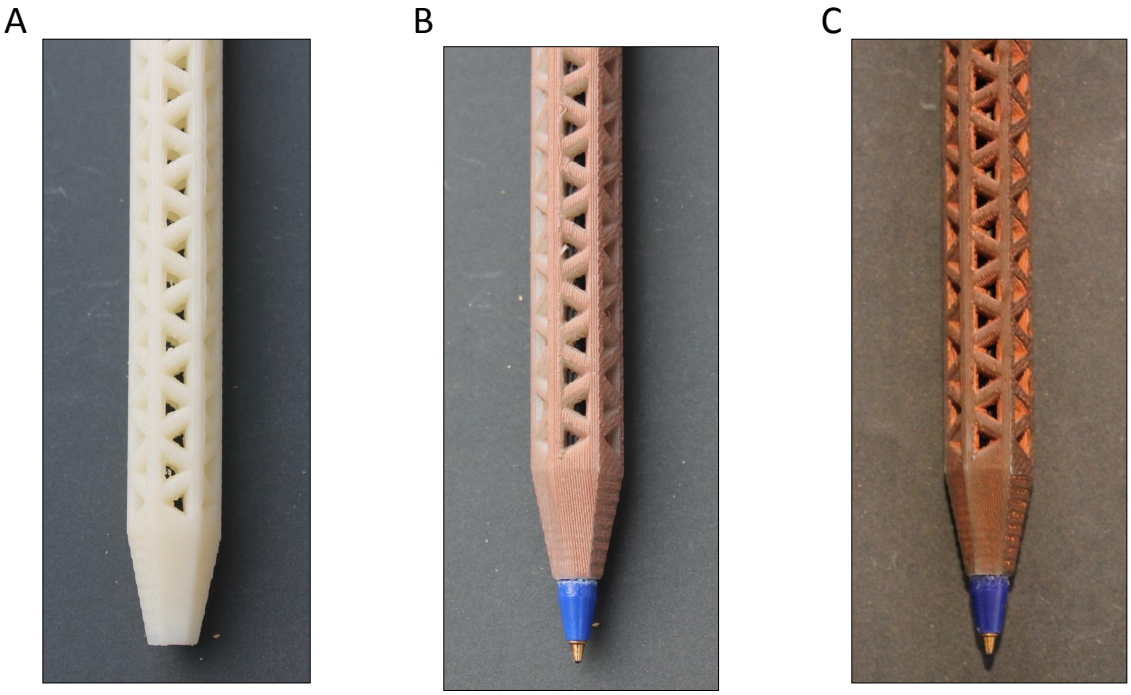
Prototype testing takes an idea, which in this case has undergone extensive laboratory based testing, and applies it to given real-world problems to evaluate its ultimate viability. This understanding of prototype testing was applied to the developed technology. In an attempt to prove the applicability of the designed, developed and optimised antimicrobial surface coatings to the application of healthcare surfaces for the mitigation of nosocomial infections, the following prototype tests were carried out.

Some of the most widely used and transported personal items include: pens, keyrings, cell-phones and access cards. It was these everyday items that were used in the prototype testing. These items are often carried in the pocket of the owner or in a bag. They may also be regarded as high contact items, interacting with both the hands of the owner and various other surfaces and environments from table tops, pockets and bags. These items were therefore ideal for consideration as real-world simulations.

Coating durability - Pens and keyrings

It was proposed that the example of pens and keyrings be used in a longitudinal coating durability assay, spanning a minimum of 12 months. Following the procedure mentioned in Chapter 3 (Page 112) a qualitative assessment of cold spray coated 3D printed pens and keyrings was investigated.

Figure 5.18 depicts the development and subsequent physical variation of a 3D printed ABS pen casing, cold spray coated with a 50:50 copper-zinc blended coating. The study took place over the course of 14 months. Sub-figures B and C illustrate the essential before- and after-use conditions of the coated pens. While a colour change is evident the coating itself exhibited good wear resistance; maintaining the cold spray deposition on the high contact surfaces.



(A) 3D printed pen case, before cold spraying.

(B) 50:50 copper-zinc blended cold spray coating.

(C) Coated pen after a year of use.

Figure 5.18: Development and physical variation investigation of a 50:50 copper-zinc cold spray coated 3D printed ABS pen case, used as such for over a year (January 2018 - March 2019).

Figure 5.19 depicts a detailed view of the 3D printer polymer layering and the copper-zinc coating present on each exposed layer. It was evident that the top surface layer, due to touch-contact exposure, had undergone the most wear as well as observing a distinct colour change - a natural and expected consequence of oxidation.

The intricate geometry had three-fold functionality. The first, with regards to additive manufacturing and the concept of generative design, meant that this pen was designed with minimal superfluous material, saving on material costs. The second, being a means of reducing the surface area in contact with skin, thereby mitigating the area available for touch-contact infection transmission. Finally, as a means of prolonging coating activity by minimising coating wear, since it was evident from Figure 5.19 that the inner, exposed layers were uniformly coated and had retained their colour and coating quality, even after over 13 months of handling and day-to-day use. Thus, prolonged antimicrobial activity was expected.

A caveat must be mentioned regarding the advantages gained by intricate 3D print geometry and surface contamination and microbial persistence. Without the biocidal activity of the cold spray coatings, bacterial adherence would be encouraged by such intricate geometries. Thus in order to successfully integrate the unique properties of 3D printing design and manufacture, with the antimicrobial coatings, it is imperative that intentional design be undertaken. The implications of every design element must be carefully considered before implementation. In this way effective design integration may be achieved.

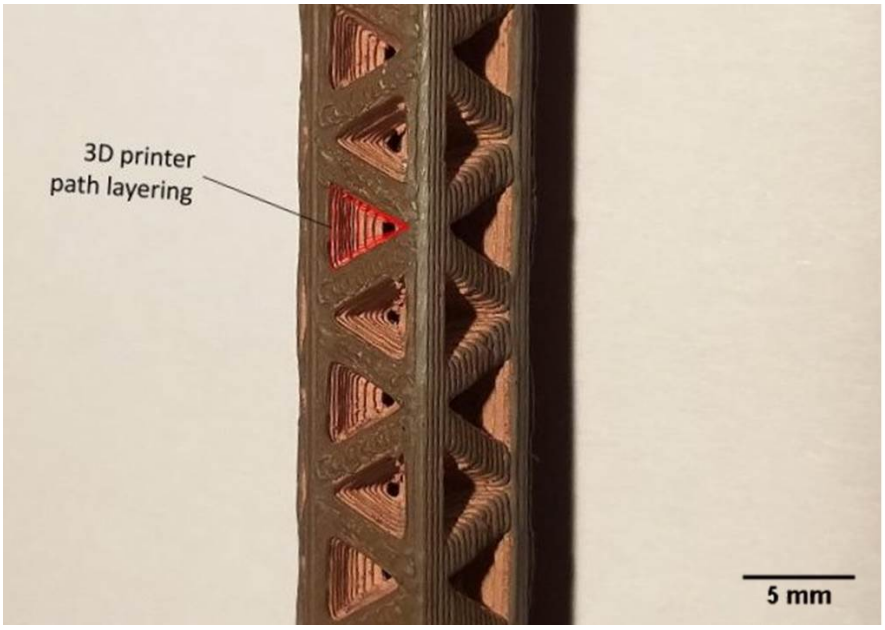
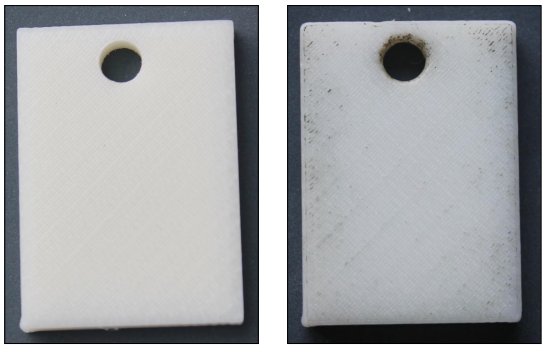


Figure 5.19: Detail view of the coated pen case after a year of active use.

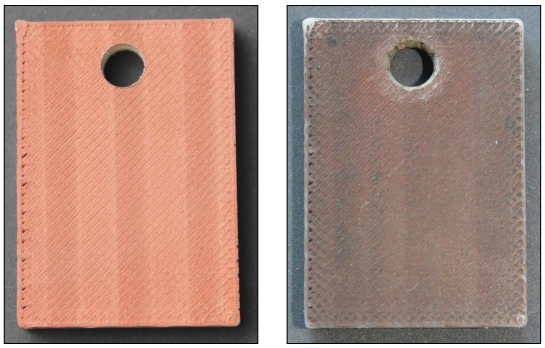
Figures 5.20 - 5.23 illustrate the surface variations of both coated and uncoated polymer substrates. Figure 5.20 depicts the before and after images of uncoated 3D printed ABS. It

was evident that this sample had undergone some wear and significant fouling. Figure 5.21 depicts the variation of a copper coating on a 3D printed ABS substrate over the course of a year. Slight wear of the keyring edges and a colour change resulting from oxidation were the main physical changes to these durable coatings.



As printed, before use. One year later.

Figure 5.20: Changes in uncoated 3D printed ABS over a year of use as a keyring.



As coated, before use. One year later.

Figure 5.21: Changes in copper coated 3D printed ABS over a year of use as a keyring.

Figure 5.22 depicts the before and after images of the solid ABS test sample keyring. Only slight wearing around the eye of the keyring was observed. The zinc coating on solid ABS, depicted in Figure 5.23, in a similar way to the copper coating, experienced only a colour change and slight wearing of the edges.



As cut, before use. One year later.

Figure 5.22: Changes in uncoated solid ABS over a year of use as a keyring.



As coated, before use. One year later.

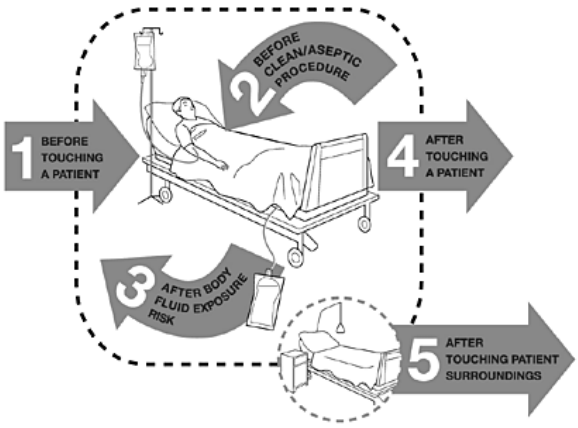
Figure 5.23: Changes in zinc coated ABS over a year of use as a keyring.

These test samples, both the antimicrobial pen and the keyrings, exhibit acceptable wear characteristics and coating durability. Apart from coating oxidation, the coatings maintained their form and quality. The nature of the cold spray coatings, such that the coating generation was fundamentally characterised by the embedment and mechanical entanglement of impacting powder particles, ensured a durable coating deposition with sufficient longevity.

Further analysis regarding surface topographical effects is discussed in Chapter 7. This includes: surface topographical effects on antimicrobial activity, a correlation analysis between surface wear and topographical effects and an investigation into the effects of substrate surface topography on the ideal cold spray particle depth-of-penetration.

This chapter set out to detail the development of cold spray coatings via polymer metallisation and characterise their properties. Using the theoretically optimum parameter sets derived, and following the experimental optimisation procedure, twenty unique and successful cold spray coating types were developed.

Chapter 6 Antimicrobial Susceptibility Testing



World Health Organization - My 5 Moments for Hand Hygiene

Entering a hospital or healthcare facility either as a patient, visitor or part of the medical team is done under the unrelenting threat of infection. It is now common to have your hands sprayed with a sanitiser upon entering a hospital and you are encouraged to use the frequently located disinfectant sprays located throughout the hospital. Along the hospital corridors, on doors and outside the wards, it is commonplace to find a WHO poster detailing the risks of contamination caused by touch-contact transmission. These are nearly always accompanied by a *Five Moments* poster depicting the five critical moments for hand hygiene. The response to hospital acquired infections is active and gaining momentum, yet many of the problems persist.

The British Broadcasting Corporation (BBC) reported on the current trends in hospital acquired infections from Scottish hospitals [194]. Four Glasgow patients had recently (January 2019) passed away from nosocomial infection complications. In addition, 110 cases of *S. aureus* infections documented per month in Scottish hospitals was reported.

In South Africa, Independent Media reported that during 2018 a severe outbreak of antibiotic-resistant *Klebsiella* took the lives of five infants at the Thelle Mogoerane Hospital in Ekurhuleni [195]. Another six were also infected.

These are just two of many such reports, highlighting the severity and unrelenting prevalence of hospital acquired infections. It was, therefore, evident that alternative containment solutions, alternative barriers to infection transmission and alternative mechanisms to actively combat nosocomial infections is a desperate and global requirement.

Inter-disciplinary research provides the opportunity for novel solutions and is a growing area of interest. It was believed that addressing the problem of surface contamination and transmission as an engineering design problem, would afford the opportunity of an alternative and ultimately effective solution to be developed.

Antimicrobial susceptibility testing was undertaken based on wet and dry contact testing. Baseline efficacy of the developed coatings, their constituent active elements and their combinations was investigated. This was performed against the five standard pathogens (*S. aureus*, *E. faecalis*, *P. aeruginosa*, *K. pneumoniae* and *C. albicans*). From these results coatings were selected for trials with a 5 wt% silver additive added to the base coating powder, prior to cold spraying. These samples underwent the same investigation against selected standard pathogens. Finally the best performing coatings were identified and tested against three resistant strains (a multi-resistant GMRSA strain, a resistant *P. aeruginosa* reference strain and a clinically resistant *C. albicans*).

6.1 Standard pathogens

In order to perform a valid antimicrobial susceptibility analysis and to be in a position to make general comments on efficacy, test pathogens were identified which covered the structural and phylogenetic classification range of micro-organisms, specifically targeting those of high prevalence. Thus, two Gram-positive (*Staphylococcus aureus* - ATCC 25923, *Enterococcus faecalis* - ATCC 29212), two Gram-negative (*Pseudomonas aeruginosa* - ATCC 27853, *Klebsiella pneumoniae* - ATCC 13887) and a yeast culture (*Candida albicans* - ATCC 10231) were used in the following coating susceptibility tests.

6.1.1 Powder efficacy

The raw cold spray feedstock powders were tested under the diffusive, wet contact test conditions. The results of this test are contained in Table 6.1. The larger the effective zone of inhibition (ZOI) the greater the antimicrobial efficacy, with regards to bacteriostatic activity.

Table 6.1: Inhibition zones for diffusion assay of cold spray feedstock powders.

Test Sample	Average Zone of Inhibition (mm)				
	S. aureus	*E. faecalis*	*K. pneumoniae*	*P. aeruginosa*	*C. albicans*
Copper Cu(1)	4.7	4.1	2.9	4.4	0.8
Copper Cu(2)	4.0	3.1	2.8	4.6	0.0
Zinc	3.0	1.4	0.8	3.0	0.0
Cu(1)75Zn	1.8	2.0	4.4	6.9	1.6
Cu(1)50Zn	1.4	0.9	3.6	6.1	0.5
Zn75Cu(1)	3.6	0.6	4.0	6.0	0.5
Silver	0.0	0.3	0.8	3.1	0.0
Ciprofloxacin	10.6	10.6	18.7	14.3	N/A
Nystatin	N/A	N/A	N/A	N/A	5.6

It was noted that the silver powder - a metal with known and effective antimicrobial properties - exhibited a significant lack of inhibitory activity. This may appear contradictory in light of the many studies purporting its antimicrobial efficacy [1, 9, 10], yet further investigation showed that this lack of activity may be a consequence of its present form. A study found that against *S. epidermidis* and *S. aureus* silver oxide thin films were antimicrobially active, yet pure silver proved inactive [5]. Thus the antimicrobial activity of silver may be attributed to the formation of oxides and the subsequent release of ions, a situation which may not have been achieved under the current test conditions.

Against the Gram-positive pathogens the high purity copper powder (99.7% copper) proved to be the most active of the tested powders. Against the Gram-negative pathogens, however, it was the copper-zinc blended powders that produced the largest zones of inhibition. Very little activity was observed from any powder against the *Candida* yeast culture. This, in fact, would foreshadow future trends from the developed coatings under diffusive, wet-contact test conditions.

A noteworthy observation related to the relative activity of the cold spray powders compared to that of the antimicrobial controls (ciprofloxacin and nystatin). The antibiotic and anti-fungal agents were more effective than the powders, and this was to be expected considering their primary use for this purpose. The activity of the powders - and later coatings - would, therefore, firstly be compared with each other and then with the antimicrobials. The anti-microbial controls were essentially there to confirm the susceptibility status of the specific microbial cultures used.

6.1.2 Standard coatings

Standard coatings, that is coatings without a silver additive, are listed in Table D.1 of Appendix D. These coatings underwent both the diffusion and dry contact antimicrobial susceptibility tests.

6.1.2.1 Diffusion assay

The standard coatings were tested against the five standard pathogens according to the diffusion test procedure detailed in the research methodology. The average extent of inhibition, measured in millimetres to the nearest 0.1 mm, for these coatings is depicted in Figure 6.1. Refer to Appendix D for the corresponding data table.

It was evident that zinc and particularly copper-zinc blended coatings exhibited enhanced antimicrobial activity against *S. aureus*, *P. aeruginosa* and *K. pneumoniae* in particular. Copper coatings, however, were more active against the Gram-positive *E. faecalis* pathogen. There was, however, no evidence of antimicrobial activity against the *C. albicans* strain, validating the lack of activity observed from the raw powders in Table 6.1.

The enhanced activity of the copper-zinc blended coatings in a wet, diffusive test environment, lead to suspected synergistic activity. Further investigation was subsequently carried out to confirm this.

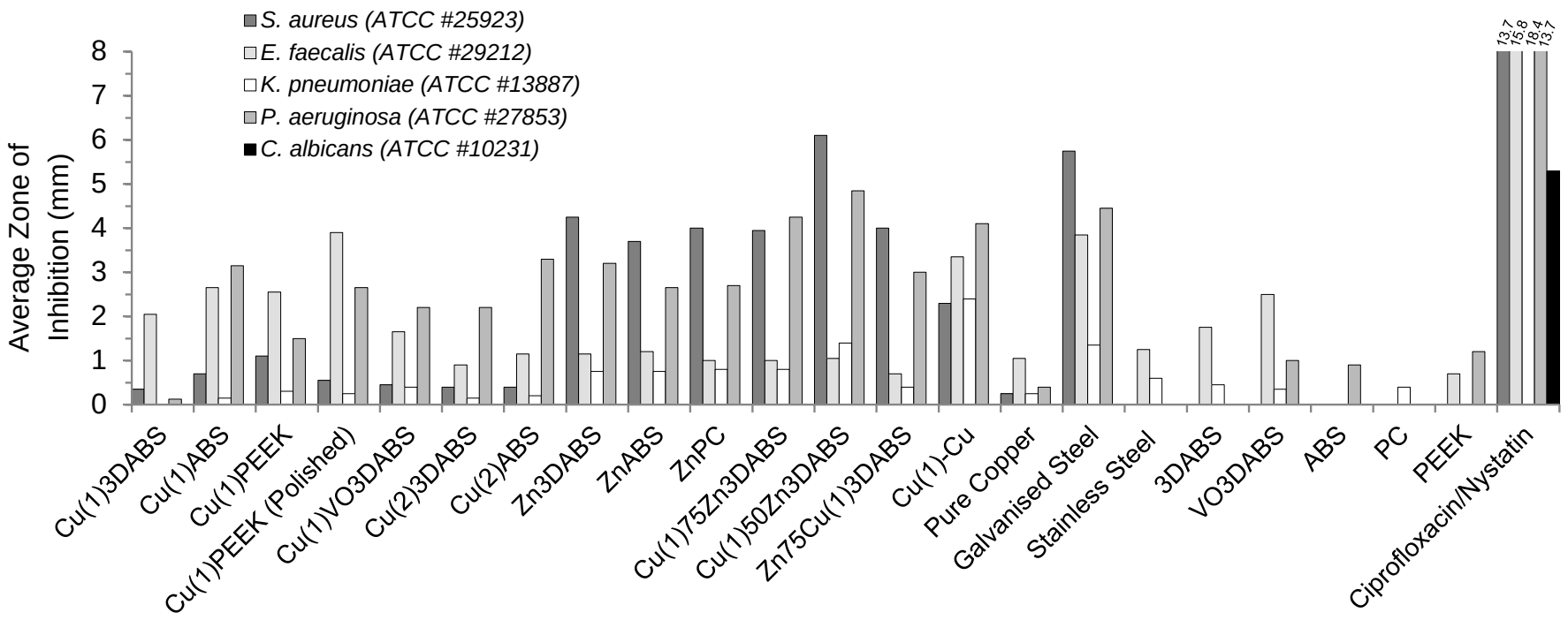


Figure 6.1: Average zones of inhibition for standard coatings against the standard bacterial and fungal pathogens.

Synergistic interactions

Figure 6.2 isolates the copper and zinc coatings which show evidence of synergistic activity.

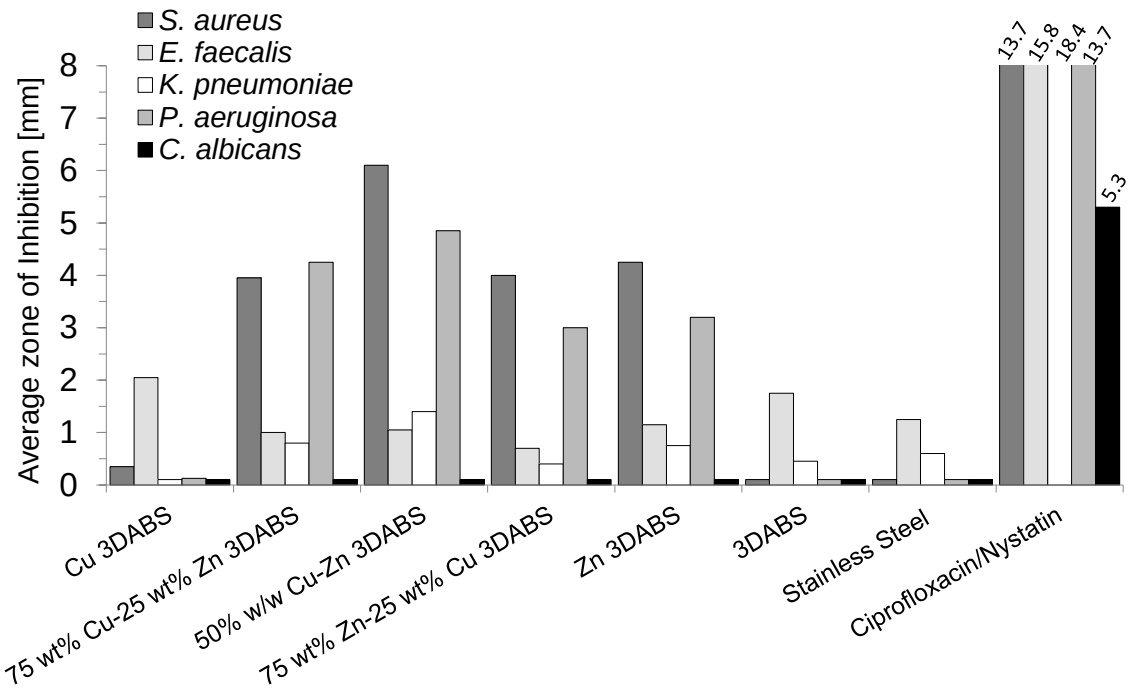


Figure 6.2: Synergistic diffusive activity from copper-zinc blended coatings against the standard pathogens.

Synergy or synergistic behaviour is defined as the interaction of two or more agents to produce a combined effect that is greater than the sum of their separate efforts. Synergistic activity was therefore confirmed for a 50:50 w/w% copper-zinc coating on a 3D printed ABS substrate, when comparing this coating's average zone of inhibition to that of the combined average of separate copper and zinc coatings on the same substrate material. Specifically the copper-zinc blended coating exhibits synergistic diffusive activity against *S. aureus*, *P. aeruginosa* and *K. pneumoniae*. Against these three pathogens the 50:50 copper-zinc synergistic coating was found to be 43% more effective (with respect to the extent of inhibition) than the combined average activity of the independent copper and zinc coatings on the same 3D printed ABS polymer substrate.

This blended coating does, however, appear to exhibit a marginal reduction in antimicrobial activity when in contact with *E. faecalis*, compared to each independent coating. This activity, however, was seen to be the same as that afforded by pure copper, with both exhibiting an average zone of inhibition of 1.05 mm; which still represents diffusive antimicrobial activity, albeit not extensively. Copper metal is a known and effective antimicrobial agent and, therefore, this reduced activity from the blended copper-zinc coating was not deemed a limitation or an effective barrier to entry for further use.

Based on the above results and reasoning the 50:50 copper-zinc blended coating on a 3D printed ABS polymer substrate in the horizontal orientation, was recognised as not only the best performing coating combination, but a highly effective material combination achieving synergistic antimicrobial activity.

Material ranking

Considering this synergistic activity and the activity of the other test samples, an efficacy ranking was carried out. Table 6.2 depicts this ranking based on the average extent of microbial inhibition across all five test pathogens. The test sample designation PCD, refers to the Positive Control Discs of Ciprofloxacin and Nystatin used in this test. Refer to Appendix D for the ranking per test pathogen.

Table 6.2: Overall efficacy ranking based on average zone of inhibition from diffusion assays of standard coatings against standard pathogens.

Overall Rank*	Test sample	Overall Average ZOI [mm]
1	PCD	13.36
2	Zinc coated/galvanised steel	3.08
3	50% w/w copper-zinc coated 3D printed ABS	2.68
4	Copper coated copper	2.43
5	75 wt% copper - 25 wt% zinc coated 3D printed ABS	2.00
6	Zinc coated 3D printed ABS	1.87
7	Zinc coated PC	1.70
8	Zinc coated solid ABS	1.66
9	75 wt% zinc - 25 wt% copper coated 3D printed ABS	1.62
10	Polished copper coated PEEK	1.47
11	Copper coated solid ABS	1.33
12	Copper coated PEEK	1.09
13	Copper-Aluminium-Alumina coated solid ABS	1.01
14	Copper coated vertically oriented 3D printed ABS	0.94
15	Vertically oriented 3D printed ABS	0.77
16	Copper-Aluminium-Alumina coated 3D printed ABS	0.73
17	Copper coated 3D printed ABS	0.51
18	3D printed ABS	0.44
19	Pure copper	0.39
20	Solid polyetheretherketone	0.38
21	Stainless steel	0.37
22	Solid ABS	0.18
23	Solid polycarbonate	0.08

*Test samples were ranked from most antimicrobially active (1) to least antimicrobially active (23).

Omitting the effects of Ciprofloxacin and Nystatin as positive control discs/dots (PCDs), the other positive controls and the negative polymeric substrate controls; the top three most

efficacious coatings in a diffusive, wet contact microbial contamination environment were:
(1) 50% w/w copper-zinc coated 3D printed ABS,
(2) Copper coated copper and
(3) 75 wt% copper - 25 wt% zinc coated 3D printed ABS.

These were followed by the zinc-polymer coatings and the third zinc-copper blended coating. Copper coatings, particularly copper coated 3D printed ABS were not significantly effective under these test conditions. The juxtaposition between the respective activities of these two metals (copper and zinc), which are known to possess innate antimicrobial properties, leads to speculation into the unique antimicrobial mechanisms of action previously discussed in the literature review.

6.1.2.2 Dry contact test

Touch-contact transmission refers to the transmission of pathogenic micro-organisms through physical contact; either via direct hand-to-hand contact or via indirect contact through touched surfaces, to a susceptible host. It was this mechanism of infection transmission which was a salient aspect of consideration in the current research.

Fourteen test samples, eight material controls and two antimicrobial agents (ciprofloxacin and nystatin), were tested against three of the standard test pathogens (*S. aureus*, *P. aeruginosa* and *C. albicans*) under simulated touch-contact conditions. These pathogens were selected as representative of Gram-positive, Gram-negative and yeast cultures, respectively. As part of scope delimitation it was these three pathogens that were selected; thereby avoiding profligate use of consumables and ensuring efficient experimentation.

The tabulated results for all test samples and their respective controls may be found in Appendix D. Each table contains the time-kill data measured in CFU/ml for each of the eight time periods (0, 0.5, 5, 10, 15, 20, 60 and 180 minutes). For each material a Pearson correlation analysis was performed to evaluate the suitability of a linear trend analysis. This analysis validated the use of the rate of antimicrobial activity (m_{ar}), which was later used as a key discriminating criterion to evaluate and compare the relative antimicrobial activity of respective coatings in a simulated touch-contact environment.

The simulated touch-contact activity of the standard coatings against the three test pathogens (*S. aureus*, *P. aeruginosa* and *C. albicans*) was evaluated according to coating type. Figure 6.3, Figure 6.4, Figure 6.5 and Figure 6.6 depict the time-kill responses for copper, copper-aluminium-alumina, zinc and copper-zinc blended coatings against *S. aureus*.

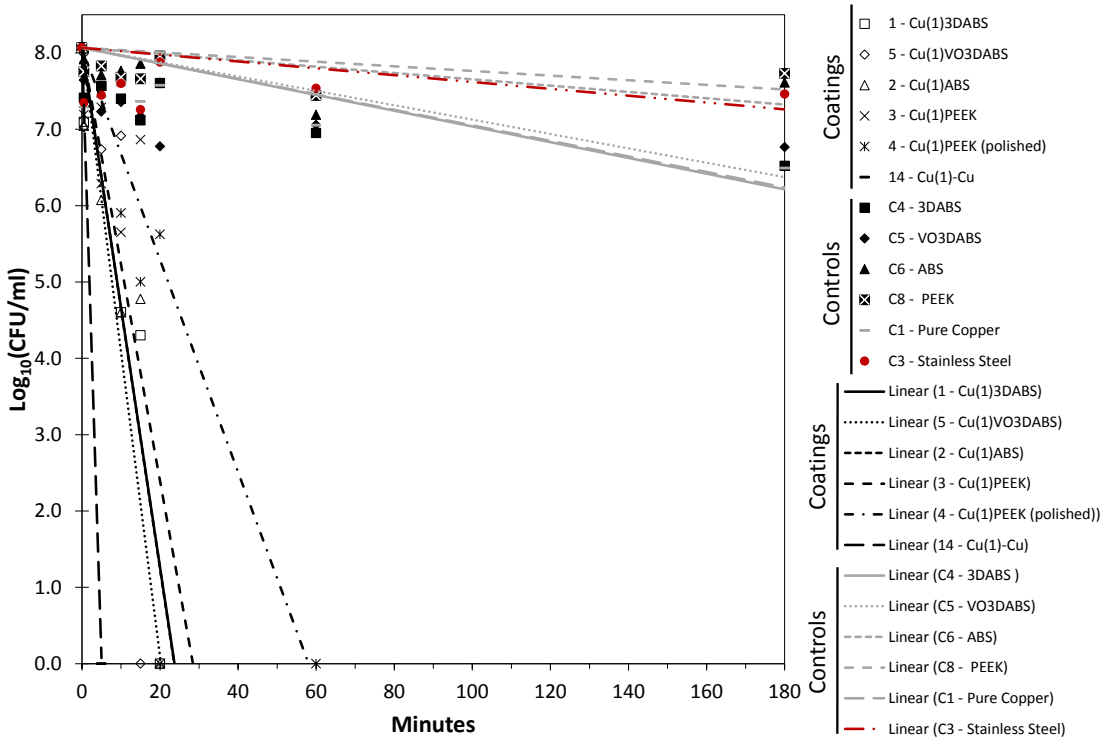


Figure 6.3: Touch-contact antimicrobial efficacy of copper coatings against *S. aureus* (ATCC 25923).

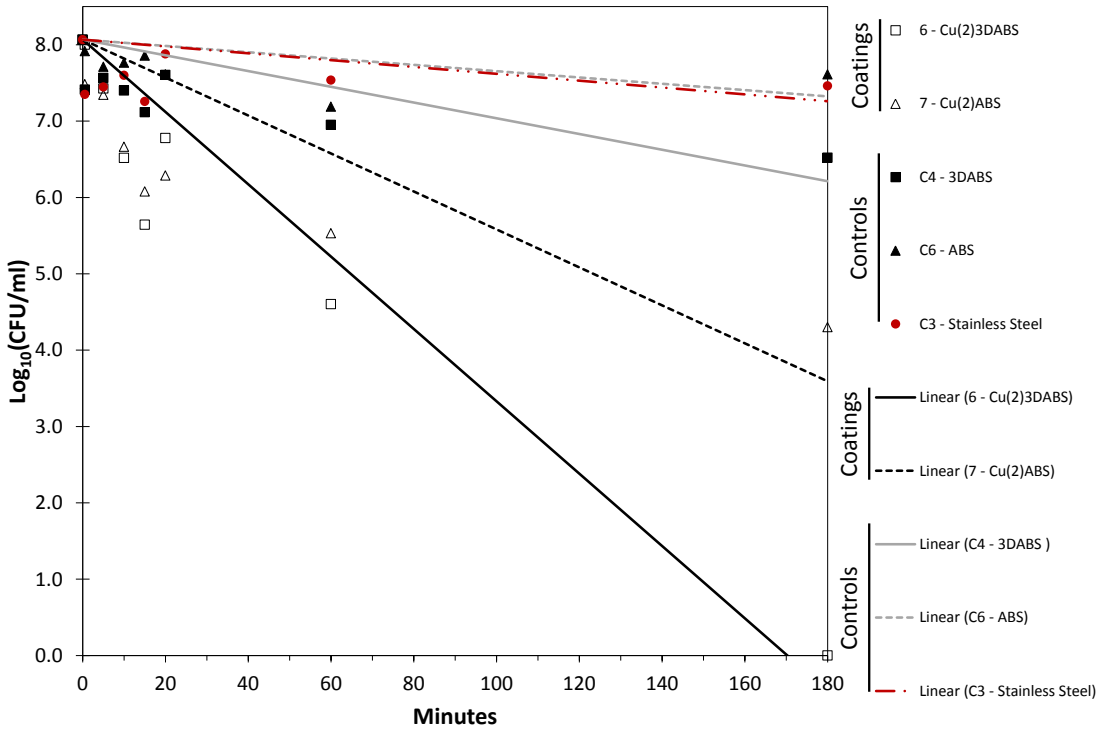


Figure 6.4: Touch-contact antimicrobial efficacy of copper-aluminium-alumina coatings against *S. aureus* (ATCC 25923).

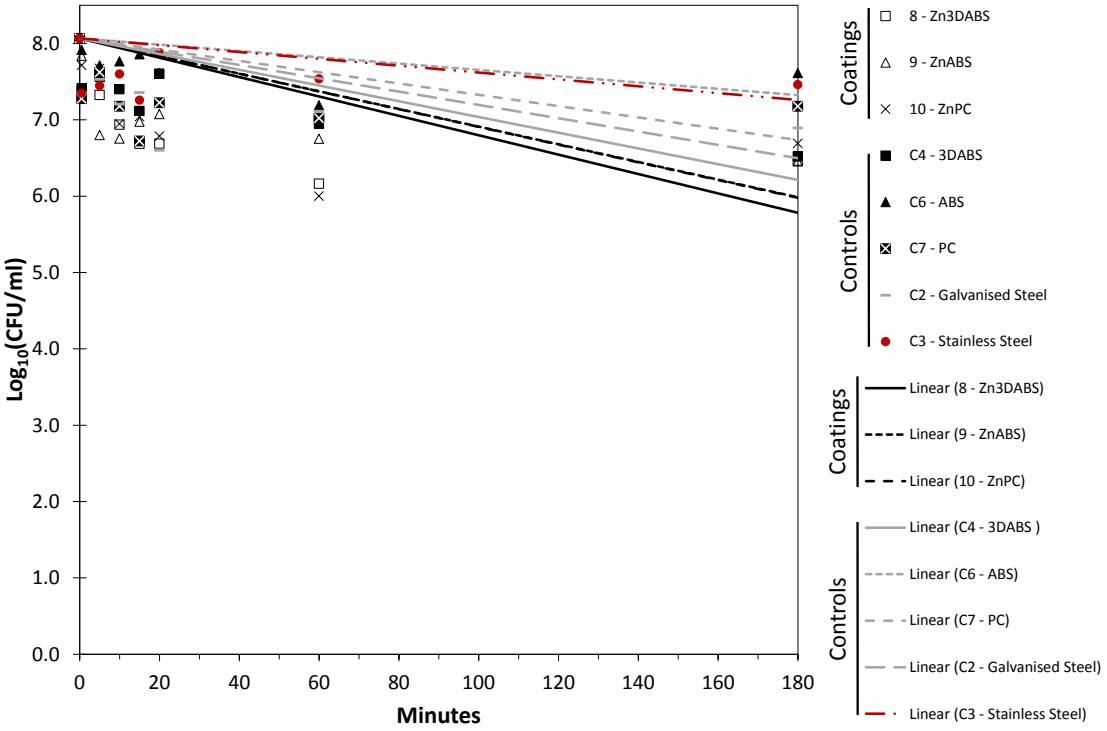


Figure 6.5: Touch-contact antimicrobial efficacy of zinc coatings against *S. aureus* (ATCC 25923).

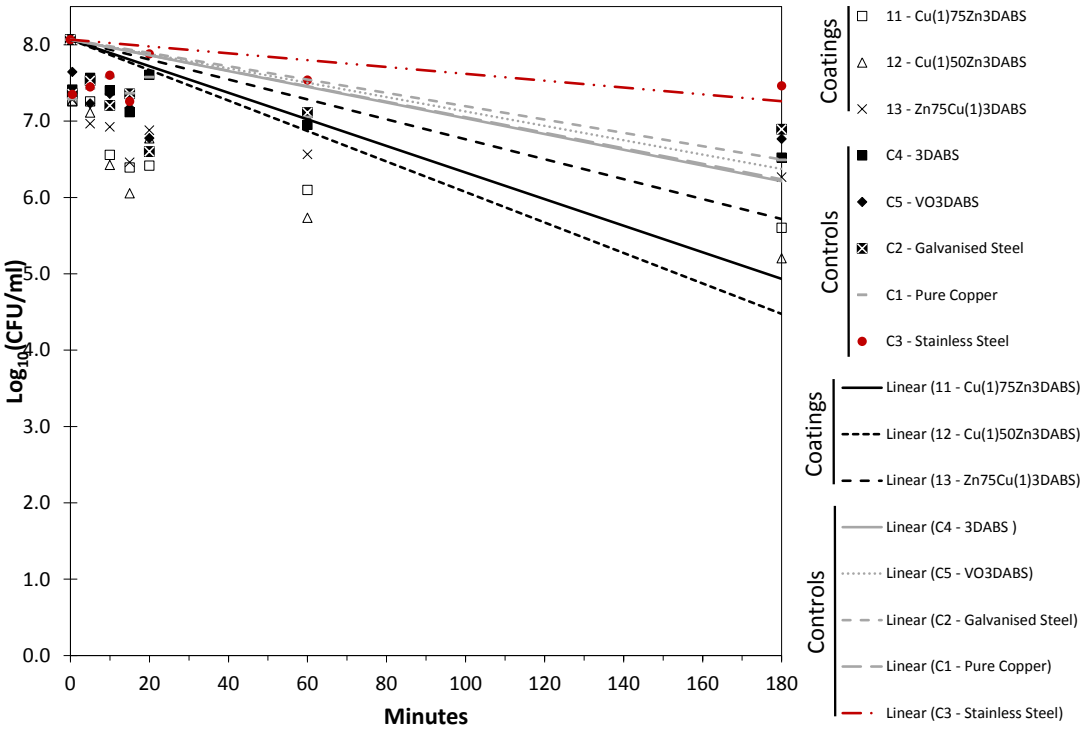


Figure 6.6: Touch-contact antimicrobial efficacy of copper-zinc blended coatings against *S. aureus* (ATCC 25923).

Figure 6.7, Figure 6.8, Figure 6.9 and Figure 6.10 depict the time-kill responses for copper, copper-aluminium-alumina, zinc and copper-zinc blended coatings against *P.aeruginosa*.

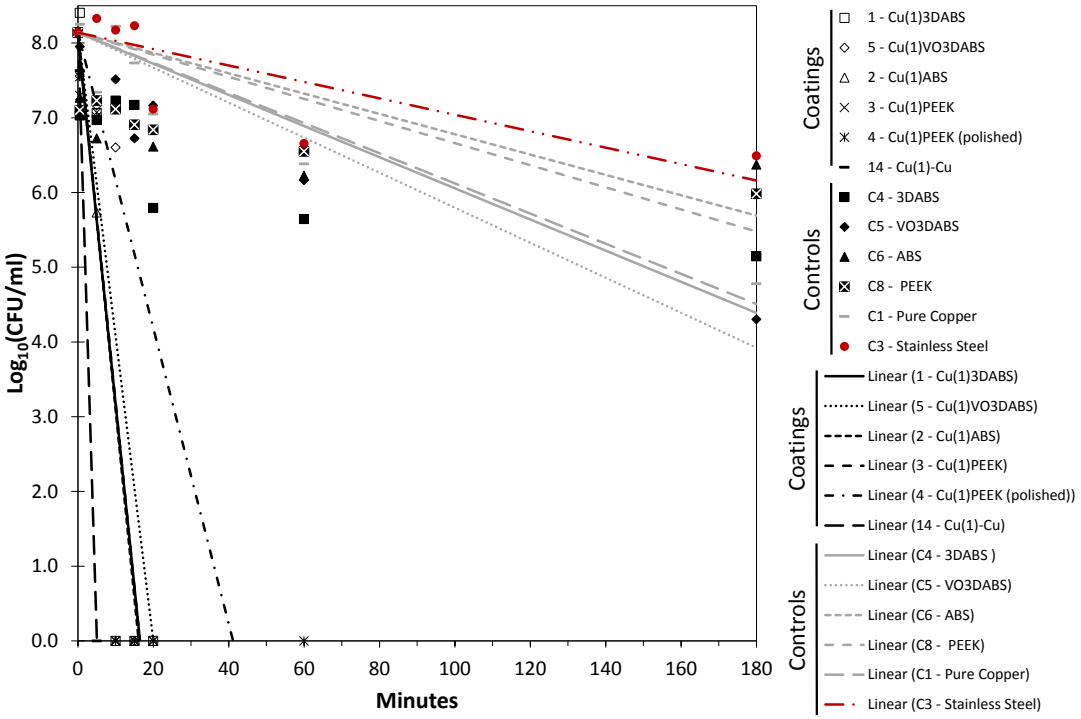


Figure 6.7: Touch-contact antimicrobial efficacy of copper coatings against *P.aeruginosa* (ATCC 27853).

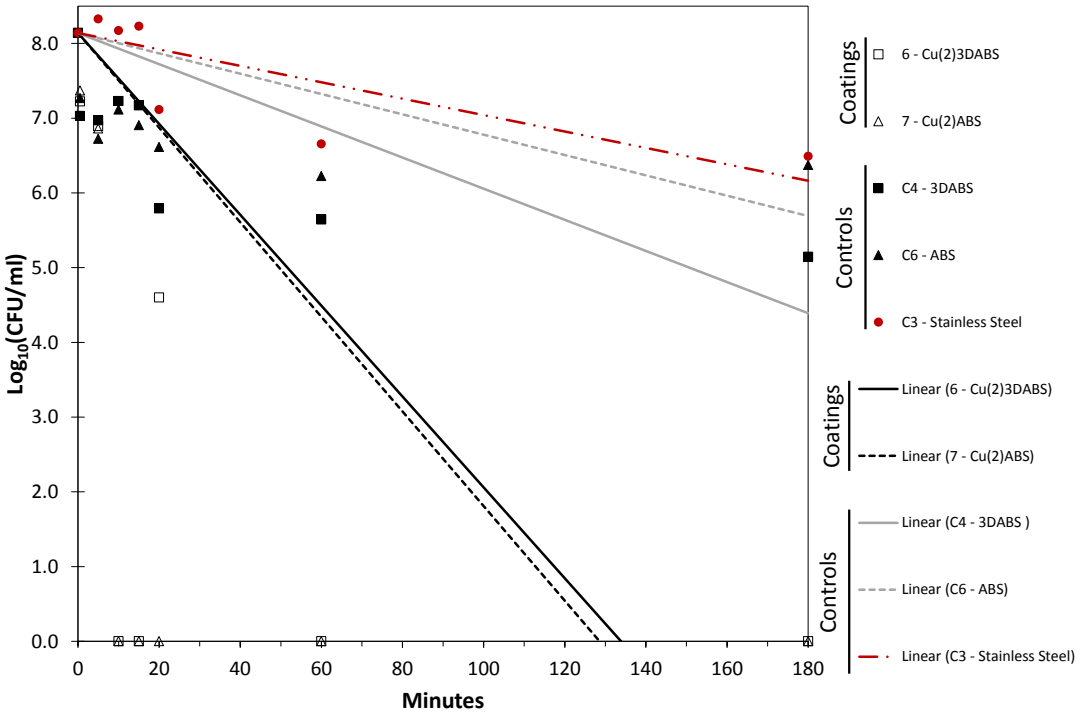


Figure 6.8: Touch-contact antimicrobial efficacy of copper-aluminium-alumina coatings against *P.aeruginosa* (ATCC 27853.

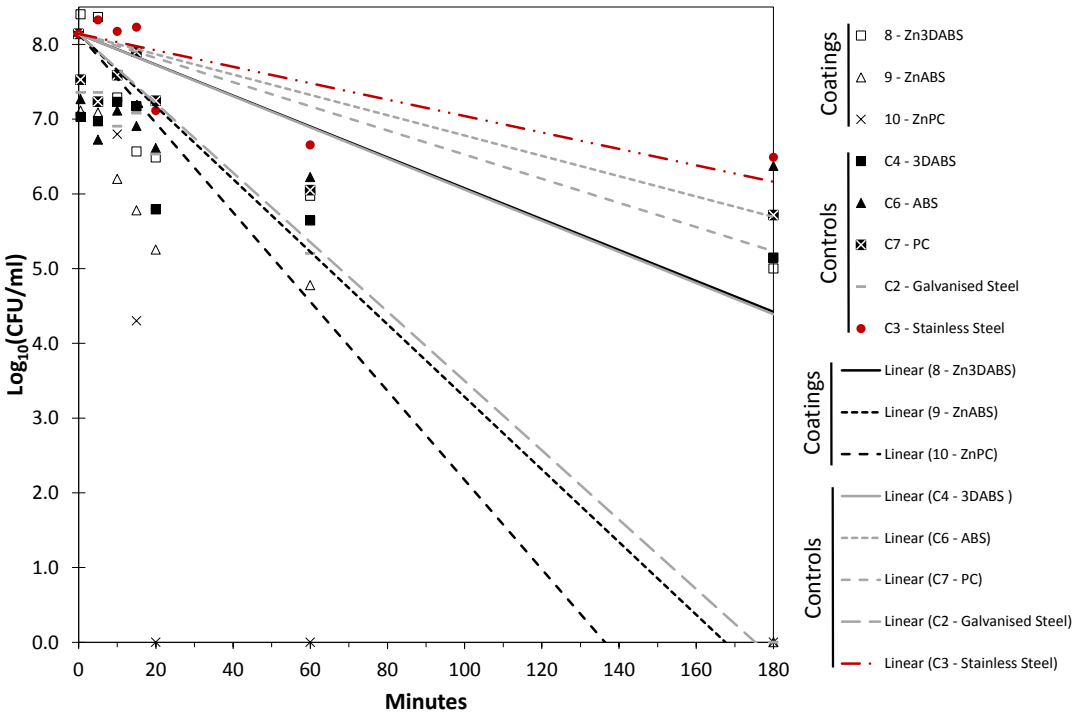


Figure 6.9: Touch-contact antimicrobial efficacy of zinc coatings against *P.aeruginosa* (ATCC 27853.

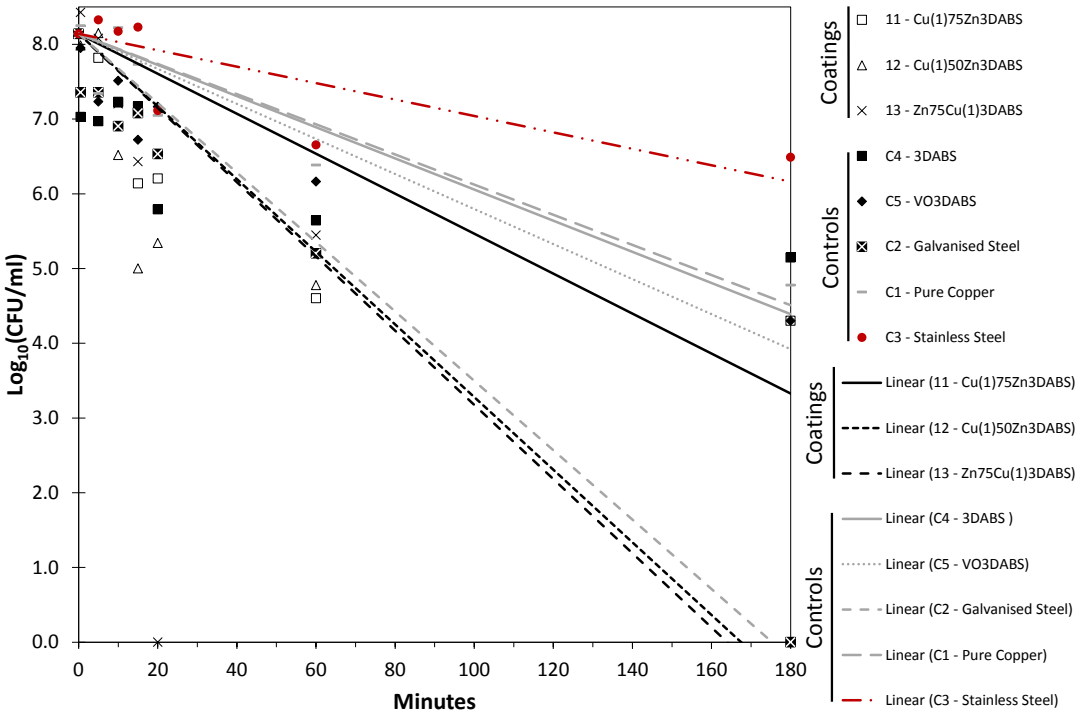


Figure 6.10: Touch-contact antimicrobial efficacy of copper-zinc blended coatings against *P.aeruginosa* (ATCC 27853.

Figure 6.11, Figure 6.12, Figure 6.13 and Figure 6.14 depict the time-kill responses for copper, copper-aluminium-alumina, zinc and copper-zinc blended coatings against *C.albicans*.

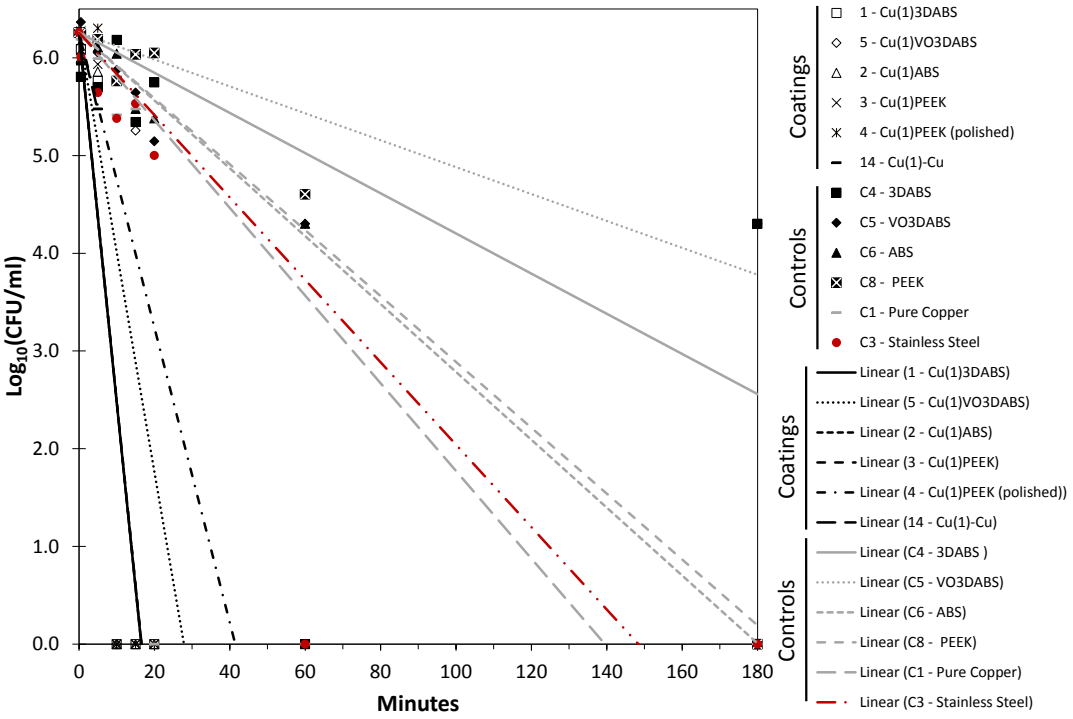


Figure 6.11: Touch-contact antimicrobial efficacy of copper coatings against *C.albicans* (ATCC 10231).

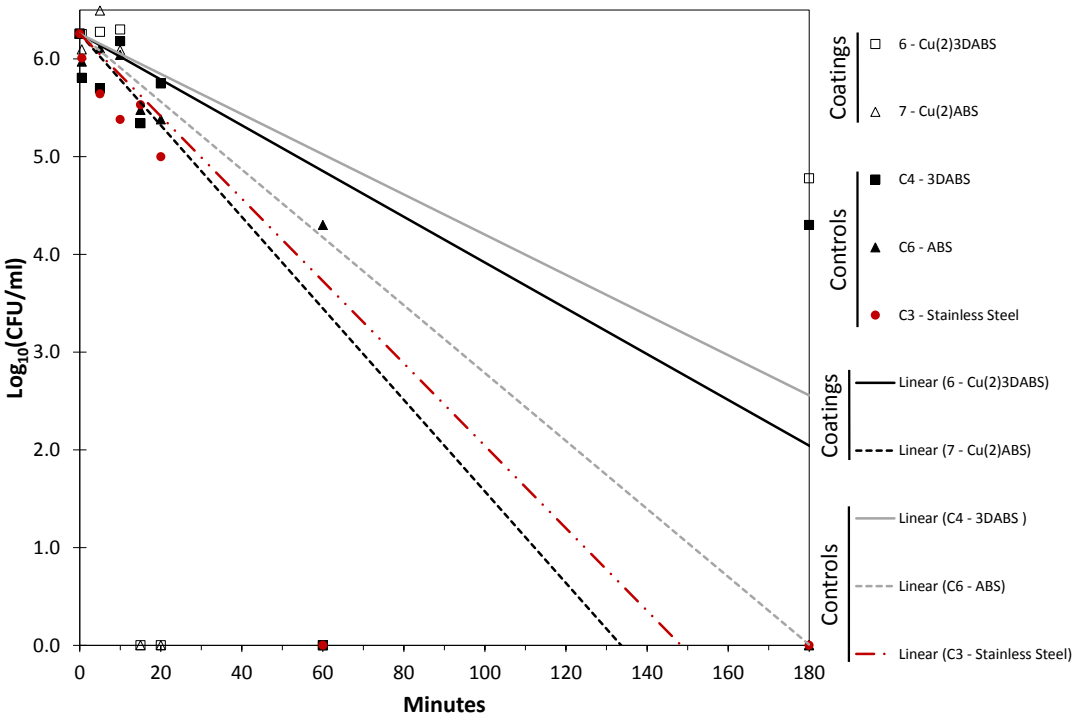


Figure 6.12: Touch-contact antimicrobial efficacy of copper-aluminium-alumina coatings against *C.albicans* (ATCC 10231).

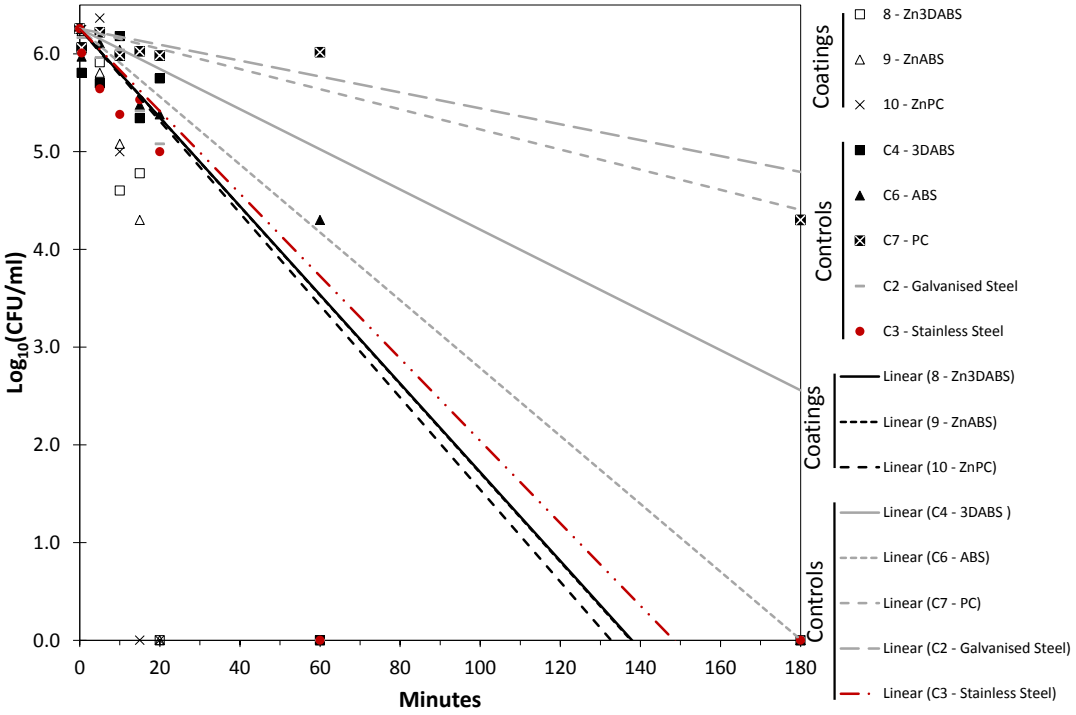


Figure 6.13: Touch-contact antimicrobial efficacy of zinc coatings against *C.albicans* (ATCC 10231).

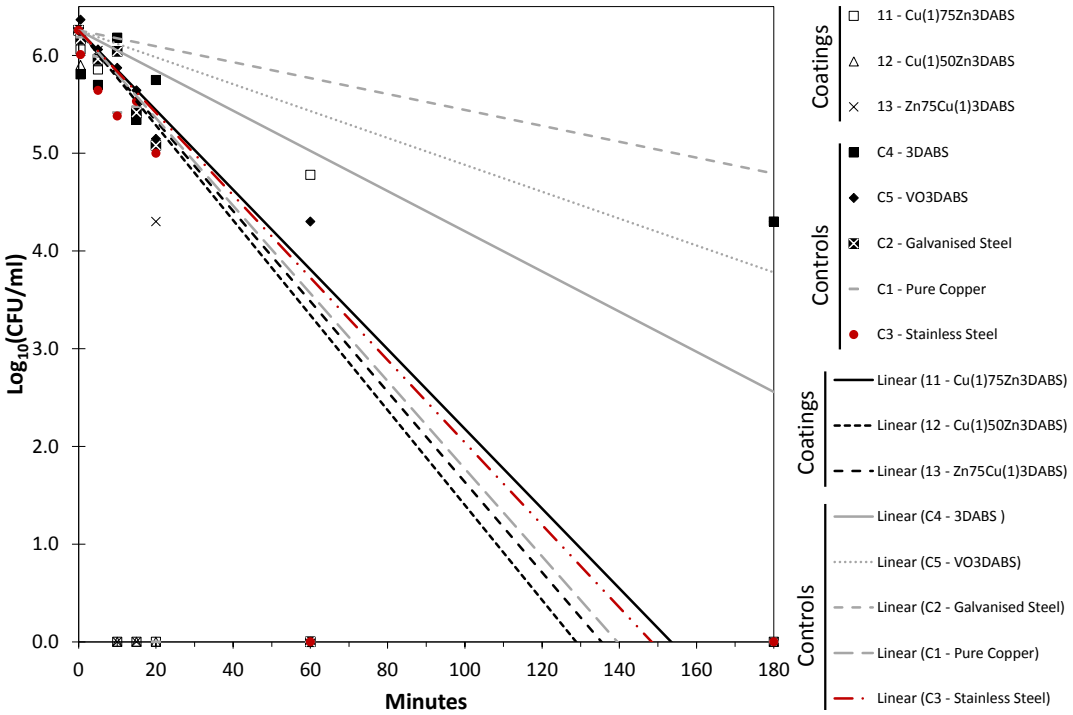


Figure 6.14: Touch-contact antimicrobial efficacy of copper-zinc blended coatings against *C.albicans* (ATCC 10231).

Summary results: best performing polymer metallised coatings

For each respective pathogen a table consolidating the susceptibility test findings from the time-kill graphs is given (Table 6.3, Table 6.4 and Table 6.5). The Pearson coefficient (R) and coefficient of determination (R^2) demonstrate the suitability of a linear regression analysis, thereby validating the use of the microbial reduction rate (m_{ar}) as the primary discriminating factor. The closer the absolute values are to one (1), the stronger the linear correlation. In addition, two other factors of determination included the highest average percentage reduction (Red.%) after a given exposure period and the average percentage reduction in viable colony forming units after 15 min to provide a standardised measure of antimicrobial activity. The results were ranked from most antimicrobially active (assigned rank number 1) to the least antimicrobially active.

The overall best performing coating-substrate combination was that of a cold spray copper coating on a copper metal substrate, with complete microbial elimination against all standard pathogens within just 10 min.

Table 6.3: Ranked dry contact antimicrobial test results for standard coatings against the *S. aureus* (ATCC 25923).

Test sample	*Staphylococcus aureus* (ATCC 25923)					
	R	R^2	m_{ar}	Red.%[1]	Red.% @ 15 min.	Rank (m_{ar})
Copper coated 3D printed ABS	-0.939	0.882	0.340	100% @ 20 min	99.98	3
Copper coated solid ABS	-0.928	0.861	0.340	100% @ 20 min	99.94	4
Copper coated PEEK	-0.789	0.623	0.280	100% @ 20 min	92.74	5
Polished copper coated PEEK	-0.985	0.970	0.130	100% @ 60 min	99.90	6
Copper coated vertically oriented 3D printed ABS	-0.827	0.684	0.390	100% @ 15 min	100.00	2
Copper-Aluminium-Alumina coated 3D printed ABS	-0.974	0.949	0.040	100% @ 180 min	99.56	7
Copper-Aluminium-Alumina coated solid ABS	-0.871	0.759	0.020	99.89% @ 180 min	98.80	11
Zinc coated 3D printed ABS	-0.562	0.316	0.040	97.68% @ 60 min	95.16	8
Zinc coated solid ABS	-0.581	0.338	0.030	94.63% @ 10 min	90.54	10
Zinc coated PC	-0.521	0.271	0.040	98.41% @ 60 min	89.01	9
75 wt% copper - 25 wt% zinc coated 3D printed ABS	-0.731	0.534	0.010	98.01% @ 60 min	97.53	13
50% w/w copper-zinc coated 3D printed ABS	-0.764	0.584	0.020	99.14% @ 60 min	98.87	12
75 wt% zinc - 25 wt% copper coated 3D printed ABS	-0.615	0.378	0.010	97.12% @ 15 min	97.12	14
Copper coated copper	-0.996	0.992	1.590	100% @ 5 min	100.00	1
Pure copper	-0.855	0.731	0.010	82.89% @ 180 min	76.83	15
Zinc coated/galvanised steel	-0.468	0.219	0.000	84.83% @ 10 min	77.33	19
Stainless steel	-0.187	0.035	0.000	/	0.00	20
3D printed ABS	-0.820	0.672	0.006	14.38% @ 180 min	1.09	16
Vertically oriented 3D printed ABS	-0.591	0.349	0.005	12.15% @ 180 min	0.92	17
Solid ABS	-0.441	0.194	0.000	-0.99% @ 180 min	-0.07	21
Solid polycarbonate	-0.259	0.067	0.003	7.19% @ 180 min	0.54	18
Solid polyetheretherketone	-0.292	0.085	-0.002	-3.72% @ 180 min	-0.28	22

[1] Relative to stainless steel

Table 6.4: Ranked dry contact antimicrobial test for standard coatings against the *P. aeruginosa* (ATCC 27853).

Test sample	*Pseudomonas aeruginosa* (ATCC 27853)					
	R	R^2	m_{ar}	Red.%[1]	Red.% @ 15 min.	Rank (m_{ar})
Copper coated 3D printed ABS	-0.934	0.872	0.680	100% @ 10 min	100.00	6
Copper coated solid ABS	-0.966	0.933	0.740	100% @ 10 min	100.00	2
Copper coated PEEK	-0.912	0.832	0.680	100% @ 10 min	100.00	7
Polished copper coated PEEK	-0.922	0.850	0.690	100% @ 10 min	100.00	3
Copper coated vertically oriented 3D printed ABS	-0.865	0.748	0.400	100% @ 15 min	100.00	8
Copper-Aluminium-Alumina coated 3D printed ABS	-0.919	0.845	0.690	100% @ 10 min	100.00	4
Copper-Aluminium-Alumina coated solid ABS	-0.925	0.856	0.690	100% @ 10 min	100.00	5
Zinc coated 3D printed ABS	-0.823	0.677	0.010	96.89% @ 60 min	96.10	16
Zinc coated solid ABS	-0.966	0.933	0.040	100% @ 180 min	99.36	10
Zinc coated PC	-0.902	0.814	0.310	100% @ 20 min	99.98	9
75 wt% copper - 25 wt% zinc coated 3D printed ABS	-0.796	0.634	0.020	99.87% @ 60 min	98.54	14
50% w/w copper-zinc coated 3D printed ABS	-0.935	0.874	0.040	100% @ 180 min	99.89	11
75 wt% zinc - 25 wt% copper coated 3D printed ABS	-0.696	0.484	0.040	100% @ 180 min	97.14	12
Copper coated copper	-0.999	0.998	1.610	100% @ 5 min	100.00	1
Pure copper	-0.942	0.887	0.010	95.85% @ 180 min	42.80	17
Zinc coated/galvanised steel	-0.995	0.990	0.040	100% @ 180 min	87.29	13
Stainless steel	-0.788	0.621	0.000	/	0.00	22
3D printed ABS	-0.766	0.587	0.010	28.64% @ 180 min	1.84	18
Vertically oriented 3D printed ABS	-0.953	0.908	0.012	36.23% @ 180 min	2.33	15
Solid ABS	-0.561	0.315	0.003	7.60% @ 180 min	0.49	21
Solid polycarbonate	-0.852	0.726	0.005	15.19% @ 180 min	0.98	19
Solid polyetheretherketone	-0.788	0.621	0.004	11.10% @ 180 min	0.71	20

[1] Relative to stainless steel

Table 6.5: Ranked dry contact antimicrobial test for standard coatings against the *C. albicans* (ATCC10231).

Test sample	*Candida albicans* (ATCC 10231)					
	R	R^2	m_{ar}	Red.%[1]	Red.% @ 15 min.	Rank (m_{ar})
Copper coated 3D printed ABS	-0.906	0.821	0.480	100% @ 10 min	100.00	2
Copper coated solid ABS	-0.897	0.805	0.470	100% @ 10 min	100.00	4
Copper coated PEEK	-0.896	0.803	0.480	100% @ 10 min	100.00	3
Polished copper coated PEEK	-0.873	0.762	0.460	100% @ 10 min	100.00	8
Copper coated vertically oriented 3D printed ABS	-0.700	0.490	0.180	100% @ 20 min	57.32	12
Copper-Aluminium-Alumina coated 3D printed ABS	-0.772	0.596	0.220	100% @ 15 min	100.00	11
Copper-Aluminium-Alumina coated solid ABS	-0.778	0.605	0.230	100% @ 15 min	100.00	10
Zinc coated 3D printed ABS	-0.864	0.746	0.180	100% @ 20 min	85.77	13
Zinc coated solid ABS	-0.891	0.794	0.180	100% @ 20 min	95.26	14
Zinc coated PC	-0.868	0.753	0.260	100% @ 15 min	100.00	9
75 wt% copper - 25 wt% zinc coated 3D printed ABS	-0.898	0.806	0.470	100% @ 10 min	100.00	5
50% w/w copper-zinc coated 3D printed ABS	-0.887	0.787	0.470	100% @ 10 min	100.00	6
75 wt% zinc - 25 wt% copper coated 3D printed ABS	-0.888	0.789	0.470	100% @ 10 min	100.00	7
Copper coated copper	-0.920	0.846	0.490	100% @ 10 min	100.00	1
Pure copper	-0.992	0.984	0.150	100% @ 60 min	28.86	15
Zinc coated/galvanised steel	0.611	0.373	0.010	53.74% @ 20 min	38.34	16
Stainless steel	-0.995	0.990	0.000	/	0.00	18
3D printed ABS	-0.411	0.169	-0.022	-9.03% @ 60 min	-5.76	20
Vertically oriented 3D printed ABS	-0.801	0.642	-0.028	-11.87% @ 60 min	-7.57	21
Solid ABS	-0.997	0.994	-0.008	-3.14% @ 60 min	-2.00	19
Solid polycarbonate	-0.960	0.922	-0.032	-13.34% @ 60 min	-8.51	22
Solid polyetheretherketone	-0.994	0.988	0.009	-3.56% @ 60 min	-2.27	17

[1] Relative to stainless steel

Considering polymer metallised coatings, against *Staphylococcus aureus* a cold spray copper coating on a vertically orientated 3D printed ABS substrate was seen to be the most effective. Figure 6.15 depicts the time-kill graph for this test case. The coating observed complete bacterial elimination within a 15 minute exposure period compared to a 98.5% reduction in viable colony forming units after 3 hrs for pure copper.

The best performing polymer based material against *Pseudomonas aeruginosa* was seen to be a cold spray copper coating on an ABS substrate (Figure 6.16). This material observed complete bacterial elimination within a 10 min exposure period compared to a 99.97% reduction in viable CFUs after 3 hrs for pure copper.

A cold spray copper coating on 3D printed ABS (horizontal orientation) outperformed pure copper metal against the yeast *C. albicans* (Figure 6.17). The cold spray coating was seen to achieve the same effect as copper metal, yet in a sixth of the time.

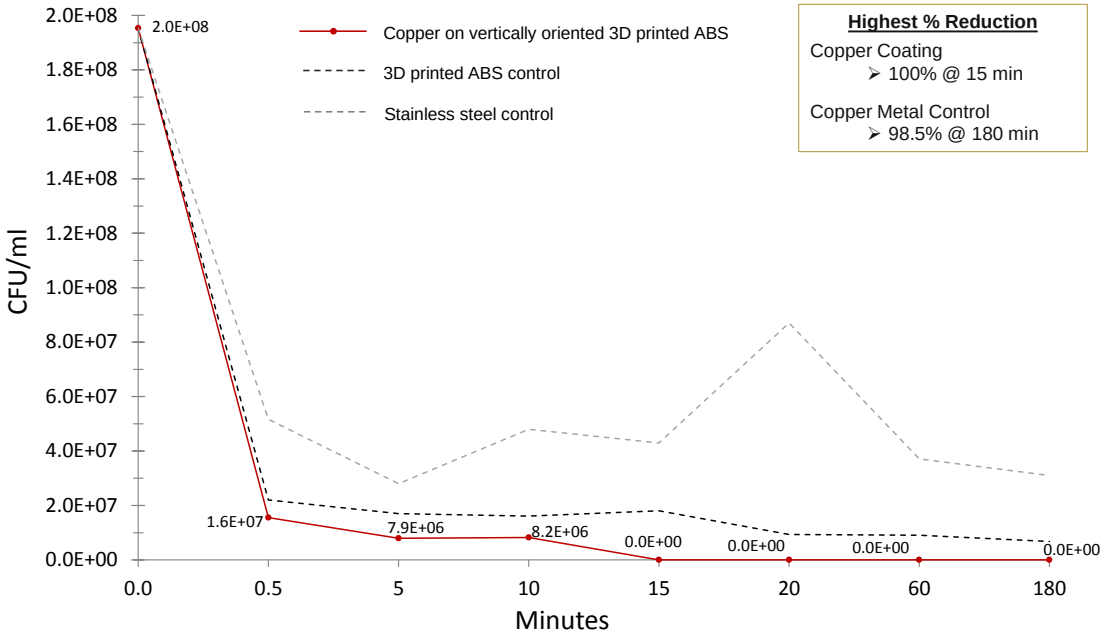


Figure 6.15: Viable CFU/ml per sampling period for a cold spray copper coating on vertically oriented 3D printed ABS against *Staphylococcus aureus*.

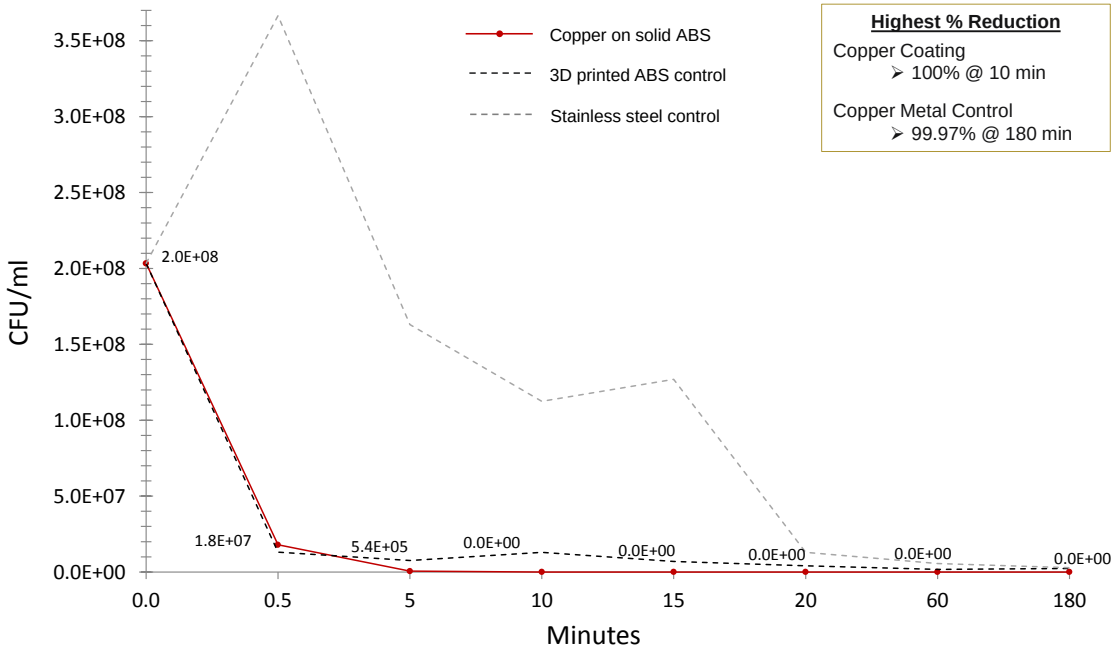


Figure 6.16: Viable CFU/ml per sampling period for a cold spray copper coating on solid ABS against *Pseudomonas aeruginosa*.

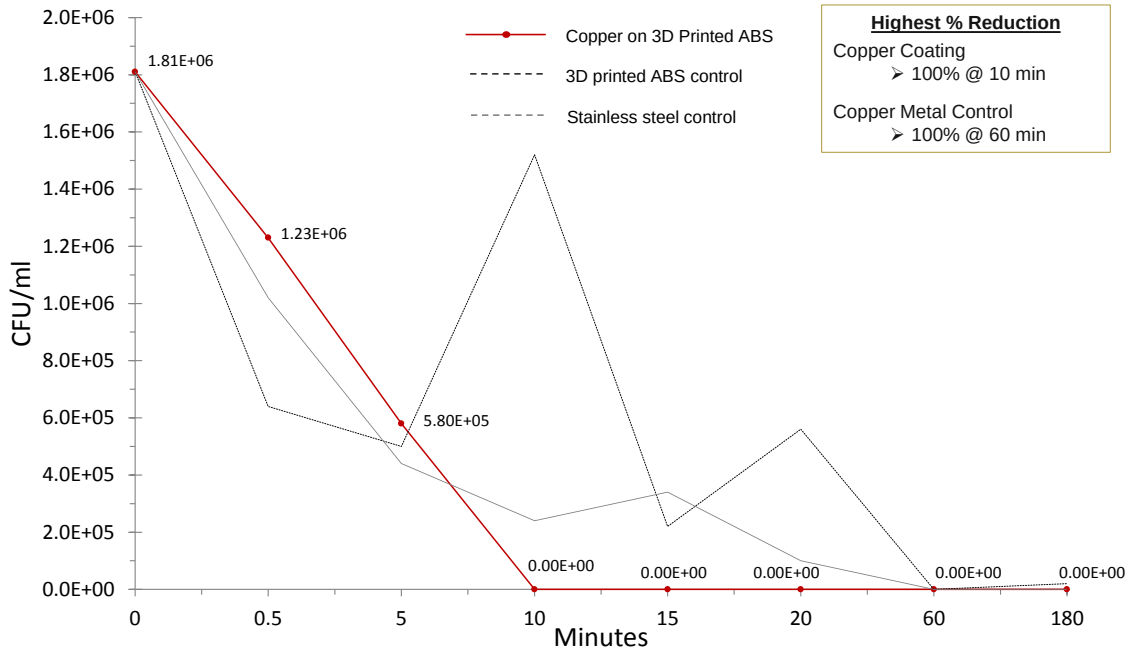


Figure 6.17: Viable CFU/ml per sampling period for a cold spray copper coating on 3D printed ABS against *Candida albicans*.

The accelerated rate of antimicrobial efficacy, observed from these developed coatings, was a desirable property. The quicker microbial elimination takes place the lower the risk of pathogenic transmission either to a contacting object or person.

Table 6.6 contains the overall efficacy ranking based on the m_{ar} value. It was observed that the copper containing coatings, in general, outperform those coatings containing zinc powders. In a dry contact environment copper was therefore seen to be more antimicrobially active than zinc. Copper's heightened performance in a dry contact environment supports claims made in previous studies [66, 80]. Looking specifically at the best performing material combination, that of a cold spray copper coating on a copper metal substrate, it was evident that the coated metal was considerably more effective than an uncoated metal sample. Where uncoated copper metal achieved an average maximum microbial percentage reduction of 98.5% in 2 hrs and 20 min, the coated samples consistently achieved complete microbial elimination within only 10 min.

The top three best performing cold spray coatings in a dry, touch-contact environment against standard test pathogens, were that of:
(1) Copper coated copper,
(2) Copper coated solid ABS and
(3) Copper coated 3D printed ABS.

From a dry, touch-contact perspective the reverse to what was observed for the wet, diffusive tests occurred. That is copper coatings were more antimicrobially active than zinc coatings.

Table 6.6: Overall efficacy ranking for standard coatings tested via the dry contact test procedure against the standard pathogens.

Sample	Ranking based on m_{ar}			Average rank	Overall efficacy rank
	S. aureus	*P. aeruginosa*	*C. albicans*		
Copper coated copper	1	1	1	1.00	1
Copper coated solid ABS	4	2	4	3.33	2
Copper coated 3D printed ABS	3	6	2	3.67	3
Copper coated PEEK	5	7	3	5.00	4
Polished copper coated PEEK	6	3	8	5.67	5
Copper-Aluminium-Alumina coated 3D printed ABS	7	4	11	7.33	6
Copper coated vertically oriented 3D printed ABS	2	8	12	7.33	7
Copper-Aluminium-Alumina coated solid ABS	11	5	10	8.67	8
Zinc coated PC	9	9	9	9.00	9
50% w/w copper-zinc coated 3D printed ABS	12	11	6	9.67	10
75 wt% copper - 25 wt% zinc coated 3D printed ABS	13	14	5	10.67	11
75 wt% zinc - 25 wt% copper coated 3D printed ABS	14	12	7	11.00	12
Zinc coated solid ABS	10	10	14	11.33	13
Zinc coated 3D printed ABS	8	16	13	12.33	14
Pure copper	15	17	15	15.67	15
Zinc coated/galvanised steel	19	13	16	16.00	16
Vertically oriented 3D printed ABS	17	15	21	17.67	17
3D printed ABS	16	18	20	18.00	18
Solid polyetheretherketone	22	20	17	19.67	19
Solid polycarbonate	18	19	22	19.67	20
Stainless steel	20	22	18	20.00	21
Solid ABS	21	21	19	20.33	22

Ranked in order of most antimicrobially active (1) to the least antimicrobially active test sample/control sample (22)

6.1.3 Silver additives

Based on the standard coating tests six coating types were selected to be adapted with the inclusion of a 5 wt% silver additive. These six, silver additive coatings are listed in Table D.2. Their selection was based on previous antimicrobial efficacy in wet and dry test environments, as well as the type of substrate, particularly to include the 3D printed ABS substrates in both the horizontal and vertical orientations.

6.1.3.1 Diffusion assay

These coating were then investigated in terms of their diffusive antimicrobial activity. The average zone of inhibition results are tabulated in Appendix D and graphed below in Figure 6.18.

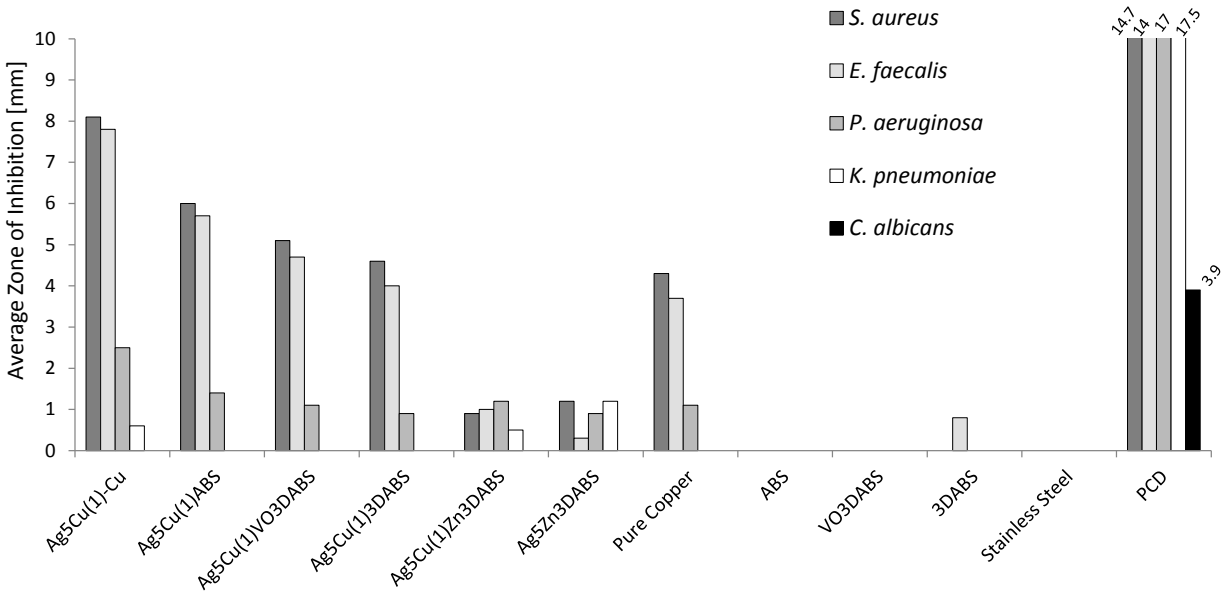


Figure 6.18: Average zones of inhibition for special, silver additive, coatings against the standard bacterial and fungal pathogens.

It was suggested that the addition of silver would further improve antimicrobial activity, which was seen to be the case with copper coatings. Previous studies explain this collaborative behaviour of silver and copper in terms of their independent antimicrobial mechanisms of action, whereby copper breaches cell walls granting access to the silver ions [9]. Yet the opposite was observed for zinc coatings, where a significant reduction in antimicrobial activity was observed through the addition of a silver additive. Figure 6.19 illustrates direct comparisons between coatings with and without silver. Figure 6.19 F depicts the associated bacteriostatic antimicrobial activity of the positive controls: ciprofloxacin and nystatin.

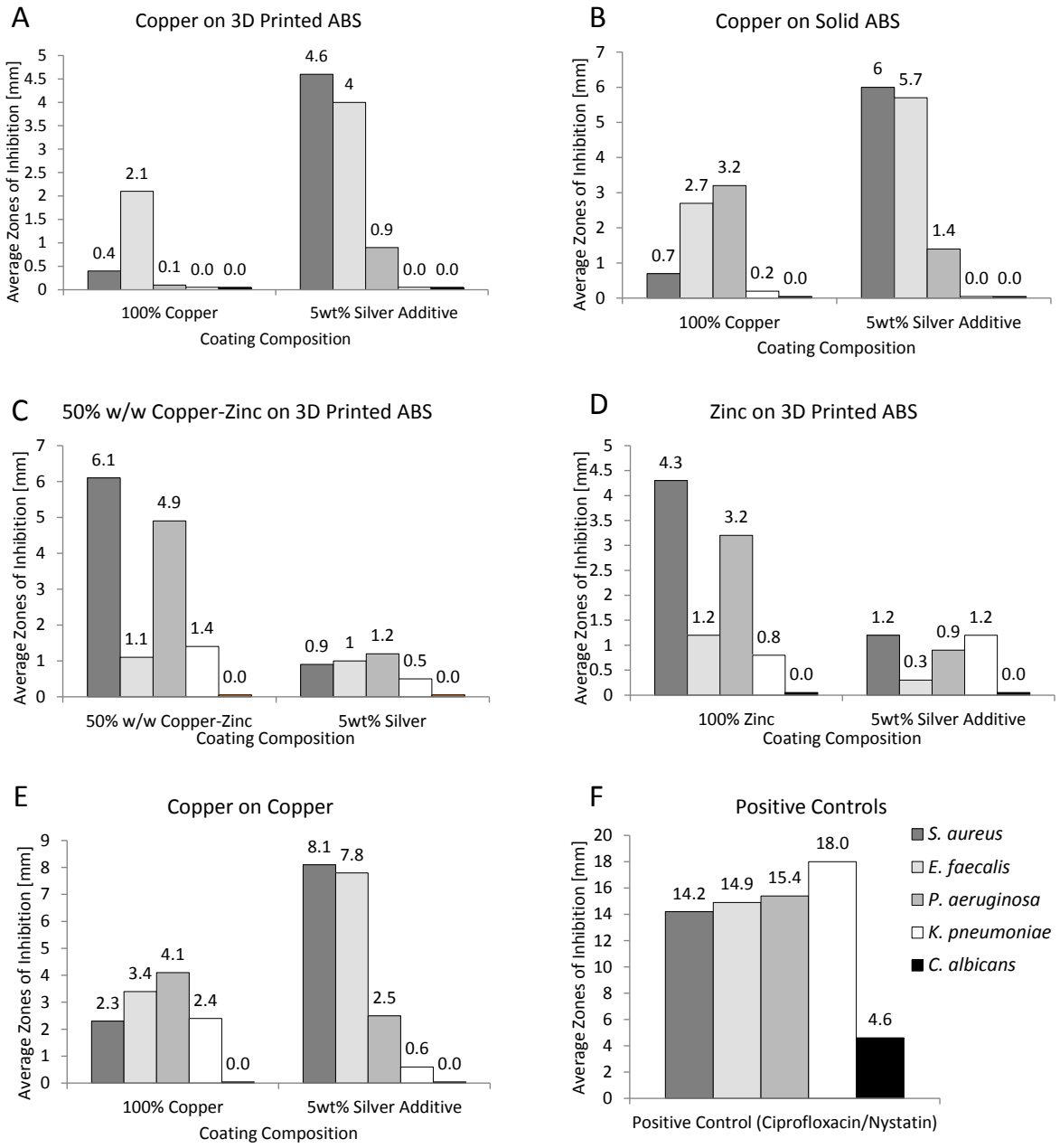


Figure 6.19: Graphical comparison between diffusive antimicrobial activity from coatings with and without a 5wt% silver additive.

The addition of silver to copper containing coatings (Figure 6.19 A, B and E) was seen to result in a 92% increase in the average size of the zones of inhibition. Conversely the addition of silver to the 50:50 copper-zinc blended coating (Figure 6.19 C) and the zinc coating on 3D printed ABS (Figure 6.19 D) lead to a reduction in effective zone of inhibition size by 73% and 62% respectively. It was therefore inferred that silver metal, as a powder additive, is effective in enhancing the antimicrobial activity of copper cold spray coatings in a diffusive environment; and yet not for zinc containing coatings. The choice of coating composition

and the interaction of the various coating constituents was seen to significantly influence efficacy and therefore should be taken into consideration when designing and implementing such coated surfaces.

A direct comparison was made between the original coatings and the coatings with a 5 wt% silver additive. The results for the two bacterial strain types are depicted in Table 6.7 and Table 6.8. Neither the original coatings nor the silver additive samples showed any antimicrobial activity against the yeast, *C. albicans* in a diffusive test environment and were therefore omitted from this comparison.

Table 6.7: Comparison between diffusive antimicrobial activity from coatings with and without a silver additive against Gram-positive bacteria (*S. aureus* and *E. faecalis*).

Test Sample	Average ZOI [mm]	Best Performing
Copper coated copper	2.8	5 wt% silver - 95 wt% copper coated copper
5 wt% silver - 95 wt% copper coated copper	8.0	
Copper coated solid ABS	1.7	5 wt% silver - 95 wt% copper coated solid ABS
5 wt% silver - 95 wt% copper coated solid ABS	5.9	
Copper coated vertically oriented 3D printed ABS	1.1	5 wt% silver - 95 wt% copper coated vertically oriented 3D printed ABS
5 wt% silver - 95 wt% copper coated vertically oriented 3D printed ABS	4.9	
Copper coated 3D printed ABS	1.2	5 wt% silver - 95 wt% copper coated 3D printed ABS
5 wt% silver - 95 wt% copper coated 3D printed ABS	4.3	
50% (w/w) copper-zinc coated 3D printed ABS	3.6	50% (w/w) copper-zinc coated 3D printed ABS
5 wt% silver - 47.5% w/w copper-zinc coated 3D printed ABS	1.0	
Zinc coated 3D printed ABS	2.7	Zinc coated 3D printed ABS
5 wt% silver - 95 wt% zinc coated 3D printed ABS	0.8	

Table 6.8: Comparison between diffusive antimicrobial activity from coatings with and without a silver additive against Gram-negative bacteria (*P.aeruginosa* and *K. pneumoniae*).

Test Sample	Average ZOI [mm]	Best Performing
Copper coated copper	3.3	Copper coated copper
5 wt% silver - 95 wt% copper coated copper	1.6	
Copper coated solid ABS	1.7	Copper coated solid ABS
5 wt% silver - 95 wt% copper coated solid ABS	0.7	
Copper coated vertically oriented 3D printed ABS	1.3	Copper coated vertically oriented 3D printed ABS
5 wt% silver - 95 wt% copper coated vertically oriented 3D printed ABS	0.6	
Copper coated 3D printed ABS	0.1	5 wt% silver - 95 wt% copper coated 3D printed ABS
5 wt% silver - 95 wt% copper coated 3D printed ABS	0.5	
50% (w/w) copper-zinc coated 3D printed ABS	3.1	50% (w/w) copper-zinc coated 3D printed ABS
5 wt% silver - 47.5% w/w copper-zinc coated 3D printed ABS	0.9	
Zinc coated 3D printed ABS	2.0	Zinc coated 3D printed ABS
5 wt% silver - 95 wt% zinc coated 3D printed ABS	1.1	

The addition of silver to the various copper coatings had a positive effect on antimicrobial activity against Gram-positive pathogens, but not against Gram-negative bacteria, except in the case of a silver and copper blended coating on 3D printed ABS. Silver as an additive to zinc coatings did not result in any improved antimicrobial activity, regardless of the pathogen for the diffusion assays.

Table 6.9 contains the combined comparative results for cold spray coating with and without a 5 wt% silver additive within a diffusive test environment.

Table 6.9: Comparison between diffusive antimicrobial activity from coatings with and without a silver additive against all standard test pathogens.

Test Sample	Average ZOI [mm]	Best Performing
Copper coated copper	2.4	5 wt% silver - 95 wt% copper coated copper
5 wt% silver - 95 wt% copper coated copper	3.8	
Copper coated solid ABS	1.3	5 wt% silver - 95 wt% copper coated solid ABS
5 wt% silver - 95 wt% copper coated solid ABS	2.6	
Copper coated vertically oriented 3D printed ABS	0.9	5 wt% silver - 95 wt% copper coated vertically oriented 3D printed ABS
5 wt% silver - 95 wt% copper coated vertically oriented 3D printed ABS	2.2	
Copper coated 3D printed ABS	0.5	5 wt% silver - 95 wt% copper coated 3D printed ABS
5 wt% silver - 95 wt% copper coated 3D printed ABS	1.9	
50% (w/w) copper-zinc coated 3D printed ABS	2.7	50% (w/w) copper-zinc coated 3D printed ABS
5 wt% silver - 47.5% w/w copper-zinc coated 3D printed ABS	0.7	
Zinc coated 3D printed ABS	1.9	Zinc coated 3D printed ABS
5 wt% silver - 95 wt% zinc coated 3D printed ABS	0.7	

A piecewise ranking for each material against each respective pathogen may be found in Appendix D.

Table 6.10 provides an overall ranking of the developed coatings, based on diffusive antimicrobial tests against the standard pathogens. Ranking in numerical order from the most to the least antimicrobially active. The top three most effective coatings, ranked in terms of decreasing zone of inhibition size, are:

(1) 5 wt% silver - 95 wt% copper coated copper,
(2) 5 wt% silver - 95 wt% copper coated solid ABS and
(3) 5 wt% silver - 95 wt% copper coated vertically oriented 3D printed ABS.

Table 6.10: Overall efficacy ranking based on average zone of inhibition from diffusion assays of special, silver additive, coatings against standard pathogens.

Overall Rank	Test sample	Overall Average ZOI [mm]
1	PCD	13.42
2	5 wt% silver - 95 wt% copper coated copper	3.8
3	5 wt% silver - 95 wt% copper coated solid ABS	2.62
4	5 wt% silver - 95 wt% copper coated vertically oriented 3D printed ABS	2.18
5	5 wt% silver - 95 wt% copper coated 3D printed ABS	1.9
6	Pure copper	1.82
7	5 wt% silver - 47.5% w/w copper-zinc coated 3D printed ABS	0.72
8	5 wt% silver - 95 wt% zinc coated 3D printed ABS	0.72
9	3D printed ABS	0.16
10	Stainless steel	0
11	Vertically oriented 3D printed ABS	0
12	Solid ABS	0

6.1.3.2 Dry contact test

For each of the three test pathogens (*S. aureus*, *P. aeruginosa* and *C. albicans*) the resulting antimicrobial efficacies of the silver additive cold spray coatings were plotted. The corresponding data tables, with corresponding linear regression analysis via Pearson's correlation coefficient, are included in Appendix D. Figure 6.20 depicts the time-kill trend for silver additive test samples against *S. aureus*.

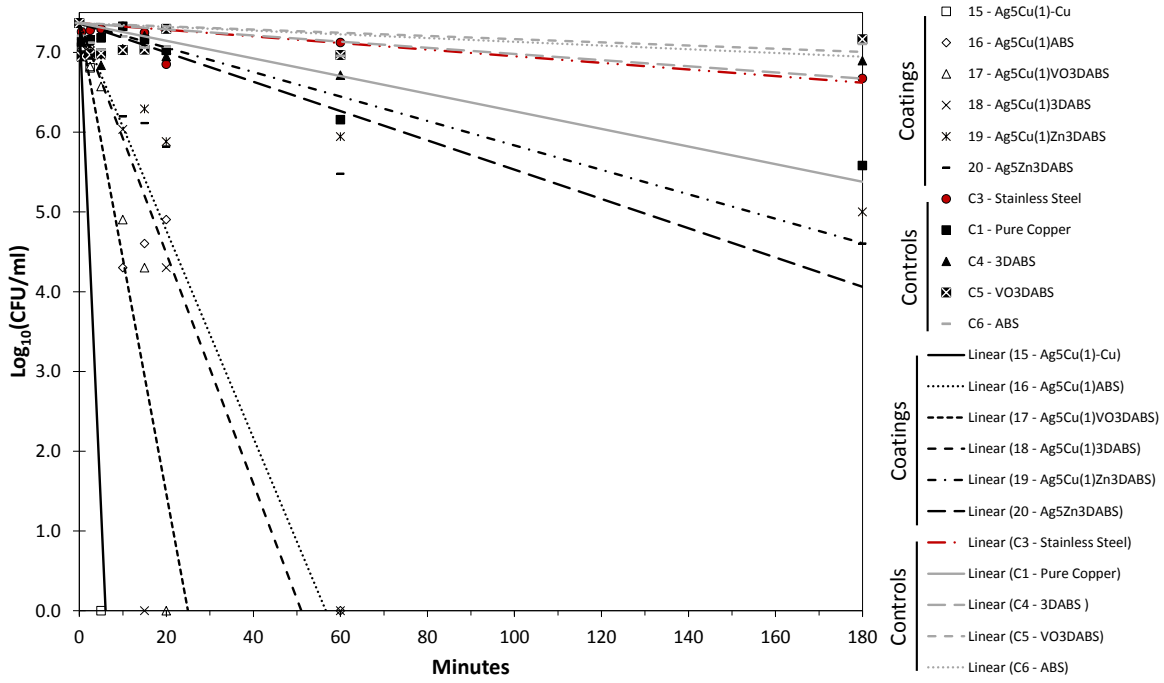


Figure 6.20: Touch-contact antimicrobial efficacy of cold spray coatings, with a 5 wt% silver additive, against *S. aureus* (ATCC 25923).

Figure 6.21 depicts the time-kill trend for silver additive test samples against *P. aeruginosa*.

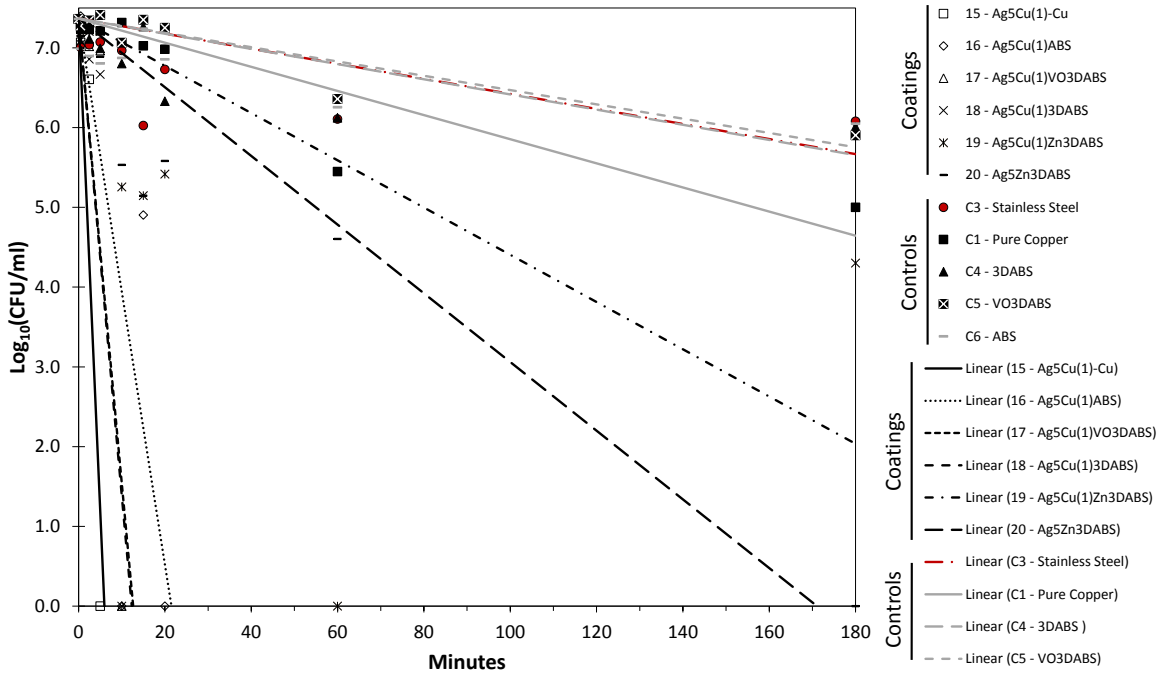


Figure 6.21: Touch-contact antimicrobial efficacy of cold spray coatings, with a 5 wt% silver additive, against *P. aeruginosa* (ATCC 27853).

Figure 6.22 depicts the time-kill trend for silver additive test samples against *C. albicans*.

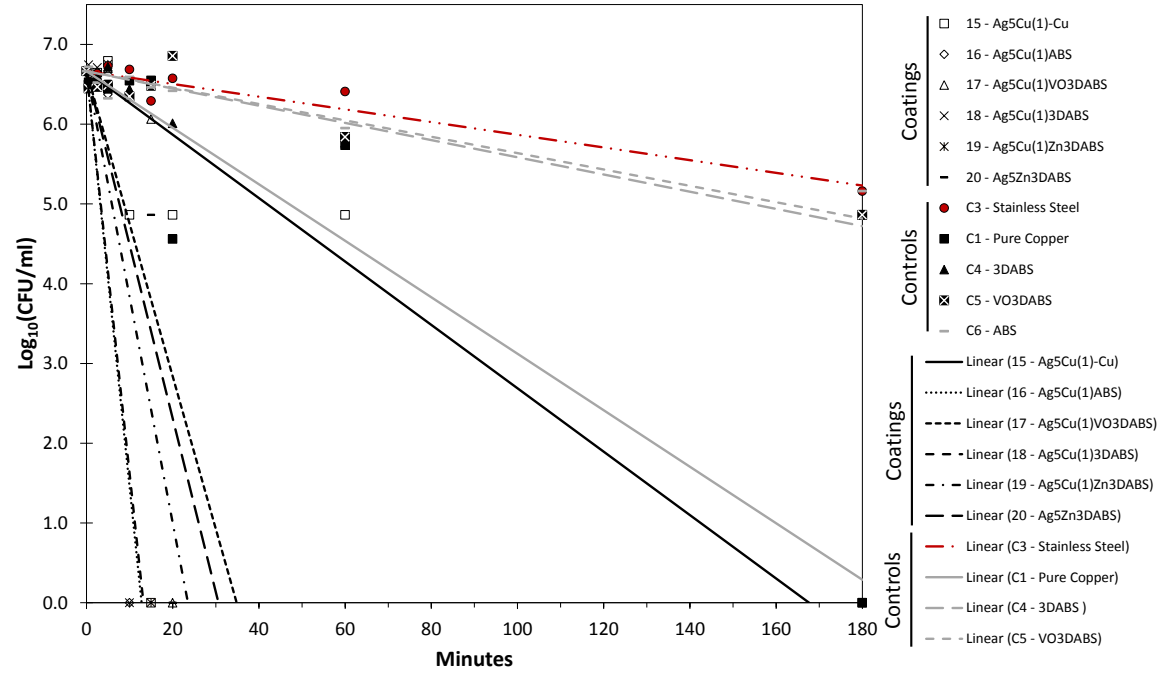


Figure 6.22: Touch-contact antimicrobial efficacy of cold spray coatings, with a 5 wt% silver additive, against *C. albicans* (ATCC 10231).

It was evident that all cold spray coatings exhibited effective and efficient biocidal activity, outperforming that of copper metal, a known antimicrobial agent. This result reflected that of a similar study, which investigated the antimicrobial potential of laser cladded copper-silver coatings on stainless steel substrates [80]. While the paper's authors suggest that the enhanced activity was due to a synergistic relationship between the copper and silver metals, it is here proposed that the coating method itself and the related surface topography may be additional influencing factors. This does not rule out a collaborative interaction between the two metals, but proposed an additional contributing factor. Further analysis to this effect is made in Chapter 7.

The extent of efficacy, to which the majority of coatings achieved complete microbial elimination, was evaluated using three main parameters. The first being the rate of microbial reduction (m_{ar}) [Log_{10}(CFU/ml)/min], the second the highest percentage reduction with the corresponding contact time (Red.%) and thirdly the percentage reduction at a 15 minute exposure period (Red.% @ 15 min). A summary of these results is given in Table 6.11, Table 6.12 and Table 6.13 for each respective pathogenic strain. In addition the associated efficacy ranking, based on the microbial reduction rate (m_{ar}), is given.

Table 6.11: Summary results for dry contact antimicrobial test for silver additive coatings against *S. aureus*.

Test sample	*Staphylococcus aureus* (ATCC 25923)					
	R	R^2	m_{ar}	Red.%[1]	Red.% @ 15 min.	Rank (m_{ar})
5 wt% silver - 95 wt% copper coated copper	-0.907	0.823	1.210	100% @ 5 min	100.00	1
5 wt% silver - 95 wt% copper coated solid ABS	-0.960	0.922	0.130	100% @ 60 min	99.80	4
5 wt% silver - 95 wt% copper coated vertically oriented 3D printed ABS	-0.945	0.893	0.290	100% @ 20 min	99.90	2
5 wt% silver - 95 wt% copper coated 3D printed ABS	-0.788	0.621	0.140	100% @ 15 min	100.00	3
5 wt% silver - 47.5% w/w copper-zinc coated 3D printed ABS	-0.858	0.736	0.010	97.55% @ 180 min	90.27	5
5 wt% silver - 95 wt% zinc coated 3D printed ABS	-0.848	0.719	0.010	99.02% @ 180 min	93.54	6
Pure copper	-0.945	0.893	0.010	90.69% @ 180 min	27.99	7
Stainless steel	-0.823	0.677	0.000	/	/	8
3D printed ABS	-0.415	0.172	0.000	-0.82% @ 180 min	-0.06	9
Vertically oriented 3D printed ABS	0.128	0.016	-0.002	-5.99% @ 180 min	-0.45	11
Solid ABS	-0.269	0.072	-0.002	-5.17% @ 180 min	-0.39	10

[1] Relative to stainless steel

Table 6.12: Summary results for dry contact antimicrobial test for silver additive coatings against *P. aeruginosa*.

Test sample	*Pseudomonas aeruginosa* (ATCC 27853)					
	R	R^2	m_{ar}	Red.%[1]	Red.% @ 15 min.	Rank (m_{ar})
5 wt% silver - 95 wt% copper coated copper	-0.918	0.843	1.220	100% @ 5 min	100.00	1
5 wt% silver - 95 wt% copper coated solid ABS	-0.799	0.638	0.330	100% @ 20 min	99.52	4
5 wt% silver - 95 wt% copper coated vertically oriented 3D printed ABS	-0.893	0.797	0.570	100% @ 10 min	100.00	3
5 wt% silver - 95 wt% copper coated 3D printed ABS	-0.910	0.828	0.590	100% @ 10 min	100.00	2
5 wt% silver - 47.5% w/w copper-zinc coated 3D printed ABS	-0.483	0.233	0.120	100% @ 60 min	99.30	5
5 wt% silver - 95 wt% zinc coated 3D printed ABS	-0.967	0.935	0.030	100% @ 180 min	99.16	6
Pure copper	-0.913	0.834	0.010	95.54% @ 60 min	36.28	7
Stainless steel	-0.653	0.426	0.000	/	/	9
3D printed ABS	-0.760	0.578	0.000	0.33% @ 180 min	0.02	8
Vertically oriented 3D printed ABS	-0.931	0.867	-0.001	-1.59% @ 180 min	-0.10	10
Solid ABS	-0.829	0.687	-0.001	-1.9% @ 180 min	-0.12	11

[1] Relative to stainless steel

Table 6.13: Summary results for dry contact antimicrobial test for silver additive coatings against *C. albicans*.

Test sample	*Candida albicans* (ATCC 10231)					
	R	R^2	m_{ar}	Red.%[1]	Red.% @ 15 min.	Rank (m_{ar})
5 wt% silver - 95 wt% copper coated copper	-0.668	0.446	0.320	100% @ 15 min	100.00	2
5 wt% silver - 95 wt% copper coated solid ABS	-0.894	0.799	0.510	100% @ 10 min	100.00	1
5 wt% silver - 95 wt% copper coated vertically oriented 3D printed ABS	-0.762	0.581	0.180	100% @ 20 min	66.85	6
5 wt% silver - 95 wt% copper coated 3D printed ABS	-0.803	0.645	0.280	100% @ 15 min	100.00	3
5 wt% silver - 47.5% w/w copper-zinc coated 3D printed ABS	-0.786	0.618	0.280	100% @ 15 min	100.00	4
5 wt% silver - 95 wt% zinc coated 3D printed ABS	-0.845	0.714	0.210	100% @ 20 min	97.92	5
Pure copper	-0.949	0.901	0.030	100% @ 180	-0.87	7
Stainless steel	-0.957	0.916	0.000	/	/	11
3D printed ABS	-0.957	0.916	0.003	9.65% @ 180 min	0.64	8
Vertically oriented 3D printed ABS	-0.945	0.893	0.002	7.92% @ 180 min	0.53	9
Solid ABS	-0.972	0.945	0.001	2.76% @ 180 min	0.18	10

[1] Relative to stainless steel

The overall efficacy ranking for the silver additive coatings against the three standard pathogens is given in Table 6.14.

Table 6.14: Overall efficacy ranking for special coatings tested via the dry contact test procedure against the standard pathogens.

Sample	Ranking based on m_{ar}			Average rank	Overall efficacy ranking
	S. aureus	*P. aeruginosa*	*C. albicans*		
5 wt% silver - 95 wt% copper coated copper	1	1	2	1.33	1
5 wt% silver - 95 wt% copper coated 3D printed ABS	3	2	3	2.67	2
5 wt% silver - 95 wt% copper coated solid ABS	4	4	1	3.00	3
5 wt% silver - 95 wt% copper coated vertically oriented 3D printed ABS	2	3	6	3.67	4
5 wt% silver - 47.5% w/w copper-zinc coated 3D printed ABS	5	5	4	4.67	5
5 wt% silver - 95 wt% zinc coated 3D printed ABS	6	6	5	5.67	6
Pure copper	7	7	7	7.00	7
3D printed ABS	9	8	8	8.33	8
Stainless steel	8	9	11	9.33	9
Vertically oriented 3D printed ABS	11	10	9	10.00	10
Solid ABS	10	11	10	10.33	11

Ranking from most antimicrobially active at 1, to the least antimicrobially active – neutral/inert – at 11.

Comparison between standard coatings and silver additive coatings

Silver's potential additive effects on touch-contact antimicrobial activity was investigated. Table 6.15, Table 6.16 and Table 6.17 tabulate the results for antimicrobial activity against *S. aureus*, *P. aeruginosa* and *C. albicans*.

Table 6.15: Silver additive effects - cold spray coatings against *S. aureus*.

Test Sample	Relative antimicrobial rate (m_{ar})	Highest relative percentage reduction	Relative percentage reduction @ 15 minutes	Best Performing
Copper coated copper	1.59	100% @ 5 min	100	Copper coated copper
5 wt% silver - 95 wt% copper coated copper	1.21	100% @ 5 min	100	
Copper coated solid ABS	0.34	100% @ 20 min	99.94	Copper coated solid ABS
5 wt% silver - 95 wt% copper coated solid ABS	0.13	100% @ 60 min	99.8	
Copper coated vertically oriented 3D printed ABS	0.39	100% @ 15 min	100	Copper coated vertically oriented 3D printed ABS
5 wt% silver - 95 wt% copper coated vertically oriented 3D printed ABS	0.29	100% @ 20 min	99.9	
Copper coated 3D printed ABS	0.34	100% @ 20 min	99.98	Copper coated 3D printed ABS
5 wt% silver - 95 wt% copper coated 3D printed ABS	0.14	100% @ 15 min	100	
50% w/w copper-zinc coated 3D printed ABS	0.02	99.14% @ 60 min	98.87	50% w/w copper-zinc coated 3D printed ABS
5 wt% silver - 47.5% w/w copper-zinc coated 3D printed ABS	0.01	97.55% @ 180 min	90	
Zinc coated 3D printed ABS	0.04	97.68% @ 60 min	95.16	Zinc coated 3D printed ABS
5 wt% silver - 95 wt% zinc coated 3D printed ABS	0.01	99.02% @ 180 min	93.54	

Table 6.16: Silver additive effects - cold spray coatings against *P. aeruginosa*.

Test Sample	Relative antimicrobial rate (m_{ar})	Highest relative percentage reduction	Relative percentage reduction @ 15 minutes	Best Performing
Copper coated copper	1.61	100% @ 5 min	100	Copper coated copper
5 wt% silver - 95 wt% copper coated copper	1.22	100% @ 5 min	100	
Copper coated solid ABS	0.74	100% @ 10 min	100	Copper coated solid ABS
5 wt% silver - 95 wt% copper coated solid ABS	0.33	100% @ 20 min	100	
Copper coated vertically oriented 3D printed ABS	0.4	100% @ 15 min	100	5 wt% silver - 95 wt% copper coated vertically oriented 3D printed ABS
5 wt% silver - 95 wt% copper coated vertically oriented 3D printed ABS	0.57	100% @ 10 min	100	
Copper coated 3D printed ABS	0.68	100% @ 10 min	100	Copper coated 3D printed ABS
5 wt% silver - 95 wt% copper coated 3D printed ABS	0.59	100% @ 10 min	100	
50% w/w copper-zinc coated 3D printed ABS	0.04	100% @ 180 min	99.89	5 wt% silver - 47.5% w/w copper-zinc coated 3D printed ABS
5 wt% silver - 47.5% w/w copper-zinc coated 3D printed ABS	0.12	100% @ 60 min	99	
Zinc coated 3D printed ABS	0.01	96.89% @ 60 min	96.1	5 wt% silver - 95 wt% zinc coated 3D printed ABS
5 wt% silver - 95 wt% zinc coated 3D printed ABS	0.03	100% @ 180 min	99	

Table 6.17: Silver additive effects - cold spray coatings against *C. albicans*.

Test Sample	Relative antimicrobial rate (m_{ar})	Highest relative percentage reduction	Relative percentage reduction @ 15 minutes	Best Performing
Copper coated copper	0.49	100% @ 10 min	100	Copper coated copper
5 wt% silver - 95 wt% copper coated copper	0.32	100% @ 15 min	100	
Copper coated solid ABS	0.47	100% @ 10 min	100	5 wt% silver - 95 wt% copper coated solid ABS
5 wt% silver - 95 wt% copper coated solid ABS	0.51	100% @ 10 min	100	
Copper coated vertically oriented 3D printed ABS	0.18	100% @ 20 min	57.32	No preference
5 wt% silver - 95 wt% copper coated vertically oriented 3D printed ABS	0.18	100% @ 20 min	66.852	
Copper coated 3D printed ABS	0.48	100% @ 10 min	100	Copper coated 3D printed ABS
5 wt% silver - 95 wt% copper coated 3D printed ABS	0.28	100% @ 15 min	100	
50% w/w copper-zinc coated 3D printed ABS	0.47	100% @ 10 min	100	50% w/w copper-zinc coated 3D printed ABS
5 wt% silver - 47.5% w/w copper-zinc coated 3D printed ABS	0.28	100% @ 15 min	100	
Zinc coated 3D printed ABS	0.18	100% @ 20 min	85.77	5 wt% silver - 95 wt% zinc coated 3D printed ABS
5 wt% silver - 95 wt% zinc coated 3D printed ABS	0.21	100% @ 20 min	97.923	

Against *Staphylococcus aureus* a silver additive is seen to offer no antimicrobial advantage. In light of this a standard coating, without the addition of a silver additive, was deemed to be the more desirable coating formulation.

Isolated coatings showed improved rates of antimicrobial activity after the addition of the silver additive against the *P. aeruginosa* strain, with the most significant improvement coming from a copper-zinc blended coating on 3D printed ABS. For this test case the silver additive instigated a microbial reduction rate three times greater than a standard coating.

No significant advantage against the yeast pathogen, *Candida albicans*, was observed for coatings with a silver additive. Marginal increased rates of antimicrobial reduction were observed for copper coated solid ABS and zinc coated 3D printed ABS with the addition of 5 wt% silver powder, yet not to a fiscally viable extent.

A caveat, based on the findings from a study into antimicrobial copper and silver interactions, suggests caution when considering metallic combinations for antimicrobial applications, thereby proposing adequate consideration of the intended application, metal combinations and their associated effects, since both synergistic and antagonistic antimicrobial behaviour has been observed [65].

In addition to the different metal powder combinations, the substrate materials have also differed. Substrate design, using additive manufacturing techniques, allows for potential functional substrate development. As a means of investigating the effects of 3D printing build orientation, in particular, a surface topography analysis was conducted. This analysis was presented in Chapter 5, Section 5.5.2, on pages 192 - 194 and will be used in a consolidative analysis in the following chapter as a means of investigating the role surface topography plays in antimicrobial efficacy.

6.2 Resistant pathogens

The five best performing materials from the preceding susceptibility tests were tested against the resistant microbial strains (Gentamicin-methicillin-resistant *S. aureus* (GMRSA), resistant reference *P. aeruginosa*[i] and clinically resistant *C. albicans*[ii]). These three pathogens represent a branch of nosocomial infections posing a serious threat to the healthcare industry. This takes the concern of contracting an infection while in hospital to a new and life-threatening level. If the developed coatings were able to exhibit sufficient levels of inhibitory or biocidal activity against these resistant pathogenic strains they would offer a viable and alternative means to infection control and prevention within hospitals.

The five cold spray coatings identified and selected for these antimicrobial tests are given as follows:

[i] Azlocillin-carbenicillin-resistant *Pseudomonas aeruginosa* (DSM 46316).
[ii] Fluconazole-resistant *Candida albicans* (Wits *C. albicans* 4122).

1. 5 wt% silver - 95 wt% copper coated copper.
2. 50% w/w copper-zinc coated 3D printed ABS (hor.)
3. Copper coated copper
4. Copper coated solid ABS
5. Copper coated 3D printed ABS (hor.)

The choice of coatings to be included in this analysis was based on antimicrobial efficacy, selecting those exhibiting the highest levels of efficacy against the standard pathogens in both a wet and dry contact environment. In addition, practical considerations regarding the scale of these tests limited the selection to only the top five coatings. This decision does not, however, reflect the inability (perceived or actual) of the other coating types as effective self-sanitising surfaces against these resistant and multi-drug resistant pathogens.

6.2.1 Diffusion assay

The results for the diffusive assay are presented in Figure 6.23. The accompanying data table may be found in Appendix D.

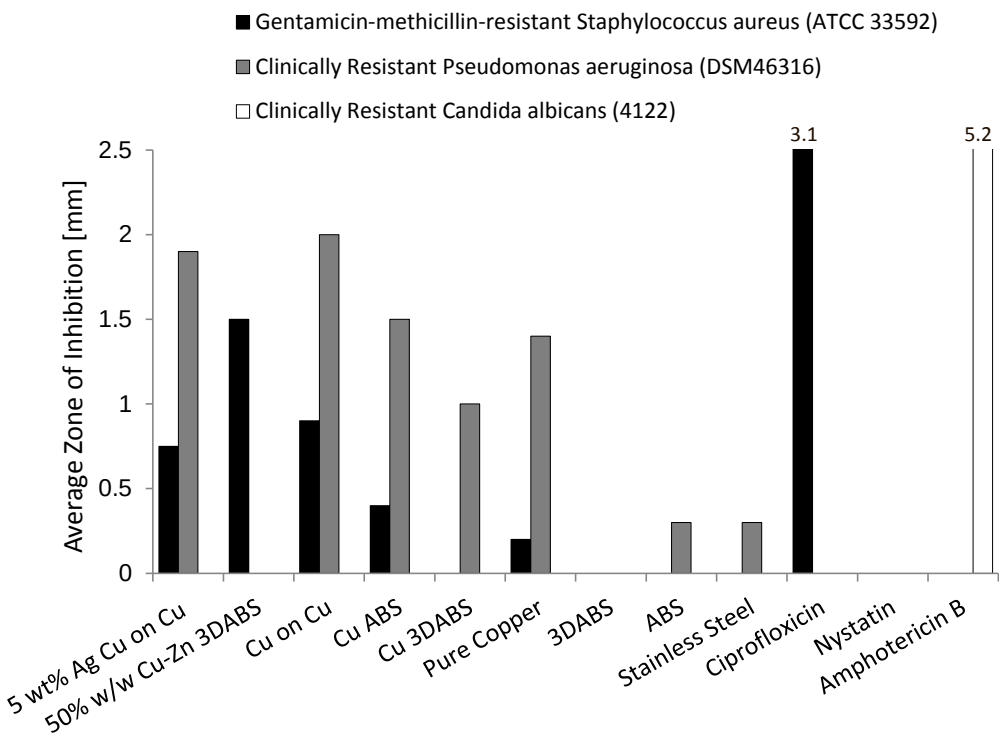


Figure 6.23: Average microbial inhibition for cold spray coatings against resistant pathogens GMRSA, *P. aeruginosa* and a clinically resistant *C. albicans*.

The key results show that copper was more active against the Gram-negative strain, while a copper-zinc blend shows significant improvement against the multi-drug resistant Gram-positive strain. Again no activity was observed against the pathogenic yeast and a silver additive offered no significant antimicrobial enhancement. The results for the diffusive assay under these conditions are given in Table 6.18. Table 6.19 ranks the five test samples and their relevant control samples against the three resistant and multi-resistant pathogens.

Table 6.18: Diffusion assay efficacy ranking per culture and resistant pathogen type.

Rank	Gentamicin-methicillin-resistant Staphylococcus aureus (ATCC #33592)		Clinically Resistant Pseudomonas aeruginosa (DMS46316)		Clinically Resistant Candida albicans (#4122)	
	Test Sample	ZOI [mm]	Test Sample	ZOI [mm]	Test Sample	ZOI [mm]
1	Ciprofloxicin	3.10	Cu(1)-Cu	2.00	Amphotericin B	5.20
2	Cu(1)50Zn3DABS	1.50	Ag5Cu(1)-Cu	1.90	Ag5Cu(1)-Cu	0.00
3	Cu(1)-Cu	0.90	Cu(1)ABS	1.50	Cu(1)50Zn3DABS	0.00
4	Ag5Cu(1)-Cu	0.75	Pure Copper	1.40	Cu(1)-Cu	0.00
5	Cu(1)ABS	0.40	Cu(1)3DABS	1.00	Cu(1)ABS	0.00
6	Pure Copper	0.20	ABS	0.30	Cu(1)3DABS	0.00
7	Cu(1)3DABS	0.00	Stainless Steel	0.30	Pure Copper	0.00
8	3DABS	0.00	Cu(1)50Zn3DABS	0.00	3DABS	0.00
9	ABS	0.00	3DABS	0.00	ABS	0.00
10	Stainless Steel	0.00	Ciprofloxicin	0.00	Stainless Steel	0.00
11	Nystatin	/	Nystatin	/	Nystatin	0.00
12	Amphotericin B	/	Amphotericin B	/	Ciprofloxicin	/

Table 6.19: Efficacy ranking for selected cold spray coatings against resistant pathogenic strains in a diffusive test environment.

Overall Rank	Test sample	Overall Average ZOI [mm]
1	Copper coated copper	0.97
2	5 wt% silver - 95 wt% copper coated copper	0.88
3	Copper coated solid ABS	0.63
4	Copper metal	0.53
5	50% (w/w) copper-zinc coated 3D printed ABS (hor.)	0.5
6	Copper coated 3D printed ABS (hor.)	0.33
7	Solid ABS	0.1
8	Stainless Steel	0.1
9	3D printed ABS (hor.)	0

6.2.2 Dry contact test

These same coatings were then tested under simulated touch-contact activity, by way of the adapted time-kill assay. The results are graphed in Figure 6.24 - Figure 6.26, with the corresponding data tables given in Appendix D.

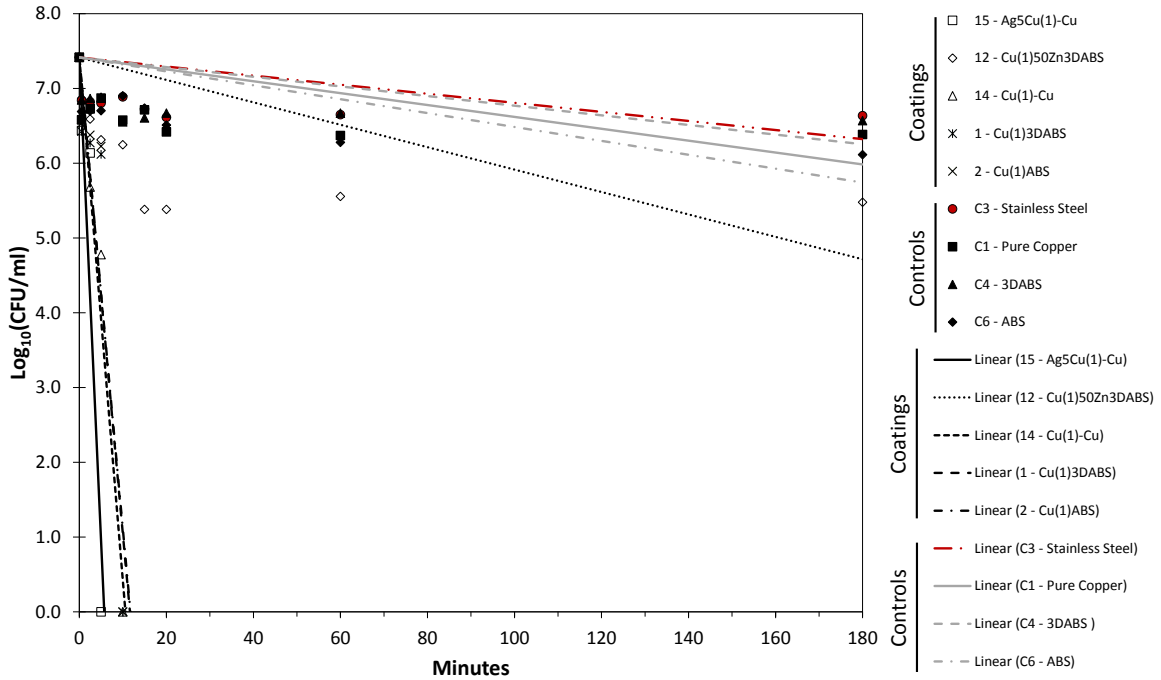


Figure 6.24: Touch-contact antimicrobial efficacy of cold spray coatings against Gentamicin-methicillin-resistant *Staphylococcus aureus* (ATCC 33592).

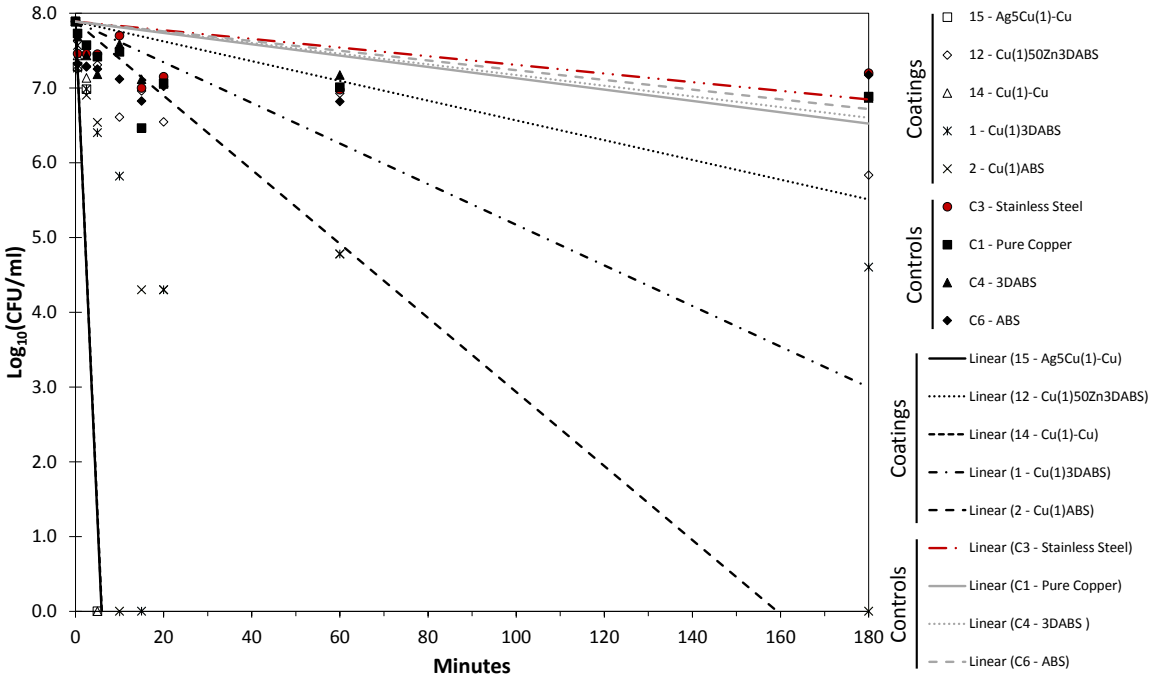


Figure 6.25: Touch-contact antimicrobial efficacy of cold spray coatings against Reference *Pseudomonas aeruginosa* (DSM 46316).

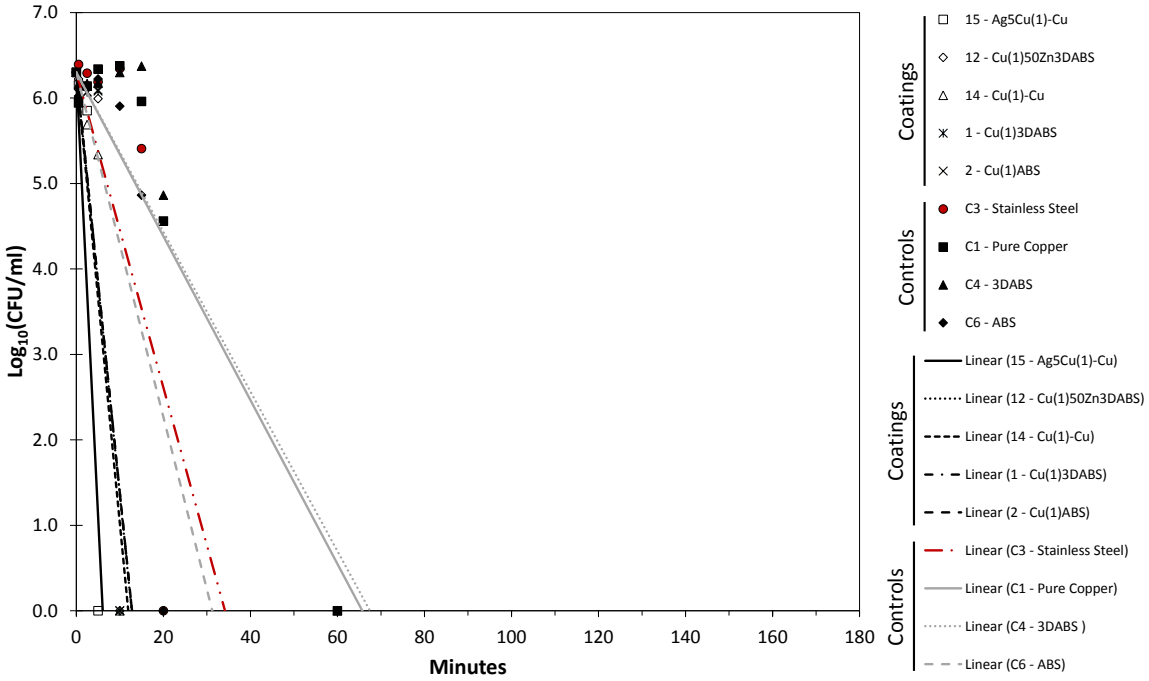


Figure 6.26: Touch-contact antimicrobial efficacy of cold spray coatings against Clinically Resistant *Candida albicans* (Ref. No. 4122).

These results confirm effective and efficient antimicrobial activity from the selected cold spray coatings against resistant pathogenic strains in a dry, touch-contact environment. Table 6.20,

Table 6.21 and Table 6.22 summarise the dry contact test results for test coatings against the resistant pathogenic strains. Included in each table is a ranking based on the effective rate of microbial reduction (m_{ar}), with 1 being the most antimicrobially active and 9 the least.

Table 6.20: Summary results for dry contact antimicrobial test for developed coatings against gentamicin methicillin resistant *S. aureus* (ATCC 33592).

Test sample	Gentamicin Methicillin Resistant *Staphylococcus aureus* (ATCC 33592)					
	R	R^2	m_{ar}	Red.%[1]	Red.% @ 15 min.	Rank (m_{ar})
5 wt% silver - 95 wt% copper coated copper	-0.930	0.865	1.290	100% @ 5 min	100.00	1
50% w/w copper-zinc coated 3D printed ABS	-0.514	0.264	0.010	98,86% @ 15 min	98.86	5
Copper coated copper	-0.983	0.966	0.690	100% @ 10 min	100.00	2
Copper coated solid ABS	-0.922	0.850	0.630	100% @ 10 min	100.00	3
Copper coated 3D printed ABS	-0.925	0.856	0.630	100% @ 10 min	100.00	4
Pure copper	-0.488	0.238	0.000	88.08% @ 60 min	77.21	8
Stainless steel	-0.428	0.183	0.000	/	0.00	9
3D printed ABS	-0.422	0.178	0.000	1.14% @ 180 min	0.08	7
Solid ABS	-0.713	0.508	0.003	9.12% @ 180 min	0.66	6

[1] Relative to stainless steel

Table 6.21: Summary results for dry contact antimicrobial test for developed coatings against resistant reference *P. aeruginosa* (DSM 46316).

Test sample	Resistant Reference *Pseudomonas aeruginosa* (DSM 46316)					
	R	R^2	m_{ar}	Red.%[1]	Red.% @ 15 min.	Rank (m_{ar})
5 wt% silver - 95 wt% copper coated copper	-0.917	0.841	1.330	100% @ 5 min	100.00	1
50% w/w copper-zinc coated 3D printed ABS	-0.779	0.607	0.010	94.07% @ 20 min	85.56	5
Copper coated copper	-0.912	0.832	1.310	100% @ 5 min	100.00	2
Copper coated solid ABS	-0.637	0.406	0.670	100% @ 180 min	99.97	3
Copper coated 3D printed ABS	-0.234	0.055	0.410	100% @ 15 min	100.00	4
Pure copper	-0.470	0.221	0.000	95.71% @ 15 min	95.71	8
Stainless steel	-0.408	0.166	0.000	/	0.00	9
3D printed ABS	-0.638	0.407	0.001	3.68% @ 180 min	0.27	6
Solid ABS	-0.228	0.052	0.001	1.84% @ 180 min	0.13	7

[1] Relative to stainless steel

Table 6.22: Summary results for dry contact antimicrobial test for developed coatings against the clinically resistant *C. albicans* (4122).

Test sample	Clinically Resistant *Candida albicans* (#4122)					
	R	R^2	m_{ar}	Red.%[1]	Red.% @ 15 min.	Rank (m_{ar})
5 wt% silver - 95 wt% copper coated copper	-0.907	0.823	0.990	100% @ 5 min	100.00	1
50% w/w copper-zinc coated 3D printed ABS	-0.895	0.801	0.450	100% @ 10 min	100.00	3
Copper coated copper	-0.933	0.870	0.480	100% @ 10 min	100.00	2
Copper coated solid ABS	-0.884	0.781	0.450	100% @ 10 min	100.00	4
Copper coated 3D printed ABS	-0.885	0.783	0.450	100% @ 10 min	100.00	5
Pure copper	-0.967	0.935	0.000	100% @ 60 min	-27.81	7
Stainless steel	-0.785	0.616	0.000	/	0.00	8
3D printed ABS	-0.960	0.922	-0.003	-4.99% @ 60 min	-0.80	9
Solid ABS	-0.824	0.679	0.000	0.67% @ 60 min	0.11	6

[1] Relative to stainless steel

Figure 6.27, Figure 6.28 and Figure 6.29 depict the time-kill graphs for copper containing samples tested against the resistant pathogen gentamicin-methicillin-resistant *Staphylococcus aureus* (ATCC 33592), a reference resistant strain of *Pseudomonas aeruginosa* (DSM 46316) and a clinically resistant *Candida albicans* (Ref. No. 4122), respectively. Comparing the highest average percentage reductions across all three tested pathogens and comparing the activity of cold spray coated materials with the activity of copper metal it was evident that the cold spray coatings work faster to eliminate contacting micro-organisms. Copper metal, a known antimicrobial agent, was observed to achieve only a 94.6% microbial reduction over a 45 min exposure period. The copper cold spray coatings, however, were significantly more effective; with a copper coating on 3D printed ABS achieving complete microbial elimination within 12 min. This was bettered by a copper coating on copper metal in an exposure time of just 8 min. The best performing combination, however, was a copper coating with a 5 wt% silver additive on a copper metal substrate, which achieved complete microbial elimination against all resistant and multi-resistant pathogens tested within only 5 min.

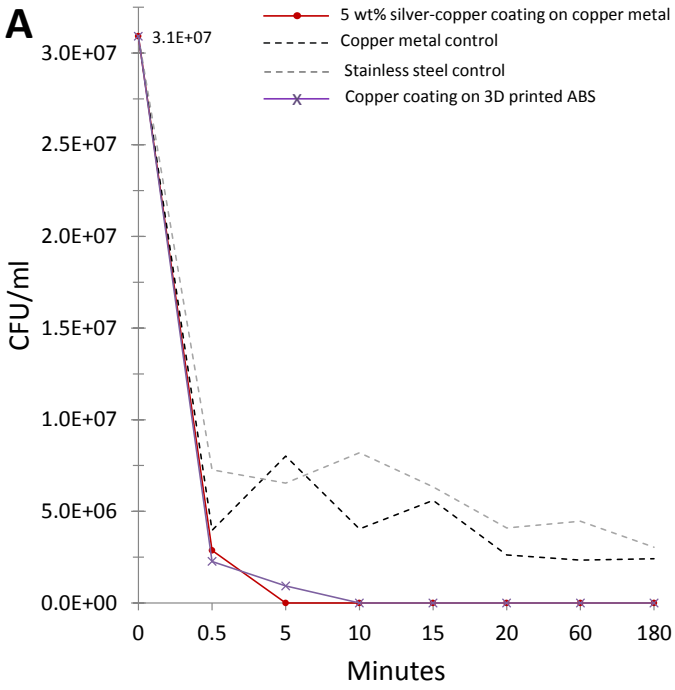


Figure 6.27: Viable CFU/ml per sampling period for copper coatings against the multi-resistant gentamicin methicillin resistant *S. aureus* (ATCC 33592).

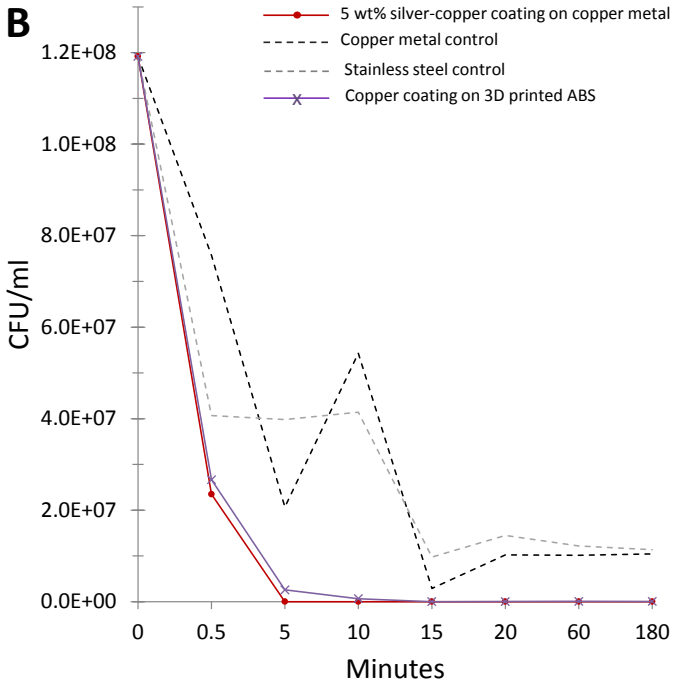


Figure 6.28: Viable CFU/ml per sampling period for copper coatings against resistant reference *P. aeruginosa* (DSM 46316).

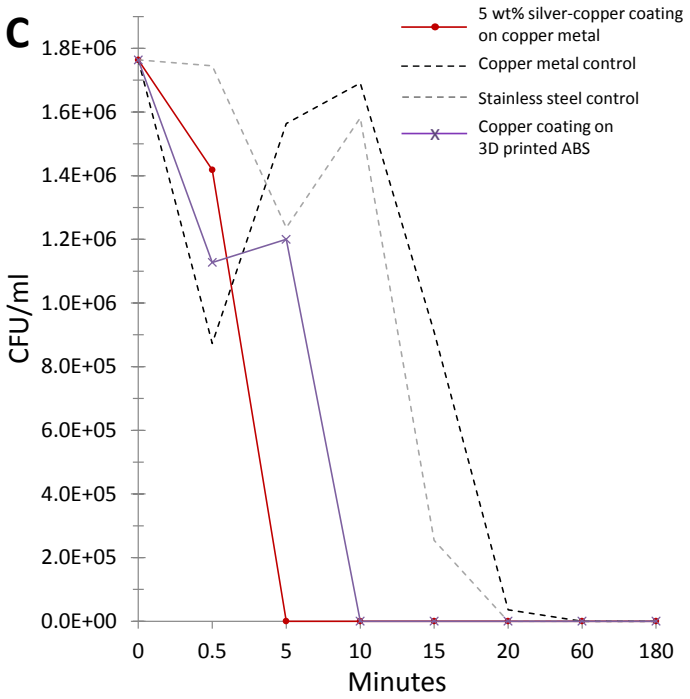


Figure 6.29: Viable CFU/ml per sampling period for copper coatings against clinically resistant *C. albicans* (4122).

In order to prevent the transfer of potentially pathogenic micro-organisms from a previously contaminated surface to the hands of a patient, visitor or member of the hospital staff any designed antimicrobial agent should work as efficiently as possible to eliminate or render such pathogens inactive. Based on various studies a review article proposed that five minutes be a target benchmark time for bacterial elimination from touch-contact surfaces [5]. Five minutes was suggested as the average time between someone touching a surface and that very same surface being touched again by another person within a hospital.

Therefore, the standard for antimicrobial efficacy is high, yet achievable; based on the findings of a copper cold sprayed coating with a 5 wt% silver additive on a copper substrate.

Table 6.23 summarises the touch-contact antimicrobial activity of the best performing materials, which includes two with 3D printed substrates and two with blended powder coatings. The efficacy of the test samples was used to rank the test samples; from 1 as the most active to 9 as the least antimicrobially active.

Table 6.23: Overall efficacy ranking for developed coatings tested via the dry contact test procedure against the resistant pathogens.

Sample	Ranking* based on m_{ar}			Average rank	Overall Efficacy ranking
	GMRSA	RPA	CRCA		
5 wt% silver - 95 wt% copper coated copper	1	1	1	1.00	1
Copper coated copper	2	2	2	2.00	2
Copper coated solid ABS	3	3	4	3.33	3
50% w/w copper-zinc coated 3D printed ABS	5	5	3	4.33	4
Copper coated 3D printed ABS	4	4	5	4.33	5
Solid ABS	6	7	6	6.33	6
3D printed ABS	7	6	9	7.33	7
Pure copper	8	8	7	7.67	8
Stainless steel	9	9	8	8.67	9

*The antimicrobial efficacy ranking was made in numerical order from most active to the least active.

The antimicrobial susceptibility tests conducted thus far have highlighted, not only the antimicrobial efficacy of these novel materials, but supported the goal of implementing this technology within the healthcare environment. These results encouraged the start of pilot trials.

6.3 Prototype testing

Pilot studies were undertaken on the developed prototypes, which represented ideal test surfaces for touch-contact microbial transmission trials and coating durability.

6.3.1 Autoclave sterilisation effects

Related to the observations of coating durability, made in Chapter 5, is the question of continued antimicrobial activity under active use. As a means of investigating this an application specific test scenario was investigated - that of autoclave sterilisation.

Autoclave sterilisation uses high temperature (121°C), high pressure (15 Psi) and steam to achieve effective sterilisation. As a common, 30 minute, sterilisation process for medical equipment this represented a relevant and comparatively harsh condition for the developed coatings to undergo. It was, therefore, appropriate to investigate the durability of the coated polymers with respect to physical changes and antimicrobial ability under these conditions.

Analysis took the form of both physical surface inspections as well as antimicrobial efficacy. Figure 6.30 depicts the surfaces of three test sample types, before and after autoclave sterilisation. Two of the three types observed slight changes with no detrimental or enhancing effects: ABS observed slight warping of the edges yet not to a considerable degree and the copper blended coated sample observed a marginal colour change. The zinc coated ABS sample, however, observed a physical change to the zinc coating, deduced to be a result of a chemical reaction causing the formation of zinc hydroxide, known commonly as *white rust*.

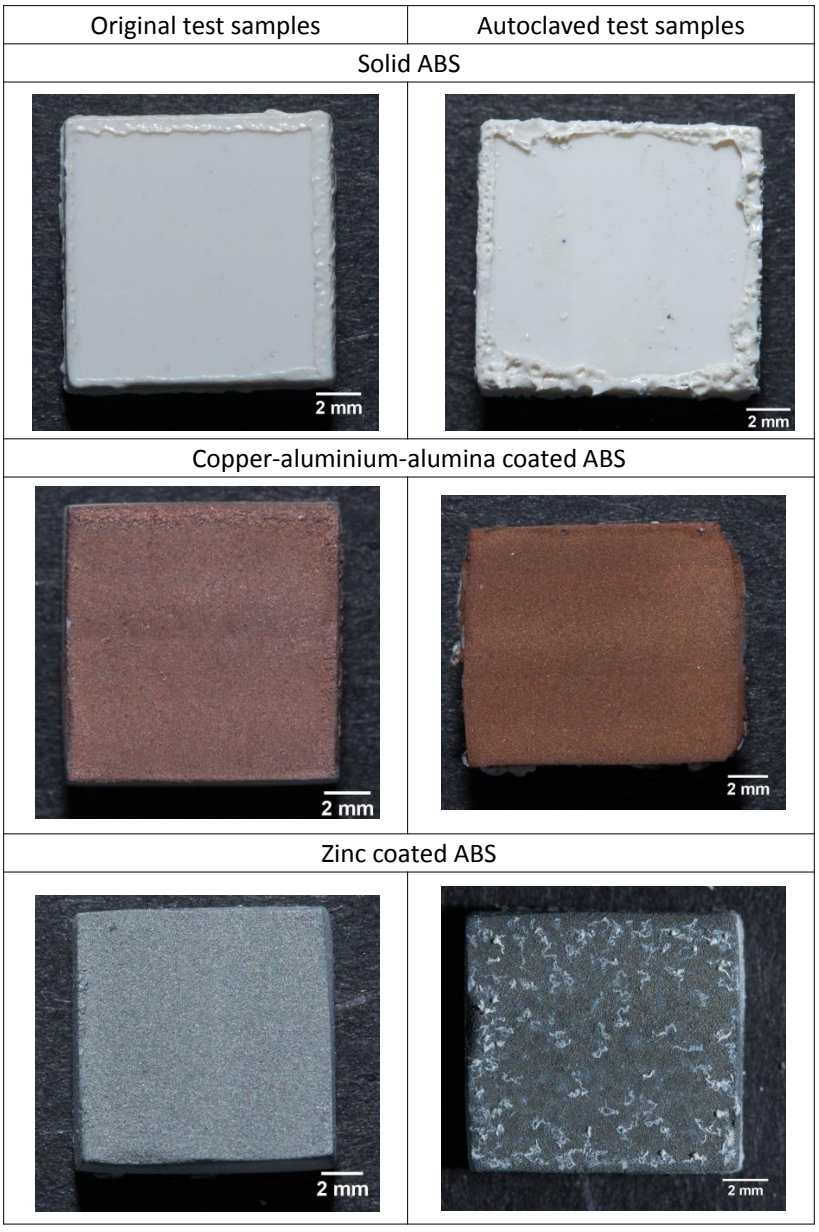


Figure 6.30: Visual comparison between original test samples and autoclaved samples for solid ABS, copper-aluminium-alumina coated ABS and zinc coated ABS.

On newly galvanised or zinc coated surfaces there is a higher chance of the formation of *white rust*, which manifests as a white powdery deposit on the surface [196]. The autoclave process

accelerated this natural process. The formation of this compound, while fundamentally detrimental to the coating integrity, may offer an antimicrobial advantage.

Both antimicrobial susceptibility test procedures were carried out for this investigation. Table 6.24 tabulates the diffusive assay results for both alcohol dipped and autoclave sterilised samples, respectively. The data tables for each tested material against each of the three standard pathogens (*S. aureus*, *P. aeruginosa* and *C. albicans*) may be found in Appendix D.

Table 6.24: Comparison between alcohol dip and autoclave sterilisation effects on diffusive antimicrobial activity.

Cold spray coating types	Ave. ZOI alcohol dip [mm]	Ave. ZOI autoclave sterilisation [mm]	% Diff.	Comment
Copper coated polymers	1.03	1.05	2%	No significant difference
Zinc coated polymers	1.83	2.08	14%	Significant improvement
50:50 Copper-zinc coated 3D printed ABS	2.43	3.27	35%	Significant improvement

Copper coated polymers, including copper coatings on ABS, 3D printed ABS (hor. and vert.) and the thermoplastic PEEK substrates, were seen to observe no significant change in activity after autoclave sterilisation. Interestingly the zinc containing samples observed significant improvement with regards to the resultant extent of the zone of inhibition, with a 50:50 copper-zinc blended coating on 3D printed ABS (hor.) observing a 35% improvement in observed antimicrobial activity. This may be explained with regards to the formation of the zinc hydroxide deposits. It is known that zinc oxides are antimicrobially active, capable of producing reactive oxygen species (ROS) and zinc ions which attack micro-organisms [1,5]. A three prong attack was therefore realised: (1) with the antimicrobial activity of zinc and its oxides, (2) generated ions and through the (3) generation of ROS [197].

Over time the zinc coatings may form stable oxides, which in a wet environment may produce zinc ions (Zn^{2+}) [198]. Ultraviolet exposure via sunlight may generate hydrogen peroxide (H_2O_2) as a ROS. The zinc hydroxide (*white rust*) may also undergo a chemical reaction ($Zn(OH)_{2(s)} \Longleftrightarrow {Zn^{2+}}_{(aq)} + 2{OH^{-}}_{(aq)}$) to produce zinc ions and hydroxyl radicals [199,200]. All such processes subsequently aid and actively enhance antimicrobial activity.

While positive results were observed for zinc coatings in a diffusive environment as a result of autoclave sterilisation, the same cannot be said for efficacy in a dry, touch-contact environment. Table 6.25 contains the antimicrobial results and comparative data for the dry contact tests. The corresponding data tables may be found in Appendix D.

Table 6.25: Comparison between alcohol dip and autoclave sterilisation effects on touch-contact antimicrobial activity.

Cold spray coating types	Ave. m_{ar} alcohol dip [Log10(CFU/ml)/min]	Ave. m_{ar} autoclave sterilisation [Log10(CFU/ml)/min]	% diff.	Comment
Copper coated 3D printed ABS	0.34	0.03	-91%	Significant reduction
Zinc coated solid ABS	0.03	0.01	-67%	Significant reduction
50:50 Copper-zinc coated 3D printed ABS	0.02	0.01	-50%	Significant reduction

All three polymer metallised test samples observed significant reduction in antimicrobial efficacy after autoclave sterilisation. Thus considering the coatings, their intended applications and required sterilisation, alternative cleaning protocols should be developed. Autoclave sterilisation may be an acceptable option for zinc coated polymers working in a wet, diffusive operating environment; yet for other coatings, with dry contact applications autoclave sterilisation should be avoided wherever possible. Alternative sterilisation techniques do exist, including ultraviolet exposure, bleaching, alcohol baths and even radiation exposure.

6.3.2 Security access cards

A previous study highlighted the concern of contaminated security access cards within hospitals and, therefore, became another point of prototype priority [60].

Cold spray coated 3D printed polymer security access cards were prepared, together with uncoated controls. Three coating types were tested: copper, 50:50 copper-zinc and zinc. These cards were then exposed to healthcare associated environments over the course of seven days. These environments included: the Charlotte Maxeke Johannesburg Academic Hospital (patient bedside tables, patient bathrooms), primary healthcare clinics, pharmacies, public spaces within the University of the Witwatersrand Medical School (cafeteria, lecture theatres, bathrooms and computer labs) as well as the card scanners in and around the university campus.

Table 6.26 contains the contamination levels present on the different card types. The microbial assay incubated for both bacterial and fungal contamination as appropriate.

Table 6.26: Microbial contamination of cold spray coated and uncoated security access cards after seven days exposure to various high-contact and high-risk surfaces and environments.

Test Samples		Bacterial CFUs	Fungal CFUs
Zinc Coated 3D Printed Access Card	Coating	0	6
	Control	12	107
Copper Coated 3D Printed Access Card	Coating	0	9
	Control	103	32
50/50 Copper-Zinc Coated 3D Printed Access Card	Coating	2	16
	Control	8	16
Standard Commercially Available Access Card	Control	5	3

The standout results include the exceptional activity exhibited by the copper and zinc coated cards, with zero bacterial growth and significantly reduced fungal growth, when compared to the test controls. The coatings under these test conditions exhibit a high degree of bacteriostasis, similar to that observed in the laboratory based wet, diffusive assays. As an initial pilot study this result suggested a good translation of laboratory based results to that of real-world applications.

6.3.3 Antimicrobial smartphone cover

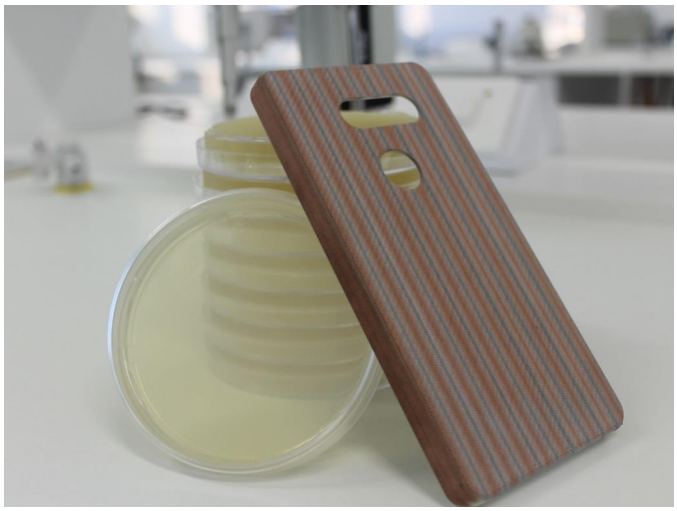


Figure 6.31: Copper and zinc coated 3D printed smartphone cover.

The antimicrobial smartphone cover, as depicted in Figure 6.31, was used in a longitudinal contamination study within the microbiology laboratories at the University of the Witwatersrand's Medical School. The smartphone cover was used under normal, everyday conditions over a period of three weeks, within a high contamination risk environment.

There is an increasing trend, within the healthcare environment, of medical personnel making use of mobile devices within hospitals and other healthcare environments. According to the Epocrates 2013 Mobile Trends Report, as of 2014 approximately nine out of ten medical practitioners would have adopted mobile devices within the healthcare environment [57]. By 2019 this prediction is expected to rise even further, with a growing trend towards multiple device ownership (personal and work related) becoming the norm.

The use of such devices is suggested as a means to provide better care for patients. Easy access to patient electronic health records and related communications between the doctors, nurses and associated medical staff is the ultimate intention [57, 58]. While abuse of such technology, for personal communications, will need to be controlled [59], the fact remains that this technology is being used, and will undoubtedly continue to be used within the healthcare industry.

The underlying issue is that of infection transmission. While these devices have been referred to as being "the prescription for improved patient care" [57] by some, others have offered a more disturbing sentiment, naming such devices "pocket-sized Trojan horses" that travel "in and out of the hospital and between rooms, spreading germs along the way" [59].

Figure 6.32 and Figure 6.33 depict the average viable microbial colony forming units isolated daily from the smartphone and antimicrobial cover surfaces over the three week study period. For further information regarding the bacterial and fungal results Appendix D contains additional tabulated data.

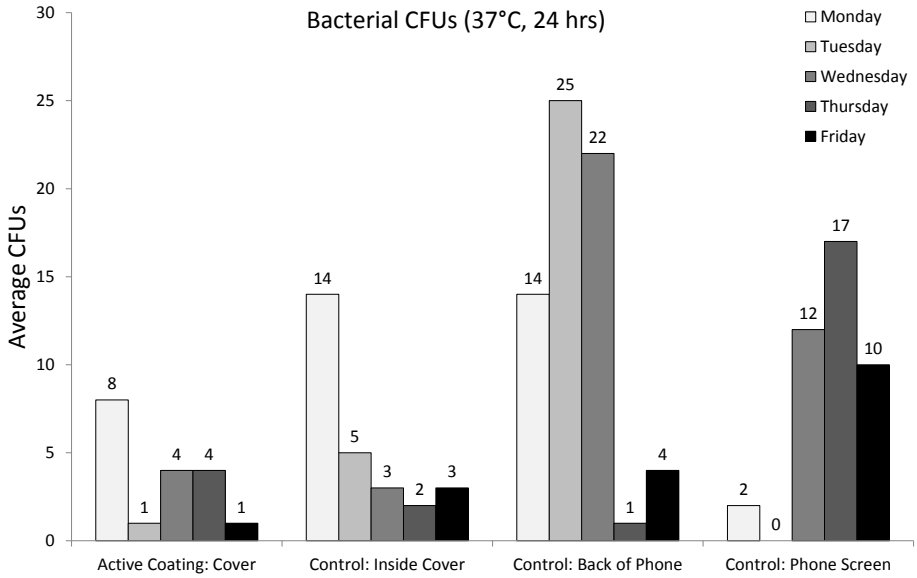


Figure 6.32: Average viable bacterial colony forming units isolated daily from the smartphone and antimicrobial 3D printed cover.

A reduction in bacterial contamination exceeding 55% was observed from the active coating surface. This study was carried out in a high risk environment considering the daily handling of numerous bacterial and fungal pathogens from the laboratory technician who agreed to take part. Previous studies, employing the use of copper metal surfaces within hospitals, have reported varying degrees of effectiveness. In general their bacterial reduction statistics were more favourable [66,82,83]. A direct comparison between such studies and the one presented here cannot, however, be made; due to variable test conditions.

It was noted that in terms of contamination levels, the screen of the phone had approximately 40% less bacterial contamination than the back of the phone, suggesting that the use of an effective antimicrobial cover, which covers the back and sides of the phone, would provide protection for the majority of contamination sites. A link is made between surfaces of infrequent use and higher levels of contamination. The back and inside cover of the phone observed the highest levels of contamination. The inside cover is handled the least yet observes high contamination levels, prompting carefully consideration of where these antimicrobials should actually be applied. A similar observation was made in a study of security swipe cards, where cards kept in pockets or wallets were associated with higher levels of contamination [60]. Thus these coatings may be required for both high contact and seldomly contacted surfaces.

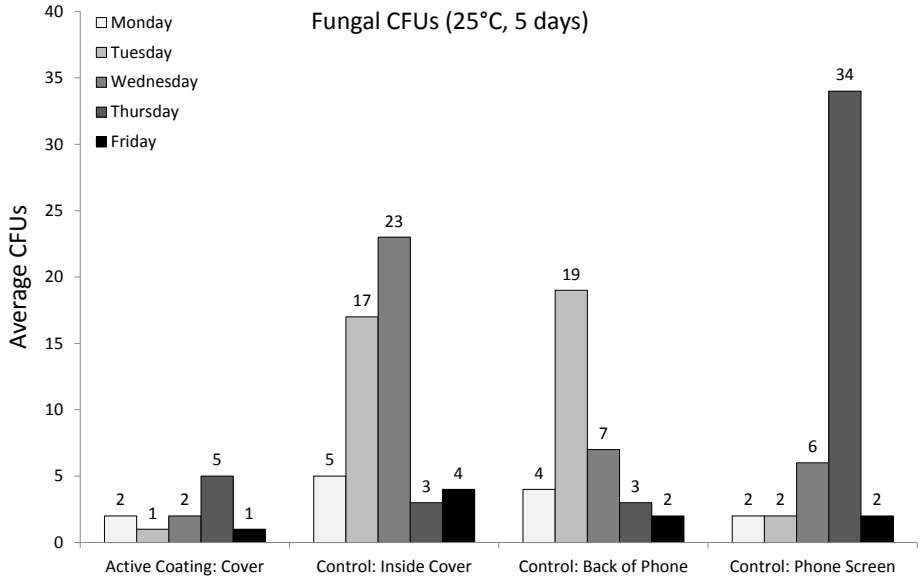


Figure 6.33: Average viable fungal colony forming units isolated daily from the smartphone and antimicrobial 3D printed cover.

Considering fungal contamination it was found that the active coating had four and a half times fewer colony forming units present on its surface than what was found on the (non-antimicrobial) control surfaces.

This result suggested that while the copper and zinc coated smartphone cover does not exhibit complete microbial elimination, it does significantly reduce the pathogenic load present on its surface. Therefore, under *real world* conditions these developed coatings are still effective as antimicrobial agents.

Based on these findings, as well as the laboratory based studies, the developed materials - integrating the technologies of cold spray and 3D printing, together with antimicrobially active metals - have exhibited effective and enhanced antimicrobial activity, with proven applications within the healthcare industry.

Chapter 7 Research Consolidation

"'The time has come', the Walrus said, 'to talk of many things: of shoes - and ships - and sealing wax, of cabbages and kings, and why the sea is boiling hot - and whether pigs have wings.'"

Lewis Carroll, Alice through the Looking Glass

Considering the preceding analyses, from the theoretical modelling and experimental cold spray optimisation, through coating characterisation and finally antimicrobial susceptibility testing, an important question arose regarding the design requirements for such antimicrobial coatings. Ultimately, *what makes the best performing coating perform the best?* This question relates to a number of performance requirements, including: coating viability, coating durability and ultimately antimicrobial efficacy.

7.1 Antimicrobial inferences and mechanisms of action

Chapter 6 set out to investigate the antimicrobial activity of the developed cold spray metallised polymer materials. The process sought to answer a number of questions related to efficacy, mechanism of action, and application potential within a hospital environment. In this section the answers obtained from the previous chapter are explored, looking specifically at three areas:
(1) Antimicrobial efficacy and environmental conditions.
(2) Mitigation potential against resistant and multi-resistant pathogens.
(3) Real world application considerations.

7.1.1 Antimicrobial efficacy and environmental conditions

In answer to the questions related to the validity of the claimed antimicrobial efficacy the developed cold spray coatings, both as polymer metallised coatings as well as conventional

metal on metal coatings (copper coated copper), exhibited effective antimicrobial efficacy. This activity varied based on coating type, constituent materials and test environment (wet, diffusive vs dry, touch-contact simulated conditions); yet it was confirmed that cold spray coatings on polymer substrates, using antimicrobially active metals, do indeed provide mitigation of nosocomial infection transmission.

Wet contact conditions

Comparing the antimicrobial inhibitory behaviour of the raw cold spray feedstock powders to the corresponding best performing coated material it was found that copper was more effective in micro-sized powder form, whereas zinc was more effective within a coating matrix. The average zone of inhibition (ZOI) for a copper coated copper sample was found to be 27% smaller than the corresponding copper powder. For a zinc coating on 3D printed ABS, however, the ZOI was 14% larger than its corresponding powder efficacy.

A similar comparison was made considering base metal vs coated metal activity. It was found that copper coatings were, on average, three times more effective than solid copper metal. Conversely, zinc coatings were, on average, 44% less effective that galvanised (zinc coated) steel, in terms of effective ZOI size.

A 50:50 copper-zinc blended coating while achieving a ZOI only 7% larger than the corresponding powder blend did, nonetheless, achieve synergistic activity against the pathogens of *S. aureus*, *P. aeruginosa* and *K. pneumoniae*, with a 43% increase in ZOI size compared to the combined average ZOI for the independent copper and zinc coatings.

Silver powder, intended as a low percentage coating additive, proved to be more effective as a coating than in powder form, with an average ZOI four and a half times that of the silver powder alone when combined with copper as a coating for copper metal against all five standard test pathogens. The use of silver as an additive had mixed results, considering efficacy in a wet vs dry environment and when comparing efficacy against different pathogenic types. Silver was seen to be an effective additive particularly against Gram-positive pathogens in a diffusive environment. Yet in a dry, touch-contact environment silver, as a 5 wt% additive, only offered considerable antimicrobial enhancement over standard coatings in the case of the 50:50 copper-zinc blended coating on 3D printed ABS against the Gram-negative *P. aeruginosa* strain.

Dry contact conditions

As with the wet contact conditions, comparisons were made between cold spray coatings and their base metal counterparts under dry, touch-contact conditions. The efficacy of copper and zinc coatings were compared to their metal counterparts tested against the standard pathogens of *S. aureus*, *P. aeruginosa* and *C. albicans*. Two points of comparison were

selected:
(1) The rate of microbial reduction (m_{ar}) [$\log_{10}$(CFU/ml)/min] and
(2) The percentage microbial reduction after 15 min of microbial exposure.

Table 7.1 contains the average rates of microbial reduction for copper and zinc coatings and their respective metal counterparts. Both coating types were seen to have a reduction rate greater than five times the respective metal control.

Table 7.1: Comparison between copper and zinc coatings and their metal counterparts with regards to the average rate of microbial reduction (m_{ar}) [$\log_{10}$(CFU/ml)/min].

	m_{ar}	
Metal	Coating	Metal
Copper	0.45	0.06
Zinc	0.12	0.02

Table 7.2 provides the second criterion for comparison: that of the percentage reduction after a 15 min exposure to the standard test pathogens *S. aureus*, *P. aeruginosa* and *C. albicans*. These results corroborate those obtained from the m_{ar} value: The cold spray coatings are more effective than the associated base metals in a dry, touch-contact environment.

Table 7.2: Comparison between copper and zinc coatings and their metal counterparts with regards to the percentage reduction in viable CFUs over a 15 min exposure period.

	Red. % @ 15 min.	
Metal	Coating	Metal
Copper	96.7	49.5
Zinc	94.6	67.7

7.1.2 Mitigation potential against resistant and multi-resistant pathogens

Wet contact conditions

From Table 7.3 it is observed that besides copper metal against *P. aeruginosa* strains, all test samples and controls observed a reduction in antimicrobial activity against the resistant strains[i]. This was to be expected considering the inherent resistivity and hardiness of resistant pathogenic strains. The extent of microbial reduction was, however, of particular interest. Considering both pathogenic types (standard and resistant) the cold spray coatings still

[i]It is suspected that the increased activity apparent for the copper metal against the resistant *P. aeruginosa* strain may be accounted for by slight variations in the copper samples used or in the concentration of the inoculate.

performed comparatively better than the antibiotic control. For the case of test samples against the resistant *P. aeruginosa* strains, where Ciprofloxacin, as the antibiotic control, exhibited no antimicrobial activity the cold spray coatings still actively inhibited the growth of viable colony forming units.

Table 7.3: Comparison between diffusive antimicrobial efficacy of coatings against standard and resistant pathogenic strains of *S. aureus* and *P. aeruginosa*.

Pathogen	Test sample	Average ZOI [mm]		% diff.
		Standard strain	Resistant strain	
S. aureus	Ciprofloxacin	13.65	3.10	77.3
	Copper coating on ABS and 3D printed ABS (Average)	0.53	0.20	62.3
	Copper coated copper	2.30	0.90	60.9
	Copper metal	0.25	0.20	20.0
P. aeruginosa	Ciprofloxacin	13.65	0.00	100.0
	Copper coating on ABS and 3D printed ABS (Average)	1.64	1.25	23.8
	Copper coated copper	4.10	2.00	51.2
	Copper metal	0.40	1.40	-250.0

Coincidentally, the antibiotic control, Ciprofloxacin, was seen to exhibit the same average bacteriostatic activity against both pathogenic strains, with an average zone of inhibition of 13.65 mm.

Dry contact conditions

The results for dry contact conditions, with regards to standard vs resistant pathogens provides further evidence for the effective antimicrobial activity of the developed coatings even against resistant pathogenic strains. Table 7.4 tabulates the comparative results for cold spray coatings against three pathogens (*S. aureus*, *P. aeruginosa* and *C. albicans*) expressed as both standard and resistant strains. The average rate of microbial reduction (m_{ar}) and the percentage reduction after a 15 min exposure were used as deterministic criteria.

Against the resistant strains copper metal observed the same rate of microbial reduction as stainless steel, suggesting that the metal in fact had no attributable antimicrobial activity. The cold spray coatings, however, were seen to offer effective antimicrobial activity. It was concluded that the resistivity of the micro-organisms does not significantly affect the performance of the cold spray coatings. Two exceptions, however, were that of copper coated copper and the 50:50 copper-zinc blended coating on 3D printed ABS. This latter coating achieved a 75% reduction in the antimicrobial rate against the resistant *P. aeruginosa* strain when compared with the standard strain. Even under this circumstance the coating still managed to achieve a reasonable 86% microbial reduction after 15 min exposure and went

Table 7.4: Comparison between touch-contact antimicrobial efficacy of coatings against standard and resistant pathogenic strains of *S. aureus*, *P. aeruginosa* and *C. albicans*.

Pathogen	Test sample	Standard strain		Resistant strain		% reduction in (m_{ar})	% reduction in Red. % @15 min)
		Average m_{ar}*	Red. % @ 15 min	Average m_{ar}*	Red. % @ 15 min		
S. aureus	50% w/w copper-zinc blended coating on 3D printed ABS (hor.)	0.02	98.87	0.01	98.86	50	0.01
	Copper coating on ABS and 3D printed ABS (Average)	0.34	99.96	0.63	100.00	-85	-0.04
	5 wt% silver - 95 wt% copper coated copper	1.21	100.00	1.29	100.00	-7	No change
	Copper coated copper	1.59	100.00	0.69	100.00	57	No change
	Copper metal	0.01	76.83	0.00	77.21	100	-0.49
	Stainless steel	0.00	0.00	0.00	0.00	No change	No change
P. aeruginosa	50% w/w copper-zinc blended coating on 3D printed ABS (hor.)	0.04	99.89	0.01	85.56	75	14.35
	Copper coating on ABS and 3D printed ABS (Average)	0.71	100.00	0.54	99.99	24	0.01
	5 wt% silver - 95 wt% copper coated copper	1.22	100.00	1.33	100.00	-9	No change
	Copper coated copper	1.61	100.00	1.31	100.00	19	No change
	Copper metal	0.01	42.80	0.00	95.71	100	-123.62
	Stainless steel	0.00	0.00	0.00	0.00	No change	No change
C. albicans	50% w/w copper-zinc blended coating on 3D printed ABS (hor.)	0.47	100.00	0.45	100.00	4	No change
	Copper coating on ABS and 3D printed ABS (Average)	0.48	100.00	0.45	100.00	6	No change
	5 wt% silver - 95 wt% copper coated copper	0.32	100.00	0.99	100.00	-209	No change
	Copper coated copper	0.49	100.00	0.48	100.00	2	No change
	Copper metal	0.01	28.86	0.00	/	100	N/A
	Stainless steel	0.00	0.00	0.00	0.00	No change	No change

*[Log10(CFU/ml)/min]

on to achieve a ten-fold reduction within 20 min. No other cold spray test sample, though, exhibited anything less than a 90% reduction after 15 min, with the majority achieving complete microbial elimination despite the presence of high risk, resistant and multi-resistant pathogens.

In terms of coating performance in a touch contact environment, the developed coatings performed exceptionally well against both standard and resistant pathogen strains. A standout

result was that of the 5 wt% silver - 95 wt% copper coated copper sample, which achieved complete microbial elimination against all tested resistant and multi-resistant infectious pathogens, within only 5 min of exposure to a culture solution at a concentration exceeding 2 million viable CFU/ml. This coating achieved an average microbial reduction rate of 1.2 $\log_{10}$(CFU/ml)/min; which corresponds to an approximately 93.7% reduction in viable colony forming units every minute.

7.1.3 Real world application considerations

Three potential real world applications were investigated in Chapter 6: antimicrobial pens (and keyrings), security access cards and a 3D printed smartphone cover. All three represent practical, everyday items all found within hospitals that patients, visitors and medical staff bring in as personal items. These high contact surfaces are known contributors to infection transmission.

Considering particularly the use of mobile devices within hospitals by medical staff, measures need to be put in place to mitigate the risk of infection transmission - a known and growing concern in hospitals [56]. The option of 3D printed, cold spray antimicrobial coated mobile device covers was one proposed solution. The fact that these devices are small, means that effective manufacturing costs are lowered. Additionally, the potential benefit offered by these specialised protective covers validates this application as a relevant and necessary opportunity.

The results of the pilot studies confirm and validate the antimicrobial activity reported from the laboratory trials. The examples used do not, however, represent all possible applications, which may include many other hospital surfaces (e.g. hand rails, table tops, buttons, medical and clerical equipment and items), but may also be extended to other applications for both personal, commercial and industrial use.

For each application, a critical suitability evaluation was required to identify the key operating conditions and surface requirements of that particular application. It was evident that copper coatings perform well in a dry, touch-contact environment; while zinc is better suited to a wet, diffusive environment. This reflected observations made in previous studies [66,80], with regards to higher copper ion absorption in a dry contact environment. Careful selection of coating metals and powder blends is therefore advised to account for the intended application and environmental conditions.

These developed coatings should not, however, be limited to these singular applications; where the opportunity exists for multiple and integrated surface coating applications. These may include medical equipment, surgical tools and hospital surfaces. Application potential,

however, extends beyond the healthcare industry with relevance in a diverse range of operational environments: from public transport, food production and building materials, to consumer goods and personal and household surfaces.

7.1.4 Human toxicity concerns

Toxicity effects are an important consideration, which relates to the development of materials that are safe for human use. This is critically important when working within the framework of the healthcare industry. In this way the form of the final product needs to be safe. The following briefly outlines the concerns and supporting evidence for the safe use of this technology.

Considering copper, zinc and silver metals with respect to potential toxicity effects, it was noted that copper and zinc are essential nutrients and are therefore not inherently toxic [67, 68].

Silver, however, since it has no known beneficial effects on human health affords some concern from the United States Environmental Protection Agency (EPA) [68]. This concern is specifically with regards to soluble solutions, and therefore not of critical concern for coated surfaces. Metal toxicity, however, depends on a number of factors: dose, route of exposure, chemical species as well as the age, gender, genetics and nutritional status of exposed individuals [67]. The risk of exposure and detrimental effects was related primarily to exposure through ingestion, either by way of contaminated drinking water, foods and inhalation. For the current application of touch-contact antimicrobial surfaces the risk is primarily with regards to absorption through the skin - the site of contact. Fortunately human skin provides a good barrier to metal absorption, due to the low permeability of the dermal layer [68]. Additionally copper, zinc and silver are not priority metals and are not considered carcinogens [67] [69].

It was reported that confining the application of antimicrobially active metals to surfaces safeguards against the toxicity effects of the metals [71]. While many metals may be toxic to both bacterial and eukaryotic cells at high doses they are known to have 'divergent metal transport systems and metalloproteins' [71] whereby the activity of metal compounds is different for bacterial and mammalian cells [71], thereby making their use in antimicrobial applications that much safer. For completeness, the following details the extreme (rare and unlikely) risks from the use of these metals.

Copper

While copper is an essential bodily nutrient, in excess this metal can become potentially toxic

inducing cellular damage leading to Wilson disease, linked to the accumulation of copper in organs [67]. Other potential toxic effects include: salivation, epigastric pain, nausea, vomiting and diarrhoea - all of which are associated with ingestion [72]. From a touch-contact perspective, excessive exposure may lead to temporary dermatitis, that is irritation and inflammation of the skin [73].

Silver
Silver exposure offers no significant health risks, besides causing argyria (a bluish/grey discolouration of the skin and other organs) in rare cases, due to excessive exposure to silver [1,73]. Arygria is not life-threatening, nor associated with other ill effects [74]. Additional toxicological effects related to the ingestion of silver, include: anaemia, cardiac enlargement, growth retardation and liver degeneration [72].

Zinc
Zinc metal is not stored in the body and therefore excessive exposure results in reduced absorption and increased excretion [72]. Symptoms of acute zinc poisoning include: nausea, vomiting, epigastric pain, abdominal cramps and diarrhoea; while chronic toxicity may lead to interactions with essential copper retention [72]. All of these potential consequences are a response of ingestion and not from physical contact.

Based on the above literature it was concluded that while these metals may possess certain, yet rare, health concerns under specific exposure conditions, the risk under the given intended operational conditions is sufficiently low to support progression of this research.

7.2 Surface topography effects on antimicrobial activity

Based on preliminary cold spray trials with polymer metallisation, copper cold spray coatings were seen to outperform copper metal under antimicrobial test scenarios. It was speculated that surface topography, specifically the increase in coated surface area (characterised by the increased surface roughness) was a contributing factor in achieving enhanced antimicrobial activity. This speculation was subsequently put to the test. The surface topographical effects were compared to the antimicrobial activity under both wet and dry contact conditions.

7.2.1 Diffusive antimicrobial activity

Figure 7.1 illustrates the relationship between surface topographical quantities and the effective antimicrobial activity given by the extent of inhibition from copper cold spray coatings against the five respective standard test pathogens, under diffusive (wet-contact) test conditions. Figure 7.2 presents the same information for zinc.

7.2.2 Dry contact antimicrobial activity

Figure 7.3 and Figure 7.4 depict the relationships between surface topographical qualities and the effective touch-contact antimicrobial activity given by the average rate of microbial reduction (m_{ar}) for copper and zinc cold spray coatings, respectively; against the three standard test pathogens (*S. aureus*, *P. aeruginosa*, *C. albicans*). The associated data tables may be found in Appendix F.

A strong linear correlation (Pearson correlation coefficient $R > |0.8| == R^2 > 0.64$) between a surface profile quantity and the corresponding measure of antimicrobial activity would be indicative of a strong possibility of antimicrobial activity to be influenced by coating surface topography. In addition a moderate linear correlation (Pearson correlation coefficient $|0.5| < R < |0.8| == 0.25 < R^2 < 0.64$) between a surface profile quantity and the corresponding measure of antimicrobial activity would be indicative of a moderate chance of antimicrobial activity to be influenced by coating surface topography. Consistency of results between coating metals (copper and zinc) and between antimicrobial test would strengthen these trends, validating a correlation between surface topography and antimicrobial activity.

In all four aforementioned graphs the trendlines are indicative of linear correlation, with a dashed line representing a strong linear correlation and a dotted line representing a moderate linear correlation.

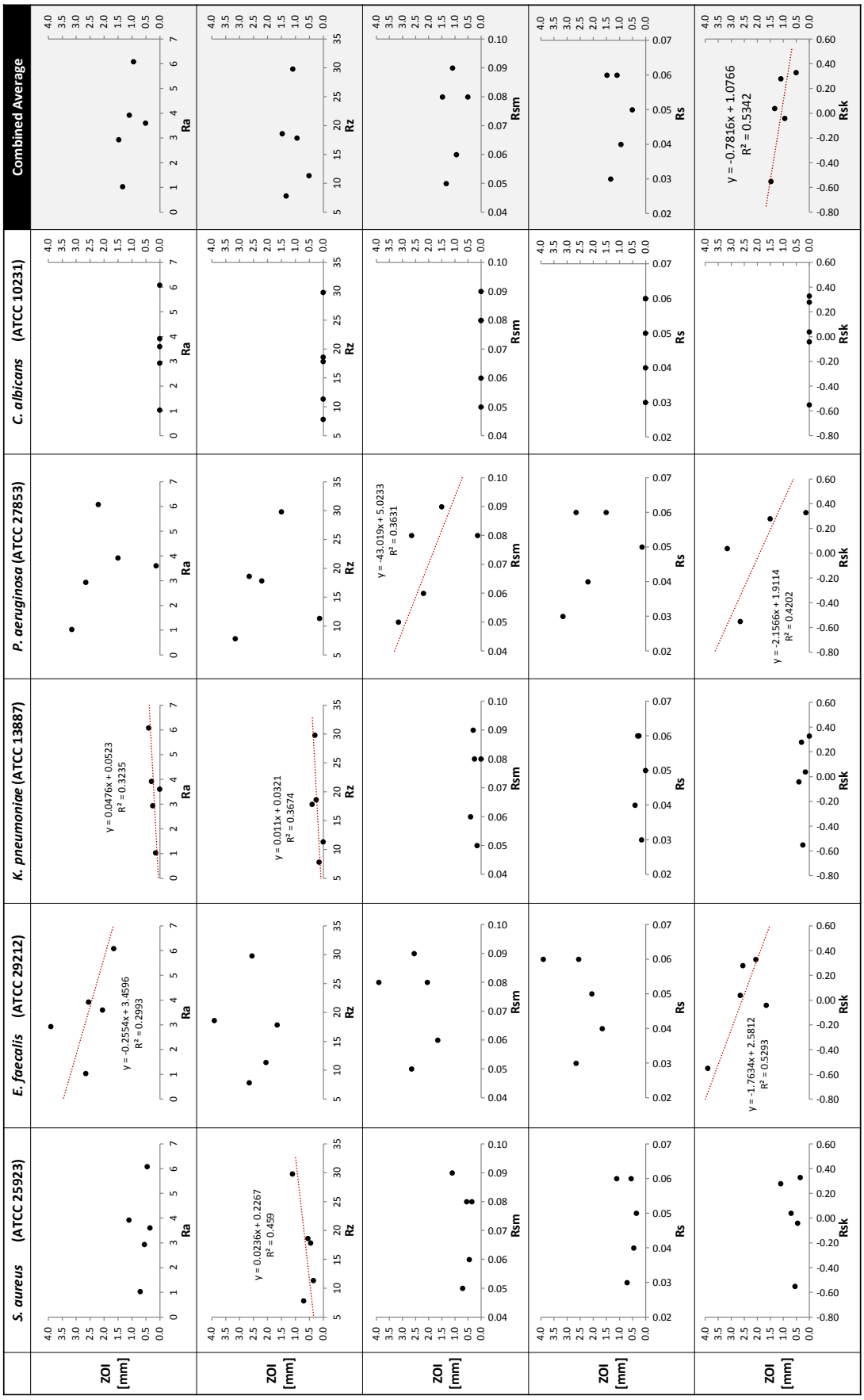


Figure 7.1: Antimicrobial diffusive activity against surface profile features for copper cold spray coatings.

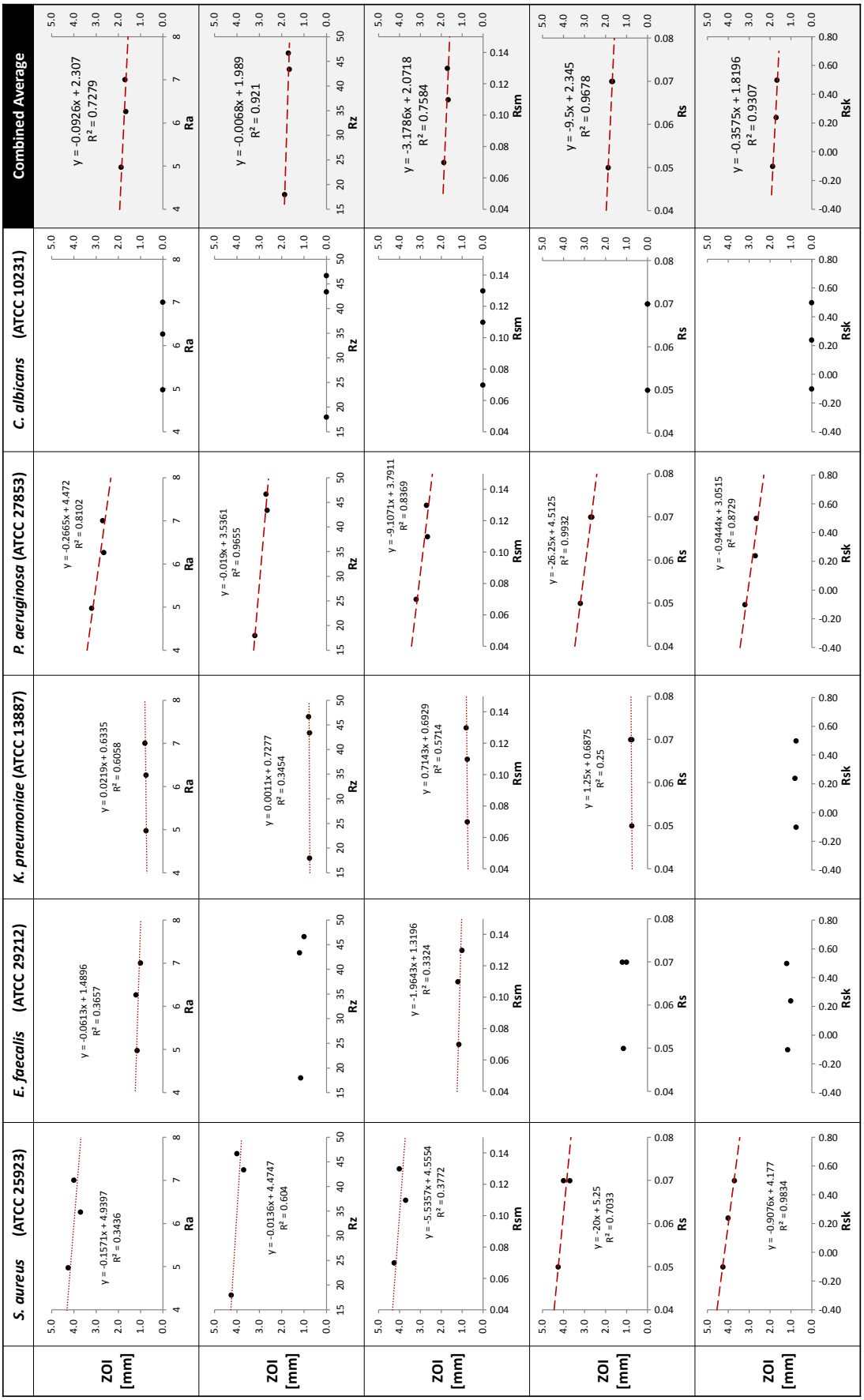


Figure 7.2: Antimicrobial diffusive activity against surface profile features for zinc cold spray coatings.

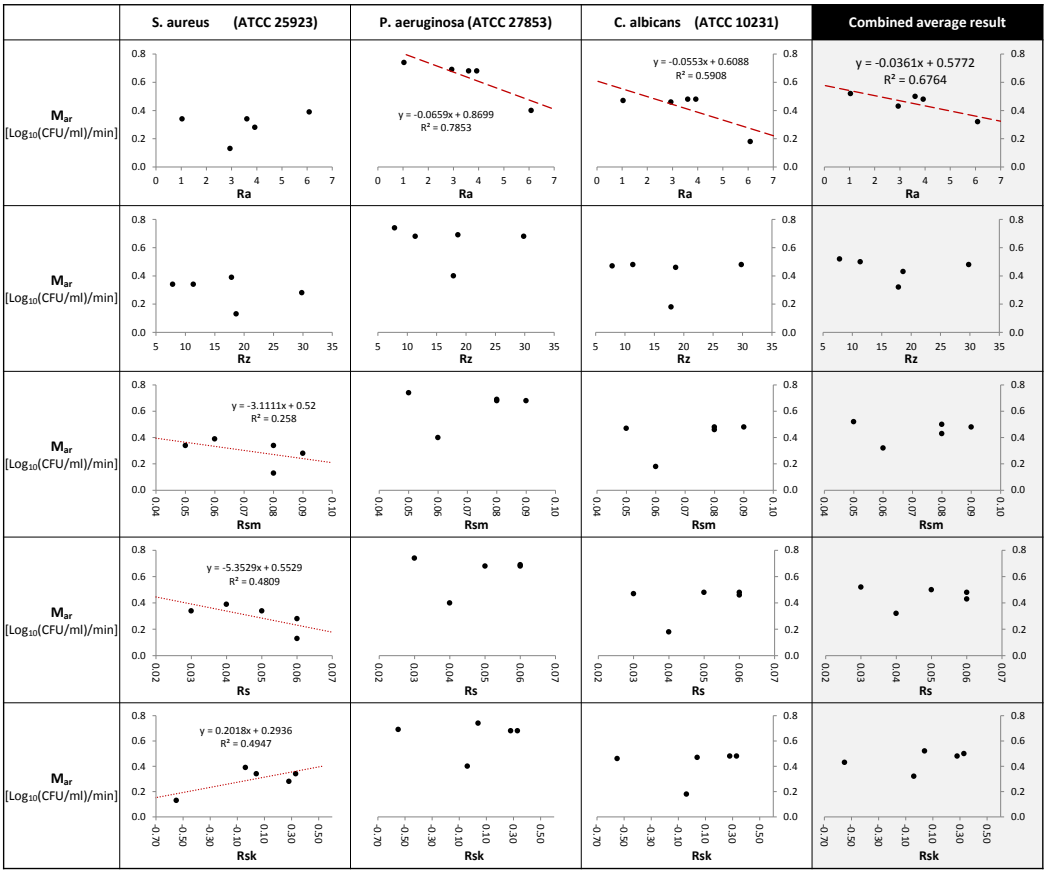


Figure 7.3: Antimicrobial touch-contact activity against surface profile features for copper cold spray coatings.

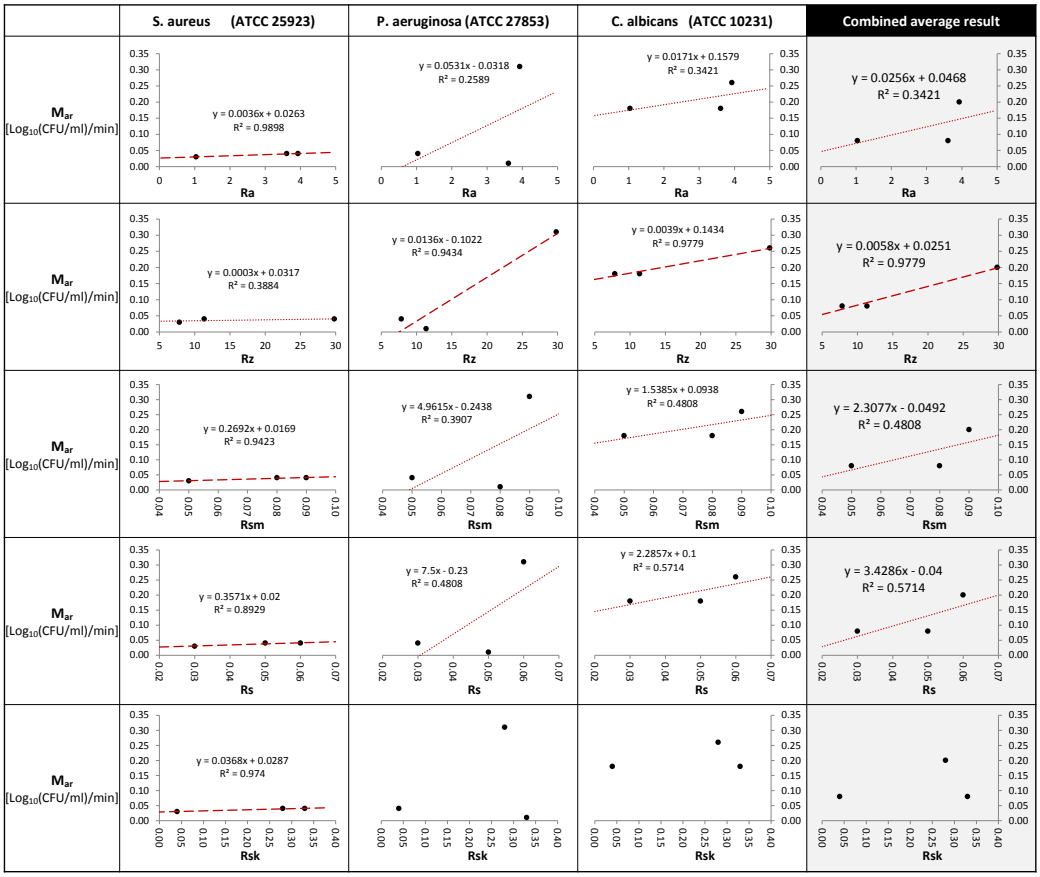


Figure 7.4: Antimicrobial touch-contact activity against surface profile features for zinc cold spray coatings.

Wet contact conditions

Considering the wet contact conditions and Figure 7.1 and Figure 7.2 it was found that the different coating metals confer different mechanisms of action on the respective micro-organisms.

The two coating types (copper and zinc) are observed to exhibit differing roughness-to-ZOI relationships. Specifically it was found that copper coatings had, on average, a statistically moderate agreement with a linear correlation demonstrating a decreasing trend between profile skewness (Rsk) and average zone of inhibition; while zinc coatings observed, on average, a statistically strong linear correlation, also as a decreasing trend, between all five roughness quantities and the average zone-of-inhibition. These general observations did not, however, hold true for all individual situations.

Individual relationships, at varying levels of linearity, exist between surface profile quantities and independent pathogens. These may be appropriate for specific applications of known contamination; otherwise the general, combined average result, provides the most appropriate source of generalisation.

With regards to profile skewness (Rsk) either this property exhibited no effect on diffusive antimicrobial activity, or where it did, it appeared to lead to a reduced diffusive antimicrobial activity (as its value shifts from negative to positive). Physically, the profile skewness relates to the asymmetry of a profile about a mean line; such that a negative value may be regarded as a profile with a higher surface contact area and a positive value indicative of a profile with a lower surface contact area. It may then be possible to suggest that the smaller zones of inhibition, that is, reduced diffusive antimicrobial activity exhibited against some pathogens, may be a consequence of a reduced contact area. There is unfortunately insufficient data to prove this postulation and so further research is required. At present it has been shown that surface profile does, under certain conditions, influence wet contact antimicrobial activity.

Dry contact conditions

With regards to dry, touch-contact activity, with specific reference to Figure 7.3 and Figure 7.4 a similar, yet more extreme, case of differing antimicrobial mechanisms of action conferred by the coatings metals (copper and zinc) is observed.

In a simulated touch-contact environment copper coatings with *smoother* coatings, at lower Ra values, achieved increased rates of antimicrobial efficacy. It was noted, however, that all other surface topography quantities do not observe any significant trends. The antimicrobial efficacy remains relatively unaffected by the other four roughness quantities measured (Rz, Rsm, Rs, Rsk).

In the same test environment, under equivalent test conditions, zinc coatings were found to demonstrate the opposite response. Improved rates of antimicrobial activity were achieved from *rougher* coatings. The coating profile quantities of arithmetic mean deviation (Ra), maximal profile height (Rz), mean roughness spacing (Rsm) and the mean spacing between profile peaks (Rs) all positively contributed to an increased rate of antimicrobial activity. These results were most significant against *P. aeruginosa* and *C. albicans*. Profile skewness exhibited no correlation with microbial reduction rate in a dry environment.

For zinc coatings in a dry, touch-contact environment it would appear that the antimicrobial efficacy is dictated more by the surface profile than by the constituent zinc metal. Looking critically at the ordinate axes scale for both the copper and zinc coatings the following was deduced. It was seen that the rate of microbial reduction for copper coatings extends to 0.8 $\log_{10}$(CFU/ml)/min, with around 75% of results grouped in the range 0.4 to 0.7 $\log_{10}$(CFU/ml)/min. Comparatively for the zinc coatings the vertical scale only extends to 0.35 $\log_{10}$(CFU/ml)/min, with the around 75% of results achieving a rate of microbial reduction less than 0.2 $\log_{10}$(CFU/ml)/min. While zinc coatings are seen to be significantly influenced by surface topography; copper coatings are not, yet are significantly more antimicrobially active that zinc coatings under that same dry contact conditions.

The surface profilometry analysis, following the ISO 4288:1996 surface texture test method, was carried out in response to the suspected relationship between surface topography and antimicrobial activity. This analysis was conducted independently for both wet and dry contact antimicrobial susceptibility tests. Based on this test method and considering five key roughness parameters (Ra, Rz, Rsm, Rs and Rsk), there was no generalised and direct correlation between surface topography and antimicrobial efficacy; and yet under certain circumstances, based on particular coating combinations and specific operating environments, surface profile was found to influence antimicrobial activity.

Considering copper metal-on-metal coatings, however, it may be suggested that while surface topography may play a contributory role, a key factor influencing antimicrobial efficacy relates to the diffusion of ions. In a wet contact environment a copper cold spray coating on a copper substrate achieved three times greater efficacy than the uncoated metal, based on the size of the zone-of-inhibition, and in a dry contact environment the rate of antimicrobial efficacy from such a coating was five times greater than the metal alone. An increase in the diffusion of ions is believed to be a key factor affording this heightened activity. It is widely accepted that the generation and diffusion of metal ions plays a fundamental role in the antimicrobial mechanism of action of such metals [1,5,9]. The increased rate of microbial elimination when comparing coatings on copper substrates to those on polymer substrates may be a consequence of improved ion diffusivity. It was postulated, in a study investigating cold spray of copper onto aluminium substrates [87], that the cold spray process for such

metal-on-metal depositions results in impact hardening of the coatings and, due to known relationships between hardness and ion diffusivity, enhanced diffusion of cupric copper ions needed for microbial destruction is subsequently achieved. A similar mechanism is proposed here for copper coated copper.

The use of additive manufacturing techniques, in terms of both cold spray and polymer 3D printing, provides a unique opportunity for functional surface design. This encompasses: coating development (as previously investigated in Chapter 5, Section 5.5.2 *3D Printing design for effective coating development*), component design (considering the ultimate application of these antimicrobial coatings), coating durability and, of course, antimicrobial efficacy. Considering antimicrobial activity from 3D printed ABS substrates with both horizontal and vertical build orientations, with a copper cold spray coating, it was previously shown in Chapter 6 that these coatings were effective in both a wet and dry contact environment. While perhaps not leading to heighten activity in general, when compared with copper coatings on solid ABS substrates, these copper coated 3D printed coatings were still far superior to copper metal alone in terms of antimicrobial efficacy and provide a versatile solution to such surface coatings.

Based on this, a combination of factors are believed to be responsible for the heightened activity of cold spray coatings, considering both metal-on-metal and polymer metallised coatings. These factors may be underpinned by the contact surface area, which for cold spray coatings is inherently increased, such that an increased area of direct contact is achieved - which a study by Mathews, et al. [70] showed to be a key contributor to antimicrobial activity - and at the same time affording increased ion diffusion - an agreed mechanism of action for such oligodynamic metals [70, 80, 204]. Additionally, the unique embedded deposition mechanism achieved by cold spray polymer metallisation may contribute to the release of ions, in a similar way to that observed by Vucko, et al. [91] in their antifouling study. To investigate the coating specific mechanisms of action in greater detail it is suggested that a further surface topography study using Atomic Force Microscopy (AFM) be carried out in addition to an immersed ion diffusion assay, using an Inductively Coupled Plasma Mass Spectrometer (ICP-MS) as part of a ion concentration analysis.

7.3 Surface wear and topography correlation analysis

7.3.1 Coating wear characteristics

Following the ASTM G99 *standard test method for wear testing with a pin-on-disc apparatus*, a complete evaluation of wear resistance was carried out. The two criteria used to quantify the

sliding wear resistance and surface behaviour of the coatings are that of the wear coefficient (k) and the coefficient of friction (μ). These parameters of wear were compared with two different polymer substrates for different cold spray coatings. Copper, zinc and 50:50 copper-zinc blended coatings with corresponding solid ABS and 3D printed ABS (hor.) substrates were used in this analysis. Figure 7.5 and Figure 7.6 illustrate the observed relationships for polymer substrates with different metal coatings with respect to the coefficient of friction (μ) and wear coefficient (k), respectively. Test data represents the experimentally valid[ii] results for a single test specimen for each coating combination each with multiple corresponding data points.

Copper coatings were seen to confer higher wear resistance, with much lower wear coefficients observed for both an ABS substrate and a 3D printed ABS substrate. With regards to the coefficient of friction no significant difference was observed amongst the three coating types.

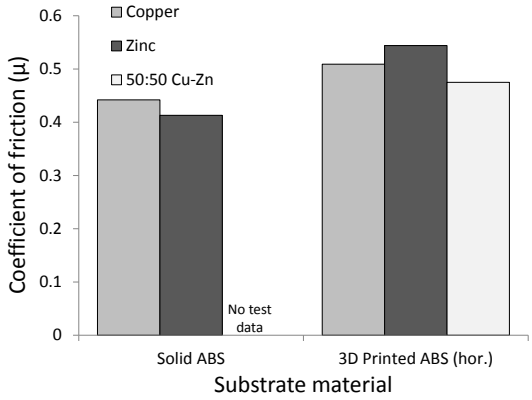


Figure 7.5: Coefficient of friction (μ) trends for copper, zinc and 50:50 copper-zinc cold spray coatings on solid ABS and 3D printed ABS (hor.) substrates.

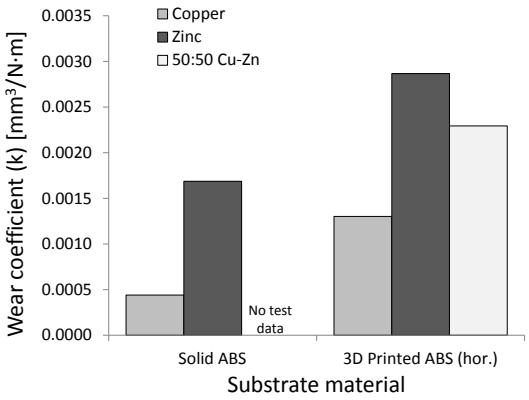


Figure 7.6: Wear coefficient (k) trends for copper, zinc and 50:50 copper-zinc cold spray coatings on solid ABS and 3D printed ABS (hor.) substrates.

Material hardness, as a qualitative measure of material strength, represents a resistance to either indentation or scratching [203]. It is therefore inferred that there is a correlation between hardness and wear resistance for materials [203]. By making the fair, but limited assumption, that materials of higher hardness reflect higher wear resistance properties, the wear resistance effects for both copper and zinc based coatings were compared to their corresponding sheet metals.

[ii] A wear test validation test was conducted so as to validate the results and accuracy of the test data. The copper coating on 3D printed ABS and uncoated 3D printed ABS were tested in triplicate. According to the standard the calculated coefficient of variation must be less than 20% for the procedure to be confirmed as an experimentally valid procedure. Refer to Table C.27 in Appendix C for the validating results.

As discussed above, copper coatings, in general, exhibit higher wear resistance than zinc coatings. Given that the average Vickers Hardness for copper (annealed) is HV = 50 which is higher than that of zinc (HV = 30), an agreement between coating wear resistance and constituent metal hardness is observed. Interpreting the results in this way suggests that the wear effects observed for the cold spray coatings may, in part, be linked to the constituent metal of such coatings. That is, for example, the higher wear resistance of copper cold spray coatings may be a consequence of hardness properties conferred by the constituent copper metal in the coating.

Substrate properties for the cold spray coatings, however, have an additional impact on coating wear properties. The following sub-section discusses these additional substrate effects.

7.3.2 Substrate wear characteristics

A similar analysis was carried out to evaluate the effect substrate material played in wear phenomena for cold spray coated polymer metallisation. Figure 7.7 and Figure 7.8 depict the coefficients of friction and wear for copper and zinc coatings on different polymer substrates (and a copper substrate). Zinc coatings were, again, observed to wear more easily than equivalent copper coatings on the same polymer substrates.

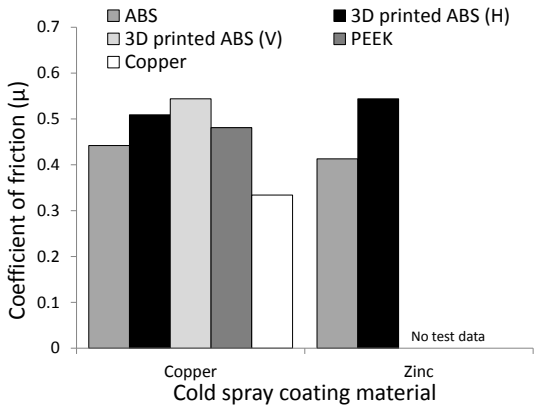


Figure 7.7: Coefficient of friction (μ) trends for various polymer substrates with copper and zinc cold spray coatings.

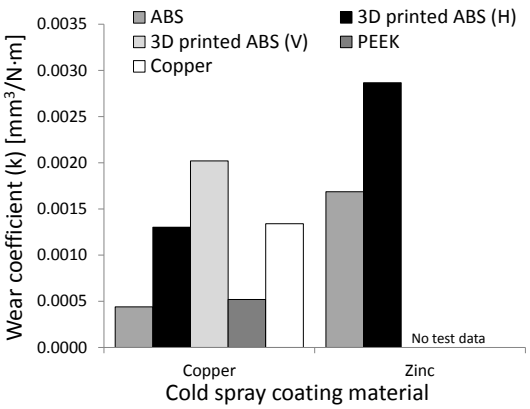


Figure 7.8: Wear coefficient (k) trends for various polymer substrates with copper and zinc cold spray coatings.

It was evident that cold spray coatings on smoother more dense substrates (e.g. solid ABS and PEEK), result in a lower frictional coefficient and lower resultant wear, when compared to coatings on 3D printed ABS, which has a distinct surface profile characterised by larger roughness values. As the substrate roughness increases there was a corresponding increase in the rate of wear and in the coefficient of friction.

7.3.3 Further roughness effects - coatings and substrates

A suspected relationship between surface roughness and wear properties was deduced. Surface roughness effects were not able to be integrated into the coating optimisation procedure since the desired effects were unknown. The following analysis, however, provides a better understanding of surface topographical effects on polymer metallised materials.

Variations in surface topography of the substrate material was investigated for its influence on coating wear properties, using copper and zinc coatings as examples. Figure 7.9 depicts the relationships between surface topographical features and the friction (μ) and wear (k) coefficients for copper coatings on various polymer ABS substrates.

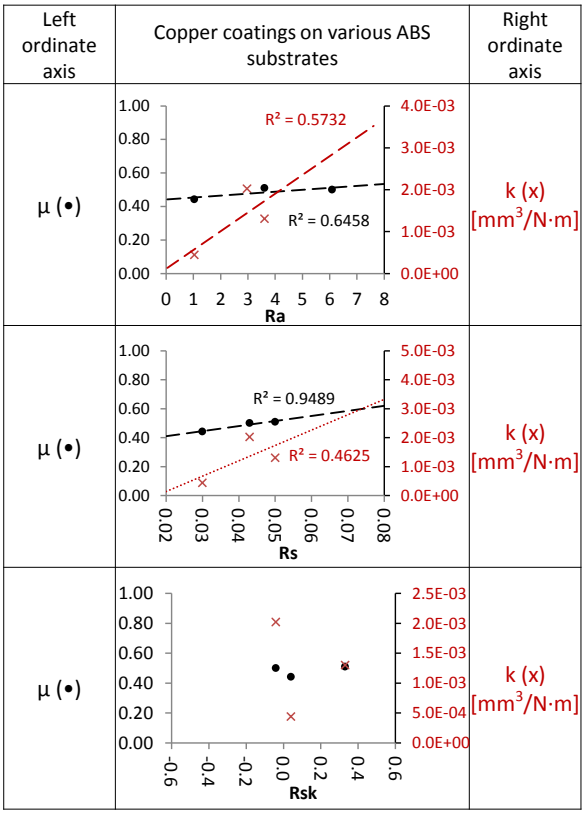


Figure 7.9: Correlations between surface topographical features of copper coatings on various ABS substrates against friction (μ) and wear (k) coefficients.

Based on a Pearson correlation analysis, there was a strong positive correlation between surface roughness (Ra) and mean peak spacing (Rs) and friction. Surface roughness (Ra) was also strongly correlated with wear such that an increased coating roughness corresponds with an increased rate of wear. This trend was confirmed with zinc coatings on ABS, as well as polished copper coatings on PEEK substrates. The corresponding tabulated data for these two test cases may be found in Table F.1 and F.2 in Appendix F.

7.3.4 Wear property effects of cold spray polymer metallisation

The influence cold spray polymer metallised coatings have on wear rate required further evaluation. Based on the preceding results it was suggested that rather than improving wear performance these developed coatings in fact impair wear resistance.

Table 7.5 contains the calculated percentage differences between coated polymer substrates and their corresponding substrates in terms of their respective coefficient of friction (μ) and wear coefficient (k). A positive percentage difference represents a situation where the coating in a coating-substrate pairing has higher values of the respective quantity (μ or k) when compared to the corresponding substrate material.

Table 7.5: Percentage difference in wear properties comparing cold spray coated samples to their corresponding polymer substrates.

Coating/substrate combinations	% diff. μ	% diff. k
CuABS - ABS	63.10	-51.47
Cu3DABS(H) - 3DABS(H)	38.69	112.32
CuPEEK - PEEK	96.33	1014.29
CuPEEK (polished) - PEEK	84.49	428.57
Cu3DABS(V) - 3DABS(V)	25.94	122.79
Zn3DABS(H) - 3DABS(H)	48.23	367.39
ZnABS - ABS	52.40	86.03
ZnPC - PC	-2.51	-8.11
Cu(1)Zn3DABS(H) - 3DABS(H)	29.43	273.91
Average percentage difference	48	261

Only a copper coated ABS and a zinc coating on a polycarbonate substrate were found to have comparatively lower wear rates than their corresponding substrates. This was the desired response as it suggests that those cold spray coatings, besides affording effective antimicrobial activity, also offer additional protection against physical wear - thereby prolonging operational life. In lieu of the computed average percentage differences it was found that, in general, a coated sample wears more than two and a half times faster than the uncoated substrates.

7.3.5 Overall surface wear and topographical effects

Based on the above findings, Figure 7.10 illustrates the combined relationships for coatings and substrates in terms of friction and wear qualities. Dotted and dashed trend lines represent moderate and strong linear correlations, respectively. The associated data table (Table F.3) and Pearson correlation analysis (Table F.4) may be found in Appendix F.

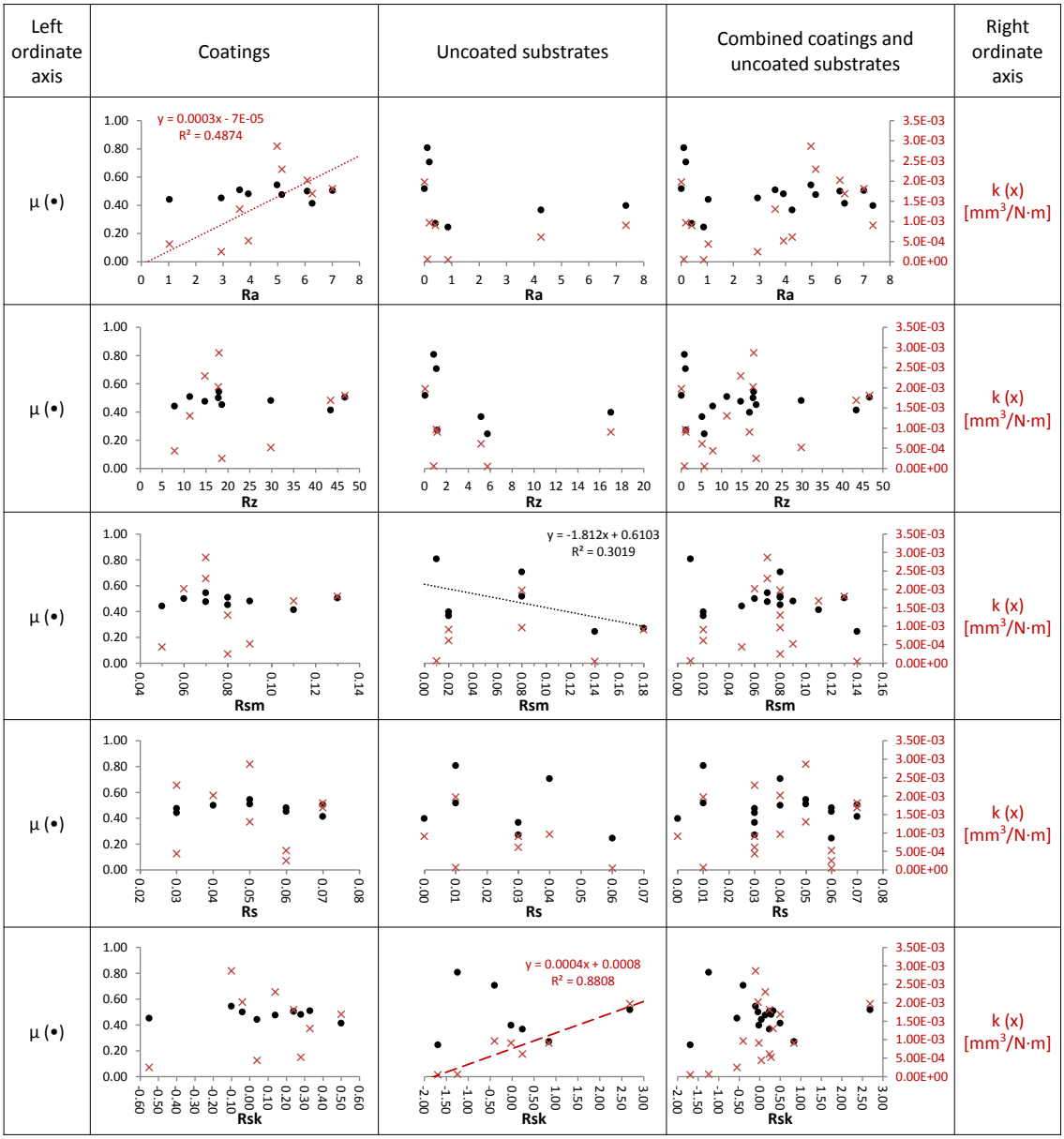


Figure 7.10: Surface topographical effects on wear properties.

A general observation related to coefficient of friction suggests that there is high variability in the coefficient of friction for surfaces of low roughness values (i.e. an Ra value below 1 μm). At higher Ra values there was no significant effect on friction coefficient.

Looking at specific results three key trends were observed:

1. There is a moderate (positive) relationship between arithmetic mean roughness (Ra) and wear rate (k) for cold spray coatings, such that an increased roughness corresponds with a reduced wear resistance.

While an increased wear with increased roughness which leads to reduced life, is undesirable; an increased roughness, while resulting in increased wear leads to the progressive exposure of *fresh* coating material due to the distinguishing particle embedment of cold spray polymer metallisation. Continued antimicrobial activity is therefore expected under these circumstances, until such time as the embedded deposition layer is completely worn through. The former interpretation considers the physical integrity of the coating, while the latter includes the functionality. So in general a smoother surface profile is desirable; yet an allowance is made for rougher surface topographies, provided sufficient deposition and metal particle entanglement has been achieved via the cold spray process.

2. There was a moderate (negative) relationship between mean profile spacing (Rsm) and friction for substrate materials. This suggested that the greater the spacing between profile elements the lower the friction. Depending on the application and system requirements this may be a desirable property, yet considering the equivalent comparison for coated samples, where no relationship exists, this observation was of no consequence in this research which pertains specifically to metal coatings on polymer substrates.

3. A strong (positive) relationship exists between profile skewness (Rsk) and wear rate for uncoated substrates. In a similar manner to the second trend, this observation had little consequence in this research. For completeness, though, this relationship does agree with what would be expected, such that a surface with a low contact surface area (Rsk $>$ 0) will wear faster than a surface with a larger contact surface area (Rsk $<$ 0), which would be able to resist wear to a greater degree. Figure 7.11 illustrates the physical interpretation of profile skewness (Rsk).

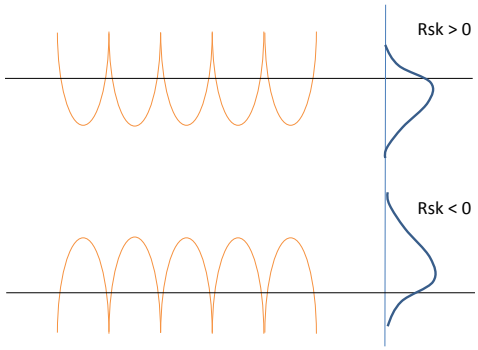
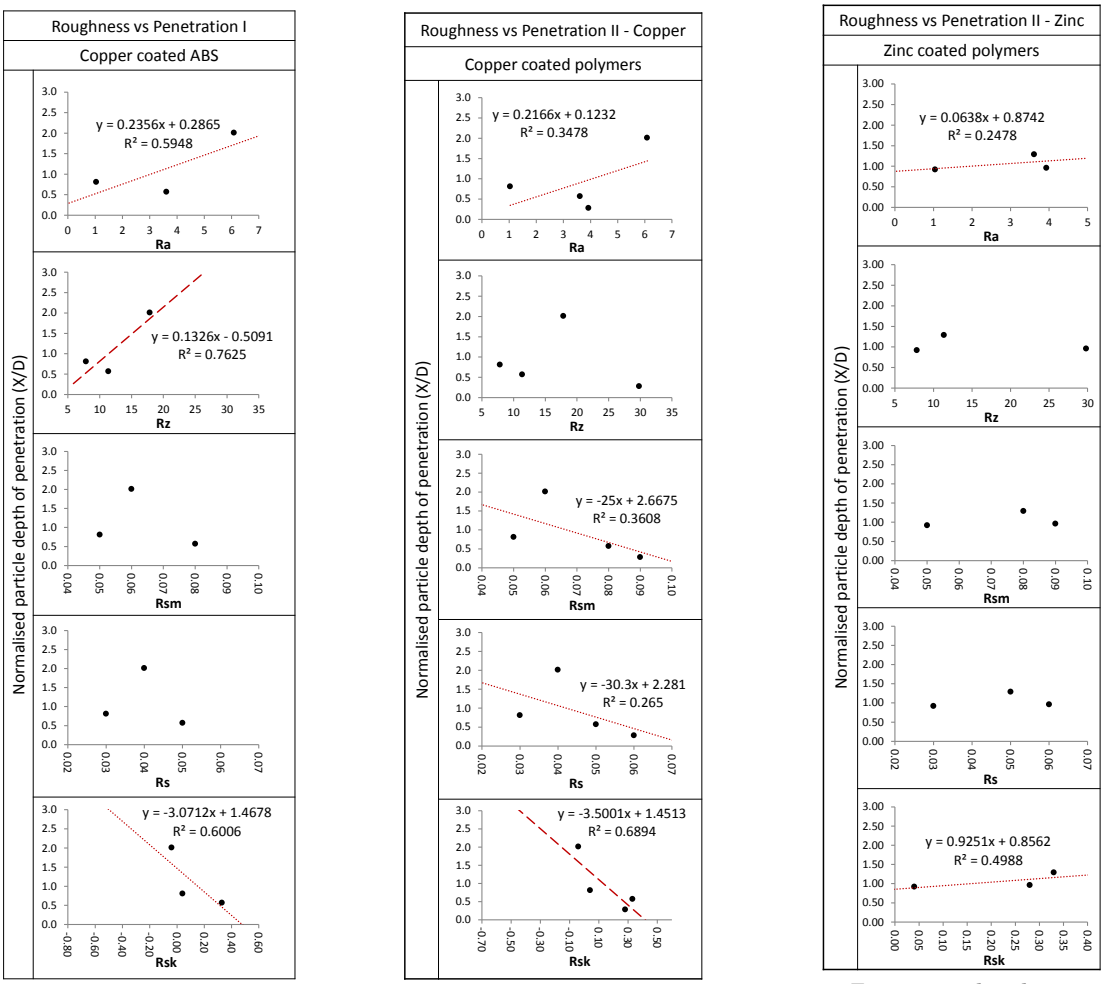


Figure 7.11: Graphical illustration of skewness of profile (Rsk) surface topography parameter.

7.4 Substrate topography effects on particle penetration

The use of particle depth-of-penetration as a relevant criterion for cold spray metallisation of polymers was investigated. The influence that substrate surface topography has on the ideal particle depth-of-penetration was also investigated. Figure 7.12 depicts the experimental depth of penetration results illustrating the effect substrate surface topography has on particle penetration. Both copper and zinc coatings were evaluated based on a number of coating-substrate combinations. The corresponding Pearson correlation analysis may be found in Tables F.5 to F.7 of Appendix F .



Copper coated ABS Copper coated polymers Zinc coated polymers

Figure 7.12: Substrate surface topographical effects on particle depth-of-penetration for different copper and zinc coated polymer substrate combinations.

Arithmetic mean surface roughness (Ra) showed a common and consistent increasing trend, such that an increase in surface roughness corresponds with an increase in the required particle depth-of-penetration. This, therefore suggests that the rougher the substrate surface, the deeper particles are required to be embedded to achieve a viable cold spray deposition.

7.5 Cold spray polymer metallisation

7.5.1 Preliminary Cost Benefit Analysis of Additive Manufacturing

The cost of additive manufacturing is a important consideration. Considering a part production cost breakdown, it has been suggested that machine costs account for 50 - 75% of direct production costs, while materials, including model and support materials account for 20 - 40% and labour between 5 and 30% [97][iii]. Another aspect to consider is the specific type of additive manufacturing process being used: from polymer 3D printing with a fused deposition modelling approach, to direct metal laser sintering. There is a considerable range. This would also influence the allocation of costs.

A significant initial expense for manufacture start-up is, however, expected; supplemented by running costs associated with consumables, necessary maintenance and labour coats. Machine costs, however, have reduced significantly such that from 2001 to 2011 the cost of an additive manufacturing system has reduced by 51% [98, 99]. Going back even further, in the 1990's a new additive manufacturing system may have cost around $100 000, whereas a new system may be purchased for $500 as of 2018[iv] [96], making the use of additive manufacturing technologies more affordable and appealing.

At the 2017 RAPDASA additive manufacturing conference, held in Durban, South Africa, Terry Wohlers (a leading expert in rapid product development and additive manufacturing) reported that between 2012 and 2016 there had been a 26.7% rise in worldwide revenues from additive manufacturing [100]. Worldwide revenues as of 2016 were reportedly $6.1 billion, with Europe, United States, China and Japan current leaders in additive manufacturing systems. From the aforementioned talk by Baker Baynes it was reported that in 2017 South Africa had 5600 3D printers, 450 of which were industrial units, according to the Council for Scientific and Industrial Research (CSIR). The growth of advanced technologies, specifically additive manufacturing, within South Africa is indicative of the growth in this technology and associated research interests.

[iii] The cost breakdown, given by Hopkinson, Hague and Dickens [97], was published in 2006 and since then the technology has advanced considerably so this may not be entirely applicable today, but it does provide an idea of the allocation of costs.

[iv] This statistic does not reflect the actual cost of either the polymer 3D printer or the cold spray unit used in this study

7.5.2 Depth-of-penetration comparisons

Particle depth-of-penetration was used as the key discriminating criterion for theoretical cold spray parameter optimisation. As such, it was this quantity which was to be critically evaluated. Table 7.6 contains the normalised depth of particle penetration data for theoretical and experimentally optimum parameter sets together with their theoretically targeted and predicted values[v] for various copper and zinc coatings on polymer substrates. A corresponding plot of the theoretical targets, theoretical model predictions and the physically achieved normalised depths-of-penetration for the experimentally optimum parameter sets is presented in Figure 7.13.

Table 7.6: Normalised depth of particle penetration (X/D) data for theoretical and experimentally optimum parameter sets together with their theoretically targeted and predicted values for various copper and zinc coatings on polymer substrates.

Normalised particle depth-of-penetration	Copper coated solid ABS	Copper coated 3D printed ABS (hor.)	Copper coated 3D printed ABS (vert.)	Copper coated PEEK	Zinc coated ABS	Zinc coated 3D printed Abs (hor.)	Zinc coated PC
Theoretically optimum parameter sets							
Theoretical target	1.88	1.85	1.85	1.54	1.70	1.67	1.50
Theoretical model prediction	2.25	2.25	2.25	1.50	2.02	2.02	1.72
Experimental reality	0.93	0.61	1.09	0.26	0.42	1.28	/
Experimentally optimum parameter sets							
Theoretical model prediction	1.77	1.77	1.77	0.88	1.76	1.76	1.21
Experimental reality	0.81	0.57	2.01	0.28	0.92	1.29	0.96

[v]It is to be noted that the theoretical model predictions presented here may differ from those presented in Chapter 4. This is due to continuous modifications made to the theoretical model. All research aspects presented in this study underwent continuous cycles of development and weren't isolated as independent research outcomes.

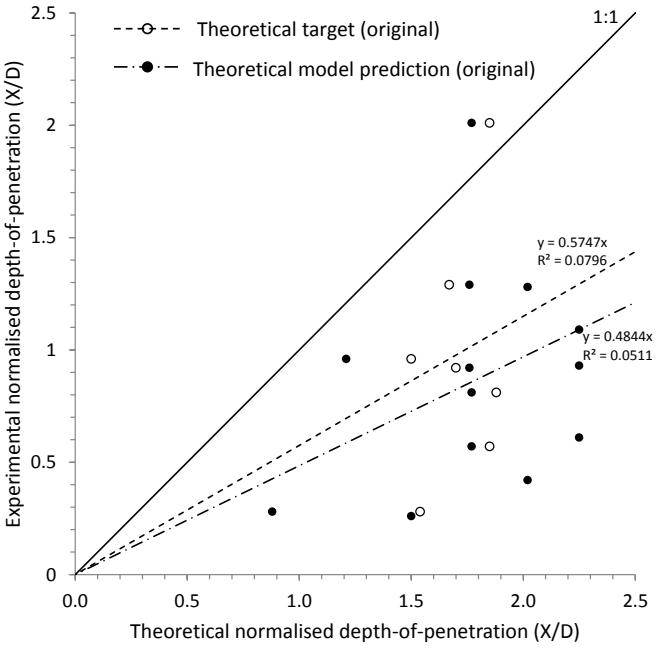


Figure 7.13: Comparison between both the targeted and theoretically predicted depths-of-penetration and the experimental depths-of-penetration for a range of cold spray polymer metallised coatings, using the originally developed theoretical model and target penetration equation.

It is evident that while the theoretical model's predictions and theoretically targeted particle penetrations do provide a suitable starting point for experimental analysis, they do not, in fact, accurately correspond to the penetrations observed in reality. This suggested that both models (the empirical depth-of-penetration targeting model and the theoretically predictive models), while consistent and fairly precise in their theoretical predictions, are not sufficiently accurate. The use of such theoretical models did, however, provide a suitable starting point for experimental analysis, thus removing the need for random experimental trials. Additionally, this structured approach ensured far greater confidence in final parameter selection as a local optimum.

Considering the effects cold spray process parameters have on particle depth-of-penetration, based on historical studies, experimental testing and theoretical modelling, a number of general trends are observed. Not only did these trends support the development of the theoretical cold spray model and independent parameter effects and variation (IPEV) decision framework, as two principal research outcomes; but they later assisted in re-evaluating the theoretical model. Again, the understanding of cycles of development underpinning this study is reinforced. Reference is made to both the literature review (particularly the discussion on page 57 related to the results of a CFD cold spray study [127]) and the development of

the independent parameter effects and variation (IPEV) decision framework in Chapter five. The IPEV decision framework collated data from theoretical trends (page 155), experimental trends (page 159) and historical studies (page 167), which are again considered below.

The computational fluid dynamic results, achieved by an early study [127], gives particular insight into temperature and velocity effects for both the carrier gas and the spray particles in a simulated cold spray scenario. Figure 2.14 found in the literature survey on page 57, depicts these parameter effects for particle and gas flow conditions through a typical DeLaval type cold spray nozzle and within the spray gap. The increase in particle velocity and variation in particle and gas temperature all influence the effects surrounding particle/substrate impingement related to the particle depth-of-penetration.

The stand-out parameters from the aforementioned study, together with the associated literature and the theoretical and experimental approaches carried out in this study were found to be that of the operating (or stagnation) pressure and temperature as well as the nozzle standoff distance. In general, an increase in any one of these parameters (within reasonable ranges) leads to an increase in particle velocities and/or particle depth-of-penetration. The theoretical model, however, does not predict a significantly larger depth-of-penetration from a larger standoff distance. This is related to the particle impact velocity which under theoretical trials only observes a slight rise in response to fairly considerable increase in the nozzle standoff distance. Improvements in handling nozzle gap effects may yet yield higher predictive accuracy in this regard, and yet for the purposes of this study this was sufficient.

While nozzle standoff effects may be under-predicted, operating temperature effects appear be over-predicted (see Figure 5.2). From Figure 5.2 the extent to which the model predicts penetration for an operating temperature in the range 250 - 400 °C indicates a likely occurrence of severe erosive behaviour in practice; which, coincidently, would not achieve a viable coating. The penetrative depths predicted extend from approximately two particle diameter lengths to an extreme eight diameter lengths, which in reality presents as erosive effects and not ballistic penetration.

As with any piece of technology, though, improvements are possible and, therefore, based on the observations contained in Table 7.6 a good place to start was with the targeted particle depth-of-penetration model and thereafter the theoretical predictive model. In this way progression towards more accurate local optima may be achieved. Future work, however, is recommended to fully encompass the specific comments discussed above related to temperature and nozzle standoff distance effects. Further experimental analysis of nozzle flow conditions, particularly with regards to nozzle exit flow conditions (over-, vs under-expanded slow), should be undertaken to assist accordingly. Discrepancies between theoretically predicted

and experimentally achieved particle impact phenomena, may be a consequence of misrepresented design factors. What follows though is a start of a further cycle of development towards improving the experimental design tool, packaged as a versatile and quick-reference theoretical cold spray model.

7.5.3 Re-derived targeted particle depth-of-penetration

Using the experimental cold spray particle depth-of-penetration results (normalised by average embedding particle size), the associated material properties and the arithmetic mean substrate surface roughness data collated for experimentally optimum cold spray parameter set coatings, a re-derived empirical particle depth-of-penetration targeting model was devised.

Refer to Appendix F for the derivation steps and specifically Table F.8 and Figure F.1. The empirical model was based on substrate roughness effects as well as the material properties of Young's Modulus and ultimate tensile strength as used in the original empirical model detailed in Chapter 4 (Page 144).

The revised ideal depth of penetration targeting model is given by Equation 7.1, where the factor weightings are given as: A = 0.6, B = 0.2, C = 0.2, and Ra_s represents the substrate surface roughness. Equation 7.1 represents the ideal particle depth-of-penetration for cold spray coating applications for polymer metallisation.

$$\begin{aligned}\left.\frac{X}{D}\right|_{\text{TARGET new}} = &\left[0.0807\left(Ra_s\right)^2 - 0.4349\left(Ra_s\right)\right] \times A + \\ &\left[0.2324 \times e^{\left\{0.0239\left(\frac{E_p}{E_s}\right)\right\}}\right] \times B + \\ &\left[-0.0684\left(\frac{UTS_p}{UTS_s}\right)^2 + 0.583\left(\frac{UTS_p}{UTS_s}\right) - 0.2007\right] \times C\end{aligned} \tag{7.1}$$

7.5.4 Re-evaluated particle depth-of-penetration models

Considering the best suited particle depth-of-penetration predictive model (Model 1), and the results tabulated in Table 7.6, there appears to be an over-prediction in the particle depth-of-penetration. It was suggested that this be corrected with the use of a variable scaling factor, tailored to the conditions and requirements of polymer metallisation.

A variable scaling factor was derived from the relationship between the cold spray powder-substrate material density ratio and a target scaling factor, which was based on the ratio of the actual normalised particle penetration and the original theoretical normalised penetrations.

Refer to Table F.9 of Appendix F for the tabulated density ratios and target scaling factors. These were graphed as a piecewise function depicted by Figure F.2 of Appendix F. From which the variable scaling factor (η), expressed by Equation 7.2, was derived.

$$\text{Scaling factor}(\eta) = \begin{cases} 1 & \text{if } 0 < \dfrac{\rho_p}{\rho_s} \leq 4 \\ -0.124\left(\dfrac{\rho_p}{\rho_s}\right) + 1.4285 & \text{if } 4 < \dfrac{\rho_p}{\rho_s} \leq 10 \\ Unknown^{\text{vi}} & \text{if } \dfrac{\rho_p}{\rho_s} > 10 \end{cases} \tag{7.2}$$

The expression for the modified particle depth of penetration was therefore given by Equation 7.3.

$$\frac{X}{D} = \left.\frac{X}{D}\right|_{\text{Model 1}} \times \eta \tag{7.3}$$

Table 7.7 evaluates the accuracy of the modified particle depth-of-penetration model and new empirical particle depth-of-penetration targeting model, using various copper and zinc cold spray coated polymer materials as test samples. A corresponding plot of the re-derived theoretical targets, re-derived theoretical model predictions and the physically achieved normalised depths-of-penetration for the experimentally optimum parameter sets is depicted in Figure 7.14. Compared to the original penetration model the modified model was found to be more accurate across a wider range of powder-substrate combinations. Comparing the plotted gradients of (theory vs reality) for the original theoretical predictions and the predictions made after the theoretical model was re-evaluated and subsequently modified there is a considerable improvement in predictive accuracy. This improvement is also confirmed for the re-derived targeted particle depth-of-penetration model.

[vi] There is an unknown relationship between the density ratio and ideal particle depth-of-penetration where the density of the spray powder is more than ten times that of the substrate material and so under this condition no theoretical prediction may be made at present.

Table 7.7: Normalised particle depth-of-penetration data for theoretical and experimental cold spray of polymer substrates, comparing the predictive accuracy of the modified theoretical cold spray model for experimentally optimum parameter sets.

	Copper coated 3D printed ABS	Copper coated ABS	Copper coated PEEK	Zinc coated 3D printed ABS	Zinc coated ABS	Zinc coated PC
X/D actual	0.57	0.81	0.28	1.29	0.92	0.96
$X/D_{TARGETnew}$	0.59	0.78	0.57	0.62	0.81	0.78
X/D Theoretical model (original - no scaling)	1.77	1.77	0.88	1.76	1.76	1.21
Theoretical model variable scale factor	0.36	0.36	0.57	0.58	0.58	0.69
X/D theoretical model (variable scaling)	0.64	0.64	0.51	1.03	1.03	0.83

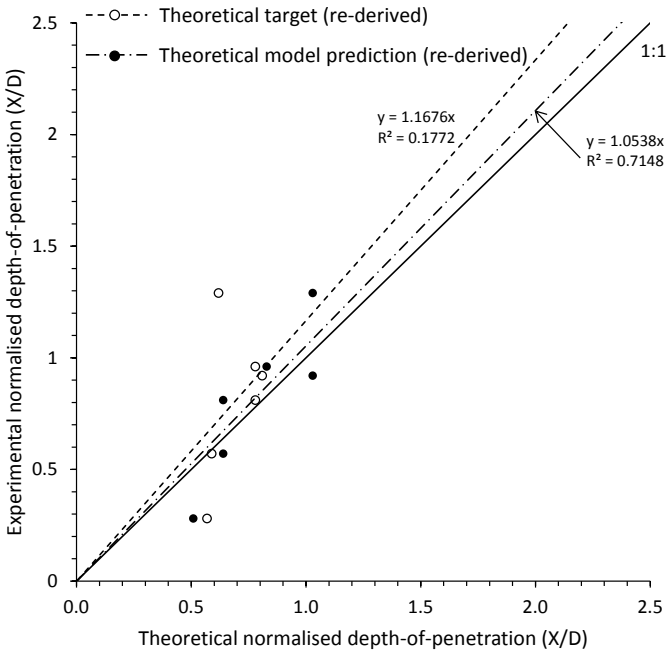


Figure 7.14: Comparison between both the targeted and predicted depths-of-penetration and the experimental depths-of-penetration for a range of cold spray polymer metallised coatings, using the re-derived theoretical model and penetration equation as well as the experimentally optimum parameter sets.

This new theoretical model was programmed into the existing Python code and integrated with the programmed Taguchi optimisation model used in re-deriving the theoretically optimum parameter sets.

7.5.5 Re-derived theoretical cold spray parameter sets

In addition to the use of the new targeted particle depth-of-penetration and the modified particle depth-of-penetration predictive algorithm, an additional means of improving the predictive accuracy was made. It was observed from the combined use of the theoretical cold spray model and the experimental cold spray analysis that parameter effects are of critical importance and that parameter levels should be carefully selected for both forms of optimisation (both theoretical and experimental). In light of this it was found that the original parameter levels for the theoretical optimisation procedure were too broad and at the same time inadvertently misrepresented a viable range of cold spray parameters for each respective coating type. This limited the accuracy of the theoretical parameter optimisation and parameter selection.

An example of this range misrepresentation is through operating temperature effects. Operating temperature, although having a link to detrimental thermal effects, plays an important role in effective cold spray deposition. The theoretical model used an initial temperature range starting at ambient temperature. This skewed the analysis, favouring the low temperature in light of a high coefficient of variation on the signal-to-noise (S/N) ratio. From an experimental cold spray perspective, these low temperatures were insufficient to achieve acceptable coating depositions. It was therefore proposed that the parameter ranges be re-evaluated. In the case of temperature this involved raising the minimum operating temperature to a minimum of 100°C, while for other parameters the theoretical parameter ranges were reduced to a more realistic range for polymer metallisation.

This change, to the theoretical analysis for the case of operating temperature, resulted in a shift from that parameter being regarded as a control factor, which should be selected to maximise the S/N ratio, to a signal factor, which targets the mean. This change, in the majority of cases, lead to the theoretical selection of operating temperature far closer to the experimentally optimum equivalent, thus improving the predictive accuracy of the theoretical cold spray model.

Two other small procedural variations were also enforced. The first provided structure to the selection of the test parameter values for Part 2 of the Taguchi Method, based on the best parameter set of Part 1. These are given below.

- Operating pressure (P_0) = ± 0.1 MPa
- Operating temperature (T_0) = ± 50°C
- Nozzle standoff distance (SOD) = ± 2 - 3 mm
- Nozzle traverse speed (V_n) = ± 5 mm/s

The second procedural variation related to small parameter variations after the completion of the Taguchi analysis, as a means of refining the predicted particle depth-of-penetration response to achieve the targeted depth-of-penetration as given by the new empirical model (Page 274). In this way the identification of the theoretically optimum parameter set may become more precise and potentially more accurate, provided the re-evaluated theoretical model itself better represents reality. These variations are given below.

- Operating pressure (P_0) = ± 0.1 MPa
- Operating temperature (T_0) = ± 10°C
- Nozzle standoff distance (SOD) = ± 5 mm
- Nozzle traverse speed (V_n) = ± 5 mm/s

Using copper and zinc coated 3D printed ABS and a tin coating on solid ABS as three independent test cases, the theoretical parameter sets were re-derived using the new particle depth-of-penetration targeting empirical model and the modified cold spray theoretical model. The resultant theoretical parameter sets are given in Table 7.8, Table 7.9 and Table 7.10.

Table 7.8: Theoretical and experimental cold spray parameter set comparisons and results for copper coated 3D printed ABS.

	Copper coated 3D printed ABS			
	Original theoretical (predicted)	Original theoretical (actual)	Experimentally optimum (actual)	New theoretical (predicted)
Throat diameter (mm)	2.5	2.5	2.5	2.5
Exit diameter (mm)	6.5	6.5	6.5	6.5
Divergent length (mm)	120	120	120	120
Spray gas	Air	Air	Air	Air
Ambient pressure (Pa)	83060	83060	83060	83060
Ambient temperature (°C)	15	15	15	15
Spray powder	Copper	Copper	Copper	Copper
Stagnation pressure (MPa)	1	1	0.75	0.8
Stagnation temperature (°C)	90	90	190	190
Initial particle temperature (°C)	15	15	15	15
Nozzle standoff distance (mm)	10	10	5	18
Nozzle traverse speed (mm/s)	10	10	15	15
Substrate material	3D Printed ABS	3D Printed ABS	3D Printed ABS	3D Printed ABS
Initial substrate temperature (°C)	15	15	15	15
Powder mean diameter (µm)	25	25	25	25
Target penetration (X/D) [µm]	1.85	/	/	0.59
Depth-of-penetration (X) [µm]	46.71	8.25	4.34	16.62
Impacting particle size (D) [µm]	25.00	13.57	9.25	25.00
X/D	1.87	0.61	0.57	0.66

Table 7.9: Theoretical and experimental cold spray parameter set comparisons and results for zinc coated 3D printed ABS.

	Zinc coated 3D printed ABS			
	Original theoretical (predicted)	Original theoretical (actual)	Experimentally optimum (actual)	New theoretical (predicted)
Throat diameter (mm)	2.5	2.5	2.5	2.5
Exit diameter (mm)	6.5	6.5	6.5	6.5
Divergent length (mm)	120	120	120	120
Spray gas	Air	Air	Air	Air
Ambient pressure (Pa)	83060	83060	83060	83060
Ambient temperature (°C)	15	15	15	15
Spray powder	Zinc	Zinc	Zinc	Zinc
Stagnation pressure (MPa)	1.05	1.05	0.8	0.55
Stagnation temperature (°C)	100	100	200	100
Initial particle temperature (°C)	15	15	15	15
Nozzle standoff distance (mm)	20	20	10	15
Nozzle traverse speed (mm/s)	10	10	15	2517
Substrate material	3D Printed ABS	3D Printed ABS	3D Printed ABS	3D Printed ABS
Initial substrate temperature (°C)	15	15	15	15
Powder mean diameter (µm)	27.5	27.5	27.5	27.5
Target penetration (X/D) [µm]	1.67	/	/	0.62
Depth-of-penetration (X) [µm]	46.08	18.92	13.21	19.99
Impacting particle size (D) [µm]	27.50	14.20	11.87	27.50
X/D	1.68	1.28	1.29	0.73

Based on the re-evaluated theoretical predictions for both a copper and zinc cold spray coating onto a 3D printed substrate, it is clear that the modifications have improved the accuracy of the models. The theoretically optimum parameter sets attained using these modified models, therefore, bear closer relation to the experimentally optimum parameter sets, thus indicating that use of such modified theoretical models would accelerate experimental optimisation.

The Python programmed theoretical cold spray model, as used in this chapter, may be viewed in Appendix A. To use the automated setting in the program for parameter set optimisation, the user responses must be commented out and the section following the main code introduction must be uncommented. A separate .CSV file containing the relevant initial parameter sets for the Taguchi Method must then be created.

Table 7.10: Theoretical cold spray parameter set comparisons and results for tin coated solid ABS.

	Tin coated ABS	
	Original theoretical (predicted)	New theoretical (predicted)
Throat diameter (mm)	2.5	2.5
Exit diameter (mm)	6.5	6.5
Divergent length (mm)	120	120
Spray gas	Air	Air
Ambient pressure (Pa)	83060	83060
Ambient temperature (°C)	15	15
Spray powder	Tin	Tin
Stagnation pressure (MPa)	0.95	0.75
Stagnation temperature (°C)	150	140
Initial particle temperature (°C)	15	15
Nozzle standoff distance (mm)	15	5
Nozzle traverse speed (mm/s)	10	7
Substrate material	ABS	ABS
Initial substrate temperature (°C)	15	15
Powder mean diameter (μm)	25	25
Target penetration (X/D) [μm]	42.08	0.62
Depth-of-penetration (X) [μm]	42.43	24.69
Impacting particle size (D) [μm]	25.00	25.00
X/D	1.7	0.99

This chapter set out to evaluate the requirements for effective antimicrobial surface coatings. In doing so, the antimicrobial effects and mechanisms of action were considered, together with the surface topographical effects. A correlation analysis was performed between surface wear and topography, and the effects substrate surface topography have on ideal particle depth-of-penetration were briefly investigated. The chapter concluded where the research began: considering cold spray polymer metallisation and the requirements and theoretical prediction of optimum system conditions.

Chapter 8 Conclusions and Recommendations

"There is a law written in the darkest of the Books of Life, and it is this: If you look at a thing nine hundred and ninety-nine times, you are perfectly safe; if you look at it the thousandth time, you are in frightful danger of seeing it for the first time."

G.K. Chesterton, The Napoleon of Notting Hill

8.1 Research conclusions

The development of antimicrobial surface coatings via cold spray and 3D printing was based around the research question: *Could the integration of cold spray and 3D printing provide a significant means to the mitigation of nosocomial infection transmission, by way of antimicrobial touch-contact materials and in such a way develop a novel surface coating for healthcare related applications?* This question itself arose from the need for an alternative solution to the global problem of hospital acquired infections together with resistant pathogenic strains. This need was to be fulfilled through an inter-disciplinary study, bridging a gap between the engineering and medical fields; towards an implementable solution to surface contamination and nosocomial infection transmission.

Surface contact sites are a significant and persistent source of infection transmission. The high prevalence of these nosocomial infections, together with insufficient compliance with cleaning protocols within hospitals, provided ample motivation for broad based counter measures to surface contact site transmission paths, using the innate antimicrobial properties of three metals: copper, silver and zinc.

It was from this research question that the three core research areas were derived: *theoretical cold spray modelling*, *experimental cold spray optimisation* and *antimicrobial susceptibility testing*. Together these research areas worked to develop a viable solution to touch-contact microbial transmission by addressing the seven research hypotheses guiding the research progression.

To reiterate the *purpose of study* the research set out to disrupt the chain of infection transmission within the hospital environment, through the development of antimicrobial surface coatings; via cold spray surface coating technology, antimicrobially active metals (copper, zinc and silver) and polymer 3D printing. A theoretical approach to polymer metallisation was ultimately a requirement for assisting parameter selection, a known area of uncertainty in the cold spray process, making use of mathematical algorithm development, together with software development and optimisation strategies. Spray powder combinations and surface coating effects were investigated; while antimicrobial susceptibility testing characterised the efficacy of the developed coatings against known pathogenic micro-organisms.

Theoretical cold spray modelling sought to mitigate parameter selection uncertainty and aid theoretical optimisation. This objective was derived from the posed research hypothesis: Hypothesis 4 - *Theoretical cold spray modelling is able to suitably represent and make accurate prediction of the cold spray coating effects as well as provide rapid selection of process parameters.* This hypothesis relies on the confirmation of the preceding three hypotheses[i]. The process parameters of operating pressure and temperature, nozzle standoff distance, nozzle traverse speed and powder feed rate, were identified and used as the key process parameters.

A theoretical cold spray model was developed which employed a particle depth-of-penetration targeting empirical model, a two stage Taguchi optimisation protocol and a comprehensive theoretical algorithm based on particle depth-of-penetration, for effective cold spray polymer metallisation. This model integrated various design elements, making use of modular components. The Taguchi Method was effective in robust system design for ideal, theoretical parameter selection.

Together with the theoretical model and its theoretical optimisation, experimental optimisation was a key research outcome, designed to effect change towards cold spray polymer metallisation for functional surface coating development. Cold spray metallisation was, therefore, achieved based on the theoretical analyses and experimental optimisation procedure devised, thus confirming Hypothesis 5 - *Polymer metallisation via cold spray is possible, across a range of thermoplastic polymers, including metallisation of 3D printed Acrylonitrile Butadiene Styrene (ABS).* Functional surface design via additive manufacturing was a goal achieved in the pursuit of cold spray polymer metallisation.

[i] Hypothesis 1 - *Mathematical modelling, using spray particle depth-of-penetration as the key discriminating criterion, is able to accurately predict cold spray parameter set effects.*
Hypothesis 2 - *The Taguchi Method is a suitable tool for cold spray parameter set selection.*
Hypothesis 3 - *An empirical model, based on the properties of the relevant cold spray powders and target substrate materials, is able to effectively determine a target particle depth-of-penetration for ideal coating quality.*

With the aid of an independent parameter effects selection and variation decision framework, which was designed as a tool for cold spray coating assessment based on five known detrimental coating effects (lack of deposition, lack of depositional consistency, lack of coating densification, thermal effects and erosive features), and a novel optimisation procedure; 20 unique cold spray coating-substrate combinations were developed. It was found that cold spray of dissimilar materials, particularly for polymer metallisation, involves high levels of parameter sensitivity with consequent careful parameter selection required. The key areas of coating characterisation were with regards to particle depth-of-penetration, surface topography and coating wear resistance.

Additive manufacturing played a central role in the development of these surface coatings, both as the coating material deposition (via cold spray) and for the polymer substrates themselves (via polymer FDM 3D printing). The use of the latter was particularly important in investigating the effects of surface topography. This integrated and novel, multi-step and multi-material approach to additive manufacturing led to the additional design goal of functional and versatile design for retrofitting capabilities as well as enhanced antimicrobial performance.

A shift away from the idea of additive manufacturing and 3D printing as simply prototyping tools, has been made. The design freedom and customisation afforded by additive manufacturing techniques has allowed the development of these functional coatings. Specifically cold spray, as a specialised deposition technique, offers high levels of process control for the generation of coatings. Additionally, 3D printing has influenced coating deposition, antimicrobial efficacy and wear phenomena.

The primary goal of this research was to develop antimicrobial surface coatings, which may find effective application within the healthcare industry. As such the antimicrobial susceptibility testing was to confirm Hypothesis 6 - *Cold spray surface coatings on polymer substrates, using antimicrobially active metals, mitigate nosocomial infection transmission.* The antimicrobially active surface coatings that were developed were not designed to replace existing hospital cleaning protocols, but to supplement them. Based on literature this is a fundamental issue whereby the compliance with cleaning and sanitising protocols are reportedly very low.

The results of the antimicrobial susceptibility tests proved the enhanced efficacy of these cold spray coatings. Synergistic activity in a diffusive, wet contact environment was confirmed for a 50:50 copper-zinc blended coating on 3D printed ABS substrates; which against *S. aureus*, *P. aeruginosa* and *K. pneumoniae* was found to be 43% more effective than the combined average for independent copper and zinc coatings on 3D printed ABS. The addition of a silver additive was found to improve copper's performance in a diffusive test environment,

whereas the same 5wt% silver additive for zinc containing samples lead to a significantly reduced antimicrobial activity in the same environment. In a dry, touch-contact environment this silver additive offered no enhancement against *S. aureus* nor *C. albicans*, but was found to enhance the microbial reduction potential for the 50:50 copper-zinc coating blend, by a factor of three, against *P. aeruginosa*.

The developed coatings also performed well against resistant pathogens. In a wet contact environment copper was found to be more active against azlocillin-carbenicillin-resistant *Pseudomonas aeruginosa* (DSM 46316), while the 50:50 copper-zinc blend showed enhanced diffusive activity against gentamicin methicillin resistant *S. aureus* (ATCC 33592). No activity was observed against fluconazole-resistant *Candida albicans* (Wits *C. albicans* 4122) and silver offered no antimicrobial advantage. In a dry, touch-contact environment the three top coatings performed exceptionally well. A copper coating on 3D printed ABS achieved complete microbial elimination within 12 min, while a copper-on-copper coating achieved the same in just 8 min. The standout result was that of a copper coating with a 5wt% silver additive on a copper metal substrate, which against all three resistant pathogenic strains achieved complete microbial elimination within just 5 min. This material, therefore, achieves the set benchmark time for bacterial elimination from touch-contact surfaces within a healthcare environment [5].

Based on prototype trials, the coatings were found to be sufficiently durable and comparatively effective antimicrobial surfaces. Zinc coatings undergoing autoclave sterilisation were found to exhibit enhanced antimicrobial activity in a diffusive environment, attributed to the formation of zinc hydroxide.

Antimicrobial activity of the coatings varied based on coating type, constituent materials and test environment, and yet cold spray coatings on polymer substrates were found to provide significant mitigation of nosocomial infection transmission, thereby confirming Hypothesis 6. Copper coatings were more active in a dry, touch contact environment, whereas zinc containing coatings performed well in a diffusive, wet contact environment. In a dry, touch-contact environment, cold spray coatings had, on average, a microbial reduction rate five times greater than their corresponding base metals.

Finally, Hypothesis 7 - *Antimicrobial efficacy is enhanced by a corresponding increase in surface contact area observed in an increase in arithmetic mean surface roughness*, was addressed through a detailed evaluation of surface topographical and coating composition effects.

The diffusion of metal ions and direct microbial contact are two key factors when considering antimicrobial mechanism of action from surfaces [5, 70, 80, 87, 91, 204]. Based on this and the various elements of this current study, it appears that a number of interrelated factors may be

used to explain the enhanced antimicrobial activity exhibited by these novel surface coatings. Surface contact area is indeed one influencing factor, and yet considering the arithmetic mean surface roughness as the root cause of this, may limit this view. Considering the wider study, surface topography had varying effects, depending on the prevailing operating environment.

Under diffusive, wet-contact conditions a smoother coating, in general, was found to be more antimicrobially active. While smoother (low arithmetic mean roughness) copper coatings in a dry, touch-contact environment followed this trend, zinc containing coatings performed better with rougher surface coatings. The surface topography of the zinc coatings played a comparatively larger role in the exhibited antimicrobial activity in a dry contact environment than the constituent zinc metal itself, which wasn't exceptionally effective under such conditions. It was also found that the required average particle depth-of-penetration, for a sufficient coating, is increased with an increased substrate roughness.

So in response to Hypothesis 7, surface profile, which does include arithmetic mean surface roughness, was found to influence antimicrobial activity, yet not in the generalised way initially proposed. This influence is dependent on a far greater number of factors, including for example: the coating composition (with regards to the substrate material and structure, as well as the coating's constituent metals), the type of contamination (wet/dry contact environment) and even the type of pathogens present in that environment (Gram-positive vs Gram-negative bacteria and fungal contaminants). The study results therefore go beyond the purview of the initial hypothesis and subsequently provides relevant scope for future study in this field.

Besides a zinc coating on polycarbonate and a copper coating on solid ABS, cold spray coated samples were found, on average, to wear two and a half times faster than their respective uncoated substrates, based on the ASTM G99 *standard test method for wear testing with a pin-on-disc apparatus*. The aforementioned zinc and copper coatings were the only coatings to exhibit lower wear rates than their corresponding substrates. Arithmetic mean roughness was found to be strongly correlated with wear such that an increased coating roughness lead to an increased wear rate. Provided the cold spray metallisation has penetrated the polymer substrate sufficiently, this should not be significantly detrimental to antimicrobial performance, since as a surface layer is worn away, fresh metal sub-layers are revealed, thereby prolonging operational longevity.

Based on cold spray parameter selection, all process parameters (P_0, T_0, SOD, PFR) barring nozzle traverse speed were found to increase the coating roughness.

As a special application, antimicrobial mobile device covers were identified in response to the rise in mobile device use from visitors, patients and medical staff within hospitals and their

consequent impact on infection prevalence. The prototype trial that was conducted proved the viability of these coatings for real world applications. An alternating copper and zinc stripe-coated 3D printed smartphone cover was found to reduce bacterial contamination by over 55% and fungal contamination by over 75% over the course of a three week pilot study.

The implications of this research are that real world applications are feasible, where such technology offers an alternative barrier to infection transmission and alternative mechanisms to actively combat hospital acquired infections. An international patent application, in agreement with the Patent Cooperation Treaty, has successfully entered the National Phase, with the title: *Method of Applying an Antimicrobial Surface Coating to a Substrate*[ii]. As of July 2020 the patent has been filed with jurisdiction in the following countries/regions: South Africa (Ref: 2020/01762), United States of America (Ref: 16/652,389), China (Reference pending) and Europe (Reference pending). The novelty of this technology and its inherent utility, within the scope of infection prevention and control, confirms the feasibility of future possibilities.

8.2 Future recommendations

There is continuity in research and as such the following future recommendations were identified for further study:

- The theoretical cold spray model algorithm included the plan and details for the use of submerged jet modelling as a means to evaluate substrate temperatures after jet impingement. This analysis was, however, unsuccessful and omitted from the final model. Further research would benefit from a review of this analysis, or through the inclusion of an alternative heat transfer analysis for such an evaluation.
- Experimental analysis of both gas and particle conditions within the nozzle and nozzle gap may inform modifications to the theoretical model, thus mitigating any discrepancies between theoretically predicted and experimentally achieved particle impact phenomena. In this way an improved theoretical cold spray model may be developed.

  Using particle visualisation and measurement software, such as the VisiSize system produced by Oxford Lasers, accurate correlations between theoretical and experimental velocities may be used to further theoretical model design.

[ii] Patent inventors: Michael David Ian Lucas, Ionel Botef, Sandy van Vuuren.
International Application Number: PCT/IB2018/057488.
International Publication Number: WO 2019/064216 AI.

The use of a novel particle compression test, as developed by Assadi and Gärtner [175] is suggested as a means to improve theoretical cold spray penetration predictions based on an accurate representation of the feedstock powder particle ultimate tensile strength.

- The Scope Delimitation (see page 6) detailed the research boundaries that were instituted for this research. Further studies may benefit from their variation.

  One such constraint was that of the 3D printer and subsequent 3D printing material. Further insight into surface topographical effects and substrate composition effects may be gained by including other 3D printed substrate materials with different process parameters. A suggested area for enhanced 3D printing, related to the design and manufacture of antimicrobial surface coatings, is that of surface topography. Sequential layer build-up and the associated build orientation was used in this study to explore surface topographical effects on both coating development and antimicrobial efficacy. Further design potential exists for user controlled extrusion patterns and properties for polymer 3D printing. With this development, refined substrate surfaces may be designed to achieve optimal deposition characteristics and commensurate antimicrobial activity, tailored to a specific operating environment.

  Another research constraint related to the selected test micro-organisms for the antimicrobial susceptibility tests. For this study they were selected based on their prevalence as nosocomial infections and their structural and phylogenetic classifications, but there are many other such pathogens affecting hospital care. A few of which include: *Escherichia coli* or *Acinetobacter baumannii* as Gram-negative pathogens, or *Clostridium difficile* or *Listeria monocytogenes* as Gram-positive pathogens. Furthermore, *Aspergillus niger* as a suitable model for fungal mould studies may be considered. A further study including additional test species may provide further insight into the mechanism of antimicrobial action achieved by the three selected antimicrobial metals.

- In light of the current and global coronavirus (SARS-CoV-2) outbreak [232], extension of this research to investigate the effectiveness against viruses is strongly suggested. The outbreak was first reported from Wuhan, China on 31 December 2019, and as of 30 January 2020 declared a Public Health Emergency of International Concern [233]. Strategies for containment and ultimate elimination of such viral outbreaks, in addition to bacterial and fungal infections, requires successful restriction of infectious agent transmission, which this technology ultimately intends to achieve.

- Further antimicrobial assays may be conducted, related specifically to the prolonged activity of the developed coatings. One such test procedure is that of the EPA continuous kill test protocol, which involves re-inoculation with a test culture every 4 hrs for 24 hrs. In addition to this, the abrasion and chemical exposure process detailed in the US EPA's *Protocol for the evaluation of bactericidal activity of hard, non-porous*

copper containing surface products (2016), which is designed to mimic a certain degree of normal and relevant physical wear, may be considered.

- It was suggested by an infection control and prevention expert at the 5th International Conference on Prevention and Infection Control (ICPIC 2019) that an additional study into the antimicrobial efficacy of these coatings, in the presence of organic matter, would be an important next step. This would further test the efficacy of these coatings and provide a bridge to clinical trials. A suggested study methodology would use fetal calf serum (FCS) to simulate organic surface loading (biological soiling) by blood, vomit, etc. The FCS, at a set concentration anywhere between 1% and 10%[iii], is incorporated into the bacterial suspensions used to contaminate the surfaces. Such tests are designed to simulate possible real-world conditions within a hospital environment.

- Given the successful development of single pass cold spray coatings, it would be beneficial to further investigate coating build-up, with multi-pass layering.

- Further research may look at improving the wear resistance of the various coating types.

- Toxicity tests would be a beneficial additional study, considering the intention to see these materials integrated into the healthcare industry. Based on the literature review, these coatings are not expected to pose a health risk, but such a study would confirm this.

  - One example of such a study may include a dermal penetration test. Sigma Aldrich supplies a synthetic human skin analogue (Strat-M) which may be a suitable model for touch-contact diffusivity safety.

- A further study into surface wettability may provide further evidence of the specific mechanisms of action of the metals against micro-organisms.

- Capillary cold spray, for refined and intentional surface topography design, is a further avenue of research to explore the effects of surface topography as a mechanism to prevent microbial attachment, while affording contact killing activity due to the selected coating metal.

- A longitudinal pilot study in a working, real world environment - such as a hospital - would be beneficial as a means of transitioning this technology into the commercial space, while exploring the long term durability and sustained efficacy of these effective antimicrobial coatings.

- Extend the technology to other applications, including: public transport, food production plants, consumer goods as well as personal and household surfaces.

[iii] Based on discussions with the deputy director of the Squina International Centre for Infection Control, Margie O'Donoghue (PhD)

Nosocomial infections have been a persistent and prevailing problem within the healthcare industry, exacerbated by resistant microbial strains, such that the hospital has become a high risk environment. Touch-contact surfaces provide a common intermediary for infection transmission and were, therefore, the perfect target for critical assessment, effective solution development and targeted implementation for the mitigation of surface contamination. Through the use of integrated additive manufacturing techniques of cold spray and polymer 3D printing, design and development of effective antimicrobial surface coatings was achieved. Enhanced antimicrobial activity was demonstrated from these surface coatings. Cold spray polymer metallised copper, silver and zinc coatings - based on carefully selected material combinations and controlled parameter settings - are, therefore, realised as effective contact killing surfaces.

Glossary

"We are at risk of speculating about the speculation about which we speculate."

Andrew Charlton, Managing director of Aviation Advocacy, Geneva Switzerland

This research bridged both the engineering and medical fields as an interdisciplinary, biomedical engineering study; thus the multidisciplinary nature of the study brought with it certain terms unique to each field of study. Below is a list of such terms.

3D Printing (Eng) A sub-set of additive manufacturing, whereby designed parts are created through successive layer deposition. The Fused Deposition Modelling (FDM), as patented by Stratasys Inc., uses material extrusion to achieve layered component development [162].

Additive Manufacturing (Eng) Additive manufacturing is seen as both the umbrella term for rapid manufacturing technologies as well as a technological manufacturing advancement made possible by: computer system advances, Computer Aided Design (CAD), advanced positioning systems and adapted printing technologies [162]. There are many branches to core additive manufacturing, including material extrusion techniques (FDM - 3D printing) and material jetting (cold spray technology). These processes work towards rapid part creation, through a layered or multi-axis generative approach to manufacture, either independently or as an integrated, multi-process and multi-material approach. (Alternative synonymous terms: direct digital manufacturing, rapid manufacturing, layer-based manufacturing, solid free-form fabrication [162]).

Adiabatic Flow (Eng) Fluid flow which does not undergo heat transfer.

Adiabatic Shear Instability (Eng) A common metal-on-metal cold spray bonding feature, whereby shear loading and thermal softening during particle impingement, causes material to be ejected as an interfacial jet away from the particle impingement zone. This ejecta lands on the surrounding surface, forming a metallurgical bond. [113]

Antimicrobial Resistance (Med) The means by which micro-organisms resist the effects of antimicrobial agents. For example, reduced permeability of the cell membranes, reducing the effectiveness of an antimicrobial agent, constitutes antimicrobial resistance.

Antimicrobials (Med) Agents that kill or significantly inhibit the growth of micro-organisms.

Argyria (Med) A medical condition causing a bluish/grey discolouration of the skin and other organs, due to excessive exposure to silver [73].

Bacteriostatic (Med) A term used to describe the extent of antimicrobial ability related to the inhibition of microbial growth, rather than inducing a lethal biocidal effect [224].

Biocidal (Med) A property of a substance, chemical or entity that inflicts fatal activity against organisms, used specifically in this context to refer to an agent which may exert a killing effect on micro-organisms.

Biocide (Med) A chemical agent with the innate ability to kill living organisms [71].

Biot Number (Eng) The ratio of internal to external thermal resistance of a solid body, which gives an indication of the importance of internal thermal diffusivity to be considered for heat transfer analysis [150].

Choked Flow (Eng) A flow-limiting-condition whereby the flow achieves and is restricted to, a maximum mass flow rate. In a converging-diverging nozzle flow arrangement, this occurs when the flow through the throat (point of minimum cross-sectional area) becomes sonic (M = 1). At this critical flow point the maximum mass flow rate is achieved.

Coefficient of Variation (Stats) A statistical quantity used to compare system variability. This calculated quantity may be used to identify control and signal factors, based on its magnitude. As the coefficient of variation increases so too does system variability. The coefficient of variation is defined as the quotient of standard deviation and the mean response.

Cold Spray (Eng) A diverse, solid state material deposition technique, well suited to repair and restorative processes, surface coating processes and additive manufacturing applications. Cold spray is a low temperature deposition process, capable of *coating* dissimilar materials. With a wide and diverse range of application, cold spray is an emerging technology, branching into the additive manufacturing domain.

Control Factors (Stats) Factors in a statistical analysis which, when carefully selected, reduce variability caused by noise.

Critical Particle Velocity (Eng) A criterion for effective cold spray deposition, defined as the minimum particle velocity required for effective particle-substrate bonding and subsequent coating formation. The critical particle velocity is dependent on both the feedstock powder material and the substrate material properties as well as coating

conditions and requirements. (Unfortunately many predictions of this quantity neglect independent substrate material properties and therefore assume cold spray of *like* materials).

Cytotoxicity (Med) The extent to which an entity is destructive to living cells [223].

Dermatitis (Med) Inflammation or irritation of the skin.

Design Space (Stats) A statistical system space, comprised of the collective design variables.

Design Variables (Stats) The variable inputs to a statistical experiment.

Ejecta (Eng) Material ejected from a particle-substrate impact, a consequence of cold spray particle impingement. This ejected material then lands on the surface adjacent to the site of impact, assisting in the formation of a bonded coating. Ejecta are primarily caused by the melting of the substrate material at the crater lip, along the outer interface of a particular particle-substrate impingement interaction.

Endogenous Infections (Med) Disease causing agents residing within the host, previously asymptomatic. Possible instigating factors include compromised immune systems.

Exogenous Infections (Med) Infections that originate or are transmitted outside of the host organism, as demonstrated by the spread of nosocomial infections.

Feasibility Space (Stats) The statistical region where design variables result in system responses that fall within the boundaries of the pre-defined constraints [161]. That is the collective group of experimental outcomes that result in a viable response, within which the local and global optimums reside.

Fomites (Med) Inanimate surfaces with a propensity for harbouring infectious agents.

Global Optimum (Stats) The point in a defined feasibility space that produces the overall, most effective response characteristic, thereby representing the desired system design for a specific design specification.

Gram Stain (Med) A staining method used to differentiate bacteria [224]. A Gram-positive bacterium has a thick peptidoglycan layer, whereas a Gram-negative bacterium has a thin peptidoglycan layer. The structure and extent of the peptidoglycan layer affects gram stain dye retention, thereby providing a means to distinguish bacterial types.

Hospital Acquired Infections (Med) Infections with a point of origin linked physically and temporally with a patient's stay in hospital or similar healthcare facility.

Isentropic Flow (Eng) Reversible and adiabatic flow.

Local Optimum (Stats) A design point which, in relation to surrounding feasibility points, produces the best response characteristic.

Mechanical Entanglement (Eng) A bonding mechanism in cold spray deposition, whereby impacting spray particles embed in the target substrate and become entangled in the surrounding substrate matrix. This is the fundamental bonding mechanism for polymer metallisation cold spray.

Mesophilic Contamination (Med) Pathogenic contamination by micro-organisms that survive under moderate (human body) temperatures [4].

Noise (Eng) Unwanted disturbances to a system.

Nosocomial (Med) Referring to infections acquired and/or originating from hospitals. Also known as hospital acquired infections or healthcare associated infections. Semantic differences and a lack of consensus has historically inhibited classification agreement, yet for the purposes of this study these terms all refer to infections which have as a root origin, a clinical or healthcare associated environment which may be extended to community transmission.

Oligodynamic (Med) Effective antimicrobial properties of metals even in small quantities.

Peptidoglycan (Med) A macromolecule which protects cells and defines their shape [39]. A thick peptidoglycan layer is present in Gram-positive bacteria [39].

Pychrophilic Contamination (Med) Pathogenic contamination by micro-organisms that have the propensity for surviving under extremely low temperatures, usually associated with environmental contamination [4].

Reactive Oxygen Species (Med) Highly reactive cytotoxic molecules generated through REDOX reactions, with the potential to kill micro-organisms [223]. They are effective antimicrobial agents and are a proposed product of oligodynamic metal interactions and a possible route of metal antimicrobial mechanism of action.

Response Characteristic (Stats) The specific and monitored outcome of a statistical experiment.

Signal Factors (Stats) Factors in a statistical analysis which, when carefully selected significantly influence the system mean response.

Synergy (Gen) The interaction of two or more agents to produce a combined effect greater than the sum of their separate effects.

Taguchi Method (Stats) An optimisation and system analysis tool, aimed at identifying local and global optimums in a feasibility space, while targeting robust system design. System parameters are preferentially selected to reduce system noise.

Zeolites (Med) Framework structures of hydrated aluminosilicate materials [84]. Often used as a matrix for incorporation with other materials for enhancing diffusivity.

References

[1] T. Schettler, 2016, Antimicrobials in Hospital Furnishings: Do They Help Reduce Healthcare-Associated Infections?, Healthcare Without Harm, Safer Chemicals Program, https://noharm-uscanada.org/documents/antimicrobials-hospital-furnishings-do-they-help-reduce-healthcare-associated-infections, Cited 6 August 2018.

[2] C. Lee Ventola, 2015, The Antibiotic Resistance Crisis - Part 1: Causes and Threats, Pharmacy and Therapeutics, Vol. 40(4): 277-283.

[3] C.E. Kandel, A.E. Simor and D.A. Redelmeier, 2014, Elevator Buttons as Unrecognized Sources of Bacterial Colonization in Hospitals, Open Medicine, 8(3): 81-86.

[4] G. Messina, E. Ceriale, D. Lenzi, S. Burgassi, E. Azzolini and P. Manzi, 2013, Environmental Contaminants in Hospital Settings and Progress in Disinfecting Techniques, BioMed Research International, doi:10.1155/2013/429780.

[5] V.M. Villapún, L.G. Dover, A. Cross and S. González, 2016, Antibacterial Metallic Touch Surfaces, Materials, 9: 736, doi:10.3390/ma9090736.

[6] E.E. Mann, M.R. Mettetal, R.M. May, M.C. Drinker, B.C. Stevenson, V.L. Baiamonte, J.M. Marso, E.A. Dannemiller, A.E. Parker, S.T. Reddy and M.K. Sande, 2014, Surface Micropattern Resists Bacterial Contamination Transferred by Healthcare Practitioners, Journal of Microbiology & Experimentation, 1(5), doi:10.15406/jmen.2014.01.00032.

[7] CDC, Global Health - South Africa, www.cdc.gov/globalhealth/countries/southafrica/, Cited 24 October 2018.

[8] USCDC, 2013, Antibiotic Resistance Threats in the United States, U.S. Department of Health and Human Services CDC, www.cdc.gov/drugresistance/pdf/ar-threats-2013-508.pdf, Cited 3 August 2018.

[9] R. Shrestha, D.R. Joshi, J. Gopali and S. Piya, 2009, Oligodynamic Action of Silver, Copper and Brass on Enteric Bacteria Isolated from Water of Kathmandu Valley, Nepal Journal of Science and Technology, 10: 189-193.

[10] J.L. Hobman and L.C. Crossman, 2014, Bacterial Antimicrobial Metal Ion Resistance, Journal of Medical Microbiology, 64: 471-497, doi:10.1099/jmm.0.023036-0.

[11] D. Seo, M. Sayar and K. Ogawa, 2012, SiO_2 and $MoSi_2$ Formation on Inconel 625 Surface via SiC Coating Deposited by Cold Spray, Journal of Surface & Coatings Technology, 206: 2851-2858, doi:10.1016/j.surfcoat.2011.12.010.

[12] C.B. Henderson, 1976, Drag Coefficients of Spheres in Continuum and Rarefied Flows, American Institute of Aeronautics and Astronautics Journal, 14(6), 707-708, doi:10.2514/3.61409.

[13] M. Grujicic, W.S. DeRosset and D. Helfritch, 2003, Flow Analysis and Nozzle-Shape Optimization for the Cold-Gas Dynamic-Spray Process, The Proceedings of the Institute of Mechanical Engineers, Journal of Engineering Manufacture, 217(Part B).

[14] F. Robitaille, M. Yandouzi, S. Hind and B. Jodoin, 2009, Metallic Coating of Aerospace Carbon/Epoxy Composites by the Pulsed Gas Dynamic Spraying Process, Journal of Surface & Coatings Technology, 203: 2954-2960, doi:10.1016/j.surfcoat.2009.03.011.

[15] Centerline, 2014, SST Cold Spray Systems, The SST Series P Cold Spray System, Document SST-SP-FL-PR-1.0-1114, www.supersonicspray.com, Cited July 2019.

[16] Centerline, 2010, Automatic Spray Gun System, User's Manual, Document #ASG-UM-SIP-PR-1.0-0910.

[17] C. Suetens, S. Hopkins, J. Kolman, L.D. Högberg, 2013, Surveillance Report - Point Prevalence Survey of Healthcare-Associated Infections and Antimicrobial Use in European Acute Care Hospitals 2011 - 2012, European Centre for Disease Prevention and Control, Stockholm, doi:10.2900/86011.

[18] WHO, 2011, Report on the Burden of Endemic Health Care-Associated Infection Worldwide - Clean Care is Safer Care, World Health Organisation, Geneva, Switzerland, ISBN 9789241501507.

[19] M.P. Muller, C. MacDougall, M. Lim, the Ontario Agency for Health Protection and Promotion and the PIDAC-IPC, 2016, Antimicrobial Surfaces to Prevent Healthcare-Associated Infections: A Systematic Review, Journal of Hospital Infection, 92: 7 - 13, doi:10.1016/j.jhin.2015.09.008.

[20] S. Santajit and N. Indrawattana, 2016, Mechanisms of Antimicrobial Resistance in ESKAPE Pathogens, BioMed Research International, doi:10.155/2016/2475067.

[21] I. Raza, A. Raza, S.A. Razaa, A.B. Sadar, A.U. Qureshi, U. Talib and G. Chi, 2017, Surface Microbiology of Smartphone Screen Protectors Among Healthcare Professionals, Cureus, 9(12), doi:10.7759/cureus.1989.

[22] S. Mahomed,O. Mahomed, A.W. Sturm, S. Knight and P. Moodley, 2017, Challenges with Surveillance of Healthcare-Associated Infections in Intensive Care Units in South Africa, Critical Care Research and Practice, doi:10.1155/2017/7296317.

[23] W. Lowman, 2016, Active Surveillance of Hospital-Acquired Infections in South Africa: Implementation, Impact and Challenges, South African Medical Journal, 106(5): 489 - 493, doi:10.7196/SAMJ.2016.v106i5.10783.

[24] A. Brink, C. Feldman, A. Duse, D. Gopalan, D. Grolman, M. Mer, S. Naicker, G. Paget, O. Perovic and G. Richards, 2006. Guideline for the Management of Nosocomial Infections in South Africa, The Southern African Journal of Epidemiology and Infection, 21(4): 152-160, ISSN 1015-8782.

[25] A. Dramowski and A. Whitelaw, 2017, Surveillance of Healthcare-Associated Infection in Hospitalised South African Children: Which Method Performs Best?, The South African Medical Journal, 107(1): 56 - 63, doi:10.7196/SAMJ.2017.v107i1.11431.

[26] L.B. Rice, 2008, Federal Funding for the Study of Antimicrobial Resistance in Nosocomial Pathogens: No ESKAPE, The Journal of Infectious Diseases, 197: 1079 - 1081, doi:10.1086/533452.

[27] B.E. Murray, 2018, Treatment of Enterococcal Infections, www.uptodate.com/contents/treatment-of-enterococcal-infections, Cited 5 November 2018.

[28] R.R. Roberts, R.D. Scott, B. Hota, L.M. Kampe, F. Abbasi, S. Schabowski, I. Ahmad, G.G. Ciavarella, R. Cordell, S.L. Solomon, R. Hagtvedt and R.A. Weinstein, 2010, Costs Attributable to Healthcare-Acquired Infection in Hospitalised Adults and a Comparison of Economic Methods, Med Care, 48(11): 1026 - 1035, doi:10.1097/MLR.0b013e3181ef60a2.

[29] CDC, Hand Hygiene in Healthcare Settings, Centers for Disease Control and Prevention, www.cdc.gov/handhygiene/index.html, Page last reviewed 29 April 2019 and last accessed 7 November 2019.

[30] E. Tartari, M. Borg, E. Castro-Sanchez, W. Zingg, B. Allegranzi and D. Pittet, 2019, Current Status of Hand Hygiene Monitoring and Performance Feedback Across Low-, Middle- and High Income Countries, Antimicrobial Resistance and Infection Control, 8 (Supplement 1):P131.

[31] V. Erasmus, T.J. Daha, H. Brug, J.H. Richardus, M.D. Behrendt, M.C. Vos and E.F. vam Beeck, 2010, Systematic Review of Studies on Compliance with Hand Hygiene Guideline in Hospital Care, Infection Control and Hospital Epidemiology, 31(3), doi:10.1086/650451.

[32] M. Musa, A. Lai, N.M. Mereu, M. Galletta, M. Campagne, M. Tidore, M.F. Piazza, L. Spada, M.V. Massidda, S. Colombo, P. Mura and R.C. Coppola, 2017, Assessing Hand Hygiene Compliance Among Healthcare Workers in Six Intensive Care Units, Journal of Preventative Medicine and Hygiene, 58, E231-E237.

[33] WHO, 2009, WHO Guidelines on Hand Hygiene in Health Care, https://www.who.int/gpsc/5may/tools/9789241597906/en/, Cited 6 November 2018.

[34] T. Cardoso, M. Almeida, N.D. Friedman, I. Aragão, A. Costa-Pereira, A.E. Sarmento and L. Azevedo, 2014, Classification of Healthcare-Associated Infection: A Systematic Review 10 Years after the First Proposal, BioMed Central Medicine, 12:40, doi:10.1186/1741-7015-12-40.

[35] WHO, 2002, Prevention of Hospital-Acquired Infections - A Practical Guide (2nd Ed.), World Health Organisation, www.who.int/csr/resources/publications/drugresist/WHO_CDS_CSR_EPH_2002_12/en/, Cited 6 November 2018.

[36] O. Perovic, H. Ismail, E. Van Schalkwyk, W. Lowman, E. Prentice, M. Senekal, C.N. Govind, 2018, Antimicrobial Resistance Surveillance in the South African Private Sector Report for 2016, Southern African Journal of Infectious Diseases, 33:4, 114-114, doi:10.1080/23120053.2018.1482646.

[37] S. Aryal, 2018, Differences between Gram Positive and Gram Negative Bacteria, microbiologyinfo.com/differences-between-gram-positive-and-gram-negative-bacteria/, Cited 7 November 2018.

[38] S.S. Bhimji and C.G. Unakal, 2017, Bacteria, Gram Positive, NCBI Bookshelf, www.ncbi.nlm.nih.gov/books/NBK470553/?report=printable, Cited 6 November 2018.

[39] T.J. Silhavy, D. Kahne and S. Walker, 2010, The Bacterial Cell Envelope, Cold Spring Harbor Laboratory Press, doi: 10.1101/cshperspect.a000414.

[40] O. Denis, 2016, Route of Transmission of *Staphylococcus aureus*, Comment on Transmission of Staphylococcus aureus between health-care workers, the environment, and patients in an intensive care unit: a longitudinal cohort study based on whole-genome sequencing, The Lancet Infectious Diseases, 17(2): 124 - 125, doi:10.1016/S1473-3099(16)30512-6.

[41] Infection Control Team, 2006, Vancomycin - Resistant Enterococcus, St James's Hospital, Dublin, www.stjames.ie/Patients/Infectionpreventioncontrol/VRE.pdf, Cited 1 August 2018.

[42] K. Todar, Pseudomonas aeruginosa, Todar's Online Textbook of Bacteriology, http://textbookofbacteriology.net/pseudomonas.html, Cited 7 November 2018.

[43] R. Facklam, 1980,ID# 2297, CDC Public Health Image Library, https://phil.cdc.gov/Details.aspx?pid=2297, Cited 25 July 2020.

[44] CDC, 2018, Pseudomonas aeruginosa in Healthcare Settings, Centers for Disease Control and Prevention, www.cdc.gov/hai/organisms/pseudomonas.html, Cited 7 November 2018.

[45] Public Health Agency of Canada, 2012, Pseudomonas spp. Pathogen Safety Data Sheet - Infectious Substances, www.canada.ca/en/public-health/services/laboratory-biosafety-biosecurity/pathogen-safety-data-sheets-risk-assessment/pseudomonas.html, Cited 8 August 2018.

[46] R. Podschun and U. Ullmann, 1998, *Klebsiella* spp. as Nosocomial Pathogens: Epidemiology, Taxonomy, Typing Methods, and Pathogenicity Factors, Clinical Microbiology Reviews, 11(4): 589 - 603.

[47] F.E. Tatsing Foka, A. Kumar and C.N. Ateba, 2018, Emergence of Vancomycin-Resistant Enterococci in South Africa: Implications for Public Health, South African Journal of Science, 114(9/10).

[48] H. Lochan, C. Moodley, D. Rip, C. Bamford, M. Hendricks, A. Davidson, B. Eley, 2016, Emergence of Vancomycin-Resistant *Enterococcus* at a Tertiary Paediatric Hospital in South Africa, South African Medical Journal, 106(6): 562 - 566, doi:10.7196/SAMJ.2016.v106i6.10858.

[49] C. Tsui, E.F. Kong and M.A. Jabra-Rizk, 2016, Pathogenesis of *Candida albicans* biofilm, Pathogens and Disease, 74(4), doi:10.1093/femspd/ftw018.

[50] M.A. Pfaller and D.J. Diekema, 2007, Epidemiology of Invasive Candidiasis: a Persistent Public Health Problem, Clinical Microbiology Reviews, 20(1): 133 - 163, doi:10.1128/CMR.00029-06.

[51] L.J. Strausbaugh, D.L. Sewell, T.T. Ward, M.A. Pfaller, T. Heitzman and R. Tjoelker, 1994, High Frequency of Yeast Carriage on Hands of Hospital Personnel, Journal of Clinical Microbiology, 32(9): 2299 - 2300.

[52] A. Voss, M.A. Pfaller, R.J. Hollis, J. Rhine-Chalberg and B.N. Doebbeling, 1995, Investigation of *Candida albicans* Transmission in a Surgical Intensive Care Unit Cluster by Using Genomic DNA Typing Methods, Journal of Clinical Microbiology, 33(3): 576 - 580.

[53] A. Gerhardts, T.R. Hammer, C. Balluff, H. Mucha and D. Hoefer, 2012, A Model of the Transmission of Micro-Organisms in a Public Setting and its Correlation to Pathogen Infection Risks, Journal of Applied Microbiology, 112: 614 - 621, doi:10.1111/j.1365-2672.2012.05234.x.

[54] M. Anaul Kabir, M.A. Hussain and Z. Ahmed, 2012, *Candida albicans*: A Model Organism for Studying Fungal Pathogens, International Scholarly Research Network Microbiology, doi:10.5402/2012/538694.

[55] V. Russotto, A. Cortegiani, S.M. Raineri and A. Giarratano, 2015, Bacterial Contamination of Inanimate Surfaces and Equipment in the Intensive Care Unit, Journal of Intensive Care, 3:54, doi:10.1186/s40560-015-0120-5.

[56] K.M. Angadi, R. Misra, U. Gupta, S. Jadhav and M. Sardar, 2014, Study of the Role of Mobile Phones in the Transmission of Hospital Acquired Infections, Medical Journal of Dr. D.Y. Patil university, 7(4): 435 - 438, doi:10.4103/0975-2870.135256.

[57] Samsung, Tablets the Prescription for Improved Patient Care, http://www.samsung.com/za/business-images/insights/2016/SAMSUNG-HEALTHCARE-INFOGRAPHI-FINAL-SEP14J-0.pdf, Cited 9 February 2017.

[58] Alcatel-Lucent, 2014, Empowering Nurses with Wireless Phones - Five Best Practices and Real World Case Studies, http://enterprise.alcatel-lucent.com/assets/documents/E2014014232EN_Nurse_Mobility_Whitepaper.pdf, Cited 13 January 2017.

[59] C. Scott, 2015, Do Cell Phones Spread Infections in Hospitals?, Healthline, www.healthline.com/health-news/do-cell-phones-spread-infections-in-hospitals-072215#5, Cited 13 January 2017.

[60] M.J. Sultan, A. Alm, A. Hindmarsh and R.A. Greatorex, 2009, Security Swipe Cards and Scanners are a Potential Reservoir for Hospital-Acquired Infection, Annals of the Royal College of Surgeons of England, 91: 155 - 158, doi:10.1308/003588409X358962.

[61] J.R. Price, K. Cole, A. Bexley, V. Kostiou, D.W. Eyre, T. Golubchik, D.J. Wilson, D.W. Crook, A.S. Walker, T.E.A. Peto, M.J. Llewelyn, J. Paul and the Modernising Medical Microbiology Informatics Group, 2017, Transmission of *Staphylococcus aureus* between health-care workers, the environment, and patients in an intensive care unit: a longitudinal cohort study based on whole-genome sequencing, The Lancet Infectious Diseases, 14: 207 - 214, doi:10.1016/S1473-3099(16)30413-3.

[62] J.F. John Jr, F.I.D.S.A, R.J. Davidson, D.E. Low, *Staphylococcus epidermidis* and other Coagulase-Negative *Staphylococci*, Infectious Diseases and Antimicrobial Agents, www.antimicrobe.org/b234.asp, Cited 7 November 2018.

[63] A. Mohammadi, A. Ebrahimi and S. Nemati, 2016, Bacterial and Fungal Contamination of Elevator Buttons in University Schools of Isfahan University of Medical Sciences, Isfahan, Iran, Health Scope, 5(4), doi:10.17795/jhealthscope-34428.

[64] C.A. Umscheid, M.D. Mitchell, J.A. Doshi, R. Agarwal, K. Williams and P.J. Brennan, Estimating the Proportion of Reasonably Preventable Hospital-Acquired Infections and Associated Mortality and Costs, Infection Control & Hospital Epidemiology, 32(2): 101 114, doi:10.1086/657912.

[65] J.A. Garza-Cervantes, A. Chávez-Reyes, E.C. Castillo, G. García-Rivas, O.A. Ortega-Rivera, E. Salinas, M. Ortiz-Martínez, S.L Gómez-Flores, J.A. Peña-Martínez, A. Pepi-Molina, M.T. Treviño-González, X. Zarate, M.E. Cantú-Cárdenas, C.E. Escarcega-Gonzalez and J.R. Morones-Ramírez, 2017, Synergistic Antimicrobial Effects of Silver/Transition-metal Combinatorial Treatments, Nature Scientific Reports, 7:903, doi:10.1038/s41598-017-01017-7.

[66] G. Grass, C. Rensing and M. Solioz, 2011, Metallic Copper as an Antimicrobial Surface, Applied and Environmental Microbiology, 77(5): 1541 - 1547, doi:10.1128/AEM.02766-10.

[67] P.B. Tchounwou, C.G. Yedjou, A.K. Patlolla and D.J Sutton, 2014, Heavy Metal Toxicity and the Environment, National Institutes of Health Public Access, doi:10.1007/978-3-7643-8340-4_6.

[68] R. Goyer, 2004, Issue Paper on the Human Health Effects of Metals, Submitted to the U.S. Environmental Protection Agency Risk Assessment Forum, www.epa.gov/sites/production/files/2014-11/documents/human_health_effects.pdf, Cited 7 November 2018.

[69] American Cancer Society, 2014, Known and Probable Human Carcinogens, www.cancer.org/cancer/cancer-causes/general-info/known-and-probable-human-carcinogens.html, Cited 7 November 2018.

[70] S. Mathews, M. Hans, F. Mücklich and M. Solioz, 2013, Contact Killing of Bacteria on Copper is Suppressed if Bacterial-Metal Contact is Prevented and is Induced on Iron by Copper Ions, Applied and Environmental Microbiology, 79(8): 2605-2611, doi:10,1128/AEM,03608-12.

[71] J.A. Lemire, J.J. Harrison and R.J. Turner, 2013, Antimicrobial Activity of Metals: Mechanisms, Molecular Targets and Applications, Nature Reviews Microbiology, 11: 371 - 384, doi:10.1038/nrmicro3028.

[72] Norden, 2015, Food Contact Materials - Metals and Alloys, Nordic Guidance for Authorities, Industry and Trade, doi:10.6027/TN2015-522.

[73] C. Lewton-Brain, 1999, Metals Safety Information, Ganoksin Jewelry Making Community, www.ganoksin.com/article/metals-safety-information/, Cited 7 November 2018.

[74] A. Pietrangelo (Medically reviewed by D.R. Wilson PhD), 2017, Everything You Should Know About Argyria, Healthline, www.healthline.com/health/argyria-cure, Cited 7 November 2018.

[75] P. Held, 2015, An Introduction to Reactive Oxygen Species - Measurement of ROS in Cells, BioTek Instruments, www.biotek.com/resources/white-papers/an-introduction-to-reactive-oxygen-species-measurement-of-ros-in-cells/, Cited 8 November 2018.

[76] C.E. Santo, N. Taudte, D.H. Nies and G. Grass , 2008, Contribution of Copper Ion Resistance to Survival of *Escherichia coli* on Metallic Copper Surfaces, Applied and Environmental Microbiology, 74(4): 977 - 986, doi:10.1128/AEM.01938-07.

[77] M. Raffi, S. Mehrwan, T.M. Bhatti, J.I. Akhter, A. Hameed, W. Yawar and M. Masood ul Hasan, 2010, Investigations into the Antibacterial Behavior of Copper Nanoparticles Against *Escherichia coli*, Annals of Microbiology, 60: 75 - 80, doi:10.1007/s13213-010-0015-6.

[78] D. Wojcieszak, D. Kaczmarek, A. Antosiak, M. Mazur, Z. Rybak, A. Rusak, M. Osekowska, A. Poniedzialek, A. Gamian and B. Szponar, 2015, Influence of Cu-Ti Thin Film Surface Properties on Antimicrobial Activity and Viability of Living Cells, Materials Science And Engineering C, 56: 48 - 56, doi:10.1016/j.msec.2015.06.013.

[79] C.E. Santo, N. Taudte, D.H. Nies and G. Grass, 2011, Bacterial Killing by Dry Metallic Copper Surfaces, Applied and Environmental Microbiology, 77(3): 794 - 802, doi:10.1128/AEM.01599-10.

[80] M. Hans, J.C. Támara, S. Mathews, B. Bax, A. Hegetschweiler, R. Kautenburger, M. Solioz and F. Mücklich, 2014, Laser Cladding of Stainless Steel with a Copper-Silver Alloy to Generate Surfaces of High Antimicrobial Activity, Applied Surface Science, 320: 195 - 199, doi:10.1016/j.apsusc.2014.09.069.

[81] Copper Development Association, 2018, Copper, Pathogens and Disease, https://copperalliance.org.uk/knowledge-base/education/education-resources/copper-pathogens-disease/, Cited 8 November 2018.

[82] A.L. Casey, D. Adams, T.J. Karpanen, P.A. Lambert, B.D. Cookson, P. Nightingale, L. Miruszenko, R. Shillam, P. Christian and T.S.J. Elliott, 2010, Role of Copper in Reducing Hospital Environment Contamination, Journal of Hospital Infection, 74: 72 - 77, doi:10.1016/j.jhin.2009.08.018.

[83] F. Marais, S. Mehtar and L. Chalkley, 2009, Antimicrobial Efficacy of Copper Touch Surfaces in Reducing Environmental Bioburden in a South African Community Healthcare Facility, Journal of Hospital Infection, 74: 80 - 95, doi:10.1016/j.jhin.2009.07.010.

[84] A. Augustyn, Zeolite, Encyclopedia Britannica, www.britannica.com/science/zeolite, Cited 11 November 2018.

[85] Unknown, Keratinocytes - Structure, Function, Immunity and Differentiation, Keratinocyte Transfection Kit, www.keratinocyte-transfection.com/, Cited 12 November 2018.

[86] O. Sharifahmadian, H.R. Salimijazi, M.H. Fathi, J. Mostaghimi and L. Pershin, 2013, Study of the Antibacterial Behavior of Wire Arc Sprayed Copper Coatings, Journal of Thermal Spray Technology, 22: 371 - 379, doi:10.1007/s11666-012-9842-2.

[87] V.K. Champagne and D.J. Helfritch, 2013, A Demonstration of the Antimicrobial Effectiveness of Various Copper Surfaces, Journal of Biological Engineering, 7:8, doi:10.1186/1754-1611-7-8.

[88] Palram Industries Ltd., HYG Technology - PVC Sheets with Active Antimicrobial Action, Palram South Africa, www.palram.co.za/hyg˙technology, Cited 13 November 2018.

[89] Sharklet Technologies, Inc., The Technology of Sharklet, www.sharklet.com/our-technology/technology-overview/, Cited 13 November 2018.

[90] P.C. King, A.J. Poole, S. Horne, R. de Nys, S. Gulizia and M.Z. Jahedi, 2013, Embedment of Copper Particles into Polymers by Cold Spray, Surface & Coatings Technology, 216: 60 - 67, doi:10.1016/j.surfcoat.2012.11.023.

[91] M.J. Vucko, P.C. King, A.J. Poole, C. Carl, M.Z. Jahedi and R. de Nys, 2012, Cold Spray Metal Embedment: An Innovative Antifouling Technology, Biofouling: The Journal of Bioadhesion and Biofilm Research, 28(3): 239 - 248, doi:10.1080/08927014.2012.670849.

[92] J. Zhu, 2014, Water-Based Antimicrobial Coating for 3D Printed Medical Devices, Stratasys Inc., Materials Research & Development, www.stratasys.com, Cited 15 July 2016.

[93] S. Kondor, G.T. Grant and V.K. Ratogi, 2013, On Demand Additive Manufacturing of a Basic Surgical Kit, Journal of Medical Devices, doi:10.1115/1.4024490.

[94] K. Bohinc, G. Dražić, A. Abram, M. Jevšnik, B. Jeršek, D. Nipič, M. Kurinčič and P. Raspor, 2016, Metal Surface Characteristics Dictate Bacterial Adhesion Capacity, International Journal of Adhesion & Adhesives, 68: 39 - 46, doi:10.1016/j.ijadhadh.2016.01.008.

[95] P. Picariello, 2017, The Global Leader in Additive Manufacturing Standards, www.astm.org/COMMITTEE/F42.htm, Cited 16 November 2018.

[96] S.A.M. Tofail, E.P. Koumoulos, A. Bandyopadhyay, S. Bose, L. O'Donogue and C. Charitidis, 2018, Additive Manufacturing: Scientific and Technological Challenges, Market Uptake and Opportunities, Materials Today, 21(1): 22 - 37, doi:10.1016/j.mattod.2017.07.001.

[97] N. Hopkinson, R.J.M. Hague and P.M. Dickens, 2006, Rapid Manufacturing - An Industrial Revolution for the Digital Age, John Wiley & Sons, Ltd, The Atrium, Southern Gate, Chichester, West Sussex PO19 8SQ, England.

[98] D.S. Thomas, S.W. Gilbert, 2014, Costs and Cost Effectiveness of Additive Manufacturing, A Literature Review and Discussion, National Institute of Standards and Technology, NIST Special Publication 1176, doi: 10.6028/NIST.SP.1176.

[99] D. Thomas, 2016, Costs, Benefits, and Adoption of Additive Manufacturing: A Supply Chain Perspective, The International Journal of Advanced Manufacturing Technology, 85(5-8), 1857-1876, doi: 10.1007/s00170-015-7973-6.

[100] Wohlers associates, 2017, Update on the State of Additive Manufacturing Worldwide, 18th Annual RAPDASA Conference, Durban, South Africa, 7-10 November.

[101] R. Jiang, R. Kleer and F.T. Piller, 2017, Predicting the Future of Additive Manufacturing: A Delphi Study on Economic and Societal Implications of 3D Printing for 2030, Technological Forecasting & Social Change, 117: 84 - 97, doi:10.1016/j.techfore.2017.01.006.

[102] S.C. Ligon, R. Liska, J. Stampfl, M. Gurr and R. Mülhaupt, 2017, Polymers for 3D Printing and Customized Additive Manufacturing, Chemical Reviews, 117: 10212 - 10290, doi:10.1021/acs.chemrev.7b00074.

[103] F. Perez-Smith, 2018, Generative Design and Additive Manufacturing, Man and Machine, www.manandmachine.co.uk/generative-design-additive-manufacturing/, Cited 19 November 2018.

[104] P. Picariello, ASTM F42/ISO TC 261 Develops Additive Manufacturing Standards, ASTM International, www.astm.org/COMMITTEE/F42.htm, Cited 16 November 2018.

[105] S. Yin, P. Cavaliere, B. Aldwell, R. Jenkins, H. Liao, W. Li and R. Lupoi, 2018, Cold Spray Additive Manufacturing and Repair; Fundamentals and Applications, Additive Manufacturing, doi:10.1016/j.addma.2018.04.017.

[106] R.N. Raoelison, C. Verdy and H. Liao, 2017, Cold Gas Dynamic Spray Additive Manufacturing Today: Deposit Possibilities, Technological Solutions and Viable Applications, Materials and Design, 133: 266 - 287, doi:10.1016/j.matdes.2017.07.067.

[107] J.-Y Lee, J. An and C.K. Chua, 2017, Fundamentals and Applications of 3D Printing for Novel Materials, Applied Materials Today, 7: 120 - 133.

[108] R.C. Dykhuizen and M.F. Smith, 1998, Gas Dynamic Principles of Cold Spray, Journal of Thermal Spray Technology, 7(2): 205 - 212.

[109] A.P. Alkhimov, A.N. Papyrin, V.F. Kosarev, N.I. Nesterovich, M.M. Shushpanov and all of Novosibirsk, U.S.S.R, 1994, Gas Dynamic Spraying Method for Applying a Coating, United States Patent, Patent Number: 5,302,414.

[110] H. Koivuluoto, A. Coleman, K. Murray, M. Kearns and P. Vuoristo, 2012, High Pressure Cold Sprayed (HPCS) and Low Pressure Cold Sprayed (LPCS) Coatings Prepared from OFHC Cu Feedstock: Overview from Powder Characteristics to Coating Properties, Journal of Thermal Spray Technology, 21: 1065 - 1075, doi:10.1007/s11666-012-9790-x.

[111] I. Botef, 2013, Manufacturing - Design and Processes, Picsie Press, Sandton, South Africa.

[112] A. Moridi, S.M. Hassani-Gangaraj, M. Guagliano and M. Dao, 2014, Cold Spray Coating, Review of Materials Systems and Future Perspectives, Institute of Materials, Minerals and Mining, 36(6): 369 - 395, doi:10.1179/1743294414Y.0000000270.

[113] H. Assadi, H. Kreye, F. Gärtner and T. Klassen, 2016, Cold Spraying - A Materials Perspective, Acta Materialia, doi:10.1016/j.actamat.2016.06.034.

[114] H. Ye and J. Wang, 2014, Preparation of Aluminium Coating on Lexan by Cold Spray, Material Letters, 137: 21 - 24, doi:10.1016/j.matlet.2014.08.119.

[115] Centerline, 2010, SST Series P Portable Spray Machine, User's Manual, Document # ASG-UM-PR-2.0.0-0410.

[116] T. Schmidt, H. Assadi, F. Gärtner, H. Richter, T. Stoltenhoff, H. Kreye and T. Klassen, 2009, From Particle Acceleration to Impact and Bonding in Cold Spraying, Journal of Thermal Spray Technology, 18: 794 - 808, doi:10.1007/s11666-009-9357-7.

[117] M. Grujicic, J.R. Saylor, D.E. Beasley, W.S. de Rosset and D, Helfritch, 2003, Computational analysis of the interfacial bonding between feed-powder particles and the substrate in the cold-gas dynamic-spray process, Applied Surface Science, 219: 211-227, doi: 10.1016/S0169-4332(03)00643-3.

[118] W.S. de Rosset, 2006, Modeling Impacts for Cold-Gas Dynamic Spray, Army Research Laboratory, Weapons and Materials Research Directorate, https://apps.dtic.mil/dtic/tr/fulltext/u2/a454830.pdf, Cited 10 August 2016.

[119] J. Wu, H. Fang, S. Yoon, HJ Kim and C. Lee, 2005, Measurement of Particle Velocity and Characterization of Deposition in Aluminium Alloy Kinetic Spraying Process, Applied Surface Science, 252: 1368 - 1377, doi:10.1016/j.apsusc.2005.02.108.

[120] E. Calla, 2005, Cold Gas Spraying of Copper and Tin onto Metallic and Non Metallic Substrates (PhD Thesis), George Green Library of Science and Engineering, University of Nottingham.

[121] T. Goyal, R.S. Walia and T.S. Sidhu, 2012, Effect of Parameters on Coating Density for Cold Spray Process, Materials and Manufacturing Processes, 27: 193 - 200, doi:10.1080/10426914.2011.566906.

[122] T. Goyal, R.S. Walia and T.S. Sidhu, 2012, Study of Coating Thickness of Cold Spray Process Using Taguchi Method, Materials and Manufacturing Processes, 27: 185 - 192, doi:10.1080/10426914.2011.564249.

[123] J. Karthikeyan, 2013, Cold Spray Process, ASM Handbook Thermal Spray Technology, 5A, www.asminternational.org, Cited 27 September 2016.

[124] T. Marrocco, D.G. McCartney, P.H. Shipway and A.J. Sturgeon, 2006, Production of Titanium Deposits by Cold-Gas Dynamic Spray: Numerical Modelling and Experimental Characterization, Journal of Thermal Spray Technology, 15: 263 - 272, doi:10.1361/105996306X108219.

[125] S. Yin, M. Meyer, W. Li, H. Liao and R. Lupoi, 2016, Gas Flow, Particle Acceleration, and Heat Transfer in Cold Spray: A Review, Journal of Thermal Spray Technology, 25: 874 - 896, doi:10.1007/s11666-016-0406-8.

[126] A. Trinchi, Y.S. Yang, A. Tulloh, S.H. Zahiri and M. Jahedi, 2010, Copper Surface Coatings Formed by the Cold Spray Process: Simulations Based on Empirical and Phenomenological Data, Journal of Thermal Spray Technology, 20: 986 - 991, doi:10.1007/s11666-011-9613-5.

[127] T. Stoltenhoff, H. Kreye and H.J. Richter, 2001, An Analysis of the Cold Spray Process and its Coatings, Journal of Thermal Spray Technology, 11: 542 - 550.

[128] W.-Y. Li, C. Zhang, X.P. Guo, G. Zhang, H.L. Liao, C.-J. Li and C. Coddet, 2007, Effect of Standoff Distance on Coating Deposition Characteristics in Cold Spraying, Materials & Design, 29: 297 - 304, doi:10.1016/j.matdes.2007.02.005.

[129] Arbegast Materials Processing and Joining Lab, 2012, Cold Spray - A Guide to Best Practice, South Dakota School of Mines and Technology, www.sdsmt.edu/research/research-laboratories/amp/docs/cold-spray-best-practices/, Cited 30 September 2016.

[130] P. Richer, B. Jodoin, L. Ajdelsztajn and E.J. Lavernia, 2006, Substrate Roughness and Thickness Effects on Cold Spray Nanocrystalline Al-Mg Coatings, Journal of Thermal Spray Technology, 15: 246 - 254, doi:10.1361/105996306X108174.

[131] H. Assadi, F. Gärtner, T. Stoltenhoff and H. Kreye, 2003, Bonding Mechanism in Cold Gas Spraying, Acta Materialia, 51: 4379 - 4394, doi:10.1016/S1359-6454(03)00274-X.

[132] T. Schmidt, F. Gärtner, H. Assadi and H. Kreye, 2006, Development of a Generalised Parameter Window for Cold Spray Deposition, Acta Materialia, 54: 729 - 742, doi:10.1016/j.actamat.2005.10.005.

[133] V.K. Champagne, D.J. Helfritch, S.P.G. Dinavahi and P.F. Leyman, 2010, Theoretical and Experimental Particle Velocity in Cold Spray, Journal of Thermal Spray Technology, 20: 425 - 431, doi:10.1007/s11666-010-9530-z.

[134] H. Assadi, T. Schmidt, H. Richter, J.-O. Kliemann, K. Binder, F. Gätner, T. Klassen and H. Kreye, 2011, On Parameter Selection in Cold Spraying, Journal of Thermal Spray Technology, 20: 1161 - 1176, doi:10.1007/s11666-011-9662-9.

[135] W.-Y. Li, D.D. Zhang, C.J. Huang, S. Yin, M. Yu, F.F. Wang and H.L. Liao, 2014, Modelling of Impact Behaviour of Cold Spray Particles: Review, Surface Engineering, 30(5): 299 - 308, doi: 10.1179/1743294414Y.0000000268.

[136] A.S. Alhulaifi and G.A. Buck, 2014, A Simplified Approach for the Determination of Critical Velocity for Cold Spray Processes, Journal of Thermal Spray Technology, 23: 1259 - 1269, doi:10.1007/s11666-014-0128-8.

[137] T. Hussain, D.G. McCartney, P.H. Shipway and D. Zhang, 2008, Bonding Mechanisms in Cold Spraying: The Contributions of Metallurgical and Mechanical Components, Journal of Thermal Spray Technology, 18: 364 - 379, doi:10.1007/s11666-009-9298-1.

[138] J. Affi, H. Okazaki, M. Yamada and M. Fukumoto, 2011, Fabrication of Aluminium Coating onto CFRP Substrate by Cold Spray, Materials Transactions, 52(9): 1759 - 1763, doi:10.2320/matertrans.T-M2011807.

[139] Stratasys, 2011, uPrint SE and uPrint SE Plus - Personal 3D Printers - User Guide, Stratasys, Inc., 209226-0001.

[140] M. Pérez, G. Medina-Sänchez, A. García-Collado, M. Gupta and D. Carou, 2018, Surface Quality Enhancement of Fused Deposition Modeling (FDM) Printed Samples Based on the Selection of Critical Printing Parameters, Materials, 11, doi:10.3390/ma11081382.

[141] F. Fisher, 2011, Thermoplastics: The Strongest Choice for 3D Printing - Why ABS is a Good Choice for 3D Printing and When to use Another Thermoplastic, Stratasys Inc., www.stratasys.com, Cited 15 November 2018.

[142] C.E. Brennen, 2008, Fundamentals of Multiphase Flows, Cambridge University Press, ISBN 0521848040.

[143] P. Asinari, 2007, Multiphase Flows: Basic Physics and Engineering Modeling, University of Illinois, Department of Energetics, https://staff.polito.it/pietro.asinari/teaching/NHT˙Asinari˙Multiphase˙v1.5.PDF, Cited 12 February 2020.

[144] M. Meyer & R. Lupoi, 2015, An Analysis of the Particulate Flow in Cold Spray Nozzles, Mechanical Sciences, 6: 127 - 136, doi:10.5194/ms-6-127-2015.

[145] B. Samareh & A. Dolatabadi, 2008, Dense Particulate Flow in a Cold Gas Dynamic Spray System, Journal of Fluids Engineering, 130, doi: 10.1115/1.2957914.

[146] H. Tabbara, S. Gu, D.G. McCartney, T.S. Price and P.H. Shipway, 2010, Study on Process Optimisation of Cold Gas Spraying, Journal of Thermal Spray Technology, 20: 608 - 620, doi: 10.1007/s11666-010-9564-2.

[147] F.M. White, 2011, Fluid Mechanics 7th Edition, McGraw Hill, New York.

[148] M.C. Potter, D.C. Wiggert and B.H. Ramadan, 2012, Mechanics of Fluids 4th Edition, Cengage Learning, USA.

[149] A.P. Alkhimov, V.F. Kosarev and S.V. Klinkov, 2000, The Features of Cold Spray Nozzle Design, Journal of Thermal Spray Technology, 10(2): 375 - 381.

[150] F. Kreith and M. Bohn, 2001, Principles of Heat Transfer sixth edition, Thomson, USA.

[151] N. Menon, 2009, Analysis of non-axisymmetric underexpanded jet flow fields (PhD Thesis), Faculty of Engineering and the Built Environment, University if the Witwatersrand, Johannesburg, South Africa.

[152] J.D. Anderson Jr., 2007, Fundamentals of Aerodynamics, Fifth Edition, McGraw-Hill, New York, ISBN 978-0-07-339810-5.

[153] D. Helfritch and V. Champagne, 2008, A Model Study of Powder Particle Size Effects in Cold Spray Deposition, U.S. Army Research Laboratory, Aberdeen Proving Ground, MD, https://apps.dtic.mil/docs/citations/ADA504175, Cited 22 September 2016.

[154] K. Frank and J. Zook, 1990, Chunky Metal Penetrators Act Like Constant Mass Penetrators, In Proceedings of the 12th International Symposium on Ballistics, San Antonio, TX, 30 October - 1 November, 1: 441 - 449.

[155] C.E. Anderson , Jr., 2016, Penetration Mechanics: Analytical Modeling, In Proceedings of the International Ballistics Society Conference, May 10.

[156] R.J. Eichelberger, 1956, Experimental Test of the Theory of Penetration by Metallic Jets, Journal of Applied Physics, 27(1): 63 - 68, doi: 10.1063/1.1722198.

[157] D.R. Christman and J.W. Gehring, 1966, Analysis of High-Velocity Projectile Penetration Mechanics, Journal of Applied Physics, 37(4): 1579 - 1587, doi:10.1063/1.1708570.

[158] J.D. Clayton, 2016, Dimensional Analysis and Extended Hydrodynamic Theory Applied to Long-Rod Penetration of Ceramics, Defence Technology, 12: 334 - 342, doi:10.1016/j.dt.2016.02.004.

[159] A. Tate, 1967, A Theory for the Deceleration of Long Rods After Impact, Journal of the Mechanics and Physics of Solids, 15: 387 - 399.

[160] T. Goyal, T.S. Sidhu and R.S. Walia, 2013, Multi-Response Optimization of Process Parameters for Low Pressure Cold Spray Coating Process Using Taguchi and Utility Concept, Journal of Thermal Spray Technology, 23: 114 - 122, doi:10.1007/s11666-013-9988-6.

[161] A.R. Parkinson, R.J. Balling and J.D. Hedengren, 2013, Optimization Methods for Engineering Design - Applications and Theory, Brigham Young University, https://static1.squarespace.com/static/53eacd17e4b0588f78eb723c/t/586ea636d482e91c7a76bd61/1483646550748/Optimization+Methods+in+Engineering+Design.pdf, Cited 23 August 2016.

[162] M.P. Groover, 2013, Principles of Modern Manufacturing, 5th Edition (SI Units), John Wiley & Sons, Singapore.

[163] Unknown, 2019, Taguchi Designs, Minitab 18 Support, https://support.minitab.com/en-us/minitab/18/help-and-how-to/modeling-statistics/doe/supporting-topics/taguchi-designs/taguchi-designs/, Cited 21 November 2018.

[164] T.B. Barker, 1990, Engineering Quality by Design - Interpreting the Taguchi Approach, Marcel Dekker, INC, USA.

[165] I.E. Madu and C.N. Madu, 1999, Design Optimisation Using Signal-to-Noise Ratio, Simulation Practice and Theory, 7: 349 - 372.

[166] A. Bendell, J. Disney, W.A. Pridmore, 1989, Taguchi Methods Applications in World Industry, IFS Publications, USA.

[167] D.C. Montgomery and G.C. Runger, 2014, Applied Statistics and Probability for Engineers (6th edition), John Wiley & Son, Singapore.

[168] L. Goldberg and B. van Halle, 2009, More on Decision Tables and The Decision Model in Practice, Modern Analyst, https://www.modernanalyst.com/Resources/Articles/tabid/115/ID/2376/More-on-Decision-Tables-and-The-Decision-Model-in-Practice.aspx, Cited 30 January 2020.

[169] G. Witt, 2012, Writing Effective Business Rules, Morgan Kaufmann - Elsevier, 225 Wyman Street, Waltham, MA 02451, USA.

[170] T.W. Simpson, Taguchi's Robust Design Method, Concurrent Engineering, PennState College of Engineering, www.mne.psu.edu/simpson/courses/ie466/ie466.robust.handout.pdf, Cited 26 November 2018.

[171] Unknown, Chapter 2: Introduction to Taguchi Method, University of Massachusetts Amherst College of Engineering, www.ecs.umass.edu/mie/labs/mda/fea/sankar/chap2.html, Cited 21 November 2018.

[172] T.B. Barker, 2005, Quality by Experimental Design, 3rd edition, Capman & Hall, CRC Press, Taylor & Francis Group, 6000 Broken Sound Parkway NW, Suite 300, Boca Raton FL.

[173] J.D. Walker and C.E. Anderson Jr, 1995, A Time-Dependent Model for Long-Rod Penetration, International Journal of Impact Engineering, 16(1): 19 - 48, doi:10.1016/0734-743X(94)00032-R.

[174] S.K.M. Yi, M. Steyvers, M.D. Lee and M.J. Dry, 2012, The Wisdom of the Crowd in Combinatorial Problems, Cognitive Science, 36: 452 - 470, doi:10.1111/j.1551-6709.2011.01223.x.

[175] H. Assadi and F. Gärtner, 2020, Particle Compression Test: A Key Step towards Tailoring of Feedstock Powder for Cold Spraying, Coatings, 10:458, doi:10,3390/coatings10050458

[176] Centerline, 2015, SST-C5003 - Copper - Technical Data Sheet, Document Number: SST-TDS-C5003-PR-1.0.0-0410, www.supersonicspray.com, Cited 9 May 2019.

[177] Centerline, 2015, SST-N0056 - Nickel - Technical Data Sheet, Document Number: SST-TDS-N0056-PR-1.0.0-0410, www.supersonicspray.com, Cited 9 May 2019.

[178] Centerline, 2015, SST-Z5001 - Zinc - Technical Data Sheet, Document Number: SST-TDS-Z5001-PR-1.0.0-0410, www.supersonicspray.com, Cited 9 May 2019.

[179] Centerline, 2015, SST-S6001 - Tin - Technical Data Sheet, Document Number: SST-TDS-S6001-PR-1.0.0-0410, www.supersonicspray.com, Cited 9 May 2019.

[180] Centerline, 2013, SST-A0050 - Aluminium - Technical Data Sheet, Document Number: SST-TDS-A0050-PR-1.0.0-0410, www.supersonicspray.com, Cited 9 May 2019.

[181] Innovatest, TR-220 Surface Roughness Tester Manual, Innovatest - Advanced Materials Testing Solutions, www.innovatest-europe.com/products/portables/roughness/roughness-portable-tr220, Cited 20 September 2018.

[182] S.J. Shaffer, 2013, Tribology 101 - Introduction to the Basics of Tribology, Bruker (webinar), www.bruker.com/fileadmin/user_upload/8-PDF-Docs/SurfaceAnalysis/TMT/Webinars/Tribology_101_Webinar-1_Intro_and_Basics_29-Jan-2013.pdf, Cited 29 May 2017.

[183] R.C. Hibbler, 2010, Engineering Mechanics Statics (12th Edition), Prentice Hall, Pearson Education South Asia Ptd. Ltd, Singapore.

[184] D.M. Kennedy and M.S.J. Hashmi, 1998, Methods of Wear Testing for Advanced Surface Coatings and Bulk Materials, Journal of Materials Processing Technology, 77: 246 - 253.

[185] S.J. Cavalieri, et al., 2005, Manual of Antimicrobial Susceptibility Testing, American Society for Microbiology, Library of Congress Cataloging-in-Publication Data, ISBN 1-55581-349-6.

[186] Sigma Aldrich, (Image) Spreader, L-Shape, sterile, pack of 500 (total), HS8171B, https://www.sigmaaldrich.com/catalog/product/sigma/hs8171b?lang=en&region=ZA, Cited 6 November 2019

[187] EPA, 2016, Updated Draft Protocol for the Evaluation of Bactericidal Activity of Hard, Non-porous Copper Containing Surface Products, United States Environmental Protection Agency, www.epa.gov/pesticide-registration/updated-draft-protocol-evaluation-bactericidal-activity-hard-non-porous, Cited 22 May 2019.

[188] S. Sutton, 2011, Accuracy of Plate Counts, Journal of Validation Technology, 17(3).

[189] M. Grujicic, C.L. Zhao, C. Tong, W.S. DeRosset and D. Helfritch, 2003, Analysis of the Impact Velocity of Powder Particles in the Cold-Gas Dynamic-Spray Process, Materials Science and Engineering, A368: 222 - 230, doi:10.1016/j.msea.2003.10.312.

[190] G. Ahmadi, 2005, Particle Transport, Deposition, & Removal II, ME637 - Online Curriculum, Clarkson University, https://webspace.clarkson.edu/projects/crcd/public_html/me637/notes/aerosols/aerosols_page3.html, Cited 11 July 2016.

[191] R.C. Dykhuizen, M.F. Smith, D.L. Gilmore, R.A. Neiser, X. Jiang and S. Sampath, 1999, Impact of High Velocity Cold Spray Particles, Journal of Thermal Spray Technology, 8: 559 - 564.

[192] P.C. King, G. Bae, S.H. Zahiri, M. Jahedi and C. Lee, 2009, An Experimental and Finite Element Study of Cold Spray Copper Impact onto Two Aluminium Substrates, Journal of Thermal Spray Technology, 19: 620 - 634, doi:10.1007/s11666-009-9454-7.

[193] T. Schmidt, F. Gaertner, H. Kreye and T. Klassen, 2007, Particle Impact Conditions and Corresponding Coating Properties in Cold Spraying, Cold Spray 2007 Conference, October 8-9, Akron, Ohio, USA.

[194] BBC, 2019, Why do Patients Get Ill with Hospital-Acquired Infections?, www.bbc.com/news/uk-scotland-47071813, Cited 28 February 2019.

[195] ANA Reporter, 2018, Gauteng Hospital under Scrutiny as 'More Babies Die from Infection', www.iol.co.za/news/south-africa/gauteng/gauteng-hospital-under-scrutiny-as-more-babies-die-from-infection-16962739, Cited 28 February 2019.

[196] AZoM, 2002, Galvanising - White Rust Prevention and Cure, www.azom.com/article.aspx?ArticleID=1220, Cited 12 March 2019.

[197] J. Pasquet, Y. Chevalier, J. Pelletier, E. Couval, D. Bouvier and M.-A. Bolzinger, 2014, The Contribution of Zinc Ions to the Antimicrobial Activity of Zinc Oxide, Colloids and Surface A: Physiochemical and Engineering Aspects, 457: 263 - 274, doi:10.1016/j.colsurfa.2014.05.057.

[198] D. Ercan, A. Cossu, N. Nitin and R.V. Tikekar, 2016, Synergistic Interaction of Ultraviolet Light and Zinc Oxide Photosensitizer for Enhanced Microbial Inactivation in Simulated Wash-Water, Innovative Food Science and Emerging Technologies, 33: 240 - 250, doi:10.1016/j.ifset.2015.11.015.

[199] M. Fiedot, I. Maliszewska, O. Rac-Rumijowska, P. Suchorska-Woźniak, A. Lewińska and H. Teterycz, 2017, The Relationship between the Mechanism of Zinc Oxide Crystallization and Its Antimicrobial Properties for the Surface Modification of Surgical Meshes, Materials, 10, doi:10.3390/ma10040353.

[200] J.P. Birk, 2018, Characteristic Reactions of Zinc Ions ($Zn_2{}^+$), Chemistry LibreTexts, https://chem.libretexts.org/Bookshelves/Analytical_Chemistry/Supplemental_Modules_

(Analytical_Chemistry)/Qualitative_Analysis/Characteristic_Reactions_of_Select_Metal_Ions/Characteristic_Reactions_of_Zinc_Ions_(Zn%C2%B2%E2%81%BA), Cited 12 March 2019.

[201] Y.J. Kim, J.-G. Hand and Y.J. Kim, 2004, Numerical Analysis of Flow Characteristics of an Atmospheric Plasma Torch, Cornell University, https://arxiv.org/abs/physics/0410237, Cited 23 November 2016.

[202] MatWeb, 2019, Material Property Data (Electronic dataset),www.matweb.com, Last accessed January 2020.

[203] D.R.Askeland and P.P. Fulay, 2010, Essentials of Materials Science and Engineering (Second Edition), Cengage Learning, Stamford, USA.

[204] J-S. Lee, Y-S. Lee, M-S. Kim, S-K. Hyun, C-H. Kang, J-S. So, and E-H. Yoon, 2013, Antibacterial Characteristics of Lotus-Type Porous Copper, Advances in Materials Science and Engineering, doi:10.1155/2013/608350.

[205] AGA (Electronic dataset), 2017, Zinc Metal Properties, American Galvanizers Association, https://galvanizeit.org/design-and-fabrication/design-considerations/zinc-metal-properties, Last accessed 2017.

[206] The Engineering Toolbox (Electronic dataset), www.engineeringtoolbox.com/, Last accessed 2017.

[207] V. Shah, 2007, Handbook of Plastics Testing and Failure Analysis (Third Edition), John Wiley & Sons, Inc.

[208] Unknown, Hardness Scale for Various Materials, AutoDrill, www.drill-hq.com/2011/11/hardness-scale-for-various-material, Cited January 2019.

[209] Professional Plastics (Electronic dataset), Thermal Properties of Plastic Materials, www.professionalplastics.com, Last accessed January 2017.

[210] General Electric Company, 2005, Lexan* 9030 Sheet - Product Datasheet, www.theplasticshop.co.uk/plastic_technical_data_sheets/lexan_polycarbonate_9030_technical_properties_data_sheet.pdf, Cited 12 July 2016.

[211] Victrex, 2014, Victrex PEEK 450G, www.victrex.com, Cited 13 July 2016.

[212] Ensinger, 2014, TECANAT natural - Stock Shapes, www.ensinger-online.com, Cited 16 February 2017.

[213] Unknown, ABS Material Data Sheet, http://teststandard.com/data_sheets/ABS_Data_sheet.pdf, Cited 8 July 2015.

[214] Stratasys, 2014, ABSplus-P430 - Production-Grade Thermoplastic for Design Series 3D Printers, Stratasys Inc., www.stratasys.com, Cited 17 July 2015.

[215] T. Osswald and J.P. Hernández-Ortiz, 2006, Chapter 2: Processing Properties, Polymer Processing - Modeling and Simulation, ISBNa 978156990-3988, www.hanserpublications.com/Products/195-polymer-processing.aspx, Cited 10 May 2019.

[216] Dielectric Corporation, PEEK (Polyetheretherketone) - General Material Properties, www.dielectriccorp.com/downloads/thermoplastics/peek.pdf, Cited 28 January 2019.

[217] S. Rahmati and A. Ghaei, 2013, The Use of Particle/Substrate Material Models in Simulation of Cold-Gas Dynamic-Spray Process, Journal of Thermal Spray Technology, 23: 532 - 540, doi:10.1007/s11666-013-0051-4.

[218] Keyence Corporation, 2018, Surface Roughness Analysis, www.keyence.com/ss/products/microscope/roughness/line/index.jsp, Cited 20 September 2018.

[219] Anton Paar, Advanced Mechanical Surface Testing - Biomedical Applications 3: Tribology and Frictional Behavior, www.anton-paar.com, Cited 25 June 2018.

[220] M.N. Sudin, F.R. Ramli, M.R. Alkahari and M.A. Abdullah, 2018, Comparison of Wear Behavior of ABS and ABS Composite Parts Fabricated via Fused Deposition Modelling, International Journal of Advanced and Applied Sciences, 5(1): 164 - 169, doi:10.21833/ijaas.2018.01.022.

[221] K. Boparai, R. Singh and H. Singh, 2015, Comparison of Tribological Behaviour for Nylon6-Al-Al_2O_3 and ABS Parts Fabricated by Fused Deposition Modelling, Virtual and Physical Prototyping, 10(2): 59 - 66, doi:10.1080/17452759.2015.1037402.

[222] D. Amrishraj and T. Senthilvelan, 2018, Dry Sliding Wear Behavior of ABS Composite Reinforce with Nano Zirconia and PTFE, Materials Today: Proceedings, 5: 7068 - 7077.

[223] J. Daintith and E. Martin (ed.), 2010, Oxford Dictionary of Science, Oxford University Press, Great Britain.

[224] R.S. Hine (ed.), 2008, Oxford Dictionary of Biology, Oxford University Press, Great Britain.

[225] ATCC, *Staphylococcus aureus subsp. aureus* (ATCC 25923^{TM}), https://www.lgcstandards-atcc.org/Products/All/25923.aspx, Last accessed March 2019.

[226] ATCC, *Pseudomonas aeruginosa* (ATCC 27853^{TM}), https://www.lgcstandards-atcc.org/products/all/27853.aspx, Last accessed March 2019.

[227] ATCC, *Candida albicans* (ATCC 10231^{TM}), https://www.lgcstandards-atcc.org/products/all/10231.aspx, Last accessed March 2019.

[228] ATCC, *Klebsiella pneumoniae subsp. pneumoniae* (ATCC 13887^{TM}), https://www.lgcstandards-atcc.org/products/all/13887.aspx, Last accessed March 2019.

[229] ATCC, *Enterococcus faecalis* (ATCC 29212^{TM}), https://www.lgcstandards-atcc.org/products/all/29212.aspx, Last accessed March 2019.

[230] ATCC, *Staphylococcus aureus subsp. aureus* (ATCC 33592^{TM}), https://www.lgcstandards-atcc.org/products/all/33592.aspx, Last accessed March 2019.

[231] BacDive, *Pseudomonas aeruginosa* (Schroeter 1872) Migula 1900, https://bacdive.dsmz.de/strain/24356, doi:10.13145/bacdive24356.20180622.3, Last accessed March 2019.

[232] WHO, Coronavirus disease (COVID-19) outbreak, https://www.who.int/emergencies/diseases/novel-coronavirus-2019, Last accessed March 2020.

[233] WHO, Rolling Updates on Coronavirus Disease (COVID-19), https://www.who.int/emergencies/diseases/novel-coronavirus-2019/events-as-they-happen, Last accessed April 2020.

Appendices

Appendix A - Theoretical Cold Spray Model Page 316

Appendix B - Taguchi Optimisation Procedure Page 371

Appendix C - Experimental Cold Spray Page 373

Appendix D - Antimicrobial Susceptibility Test Data Page 418

Appendix E - Coating Combinations Page 454

Appendix F - Research Consolidation Page 456

Appendix A Theoretical Cold Spray Model

Appendix A documents additional data regarding the theoretical cold spray model. The following is included:

- Model initialisation and setup Page 317
- Model nomenclature Page 317
- System constants Page 320
- Parameter Limitations Page 323
- Called functions Page 324
- System algorithm Page 327
- Python code Page 334
- Model selection Page 363

1. Model initialisation and setup

The cold spray theoretical model was programmed into Python. Python is an open source, high-level programming language. It integrates well with other programmes and software making it highly desirable for rapid and convenient use and interconnection with other applications. The following imported mathematics packages and symbol definitions were instituted.

Imported mathematics packages

From the 'math' package the following were imported: *, exp, erf, pi, sin, cos, tan, asin, acos, atan, log, log10.

Symbol definitions

```
degree_sign= u'\N{DEGREE SIGN}'
```

2. Model nomenclature

The following is a list of all terms and variables used within the main section of the model algorithm.

Model Nomenclature

D* - Nozzle throat diameter [mm - m]

D_e - Nozzle exit diameter [mm - m]

L - Nozzle diverging length [mm - m]

A* - Cross sectional area of the nozzle throat [m^2]

A_e - Cross sectional area of the nozzle exit [m^2]

SprayGas - Cold spray gas (air,nitrogen or helium)

γ - Ratio of specific heats

k_1 - Mach number analytical function constant [189]

k_2 - Mach number analytical function constant [189]

$M_{eApprox}$ - Approximated value for the nozzle exit Mach number [189]

xi - Initial guess at root value

f - Function

df - Derivative of function f

M_e - Mach number at nozzle exit

P_{amb} - Ambient laboratory pressure [Pa]

T_{amb} - Ambient laboratory temperature [°C]

P_y - Gas pressure behind the shock at nozzle exit [Pa]

M_x - Mach number in front of shock at nozzle exit

P_x - Gas pressure in front of shock at nozzle exit [Pa]

$P_{o-threshold}$ - threshold stagnation pressure [Pa]

P_{o-min} - Minimum allowable stagnation pressure [Pa]

P_{o-max} - Maximum allowable stagnation pressure [Pa]

T_{o-min} - Minimum allowable stagnation temperature [°C]

T_{o-max} - Maximum allowable stagnation temperature [°C]

Powder - Cold spray powder

Po - Operating stagnation pressure [Pa/MPa]

To - Operating stagnation temperature [°C/K]

R_{bar} - Universal gas constant [kJ/kmol·K]

M_m - Molecular mass [kg/kmol]

R - Characteristic gas constant [J/kg·K]

ρ_o - Stagnation density [kg/m^3]

P_e - Gas pressure at nozzle exit along centreline [Pa]

T_e - Gas temperature at nozzle exit along centreline [K]

ρ_e - Gas density at nozzle exit along centreline [kg/m^3]

V_e - Gas velocity at nozzle exit along centreline [m/s]

μ_{ref} - Reference dynamic viscosity [·s/m^2]

T_{ref} - Reference temperature [K]

S° - Sutherland's Law constant

μ_e - Dynamic viscosity at nozzle exit [N·s/m^2]

ν_e - Gas kinematic viscosity at nozzle exit [m^2/s]

β - Nozzle angle [radians]

L° - Effective flat plate length of the nozzle wall [m]

Re_e - Gas Reynolds number at nozzle exit

h - Nozzle exit diameter [m]

$M_{e-Approx}$ - Approximate nozzle exit Mach number

V_{e-ave} - Average gas flow velocity at nozzle exit [m/s]

ρ^* - Nozzle throat density [kg/m^3]

T* - Nozzle throat temperature [K]

V* - Nozzle throat velocity [m/s]

$\dot{m}$ - Choked mass flow rate [kg/s]

ρ_{e-ave} - Average gas flow density at nozzle exit [kg/m^3]

P_{e-ave} - Average gas flow pressure [Pa]

T_{e-ave} - Average gas flow temperature [K]

ff - Friction factor

n - Power Law constant

Pg_e - Gas pressure at nozzle exit [Pa]

Tg_e - Gas temperature at nozzle exit [K]

ρ_{g-e} - Gas density at nozzle exit [kg/m^3]

Vg_e - Gas velocity at nozzle exit [m/s]

Mg_e - Gas Mach number at nozzle exit

Cp - Specific heat at constant pressure [J/kg·K]

kg - Thermal conductivity of the gas [W/m·K]

$T_{ref-sutherland}$ - Reference temperature for Sutherland's Law [K]

Pr - Prandtl Number

Nus_D - Nusselt Number as a function of nozzle diameter

hc - Average heat transfer coefficient for gas flow [W/m^2 ·K]

dp - Powder particle diameter [m]

kp - Thermal conductivity of the spray powder [W/m·K]

Bi - Biot number

ρ_p - Density of the spray powder [kg/m^3]

$Vp_{e-Approx}$ - Approximate particle velocity at nozzle exit [m/s]

$V_{e-rel-Approx}$ - Relative flow velocity [m/s]

Re_{dp} - Reynolds number as a function of spray powder diameter

Nus_{dp} - Nusselt number as a function of spray powder diameter

As - Surface area of a sphere [m^2]

mp - Mass of a spray powder particle [kg]

T_{pa} - Initial spray particle temperature [K]

α_p - Thermal diffusivity of the spray powder [m^2/s]

t_n - Particle time in nozzle [s]

Tg* - Gas temperature at nozzle throat [K]

T_{ave} - Average gas temperature in cold spray nozzle [K]

Tp_e - Particle temperature at nozzle exit [K]

Mr_e - Relative Mach number

S - Molecular speed ratio

Mg - Gas Mach number

Cd_e - Effective drag coefficient

λ - Mean free path length [m]

Kn - Knudsen number

Ap - Circular area [m^2]

Vp_e - Particle velocity at nozzle exit

SOD - Nozzle standoff distance [mm - m]

D_i - Jet impingement diameter [m]

r_i - Jet impingement radius [m]

Nus_{eo} - Nusselt number (part)

Nus_e -Average flow Nusselt number

Vnozzle - Nozzle traverse speed [m/s]

t_s - Significant time of jet contact with substrate [s]

Substrate - Cold spray substrate material

ks - Thermal conductivity of the substrate [W/m·K]

ρ_s - Density of substrate [kg/m^3]

Cp_s - Specific heat at constant pressure of the substrate [J/kg·K]

α_s - Thermal diffusivity of the substrate [m^2/s]

T_{sa} - Initial substrate temperature [K]

T_s - Substrate Temperature [K]

Tvs - Substrate Vicat softening temperature [K]

Pg_2 - Gas pressure in front of bow shock [Pa]

Tg_2 - Gas temperature in front of bow shock [K]

ρ_{g-2} - Gas density in front of bow shock [kg/m^3]

Vg_2 - Gas velocity in front of bow shock [m/s]

θ - Deflction angle caused by oblique shock wave

P_{o2} - Stagnation pressure downstream of nozzle exit [Pa]

T_{o2} - Stagnation temperature downstream of nozzle exit [K]

M_{an1} -Mach number normal to oblique shock on entry

M_{an2} - Mach number normal to oblique shock on exit

Mg_2 - Mach number downstream of nozzle exit

$Ratio_1$ - Ratio of stagnation pressure to exit pressure

$Ratio_2$ - Ratio of ambient pressure to the stagnation pressure downstream or nozzle exit

$Ratio_3$ - Ratio of the nozzle exit temperature to stagnation temperature

$Ratio_4$ - Ratio of temperature behind the expansion waves to the corresponding stagnation temperature

$\theta_{1'}$ - Flow deflection angle caused by expansion waves w.r.t. upstream flow Mach number

$\theta_{2'}$ - Flow deflection angle caused by expansion waves w.r.t. downstream flow Mach number

$\theta_{overall'}$ - Overall system flow deflection angle caused by expansion waves

Mg_3 - Mach number downstream of the Bow Shock

Tg_3 - Gas temperature downstream of the bow shock [K]

Pg_3 - Gas pressure downstream of the bow shock [Pa]

$\rho_{g}-3$ - Gas density downstream of the bow shock [kg/m^3]

δ_{shock} - Bow shock standoff distance [m]

$Vrel_2$ - Relative gas flow velocity downstream of nozzle exit [m/s]

μ_2 - Dynamic viscosity in front of bow shock [N·s/m^2]

ν_2 - Kinematic viscosity in front of bow shock [m^2/s]

Re_2 - Relative Reynolds number in front of bow shock

Cd_2 - Flow drag coefficient in front of bow shock

$Vp_{i-Approx}$ - Approximate value for the particle impact velocity [m/s]

Vp_i - Particle impact velocity [m/s]

$Vrel_i$ - Relative impact velocity [m/s]

Re_i - Impact Reynolds number

Nus_i - Impact Nusselt number

Cp_p - Specific heat at constant pressure of the spray powder [J/kg·K]

t_G - Duration of spray particle within spray gap [s]

Tp_i - Particle impact temperature [K]

Pg_i - Gas pressure at point of substrate impingement [Pa]

Tg_i - Gas temperature at point of substrate impingement [K]

ρ_{g-i} - Gas density at point of substrate impingement [kg/m^3]

Vg_i - Gas velocity at point of substrate impingement [m/s]

Mg_i - Gas Mach number at point of substrate impingement

Trefp - Spray powder reference temperature [K]

Trefs - Substrate reference temperature [K]

Tp_m - Spray powder melting temperature [K]

Ts_i - Substrate temperature on impact [K]

Ts_m - Substrate melting temperature [K]

UTSs - Substrate ultimate tensile strength [Pa]

UTSp - Spray powder ultimate tensile strength [Pa]

Es - Substrate Young's Modulus

ρ_s - Substrate density

BHN_p - Spray powder Brinell hardness [Pa]

V_{crit} - Critical particle impact velocity [m/s]

$t_{penetration}$ - Duration of penetration [s]

$BHNmax_s$ - Substrate maximum Brinell hardness

$\theta_{p'}$ - Normalised particle impact temperature [K]

σ_p - Particle impact flow stress [Pa]

X - Particle depth of penetration [m]

3. System constants

The system and material properties for the cold spray model are tabulated below for convenience. Table A.1, Table A.2 and Table A.3 contain the relevant cold spray gas, powder and substrate properties used in this research. It was these properties that were parsed to the model algorithm detailed hereafter. In Table A.1 the thermal conductivity required the use of a second order polynomial equation from data given in [150].

Table A.1: Cold spray gas properties.

Property	**Units**	**Air**	**Nitrogen**	**Helium**
Specific heat ratio (γ) [147, 148]	/	1.4	1.4	1.667
Universal gas constant ($\overline{R}$) [148]	kJ/kmol·K	8.314	8.314	8.314
Molecular mass (M_m) [147, 148]	kg/kmol	28.97	28.02	4.003
Reference dynamic viscosity (μ_{ref})	N·s/m^2	1.81 x 10^{-5} [148]	1.784 x 10^{-5} [150]	1.864 x 10^{-4} [201]
Reference temperature (T_{ref})	K	293 [148]	300 [150]	273 [201]
Sutherland's Law reference temperature ($T_{ref-Sutherland}$) [147]	K	273	273	273
Sutherland's Law constant (S') [147]	K	110	111	79.4
Thermal conductivity (k) [150]	W/m·K	(-2 x 10^{-8}) x T_g^2) + (8 x 10^{-5}) x T_g) + 0.004	(-3 x 10^{-8}) x T_g^2) + (9 x 10^{-5}) x T_g) + 0.001 [i]	(-2 x 10^{-7}) x T_g^2) + (0.0005 x T_g) + 0.0021[i]

Table A.2: Cold spray feedstock powder properties.

Property	**Units**	**Copper (C5003)**	**Zinc (Z5001)**	**Nickel (N5001)**	**Tin (S6001)**	**Aluminium (A0050)**
Average particle size (dp)	μm	25 [176]	27.5 [178]	25	25	25
Density (ρ)	kg/m^3	8690 [202]	7100 [202]	8880 [202]	7265 [202]	2790 [203]
Thermal conductivity (k)	W/m·K	385 [202]	112.2 [202]	60.7 [202]	63.2 [202]	205
Particle mass (m)	kg	7.3304 x 10^{-11}	7.731 x 10^{-11}	7.265 x 10^{-11}	5.944 x 10^{-11}	2.283 x 10^{-11}
Melting temperature (T$_m$)	K	1356 [202]	692.58 [202]	1728 [202]	504.968 [202]	983
Ultimate tensile strength (UTS)	Pa	210 x 10^6 [202]	124 x 10^6 [205]	317 x 10^6 [202]	220 x 10^6 [202]	110 x 10^6 [206]
Reference temperature (T$_{ref}$)	K	293	293	293	293	293
Specific heat at constant pressure (Cp) [150]	J/kg·K	383	385	446	227	896
Bulk metal Brinell hardness (BHN$_p$)	/	89 [202]	95 [207]	187 [208]	17 [207]	73 [207]

Table A.3: Cold spray substrate properties.

Property	Units	ABS	Lexan	PEEK	PC	Copper	Zinc	Nickel	Tin	Aluminium	Stainless steel
Thermal conductivity	W/m·K	0.17 [209]	0.2 [210]	0.29 [211]	0.25 [212]	385 [202]	112.2 [202]	60.7 [202]	63.2 [202]	205 [206]	16.3 [202]
Density	kg/m^3	1040 [213]	1200 [210]	1300 [211]	1190 [212]	7764 [202]	7100 [202]	8880 [202]	7265 [202]	2790 [203]	8030 [202]
Reference temperature	K	293	293	293	293	293	293	293	293	293	293
Melting temperature	K	381 [214]	418 [210]	616 [211]	422 [212]	1356 [202]	693 [202]	1728 [202]	505 [202]	933 [206]	1672 [202]
Ultimate tensile strength	Pa	33 X 10^6 [214]	70 x 10^6 [210]	98 x 10^6 [211]	69 x 10^6 [212]	210 x 10^6 [202]	124 x 10^6 cite176	317 x 10^6 [202]	220 x 10^6 [202]	110 x 10^6 [206]	515 x 10^6 [202]
Young's Modulus	Pa	2.2 x 10^9 [214]	2.35 x 10^9 [210]	4 x 10^9 [211]	2.2 x 10^9 [212]	110 x 10^9 [202]	96.5 x 10^9 [202]	207 x 10^9 [202]	41.6 x 10^9 [202]	69 x 10^9 [206]	212 x 10^9 [202]
Brinell Hardness	/	40 [214]	22 [214]	35 [214]	22 [214]	89 [202]	95 [207]	187 [208]	17 [207]	73 [207]	217 [202]
Thermal diffusivity	m^2/s	170 x 10^{-9} [215]	/	166 x 10^{-9} [211, 216]	147 x 10^{-9} [215]	116.6 x 10^{-6} [150]	44 x 10^{-6} [150]	22.9 x 10^{-6} [150]	51.3 x 10^{-6} [150]	97.5 x 10^{-6} [150]	0.387 x 10^{-5} [150]
Specific heat at constant pressure (Cp)	J/kg·K	1424 [206]	1100 [206]	1340 [216]	1100 [206]	383 [150]	385 [150]	446 [150]	227 [150]	896 [150]	461 [150]

4. Parameter Limitations

Global system constraints

The global system constraints were enforced as a means of protecting the cold spray equipment, based on equipment limitations as given by the cold spray operating manual [16]. Operating pressure was to be greater than 0.55 MPa, but less than 1.72 MPa. Operating temperature was never to exceed 823 K ($\approx 550°C$).

Boundary powder recommendations

Boundary powder recommendations provide recommended parameter settings, but were not enforced as system limitations. These recommendations are as given by the relevant cold spray powder data sheets.

- Copper [176]
  - Operating temperature (T_0) $\rightarrow <$ 723 K
  - Nozzle standoff distance (SOD) $\rightarrow 10 <$ SOD < 15 mm
  - Nozzle traverse speed (Vn) $\rightarrow 10 <$ Vn < 500 mm/s
- Nickel [177]
  - Operating temperature (T_0) $\rightarrow <$ 823 K
  - Nozzle standoff distance (SOD) $\rightarrow 10 <$ SOD < 15 mm
  - Nozzle traverse speed (Vn) $\rightarrow 10 <$ Vn < 250 mm/s
- Zinc [178]
  - Operating temperature (T_0) $\rightarrow <$ 673 K
  - Nozzle standoff distance (SOD) $\rightarrow 10 <$ SOD < 15 mm
  - Nozzle traverse speed (Vn) $\rightarrow 10 <$ Vn < 200 mm/s
- Tin [179]
  - Operating temperature (T_0) $\rightarrow <$ 498 K
  - Nozzle standoff distance (SOD) $\rightarrow 10 <$ SOD < 15 mm
  - Nozzle traverse speed (Vn) $\rightarrow 10 <$ Vn < 250 mm/s
- Aluminium [180]
  - Operating temperature (T_0) $\rightarrow <$ 823 K
  - Nozzle standoff distance (SOD) $\rightarrow 10 <$ SOD < 15 mm
  - Nozzle traverse speed (Vn) $\rightarrow 10 <$ Vn < 500 mm/s

Boundary substrate recommendations

Boundary substrate recommendations provide recommended parameter settings, but were not enforced as system limitations. These recommendations are as given by the relevant material data sheets. The key substrate material property was that of operating temperature, which was limited to the following:

- Copper: 1356 K [202]
- Nickel: 1728 K [202]
- Zinc: 693 K [202]
- Tin: 505 K [202]
- Aluminium: 2327 K [202]
- ABS: 381 K [214]
- Lexan/Polycarbonate: 418 K [210]
- PEEK: 416 K [211]

5. Called functions

In accordance with the modular design strategy used in developing and subsequently programming the cold spray theoretical model, repeatedly used sub processes were isolated and implemented as called functions. This shortened the overall code length and reduced the risk of calculation error caused by inaccurate replication of relevant functions.

The model functions and their respective terms are detailed in Table A.4.

Table A.4: Model function nomenclature for theoretical cold spray model

Function Number	Function Name and Equation	Variable Name	Variable Symbol	Units
#1	Circular area $\left(A = \pi \frac{D}{2}^2\right)$	• Diameter • Area	D A	m m^2
#2	Basic root finding method $(x = f(x))$	• An initial guess at the root • Function in the form f(x)	x f	/ /
#3	Specific gas constant $\left(R = \frac{\overline{R}}{Mm}\right)$	• Molecular mass of gas • Universal gas constant • Characteristic gas constant	Mm $\overline{R}$ R	kg/mol J/mol·K J/kg·K

Function Number	Function Name and Equation	Variable Name	Variable Symbol	Units
#4	Ideal gas law $(P = \rho RT)$	• Chosen parameter to be calculated	Q	/
		• Pressure	P	Pa
		• Temperature	T	K
		• Density	ρ	kg/m^3
		• Characteristic gas constant	R	J/kg·K
#5	Mach number $\left(M = \frac{V}{\sqrt{\gamma RT}}\right)$	• Chosen parameter to be calculated	Q	/
		• Mach number	M	/
		• Velocity	V	m/s
		• Ratio of specific heats	γ	/
		• Characteristic gas constant	R	J/kg·K
		• Temperature	T	K
#6	Sutherland's Law [147] $\left(\mu = \mu_{ref}\left(\frac{T}{T_{ref}}\right)^{\frac{3}{2}}\frac{T_{ref}+S'}{T+S'}\right)$	• Reference dynamic viscosity	μ_{ref}	N·s/m^2
		• Temperature	T	K
		• Reference temperature	T$_{ref}$	K
		• Sutherland's Law constant	S$_{ref}$	/
		• Dynamic viscosity	μ	N·s/m^2
#7	Reynolds Number $\left(Re = \frac{V \cdot Lc}{\nu}\right)$	• Velocity	V	m/s
		• Characteristic length	Lc	m
		• Kinematic viscosity	ν	m^2/s
		• Reynoldss Number	Re	/
#8	Specific heat capacity at constant pressure $\left(Cp = \frac{\gamma \cdot R}{\gamma - 1}\right)$	• Ratio of specific heats	γ	/
		• Characteristic gas constant	R	J/kg·K
		• Specific heat capacity at constant pressure	Cp	J/kg·K
#9	Approximate particle velocity [119, 149] $\left(Vp' = \frac{V}{1+\left(0.85\sqrt{\frac{dp}{x}}\sqrt{\frac{\rho V^2}{Po}}\right)}\right)$	• Velocity	V	m/s
		• Spray particle diameter	d$_p$	m
		• Distance from the nozzle throat along diverging section	x	m
		• Density	ρ	kg/m^3
		• Operating pressure	Po	Pa
		• Approximate particle velocity	Vp'	m/s
#10	Thermal diffusivity [147] $\left(\alpha = \frac{k}{\rho Cp}\right)$	• Thermal conductivity	k	W/m·K
		• Density	ρ	kg/m63
		• Specific heat at constant pressure	Cp	J/kg·K

Function Number	Function Name and Equation	Variable Name	Variable Symbol	Units
		• Thermal diffusivity	α	m^2/s
#11	Mean free path length $\left(\lambda = 1.26\frac{\mu}{\rho\sqrt{R \cdot T}}\right)$	• Dynamic viscosity • Density • Characteristic gas constant • Temperature • Mean free path length [147]	μ ρ R T λ	N·s/m^2 kg/m^3 J/kg·K K m
#12	Knudsen Number [147] $\left(Kn = \frac{\lambda}{dp}\right)$	• Mean free path length • Spray particle diameter • Knudsen Number	λ dp Kn	m m /
#13	Cunningham correction factor [190] $\left(Cc = 1 + \frac{2\lambda}{dp}\left[1.257 + 0.4e^{-\frac{1.1dp}{2\lambda}}\right]\right)$	• Mean free path length • Spray particle diameter • Drag coefficient • Cunningham correction factor	λ dp Cd Cc	m m / /
#14	Spherical mass $\left(m = \frac{4\pi\rho}{3}\left(\frac{D}{2}\right)^3\right)$	• Density • Diameter • Mass	ρ D m	kg/m^3 m kg
#15	Nozzle angle $\left(\beta = tan^{-1}\left(\frac{2L}{De - D*}\right)\right)$	• Nozzle diverging section length • Nozzle exit diameter • Nozzle throat diameter • Nozzle angle	L De D* β	m m m rad
#16	Prandtl Number [150] $\left(Pr = \frac{Cp\mu}{k}\right)$	• Specific heat at constant pressure • Dynamic viscosity • Thermal conductivity • Prandtl Number	Cp μ k Pr	J/kg·K N·s/m^2 W/m·K /
#17	Heat transfer coefficient for the particle [150] $\left(hc = \frac{Nus \cdot k}{Lc}\right)$	• Nusselt Number • Thermal conductivity • Characteristic length • Average heat transfer coefficient	Nus k Lc hc	/ W/m·K m W/m^2 ·
#18	Biot Number [150] $\left(Bi = \frac{hc \cdot Lc}{k}\right)$	• Average heat transfer coefficient • Characteristic length • Thermal conductivity • Biot Number	hc Lc k Bi	W/m^2 · m W/m·K /
#19	Surface area of a sphere $\left(As = 4\pi\frac{D}{2}^2\right)$	• Diameter • Surface area of a sphere	D As	m m^2

Function Number	Function Name and Equation	Variable Name	Variable Symbol	Units
#20	Normalised temperature [150] $\left(\theta' = \frac{T - T_{ref}}{Tm - T_{ref}}\right)$	• Temperature	T	K
		• Reference temperature	T_{ref}	K
		• Melting temperature	Tm	K
		• Normalised temperature	θ'	/
#21	Flow stress [118] $(\sigma = UTS(1 - \theta'))$	• Ultimate tensile strength	UTS	Pa
		• Normalised temperature	θ'	/
		• Flow stress	σ	Pa
#22	Newton's root finding method $\left(x_{i+1} = x_i - \frac{f(x_i)}{f'(x_i)}\right)$	• Intermediate root value	xi	/
		• Function	f	/
		• First derivative of the function	df	/

Details of the two root finding methods used are detailed below.

Basic fixed point root finding method
An iterative fixed point method for non-linear equations was employed. This method solves equations of the form x = f(x).

An initial guess is made for the value of x. This initial guess may either be based on expected parameter ranges or via empirical formulations. This value for x is subsequently substituted into f(x) to obtain a new approximation. This process is repeated until the value for x converges, or achieves an acceptable level of accuracy.

Newton's fixed point root finding method
A similar approach to solving non-linear equations as above is made using Newton's fixed point root finding method. Here the equation is of the form $x_{i+1} = x_i - \frac{f(x_i)}{f'(x_i)}$.

6. System algorithm

The various mathematical derivations made in the process of developing the cold spray theoretical model are reproduced here.

Derivation 1: Combined heat transfer equation

This equation was used to evaluate the spray particle temperature at the nozzle exit.

Combined Heat Transfer Equation

$\dot{q} = m_P C_P \frac{dT_P}{dt}$ and $\dot{q} = \overline{h_c} A_s \Delta T$ are both heat transfer equations. Therefore equating $\dot{q}$ gives:

$$m_P C_P \frac{dT_P}{dt} = \overline{h_c} A_s \Delta T \qquad \boxed{\frac{dT_P}{dt} = \frac{dT_P}{dx} V_P}$$

$$\rightarrow dT_P V_P = \frac{\overline{h_c} A_s (T_{ge} - T_{Pe})}{m_p C_P} dx$$

$$\rightarrow \frac{dT_P}{(T_{ge} - T_{Pe})} V_P = \frac{\overline{h_c} A_s}{m_p C_P} dx$$

$$\rightarrow V_P \int_{T_{Pa}}^{T_{Pb}} \frac{dT_P}{(T_{ge} - T_{Pe})} = \int_{x_a}^{x_b} \frac{\overline{h_c} A_s}{m_p C_P} dx$$

a = initial value of the quantity

b = final value of the quantity

This is of the form: $\int (ax + b)^{-1} dx = \frac{1}{a} \ln|ax + b| + c$

$$\therefore V_P \left(\frac{1}{-1} \ln|-1('T_P') + T_{ge}| \right) \Big|_{T_{Pa}}^{T_{Pb}} = \frac{\overline{h_c} A_s x}{m_p C_P} \Big|_{x_a}^{x_b}$$

$$\rightarrow V_P \left(-\ln|-T_{Pb} + T_{ge}| + \ln|-T_{Pa} + T_{ge}| \right) = \frac{\overline{h_c} A_s x_b}{m_p C_P} - \frac{\overline{h_c} A_s x_a}{m_p C_P}$$

$$\rightarrow V_P \left(-\ln|T_{ge} - T_{Pb}| + \ln|T_{ge} - T_{Pa}| \right) = \frac{\overline{h_c} A_s x_b}{m_p C_P} - \frac{\overline{h_c} A_s x_a}{m_p C_P}$$

$$\rightarrow V_P \ln|T_{ge} - T_{Pb}| = \frac{\overline{h_c} A_s x_b}{m_p C_P} - \frac{\overline{h_c} A_s x_a}{m_p C_P} - V_P \ln|T_{ge} - T_{Pa}|$$

$$\rightarrow \ln|T_{ge} - T_{Pb}| = -\frac{1}{V_P} \left(\frac{\overline{h_c} A_s x_b}{m_p C_P} - \frac{\overline{h_c} A_s x_a}{m_p C_P} \right) + \ln|T_{ge} - T_{Pa}|$$

$$\rightarrow |T_{ge} - T_{Pb}| = e^{\left(-\left(\frac{\overline{h_c} A_s x_b}{m_p C_P V_P} - \frac{\overline{h_c} A_s x_a}{m_p C_P V_P} \right) + \ln|T_{ge} - T_{Pa}| \right)}$$

a = 0 (Nozzle throat)
b = e (Nozzle exit)
x = 0 at throat

Now for the specific case of particle temperature at the nozzle exit

IF $T_e > T_{Pa}$

$$T_{Pe} = T_{ge} - e^{\left(-\frac{\overline{h_c} A_s L}{m_p C_P V_P} + \ln|T_{ge} - T_{Po}| \right)}$$

IF $T_e < T_{Pa}$

$$T_{Pe} = T_{ge} + e^{\left(-\frac{\overline{h_c} A_s L}{m_p C_P V_P} + \ln|T_{ge} - T_{Po}| \right)}$$

Derivation 2: Particle velocity model

Based on a drag force relationship a non-linear expression for particle velocity dependent on particle properties and carrier gas velocity.

Particle Velocity Model

$$F_{drag} = m_p a$$

$$= m_p \frac{dV_P}{dt}$$

$$\therefore m_p \frac{dV_P}{dt} = \frac{C_D A_P \rho_g (V_g - V_P)^2}{2}$$

$$\boxed{\frac{dV_P}{dt} = \frac{dV_P}{dx} \cdot V_P}$$

$$\therefore \frac{V_P}{(V_g - V_P)^2} dV_P = \frac{C_D A_P \rho_g}{2m_p} dx$$

$$\rightarrow \int_{V_{Pa}}^{V_{Pb}} \frac{V_P}{(V_g - V_P)^2} dV_P = \int_{x_a}^{x_b} \frac{C_D A_P \rho_g}{2m_p} dx$$

The LHS of the equation is of the form: $\int \frac{u}{(a+bu)^2} du = \frac{1}{b^2}\left(\frac{a}{a+bu} + \ln|a+bu|\right) + c$

$$\therefore \frac{1}{(-1)^2}\left(\frac{V_g}{V_g - V_{Pb}} + \ln|V_g - V_{Pb}|\right) - \frac{1}{(-1)^2}\left(\frac{V_g}{V_g - V_{Pa}} + \ln|V_g - V_{Pa}|\right) = \frac{C_D A_P \rho_g x_b}{2m_p} - \frac{C_D A_P \rho_g x_a}{2m_p}$$

For the case in question where the particle velocity and x are zero at the throat (at position a) and the velocity required is the particle velocity at the nozzle exit.

$$\therefore \frac{V_{ge}}{V_{ge} - V_{Pe}} + \ln|V_{ge} - V_{Pe}| - (1 + \ln(V_{ge})) = \frac{C_D A_P \rho_{ge} L}{2m_p}$$

$$\rightarrow \ln|V_{ge} - V_{Pe}| - \ln(V_{ge}) + \frac{V_{ge}}{V_{ge} - V_{Pe}} - 1 = \frac{C_D A_P \rho_{ge} L}{2m_p}$$

$$\rightarrow \ln\left|\frac{V_{ge} - V_{Pe}}{V_{ge}}\right| + \frac{V_{ge}}{V_{ge} - V_{Pe}} - 1 = \frac{C_D A_P \rho_g L}{2m_p}$$

In order to apply the basic fixed point root finding method, the equation needs to be of the form x = f(x).

$$V_{P_e} = \frac{V_{ge}}{\ln\left|\frac{V_{ge} - V_{P_e}}{V_{ge}}\right| - 1 - \frac{C_D A_p \rho_e L}{2m_p}} + V_{ge}$$

Derivation 3: Substrate temperature

Employing submerged jet modelling the substrate temperature as a result of an impinging cold spray jet was derived.

The substrate temperature as a consequence of the impinging submerged jet was calculated based on certain heat transfer correlations. The flow exiting the cold spray nozzle, between the nozzle exit and the substrate, is a free jet. A free jet is a fluid flow where the flow of the jet is not constrained or supported by a parallel surface [147]. Considering the circular jet produced by the cold spray system the jet may be further classified as a submerged jet [147], since the jet is essentially an air jet issuing into a stationary air medium. Such a jet is affected by the shear stress at the substrate and a significant amount of the surrounding fluid is dragged by the jet. This entrained flow affects the flow and heat transfer characteristics of the jet. The effects of gravity are able to be neglected.

The jet can be divided into three main regions: the free jet, the stagnation region and the wall region [150] - as depicted in Figure A.1.

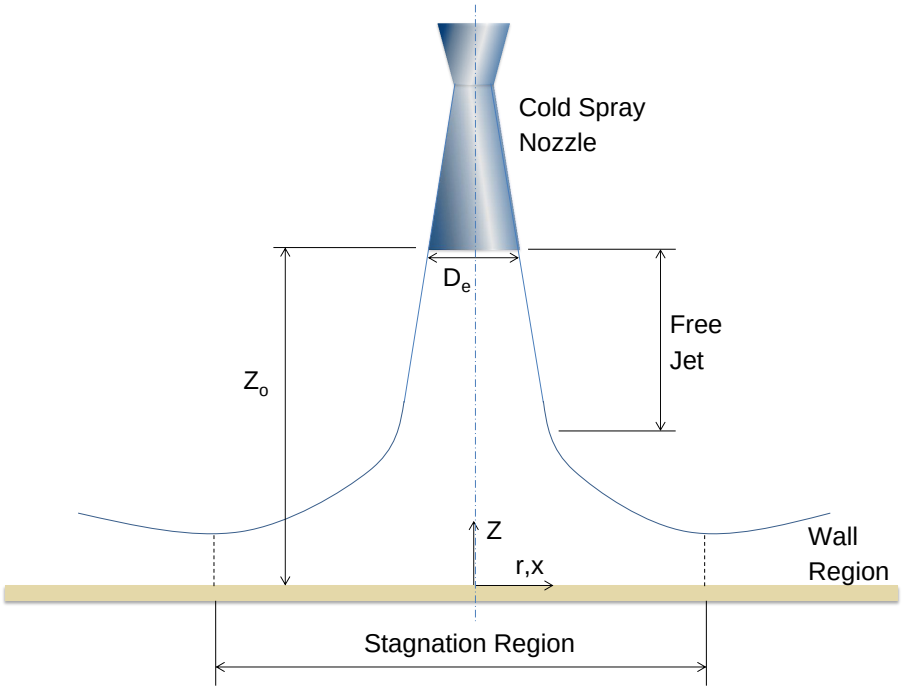


Figure A.1: Impinging cold spray jet regions

The free jet region is the region of the jet unaffected by the substrate's presence. The velocity component perpendicular to the axis of the jet was considered negligible when compared to the axial component. The stagnation region is the region of the jet that is affected by the substrate. The axial velocity decreases while the velocity component parallel to the substrate increases. The wall region observes a negligibly small axial component when compared to the flow velocity parallel to the substrate.

Modelling a single round submerged jet was conducted with the aim of estimating the jet induced substrate surface temperature. An analytical solution to transient heat conduction was carried out.

It was assumed that the effect of the jet may be modelled as a sudden application of a specified heat flux (q' - [W/m^2]). The model was derived as follows:

Substrate Temperature

Submerged jet modelling employs a specific Nusselt number calculated from:

$$\overline{N_{uD_e}} = \left[8.1{R_e}_D^{0.523} + 0.133\left(\frac{r_i}{D_e} - 4\right){R_e}_D^{0.828}\right]\left(\frac{D_e}{r_i}\right)^2 \cdot P_r^{0.33}$$

This is used in the determination of the average heat transfer coefficient of the flow.

$$\overline{h_c} = \frac{\overline{N_{uD_e}} \cdot k_f}{D_e}$$

Which itself is applied to the formula for Newton's Law of Cooling

$$\acute{q} = \overline{h_c}(T_s - T_{ge})$$

This is later substituted into the equation based on a Semi Infinite Solid heat transfer analysis. The governing equation is given by:

$$T_{s(x,t)} - T_{s_a} = \frac{2\acute{q}\left(\frac{\alpha t}{\pi}\right)^{\frac{1}{3}}}{k_s} e^{\left(\frac{-x^2}{4\alpha_s t}\right)} - \frac{\acute{q}x}{k_s} erfc\left(\frac{x}{2\sqrt{\alpha t}}\right)$$

where:

x = the perpendicular distance from the substrate surface into the material

t = the significant time of jet contact with the substrate. This value is estimated by considering the jet impingement diameter on the substrate, based on an extended nozzle exit area and the nozzle standoff distance.

$$D_i = \frac{2Z_o}{\tan(\beta)} + D_e$$

$$t = \frac{D_i}{V_{nozzle}}$$

The surface temperature is the temperature of interest. Therefore considering the case where x = 0 and substituting the heat flux suggested by Newton's Law of Cooling into the transient equation for substrate temperature, the following results.

$$T_s = T_{s_a} + \frac{2\overline{h_c}(T_s - T_{ge})\left(\frac{\alpha_s t}{\pi}\right)^{\frac{1}{2}}}{k_s}$$

The induced surface temperature is required to be less than either the substrate melting temperature or the Vicat softening temperature.

The submerged jet heat transfer method involves the following sub-procedures:

Sub-step 1 Calculate the nozzle deflection angle (β).

Called Function: *#15 - Nozzle Angle*
Parsed Variables: L, D_e, D*
Returned Value: β

Sub-step 2 Calculate the jet impingement diameter (D_i).

$$D_i = \frac{2Z_0}{tan(\beta)} + D_e \tag{A.1}$$

where:
Z_0 is the nozzle standoff distance.
D_e is the nozzle exit diameter.

Sub-step 3 Calculate the impingement radius (r_i)

$$r_i = \frac{D_i}{2} \tag{A.2}$$

Sub-step 4 Calculate the flow Reynolds number at the nozzle exit (Re_e).

Called Function: *#7 - Reynolds Number*
Parsed Variables: V_{ge}, D_e, ν_e
Returned Value: Re_e

Sub-step 5 Calculate the Prandtl Number (Pr).

Called Function: *#16 - Prandtl Number*
Parsed Variables: Cp, μ_e, k_g
Returned Value: Pr

Sub-step 6 Calculate the average flow Nusselt number at the nozzle exit (Nus_e) [150].

Assuming that the impinging jet may be modelled as a single round jet, [150] proposes the use of Equation A.3, Equation A.4 and Equation A.5.

$$Nus_{e0} = 1.29 * (Re_e^{0.5}) Pr^{0.4} \tag{A.3}$$

- If $\frac{r_i}{D_e} < 2$:

$$Nus_e = Nus_{e0}\left[\frac{tanh(0.88r_i/D_e)}{r_i/D_e}\right]^{\frac{1}{2}} \tag{A.4}$$

- If $\frac{r_i}{D_e} > 2$:

$$Nus_e = \frac{1.69Nus_{e0}}{(r_i/D_e)^{1.07}} \tag{A.5}$$

Sub-step 7 Calculate the average heat transfer coefficient of the gas flow at nozzle exit (hc).

Called Function: *#17 - Average Heat Transfer Coefficient*
Parsed Variables: Nus_e, k_g, D_e
Returned Value: hc

Sub-step 8 Calculate the effective jet impingement dwell time (t_s).

$$t_s = \frac{D_i}{V_n} \tag{A.6}$$

where V_n is the user defined[i] nozzle traverse speed.

Sub-step 9 Calculate the resultant substrate temperature (T_s).

Using Newtons Fixed Point Root Finding Method and the derived heat transfer expression Equation A.7.

$$T_s = T_{s0} + \frac{2hc(T_s - T_{ge})(\frac{\alpha_s t}{\pi})^{0.5}}{k_s} \tag{A.7}$$

where:
T_{s0} is the initial substrate temperature
α_s is the thermal diffusivity of the substrate material.
k_s is the thermal conductivity of the substrate material.

Called Function: *#22 - Newtons Method*
Parsed Variables: T_{s0}, $\mathrm{f}(\mathrm{T}_s)$, $\mathrm{f}'(\mathrm{T}_s)$
Returned Value: T_s

To avoid thermal damage to the substrate material the surface temperature calculated above should be less that the Vicat softening temperature of the substrate (T_{vs}), i.e. $T_s < T_{vs}$.

[i] For a manual parameter set check the nozzle traverse speed is user defined, yet if the model is being used in conjunction with the Taguchi optimisation procedure then this quantity is the target variable and allocated a given value as part of the optimisation protocol

7. Python code

The complete and current (March 2020) version of the Python code for the theoretical cold spray model is reproduced here. The algorithm itself underwent continuous cycles of development, based on feedback throughout the research progress. This final version was the culmination of all aspects of the current research. Previous versions were used to achieve the various developmental steps, with their results influencing this final version. What is presented here is, therefore, the latest version.

```
"""
Author: Michael David Ian Lucas
Date: Started: 2016-11-15
      Provisional completion: 2016-12-7
      Model check: 2017-01-18
      Final completion: 2019-03-20
      First Revision: 2020-02-25
      Second Revision: 2020-04-03

Programme: Theoretical Cold Spray Model

Model Description
The theoretical cold spray model is an optimisation tool for the cold spray process. The
model itself is an algorithm for determining the depth of penetration of cold spray particles
into a specified substrate.

The procedure also determines both flow and particle conditions at points of interest within
the system, namely: the nozzle exit, the bow shock and particle-substrate interactions.
Calculation of the critical particle velocity is also made, which is to be compared to the
predicted particle velocity as a way of evaluating deposition quality. Heat transfer calculations
are included, improving the accuracy of evaluated flow quantities.

The program is divided into six sections:
1 - Setup
    This section includes any mathematics that need to be imported and additional packages
    that may need to be included.

2 - Nomenclature
    A list of all variable names was included in original programme, yet omitted from inclusion
    in the PhD thesis.

3 - System Constants
    The system constants are defined in this section. It is suggested that a user confirm the
    correctness of these values before running the code, as these remain unchanged throught
    the course of the program. The system constants include the definition of material
    properties to the spray gas, spray powder, substrate.

4 - Parameter Limitations
    The model boundary conditions are defined and enforced here. These include both cold spray
    equipment limitations, cold spray powder and substrate material limitations, as well as
    user defined limits.

5 - Called Functions
    All repeatedly used and standalone functions are defined within separate functions. This is
    to aid model verification and debugging.
```

```
6 - Main Code
    All main procedural steps are built within this section, and the required functions are
    called from here. The main code itself is further divided into model steps corresponding
    with the detailed model procedure.
"""
#_____________________________________________________________________________________________________
#Setup
    #Imported packages
import math
from math import *
from math import exp
from math import erf
from math import pi
from math import sin
from math import cos
from math import tan
from math import asin
from math import acos
from math import atan
from math import log
from math import log10
import csv

    #symbol definitions
degree_sign= u'\N{DEGREE SIGN}'
#_____________________________________________________________________________________________________
#NOTE: References do not correspond with thesis references. Refer to given model algorithm.
#System Constants
    #Cold Spray Gas Properties
def GasProperties(Gas,Property,Gas_Temp):
    if Gas == "Air" or Gas == "air":
        if Property == "gamma":     #Specific Heat Ratio
            Val_Q = float(1.4)      #REF: [149][150]
        elif Property == "R_bar":   #Universal Gas Constant
            Val_Q = float(8.314)    #kJ/kmol.K REF: [150]
        elif Property == "M_m":
            Val_Q = float(28.97)    #kg/kmol REF: [150]
        elif Property == "Mu_ref":
            Val_Q = float(1.81*10**(-5)) #N.s/m^2 at 20degcel REF: [150]
        elif Property == "T_ref":
            Val_Q = float(293)      #K REF: [150]
        elif Property == "T_ref_sutherland":
            Val_Q = float(273)      #K REF: [149]
        elif Property == "S_dash":
            Val_Q = float(110)      #K REF: [149]
        elif Property == "Thermal Conductivity":
            Val_Q = float(((-2*10**(-8))*Gas_Temp**2) + ((8*10**(-5))*Gas_Temp) + 0.004)
            #W/m.K  using a second order polynomial equation from the data from REF[152]
        else:
            print "error"

    elif Gas == "Nitrogen" or Gas == "nitrogen":
        if Property == "gamma":
            Val_Q = float(1.4)      #REF: [150][149]
```

```
        elif Property == "R_bar":
            Val_Q = float(8.314)    #kJ/kmol.K REF: [150]
        elif Property == "M_m":
            Val_Q = float(28.02)    #kg/kmol REF: [Potter][White]
        elif Property == "Mu_ref":
            Val_Q = float(1.784*10**(-5)) #N.s/m^2 at 27degcel REF: [Heat]
        elif Property == "T_ref":
            Val_Q = float(300)      #K REF: [Heat]
        elif Property == "T_ref_sutherland":
            Val_Q = float(273)      #K REF: [White]
        elif Property == "S_dash":
            Val_Q = float(111)      #K [msc244]
        elif Property == "Thermal Conductivity":
            Val_Q = float(((-3*10**(-8))*Gas_Temp**2) + ((9*10**(-5))*Gas_Temp) + 0.001)
            #W/m.K using a second order polynomial equation from the data from REF[Heat]
        else:
            print "error"

    elif Gas == "Helium" or Gas == "helium":
        if Property == "gamma":
            Val_Q = float(1.667)    #REF:[Potter]
        elif Property == "R_bar":
            Val_Q = float(8.314)    #kJ/kmol.K REF: [Potter]
        elif Property == "M_m":
            Val_Q = float(4.003)    #kg/kmol REF: [Potter][White]
        elif Property == "Mu_ref":
            Val_Q = float(1.864*10**(-4)) #N.s/m^2 at 0degcel REF: [244]
        elif Property == "T_ref":
            Val_Q = float(273)      #K REF: [244]
        elif Property == "T_ref_sutherland":
            Val_Q = float(273)      #K REF: [White]
        elif Property == "S_dash":
            Val_Q = float(79.4)     #K [MSc244]
        elif Property == "Thermal Conductivity":
            Val_Q = float(((-2*10**(-7))*Gas_Temp**2) + (0.0005*Gas_Temp) + 0.0021)
        #W/m.K using a second order polynomial equation from the data from REF[Heat]
        else:
            print "error"

    else:
        print "error"

    return Val_Q

    #Cold Spray Powder Properties
def PowderProperties (Powder,Property):
    if Powder == "Copper" or Powder == "copper" or Powder == "Cu":  #C5003
        if Property == "Diameter":
            Val_Q = float(25*10**(-6)) # 25 um average value REF:[5]
        elif Property == "Density":
            Val_Q = float(8960)#kg/m^3 REF:[Matweb] assuming equivalent to cold worked
                               #copper
        elif Property == "Thermal Conductivity":
            Val_Q = float(385)      #W/m.K REF:[Matweb]
        elif Property == "Particle Mass":
```

```
        Val_Q = float(7.3304*10**(-11)) #kg
    elif Property == "Melting Temperature":
        Val_Q = float(1356)     #K REF:[Matweb]
    elif Property == "UTS":
        Val_Q = float(210*10**(6))      #Pa REF[Matweb] annealed Copper
    elif Property == "Reference Temperature":
        Val_Q = float(293)      #K
    elif Property == "Cp":
        Val_Q = float(383)      #J/kg.K [Heat]
    elif Property == "Brinell Hardness":
        Val_Q = float(89) #REF:[Matweb]
    else:
        print "error"

elif Powder == "Zinc" or Powder == "zinc" or Powder == "Zn": #Z5001
    if Property == "Diameter":
        Val_Q = float(27.5*10**(-6)) #m average value REF:[38]
    elif Property == "Density":
        Val_Q = float(7100) #kg/m^3 REF:[Matweb]
    elif Property == "Thermal Conductivity":
        Val_Q = float(112.2) #W/m.K REF:[Matweb]
    elif Property == "Particle Mass":
        Val_Q = float(7.731*10**(-11)) #kg
    elif Property == "Melting Temperature":
        Val_Q = float(692.58) #K REF:[Matweb]
    elif Property == "UTS":
        Val_Q = float(124*10**(6)) #Pa REF:[AGA - American Galvanizers Association]
    elif Property == "Reference Temperature":
        Val_Q = float(293) #K
    elif Property == "Cp":
        Val_Q = float(385) #J/kg.K [Heat]
    elif Property == "Brinell Hardness":
        Val_Q = float(95) #Average value from REF:[250]
    else:
        print "error"

elif Powder == "Nickel" or Powder == "nickel" or Powder == "Ni": #N5001
    if Property == "Diameter":
        Val_Q = float(25*10**(-6)) #m REF:[245]
    elif Property == "Density":
        Val_Q = float(8880) #kg/m^3 REF:[Matweb]
    elif Property == "Thermal Conductivity":
        Val_Q = float(60.7) #W/m.K REF:[Matweb]
    elif Property == "Particle Mass":
        Val_Q = float(7.265*10**(-11)) #kg
    elif Property == "Melting Temperature":
        Val_Q = float(1728) #K REF:[Matweb]
    elif Property == "UTS":
        Val_Q = float(317*10**(6)) #Pa REF:[Matweb]
    elif Property == "Reference Temperature":
        Val_Q = float(293) #K
    elif Property == "Cp":
        Val_Q = float(446) #J/kg.K [Heat]
    elif Property == "Brinell Hardness":
        Val_Q = float(187) #[Thesis 180]
```

```
        else:
            print "error"

    elif Powder == "Tin" or Powder == "tin" or Powder == "S": #S6001
        if Property == "Diameter":
            Val_Q = float(25*10**(-6)) #25 um REF:[37]
        elif Property == "Density":
            Val_Q = float(7265) #kg/m^3 REF:[Matweb]
        elif Property == "Thermal Conductivity":
            Val_Q = float(63.2) #W/m.K REF:[Matweb]
        elif Property == "Particle Mass":
            Val_Q = float(5.944*10**(-11)) #kg
        elif Property == "Melting Temperature":
            Val_Q = float(504.968) #K REF:[Matweb]
        elif Property == "UTS":
            Val_Q = float(220*10**(6)) #Pa REF:[Matweb]
        elif Property == "Reference Temperature":
            Val_Q = float(293) #K
        elif Property == "Cp":
            Val_Q = float(227) #J/kg.K [Heat]
        elif Property == "Brinell Hardness":
            Val_Q = float(17) #Average value from REF:[250]
        else:
            print "error"

    elif Powder == "Aluminium" or Powder == "aluminium" or Powder == "Al": #A0050
        if Property == "Diameter":
            Val_Q = float(25*10**(-6)) #25um REF:[246]
        elif Property == "Density":
            Val_Q = float(2790) #kg/m^3 REF:[Materials]
        elif Property == "Thermal Conductivity":
            Val_Q = float(205) #W/m.K REF:[EngToolBox]
        elif Property == "Particle Mass":
            Val_Q = float(2.283*10**(-11)) #kg
        elif Property == "Melting Temperature":
            Val_Q = float(933) #K REF:[EngToolBox]
        elif Property == "UTS":
            Val_Q = float(110*10**(6)) #Pa REF:[EngToolBox]
        elif Property == "Reference Temperature":
            Val_Q =  float(293) #K
        elif Property == "Cp":
            Val_Q = float(896) #J/kg.K [Heat]
        elif Property == "Brinell Hardness":
            Val_Q = float(73) #Average value from REF:[250]
        else:
            print "error"
    else:
        print "error"
    return Val_Q

    #Cold Spray Substrate Properties
def SubstrateProperties (Substrate,Property):
    if Substrate == "3D Printed ABS" or Substrate == "3d printed abs" or Substrate\
                == "ABS":
        if Property == "Thermal Conductivity":
```

```
        Val_Q = float(0.17) #W/m.K REF:[247]
    elif Property == "Density":
        Val_Q = float(1040) #kg/m^3 REF:[72]
    elif Property == "Reference Temperature":
        Val_Q =  float(293) #K
    elif Property == "Melting Temperature": #or Vicat softening temperature
        Val_Q = float(381) #K REF: [56]
    elif Property == "UTS":
        Val_Q = float(33*10**(6)) #Pa REF:[56]
    elif Property == "Young's Modulus":
        Val_Q = float(2.2*10**(9)) #Pa REF: [56]
    elif Property == "Brinell Hardness":
        Val_Q = float(40) #REF:[56][handbook of plastics testing and failure analysis]
        #brinell 100 REF:[http://gomelimpuls.by/en/product/abs-plastic]
        #Rockwell Hardness = 109.5 REF:[56]
    elif Property == "Thermal Diffusivity":
        Val_Q = float(120*10**(-9)) #m^2/s [www.scribd.com]
    elif Property == "Cp":
        Val_Q = float(1468) #J/kg.K [www.scribd.com]
    else:
        print "error"

elif Substrate == "Lexan" or Substrate == "lexan": #Lexan
    if Property == "Thermal Conductivity":
        Val_Q = float(0.2) #W/m.K REF:[94]
    elif Property == "Density":
        Val_Q = float(1200) #kg/m^3 REF:[94]
    elif Property == "Reference Temperature":
        Val_Q = float(293) #K
    elif Property == "Melting Temperature": #or Vicat softening temperature
        Val_Q = float(418) #K REF:[94]
    elif Property == "UTS":
        Val_Q = float(70*10**(6)) #Pa REF:[94]
    elif Property == "Young's Modulus":
        Val_Q = float(2.35*10**(9)) #Pa REF: [94]
    elif Property == "Brinell Hardness":
        Val_Q = float(22) #REF:[56][handbook of plastics testing and failure analysis]
    elif Property == "Thermal Diffusivity":
        Val_Q = float(150*10**(-9)) #m^2/s [www.scribd.com]
    elif Property == "Cp":
        Val_Q = float(1300) #J/kg.K [www.scribd.com]
    else:
        print "error"

elif Substrate == "PEEK" or Substrate == "peek": #PEEK 450G
    if Property == "Thermal Conductivity":
        Val_Q = float(0.29) #W/m.K REF:[96]
    elif Property == "Density":
        Val_Q = float(1300) #kg/m^3 REF:[96]
    elif Property == "Reference Temperature":
        Val_Q = float(293) #K
    elif Property == "Melting Temperature":
        Val_Q = float(616) #K 343 deg cel REF:[96]
    elif Property == "UTS":
        Val_Q = float(98*10**(6)) #Pa REF:[96]
```

```
    elif Property == "Young's Modulus":
        Val_Q = float(4*10**(9)) #Pa REF: [96]
    elif Property == "Brinell Hardness":
        Val_Q = float(35) #REF:[56][handbook of plastics testing and failure analysis]
    elif Property == "Thermal Diffusivity":
        Val_Q = float(140*10**(-9)) #m^2/s [www.scribd.com]
    elif Property == "Cp":
        Val_Q = float(1340) #J/kg.K [www.scribd.com]
    else:
        print "error"

elif Substrate == "Polycarbonate" or Substrate == "PC": #RS Components
    if Property == "Thermal Conductivity":
        Val_Q = float(0.25) #W/m.K REF:[292]
    elif Property == "Density":
        Val_Q = float(1190) #kg/m^3 REF:[292]
    elif Property == "Reference Temperature":
        Val_Q = float(293) #K
    elif Property == "Melting Temperature": #or Vicat softening temperature
        Val_Q = float(422) #K REF:[292]
    elif Property == "UTS":
        Val_Q = float(69*10**(6)) #Pa REF:[292]
    elif Property == "Young's Modulus":
        Val_Q = float(2.2*10**(9)) #Pa REF: [292]
    elif Property == "Brinell Hardness":
        Val_Q = float(22) #REF:[56][handbook of plastics testing and failure analysis]
    elif Property == "Thermal Diffusivity":
        Val_Q = float(150*10**(-9)) #m^2/s [www.scribd.com]
    elif Property == "Cp":
        Val_Q = float(1300) #J/kg.K [www.scribd.com]
    else:
        print "error"

elif Substrate == "Copper" or Substrate == "copper" or Substrate == "Cu":
    if Property == "Thermal Conductivity":
        Val_Q = float(385) #W/m.K REF:[Matweb]
    elif Property == "Density":
        Val_Q = float(7764) #kg/m^3 REF:[Matweb]
    elif Property == "Reference Temperature":
        Val_Q = float(293) #K
    elif Property == "Melting Temperature":
        Val_Q = float(1356) #K REF:[Matweb]
    elif Property == "UTS":
        Val_Q = float(210*10**(6)) #Pa REF:[Matweb]
    elif Property == "Young's Modulus":
        Val_Q = float(110*10**(9)) #Pa REF:[Matweb]
    elif Property == "Brinell Hardness":
        Val_Q = float(89) #REF:[Matweb]
    elif Property == "Thermal Diffusivity":
        Val_Q = float(116.6*10**(-6)) #m^2/s REF: [Heat]
    elif Property == "Cp":
        Val_Q = float(383) #J/kg.K [Heat]
    else:
        print "error"
```

```
elif Substrate == "Zinc" or Substrate == "zinc" or Substrate == "Zn":
    if Property == "Thermal Conductivity":
        Val_Q = float(112.2) #W/m.K REF:[Matweb]
    elif Property == "Density":
        Val_Q = float(7100) #kg/m^3 REF:[Matweb]
    elif Property == "Reference Temperature":
        Val_Q = float(293) #K
    elif Property == "Melting Temperature":
        Val_Q = float(692.58) #K REF:[Matweb]
    elif Property == "UTS":
        Val_Q = float(124*10**(6)) #Pa REF:[AGA] 37 MPa from REF:[AZOMaterials]
    elif Property == "Young's Modulus":
        Val_Q =float(96.5*10**9) #REF:[Matweb]
    elif Property == "Brinell Hardness":
        Val_Q = float(95) #Average value from REF:[250]
    elif Property == "Thermal Diffusivity":
        Val_Q = float(44.0*10**(-6)) #m^2/s REF: [Heat]
    elif Property == "Cp":
        Val_Q = float(385) #J/kg.K [Heat]
    else:
        print "error"

elif Substrate == "Nickel" or Substrate == "nickel" or Substrate == "Ni":
    if Property == "Thermal Conductivity":
        Val_Q = float(60.7) #W/m.K REF:[Matweb]
    elif Property == "Density":
        Val_Q = float(8880) #kg/m^3 REF:[Matweb]
    elif Property == "Reference Temperature":
        Val_Q = float(293) #K
    elif Property == "Melting Temperature":
        Val_Q = float(1728) #K REF:[Matweb]
    elif Property == "UTS":
        Val_Q = float(317*10**(6)) #Pa REF:[Matweb]
    elif Property == "Young's Modulus":
        Val_Q = float(207*10**9) #REF:[Matweb]
    elif Property == "Brinell Hardness":
        Val_Q = float(187) #[Thesis 180][MSc250]
    elif Property == "Thermal Diffusivity":
        Val_Q = float(22.9*10**(-6)) #m^2/s REF: [Heat]
    elif Property == "Cp":
        Val_Q = float(446) #J/kg.K [Heat]
    else:
        print "error"

elif Substrate == "Tin" or Substrate == "tin" or Substrate == "S":
    if Property == "Thermal Conductivity":
        Val_Q = float(63.2) #W/m.K REF:[Matweb]
    elif Property == "Density":
        Val_Q = float(7265) #kg/m^3 REF:[Matweb]
    elif Property == "Reference Temperature":
        Val_Q = float(293) #K
    elif Property == "Melting Temperature":
        Val_Q = float(504.968) #K REF:[Matweb]
    elif Property == "UTS":
        Val_Q = float(220*10**(6)) #Pa REF:[Matweb]
```

```
    elif Property == "Young's Modulus":
        Val_Q = float(41.6*10**9) #REF:[Matweb]
    elif Property == "Brinell Hardness":
        Val_Q = float(17) #Average value from REF:[250]
    elif Property == "Thermal Diffusivity":
        Val_Q = float(51.3*10**(-6)) #m^2/s REF: [Heat]
    elif Property == "Cp":
        Val_Q = float(227) #J/kg.K [Heat]
    else:
        print "error"

elif Substrate == "Aluminium" or Substrate == "aluminium" or Substrate == "Al":
    if Property == "Thermal Conductivity":
        Val_Q = float(205) #W/m.K REF:[EngToolBox]
    elif Property == "Density":
        Val_Q = float(2790) #kg/m^3 REF:[Materials]
    elif Property == "Reference Temperature":
        Val_Q = float(293) #K
    elif Property == "Melting Temperature":
        Val_Q = float(933) #K REF:[EngToolBox]
    elif Property == "UTS":
        Val_Q = float(110*10**(6)) #Pa REF:[EngToolBox]
    elif Property == "Young's Modulus":
        Val_Q = float(69*10**9) #Pa REF:[EngToolBox]
    elif Property == "Brinell Hardness":
        Val_Q = float(73) #Average value from REF:[250]
    elif Property == "Thermal Diffusivity":
        Val_Q = float(97.5*10**(-6)) #m^2/s REF: [Heat]
    elif Property == "Cp":
        Val_Q = float(896) #J/kg.K [Heat]
    else:
        print "error"

elif Substrate == "Stainless Steel" or Substrate == "stainless steel" or \
     Substrate == "SS":
                            #301 Stainless Steel
    if Property == "Thermal Conductivity":
        Val_Q = float(16.3) #W/m.K REF:[Matweb]
    elif Property == "Density":
        Val_Q = float(8030) #kg/m^3 REF:[Matweb]
    elif Property == "Reference Temperature":
        Val_Q =float( 293) #K
    elif Property == "Melting Temperature":
        Val_Q = float(1672) #K REF:[Matweb] lower limit
    elif Property == "UTS":
        Val_Q = float(515*10**6) #Pa REF:[Matweb]
    elif Property == "Young's Modulus":
        Val_Q = float(212*10**9) #Pa REF:[Matweb]
    elif Property == "Brinell Hardness":
        Val_Q = float(217) #REF:[Matweb]
    elif Property == "Thermal Diffusivity":
        Val_Q = float(0.387*10**(-5)) #m^2/s REF: [Heat]
    elif Property == "Cp":
        Val_Q = float(461) #J/kg.K [Heat]
    else:
```

```
            print "error"
    else:
        print "error"
    return Val_Q
#-------------------------------------------------------------------------------------------------------------
#Boundary Conditions
def BoundaryConditions (Property): #Global Constraints REF:[241]
    if Property == "Pressure" or Property == "pressure":
        P_o_min = float(0.55) #MPa
        P_o_max = float(1.72) #MPa
        return (P_o_min,P_o_max)
    elif Property == "Temperature" or Property == "temperature":
        T_o_min = "Ambient Operating Temperature"
        T_o_max = float(550) #Degrees Celcius or 823 K
        return (T_o_min,T_o_max)
    elif Property == "SOD":
        SOD_min = "5 mm"
        SOD_max = "15 mm"
        return (SOD_min,SOD_max)
    else:
        print "error"

def LocalPowderConstraints(Powder,Property):
    if Powder == "Copper" or Powder == "copper" or Powder == "Cu": #REF:[5]
        if Property == "Temperature" or Property == "temperature":
            T_o_max = float(450) #Degrees Celcius or 723 K
            return T_o_max
        elif Property == "SOD" or Property == "sod":
            SOD_min = "10 mm"
            SOD_max = "15 mm"
            return (SOD_min,SOD_max)
        elif Property == "V_nozzle":
            V_nozzle_min = "10 mm/s"
            V_nozzle_max = "500 mm/s"
            return (V_nozzle_min,V_nozzle_max)
        else:
            print "error"

    elif Powder == "Nickel" or Powder == "nickel" or Powder == "Ni":
        if Property == "Temperature" or Property == "temperature":
            T_o_max = float(550) #Degrees Celcius or 823 K"
            return T_o_max
        elif Property == "SOD" or Property == "sod":
            SOD_min = "10 mm"
            SOD_max = "15 mm"
            return (SOD_min,SOD_max)
        elif Property == "V_nozzle":
            V_nozzle_min = "10 mm/s"
            V_nozzle_max = "250 mm/s"
            return (V_nozzle_min,V_nozzle_max)
        else:
            print "error"

    elif Powder == "Zinc" or Powder == "zinc" or Powder == "Zn":  #REF:[38]
        if Property == "Temperature" or Property == "temperature":
```

```
            T_o_max = 400 #Degrees Celcius or 673 K"
            return T_o_max
        elif Property == "SOD" or Property == "sod":
            SOD_min = "10 mm"
            SOD_max = "15 mm"
            return (SOD_min,SOD_max)
        elif Property == "V_nozzle":
            V_nozzle_min = "10 mm/s"
            V_nozzle_max = "200 mm/s"
            return (V_nozzle_min,V_nozzle_max)
        else:
            print "error"

    elif Powder == "Tin" or Powder == "tin" or Powder == "S":  #REF:[37]
        if Property == "Temperature" or Property == "temperature":
            T_o_max = 225 #Degrees Celcius or 498 K"
            return T_o_max
        elif Property == "SOD" or Property == "sod":
            SOD_min = "10 mm"
            SOD_max = "15 mm"
            return (SOD_min,SOD_max)
        elif Property == "V_nozzle":
            V_nozzle_min = "10 mm/s"
            V_nozzle_max = "250 mm/s"
            return (V_nozzle_min,V_nozzle_max)
        else:
            print "error"

    elif Powder == "Aluminium" or Powder == "aluminium" or Powder == "Al":  #REF:[32]
        if Property == "Temperature" or Property == "temperature":
            T_o_max = 550 #Degrees Celcius or 823 K"
            return T_o_max
        elif Property == "SOD" or Property == "sod":
            SOD_min = "10 mm"
            SOD_max = "15 mm"
            return (SOD_min,SOD_max)
        elif Property == "V_nozzle":
            V_nozzle_min = "10 mm/s"
            V_nozzle_max = "500 mm/s"
            return (V_nozzle_min,V_nozzle_max)
        else:
            print "error"
    else:
        print "error"

def LocalSubstrateConstraints(Substrate):
    if Substrate == "Copper" or Substrate == "copper" or Substrate == "Cu": #REF:[Matweb]
        Ts_max = float(1356) #K (1083 Degrees Celcius)
        return Ts_max
    elif Substrate == "Nickel" or Substrate == "nickel" or Substrate == "Ni": #REF:[Matweb]
        Ts_max = float(1728) #K (1455 Degrees Celcius)
        return Ts_max
    elif Substrate == "Zinc" or Substrate == "zinc" or Substrate == "Zn": #REF:[Matweb]
        Ts_max = float(692.58) #K (419.58 Degrees Celcius)
        return Ts_max
```

```
    elif Substrate == "Tin" or Substrate == "tin" or Substrate == "S": #REF:[Matweb]
        Ts_max = float(504.97) #K (231.97 Degrees Celcius)
        return Ts_max
    elif Substrate == "Aluminium" or Substrate == "aluminium" or \
         Substrate == "Al": #REF:[Matweb]
        Ts_max = float(2327) #K (2054 Degrees Celcius)
        return Ts_max
    elif Substrate == "3D Printed ABS" or Substrate == "3d printed abs" or \
         Substrate == "ABS": #REF:[56]
        Ts_max = float(381) #K (108 Degrees Celcius)
        return Ts_max
    elif Substrate == "Lexan" or Substrate == "lexan" or Substrate == "Polycarbonate":
        Ts_max = float(418) #K (145 Degrees Celcius)
        return Ts_max
    elif Substrate == "PEEK" or Substrate == "peek": #REF:[96]
        Ts_max = float(416) #K (143 Degrees Celcius)
        return Ts_max
    else:
            print "error"
#____________________________Called Functions_____________________________________________
#1#
#Circular Area
def CircularArea (D):
    A = float(pi*(D/2.)**2)
    return A

#2#
#Basic Root Finding Method
##The function must be in terms of the unknown root only.
def BasicFixedPointMethod (x,f):    #x is an initial guess at the root
    x = float(x)                    #f is the function of the form f(x)
    diff = 1
    while diff > 0.0001:
        xnew = eval(f)              #The function is evaluated using initial guess
        diff = abs(x - xnew)
        x = xnew                    #Guessed value is reset
    return float(x)

#3#
#Characteristic Gas Constant
def CharacteristicGasConstant (R_bar,Mm):
    R = (R_bar/Mm)*1000. #J/kg.K
    return float(R)

#4#
#Ideal Gas Law
def IdealGasLaw (Q,P,T,rho,R):  #Q is the parameter to be calculated (pressure,
                                #temperature, density) A blank is left in place of
                                #the parameter to be calculated
    if Q == "Pressure":
        P = rho*R*T
        Val_Q = P               #Val_Q is the calculated value of requested parameter
    elif Q == "Temperature":
        T = P/(rho*R)
        Val_Q = T
```

```
    elif Q == "Density":
        rho = P/(R*T)
        Val_Q = rho
    else :
        print "Error"
    return float(Val_Q)

#5#
#Mach Number
def MachNumber (Q,M,V,gamma,R,T):
    if Q == 'Mach Number':
        M = V/sqrt(gamma*R*T)
        Val_Q = M
    elif Q == 'Velocity':
        V = M*sqrt(gamma*R*T)
        Val_Q = V
    else :
        print'Error'
    return float(Val_Q)

#6#
#Sutherland's Law
def SutherlandsLaw (Mu_ref,T,T_ref,S_dash):
    Mu = Mu_ref*((T/T_ref)**(3.0/2.0))*((T_ref + S_dash)/(T + S_dash))
    return float(Mu)

#7#
#Reynold's Number
def ReynoldsNumber (V,Lc,Nu):
    Re = float((V*Lc)/Nu)
    return Re

#8#
#Specific Heat at Constant Pressure
def SpecificHeat (gamma,R):
    Cp = float((gamma*R)/(gamma-1))
    return Cp

#9#
#Approximate Particle Velocity
#REFERENCES: [97][130][129]
def ApproximateParticleVelocity (V,dp,x,rho,Po):
    Vp_dash = float(V/(1+(0.85*sqrt(dp/x)*sqrt((rho*V**2)/Po))))
    return Vp_dash

#10#
#Thermal Diffusivity
#REFERENCE: [white]
def ThermalDiffusivity (k,rho,Cp):
    alpha = float(k/(rho*Cp))
    return alpha

#11#
#Mean Free Path Length
#REFERENCE: [white]
```

```
def MeanFreePathLength (Mu,rho,R,T):
    Lambda = float(1.26*(Mu/(rho*sqrt(R*T))))
    return Lambda

#12#
#Knudsen Number
def KnudsenNumber (Lambda,dp):
    Kn = float(Lambda/dp)
    return Kn

#13#
#Cunningham Correction Factor
#REFERENCE:[85]
def CunninghamCorrectionFactor (Lambda,dp,Cd):
    Cc = float(1+(((2*Lambda)/dp)*(1.257+(0.4*e**(-(1.1*dp)/(2.*Lambda))))))
    Cd_new = Cd/Cc
    return float(Cd_new)

#14#
#Spherical Mass
def SphericalMass (rho,D):
    m = float(rho*(4./3.)*pi*(D/2.)**3.)
    return m

#15#
#Nozzle Angle
def NozzleAngle (L,De,D_star):
    Beta = float(atan((2.*L)/(De - D_star)))  #Angle is in radians not degrees
    return Beta

#16#
#Prandtl Number
def PrandtlNumber (Cp,Mu,k):
    Pr = float((Cp*Mu)/k)
    return Pr

#17#
#Average Heat Transfer Coefficient
def AveHeatTransferCoefficient (Nus,k,Lc):
    hc = float((Nus*k)/Lc)
    return hc

#18#
#Biot Number
def BiotNumber (hc,Lc,k):
    Bi = float((hc*Lc)/k)
    return Bi

#19#
#Surface Area of Sphere
def SurfaceAreaSphere (D):
    As =float(4.*pi*(D/2)**2.)
    return As

#20#
```

```
#Normalised Temperature
def NormalisedTemperature (T,Tref,Tm):
    Theta_dash = float((T - Tref)/(Tm - Tref))
    return Theta_dash

#21#
#Flow Stress
def FlowStress (UTS,Theta_dash):
    Sigma = float(UTS(1. - Theta_dash))
    return Sigma

#22#
#Milimetre to Metre
def mmTOm (Lc):
    Val_Q = float(Lc/1000.)
    return Val_Q

#23#
#Mega-Pascals to Pascals
def MPaTOPa (P):
    Val_Q = float(P*10**6.)
    return Val_Q

#24#
#Degree Celcius to Kelvin
def degcelTOkelvin (T):
    Val_Q = float(T + 273.15)
    return Val_Q

#25#
#Newton's Root Finding Method
def NewtonsMethod(xi,f,df):
    xi = float(xi)
    diff = 1
    while diff > 0.0000000001:
       fA = eval(f)
       dfA = eval(df)
       xn = (xi - (fA/dfA))
       diff = abs(xi - xn)
       xi = xn
    return float(xi)
#_____________________________________________________________________________________________________
#Main Code
def main ():
                    #INTRODUCTION
    print "Welcome to the Theoretical Cold Spray Model \nThis programme was designed \
as an optimisation tool for the cold spray process. The model itself is an algorithm \
for determining the depth of penetration of cold spray particles into a specified \
substrate. The procedure also determines both flow and particle conditions at points \
of interest within the system, namely: the nozzle exit, the bow shock and particle-substrate \
interactions. Calculation of the critical particle velocity is also made, which is to be \
compared to the predicted particle velocity as a way of evaluating deposition quality. \
Heat transfer calculations are made, improving the accuracy of evaluated flow quantities."
    print
    Info = raw_input("Would you like additional information regarding model calculations\
```

```
 and user choices along the way (Yes or No): ")
    print
    print "Let's begin..."
    ANSWER = "Yes"
    while ANSWER == "Yes" or ANSWER == "yes":

#For automated use of programme, with corresponding CSV files containing the
#test parameter sets, uncomment this section and comment out all user inputs.
#Construct an excel file with the input data according to the row and column
#designation given below. Save file in same file directory as the python code.

##        CSVParameters = list(csv.reader(open("CSParameters_Step2_Cu3DABS_new2.csv")))
##        Column = int(raw_input("Column Number: "))
##
##        Info = CSVParameters[1][Column]
##        D_star = CSVParameters[2][Column]
##        D_star = float(D_star)
##        D_e = CSVParameters[3][Column]
##        D_e= float(D_e)
##        L = CSVParameters[4][Column]
##        L= float(L)
##        SprayGas = CSVParameters[4][Column]
##        P_amb = CSVParameters[5][Column]
##        P_amb= float(P_amb)
##        T_amb = CSVParameters[6][Column]
##        T_amb= float(T_amb)
##        Powder = CSVParameters[7][Column]
##        P_o = CSVParameters[8][Column]
##        P_o= float(P_o)
##        T_o = CSVParameters[9][Column]
##        T_o= float(T_o)
##        T_pa = CSVParameters[10][Column]
##        T_pa= float(T_pa)
##        SOD = CSVParameters[11][Column]
##        SOD= float(SOD)
##        Vnozzle = CSVParameters[12][Column]
##        Vnozzle= float(Vnozzle)
##        Substrate = CSVParameters[13][Column]
##        T_sa = CSVParameters[14][Column]
##        T_sa = float(T_sa)
##        Response_4 =CSVParameters[15][Column]
##        Response_5 = CSVParameters[16][Column]
##        Response_5 = float(Response_5)

        #Pre-Set results, for the case where not all calculations are performed
        Pg_e = "N/A"
        Pg_2 = "N/A"
        Pg_3 = "N/A"
        Tg_e = "N/A"
        Tg_2 = "N/A"
        Tg_3 = "N/A"
        Tg_i = "N/A"
        Tp_e = "N/A"
        Tp_i = "N/A"
        Ts = "N/A"
```

```
rhog_e = "N/A"
rhog_2 = "N/A"
rhog_3 = "N/A"
Vg_e = "N/A"
Vg_2 = "N/A"
Vg_3 = "N/A"
Vp_e = "N/A"
Vp_i = "N/A"
V_crit = "N/A"
X_1 = "N/A"
X_2 = "N/A"
FR = "N/A"
                #SECTION ONE: NOZZLE CALCULATIONS
#Nozzle Geometry (USER INPUT)
print "Nozzle Geometry Definition"
print "--------------------------"
D_star = float(raw_input("Nozzle throat diameter (mm): "))
D_e = float(raw_input("Nozzle exit diameter (mm): "))
L = float(raw_input("Nozzle diverging length (mm): "))
print

#GAS FLOW ANALYSIS WITHIN THE COLD SPRAY NOZZLE
#Step 6 - Determine Stagnation Pressure Threshold
D_star = mmTOm(D_star)#Conversion from mm to m
D_e = mmTOm(D_e)
L = mmTOm(L)

    #Critical nozzle areas (6.1 and 6.2)
A_star = CircularArea(D_star)
A_e = CircularArea(D_e)

    #Calculating supersonic nozzle exit Mach number (M_e) (6.3)
        #Nozzle gas (USER INPUT)
print "System Operating Conditions"
print "---------------------------"
SprayGas = raw_input("Spray gas (Air,Nitrogen or Helium): ")
        #Ratio of specific heat
gamma = float(GasProperties(SprayGas,"gamma","null"))
        #Approximated value for M_e
        #REFERENCE:[97]
k_1 = 218.0629 - (243.5764*gamma) + (71.7925*gamma**2.)
k_2 = -0.122450 + (0.281300*gamma)
M_e_Approx = ((k_1*(A_e/A_star)) + (1. - k_1))**k_2

        #M_e from Newton's Root Finding Method
xi = M_e_Approx
gamma_str = str(gamma)
A_e_str = str(A_e)
A_star_str = str(A_star)
f = "(((2/("+gamma_str+"+1))+((("+gamma_str+"-1)/("+gamma_str+"+1))*xi**2))"\
"**(("+gamma_str+"+1)/((2*"+gamma_str+")-2))) - (("+A_e_str+"/"+A_star_str+")*xi)"
df = "((((2/("+gamma_str+"+1))+((("+gamma_str+"-1)/("+gamma_str+"+1))*xi**2))"\
"**((-"+gamma_str+"+3)/((2*"+gamma_str+")-2)))*xi) - ("+A_e_str+"/"+A_star_str+")"
M_e = round(NewtonsMethod(xi,f,df),5)
```

```
    #Assume normal shock at nozzle exit (6.4)
        #Ambient pressure and temperature (USER INPUT)
P_amb = float(raw_input("Ambient pressure in lab (Pa): "))
T_amb = float(raw_input("Ambient temperature in lab (" + degree_sign + "C): "))
        #Pressure and Mach number assignment for normal shock at nozzle exit
   #M_e from Newton's Root Finding Method
xi = M_e_Approx
gamma_str = str(gamma)
A_e_str = str(A_e)
A_star_str = str(A_star)
f = "(((2/("+gamma_str+"+1))+((("+gamma_str+"-1)/("+gamma_str+"+1))*xi**2))"\
    "**(("+gamma_str+"+1)/((2*"+gamma_str+")-2))) - (("+A_e_str+"/"+\
    A_star_str+")*xi)"
df = "((((2/("+gamma_str+"+1))+((("+gamma_str+"-1)/("+gamma_str+"+1))*xi**2))"\
     "**((-"+gamma_str+"+3)/((2*"+gamma_str+")-2)))*xi) - ("+A_e_str+"/"\
     +A_star_str+")"
M_e = round(NewtonsMethod(xi,f,df),5)
P_y = P_amb     #Pressure behind shock
M_x = M_e       #Mach number in front of shock

    #Calculate gas pressure in front of the shock (6.5)
P_x = P_y/(1+(((2*gamma)/(gamma + 1))*(M_x**2 - 1)))

    #Calculating threshold stagnation pressure (6.6)
P_o_threshold = float(P_x*((1+(((gamma - 1)/2)*(M_x**2)))**(gamma/(gamma - 1))))
P_o_threshold_MPa = round(float(P_o_threshold/(10**6)),2)

#Step 7 - Calculate Nozzle Gas Exit Conditions
    #Define allowable operating pressure range (7.1)
(P_o_min,P_o_max)  = BoundaryConditions ("Pressure")
    # Ensure pressure range compliance (7.2)
if P_o_min <= P_o_threshold_MPa:
    P_o_min = P_o_threshold_MPa
elif P_o_min > P_o_threshold_MPa:
    P_o_min = P_o_min
elif P_o_max < P_o_threshold_MPa:
    print "The nozzle geometry is unacceptable and therefore supersonic flow will" \
          "not be achieved."
    #Call temperature boundary conditions
(T_o_min,T_o_max) = BoundaryConditions ("Temperature")
T_o_min = T_amb
    #Ask user for spray powder USER INPUT
Powder = raw_input("Spray powder (Copper, Zinc, Nickel, Tin, Aluminium): ")
Powder_T_o_max = LocalPowderConstraints(Powder,"Temperature")
    # Ensure temperature range compliance (7.3)
if T_o_max > Powder_T_o_max:
    T_o_max = Powder_T_o_max

P_o = float(input("Select an operating pressure in the range " + str(P_o_min)+\
                  "MPa" + " < " + str(P_o_max) + "MPa" + ": "))
P_o = MPaTOPa(P_o)
T_o = float(input("Select an operating temperature in the range " + str(T_o_min)+\
                  degree_sign + "C" + " < " + str(T_o_max)+degree_sign\
                  + "C" + ": "))
T_o = degcelTOkelvin (T_o)
```

```
    #Calculate the characteristic gas constant (7.4)
R_bar = float(GasProperties(SprayGas,"R_bar","null")) #kJ/kmol.K
M_m = float(GasProperties(SprayGas,"M_m","null")) #kg/kmol
R = float(CharacteristicGasConstant (R_bar,M_m)) #J/kg.K

    #Calculate the centreline stagnation density (7.5)
rho_o = float(IdealGasLaw("Density",P_o,T_o,"null",R))

    #Calculate the nozzle centreline exit pressure (7.6)
P_e = float(P_o/((1+(((gamma - 1)/2)*M_e**2))**(gamma/(gamma - 1))))

    #Calculate the nozzle centreline exit temperature (7.7)
T_e = float(T_o/(1+(((gamma - 1)/2)*M_e**2)))

    #Calculate the nozzle centreline exit density (7.8)
rho_e = rho_o/((1+(((gamma - 1)/2)*M_e**2))**(1/(gamma - 1)))

    #Calculate the nozzle centreline exit velocity (7.9)
V_e = MachNumber("Velocity",M_e,"null",gamma,R,T_e)

#Renaming of Properties before introduction of particle flow
Pg_e = float(P_e)
Tg_e = float(T_e)
rhog_e = float(rho_e)
Vg_e = float(V_e)
Mg_e = float(M_e)

#PARTICLE MODELLING WITH THE COLD SPRAY NOZZLE
#Step 8 - Internal particle thermal diffusivity significance based on Biot No.
    #Calculate the specific heat at constant pressure (8.1)
Cp = float(SpecificHeat (gamma,R))
    #Calculate the Prandtl number (8.2)
kg = float(GasProperties (SprayGas,"Thermal Conductivity",Tg_e))
Mu_ref = float(GasProperties(SprayGas,"Mu_ref","null"))
T_ref_sutherland = float(GasProperties(SprayGas,"T_ref_sutherland","null"))
S_dash = float(GasProperties(SprayGas,"S_dash","null"))
Mu_e = SutherlandsLaw (Mu_ref,Tg_e,T_ref_sutherland,S_dash)
Nu_e = Mu_e/rho_e
Pr = float(PrandtlNumber (Cp,Mu_e,kg))

    #Calculate the flow Reynolds number (8.3)
Re_e = float(ReynoldsNumber (V_e,D_e,Nu_e))

    #Calculate the Nusselt number (8.4)
Nus_D = float(0.023*Re_e**(0.8)*Pr**(0.3))
    #Calculate the average heat transfer coefficient for the flow (8.5)
hc = AveHeatTransferCoefficient (Nus_D,kg,D_e) #W/m^2.K

    #Calculate the Biot Number (8.6)
dp = PowderProperties (Powder,"Diameter")
kp = PowderProperties (Powder,"Thermal Conductivity")
Bi = BiotNumber (hc,dp,kp)
#print "Bi", Bi
```

```
    #Determine the average convective heat transfer coefficient (8.7)
        #Calculate an approximate value for the particle velocity at the nozzle exit
        #REFERENCE: [97][130][129]
rho_p = PowderProperties (Powder,"Density")

Vp_e_Approx = ApproximateParticleVelocity (Vg_e,dp,L,rho_p,P_o)
        #Calculate an approximate value for relative Reynolds number
V_e_rel_Approx = abs(Vg_e - Vp_e_Approx)
Mu_e = SutherlandsLaw (Mu_ref,Tg_e,T_ref_sutherland,S_dash)
Nu_e = Mu_e/rhog_e
Re_dp = ReynoldsNumber (V_e_rel_Approx,dp,Nu_e)
            #Check that Reynolds number does not lie in the following ranges REF(PhDThesis)
            #:152 (Heat pg437 McAdams)
if (Re_dp < 25) and (Re_dp > 10**5):
    print "Error. The Reynolds number is not in the required range"
        #Calculate an approximate value for the Nusselt number
Nus_dp = 0.37*Re_dp**(0.6)
        #Calclate the corresponding average convective heat transfer coefficient
hc = AveHeatTransferCoefficient (Nus_dp,kp,dp)
        #Calculate the surface area of the spray particle
As = SurfaceAreaSphere (dp)
mp = PowderProperties (Powder,"Particle Mass")

    #Thermal diffusivity significance and average particle temperature (8.8 and Step 9)
print "System Operating Conditions"
print "---------------------------"
        #Particle initial temperature (USER INPUT)
T_pa = float(input("Initial particle temperature ("+ degree_sign +"C, or ambient temperature): "))
T_pa = degcelTOkelvin (T_pa)
if Bi <= 0.1: #(9.1 A)
    if Tg_e > T_pa:
        Tp_e = Tg_e - exp(((-hc*As*L)/(mp*Cp*Vp_e_Approx)) + log(abs(Tg_e - T_pa)))
    if Tg_e < T_pa:
        Tp_e = Tg_e + exp(((-hc*As*L)/(mp*Cp*Vp_e_Approx)) + log(abs(Tg_e - T_pa)))

    #_______
    #STEPWISE CALCULATON ADDITION
    #Calculate the particle time in the nozzle
    t_n = (2*L)/(Vp_e_Approx)
    #________

elif Bi > 0.1:  #(9.1 B)

    print "The internal thermal diffusivity of the spray particle needs to be considered"
    print "Refer to the relevant calibrated charts for transient heat transfer analysis"
    print "These charts may be found in the textbook Principles of Heat Transfer (6th ed.)"
    print "By F. Kreith and M. Bohn."

#Step 10 - Calculate the Drag Coefficient
    #Calculate approximate value of the particle velocity at the nozzle exit (10.1)
    #REFERENCE: [97][130][129]
Vp_e_Approx = ApproximateParticleVelocity (V_e,dp,L,rho_p,P_o)

    #Calculate the relative Mach number (10.1)
V_e_rel_Approx = abs(Vg_e - Vp_e_Approx)
```

```
Mr_e = MachNumber ("Mach Number","null",V_e_rel_Approx,gamma,R,Tg_e)

    #Calculate the gas viscosity (10.2)
Mu_e = SutherlandsLaw (Mu_ref,Tg_e,T_ref_sutherland,S_dash)

Nu_e = Mu_e/rhog_e

    #Calculate the relative flow Reynolds number (10.3)
Re_dp = ReynoldsNumber (V_e_rel_Approx,dp,Nu_e)

    #Calcualte the effective drag coefficient (10.4)
if Mr_e < 1:    #I.e. the relative Mach number is subsonic
    #REFERENCE: [14]
    S = Mr_e*sqrt(gamma/2)
    Cd_e_part1 = (4.33 + ((3.65-(1.3*Tp_e)/Tg_e)/(1. + ((0.353*Tp_e)/Tg_e)))*exp(-0.247\
                *(Re_dp/S)))
    Cd_e_part2 = (((4.5 + 0.38*(0.03*Re_dp + 0.48*sqrt(Re_dp)))/(1. + 0.03*Re_dp + 0.48\
                *sqrt(Re_dp))) + 0.1*Mr_e**2 + 0.2*Mr_e**8)
    Cd_e_part3 = ((1 - exp(-Mr_e/Re_dp))*0.6*S)

    Cd_e = (24*(Re_dp + S*Cd_e_part1)**(-1)) + (exp(-(0.5*Mr_e)/(sqrt(Re_dp))))*Cd_e_part2\
           +Cd_e_part3

elif Mr_e > 1.75:   #I.e. the relative Mach number is supersonic
    S = Mr_e*sqrt(gamma/2)
    Mg = MachNumber ("Mach Number","null",V_e,gamma,R,Tg_e)
    Re_e = ReynoldsNumber (V_e,D_e,Mu_e)
    #REFERENCE: [14]
    Cd_e_numerator = (0.9 + (0.34/Mg**2) + 1.86*((Mg/Re_e)**0.5)*(2 + (2/S**2) + (1.058/S)*\
                     (float(Tp_e)/float(Tg_e))**0.5 - (1/S**4)))
    Cd_e_denominator = (1 + 1.86*(Mg/Re_e)**0.5)

    Cd_e = Cd_e_numerator/Cd_e_denominator

elif (Mr_e > 1) and (Mr_e < 1.75):
    S = Mr_e*sqrt(gamma/2)
    Cd_e_part1 = (4.33 + ((3.65-(1.3*Tp_e)/Tg_e)/(1 + ((0.353*Tp_e)/Tg_e)))*exp(-0.247*\
                 (Re_dp/S)))
    Cd_e_part2 = (((4.5 + 0.38*(0.03*Re_dp + 0.48*sqrt(Re_dp)))/(1 + 0.03*Re_dp + 0.48\
                *sqrt(Re_dp))) + 0.1*1**2 + 0.2*1**8)
    Cd_e_part3 = ((1 - exp(-1/Re_dp))*0.6*S)

    Cd_e_a = (24*(Re_dp + S*Cd_e_part1)**(-1)) + (exp(-(0.5*1)/(sqrt(Re_dp))))*Cd_e_part2 \
             +Cd_e_part3

    Re_e = ReynoldsNumber (V_e,D_e,Mu_e)
    #REFERENCE: [14]
    Cd_e_numerator = (0.9 + (0.34/1.75**2) + 1.86*((1.75/Re_e)**0.5)*(2 + (2/S**2) + \
                     (1.058/S)*(Tp_e/Tg_e)**0.5 - (1/S**4)))
    Cd_e_denominator = (1 + 1.86*(1.75/Re_e)**0.5)

    Cd_e_b = Cd_e_numerator/Cd_e_denominator

    Mg = MachNumber ("Mach Number","null",V_e,gamma,R,Tg_e)
```

```
    Cd_e = Cd_e_a +((4/3)*(Mg - 1)*(Cd_e_b - Cd_e_a))

    #Apply Cunningham Correction factor (10.5)
Lambda = MeanFreePathLength (Mu_e,rhog_e,R,Tg_e) #REF: [White]
Kn = KnudsenNumber (Lambda,dp)
if Kn > 0.1:
    Cd_e = CunninghamCorrectionFactor (Lambda,dp,Cd_e)

#Step 11 - Calculate the Effective Nozzle Exit Particle Velocity
Vp_e_Approx = ApproximateParticleVelocity (Vg_e,dp,L,rhog_e,P_o)
Ap = CircularArea (dp)
    #Vp_e using Newton's Fixed Point Root Finding Method
Vg_e_str = str(Vg_e)
Cd_e_str = str(Cd_e)
Ap_str = str(Ap)
rhog_e_str = str(rhog_e)
L_str = str(L)
mp_str = str(mp)

xi = Vp_e_Approx
f = "log(abs(("+Vg_e_str+" - xi)/"+Vg_e_str+")) + ("+Vg_e_str+"/("+Vg_e_str+"-xi)) - 1 - "\
    "(("+Cd_e_str+"*"+Ap_str+"*"+rhog_e_str+"*"+L_str+")/(2*"+mp_str+"))"
df = "xi/(("+Vg_e_str+"-xi)**2)"

Vp_e = NewtonsMethod(xi,f,df)

Substrate = raw_input("Cold Spray Substrate (PEEK, Lexan, 3D Printed ABS, Copper, Zinc, "\
                      "Nickel, Aluminium, Tin or Stainless Steel): ")
T_s = float(raw_input("Initial substrate temperature ("+ degree_sign +"C): "))
T_s = degcelTOkelvin(T_s)

                #SECTION TWO: GAP CALCULATIONS
#Ask the user if they want to take into account the nozzle gaps conditions with bow shock
print
print "Model Functionality"
print"--------------------"
Response_4 = raw_input("Would you like to incorporate gap effects including the bow shock "\
                       "(Yes or No): ")
if Response_4 == "Yes" or Response_4 == "yes":
    #Step 12 - Estimate the gas flow between the nozzle exit and the bow shock
    (SOD_min,SOD_max) = LocalPowderConstraints (Powder,"SOD")
    SOD = float(input("Select a nozzle standoff distance (mm) in the range " + SOD_min + " < " \
        + SOD_max+": "))
    SOD = mmTOm(SOD)
        #Calculate the flow conditions in front of the bow shock (12.1, 12.2)
    if Pg_e == P_amb:    #Design Condition
        print "Nozzle Exit flow is at the design conition"
        #It is assumed that all flow properties are constant from nozzle exit to bow shock
        Pg_2 = Pg_e
        Tg_2 = Tg_e
        rhog_2 = rhog_e
        Vg_2 = Vg_e

    elif Pg_e < P_amb:   #Overexpanded flow with oblique shocks
        print "Nozzle exit flow is overexpanded with oblique shocks"
```

```
        #REFERENCE: [white]
    Theta = 0.0698 #=4deg
    x = str(Theta)
    Theta_str = str(Theta)
    Mg_e_str = str(Mg_e)
    gamma_str = str(gamma)
    Num = "(2*(1/tan("+Theta_str+"))*(("+Mg_e_str+"**(2) * sin(x)**2) - 1))"
    Den = "(("+Mg_e_str+"**(2)*("+gamma_str+" + cos(x)**2))+2)"
    f = "atan("+Num+"/"+Den+")"
    Psi = BasicFixedPointMethod(x,f)
        #Calculate the downstream pressure
    Pg_2 = Pg_e*(1/(gamma+1))*(2*gamma*Mg_e**2*(sin(Psi))**2 - (gamma - 1))
        #Calculate the downstream density
    rhog_2 = rhog_e*(tan(Psi)/tan(Psi - Theta))
        #Calculate the downstream temperature
    Tg_2 = Tg_e*(2. + ((gamma-1.)*Mg_e**2.*(sin(Psi)**2.)))*(((2.*gamma*Mg_e**2.*\
          (sin(Psi))**2. - (gamma - 1.)))/((gamma+1.)**2.*Mg_e**2.*(sin(Psi))**2.))
        #Calculate the downstream stagnation pressure
    P_o2 = P_o*(((gamma+1)*Mg_e**2*(sin(Psi))**2)/2+(gamma-1)*Mg_e**2*(sin(Psi))**2)\
           **(gamma/(gamma-1))*((gamma+1)/(2*gamma*Mg_e**2*(sin(Psi))**2 - (gamma - 1)))\
           **(1/(gamma-1))
        #Calculate the downstream stagnation temperature
    T_o2 = T_o
        #Calculate the Mach number normal to the oblique shock upon entrance
    M_an1 = Mg_e*sin(Psi)
        #Calculate the Mach number normal to the oblique shock upon exit
    M_an2 = sqrt(((gamma-1)*M_an1**2 + 2)/(2*gamma*M_an1**2 - (gamma-1)))
        #Calculate the Mach number downstream of the oblique shock
    Mg_2 = M_an2/sin(Psi-Theta)
        #Calculate the gas velocity in front of the bow shock
    Vg_2 = Mg_2*sqrt(gamma*R*Tg_2)

elif Pg_e >P_amb:    #Underexpanded flow with expansion waves
    print "Nozzle exit flow is underexpanded with expansion waves"
    Pg_2 = P_amb
        #REFERENCE: [white]
        #Calculate the ratio of stagnation pressure to exit pressure
    Ratio_1 = (1 + (((gamma - 1)/2.)*Mg_e**2))**((-gamma)/(gamma-1))
        #Calculate the ratio of ambient pressure to the stagnation pressure
        #downstream of expansion waves
    Ratio_2 = (P_amb/Pg_e)*Ratio_1
        #Calculate the Mach number behind the expansion waves
    Mg_2 = sqrt(((Ratio_2**(-(gamma-1)/(gamma)))-1)/((gamma-1)/2.))
        #Calculate the ratio of the nozzle exit temperature to stagnation temperature
    Ratio_3 = (1+((gamma-1)/2.)*Mg_e**2)**(-1)
        #Calculate the ratio of temperature behind the expansion waves to the
        #corresponding stagnation temperature
    Ratio_4 = (1+((gamma-1)/2.)*Mg_2**2)**(-1)
        #Calculate the temperature behind the expansion waves
    T_o2 = T_o  #flow is considered adiabatic
    Tg_2 = T_o2*Ratio_4
        #Calculate the downstream density
    rhog_2 = P_amb/(R*Tg_2)
        #Calculate the downstream velocity
    Vg_2 = Mg_2*sqrt(gamma*R*Tg_2)
```

```
        #Calculate the flow deflection angle w.r.t. upstream flow Mach number
    Theta_1dash = ((gamma+1)/(gamma-1))**0.5*(atan(((gamma-1)/(gamma+1))*(Mg_e**2 - 1)\
                                                ))**0.5 - (atan(Mg_e**2 -1))**0.5
        #Calculate the flow deflection angle w.r.t. downstream flow Mach number
    Theta_2dash = ((gamma+1)/(gamma-1))**0.5*(atan(((gamma-1)/(gamma+1))*(Mg_2**2 - 1)\
                                                ))**0.5 - (atan(Mg_2**2 -1))**0.5
        #Determine the overall system flow deflection angle
    Theta_overalldash = Theta_2dash - Theta_1dash

#Step 13 - Calculate the Flow Conditions across the Bow Shock
    #Calculate the downstream Mach number (13.1)
Mg_3 = sqrt((Mg_2**2. + (2./(gamma-1.)))/((((2.*gamma)/(gamma-1.))*Mg_2**2. - 1.)))

    #Calculate the downstream flow temperature (13.2)
Tg_3 = Tg_2*(((1.+ ((gamma-1.)/2.)*Mg_2**2.)*(((((2.*gamma)/(gamma-1.))*Mg_2**2 - 1.)\
                                    )))/(((gamma+1.)**2./(2.*(gamma-1.)))*Mg_2**2.))

    #Calculate the downstream flow pressure (13.3)
#Pg_3 = Pg_2*(1+(((2*gamma)/(gamma+1))*(Mg_2**2 - 1)))
Pg_3 = Pg_2*(1+(((2*gamma)/(gamma+1))*(Mg_2**2 - 1)))

    #Calculate the downstream gas density (13.4)
rhog_3 = rhog_2*((((gamma+1.)/2.)*Mg_2**2.)/(1. + ((gamma-1.)/(2.))*Mg_2**2.))

    #Calculate the downstream flow velocity (13.5)
Vg_3 = Vg_2*(((((gamma+1.)/2.)*Mg_2**2.)/(1. + ((gamma-1.)/(2.))*Mg_2**2.)))**(-1.)
Vg_3r = Mg_3*sqrt(gamma*R*Tg_3)

#Step 14 - Calculate the Bow Shock Standoff Distance
Delta_shock = 0.143*D_e*(exp(3.24/(Mg_e**2.)))

#Step 15 - Determine the Particle Impact Velocity
    #Calculate the relative flow velocity (15.1)
Vrel_2 = abs(Vg_2 - Vp_e)
    #Calculate the flow viscosity in front of the bow shock (15.2)
Mu_2 = SutherlandsLaw(Mu_ref,Tg_2,T_ref_sutherland,S_dash)
Nu_2 = Mu_2/rhog_2

    #Calculate the relative Reynolds number (15.3)
Re_2 = ReynoldsNumber(Vrel_2,dp,Nu_2)

    #Calculate the drag coefficient (15.4)
Cd_2 = (24/Re_2)*(1+(dp/(2*SOD)))

    #Calculate the particle impact velocity (15.5)
Vp_i_Approx = Vp_e
Ap = CircularArea(dp)
rho_p = PowderProperties(Powder,"Density")
mp = SphericalMass(rho_p,dp)
x = Vp_i_Approx
Vg_2_str = str(Vg_2)
Numerator = Vg_2
Num_str = str(Numerator)
Denominator_1 = ((Cd_2*Ap*rhog_2*(SOD-Delta_shock+L))/(2*mp))
Den_1_str = str(Denominator_1)
```

```
 Denominator_2 = ((Cd_2*Ap*rhog_2*L)/(2*mp))
 Den_2_str = str(Denominator_2)
 Denominator_3 = (Vg_2/(Vg_2 - Vp_e))
 Den_3_str = str(Denominator_3)
 Denominator_4 = (log(abs(Vg_2 - Vp_e)))
 Den_4_str = str(Denominator_4)
 Denominator_5 = (log(abs(Vg_2 - x)))
 Den_5_str = str(Denominator_5)

 f = Vg_2_str+" - ("+Num_str+"/("+Den_1_str+" - "+Den_2_str+" + "+Den_3_str+" + "\
     +Den_4_str+" - "+Den_5_str+" ))"
 x = Vp_i_Approx

 Vp_i = BasicFixedPointMethod(x,f)

#Step 16 - Calculate the average particle Biot number
     #Calculate the impact Reynolds number (16.1)
 Vrel_i = abs(Vg_2 - Vp_i)
 Re_i = ReynoldsNumber(Vrel_i,dp,Nu_2)
 if (Re_i < 25) or (Re_i > 10**5):
     print "formula does not work with such a Reynolds number"

     #Calculate the associated Nusselt number (16.2)
 Nus_i = 0.37*Re_i**0.6

     #Calculate the average flow heat transfer coefficient in front of the bow shock(16.3)
 hc = (Nus_i*kg)/dp

     #Calculate the Biot number (16.4)
 Bi = (hc*dp)/kp
 #print "Bi", Bi
     #Calculate the average heat transfer coefficient of the spray particle (16.5)
 hc = (Nus_i*kp)/dp

     #PStep 17 -  Calculate the Particle Impact Temperature
 if Bi <= 0.1:    #Temperature of the spray particle is considered constant
     As = SurfaceAreaSphere(dp)
     Cp_p = PowderProperties(Powder, "Cp")
     if Tg_2 > Tp_e:
         Tp_i = Tg_2 - exp(-(((hc*As*(SOD-Delta_shock+L))/(mp*Cp*Vp_i))-((hc*As*L)/\
             (mp*Cp*Vp_i)))+(log(abs(Tg_2 - Tp_e))))

     elif Tg_2 < Tp_e:
         Tp_i = Tg_2 + exp(-(((hc*As*(SOD-Delta_shock+L))/(mp*Cp*Vp_i))-((hc*As*L)\
            /(mp*Cp*Vp_i)))+(log(abs(Tg_2 - Tp_e))))

     #STEPWISE CALCULATON ADDITION
     #Calculate the duration of particle in spray gap
     t_G = (SOD)/(abs(Vp_e + Vp_i)/2)

 elif Bi > 0.1:
     print "The internal thermal diffusivity of the spray particle needs to be considered"
     print "Refer to the relevant calibrated charts for transient heat transfer analysis"
     print "These charts may be found in the textbook Principles of Heat Transfer (6th ed.)"
     print "By F. Kreith and M. Bohn."
```

```
else:
    Pg_i = Pg_e
    Tg_i = Tg_e
    rhog_i = rhog_e
    Vg_i = Vg_e
    Mg_i = Mg_e
    Tp_i = Tp_e
    Vp_i = Vp_e

#Step 18 - Compare Critical Particle Velocities
#Parameters Used
Tp_i = Tp_i
Ts_i = T_s
Trefp = PowderProperties(Powder,"Reference Temperature")
Trefs = SubstrateProperties(Substrate,"Reference Temperature")
Tp_m = PowderProperties(Powder,"Melting Temperature")
Ts_m = SubstrateProperties(Substrate,"Melting Temperature")
UTSp = PowderProperties(Powder,"UTS")
UTSs = SubstrateProperties(Substrate,"UTS")
rho_p = PowderProperties(Powder, "Density")
rho_s = SubstrateProperties(Substrate, "Density")
Cp_p = PowderProperties(Powder, "Cp")
Es = SubstrateProperties(Substrate, "Young's Modulus")
BHN_p = PowderProperties(Powder,"Brinell Hardness")
BHNmax_s = SubstrateProperties(Substrate, "Brinell Hardness")
dp = PowderProperties(Powder,"Diameter")
mp = PowderProperties(Powder, "Particle Mass")
Vp_i = Vp_i

#MODEL 1
#REFERENCE: [91][113]
Thetap_dash = (Tp_i - Trefp)/(Tp_m - Trefp)
Sigmap = UTSp*(1 - Thetap_dash)
Vcrit_1 = sqrt(((4.*Sigmap)/(rho_p)) + 0.25*Cp_p*(Tp_m - Tp_i))

#MODEL 2 - Tate Model
#REFERENCE: [164]
Thetap_dash = (Tp_i - Trefp)/(Tp_m - Trefp) #REF: [91]
Sigmap = UTSp*(1 - Thetap_dash)#REF: [91]
Yp = abs(1.7*Sigmap)
Thetas_dash = (Ts_i - Trefs)/(Ts_m - Trefs)#REF: [91]
Sigmas = UTSs*(1 - Thetas_dash)#REF: [91]
Ys = abs(Sigmas)
Alpha_sph = ((2.*Es)/(3.*Ys))**(1./3.)
Rs = (7./3.)*log(Alpha_sph)*Ys
if Yp < Rs:
    Vcrit_2= (2.*((Rs - Yp)/(rho_p)))**(0.5)
elif Yp > Rs:
    Vcrit_2 = (2.*((Yp - Rs)/(rho_s)))**(0.5)
print

Vcrit_ave = (Vcrit_1 + Vcrit_2)/2

Response_5 =raw_input("Which method would you like to use to calculate the \
```

```
particle Critical Velocity? (Tobias Schmidt [1], Tate Model [2] or Average of the two [3]): ")

        if Response_5 == "1" or Response_5 == "Tobias Schmidt":
            Vcrit = Vcrit_1
        elif Response_5 == "2" or Response_5 == "Tate Model":
            Vcrit = Vcrit_2
        elif Response_5 == "3" or Response_5 == "Average":
            Vcrit = Vcrit_ave
        print

                #SECTION 3: PARTICLE-SUBSTRATE INTERACTIONS
        #Step 19 - Calculate the Particle Depth of Penetration
        #Model 1 - Frank and Zook
        #REFERENCE: [70]
            #Calculate the normalised temperature of the substrate (20.1)
        Thetas_dash = (Ts_i - Trefs)/(Ts_m - Trefs)

            #Calculate the temperature dependent flow stress of the substrate (20.2)
        Sigmas = abs(UTSs*(1 - Thetas_dash))

            #Calculate the extent of plastic zone in the substrate (20.3)
        Chi = ((2.*Es)/(3.*Sigmas))**(1./3.)

            #Calculate the coefficient of proportionality of the substrate (20.4)
        Zeta = (7./3.)*log(Chi)

            #Calculate the substrate resistance (20.5)
        Rs = Zeta*Sigmas

            #Calculate the  particle depth of penetration (20.5)
        X_1 = dp*((((2./3.)*(rho_p/rho_s))+0.557)/(2*1.046))*log(1 + (1.046*rho_s*Vp_i**2)/\
                                                                 (Rs)) #m
        X_1 = X_1*10**(6) #um

        #MODEL 2 - Poncelet Equation
        #REFERENCE: [255]
        Thetas_dash = (Ts_i - Trefs)/(Ts_m - Trefs)#REF: [91]
        Sigmas = UTSs*(1. - Thetas_dash)#REF: [91]
        Ys = abs(Sigmas)
        Alpha_sph = ((2.*Es)/(3.*Ys))**(1./3.)
        Rs = (7./3.)*log(Alpha_sph)*Ys
        X_2 = (dp*rho_p*Vp_i**2)/(2*Rs) #m
        X_2 = X_2*10**(6) #um

        #Model 3 - Modified Bernoulli
        #REFERENCE: [255]
        if Powder != Substrate:
            mu = (rho_s/rho_p)**0.5
            Thetas_dash = (Ts_i - Trefs)/(Ts_m - Trefs)#REF: [91]
            Sigmas = abs(UTSs*(1. - Thetas_dash))#REF: [91]
            Thetap_dash = (Tp_i - Trefp)/(Tp_m - Trefp) #REF: [91]
            Sigmap = abs(UTSp*(1. - Thetap_dash))#REF: [91]
            Sigma = abs(Sigmas-Sigmap)
            if rho_p != rho_s:
                if (Vp_i**2. + (2.*(1-mu**2.))*(Sigma/rho_s)) < 0:
```

```
                u = 0
            else:
                u = (Vp_i-(mu*(Vp_i**2. + (2.*(1-mu**2.))*(Sigma/rho_s))**0.5))/\
                    (1.- mu**2.)
        else:
            u = (Vp_i/2.) - (Sigma/rho_p*Vp_i)
        t_penetration = dp/(Vp_i-u) #time of penetration
        X_3 = u*t_penetration #m
        X_3 = X_3*10**(6) #um
    else:
        X_3 = 0
        print "Error in calculating X_3"

    #Model 4 - Christman and Gehring
    #REFERENCE: [255]
    X_4 = 0.13*((rho_p/rho_s)**(1./3.)) * ((0.5*mp*Vp_i**2.)/(BHNmax_s*10**6))\
          **(1./3.) #m
    X_4 = X_4*10**(6) #um

    #Model 5 - Extended Bernoulli (Tate)
    #REFERENCE: [254]
    if Powder != Substrate:
        mu = (rho_s/rho_p)**(0.5)
        Thetap_dash = (Tp_i - Trefp)/(Tp_m - Trefp) #REF: [91]
        Sigmap = abs(UTSp*(1. - Thetap_dash))#REF: [91]
        Yp = Sigmap*1.7
        Thetas_dash = (Ts_i - Trefs)/(Ts_m - Trefs)#REF: [91]
        Sigmas = abs(UTSs*(1. - Thetas_dash))#REF: [91]
        Ys = Sigmas
        Alpha_sph = ((2.*Es)/(3.*Ys))**(1./3.)
        Rs = (7./3.)*log(Alpha_sph)*Ys
        if Yp < Rs:
            A = 2.*(1. - mu**2.)*((Rs - Yp)/(rho_s))
        elif Yp > Rs:
            A = 2.*(1. - mu**2.)*((Yp - Rs)/(rho_p))
        if (Vp_i**(2.) + A) < 0:
            X_5 = 0
            print "Error in calculating X_5"
        else:
            X_5 = (dp/mu)*(((mu*(Vp_i**(2.) + A)**(0.5)) - Vp_i)/((mu*Vp_i) - (Vp_i**(2.) + A)**0.5)) #m
            X_5 = X_5*10**(6) #um
    else:
        X_5 = 0
        print "Error in calculating X_5"

##      #Step 21 - Calculate the Particle Flattening Ratio
##      Flattening_Ratio = 0.46*(Vp_i/Vcrit_ave)
##
##      if Powder == Substrate:
##          X_ave = (X_1 + X_2 + X_4)/3
##      else:
##          X_ave = (X_1 + X_2 + X_3 + X_4 + X_5)/5
##
##      Vel_Ratio = Vp_i/Vcrit_1
#-----------------------------------------------------------------------------------------------------
```

```
##        #Modified calculation for depth of particle penetration (18/03/2019)
##        if (rho_p/(rho_s*1.0)) <= 5:
##            Scale_factor = 1
##        elif 5 < (rho_p/rho_s) <= 10:
##            Scale_factor = (-0.1607*(rho_p/(rho_s*1.0))) + 1.7382
##        else:
##            print "ERROR - Density ratio too high - Unknown result"
##
##        X_1_modified = X_1*Scale_factor
##        X_D_modified = X_1_modified/(dp*10**6)

        #Modified calculation for depth of particle penetration (24/02/2020)
        if (rho_p/(rho_s*1.0)) <= 5:
            Scale_factor = 1
        elif 5 < (rho_p/rho_s) <= 10:
            Scale_factor = (-0.124*(rho_p/(rho_s*1.0))) + 1.4285
        else:
            print "ERROR - Density ratio too high - Unknown result"

        X_1_modified = X_1*Scale_factor
        X_D_modified = X_1_modified/(dp*10**6)
    #-------------------------------------------------------------------------------------------
        print "_____________________________________________________________________________"
        print "RESULTS"
        #Particle Depth of Penetration
        print "Particle Depth of Penetration - Original model outputs"
        print "Particle Depth of Penetration (Method One):", round(X_1,2), "um - No scale factor applied"
        #print "Particle Depth of Penetration (Method Two):", X_2, "um - No scale factor applied"
        #print "Particle Depth of Penetration (Method Three):", X_3,"um - No scale factor applied"
        #print "Particle Depth of Penetration (Method Four):", X_4, "um - No scale factor applied"
        #print "Particle Depth of Penetration (Method Five):", X_5, "um - No scale factor applied"
        print "Model 1 X/D", round(X_1/(dp*10**6),2)
        print "- - - - - - - - - - - - - - - - - - - - - - - - - - - - - - - - - - - - - - - - -"
        print "Final theoretical cold spray model, based on Chapter 7 input"
        print "Scale Factor", round(Scale_factor,2)
        print "Depth of penetration (X_1(modified))", round(X_1_modified,2), "um"
        print "Normalised depth of penetration", round(X_D_modified,2)
        print

        #Comment out the line below if using the automated model
        ANSWER = raw_input("Would you like to perform another hypothetical cold spray run?"\
                           "(Yes or No): ")

        #Uncomment the following line if  using the automated model
##      ANSWER = "yes"

        print
if __name__=="__main__":
    main()
```

8. Model Selection

In the development of an effective theoretical cold spray model it was imperative that the independent cold spray parameter effects be considered.

First, a literature survey identified ten suitable cold spray parameter sets, based on both experimental and theoretical cold spray analysis. Table A.6 contains all the pertinent design specifications from those sources as well as their findings. Where data was missing from a source a forward slash (/) was used to indicate its absence.

Table A.6: Historical cold spray trials.

		Set 1	**Set 2**	**Set 3**	**Set 4**	**Set 5**	**Set 6**	**Set 7**	**Set 8**	**Set 9**	**Set 10**
	Reference	[217]	[217]	[217]	[217]	[217]	[217]	[217]	*	*	[90]
	Method	Simulation - JC Model	Simulation - GZ Model	Simulation - VA Model	Simulation - PTW Model	Simulation - MZA Model	Simulation - MKHL Model	Experimental	Analytical Model	Experimental	Experimental
Cold Spray Properties	Throat Diameter (mm)	/	/	/	/	/	/	/	2.5	2.5	2.41
	Exit Diameter (mm)	/	/	/	/	/	/	/	6.5	6.5	6
	Divergent Length (mm)	/	/	/	/	/	/	/	120	120	130
	Spray Gas	/	/	/	/	/	/	/	Air	Air	Nitrogen
	Ambient Pressure (Pa)	/	/	/	/	/	/	/	101325	83060	101325
	Ambient Temperature (°C)	/	/	/	/	/	/	/	20	20	20
	Spray Powder	Copper	Copper	Copper	Copper	Copper	Copper	Copper	Copper	Copper	Copper
	Stagnation Pressure (MPa)	/	/	/	/	/	/	/	0.827	0.827	2.5
	Stagnation Temperature (K)	297	297	297	297	297	297	297	473	473	623
	Initial Particle Temperature (°C)	20	20	20	20	20	20	20	20	20	20
	Standoff Distance (mm)	/	/	/	/	/	/	/	/	20	30
	Traverse Speed (mm/s)	/	/	/	/	/	/	/	/	10	500
	Substrate Material	Copper	Copper	Copper	Copper	Copper	Copper	Copper	ABS	ABS	PC
	Initial Substrate Temperature (C)	20	20	20	20	20	20	20	20	20	20
	Powder Mean Diameter (μm)	20	20	20	20	20	20	20	25	25	26.9
	Powder Feed Rate	/	/	/	/	/	/	/	/	20%	0.7 kg/h
Results	Gas Exit Velocity (m/s)	/	/	/	/	/	/	/	821.15	/	/
	Particle Exit Velocity (m/s)	500	500	500	500	500	500	500	421.02	/	/
	Particle Impact Velocity (m/s)	/	/	/	/	/	/	/	421.02	/	/
	Critical Particle Velocity (m/s)	300	1150	400	525	420	400	475	/	/	570
	Depth of Penetration (μm)	15.2	8	15.3	12.4	15.9	11.7	13	42.29	51.84	18

* Preliminary version of current theoretical model, with associated experimental analysis

Predictive accuracy (MS_1)

Table A.7 contains the parameter set values for the equivalent theoretical cold spray runs based on the parameter values contained in Table A.6.

Table A.7: Equivalent theoretical cold spray parameter sets (see Table A.6).

			Set 1	Set 2	Set 3	Set 4	Set 5	Set 6	Set 7	Set 8	Set 9	Set 10
Cold Spray Properties		Throat Diameter (mm)	2.5	2.5	2.5	2.5	2.5	2.5	2.5	2.5	2.5	2.41
		Exit Diameter (mm)	6.5	6.5	6.5	6.5	6.5	6.5	6.5	6.5	6.5	6
		Divergent Length (mm)	120	120	120	120	120	120	120	120	120	130
		Spray Gas	Air	Air	Air	Air	Air	Air	Air	Air	Air	Nitrogen
		Ambient Pressure (Pa)	101325	101325	101325	101325	101325	101325	101325	101325	83060	101325
		Ambient Temperature (°C)	20	20	20	20	20	20	20	20	20	20
		Spray Powder	Copper	Copper	Copper	Copper	Copper	Copper	Copper	Copper	Copper	Copper
		Stagnation Pressure (MPa)	1.2	1.2	1.2	1.2	1.2	1.2	1.2	0.827	0.827	2.5
		Stagnation Temperature (K)	297	297	297	297	297	297	297	473	473	623
		Initial Particle Temperature (°C)	20	20	20	20	20	20	20	20	20	20
		Standoff Distance (mm)	12.5	12.5	12.5	12.5	12.5	12.5	12.5	20	20	30
		Traverse Speed (mm/s)	10	10	10	10	10	10	10	10	10	500
		Substrate Material	Copper	Copper	Copper	Copper	Copper	Copper	Copper	3D ABS	3D ABS	PC
		Initial Substrate Temperature (°C)	20	20	20	20	20	20	20	20	20	20
		Powder Mean Diameter (μm)	20	20	20	20	20	20	20	25	25	26.9
		Powder Feed Rate	/	/	/	/	/	/	/	/	/	/
Results		Gas Exit Velocity (m/s)	557.82	557.82	557.82	557.82	557.82	557.82	557.82	687.5	692.6	807.67
		Particle Exit Velocity (m/s)	252.12	252.12	252.12	252.12	252.12	252.12	252.12	274.95	268.13	460.27
		Particle Impact Velocity (m/s)	252.74	252.74	252.74	252.74	252.74	252.74	252.74	275.51	268.7	462.6
	Critical Particle Velocity (m/s)	Model 1	453.94	453.94	453.94	453.94	453.94	453.94	453.94	425.75	426.02	398.29
		Model 2	359.84	359.84	359.84	359.84	359.84	359.84	359.84	670.37	670.96	459.67
		Average	406.89	406.89	406.89	406.89	406.89	406.89	406.89	548.06	548.49	428.98
	Depth of Penetration (m)	Model 1	5.5	5.5	5.5	5.5	5.5	5.5	5.5	46.29	44.57	69.21
		Model 2	5.98	5.98	5.98	5.98	5.98	5.98	5.98	87.43	83.14	157.34
		Model 3	N/A	N/A	N/A	N/A	N/A	N/A	N/A	10.86	10	41.49
		Model 4	4.06	4.06	4.06	4.06	4.06	4.06	4.06	10.96	10.78	18.07
		Model 5	N/A	N/A	N/A	N/A	N/A	N/A	N/A	44.96	44.01	65.75
		Average	5.18	5.18	5.18	5.18	5.18	5.18	5.18	40.1	38.5	70.37

The percentage difference in published vs theoretical particle penetration was made using Equation 3.2. These results were included in the combined variability analysis table (Table A.13).

Coefficient of variation (MS_2)

As a means of evaluating each penetrative model's reaction to variation, in the pursuit of a robust model, the coefficient of variation was applied to theoretical data from two independent cold spray runs acted on by *high* and *low* parameter variation. The first parameter set simulated a copper cold spray of a copper substrate, where the feedstock powder had an average particle size of 25 μm with air as the carrier gas. The results are presented in Table A.8. A graphical representation of the independent parameter effects is given in Figure A.2.

The second parameter set simulated a copper cold spray coating on an ABS substrate, where the feedstock powder had an average particle size of 25 μm with air as the carrier gas. The

Table A.8: Independent parameter variation on a copper-copper theoretical coating.

Parameter	Low	Nominal	High	Particle depth-of-penetration (X) [µm]											
				Model 1			Model 2			Model 4			Average		
				Low	Desired	High	Low	Desired	High	Low	Desired	High	Low	Desired	High
Throat Diameter (mm)	1	4	5	2.61	7.63	7.2	2.47	8.53	7.93	2.8	4.23	4.13	2.63	6.8	6.42
Exit Diameter (mm)	5	6	10	7.32	7.63	8.12	8.1	8.53	9.22	4.16	4.23	4.34	6.53	6.8	7.23
Divergent Length (mm)	30	100	150	5.68	7.63	8.97	5.94	8.53	10.49	3.75	4.23	4.53	5.12	6.8	7.99
Ambient Pressure (Pa)	69700	101325	101325	7.63	7.63	7.63	8.53	8.53	8.53	4.23	4.23	4.23	6.8	6.8	6.8
Ambient Temperature (°C)	5	20	30	7.63	7.63	7.63	8.53	8.53	8.53	4.23	4.23	4.23	6.8	6.8	6.8
Stagnation Pressure (MPa)	0.759	1.2	1.548	6.43	7.63	8.36	6.91	8.53	9.58	3.94	4.23	4.39	5.76	6.8	7.44
Stagnation Temperature (°C)	0	24	405	7.34	7.63	10.93	8.13	8.53	13.69	4.16	4.23	4.97	6.55	6.8	9.86
Initial Particle Temperature (°C)	5	20	30	7.63	7.63	7.63	8.53	8.53	8.53	4.23	4.23	4.23	6.8	6.8	6.8
Nozzle Standoff Distance (mm)	5	12.5	100	7.63	7.63	7.71	8.52	8.53	8.64	4.25	4.23	4.24	6.79	6.8	6.86
Nozzle Traverse Speed (mm/s)	3	10	450	7.67	7.63	7.9	8.59	8.53	8.48	4.23	4.23	4.23	6.83	6.8	6.77
Initial Substrate Temperature (°C)	5	20	30	7.56	7.63	9.76	8.43	8.53	11.74	4.23	4.23	4.69	6.74	6.8	8.73

results are presented in Table A.9. A graphical representation of the independent parameter effects is given in Figure A.3.

Table A.9: Independent parameter variation on a copper-ABS theoretical coating.

Parameter	Low	Nominal	High	Particle depth-of-penetration (X) [µm]																	
				Model 1			Model 2			Model 3			Model 4			Model 5			Average		
				Low	Desired	High	Low	Desired	High	Low	Desired	High	Low	Desired	High	Low	Desired	High	Low	Desired	High
Throat Diameter (mm)	1	4	5	6.35	35.39	55.82	9.05	61.77	113.12	N/A	12.64	7.67	6.41	11.18	10.87	21.82	47.44	40.35	7.55	33.68	45.57
Exit Diameter (mm)	5	6	10	51.08	35.39	16.76	99.94	61.77	25.68	8.34	12.64	39.47	10.93	11.18	10.35	41.45	47.44	63.2	42.35	33.68	31.09
Divergent Length (mm)	30	100	150	19.9	35.39	44.16	31.15	61.77	82.12	5.94	12.64	15.98	9.12	11.18	12.04	40.73	47.44	50.45	21.37	33.68	40.95
Ambient Pressure (Pa)	69700	83060	101325	35.39	35.39	35.32	61.77	61.77	61.63	12.34	12.64	15.17	11.18	11.18	11.17	47.07	47.44	50.43	33.55	33.68	34.74
Ambient Temperature (°C)	5	20	30	35.39	35.39	35.39	61.77	61.77	61.77	12.64	12.64	12.64	11.18	11.18	11.18	47.44	47.44	47.44	33.68	33.68	33.68
Stagnation Pressure (MPa)	0.759	0.827	1.548	34.19	35.39	44.58	59.18	61.77	83.16	14.55	12.64	16.35	11.03	11.18	12.26	49.88	47.44	50.68	33.77	33.68	41.41
Stagnation Temperature (°C)	0	200	405	18.37	35.39	199.91	28.45	61.77	1361.72	13.28	12.64	13.22	10.03	11.18	12.05	47.95	47.44	44.85	23.62	33.68	326.35
Initial Particle Temperature (°C)	5	20	30	35.39	35.39	35.39	61.77	61.77	61.77	12.64	12.64	12.64	11.18	11.18	11.18	44.44	47.44	47.44	33.68	33.68	33.68
Nozzle Standoff Distance (mm)	5	20	100	35.22	35.39	36.2	61.4	61.77	63.57	12.6	12.64	12.85	11.17	11.18	11.25	47.41	47.44	47.62	33.56	33.68	35.3
Nozzle Traverse Speed (mm/s)	3	10	450	36.79	35.39	75.14	64.87	61.77	176.35	12.2	12.64	8.48	11.18	11.18	11.18	46.89	47.44	40.78	34.38	33.68	62.39
Initial Substrate Temperature (°C)	5	20	30	36.19	35.39	34.88	63.53	61.77	60.67	12.38	12.64	12.81	11.18	11.18	11.18	47.12	47.44	47.65	34.08	33.68	33.44

The combined average values for the coefficient of variation for each method (under both test scenarios) was computed for each independent process parameter. The results are tabulated in Table A.10 and represent a measure of the variability in each theoretical cold spray process parameter. The larger the coefficient of variation the greater the variability and therefore the uncertainty in parameter value.

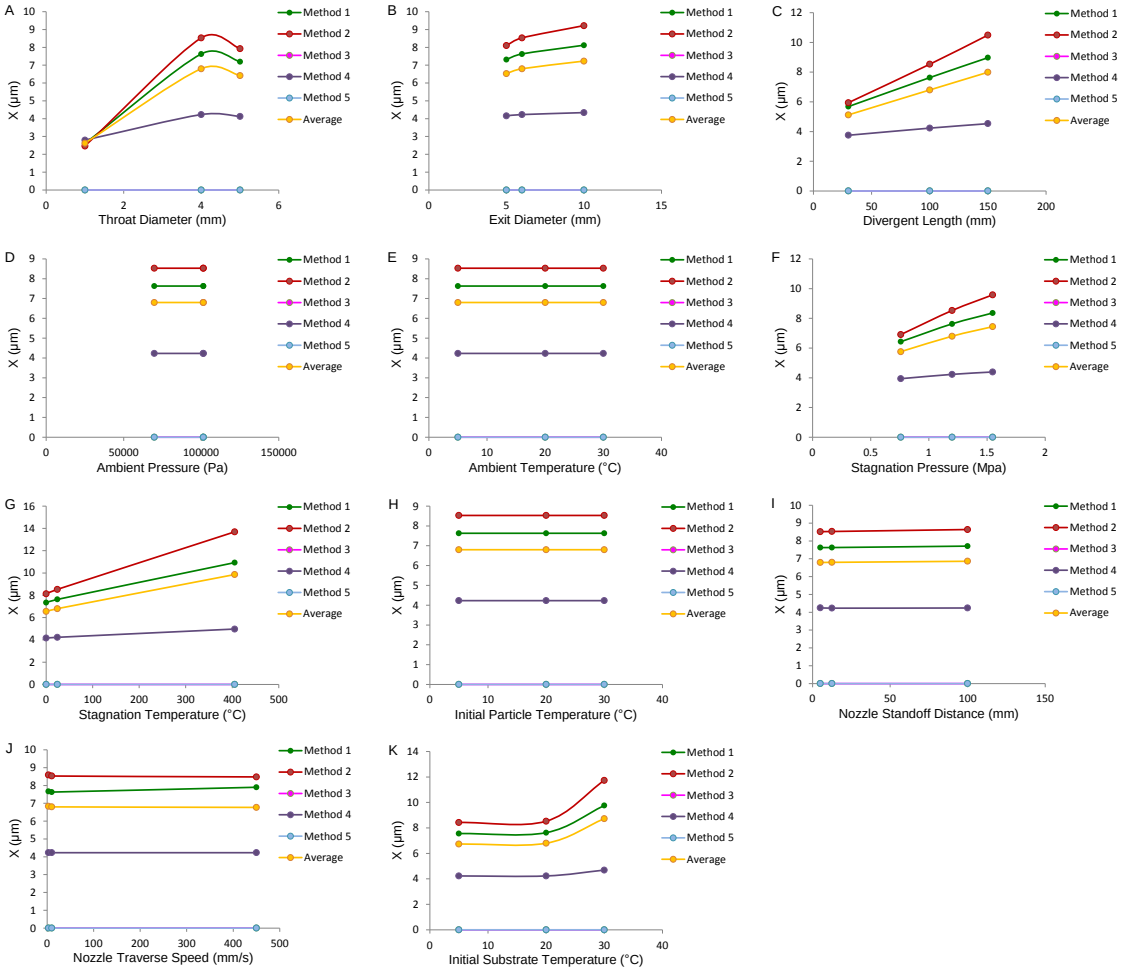


Figure A.2: Theoretical independent parameter effects on particle depth-of-penetration, using the developed theoretical model and a copper cold spray on a copper substrate scenario.

Table A.10: Combined average coefficient of variation values for each depth-of-penetration method with respect to each process parameter.

Parameter	Average Cv Values				
	Method 1	Method 2	Method 3	Method 4	Method 5
Throat Diameter (mm)	0.6215	0.6889	N/A	0.248	0.36207
Exit Diameter (mm)	0.2759	0.33	0.83718	0.0304	0.221608
Divergent Length (mm)	0.2967	0.357	0.443823	0.1168	0.10769
Ambient Pressure (Pa)	0.0006	0.0007	0.116156	0.0003	0.038134
Ambient Temperature (°C)	0	0	0	0	0
Stagnation Pressure (MPa)	0.1399	0.1774	0.127832	0.0564	0.034211
Stagnation Temperature (°C)	0.7084	0.9388	0.027092	0.0961	0.035558
Initial Particle Temperature (°C)	0	0	0	0	0.037297
Standoff Distance (mm)	0.0104	0.0132	0.010577	0.0031	0.002392
Traverse Speed (mm/s)	0.2391	0.3264	0.205766	0	0.08208
Initial Substrate Temperature (°C)	0.0845	0.11	0.017174	0.0303	0.00563

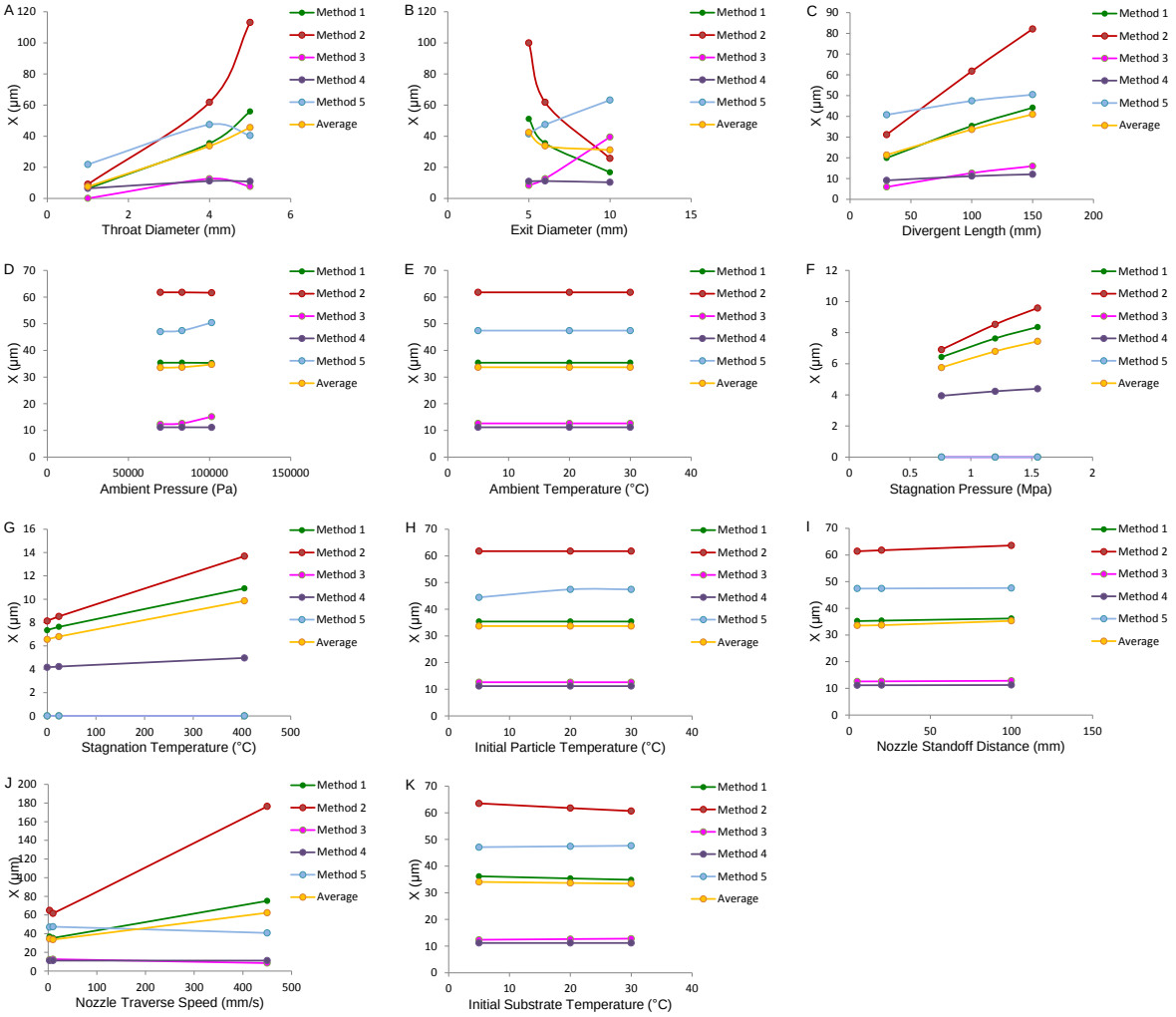


Figure A.3: Theoretical independent parameter effects on particle depth-of-penetration, using the developed theoretical model and a copper cold spray on an ABS polymer substrate scenario.

These coefficients of variation were then used to evaluate the variability in the ten parameter sets from Table A.6; evaluating the respective CV value for those missing process parameters from the literature findings and calculating the combined average. These results are tabulated in the combined variability analysis table (Table A.13) as a percentage value, such that the penetrative models with smaller %CV values represent robust models with higher confidence in selected parameter sets.

Measures of central tendency (MS_3)

Each particle penetration model was run 1000 times based on randomly defined parameter sets. Corresponding parameter sets were used for each model through this analysis. The number of times the predicted penetration for each model which lay closest to the mean of the five models was tabulated and recorded in Table A.11. Similarly, Table A.12 contains a

Table A.11: Number of time each particle penetrative model achieved a predicted response closest to the mean predicted penetration from all five penetration models, based on 1000 random cold spray parameter sets.

Particle penetration model	Number of times closest to mean response	Percentage of all trial runs
Model 1	503	50.3%
Model 2	346	34.6%
Model 3	97	9.7%
Model 4	0	0%
Model 5	54	5.4%

Table A.12: Number of time each particle penetrative model achieved a median response with respect to all five penetration models, based on 1000 random cold spray parameter sets.

Particle penetration model	Number of times as median response	Percentage of all trial runs
Model 1	694	69.4%
Model 2	84	8.4%
Model 3	129	12.9%
Model 4	0	0%
Model 5	93	9.3%

record of the number of times each respective model achieved a median penetrative response with respect to each of the five penetration models.

The Measures of Central Tendency combined method score was calculated by finding the average percentage value and subtracting that value from 100. The final results are tabulated in Table A.13 for all three respective methods. The Measures of Central Tendency score is a general factor and so it may be applied to each trial run related to the Predictive Accuracy methodology.

Table A.13: Combined variability analysis table for theoretical particle depth-of-penetration model selection.

	Model 1			Model 2			Model 3			Model 4			Model 5		
	MS1	MS2	MS3	MS1	MS2	MS3	MS1	MS2	MS3	MS1	MS2	MS3	MS1	MS2	MS3
Run 1	63.82	16.69	40.2	60.66	20.04	78.5	N/A	19.54	88.7	73.29	4.85	100	N/A	8.91	92.7
Run 2	31.25	16.69	40.2	25.25	20.04	78.5	N/A	19.54	88.7	49.25	4.85	100	N/A	8.91	92.7
Run 3	64.05	16.69	40.2	60.92	20.04	78.5	N/A	19.54	88.7	73.46	4.85	100	N/A	8.91	92.7
Run 4	55.65	16.69	40.2	51.77	20.04	78.5	N/A	19.54	88.7	67.26	4.85	100	N/A	8.91	92.7
Run 5	65.41	16.69	40.2	62.39	20.04	78.5	N/A	19.54	88.7	74.47	4.85	100	N/A	8.91	92.7
Run 6	52.99	16.69	40.2	48.89	20.04	78.5	N/A	19.54	88.7	65.3	4.85	100	N/A	8.91	92.7
Run 7	57.69	16.69	40.2	54	20.04	78.5	N/A	19.54	88.7	68.77	4.85	100	N/A	8.91	92.7
Run 8	9.46	12.48	40.2	106.74	16.98	78.5	74.32	10.82	88.7	74.08	0.16	100	6.31	4.22	92.7
Run 9	14.02	0	40.2	60.38	0	78.5	80.71	0	88.7	79.21	0	100	15.1	0	92.7
Run 10	284.5	6.48	40.2	774.11	8.74	78.5	130.5	6.78	88.7	0.39	0.61	100	265.28	3.26	92.7
Average	69.9	13.6	40.2	130.5	16.6	78.5	95.2	15.4	88.7	62.5	3.5	100	95.6	7.0	92.7
MS		47			86			70			52			68	

The predictive model with the lowest variability, i.e. the lowest Method score (MS), was selected as the model to be used for further calculations and trial cold spray run testing. Model 1 was, therefore, seen to be the most robust predictive method and was subsequently used within the theoretical optimisation protocol - the Taguchi Method.

Appendix B Taguchi Optimisation Procedure

Taguchi Method initialisation

In order to run the Taguchi optimisation procedure an initial set of parameter values at various levels was required. Table B.1 contains the initial parameter sets for all theoretical cold spray coatings.

Table B.1: Initial parameter levels for all theoretical cold spray powder-substrate combinations.

Copper (C5003) - ABS				
Independent Variables	**Level 1**	**Level 2**	**Level 3**	**Units**
Stagnation Pressure	0.6	0.8	1.0	Mpa
Stagnation Temperature	0	125	250	°C
Nozzle Standoff Distance	10	20	30	mm
Nozzle Traverse Speed	10	25	40	mm/s

Copper (C5003) - PC				
Independent Variables	**Level 1**	**Level 2**	**Level 3**	**Units**
Stagnation Pressure	0.6	0.8	1.0	Mpa
Stagnation Temperature	0	125	250	°C
Nozzle Standoff Distance	10	20	30	mm
Nozzle Traverse Speed	10	25	40	mm/s

Copper (C5003) - PEEK				
Independent Variables	**Level 1**	**Level 2**	**Level 3**	**Units**
Stagnation Pressure	0.6	0.8	1.0	Mpa
Stagnation Temperature	0	125	250	°C
Nozzle Standoff Distance	10	20	30	mm
Nozzle Traverse Speed	10	25	40	mm/s

Nickel (N5001) - ABS				
Independent Variables	**Level 1**	**Level 2**	**Level 3**	**Units**
Stagnation Pressure	0.6	0.8	1.0	Mpa
Stagnation Temperature	0	125	250	°C
Nozzle Standoff Distance	10	20	30	mm
Nozzle Traverse Speed	10	25	40	mm/s

Nickel (N5001) - PC				
Independent Variables	**Level 1**	**Level 2**	**Level 3**	**Units**
Stagnation Pressure	0.6	0.8	1.0	Mpa
Stagnation Temperature	0	125	250	°C
Nozzle Standoff Distance	10	20	30	mm
Nozzle Traverse Speed	10	25	40	mm/s

Nickel (N5001) - PEEK				
Independent Variables	**Level 1**	**Level 2**	**Level 3**	**Units**
Stagnation Pressure	0.6	0.8	1.0	Mpa
Stagnation Temperature	0	125	250	°C
Nozzle Standoff Distance	10	20	30	mm
Nozzle Traverse Speed	10	25	40	mm/s

Zinc (Z5001) - ABS				
Independent Variables	**Level 1**	**Level 2**	**Level 3**	**Units**
Stagnation Pressure	0.6	0.75	0.9	Mpa
Stagnation Temperature	0	100	200	°C
Nozzle Standoff Distance	10	20	0	mm
Nozzle Traverse Speed	10	25	40	mm/s

Zinc (Z5001) - PC				
Independent Variables	**Level 1**	**Level 2**	**Level 3**	**Units**
Stagnation Pressure	0.6	0.75	0.9	Mpa
Stagnation Temperature	0	100	200	°C
Nozzle Standoff Distance	10	20	0	mm
Nozzle Traverse Speed	10	25	40	mm/s

Zinc (Z5001) - PEEK				
Independent Variables	**Level 1**	**Level 2**	**Level 3**	**Units**
Stagnation Pressure	0.7	0.9	1.0	Mpa
Stagnation Temperature	0	125	250	°C
Nozzle Standoff Distance	10	20	30	mm
Nozzle Traverse Speed	10	25	40	mm/s

Tin (S6001) - ABS				
Independent Variables	**Level 1**	**Level 2**	**Level 3**	**Units**
Stagnation Pressure	0.65	0.8	0.95	Mpa
Stagnation Temperature	0	100	200	°C
Nozzle Standoff Distance	10	20	30	mm
Nozzle Traverse Speed	10	25	40	mm/s

Tin (S6001) - PC				
Independent Variables	**Level 1**	**Level 2**	**Level 3**	**Units**
Stagnation Pressure	0.65	0.8	0.95	Mpa
Stagnation Temperature	0	100	200	°C
Nozzle Standoff Distance	10	20	30	mm
Nozzle Traverse Speed	10	25	40	mm/s

Tin (S6001) - PEEK				
Independent Variables	**Level 1**	**Level 2**	**Level 3**	**Units**
Stagnation Pressure	0.7	0.9	1.1	Mpa
Stagnation Temperature	0	100	200	°C
Nozzle Standoff Distance	10	20	30	mm
Nozzle Traverse Speed	10	20	30	mm/s

Aluminium (A0050) - ABS				
Independent Variables	**Level 1**	**Level 2**	**Level 3**	**Units**
Stagnation Pressure	0.7	0.9	1.1	Mpa
Stagnation Temperature	0	125	250	°C
Nozzle Standoff Distance	10	20	30	mm
Nozzle Traverse Speed	10	25	40	mm/s

Aluminium (A0050) - PC				
Independent Variables	**Level 1**	**Level 2**	**Level 3**	**Units**
Stagnation Pressure	0.7	0.9	1.1	Mpa
Stagnation Temperature	0	125	250	°C
Nozzle Standoff Distance	10	20	30	mm
Nozzle Traverse Speed	10	25	40	mm/s

Aluminium (A0050) - PEEK				
Independent Variables	**Level 1**	**Level 2**	**Level 3**	**Units**
Stagnation Pressure	0.7	0.9	1.1	Mpa
Stagnation Temperature	0	125	250	°C
Nozzle Standoff Distance	10	20	30	mm
Nozzle Traverse Speed	10	25	40	mm/s

In addition to the initial parameter values of the parameters to be optimised the Taguchi Method also factors in noise factors. The initial noise factor values are tabulated in Table B.2.

Table B.2: Initial noise factor levels.

Copper (C5003)			
Noise Factors	Level 1	Level 2	Units
Ambient Pressure	83060	101325	Pa
Ambient Temperature	15	25	°C
Powder Diameter	20	25	µm

Tin (S6001)			
Noise Factors	Level 1	Level 2	Units
Ambient Pressure	83060	101325	Pa
Ambient Temperature	15	25	°C
Powder Diameter	20	25	µm

Nickel (N5001)			
Noise Factors	Level 1	Level 2	Units
Ambient Pressure	83060	101325	Pa
Ambient Temperature	15	25	°C
Powder Diameter	20	25	µm

Aluminium (A0050)			
Noise Factors	Level 1	Level 2	Units
Ambient Pressure	83060	101325	Pa
Ambient Temperature	15	25	°C
Powder Diameter	20	25	µm

Zinc (Z5001)			
Noise Factors	Level 1	Level 2	Units
Ambient Pressure	83060	101325	Pa
Ambient Temperature	15	25	°C
Powder Diameter	22	27.5	µm

Appendix C Experimental Cold Spray

Appendix C documents additional data from the experimental cold spray analysis. The following is included:

- Cold spray standard operating procedure Page 374
- Cold spray optimisation quality checks Page 376
- Cold mounting standard operating procedure procedure Page 384
- Grinding and polishing standard operating procedures Page 385
- Cold spray run card template Page 386
- Independent cold spray parameter effects Page 388
- Complete experimental cold spray optimisation trials Page 390
- Listed experimental cold spray test samples Page 390
- Surface topography standard operating procedure Page 390
- Surface wear test standard operating procedure Page 397
- Surface wear testing: literature review Page 400
- Coating characterisation Page 400

Cold spray standard operating procedure

The following details the Standard Operating Procedure for the cold spray equipment, including the apparatus and setup, the operating procedure and the precautions related to operator safety instructions.

Apparatus and setup
The cold spray system consists of the following key components:

- Cold spray control unit. This component controls the powder feed rate, operating pressure and temperature.
- Spray cabinet. An isolated spray booth containing the substrate to be coated and the cold spray nozzle.
- Computer interface. The nozzle motion is programmed and executed through the computer interface.

Cold spray operating procedure

Due to the specificity of the cold spray system, parts of the following procedure have been included directly from the Centerline SST operation manual [16].

1. Place the sample within the spray cabinet, ensuring precise alignment.
2. Adjust the standoff distance of the nozzle for the specific parameter set being used.
3. Pull out all e-stops, close the doors, check the water level, which must remain between the two limits.
4. Power both electrical panels on.
5. Switch compressor on and ensure pressure builds to nine bar.
6. Turn on the computer and wait for it to boot up.
7. Start the IAI software on the computer.
8. Program the robotic nozzle arm motion on the computer interface.
9. Save the program.
10. Plug in all the cables between the IAI controller, the E-stop for the IAI and the connections to the computer.
11. Write the desired program to the cold spray PLC (Programmable Logic Controller).

12. Turn on the down-draft motor (F1 on the control panel).
13. Turn on the portable spray unit.
14. Select the empty powder hopper on the control panel.
15. Run the program as a dry run to confirm that the program was coded correctly and runs without errors.
16. Attach the feedstock powder container to the powder hoppers by: unlatching, pivoting the assembly down and screwing the container onto the hopper, pivoting the powder hopper back up and re-latching the assembly.
17. On the control panel select the powder filled hopper and create a new program by selecting the desired parameter set.
18. Run the program.
19. Repeat the previous step for further cold spray layers.

Precautions

The following precautions should be considered and acted on when conducting a cold spray procedure:

- Ensure all equipment and systems are fully operational, especially the ventilator.
- Ensure the ventilator water is clean and at the correct level.
- Avoid powder spills or spray cabinet leakages. In the case of the former, vacuum up spills using an industrial filtered vacuum cleaner; in the case of the latter, initiate an emergency stop, evacuate spray room until powder has settled and them commence cleaning and fixing of the leak.
- Mandatory personal protective equipment (PPE) must be worn at all times when operating the cold spray equipment. These include: safety glasses, ear plugs, dust mask, dust coat, latex gloves, safety boots.
- Do not open the spray cabinet during, or immediately after the spray procedure. Allow for complete chamber venting before opening the spray cabinet after spraying.

Cold spray optimisation quality checks

The following details the quality checks that were made as part of the experimental cold spray optimisation procedure.

Physical Observations

The physical observations were made using non-destructive testing (NDT) techniques making use of observations, measurements and calculations.

General appearance

Background

A qualitative summary of the spray features was to be made. These features are based on visual (naked-eye) observations, regarding: perceived thickness, width, continuity and surface finish. A statement regarding the wipe test may be given, regarding observed particle impacts and impact location spread, if visible. A note regarding the effect of the cold spray jet impingement on the substrate may be made, with respect to thermal and mechanical effects in relation to erosion and abrasion.

Target response

The desired surface coating is one of uniform, dense powder dispersion, with minimal substrate distortion.

Apparatus, instrumentation and setup

- Canon EOS 1100D Camera
- NIS-Elements D stereoscopic microscope on Nikon DS-U3

Procedure

View the surface coating and coating-substrate interface at various angles, under good lighting. Make note of general appearance and distinguishing features.

Precautions

Avoid contact with the coating while handling the samples, thus preventing cross-contamination.

Run consistency

Background

Single pass and multi-pass coatings were evaluated by way of naked eye observations.

Target response

The surface coating should exhibit a consistent profile along a cold spray run, with negligible variation in appearance. A rounded build-up profile should be achieved along the width of the run, indicative of standard coating with a round nozzle [16].

Apparatus, instrumentation and setup

- Canon EOS 1100D Camera
- NIS-Elements D stereoscopic microscope on Nikon DS-U3

Procedure

View the sample's surface and coating-substrate interface at various angles, under good lighting. Comment on the consistency of the coating, both along and across the run itself.

Precautions

The type of nozzle used has an effect on the coating build-up profile; which should be considered when evaluating the run consistency [16]. The round nozzle, as used in the current research, produced a rounded shape with a noticeable thickening of the coating towards the centreline of each respective run [16].

Average run width

Background

As an indication of jet impingement conditions and the dispersion of powder particles within the jet, a measure of the run width was an important criterion.

Target response

The coating width, in millimetres, should lie within a tolerance band defined by ±10% of the theoretical impingement diameter (Di). This tolerance band may be expressed by Equation C.1.

$$\frac{90}{100}\left[\frac{SOD}{\frac{L}{D_e - D*}} + D_e\right] \leq \text{Target run width} \leq \frac{110}{100}\left[\frac{SOD}{\frac{L}{D_e - D*}} + D_e\right] \tag{C.1}$$

where:

SOD = Nozzle standoff distance [mm]

L = Diverging length of nozzle [mm]

D_e = Nozzle exit diameter [mm]

D* = Nozzle throat diameter [mm]

Apparatus, instrumentation and setup
Vernier Caliper (accuracy 0.02 mm).

Procedure
Take measurements at five random points along the length of the respective run, and calculate the mean width.

Precautions
The run width does taper on either side due to the rounded build-up profile thus measurements must be taken from points of effectual coating and not dispersed impact zones. This will introduce a measure of uncertainty, which should be controlled by multiple measurements made by the same experimenter (avoiding opinionated variation).

Coating mass
Background
The mass (m) of the deposited powder coating provides an indication of the quality of the coating as a function of the selected system parameters. While this test does not look directly at the quality of the coating, it gives an idea of the deposition efficiency of the system, which is another important criterion considering manufacturability of the material.

Target response
A higher-the-better response characteristic was used when making direct comparisons between coatings.

Apparatus, instrumentation and setup
An isolated digital scale.

Procedure
An uncoated, single pass and a five pass coating run are weighed and measurements made. The respective coating mass must be calculated accordingly.

Precautions
Avoid any source of contamination by keeping each sample isolated between cold spray equipment and scale, and measurements should be made directly before and after spraying, as required.

Notes
While the calculation of coating mass is important and possible in theory, it was later found that this could not be accurately quantified in the current research. Wasteful use of material, with regards to excessive deposition for the sake of generating thick coatings, was avoided. Therefore, the research aimed to deposit the least effective quantity of feedstock powder onto

the respective substrates and in doing so lead to coatings with effective deposition, yet lacking significant coating thickness and therefore mass.

Calculated coating thickness

Background

The coating thickness is an indicator of coating quality that relates directly to the cold spray process parameters. While the coating thickness was to be measured directly during microscopy analyses a preliminary average thickness may be calculated, based on the coating mass, spray area and the density of the spray powder material. This method does assume that the coating and the as sprayed material have the same density.

Target response

A higher-the-better response characteristic was used when making direct comparisons between coatings. A thicker coating means a longer product life; since a thicker coating will take longer to erode.

Apparatus, instrumentation and setup

Vernier Caliper (accuracy 0.02mm) or ruler (accuracy 0.5mm)

Procedure

The following procedure is to be followed:

1. Measure the sprayed area (length x width) using either the Vernier Caliper or ruler.
2. Using the spray powder material density (ρ), the measured spray area (l x w) and the previously calculated coating mass (m), calculate the average coating thickness (t) using Equation C.2.

$$t = \frac{m}{\rho l w} \tag{C.2}$$

Precautions

Although the dimensions of the substrate material and average run width are known the sprayed area should be measured directly to prevent any errors (either new or existing) from being introduced.

Notes

As with coating mass this quantity may be too small to be significant for the purposes of this research.

Powder deposition rate

Background

The deposition rate is a measure of the amount of powder material that coats the substrate over the spraying time period. This criterion is an indicator of process parameter selection adequacy, but may also provide a means of evaluating coating quality as a function of coating efficiency.

Target response
A higher-the-better response characteristic was desired. Therefore a larger deposition rate may be used as a criterion for effective optimisation.

Apparatus, instrumentation and setup
Stopwatch (or calculate spraying time using nozzle traverse speed and run length)

Procedure

1. Each cold spray run should be timed from the point the jet impinges on the substrate to when it leaves the substrate after completing a single pass. For a multi-pass run the sum of individual passes was calculated.
2. Using Equation C.3 and the previously calculated coating mass the powder deposition rate [kg/s] may be calculated.

$$\text{Powder deposition rate} = \frac{\text{Coating mass}}{\text{Effective spray time}} \tag{C.3}$$

Precautions
Unavoidable errors will be introduced if the spraying time is determined using a stopwatch. Preferably use the user set nozzle traverse speed and the run length.

Notes
As with coating mass and coating thickness this quantity may be too small to be significant for the purposes of this research.

Electrical conductivity
Background
Of interest was whether the cold spray coatings developed were conductive or not.

Apparatus, instrumentation and setup
A multimeter was used to measure the electrical conductivity along the length of a respective cold spray run.

Procedure
The probes were place 10 - 20 mm apart and the electrical conductivity recorded.

Precautions
If the coatings were in fact conductive then the conductivity (S/m) must be accurately measured. This required recording the exact straight line distance between the two probes when taking the reading.

Notes
The developed coatings were not expected to be highly conductive (or conductive at all), since the polymer metallisation process essentially produces embedded metal particles in a polymer matrix. This mechanical entanglement prevents continuous contact between adjacent metal deposits and therefore prevents effective conductivity.

Optical analysis

Stereoscopic microscopy

Background
The use of a stereoscopic microscope allows for higher magnification observations to be made, while incorporating the impression of depth. Both qualitative and quantitative testing may be carried out. The former being that of general appearance and surface area coverage; while the latter includes run width measurements and, with the use of digital imaging software, a quantitative analysis into surface area coverage may be made.

Target response
The target responses are specific to each output of the stereoscopic microscopy analysis, as given below:

General Appearance: Uniform, dense powder dispersion, with minimal substrate distortion.

Surface Area Coverage: Maximum surface area coverage was desired. The surface coating should exhibit a consistent profile along a run, with negligible variation in appearance. A rounded build-up profile should be achieved along the width of the run, indicative of standard coating with a round nozzle. Quantified percentage area coverage was estimated using 8 bit top view images and ImageJ threshold settings for area analysis set at a red display setting with a min/max threshold setting of 180/255. This was standardised for all test images.

Average Run Width: The coating width, in millimetres, should lie within a tolerance band defined by ±10% of the theoretical impingement diameter (Di), as calculated by Equation C.1.

Apparatus, instrumentation and setup
A stereoscopic microscope (NIS-Elements D on Nikon DS-U3) and Vernier Calipers.

Microscopy standard operating procedure

The following procedure was followed for microscopy analysis and is standard for all microscopy types.

1. Switch on the microscope, lighting and associated computer interface.
2. Start the relevant computer program.
3. Set the observation stage directly below lens at its maximum standoff distance.
4. Mount sample on stage, ensuring the sample surface is horizontal and as flat as possible.
5. Set microscope to its lowest magnification setting and use firstly the coarse focus and then fine focus to focus on a desired area of the sample surface.
6. Proceed to increase magnification, adjusting the course and then fine focus in turn, until adequate resolution is achieved.
7. Take an image using the computer interface.
    7.1. Comment on surface area coverage.
    7.2. Record run width.
8. Repeat process of additional areas of interest and samples.
9. Export images to an appropriate file.
10. Switch microscope and computer off and cover with protective cover.
11. Using suitable image analysis software (e.g. ImageJ) quantitatively evaluate the percentage of surface area coverage and comment on coating uniformity.

Precautions

The following precautions are common to all types of assisted optical observation techniques:

1. Ensure sample is level to obtain the clearest possible image.
2. Avoid contaminating the microscopic device or sample, by cross-contamination. This may require placing the sample between two glass sheets and wearing gloves when working on the device.
3. Ensure the sample top surface never comes in contact with the optical lens of the microscope.

Optical microscopy

Background

Both a top view and a cross-sectional view of the surface coating may be made with the use of a high resolution optical microscope.

Target response

The target responses are specific to each output of the optical microscopy analysis, as given below:

General appearance (top view): Uniform, dense powder dispersion, with minimal substrate distortion.

Surface area coverage (top view): Maximum surface area coverage - Larger-the-Better. The surface coating should exhibit a consistent profile along a run, with negligible variation in appearance. A rounded build-up profile should be achieved along the width of the run, indicative of a standard coating with a round nozzle.

Particle impact observations (top view): Single particle impacts.

General appearance (cross-sectional view): Uniform, thick, dense coating, with minimal substrate distortion or excessive intermixing. Transition layer should be evident, but not extensive. Minimal surface and transition irregularity should be observed.

Coating consistency (cross-sectional view): The surface coating should exhibit a consistent profile along a run, with negligible variation in appearance. A rounded build-up profile should be achieved along the width of the run, indicative of standard coating with a round nozzle.

Particle impact observations (cross-sectional view): Sufficient embedment, defined by the calculated target particle depth-of-penetration. Both theoretical and actual depth of penetration should lie within a $\pm 10\%$ tolerance band about the target response. Particle-substrate mixing, associated with particle flattening and lack of surrounding void space, was desired for a strong mechanical bond.

Coating thickness (Cross-Sectional View): Larger-the-Better
Coating thickness measurement was based on the ASTM B487-85 *standard test method for measurement of metal and oxide coating thickness by microscopical examination of cross section*. This included the following steps:

1. Obtain a micrograph of the coating cross-section.
2. Import image into suitable image processing software, for example ImageJ.
3. Overlay a boundary for the top of the coating and the bottom part - beyond which no particle deposits are present.
4. Make at least five measurements between the top and bottom boundary. Ensure measurements are made perpendicular to the average coating-substrate boundary.
5. Calculate the arithmetic mean coating thickness.

The accuracy of the coating thickness should be around 0.8 μm based on the ASTM B487-85 standard.

Transition thickness (Cross-Sectional View): Smaller-the-Better, provided that a uniform, thick, dense coating is achieved, otherwise a higher level of transition irregularity is acceptable.

Flattening ratio: The flattening ratio, given by Equation 5 [135], should lie within the range: $1.25 < FR < 2.25$. This, however, was not necessarily relevant for polymer metallisation and was therefore used with discretion.

Compression ratio: The compression ratio, given by Equation 6 [135], should lie within the range: $30 < CR < 50$. As with the flattening ratio this quantity was not considered particularly relevant for cold spray polymer metallisation and therefore used with discretion.

Apparatus, instrumentation and setup

- SM-Lux, Pol, Leitz Wetzlar, Germany, with a 3.0 megapixel Moticam 2300.
- Leica DM6000M with Leica DF490 camera mount.
- Motic BA310Met, with LM Plan objective lenses.

Cold mounting standard operating procedure

Test samples required for microscopy and wear test analysis were cold mounted in the transparent Technovit 4004 cold curing resin from Kulzer. The details and procedure for mixing the two part, exothermic resin is given below. A mixing ratio of 2:1 (powder:liquid) was used.

1. Lubricate mounting cups with Vaseline, to aid sample removal after curing.
2. Secure test samples with mounting clip in mounting cups.
3. Measure out 10 g of liquid into a beaker.
4. Add 10 g of powder and mix thoroughly, with a glass spatula.
5. Add the remaining 10 g of powder.
6. Stir gently for 40 seconds. Avoid introducing air bubbles.
7. Tap beaker gently to remove any air bubbles for 10 seconds.
8. Stir gently for a further 20 seconds.
9. Pour the resin mixture slowly into mounting cups.

10. Allow resin to cure for 10 minutes.
11. Pop cured cold mounted samples out of mounting cups.
12. Repeat the mounting process for the remaining test samples.

Precautions

- The chemicals used in the mounting process do give off fumes, so it was advisable to perform the mounting process in a well ventilated environment.
- No more than 30 g of resin was to be mixed at any given time so as to avoid excessive heat generation.

Grinding and polishing standard operating procedures

Cross-sectional cold mounted test samples undergoing microscopy analysis were required to be ground and polished according to the following procedure.

Plane grinding

- Silicon-Carbide (SiC) foil (US # 280 or FEPA P# 320).
  - grain size μm
  - water lubricated
  - 250 rpm
  - grind until plane
- SiC foil (US# 360 or FEPA P# 500)
  - water lubricated
  - grain size 30 μm
  - 250 rpm
  - grind until plane
- SiC foil (US # 500 or FEPA P# 1000)
  - water lubricated
  - grain size 18 μm
  - 250 rpm
  - grind until plane

Fine grinding

- MD-Largo (Struers) or QuickStep 250 (Proscience Laboratory Solutions (PLS))
- grain size 9 μm
- lubricated with ultra diamond solution (# 812-509M (Leco) or DP suspension poly (PLS))
- 250 rpm
- 30 N load
- 5 min duration

Diamond polishing

- MD-Mol (Struers) or Samba-N (PLS)
  - grain size 3 μm
  - lubricated with ultra diamond suspension (# 812-507M (Leco) or Magnum top-duo (3 μm) (PLS))
  - 250 rpm
  - 20 N load
  - 5 min duration
- Mag-Napal (Struers) or Mambo (PLS)
  - grain size 1 μm
  - polished with Magnum top-duo (1 μm) (PLS)
  - 250 rpm
  - 15 N load
  - 2 min duration

Oxide polishing

- MD-Nap (struers)
- lubricated with colloidal silica 0.05 μm (Leco)
- 250 rpm
- 10 N load
- 1 min duration

Cold spray run card template

Experimental cold spray optimisation and characterisation was carried out on numerous test samples. Table C.1 depicts a template cold spray run card which accompanied each test sample, ensuring accurate records were kept of each individual test sample.

Table C.1: Cold spray run card template.

Start Date(Time): End Date(Time): Cold Spray Optimisation - Run Card Run Reference Number: Sheet 1

Cold Spray Parameter Set			Physical Observations	Comments on the cold spray run:		
Ambient Conditions	Air Pressure (Pa)		General Appearance	Line 1		
	Air Temperature (°C)			Line 2		
	Powder Temperature (°C)			Line 3		
	Substrate Temperature (°C)		Run Consistency	Line 2		
Powder Properties	Spray Material			Line 3		
	Mean Particle Size (μm)		Average Run Width (mm)	(mm)	theory	actual
	Powder Material Density (kg/m^3)			Line 2		
	Powder Morphology			Line 3		
Substrate Properties	Substrate Material		Substrate Mass	Uncoated		
	Length (mm)		Coating Mass (g)	Line 1		
	Width (mm)			Line 2		
	Thickness (mm)			Line 3		
Nozzle Geometry	Throat Diameter (mm)		Coating Thickness	(mm)	measure	calc
	Exit Diameter (mm)			Line 2		
	Diverging Length (mm)			Line 3		
Cold Spray Process Parameters	Operating Pressure (Mpa)		Deposition Rate	(g/s)		
	Operating Temperature (°C)		Deposition Efficiency	%		
	Nozzle Standoff Distance (mm)		Electrical Continuity (yes or no)	Line 1		
	Nozzle Traverse Speed (mm/s)			Line 2		
	Powder Feed Rate (%)			Line 3		
	Powder Feed Rate (g/s)					
Calculated mass of powder sprayed (g)						

Mechanical Property Testing						
Surface Roughness	Line 2:		Average Ra (μm)	Line 2:		
	Line 3:			Line 3:		
Vickers Hardness			VH - Line 2			
			VH - Line 3			
Scratch Test			L_c - Line 2			
			L_c - Line 3			

Notes:

Optical Analysis						
Stereoscopic Microscopy	General Appearance	Line 1				
		Line 2				
		Line 3				
	Surface Area Coverage	Line 2				
		Line 3				
	Average Width	Line 2		Max Width of Uniform Coating	Line 2	
		Line 3			Line 3	
Optical Microscopy	General Appearance (Top View - t.v)	Line 1				
		Line 2				
		Line 3				
	Surface Area Coverage (t.v)	Line 2				
		Line 3				
	Particle Impact Observations (t.v)	Line 1				
	General Appearance (Cross-Sectional View - csv)	Line 1				
		Line 2				
		Line 3				
	Coating Consistency (csv)	Line 2				
		Line 3				
	Particle Impact Observations (csv)	Line 1	Depth of Penetration (μm)	Target		Theory
			Comments:			Actual
	Porosity (csv) [%]	Line 2		Line 3		
	Surface Irregularity (μm)	Line 2		Line 3		
	Transition Irregularity (μm)	Line 2		Line 3		
	Coating Thickness (μm)	Line 2		Line 3		
	Transition Thickness (μm)	Line 2		Line 3		
	Flattening Ratio (D/d_p)		Compression Ratio		COMPLETED	

Figures: Tables: References:

Independent cold spray parameter effects

Cold spray parameter effects, variations and selection were three fundamental areas of investigation that were considered throughout the course of this research.

High-low cold spray parameter variations

As part of the development of an independent parameter effects and variation decision framework Table C.2 was used to investigate the effect independent variation in cold spray process parameters (operating pressure and temperature, nozzle standoff distance, nozzle traverse speed and powder feed rate) have on various criteria for single and multi-pass coatings. Wipe test data was also required for the evaluation of particle depth-of-penetration and average impacting particle size.

Table C.2: Experimental parameter effects for high-low parameter variation.

Experimental Trend Criteria		Cold Spray Parameters of Interest														
		Operating Pressure			Operating Temperature			Nozzle Standoff Distance			Nozzle Traverse Speed			Powder Feed Rate		
		Low	Medium	High	Low	Medium	High	Low	Medium	High	Low	Medium	High	Low	Medium	High
Particle Depth-of-Penetration (μm)	Wipe test	3.26	5.48	3.93	4.24	5.48	6.57	2.49	5.48	6.82	3.31	5.48	2.87	6.36	5.48	7.5
Average Impacting Particle Size (μm)	Wipe test (t-v)	3.84	3.58	5.08	3.91	3.58	6.76	3.85	3.58	4.82	4.37	3.58	4.45	6.08	3.58	4.19
	Wipe test (c-s)	3.54	4.63	2.01	2.27	4.63	5.25	2.8	4.63	5.47	3.66	4.63	3.47	4.51	4.63	4.16
Surface Roughness (Ra)[μm]	Single pass	0.86	1.03	1.16	1.14	1.03	1.24	1.05	1.03	1.14	1.22	1.03	1.15	1.16	1.03	1.29
	Multi pass	1.59	1.35	1.36	1.40	1.35	1.90	1.38	1.35	1.53	1.41	1.35	1.34	1.65	1.35	1.46
Surface Area Coverage (%)	Single pass	99.03	98.19	94.67	97.28	98.19	98.86	99.44	98.19	99.5	99.66	98.19	99.58	99.37	98.19	99.57
	Multi pass	99.27	99.08	99.03	95.39	99.08	100	98.82	99.08	98.69	97.93	99.08	99.18	99.49	99.08	99.37

Independent cold spray parameter effects on surface topography

The parameter effects on a single pass coating, based on independent parameter variation for cold spray of a copper-aluminium-alumina blended powder on ABS polymer substrates are tabulated in Table C.3 together with the Pearson correlation coefficient tabulated in Table C.4. The corresponding results for multi-pass coatings (5 layers) are given by Table C.5 and Table C.6, respectively.

Table C.3: Surface topographical effects from independent cold spray parameter variation (single pass coatings).

Surface Roughness Parameters	Operating pressure			Operating temperature			Nozzle standoff distance			Nozzle traverse speed			Powder feed rate		
	low	med	high	low	med	high	low	med	high	low	med	high	low	med	high
Ra (μm)	0.863	1.189	1.161	1.14	1.189	1.235	1.048	1.189	1.138	1.223	1.189	1.153	1.16	1.189	1.289
Rz (μm)	7.479	7.716	8.966	7.773	7.716	11.162	9.014	7.716	10.288	9.707	7.716	9.785	9.786	7.716	10.823
Rsm (mm)	0.058	0.054	0.073	0.076	0.054	0.06	0.07	0.054	0.07	0.074	0.054	0.059	0.07	0.054	0.069
Rs (mm)	0.048	0.035	0.05	0.05	0.035	0.049	0.048	0.035	0.051	0.052	0.035	0.047	0.05	0.035	0.047
Rq (μm)	1.11	1.507	1.497	1.429	1.507	1.593	1.346	1.507	1.487	1.561	1.507	1.451	1.489	1.507	1.668
Rsk	-0.173	-0.133	0.452	-0.214	-0.133	-0.079	0.08	-0.133	0.598	-0.298	-0.133	-0.015	-0.021	-0.133	0.154

Table C.4: Pearson correlation coefficient (R) for surface topographical effects from independent cold spray parameter variation (single pass coatings).

	P_0	T_0	SOD	V_n	PFR
Ra (μm)	0.825	1.000	0.630	-1.000	0.953
Rz (μm)	0.931	0.859	0.495	0.033	0.328
Rsm (mm)	0.749	-0.703	0.000	-0.721	-0.056
Rs (mm)	0.123	-0.060	0.176	-0.286	-0.189
Rq (μm)	0.855	1.000	0.803	-1.000	0.908
Rsk	0.893	0.993	0.689	0.995	0.605

Table C.5: Surface topographical effects from independent cold spray parameter variation (multi-pass coatings).

Surface Roughness Parameters	Operating pressure			Operating temperature			Nozzle standoff distance			Nozzle traverse speed			Powder feed rate		
	low	med	high	low	med	high	low	med	high	low	med	high	low	med	high
Ra (μm)	1.593	1.387	1.361	1.398	1.387	1.897	1.377	1.387	1.531	1.409	1.387	1.338	1.654	1.387	1.463
Rz (μm)	12.988	9.504	10.48	13.359	9.504	15.34	10.043	9.504	11.326	12.51	9.504	11.529	13.69	9.504	11.655
Rsm (mm)	0.074	0.06	0.077	0.085	0.06	0.067	0.073	0.06	0.081	0.076	0.06	0.076	0.073	0.06	0.067
Rs (mm)	0.055	0.037	0.052	0.062	0.037	0.051	0.05	0.037	0.051	0.053	0.037	0.051	0.054	0.037	0.049
Rq (μm)	2.031	1.752	1.724	1.822	1.752	2.402	1.737	1.752	1.94	1.825	1.752	1.778	2.091	1.752	1.838
Rsk	-0.364	-0.534	-0.211	0.157	-0.534	-0.332	0.043	-0.534	-0.355	0.134	-0.534	0.563	-0.217	-0.534	-0.155

Table C.6: Pearson correlation coefficient (R) for surface topographical effects from independent cold spray parameter variation (multi-pass coatings).

	P	T	SOD	V_n	PFR
Ra (μm)	-0.913	0.856	0.894	-0.977	-0.694
Rz (μm)	-0.698	0.334	0.685	-0.320	-0.486
Rsm (mm)	0.165	-0.698	0.377	0.000	-0.461
Rs (mm)	-0.156	-0.439	0.064	-0.115	-0.286
Rq (μm)	-0.904	0.813	0.897	-0.635	-0.718
Rsk	0.473	-0.688	-0.674	0.388	0.152

Complete experimental cold spray optimisation trials

All 69 possible experimental cold spray trials for each coating is listed in Table C.7. The table includes the sample reference number, the respective optimisation level and the parameter instructions. It should be recalled that this optimisation framework was coupled with the experimental parameter selection model, thereby reducing the total number of experimental trials required in order to achieve sufficient optimisation.

Listed experimental cold spray test samples

The reference codes for all the cold spray test samples are listed in Table C.8 for Levels A, B and C of the experimental optimisation procedure. The optimum test samples from these cold spray trials are highlighted orange.

All cold spray trials followed the experimental procedure governed by the test details given in Table C.7, except for the cold spray of zinc onto a polycarbonate substrate. For this material combination, after the completion of the standard Level B procedure, it was decided that operating temperature was of particular importance in the pursuit of a suitable coating. It was for this reason that experimentation deviated from the structured optimisation procedure, opting for an alternative procedure involving the variation of operating temperature, over a wide range with associated tests conducted at a 15 unique points within this range.

Surface topography standard operating procedure

Surface topography analysis was used as a means of characterising cold spray coatings and later used to investigate the effects of surface profile (both substrate and coatings) on various coating qualities, including: antimicrobial efficacy and wear resistance.

Applicable terminology

The following terms are relevant to the surface topographical analysis undertaken.

Surface roughness: Microscopic surface asperities.

Sampling length: A section of a surface profile, isolated for representative analysis.

Evaluation length: The length of the evaluated surface, made up of a number of sampling lengths (usually five sampling lengths make up the effective evaluation length).

Table C.7: Cold spray parameter sets for experimental optimisation procedure

Test Number	Ref. Number	Optimisation Level	Optimisation Level Number	Parameter Set Selection
1	___ ___ (A1)1	A - Theoretical Parameter Set	1	Theoretically optimum parameter set used
2	___ ___ (A2)2	A - Theoretical Parameter Set	2	Theoretically optimum parameter set used
3	___ ___ (A2)3	A - Theoretical Parameter Set	3	Theoretically optimum parameter set used
4	___ ___ (B1)4	B - High-Low Variation	1	(1.25Po),(1.5To),(1.5SOD),(1.5V_{nozzle}),(1.5PFR)
5	___ ___ (B2)5	B - High-Low Variation	2	(1.25Po),(1.5To),(1.5SOD),(1.5Vnozzle),(0.5PFR)
6	___ ___ (B3)6	B - High-Low Variation	3	(1.25Po),(1.5To),(1.5SOD),(0.5V_{nozzle}),(1.5PFR)
7	___ ___ (B4)7	B - High-Low Variation	4	(1.25Po),(1.5To),(1.5SOD),(0.5V_{nozzle}),(0.5PFR)
8	___ ___ (B5)8	B - High-Low Variation	5	(1.25Po),(1.5To),(0.5SOD),(1.5V_{nozzle}),(1.5PFR)
9	___ ___ (B6)9	B - High-Low Variation	6	(1.25Po),(1.5To),(0.5SOD),(1.5V_{nozzle}),(0.5PFR)
10	___ ___ (B7)10	B - High-Low Variation	7	(1.25Po),(1.5To),(0.5SOD),(0.5V_{nozzle}),(1.5PFR)
11	___ ___ (B8)11	B - High-Low Variation	8	(1.25Po),(1.5To),(0.5SOD),(0.5V_{nozzle}),(0.5PFR)
12	___ ___ (B9)12	B - High-Low Variation	9	(1.25Po),(0.5To),(1.5SOD),(1.5V_{nozzle}),(1.5PFR)
13	___ ___ (B10)13	B - High-Low Variation	10	(1.25Po),(0.5To),(1.5SOD),(1.5V_{nozzle}),(0.5PFR)
14	___ ___ (B11)14	B - High-Low Variation	11	(1.25Po),(0.5To),(1.5SOD),(0.5V_{nozzle}),(1.5PFR)
15	___ ___ (B12)15	B - High-Low Variation	12	(1.25Po),(0.5To),(1.5SOD),(0.5V_{nozzle}),(0.5PFR)
16	___ ___ (B13)16	B - High-Low Variation	13	(1.25Po),(0.5To),(0.5SOD),(1.5V_{nozzle}),(1.5PFR)
17	___ ___ (B14)17	B - High-Low Variation	14	(1.25Po),(0.5To),(0.5SOD),(1.5V_{nozzle}),(0.5PFR)
18	___ ___ (B15)18	B - High-Low Variation	15	(1.25Po),(0.5To),(0.5SOD),(0.5V_{nozzle}),(1.5PFR)
19	___ ___ (B16)19	B - High-Low Variation	16	(1.25Po),(0.5To),(0.5SOD),(0.5V_{nozzle}),(0.5PFR)
20	___ ___ (B17)20	B - High-Low Variation	17	(0.75Po),(1.5To),(1.5SOD),(1.5V_{nozzle}),(1.5PFR)
21	___ ___ (B18)21	B - High-Low Variation	18	(0.75Po),(1.5To),(1.5SOD),(1.5V_{nozzle}),(0.5PFR)
22	___ ___ (B19)22	B - High-Low Variation	19	(0.75Po),(1.5To),(1.5SOD),(0.5V_{nozzle}),(1.5PFR)
23	___ ___ (B20)23	B - High-Low Variation	20	(0.75Po),(1.5To),(1.5SOD),(0.5V_{nozzle}),(0.5PFR)
24	___ ___ (B21)24	B - High-Low Variation	21	(0.75Po),(1.5To),(0.5SOD),(1.5V_{nozzle}),(1.5PFR)
25	___ ___ (B22)25	B - High-Low Variation	22	(0.75Po),(1.5To),(0.5SOD),(1.5V_{nozzle}),(0.5PFR)
26	___ ___ (B23)26	B - High-Low Variation	23	(0.75Po),(1.5To),(0.5SOD),(0.5V_{nozzle}),(1.5PFR)
27	___ ___ (B24)27	B - High-Low Variation	24	(0.75Po),(1.5To),(0.5SOD),(0.5V_{nozzle}),(0.5PFR)
28	___ ___ (B25)28	B - High-Low Variation	25	(0.75Po),(0.5To),(1.5SOD),(1.5V_{nozzle}),(1.5PFR)
29	___ ___ (B26)29	B - High-Low Variation	26	(0.75Po),(0.5To),(1.5SOD),(1.5V_{nozzle}),(0.5PFR)
30	___ ___(B27)30	B - High-Low Variation	27	(0.75Po),(0.5To),(1.5SOD),(0.5V_{nozzle}),(1.5PFR)
31	___ ___(B28)31	B - High-Low Variation	28	(0.75Po),(0.5To),(1.5SOD),(0.5V_{nozzle}),(0.5PFR)
32	___ ___(B29)32	B - High-Low Variation	29	(0.75Po),(0.5To),(0.5SOD),(1.5V_{nozzle}),(1.5PFR)
33	___ ___(B30)33	B - High-Low Variation	30	(0.75Po),(0.5To),(0.5SOD),(1.5V_{nozzle}),(0.5PFR)
34	___ ___ (B31)34	B - High-Low Variation	31	(0.75Po),(0.5To),(0.5SOD),(0.5V_{nozzle}),(1.5PFR)
35	___ ___ (B32)35	B - High-Low Variation	32	(0.75Po),(0.5To),(0.5SOD),(0.5V_{nozzle}),(0.5PFR)
36	___ ___ (C1)36	C - Independent Variation	1	Best of B with P = 0.9P
37	___ ___ (C2)37	C - Independent Variation	2	Best of B with P = 0.95P
38	___ ___ (C3)38	C - Independent Variation	3	Best of B with P = 1.05P
39	___ ___ (C4)39	C - Independent Variation	4	Best of B with P = 1.1P
40	___ ___ (C5)40	C - Independent Variation	5	Best of B with T = 0.5T
41	___ ___ (C6)41	C - Independent Variation	6	Best of B with T = 0.8T
42	___ ___ (C7)42	C - Independent Variation	7	Best of B with T = 0.9T
43	___ ___ (C8)43	C - Independent Variation	8	Best of B with T = 1.1T
44	___ ___ (C9)44	C - Independent Variation	9	Best of B with T = 1.2T
45	___ ___ (C10)45	C - Independent Variation	10	Best of B with T = 1.5T
46	___ ___ (C11)46	C - Independent Variation	11	Best of B with SOD = 0.8SOD
47	___ ___ (C12)47	C - Independent Variation	12	Best of B with SOD = 1.2SOD
48	___ ___ (C13)48	C - Independent Variation	13	Best of B with V_{nozzle} = 0.8 V_{nozzle}
49	___ ___ (C14)49	C - Independent Variation	14	Best of B with V_{nozzle} = 1.2 V_{nozzle}
50	___ ___ (C15)50	C - Independent Variation	15	Best of B with -5% PFR
51	___ ___ (C16)51	C - Independent Variation	16	Best of B with +5% PFD
52	___ ___ (D1r1)52	D - Combined Parameter Effect	1	Nominal = Combined best elements of C
53	___ ___ (D2r1)53	D - Combined Parameter Effect	2	1.025(Nominal)
54	___ ___ (D3r1)54	D - Combined Parameter Effect	3	0.975(Nominal)
55	___ ___ (D4r1)55	D - Combined Parameter Effect	4	P = 1.025P, Nominal
56	___ ___ (D5r1)56	D - Combined Parameter Effect	5	T = 1.025T, Nominal
57	___ ___ (D6r1)57	D - Combined Parameter Effect	6	P = 0.975P, Nominal
58	___ ___ (D7r1)58	D - Combined Parameter Effect	7	T = 0.975T, Nominal
59	___ ___ (D8r1)59	D - Combined Parameter Effect	8	P = 1.025P, T = 0.975T, Nominal
60	___ ___ (D9r1)60	D - Combined Parameter Effect	9	P = 0.975P, T = 1.025T, Nominal
61	___ ___ (D1r2)61	D - Combined Parameter Effect	10	Nominal = Best of Dr1
62	___ ___ (D2r2)62	D - Combined Parameter Effect	11	1.025(Nominal)
63	___ ___ (D3r2)63	D - Combined Parameter Effect	12	0.975(Nominal)
64	___ ___ (D4r2)64	D - Combined Parameter Effect	13	P = 1.025P, Nominal
65	___ ___ (D5r2)65	D - Combined Parameter Effect	14	T = 1.025T, Nominal
66	___ ___ (D6r2)66	D - Combined Parameter Effect	15	P = 0.975P, Nominal
67	___ ___ (D7r2)67	D - Combined Parameter Effect	16	T = 0.975T, Nominal
68	___ ___ (D8r2)68	D - Combined Parameter Effect	17	P = 1.025P, T = 0.975T, Nominal
69	___ ___ (D9r2)69	D - Combined Parameter Effect	18	P = 0.975P, T = 1.025T, Nominal

Table C.8: Experimental cold spray optimisation: List of all cold spray runs for all levels.

LEVEL B			LEVEL C			LEVEL D		
	Copper coatings	$CuAlAl_2O_3$ coatings		Zinc coatings	Copper coatings	$CuAlAl_2O_3$ coatings	Copper coatings	$CuAlAl_2O_3$ coatings
Copper - 3DABS	Cu(1)3DABS(B17)20	Cu(2)3DABS(B17)20	Zinc - 3DABS	Zn3DABS(B21)24	Cu(1)PC(C1)36	Cu(2)PC(C1)36	Cu(1)PC(D1r1)50	Cu(2)PC(D1r1)50
	Cu(1)3DABS(B17+T)20	Cu(2)3DABS(B17+T)20		Zn3DABS(B21+T)24	Cu(1)PC(C2)37	Cu(2)PC(C2)37	Cu(1)PC(D2r1)51	Cu(2)PC(D2r1)51
	Cu(1)3DABS(B19)22	Cu(2)3DABS(B17+PFR)20		Zn3DABS(B21+PFR)24	Cu(1)PC(C3)38	Cu(2)PC(C8)43	Cu(1)PC(D3r1)52	Cu(2)PC(D3r1)52
	Cu(1)3DABS(B19+T)22	Cu(2)3DABS(B19)22		Zn3DABS(B23)26	Cu(1)PC(C4)39	Cu(2)PC(C9)44	Cu(1)PC(D4r1)53	Cu(2)PC(D4r1)53
	Cu(1)3DABS(B21)24	Cu(2)3DABS(B19+T)22		Zn3DABS(B21+T)26	Cu(1)PC(C8)43	Cu(2)PC(C10)45	Cu(1)PC(D5r1)54	Cu(2)PC(D5r1)54
	Cu(1)3DABS(B21+T)24	Cu(2)3DABS(B19+PFR)22		Zn3DABS(B21+PFR)26	Cu(1)PC(C9)44	Cu(2)PC(C12)47	Cu(1)PC(D6r1)55	Cu(2)PC(D6r1)55
	Cu(1)3DABS(B23)26	Cu(2)3DABS(B21)24	Zinc - ABS	ZnABS(B21)24	Cu(1)PC(C10)45	Cu(2)PC(C13)48	Cu(1)PC(D7r1)56	Cu(2)PC(D7r1)56
	Cu(1)3DABS(B23+T)26	Cu(2)3DABS(B21+T)24		ZnABS(B21+T)24	Cu(1)PC(C11)46	Cu(2)PC(C14)49	Cu(1)PC(D8r1)57	Cu(2)PC(D8r1)57
Copper - ABS	Cu(1)ABS(B17)20	Cu(2)3DABS(B21+PFR)24		ZnABS(B21+PFR)24	Cu(1)PC(C13)48	Cu(2)PC(C15)50	Cu(1)PC(D9r1)58	Cu(2)PC(D9r1)58
	Cu(1)ABS(B17+T)20	Cu(2)3DABS(B23)26		ZnABS(B23)26	Cu(1)PC(C14)49	Cu(2)PC(C16)51	Cu(1)PC(D1r2)50	Cu(2)PC(D1r2)50
	Cu(1)ABS(B19)22	Cu(2)3DABS(B23+T)26		ZnABS(B23+T)26	Cu(1)PC(C15)50	Cu(2)PC(Cspecial1)	Cu(1)PC(D2r2)51	Cu(2)PC(D2r2)51
	Cu(1)ABS(B19+T)22	Cu(2)3DABS(B23+PFR)26		ZnABS(B23+PFR)26	Cu(1)PC(C16)51	Cu(2)PC(Cspecial2)	Cu(1)PC(D3r2)52	Cu(2)PC(D3r2)52
	Cu(1)ABS(B21)24	Cu(2)ABS(B17)20	Zinc - ABS	ZnPC(B25)28			Cu(1)PC(D4r2)53	Cu(2)PC(D4r2)53
	Cu(1)ABS(B21+T)24	Cu(2)ABS(B17+T)20		ZnPC(B25+T)28			Cu(1)PC(D5r2)54	Cu(2)PC(D5r2)54
	Cu(1)ABS(B23)26	Cu(2)ABS(B17+PFR)20		ZnPC(B25+SOD)28			Cu(1)PC(D6r2)55	Cu(2)PC(D6r2)55
	Cu(1)ABS(B23+T)26	Cu(2)ABS(B19)22		ZnPC(B25+Vn)28			Cu(1)PC(D7r2)56	Cu(2)PC(D7r2)56
Copper - PC	Cu(1)PC(B25)28	Cu(2)ABS(B19+T)22		ZnPC(B26)29			Cu(1)PC(D8r2)57	Cu(2)PC(D8r2)57
	Cu(1)PC(B25+P)28	Cu(2)ABS(B19+PFR)22		ZnPC(B26+T)29			Cu(1)PC(D9r2)58	Cu(2)PC(D9r2)58
	Cu(1)PC(B25+T)28	Cu(2)ABS(B21)24		ZnPC(B26+SOD)29				
	Cu(1)PC(B26)29	Cu(2)ABS(B21+T)24		ZnPC(B26+Vn)29				
	Cu(1)PC(B26+P)29	Cu(2)ABS(B21+PFR)24		ZnPC(B26*)29T1				
	Cu(1)PC(B26+T)29	Cu(2)ABS(B23)26		ZnPC(B26*)29T2				
Copper - PEEK	Cu(1)PEEK(B17)20	Cu(2)ABS(B23+T)26		ZnPC(B26*)29T3				
	Cu(1)PEEK(B17-T)20	Cu(2)ABS(B23+PFR)26		ZnPC(B26*)29T4				
	Cu(1)PEEK(B17+P)20	Cu(2)PC(B25)28		ZnPC(B26*)29T5				
	Cu(1)PEEK(B19)22	Cu(2)PC(B26)29		ZnPC(B26*)29T6				
	Cu(1)PEEK(B19-T)22	Cu(2)PC(B27)30		ZnPC(B26*)29T7				
	Cu(1)PEEK(B19+P)22	Cu(2)PC(B28)31		ZnPC(B26*)29T8				
	Cu(1)PEEK(B21)24	Cu(2)PC(B29)32		ZnPC(B26*)29T9				
	Cu(1)PEEK(B21-T)24	Cu(2)PC(B30)33		ZnPC(B26*)29T10				
	Cu(1)PEEK(B21+P)24	Cu(2)PC(B31)34		ZnPC(B26*)29T11				
	Cu(1)PEEK(B23)26	Cu(2)PC(B32)35		ZnPC(B26*)29T12				
	Cu(1)PEEK(B23-T)26			ZnPC(B26*)29T13				
	Cu(1)PEEK(B23+P)26			ZnPC(B26*)29T14				
				ZnPC(B26*)29T15				

Optimum Coating

Privileged direction: The direction in which roughness varies or observes a maximum/minimum roughness.

Anisotropic: Properties are orientation dependent.

Isotropic: Properties are orientation independent.

Rectangular anisotropy: Maximum and minimum values of an observed properties occur at 90° to each other. (These surfaces are also known as orthotropic surfaces).

Periodic: A surface which has features which occur with uniform, repeating intervals.

Non-periodic: A surface with no discernible regular patterns.

Equipment
A TR220 surface roughness tester, with standard TS100 inductive diamond stylus pickup, with a tip radius of 5 μm and 90° stylus angle was used [181]. TimeSurf software was used for data retrieval and initial processing.

- Display resolution: 0.001 μm
- Max tracing length: 17.5 mm
- Min tracing length: 1.3 mm
- Tolerance: $\leq \pm 10\%$
- Repeatability: $< 6\%$

Standard operating procedure (SOP) - Stylus profilometry
The following procedure is based primarily on ISO 4288:1996 (Geometrical Product Specifications (GPS), Surface texture: Profile method: Rules and procedures for the assessment of surface texture) with additions from [181, 218].

1. Connect surface roughness tester and computer interface.
2. Insert the TimeSurf software dongal.
3. Open TimeSurf software.
4. Select 'connect'.
5. Secure the sample below the stylus, aligned with the test direction of interest.

6. Lower the stylus onto the target surface. Ensure the sample being tested is secure, level and has sufficient tracing length available.

7. Select 'pickup' and adjust the calibration until zero is recorded (±0.1).

8. Select 'configure'.

    - Set track length (dependent on substrate surface - ISO 4288).

    - Set cutoff length (dependent on substrate surface - ISO 4288).

    - Set sampling range (Auto).

    - Set filter (RC).

    - Set the unit of measure (Metric).

9. Surface profile measurements.

    9.1. Decide whether surface topography is periodic or non-periodic.

    - This understanding of periodic and non-periodic surfaces may be extended to anisotropic and isotropic surfaces. Vertically oriented 3D printed ABS substrate samples were observed to exhibit rectangular, anisotropic surfaces.

    - If the surface surface topography is non-periodic then proceed with step 10, otherwise for periodic surfaces start at step 11.

10. Measurement procedure for non-periodic roughness profiles.

    10.1. Estimate the unknown roughness profile parameter Ra, Rz, Rz1max or RSM by any preferred means (visual inspection, roughness comparison, graphical analysis of a total profile trace).

    10.2. Estimate the sampling length (cutoff value λc) from Table C.9, Table C.10 and Table C.11 based on RSm (mean width of profile elements or mean groove width), Ra (arithmetic mean deviation) and Rz (maximum height of profile) respectively.

    10.3. Use the surface roughness tester to obtain a representative value for Ra, Rz, Rz1max or RSm using the estimated sampling length.

    10.4. Compare the measured value of Ra, Rz, R_{z1max} or RSm with the range of values of Ra, Rz, R_{z1max} or RSm in Table C.9, Table C.10 and Table C.11 corresponding to the estimated sampling length. If the measured value falls outside the range of values for the estimated sampling length, then adjust the sampling length to the respective higher or lower sampling length setting indicated and corresponding with the measured value.

    Following this, measure a representative value using this adjusted sampling length and compare with Table C.9, Table C.10 and Table C.11.

10.5. Obtain a representative value of Ra, Rz, R_{z1max} or RSm for one sampling length smaller, provided this setting has not previously been tried. Check agreement from Table C.9, Table C.10 and Table C.11.

10.6. Use the shortest agreeable sampling length for the final measurements and proceed with step 12.

11. Procedure for periodic roughness profiles.

11.1. Estimate graphically the parameter RSm of the surface of unknown roughness by way of a trial run.

11.2. Determine the recommended cut-off wavelength/sampling length value for the estimated RSm value in Table C.9.

11.3. Measure the RSm value using this cut-off wavelength.

11.4. Adjust the selected sampling length based on the measured RSm value and the Table C.9 corresponding sampling length.

11.5. Once a corresponding cutoff wavelength has been accepted proceed with step 12.

12. Make three readings in one orientation and another three in the orthogonal direction.

13. For isotropic surfaces the results for both orientations may be averaged. For anisotropic surfaces the results should be analysed independently.

14. Analyse the primary profile and compare coated surfaces to related uncoated substrates.

15. Record and consider all relevant roughness parameters based on a desired analysis.

16. Repeat the procedure for all test samples (coated, uncoated and control samples).

Table C.9: Sampling lengths for measurement of the parameters of periodic roughness profiles and for measurement of the RSm of periodic/non-periodic profile curves [218].

RSm [mm]	Sampling length [mm]	Evaluation length [mm]
$0.013 < \text{RSm} \leq 0.04$	0.08	0.40
$0.04 < \text{RSm} \leq 0.13$	0.25	1.25
$0.13 < \text{RSm} \leq 0.40$	0.80	4.00
$0.4 < \text{RSm} \leq 1.30$	2.50	12.50
$1.3 < \text{RSm} \leq 4.00$	8.00	40.00

Table C.10: Roughness sampling lengths for the measurement of Ra, Rq, Rsk and R$\triangle$q of non-periodic profiles [218].

Ra [μm]	Sampling length [mm]	Evaluation length [mm]
$0.006 < \text{Ra} \leq 0.02$	0.08	0.40
$0.02 < \text{Ra} \leq 0.10$	0.25	1.25
$0.1 < \text{Ra} \leq 2.00$	0.80	4.00
$2 < \text{Ra} \leq 10.00$	2.50	12.50
$10 < \text{Ra} \leq 80.00$	8.00	40.00

Table C.11: Roughness sampling lengths for the measurement of Rz, Rv, Rp, Rc and Rt of non-periodic profiles [218].

Rz [μm]	Sampling length [mm]	Evaluation length [mm]
$0.025 < \text{Rz} \leq 0.10$	0.08	0.40
$0.1 < \text{Rz} \leq 0.50$	0.25	1.25
$0.5 < \text{Rz} \leq 10.00$	0.80	4.00
$10 < \text{Rz} \leq 50.00$	2.50	12.50
$50 < \text{Rz} \leq 200.00$	8.00	40.00

Key Roughness Parameters [181]

Ra - Arithmetic mean deviation of profile [μm].

Rq - Root mean square deviation of profile [μm].

Rz - Maximum height of profile (per sampling length) [μm].

Ry - Maximum height of profile (across evaluation length) [μm].

Rt - Total height for peak and valley of profile [μm].

- The vertical distance between the maximum profile peak height and the maximum profile valley depth along the evaluation length.

Rp - Maximum peak height of profile [μm].

- The distance from the top line of the profile peak to the middle line in the sampling length.

Rv - Maximum peak valley profile [μm].

- The distance from the bottom line of the profile valley to the middle line within the sampling length.

RSm - Mean spacing for the microscopic roughness of the profile [mm].

Rs - Mean spacing between individual peaks of the profile [mm].

Rsk - Skewness profile.
- Measurement of the asymmetry of the amplitude distribution.

Surface wear test standard operating procedure

The following test procedure was based on the ASTM G99 *standard test method for wear testing with a pin-on-disc apparatus*, and the CSM tribometer: friction and sliding wear test procedure as arranged by the School of Chemical and Metallurgical Engineering at the University of the Witwatersrand, Johannesburg, South Africa.

Equipment
A CSM Tribometer (01-02536) with Tribo-X (Tribo-X 4.5) software was used to carry out and perform initial data retrieval and processing the wear test procedure. Stainless steel balls (STEEL AISI 420 BALL - Anton Paar), of diameter 6 mm, were used as the static contacting surface. Round discs with a diameter of 30 mm were prepared of each tested material/coating type.

Standard operating procedure (SOP) - Pin-on-disc

1. Select and prepare test samples.
    1.1. 6 mm stainless steel balls to be used as the static partner.
    1.2. Disc specimens with a diameter of 30 mm prepared by cold mounting (see the cold mounting procedure) 12 x 12 mm test samples.
    1.3. Clean all test samples with a soft, anti-pill cloth.
    1.4. Ensure samples are dry before testing commences.
2. Ensure all cables are correctly and securely connected to the tribometer and the PC.
3. Connect the electricity cables to the power supply plug for both the tribometer and PC.
4. Turn the computer and the tribometer on.
5. Secure a test sample into the sample mandrel.
    5.1. Open the mandrel.
    5.2. Load the sample.

5.3. Check that the sample is secure and level. The sample should be perpendicular ($\pm 1^{\circ}$) to the axis of rotation.

6. Insert the stainless steel ball into the ball holder and use the screw to fix it in place.

7. Place a thin card between the sample surface. This is to ensure that once the static ball is lowered onto the sample surface no load is applied, thus avoiding pre-loading of the sample.

8. Slide the ball holder into the sleeve of the elastic blade.

   8.1. The flat edge must be oriented towards the sample mandrel.

   8.2. Lower the arm, resting the ball on the card.

   8.3. Lock the ball holder in place, with an Allen key.

   8.4. Remove the card and confirm a small gap is present between the two interacting bodies.

   8.5. Re-check alignment.

9. Place the selected applied load (1 - 10 N) above the ball holder.

10. Use a spirit level to confirm the eccentric arm is horizontal and facing towards the test sample.

11. Run the Tribo-X software on a computer.

12. Select a 'new' run.

13. Name the run based on the test sample and/or static partner.

14. Open the tribometer parameter selection pane.

15. Set all experimental parameters

    15.1. Acquisition rate (Hz), sample temperature (°C), humidity (%), applied load (N), ball radius (mm), linear speed (cm/s) and sliding distance (m).

16. Set all sample properties.

    16.1. Coating, substrate, cleaning protocols and material supplier.

17. Set all the static friction partner properties.

    17.1. Coating (not applicable), material, cleaning, supplier, dimensions and geometry.

18. Click 'OK'.

19. Click 'Start' for initialisation.

19.1. Raise the arm to the horizontal position such that no load is applied.

19.2. Click 'OK', then 'Start'.

20. Lower the arm when initialisation is complete and then start the test.

21. Ensure that the test runs to completion.

22. Raise the arm once completed.

23. Save test data.

24. Remove the sample from the mandrel.

25. Note any surface features on or near the wear scar.

25.1. Look particularly for protrusions, displaced material, discolouration and micro-cracking or spotting.

26. Clean samples using a soft, dry, anti-pill cloth.

27. Re-examine the sample.

28. Remove ball holder and applied load from the tribometer.

29. Repeat steps 5 - 28 for all remaining samples.

30. Return all equipment and tidy up the workstation.

31. Export all saved data.

32. Using linear measures (either electronic distance gauging or profilometry) evaluate disc wear.

32.1. Using electronic distance gauging view the sample under appropriate magnification and use relevant image processing software (ImageJ) to measure the wear track width.

32.2. Wear scar measurements should be made at at least two representative locations.

32.3. Assuming no significant pin wear use the appropriate geometric relation given by Equation C.4.

$$\text{Disc volume loss} = \frac{\pi(\text{wear track radius (mm)})(\text{track width (mm)})^3}{6(\text{sphere radius (mm)})} \tag{C.4}$$

32.4. Where significant ball wear was observed both disc and ball volume loss are required to be calculated.

- Disc volume loss

·Profilimetry across wear track.

·Cross-sectional area of wear track recorded (A_w).

·Wear track circumference calculated (C_w).

·Wear track volume loss = A_w x C_w.

- Ball volume loss

·Measure wear scar diameter using microscopy analysis (ϕ).

·Calculate the distance from the wear plane to the original sphere tip (h).

$$h = R - rtan\alpha \tag{C.5}$$

where $\alpha = cosi^{-1}(r/R)$ is the contact angle calculated from the wear scar radius (r) and the ball radius (R).

·Calculate the ball radius.

·Calculate the ball volume loss using Equation C.6.

$$V_{cap} = \frac{1}{3}\pi h^2(3R - h) \tag{C.6}$$

33. Calculate the average wear coefficient (k) for each test sample, using Equation C.7.

$$k = \frac{\text{(Disc volume loss (mm\^3))}}{\text{(applied load (N)} \times \text{Sliding distance (m))}} \tag{C.7}$$

34. Record the average friction coefficient for each sample.

35. Repeat the preceding steps for a randomly selected coating and control pair.

    35.1. This data will be used to confirm test validity based on a precision analysis.

    35.2. Check test precision for disc wear loss by calculating the coefficient of variation (CV). The resultant percentage CV value should be less than 20%.

Surface wear testing: literature review

Table C.12 contains the key parameter sets of published literature results regarding surface wear testing, related to testing of polymeric materials.

Coating characterisation

The results of the coating characterisation procedure are tabulated below. This includes the specific and comprehensive particle depth-of-penetration data (Table C.13 - Table C.16), the

Table C.12: Published literature surface wear test parameter sets.

	References					
	ASTM G99	[219]	[220]	[221]	[222]	[185]
Applied load [N]	Max 10 N	10	5 - 20	5 - 20	10	5 - 20
Linear speed [m/s]	/	0.08	0.63	1.36	0.5 - 2	0.63
Sliding distance [m]	/	250	113.4 - 189	408 - 816	500	189 - 378
Pin material	/	Stainless steel	3D printed ABS	3D printed ABS	ABS Composite	3D printed ABS
Disc material	/	Various polymers	SiC (600 grit)	SiC (600 grit)	/	SiC (600 grit)
Pin diameter [mm]	6	6	10	10	/	10
Disc diameter [mm]	30	/	/	/	/	/
Disc thickness [mm]	15	/	/	/	/	/
Sample thickness [mm]	2 - 5	/	/	/	/	/

surface topography analysis (including the results for the theoretically optimum parameter set coatings in Table C.17 and the experimentally optimum parameter set results in Table C.18 - Table C.22) and the coating wear resistance test data (including the screening tests in Table C.25 and Figure C.1 as well as the combined results Table C.26 and validation data Table C.27).

Particle depth-of-penetration

Table C.13: Coating characterisation of theoretically optimum parameter sets - particle size and shape analysis.

	Particle area (A) [µm^2]				Particle perimeter (P) [µm]				Circularity (C)				Equivalent diameter (D) [µm]			
	A_1	A_2	A_3	Ave	P_1	P_2	P_3	Ave	C_1	C_2	C_3	Ave	D_1	D_2	D_3	Ave
Copper coated 3D printed ABS (hor.)	172.78	171.76	96.73	147.09	62.04	90.86	38.84	63.91	0.56	0.26	0.81	0.54	14.83	14.79	11.10	13.57
Copper coated solid ABS	183.41	18.42	58.45	86.76	67.37	17.08	39.62	41.36	0.51	0.79	0.47	0.59	15.28	4.84	8.63	9.58
Copper coated PEEK	10.06	43.26	3.62	18.98	13.03	32.18	7.28	17.50	0.75	0.53	0.86	0.71	3.58	7.42	2.15	4.38
Copper coated vertically oriented 3D printed ABS	114.66	245.28	57.50	139.15	49.73	87.80	30.87	56.14	0.58	0.40	0.76	0.58	12.08	17.67	8.56	12.77
Cu-Al-Al_2O_3 coated 3D printed ABS (hor.)	123.08	13.61	16.80	51.16	63.76	16.77	17.22	32.58	0.38	0.61	0.71	0.57	12.52	4.16	4.62	7.10
Cu-Al-Al_2O_3 coated solid ABS	76.52	37.27	97.97	70.59	32.86	26.37	50.14	36.46	0.89	0.67	0.49	0.68	9.87	6.89	11.17	9.31
Zinc coated 3D printed ABS (hor.)	118.81	187.00	173.65	159.82	42.60	60.47	52.76	51.95	0.82	0.64	0.78	0.75	12.30	15.43	14.87	14.20
Zinc coated solid ABS	220.83	714.38	221.03	385.41	64.04	167.25	70.09	100.46	0.68	0.32	0.57	0.52	16.77	30.16	16.78	21.23
Zinc coated PC	16.27	/	/	16.27	16.50	/	/	16.50	0.75	/	/	0.75	4.55	/	/	4.55
50% w/w copper-zinc coated 3D printed ABS (hor.)	53.92	50.63	58.92	54.49	42.27	31.60	33.61	35.83	0.38	0.64	0.66	0.56	8.29	8.03	8.66	8.33

Table C.14: Coating characterisation of theoretically optimum parameter sets - particle depth-of-penetration analysis.

	Area above surface (A_{Above})[µm^2]				Area below surface (A_{Below})[µm^2]				Percentage particle embedment (%embedded)				Maximum depth-of-penetration (X)[µm]				Normalised particle depth-of-penetration (X/D)			
	1	2	3	Ave	1	2	3	Ave	1	2	3	Ave	1	2	3	Ave	1	2	3	Ave
Copper coated 3D printed ABS (hor.)	50.74	46.89	25.00	40.88	116.89	160.24	71.93	116.35	69.73	77.36	74.21	73.77	11.93	5.98	6.83	8.25	0.80	0.40	0.62	0.61
Copper coated solid ABS	119.97	0.00	40.65	53.54	53.88	18.42	13.58	28.63	30.99	100.00	25.04	52.01	8.11	9.96	1.71	6.59	0.53	2.06	0.20	0.93
Copper coated PEEK	9.12	3.74	1.50	4.79	0.78	7.41	1.58	3.25	7.85	66.46	51.23	41.85	0.67	1.26	0.93	0.95	0.19	0.17	0.43	0.26
Copper coated vertically oriented 3D printed ABS	53.32	109.42	0.00	54.25	65.22	147.90	57.50	90.20	55.02	57.48	100.00	70.83	6.54	13.89	16.50	12.31	0.54	0.79	1.93	1.09
Cu-Al-Al_2O_3 coated 3D printed ABS (hor.)	81.00	3.62	2.04	28.89	53.75	9.24	14.19	25.73	39.89	71.85	87.40	66.38	8.52	2.81	4.25	5.19	0.68	0.67	0.92	0.76
Cu-Al-Al_2O_3 coated solid ABS	36.28	18.01	40.61	31.63	38.41	17.66	55.49	37.19	51.42	49.51	57.74	52.89	5.56	3.87	6.21	5.21	0.56	0.56	0.56	0.56
Zinc coated 3D printed ABS (hor.)	25.86	0.00	116.97	47.61	84.88	186.97	106.71	126.19	76.65	100.00	47.71	74.78	9.09	39.33	8.34	18.92	0.74	2.55	0.56	1.28
Zinc coated solid ABS	148.96	390.02	161.60	233.53	67.05	318.73	53.30	146.36	31.04	44.97	24.80	33.60	4.77	20.85	4.87	10.16	0.28	0.69	0.29	0.42
Zinc coated PC	/	/	/	/	/	/	/	/	/	/	/	/	/	/	/	/	/	/	/	/
50% w/w copper-zinc coated 3D printed ABS (hor.)	39.22	0.00	24.58	21.27	14.00	50.63	29.22	31.29	26.31	100.00	54.31	60.21	2.86	8.43	5.43	5.57	0.35	1.05	0.63	0.67

Table C.15: Coating characterisation of experimentally optimum parameter sets - particle size and shape analysis.

	Particle area (A) [µm^2]				Particle perimeter (P) [µm]				Circularity (C)				Equivalent diameter (D) [µm]			
	1	2	3	Ave	1	2	3	Ave	1	2	3	Ave	1	2	3	Ave
Copper coated 3D printed ABS (hor.)	26.91	31.07	191.63	83.20	21.94	21.74	68.72	37.47	0.70	0.83	0.51	0.68	5.85	6.29	15.62	9.25
Copper coated solid ABS	21.24	92.08	102.87	72.06	21.93	49.96	47.19	39.70	0.56	0.46	0.58	0.53	5.20	10.83	11.44	9.16
Copper coated PEEK	8.39	/	/	8.39	12.69	/	/	12.69	0.65	/	/	0.65	3.27	/	/	3.27
Copper coated vertically oriented 3D printed ABS	86.23	230.02	60.01	125.42	42.74	80.11	49.06	57.30	0.59	0.45	0.31	0.45	10.48	17.11	8.74	12.11
Cu-Al-Al_2O_3 coated 3D printed ABS (hor.)	25.57	51.09	34.82	37.16	12.54	30.52	22.21	21.76	0.66	0.69	0.89	0.75	5.71	8.07	6.66	6.81
Cu-Al-Al_2O_3 coated solid ABS	100.18	94.00	57.15	83.78	41.98	40.93	39.95	40.95	0.71	0.71	0.45	0.62	11.29	10.94	8.53	10.25
Zinc coated 3D printed ABS (hor.)	99.13	209.71	50.82	119.89	42.88	57.66	27.62	42.72	0.68	0.79	0.84	0.77	11.23	16.34	8.04	11.87
Zinc coated solid ABS	348.32	480.73	125.49	318.18	87.04	108.14	45.81	80.33	0.57	0.52	0.75	0.61	21.06	24.74	12.64	19.48
Zinc coated PC	4.35	/	/	4.35	8.02	/	/	8.02	0.85	/	/	0.85	2.35	/	/	2.35
50% w/w copper-zinc coated 3D printed ABS	12.12	172.17	/	92.14	14.04	65.77	/	39.90	0.77	0.50	/	0.64	3.93	14.81	/	9.37
Copper coated copper (grit blasted substrate)	143.82	168.86	207.05	173.24	88.84	88.30	141.50	106.22	0.23	0.27	0.13	0.21	13.53	14.66	16.24	14.81
Copper coated copper (no grit blasting)	/	/	/	/	/	/	/	/	/	/	/	/	/	/	/	/
5wt% Ag - 47.5% (w/w) Cu-Zn coated 3D printed ABS (hor.)	23.93	101.67	60.57	62.06	22.72	45.33	30.17	32.74	0.58	0.62	0.84	0.68	5.52	11.38	8.78	8.56

Table C.16: Coating characterisation of experimentally optimum parameter sets - particle depth-of-penetration analysis.

	Area above surface (A_{Above})[µm^2]				Area below surface (A_{Below})[µm^2]				Percentage particle embedment (%embedded)				Maximum depth-of-penetration (X)[µm]				Normalised particle depth-of-penetration (X/D)			
	1	2	3	Ave	1	2	3	Ave	1	2	3	Ave	1	2	3	Ave	1	2	3	Ave
Copper coated 3D printed ABS (hor.)	0.00	11.44	140.59	50.68	26.91	17.48	52.82	32.40	100.00	60.43	27.31	62.58	5.04	3.45	4.52	4.34	0.86	0.55	0.29	0.57
Copper coated solid ABS	9.94	22.95	55.61	29.50	15.84	80.42	57.61	51.29	61.44	77.80	50.89	63.37	4.20	11.46	6.56	7.41	0.81	1.06	0.57	0.81
Copper coated PEEK	5.57	/	/	5.57	0.97	/	/	0.97	14.88	/	/	14.88	0.93	/	/	0.93	0.28	/	/	0.28
Copper coated vertically oriented 3D printed ABS	0.00	0.00	0.00	0.00	86.23	230.03	60.01	125.42	100.00	100.00	100.00	100.00	21.83	34.39	16.80	24.34	2.08	2.01	1.92	2.01
Cu-Al-Al_2O_3 coated 3D printed ABS (hor.)	14.51	22.24	22.44	19.73	24.13	39.09	16.64	26.62	62.46	63.74	42.58	56.26	4.38	4.98	3.41	4.26	0.77	0.62	0.51	0.63
Cu-Al-Al_2O_3 coated solid ABS	60.00	58.83	34.34	51.06	38.01	32.03	20.28	30.10	38.78	35.25	37.13	37.05	5.88	5.50	3.30	4.89	0.52	0.50	0.39	0.47
Zinc coated 3D printed ABS (hor.)	0.00	148.95	0.00	49.65	99.13	56.18	50.82	68.71	100.00	27.39	100.00	75.80	20.42	5.44	13.78	13.21	1.82	0.33	1.71	1.29
Zinc coated solid ABS	105.64	70.45	95.34	90.48	239.09	407.45	27.15	224.56	69.36	85.26	22.17	58.93	23.97	31.62	4.30	19.96	1.14	1.28	0.34	0.92
Zinc coated PC	0.26	/	/	0.26	6.92	/	/	6.92	96.32	/	/	96.32	2.27	/	/	2.27	0.96	/	/	0.96
50% w/w copper-zinc coated 3D printed ABS	24.10	49.87	/	36.99	22.59	138.41		80.50	48.38	73.51		60.94	4.43	7.35	/	5.89	1.13	0.50	/	0.81
Copper coated copper (grit blasted substrate)	143.82	168.86	207.05	173.24	0.00	0.00	0.00	0.00	0.00	0.00	0.00	0.00	0.00	0.00	0.00	0.00	0.00	0.00	0.00	0.00
Copper coated copper (no grit blasting)	/	/	/	/	0.00	0.00	0.00	0.00	/	/	/	0.00	0.00	0.00	0.00	0.00	/	/	/	0.00
5wt% Ag - 47.5% (w/w) Cu-Zn coated 3D printed ABS (hor.)	0.00	15.51	56.18	23.90	23.93	124.89	51.99	66.94	100.00	88.95	48.06	79.01	8.77	8.12	5.21	7.37	1.59	0.71	0.59	0.97

Surface topography analysis

Table C.17: Arithmetic mean profile deviations (Ra) [μm] for single and multi-pass cold spray coatings and their uncoated substrates made according to ISO 4288 for theoretically optimum cold spray coatings.

Analysed samples	Single pass coating											Five pass coating										
	Sample 1 (A1)			Sample 2 (A2)			Sample 3 (A3)			Ave.	SD	Sample 1 (A1)			Sample 2 (A2)			Sample 3 (A3)			Ave.	SD
	Ra_1	Ra_2	Ra_3	Ra_4	Ra_5	Ra_6	Ra_7	Ra_8	Ra_9			Ra_1	Ra_2	Ra_3	Ra_4	Ra_5	Ra_6	Ra_7	Ra_8	Ra_9		
Copper coated 3D printed ABS	10.59	9.416	7.56	8.151	8.6	8.188	8.857	8.85	10.2	8.935	0.98	12.13	9.61	9.924	10.26	9.85	9.746	10.18	11.2	11.98	10.542	0.97
Copper coated solid ABS	1.023	0.87	0.804	0.671	0.882	0.92	0.886	0.937	0.882	0.875	0.1	1.056	0.91	1.032	0.846	0.992	1.046	0.901	1.25	1.182	1.024	0.13
Copper coated PEEK	3.154	3.474	2.874	/	/	/	/	/	/	3.167	0.3	3.069	3.425	2.685	/	/	/	/	/	/	3.06	0.37
Polished copper coated PEEK	2.35	1.528	1.207	/	/	/	/	/	/	1.695	0.59	2.184	2.574	2.287	/	/	/	/	/	/	2.348	0.2
Copper coated vertically oriented 3D printed ABS	13.03	12.72	12.97	/	/	/	/	/	/	12.907	0.16	10.25	8.415	8.375	/	/	/	/	/	/	9.013	1.07
Copper-Aluminium-Alumina coated 3D printed ABS	20.09	26.25	/	21.36	/	/	/	/	/	22.567	3.25	/	/	/	/	/	/	/	/	/	/	/
Copper-Aluminium-Alumina coated solid ABS	0.817	0.984	1.032	1.039	1.081	1.112	0.895	1.182	1.097	1.027	0.11	1.29	1.351	1.479	1.219	1.566	1.317	1.199	1.452	1.299	1.352	0.12
Zinc coated 3D printed ABS	/	/	/	7.715	7.04	/	/	/	/	7.378	0.48	/	/	/	7.71	/	/	/	/	/	7.71	/
Zinc coated solid ABS	1.625	1.888	1.526	2.255	2.371	1.6	1.856	2.327	1.725	1.908	0.33	2.516	3.295	2.019	2.58	2.469	2.417	2.276	2.537	2.472	2.509	0.34
Zinc coated PC	11.17	/	/	/	/	/	15.56	/	/	13.365	3.1	/	/	/	/	/	/	/	/	/	/	/
Pure copper	0.121	0.103	0.181	0.253	0.225	0.25	/	/	/	0.189	0.07	0.121	0.103	0.181	0.253	0.225	0.25	/	/	/	0.189	0.07
Zinc coated/galvanised steel	0.928	1.183	1.101	0.662	0.743	0.523	/	/	/	0.857	0.26	0.928	1.183	1.101	0.662	0.743	0.523	/	/	/	0.857	0.26
Stainless steel	0.099	0.113	0.095	0.13	0.136	0.091	/	/	/	0.111	0.02	0.099	0.113	0.095	0.13	0.136	0.091	/	/	/	0.111	0.02
3D printed ABS	10.61	12.57	9.39	/	/	/	/	/	/	10.857	1.6	10.61	12.57	9.39	/	/	/	/	/	/	10.857	1.6
Vertically oriented 3D printed ABS	14.89	14.11	14.15	/	/	/	/	/	/	14.383	0.44	14.89	14.11	14.15	/	/	/	/	/	/	14.383	0.44
Solid ABS	0.246	0.197	0.223	/	/	/	/	/	/	0.222	0.02	0.246	0.197	0.223	/	/	/	/	/	/	0.222	0.02
Solid polycarbonate	0.007	0.006	0.01	/	/	/	/	/	/	0.008	0	0.007	0.006	0.01	/	/	/	/	/	/	0.008	0
Solid polyetheretherketone	0.904	0.975	0.505	/	/	/	/	/	/	0.795	0.25	0.904	0.975	0.505	/	/	/	/	/	/	0.795	0.25

Table C.18: Arithmetic mean profile deviations (Ra) [μm] for single and multi-pass cold spray coatings and their uncoated substrates made according to ISO 4288 in two orthogonal sampling orientations for experimentally optimum cold spray coatings.

Analysed samples	Single pass coating (including uncoated substrates)											Multi-pass (2 layer) coating (including uncoated substrates)										
	Orientation 1			Average	SD	Orientation 2			Average	SD	Overall average	SD	Orientation 1			Average	SD	Orientation 2			Average	SD	Overall average	SD
	Ra_1	Ra_2	Ra_3			Ra_1	Ra_2	Ra_3					Ra_1	Ra_2	Ra_3			Ra_1	Ra_2	Ra_3				
Copper coated 3D printed ABS	3.157	3.291	4.168	3.539	0.55	4.247	3.181	3.603	3.677	0.5	3.61	0.5	2.658	3.302	4.314	3.425	0.83	4.608	4.097	2.699	3.801	0.99	3.61	0.9
Copper coated solid ABS	0.939	0.885	1.311	1.045	0.23	1.026	1.058	1.013	1.032	0	1.04	0.1	1.343	1.585	1.3	1.409	0.15	1.021	1.035	0.97	1.009	0.03	1.21	0.1
Copper coated PEEK	2.722	4.806	3.945	3.824	1.05	4.194	3.847	4.063	4.035	0.2	3.93	0.6	2.878	3.564	3.102	3.181	0.35	3.183	3.319	2.821	3.108	0.26	3.14	0.3
Polished copper coated PEEK	2.864	3.135	3.071	3.023	0.14	2.471	3.299	2.821	2.864	0.4	2.94	0.3	3.042	2.92	3.149	3.037	0.11	2.431	3.024	2.42	2.625	0.35	2.83	0.2
Copper coated vertically oriented 3D printed ABS	2.701	3.503	2.708	2.971	0.46	7.88	9.014	10.74	9.211	1.4	6.09	0.9	/	/	/	/	/	/	/	/	/	/	/	/
Copper-Aluminium-Alumina coated 3D printed ABS	4.64	4.422	4.578	4.547	0.11	4.143	4.322	4.303	4.256	0.1	4.4	0.1	3.805	4.158	2.934	3.632	0.63	4.254	3.455	3.988	3.899	0.41	3.77	0.5
Copper-Aluminium-Alumina coated solid ABS	1.027	1.031	1.216	1.091	0.11	1.342	1.566	1.313	1.407	0.1	1.25	0.1	1.828	1.714	1.667	1.736	0.08	1.46	2.229	1.477	1.722	0.44	1.73	0.3
Zinc coated 3D printed ABS	6.754	4.526	5.422	5.567	1.12	4.665	4.508	4.023	4.399	0.3	4.98	0.7	5.646	5.532	3.787	4.988	1.04	6.414	5.848	5.804	6.022	0.34	5.51	0.7
Zinc coated solid ABS	5.386	5.752	5.646	5.595	0.19	6.117	7.184	7.549	6.95	0.7	6.27	0.4	7.442	6.284	6.883	6.87	0.58	6.152	6.9	6.248	6.433	0.41	6.65	0.5
Zinc coated PC	5.079	8.507	7.448	7.011	1.76	/	/	/	/	/	7.01	1.8	7.871	/	/	7.871	/	/	/	/	/	/	/	/
75 wt% copper - 25 wt% zinc coated 3D printed ABS	4.803	3.736	4.7	4.413	0.59	4.818	6.018	7.207	6.014	1.2	5.21	0.9	4.643	4.88	4.034	4.519	0.44	4.515	4.991	4.44	4.649	0.3	4.58	0.4
50% w/w copper-zinc coated 3D printed ABS	5.661	5.216	6.002	5.626	0.39	4.971	4.442	4.684	4.699	0.3	5.16	0.3	5.384	3.822	4.302	4.503	0.8	4.434	4.266	4.014	4.238	0.21	4.37	0.5
75 wt% zinc - 25 wt% copper coated 3D printed ABS	5.96	5.73	5.123	5.604	0.43	4.837	6.126	5.148	5.37	0.7	5.49	0.6	4.333	5.784	6.16	5.426	0.96	4.338	6.497	7.651	6.162	1.68	5.79	1.3
Copper Metal	0.121	0.103	0.181	0.135	0.04	0.253	0.225	0.25	0.243	0	0.19	0	/	/	/	/	/	/	/	/	/	/	/	/
Galvanised steel	0.928	1.183	1.101	1.071	0.13	0.662	0.743	0.523	0.643	0.1	0.86	0.1	/	/	/	/	/	/	/	/	/	/	/	/
Stainless steel	0.099	0.113	0.095	0.102	0.01	0.13	0.136	0.091	0.119	0	0.11	0	/	/	/	/	/	/	/	/	/	/	/	/
3D printed ABS	3.584	5.008	4.56	4.384	0.73	4.703	3.761	3.942	4.135	0.5	4.26	0.6	3.584	5.008	4.56	4.384	0.73	4.703	3.761	3.942	4.135	0.5	4.26	0.6
Vertically oriented 3D printed ABS	0.164	0.381	0.458	0.334	0.15	14.89	14.11	14.15	14.383	0.4	7.36	0.3	0.164	0.381	0.458	0.334	0.15	14.89	14.11	14.15	14.383	0.44	7.36	0.3
Solid ABS	0.294	0.268	0.275	0.279	0.01	0.866	0.299	0.455	0.54	0.3	0.41	0.2	0.294	0.268	0.275	0.279	0.01	0.866	0.299	0.455	0.54	0.29	0.41	0.2
Solid polycarbonate	0.004	0.005	0.006	0.005	0	0.005	0.007	0.008	0.007	0	0.01	0	0.004	0.005	0.006	0.005	0	0.005	0.007	0.008	0.007	0	0.01	0
Solid polyetheretherketone	1.12	1.4	0.493	1.004	0.46	0.816	0.91	0.506	0.744	0.2	0.87	0.3	1.12	1.4	0.493	1.004	0.46	0.816	0.91	0.506	0.744	0.21	0.87	0.3

Table C.19: Maximal profile height (Rz) [μm] measurements for single and multi-pass cold spray coatings and their uncoated substrates made according to ISO 4288 in two orthogonal sampling orientations for experimentally optimum cold spray coatings.

Analysed samples	Single pass coating (including uncoated substrates)											Multi-pass coating (including uncoated substrates)										
	Orientation 1			Average	SD	Orientation 2			Average	SD	Overall average	SD	Orientation 1			Average	SD	Orientation 2			Average	SD	Overall average	SD
	Rz_1	Rz_2	Rz_3			Rz_1	Rz_2	Rz_3					Rz_1	Rz_2	Rz_3			Rz_1	Rz_2	Rz_3				
Copper coated 3D printed ABS	8.804	12.33	10.78	10.638	1.77	17.51	10.96	7.781	12.084	5	11.36	3.4	6.96	9.007	8.46	8.142	1.06	6.585	7.765	5.734	6.695	1.02	7.42	1
Copper coated solid ABS	7.203	6.195	9.523	7.64	1.71	8.453	8.007	7.726	8.062	0.4	7.85	1.1	10.81	10.39	10.3	10.5	0.27	7.437	7.265	7.281	7.328	0.1	8.91	0.2
Copper coated PEEK	19.3	37.52	26.72	27.847	9.16	34.14	28.78	32.45	31.79	2.7	29.82	5.9	21.92	22.87	23.83	22.873	0.96	21.78	25.19	20.67	22.547	2.36	22.71	1.7
Polished copper coated PEEK	18.08	20.34	19.58	19.333	1.15	16.06	20.34	17.43	17.943	2.2	18.64	1.7	20.39	18.82	20.97	20.06	1.11	16.46	20.05	15.92	17.477	2.24	18.77	1.7
Copper coated vertically oriented 3D printed ABS	14.5	11.9	14.23	13.543	1.43	20.83	22.47	23.24	22.18	1.2	17.86	1.3	/	/	/	/	/	/	/	/	/	/	/	/
Copper-Aluminium-Alumina coated 3D printed ABS	7.148	11.54	10.33	9.673	2.27	11.43	8.218	9.382	9.677	1.6	9.68	1.9	10.51	14.61	11.21	12.11	2.19	16.63	13.46	16.69	15.593	1.85	13.85	2
Copper-Aluminium-Alumina coated solid ABS	8.296	7.945	9.898	8.713	1.04	10.75	12.36	10.42	11.177	1	9.95	1	13.66	11.76	10.56	11.993	1.56	11.62	17.76	11.14	13.507	3.69	12.75	2.6
Zinc coated 3D printed ABS	22	21.1	18	20.367	2.1	16.1	18	12.93	15.677	2.6	18.02	2.4	17.06	11.71	12.14	13.637	2.97	22.29	19.44	18.07	19.933	2.15	16.79	2.6
Zinc coated solid ABS	38.53	44.48	37.17	40.06	3.89	38.81	50.63	50.94	46.793	6.9	43.43	5.4	52.38	40.97	46.98	46.777	5.71	43.07	46.21	42.28	43.853	2.08	45.32	3.9
Zinc coated PC	33.78	55.99	50.35	46.707	11.54	/	/	/	/	/	46.71	11.5	52.43	/	/	52.43	/	/	/	/	/	/	/	/
75 wt% copper - 25 wt% zinc coated 3D printed ABS	18.57	13.63	12.33	14.843	3.29	6.789	11.59	12.19	10.19	3	12.52	3.1	12.34	14.18	15.78	14.1	1.72	16.99	21.36	17.36	18.57	2.42	16.34	2.1
50% w/w copper-zinc coated 3D printed ABS	13.09	11.15	17.51	13.917	3.26	17.68	12.91	16.33	15.64	2.5	14.78	2.9	14.22	18.29	16.14	16.217	2.04	16.41	13.87	13.27	14.517	1.67	15.37	1.9
75 wt% zinc - 25 wt% copper coated 3D printed ABS	14.1	16.96	19.32	16.793	2.61	17.48	12.02	17.21	15.57	3.1	16.18	2.9	10	11.44	15.52	12.32	2.86	14.02	24.4	15.79	18.07	5.55	15.2	4.2
Copper Metal	0.734	0.593	1.123	0.817	0.27	1.48	1.382	1.33	1.397	0.1	1.11	0.2	/	/	/	/	/	/	/	/	/	/	/	/
Galvanised steel	3.697	3.189	4.169	3.685	0.49	2.128	1.933	2.246	2.102	0.2	2.89	0.3	/	/	/	/	/	/	/	/	/	/	/	/
Stainless steel	1.001	0.771	0.732	0.835	0.15	0.898	0.896	0.851	0.882	0	0.86	0.1	/	/	/	/	/	/	/	/	/	/	/	/
3D printed ABS	4.398	2.343	8.273	5.005	3.01	1.835	6.585	7.664	5.361	3.1	5.18	3.1	4.398	2.343	8.273	5.005	3.01	1.835	6.585	7.664	5.361	3.1	5.18	3.1
Vertically oriented 3D printed ABS	0.562	0.203	0.851	0.539	0.32	32.75	33	34.7	33.483	1.1	17.01	0.7	0.562	0.203	0.851	0.539	0.32	32.75	33	34.7	33.483	1.06	17.01	0.7
Solid ABS	1.515	1.085	0.992	1.197	0.28	1.421	1.429	0.71	1.187	0.4	1.19	0.3	1.515	1.085	0.992	1.197	0.28	1.421	1.429	0.71	1.187	0.41	1.19	0.3
Solid polycarbonate	0.07	0.039	0.101	0.07	0.03	0.101	0.07	0.039	0.07	0	0.07	0	0.07	0.039	0.101	0.07	0.03	0.101	0.07	0.039	0.07	0.03	0.07	0
Solid polyetheretherketone	6.164	7.906	3.929	6	1.99	6.921	5.64	3.992	5.518	1.5	5.76	1.7	6.164	7.906	3.929	6	1.99	6.921	5.64	3.992	5.518	1.47	5.76	1.7

Table C.20: Mean roughness profile spacing (Rsm) [mm] for single and multi-pass cold spray coatings and their uncoated substrates made according to ISO 4288 in two orthogonal sampling orientations for experimentally optimum cold spray coatings.

Analysed samples	Single pass coating (including uncoated substrates)											Multi-pass coating (including uncoated substrates)										
	Orientation 1			Average	SD	Orientation 2			Average	SD	Overall average	SD	Orientation 1			Average	SD	Orientation 2			Average	SD	Overall average	SD
	Rsm_1	Rsm_2	Rsm_3			Rsm_1	Rsm_2	Rsm_3					Rsm_1	Rsm_2	Rsm_3			Rsm_1	Rsm_2	Rsm_3				
Copper coated 3D printed ABS	0.062	0.075	0.055	0.064	0.01	0.08	0.108	0.07	0.086	0	0.08	0	0.07	0.047	0.008	0.042	0.03	0.02	0.044	0.072	0.045	0.03	0.04	0
Copper coated solid ABS	0.048	0.041	0.053	0.047	0.01	0.047	0.046	0.041	0.045	0	0.05	0	0.048	0.059	0.047	0.051	0.01	0.041	0.039	0.037	0.039	0	0.05	0
Copper coated PEEK	0.068	0.106	0.094	0.089	0.02	0.102	0.087	0.099	0.096	0	0.09	0	0.071	0.08	0.076	0.076	0	0.079	0.077	0.075	0.077	0	0.08	0
Polished copper coated PEEK	0.087	0.088	0.086	0.087	0	0.07	0.082	0.078	0.077	0	0.08	0	0.087	0.076	0.079	0.081	0.01	0.066	0.077	0.071	0.071	0.01	0.08	0
Copper coated vertically oriented 3D printed ABS	0.058	0.062	0.041	0.054	0.01	0.05	0.054	0.068	0.057	0	0.06	0	/	/	/	/	/	/	/	/	/	/	/	/
Copper-Aluminium-Alumina coated 3D printed ABS	0.057	0.066	0.072	0.065	0.01	0.038	0.039	0.033	0.037	0	0.05	0	0.099	0.054	0.061	0.071	0.02	0.05	0.057	0.074	0.06	0.01	0.07	0
Copper-Aluminium-Alumina coated solid ABS	0.036	0.037	0.039	0.037	0	0.047	0.049	0.043	0.046	0	0.04	0	0.048	0.049	0.046	0.048	0	0.045	0.049	0.042	0.045	0	0.05	0
Zinc coated 3D printed ABS	0.078	0.066	0.066	0.07	0.01	0.086	0.07	0.039	0.065	0	0.07	0	0.048	0.047	0.074	0.056	0.02	0.087	0.044	0.105	0.079	0.03	0.07	0
Zinc coated solid ABS	0.104	0.108	0.106	0.106	0	0.107	0.125	0.118	0.117	0	0.11	0	0.143	0.107	0.122	0.124	0.02	0.106	0.12	0.109	0.112	0.01	0.12	0
Zinc coated PC	0.101	0.144	0.131	0.125	0.02	/	/	/	/	/	0.13	0	0.125	/	/	0.125	/	/	/	/	/	/	/	/
75 wt% copper - 25 wt% zinc coated 3D printed ABS	0.063	0.063	0.063	0.063	0	0.022	0.071	0.089	0.061	0	0.06	0	0.039	0.042	0.068	0.05	0.02	0.063	0.064	0.067	0.065	0	0.06	0
50% w/w copper-zinc coated 3D printed ABS	0.067	0.042	0.074	0.061	0.02	0.094	0.072	0.073	0.08	0	0.07	0	0.068	0.071	0.045	0.061	0.01	0.052	0.048	0.103	0.068	0.03	0.06	0
75 wt% zinc - 25 wt% copper coated 3D printed ABS	0.065	0.083	0.131	0.093	0.03	0.084	0.077	0.091	0.084	0	0.09	0	0.055	0.064	0.057	0.059	0	0.067	0.038	0.054	0.053	0.01	0.06	0
Copper Metal	0.076	0.124	0.068	0.089	0.03	0.066	0.058	0.061	0.062	0	0.08	0	/	/	/	/	/	/	/	/	/	/	/	/
Galvanised steel	0.09	0.156	0.152	0.133	0.04	0.04	0.137	0.062	0.08	0.1	0.11	0.1	/	/	/	/	/	/	/	/	/	/	/	/
Stainless steel	0.016	0.012	0.015	0.014	0	0.015	0.013	0.015	0.014	0	0.01	0	/	/	/	/	/	/	/	/	/	/	/	/
3D printed ABS	0.007	0	0.042	0.016	0.02	0.021	0	0.021	0.014	0	0.02	0	0.007	0	0.042	0.016	0.02	0.021	0	0.021	0.014	0.01	0.02	0
Vertically oriented 3D printed ABS	0.028	0.012	0.051	0.03	0.02	0	0	0	0	0	0.02	0	0.028	0.012	0.051	0.03	0.02	0	0	0	0	0	0.02	0
Solid ABS	0.292	0.189	0.147	0.209	0.07	0.081	0.249	0.149	0.16	0.1	0.18	0.1	0.292	0.189	0.147	0.209	0.07	0.081	0.249	0.149	0.16	0.08	0.18	0.1
Solid polycarbonate	0.106	0.023	0.076	0.068	0.04	0.122	0.093	0.074	0.096	0	0.08	0	0.106	0.023	0.076	0.068	0.04	0.122	0.093	0.074	0.096	0.02	0.08	0
Solid polyetheretherketone	0.145	0.225	0.127	0.166	0.05	0.093	0.132	0.088	0.104	0	0.14	0	0.145	0.225	0.127	0.166	0.05	0.093	0.132	0.088	0.104	0.02	0.14	0

Table C.21: Mean profile peak spacing (Rs) [mm] for single and multi-pass cold spray coatings and their uncoated substrates made according to the ISO 4288 standard in two orthogonal sampling orientations for experimentally optimum cold spray coatings.

Analysed samples	Single pass coating (including uncoated substrates)											Multi-pass coating (including uncoated substrates)										
	Orientation 1			Average	SD	Orientation 2			Average	SD	Overall average	SD	Orientation 1			Average	SD	Orientation 2			Average	SD	Overall average	SD
	Rs_1	Rs_2	Rs_3			Rs_1	Rs_2	Rs_3					Rs_1	Rs_2	Rs_3			Rs_1	Rs_2	Rs_3				
Copper coated 3D printed ABS	0.038	0.038	0.04	0.039	0	0.081	0.053	0.036	0.057	0	0.05	0	0.042	0.035	0.036	0.038	0	0.031	0.036	0.025	0.031	0.01	0.03	0
Copper coated solid ABS	0.028	0.027	0.035	0.03	0	0.031	0.031	0.03	0.031	0	0.03	0	0.036	0.034	0.032	0.034	0	0.026	0.027	0.028	0.027	0	0.03	0
Copper coated PEEK	0.05	0.067	0.054	0.057	0.01	0.064	0.06	0.06	0.061	0	0.06	0	0.049	0.053	0.049	0.05	0	0.053	0.054	0.05	0.052	0	0.05	0
Polished copper coated PEEK	0.057	0.057	0.054	0.056	0	0.05	0.058	0.054	0.054	0	0.06	0	0.055	0.052	0.053	0.053	0	0.047	0.054	0.048	0.05	0	0.05	0
Copper coated vertically oriented 3D printed ABS	0.031	0.037	0.027	0.032	0.01	0.06	0.038	0.062	0.053	0	0.04	0	/	/	/	/	/	/	/	/	/	/	/	/
Copper-Aluminium-Alumina coated 3D printed ABS	0.027	0.037	0.026	0.03	0.01	0.039	0.027	0.026	0.031	0	0.03	0	0.027	0.032	0.033	0.031	0	0.036	0.032	0.033	0.034	0	0.03	0
Copper-Aluminium-Alumina coated solid ABS	0.024	0.025	0.027	0.025	0	0.03	0.033	0.029	0.031	0	0.03	0	0.029	0.029	0.029	0.029	0	0.031	0.039	0.03	0.033	0	0.03	0
Zinc coated 3D printed ABS	0.041	0.045	0.046	0.044	0	0.04	0.069	0.051	0.053	0	0.05	0	0.05	0.048	0.04	0.046	0.01	0.069	0.056	0.064	0.063	0.01	0.05	0
Zinc coated solid ABS	0.065	0.07	0.063	0.066	0	0.064	0.069	0.073	0.069	0	0.07	0	0.078	0.07	0.07	0.073	0	0.063	0.075	0.067	0.068	0.01	0.07	0
Zinc coated PC	0.061	0.079	0.07	0.07	0.01	/	/	/	/	/	0.07	0	0.076	/	/	0.076	/	/	/	/	/	/	/	/
75 wt% copper - 25 wt% zinc coated 3D printed ABS	0.042	0.03	0.026	0.033	0.01	0.021	0.029	0.028	0.026	0	0.03	0	0.024	0.027	0.036	0.029	0.01	0.031	0.035	0.036	0.034	0	0.03	0
50% w/w copper-zinc coated 3D printed ABS	0.038	0.029	0.03	0.032	0	0.042	0.032	0.032	0.035	0	0.03	0	0.035	0.042	0.038	0.038	0	0.035	0.03	0.032	0.032	0	0.04	0
75 wt% zinc - 25 wt% copper coated 3D printed ABS	0.044	0.035	0.053	0.044	0.01	0.037	0.034	0.036	0.036	0	0.04	0	0.026	0.044	0.029	0.033	0.01	0.036	0.036	0.04	0.037	0	0.04	0
Copper Metal	0.047	0.039	0.056	0.047	0.01	0.027	0.029	0.026	0.027	0	0.04	0	/	/	/	/	/	/	/	/	/	/	/	/
Galvanised steel	0.043	0.046	0.048	0.046	0	0.048	0.041	0.038	0.042	0	0.04	0	/	/	/	/	/	/	/	/	/	/	/	/
Stainless steel	0.012	0.007	0.008	0.009	0	0.008	0.008	0.011	0.009	0	0.01	0	/	/	/	/	/	/	/	/	/	/	/	/
3D printed ABS	0.008	0.011	0.051	0.023	0.02	0.032	0.02	0.048	0.033	0	0.03	0	0.008	0.011	0.051	0.023	0.02	0.032	0.02	0.048	0.033	0.01	0.03	0
Vertically oriented 3D printed ABS	0.005	0.004	0.008	0.006	0	0	0	0	0	0	0	0	0.005	0.004	0.008	0.006	0	0	0	0	0	0	0	0
Solid ABS	0.042	0.025	0.025	0.031	0.01	0.037	0.041	0.026	0.035	0	0.03	0	0.042	0.025	0.025	0.031	0.01	0.037	0.041	0.026	0.035	0.01	0.03	0
Solid polycarbonate	0.009	0.007	0.008	0.008	0	0.012	0.01	0.007	0.01	0	0.01	0	0.009	0.007	0.008	0.008	0	0.012	0.01	0.007	0.01	0	0.01	0
Solid polyetheretherketone	0.086	0.092	0.063	0.08	0.02	0.049	0.051	0.03	0.043	0	0.06	0	0.086	0.092	0.063	0.08	0.02	0.049	0.051	0.03	0.043	0.01	0.06	0

Table C.22: Profile skewness (Rsk) for single and multi-pass cold spray coatings and their uncoated substrates made according to ISO 4288 in two orthogonal sampling orientations for experimentally optimum cold spray coatings.

Analysed samples	Single pass coating (including uncoated substrates)											Multi-pass coating (including uncoated substrates)										
	Orientation 1			Average	SD	Orientation 2			Average	SD	Overall average	SD	Orientation 1			Average	SD	Orientation 2			Average	SD	Overall average	SD
	Rsk_1	Rsk_2	Rsk_3			Rsk_1	Rsk_2	Rsk_3					Rsk_1	Rsk_2	Rsk_3			Rsk_1	Rsk_2	Rsk_3				
Copper coated 3D printed ABS	1.134	-0.41	0.18	0.301	0.78	-0.322	0.738	0.656	0.357	0.6	0.33	0.7	0.898	0.592	0.003	0.498	0.45	0.221	0.457	0.535	0.404	0.16	0.45	0.3
Copper coated solid ABS	-0.083	0.045	0.202	0.055	0.14	0.141	-0.103	0.057	0.032	0.1	0.04	0.1	0.744	-0.194	0.323	0.291	0.47	0.561	0.506	0.176	0.414	0.21	0.35	0.3
Copper coated PEEK	0.21	0.35	0.128	0.229	0.11	0.843	-0.051	0.216	0.336	0.5	0.28	0.3	0.121	-0.003	-0.035	0.028	0.08	0.145	0.183	0.186	0.171	0.02	0.1	0.1
Polished copper coated PEEK	-0.533	-0.635	-0.385	-0.518	0.13	-0.523	-0.62	-0.583	-0.575	0	-0.55	0.1	-0.549	-0.248	-0.271	-0.356	0.17	-0.385	-0.153	-0.352	-0.297	0.13	-0.33	0.2
Copper coated vertically oriented 3D printed ABS	0.669	0.806	-0.52	0.318	0.73	-0.257	-0.525	-0.385	-0.389	0.1	-0.04	0.4	/	/	/	/	/	/	/	/	/	/	/	/
Copper-Aluminium-Alumina coated 3D printed ABS	-0.374	-0.555	-0.274	-0.401	0.14	1.63	1.56	1.844	1.678	0.1	0.64	0.1	0.749	0.123	-0.891	-0.006	0.83	0.039	-0.877	-0.835	-0.558	0.52	-0.28	0.7
Copper-Aluminium-Alumina coated solid ABS	0.731	0.348	0.735	0.605	0.22	0.69	1.226	0.258	0.725	0.5	0.67	0.4	0.96	-0.038	-0.073	0.283	0.59	1.474	2.535	1.808	1.939	0.54	1.11	0.6
Zinc coated 3D printed ABS	-0.008	-0.485	-0.075	-0.189	0.26	0.353	0.083	-0.445	-0.003	0.4	-0.1	0.3	0.051	0.002	0.215	0.089	0.11	-0.235	0.616	-0.334	0.016	0.52	0.05	0.3
Zinc coated solid ABS	0.851	0.746	0.229	0.609	0.33	0.468	0.286	0.404	0.386	0.1	0.5	0.2	-0.027	0.284	-0.085	0.057	0.2	0.357	0.56	0.197	0.371	0.18	0.21	0.2
Zinc coated PC	0.552	0.122	0.038	0.237	0.28	/	/	/	/	/	0.24	0.3	0.025	/	/	0.025	/	/	/	/	/	/	/	/
75 wt% copper - 25 wt% zinc coated 3D printed ABS	-0.11	0.788	0.834	0.504	0.53	-0.217	0.258	0.418	0.153	0.3	0.33	0.4	0.391	-0.265	-0.13	-0.001	0.35	-0.125	-0.571	0.775	0.026	0.69	0.01	0.5
50% w/w copper-zinc coated 3D printed ABS	-1.214	-0.742	-0.86	-0.939	0.25	1.176	1.181	1.303	1.22	0.1	0.14	0.2	-0.564	0.261	-0.769	-0.357	0.55	0.409	0.269	0.954	0.544	0.36	0.09	0.5
75 wt% zinc - 25 wt% copper coated 3D printed ABS	0.649	0.527	0.717	0.631	0.1	-0.846	0.23	-0.584	-0.4	0.6	0.12	0.4	-0.469	0.319	-0.286	-0.145	0.41	0.426	0.666	0.307	0.466	0.18	0.16	0.3
Copper Metal	-0.324	-0.249	-1.253	-0.609	0.56	-0.016	-0.377	-0.162	-0.185	0.2	-0.4	0.4	/	/	/	/	/	/	/	/	/	/	/	/
Galvanised steel	0.321	-0.284	-0.956	-0.306	0.64	0.859	-0.315	0.352	0.299	0.6	0	0.6	/	/	/	/	/	/	/	/	/	/	/	/
Stainless steel	-2.2	-0.973	-0.875	-1.349	0.74	-0.745	-1.031	-1.626	-1.134	0.4	-1.24	0.6	/	/	/	/	/	/	/	/	/	/	/	/
3D printed ABS	-1.491	-1.629	-0.872	-1.331	0.4	1.957	1.766	1.726	1.816	0.1	0.24	0.3	-1.491	-1.629	-0.872	-1.331	0.4	1.957	1.766	1.726	1.816	0.12	0.24	0.3
Vertically oriented 3D printed ABS	1	-1.183	0.958	0.258	1.25	-0.313	-0.3	-0.295	-0.303	0	-0.02	0.6	1	-1.183	0.958	0.258	1.25	-0.313	-0.3	-0.295	-0.303	0.01	-0.02	0.6
Solid ABS	1.15	-0.65	1.166	0.555	1.04	1.63	1.729	-0.007	1.117	1	0.84	1	1.15	-0.65	1.166	0.555	1.04	1.63	1.729	-0.007	1.117	0.97	0.84	1
Solid polycarbonate	2.884	2.578	2.383	2.615	0.25	3.261	2.532	2.48	2.758	0.4	2.69	0.3	2.884	2.578	2.383	2.615	0.25	3.261	2.532	2.48	2.758	0.44	2.69	0.3
Solid polyetheretherketone	-1.406	-2.595	-2.664	-2.222	0.71	-1.714	-0.912	-0.825	-1.15	0.5	-1.69	0.6	-1.406	-2.595	-2.664	-2.222	0.71	-1.714	-0.912	-0.825	-1.15	0.49	-1.69	0.6

Coating wear resistance

The tabulated results for the wear resistance screening tests are given in Table C.25, with the corresponding graphical parameter variation effects depicted in Figure C.1. The combined wear test results are summarised in Table C.26.

Table C.23: Pin-on-disc screening wear test results for copper coated solid ABS test samples - Distance variation.

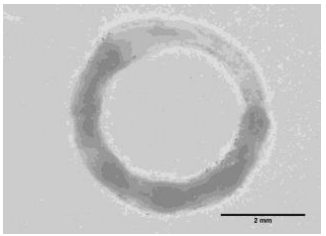
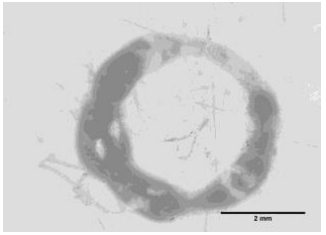
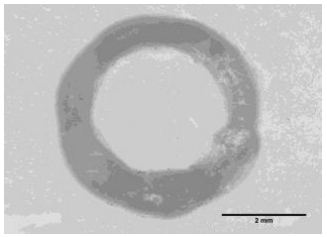
Distance Variation	A	Cu(1)ABS	**Acquisition Parameters**		**Units**	**0.358**	0.021	Metallurgical Microscope (high magnification)	Width 1 (mm)	0.45449	7.62E-02	**3.05E-04**	Coating was worn through, with a few sections that were not worn through. Powdery coating debris was observed on the edge of the wear track. Debris on ball with no observable wear.	
			Acquisition Rate	30	Hz				Width 2 (mm)	0.58133				
			Test Duration	6.63	min				Width 3 (mm)	0.65531				
			Tribological Environment						Width 4 (mm)	0.7152				
			Sample temperature	22	°C			Stereoscopic Microscopy (Low magnification)	Circular outer area	17.742				
			Humidity	53	%				Circular outer radius	2.376				
			Disc specification						Circular inner area	8.885				
			Coating	Copper	/				Circular inner radius	1.682				
			Substrate	Solid ABS	/				Track width	0.694				
			Cleaning	Dry cloth	/			Average track width (mm) excluding stereo width		0.602				
			Ball specifications					Standard deviation excluding stereo width measurement		0.11				
			Material	Stainless steel	/									
			Geometry	Ball	/									
			Diameter	6	mm									
			Tribometer test parameters											
			Applied load	5	N									
			Wear track radius	2	mm									
			Sliding distance	50	m									
			Linear speed	12.57	cm/s									
	B	Cu(1)ABS	**Acquisition Parameters**		**Units**	**0.32**	0.02	Metallurgical Microscope (high magnification)	Width 1 (mm)	0.51439	1.18E-01	**2.36E-04**	Uneven wear track pattern. Coating worn through over the majority of the wear track. Debris observed on side of wear track.	
			Acquisition Rate	30	Hz				Width 2 (mm)	0.48333				
			Test Duration	13.26	min				Width 3 (mm)	0.74694				
			Tribological Environment						Width 4 (mm)	1.043				
			Sample temperature	25	°C			Stereoscopic Microscopy (Low magnification)	Circular outer area	17.613				
			Humidity	44	%				Circular outer radius	2.368				
			Disc specification						Circular inner area	7.642				
			Coating	Copper	/				Circular inner radius	1.56				
			Substrate	Solid ABS	/				Track width	0.808				
			Cleaning	Dry cloth	/			Average track width (mm) excluding stereo width		0.697				
			Ball specifications					Standard deviation excluding stereo width measurement		0.26				
			Material	Stainless steel	/									
			Geometry	Ball	/									
			Diameter	6	mm									
			Tribometer test parameters											
			Applied load	5	N									
			Wear track radius	2	mm									
			Sliding distance	100	m									
			Linear speed	12.57	cm/s									
	C	Cu(1)ABS	**Acquisition Parameters**		**Units**	**0.298**	0.012	Metallurgical Microscope (high magnification)	Width 1 (mm)	1.12039	3.28E-01	**4.37E-04**	Coating completely worn through. Coating and substrate debris on side of wear track. Coating debris on ball, with no significant ball wear.	
			Acquisition Rate	30	Hz				Width 2 (mm)	0.90898				
			Test Duration	19.89	min				Width 3 (mm)	1.07456				
			Tribological Environment						Width 4 (mm)	0.81385				
			Sample temperature	22	°C			Stereoscopic Microscopy (Low magnification)	Circular outer area	19.726				
			Humidity	53	%				Circular outer radius	2.506				
			Disc specification						Circular inner area	7.642				
			Coating	Copper	/				Circular inner radius	1.56				
			Substrate	Solid ABS	/				Track width	0.946				
			Cleaning	Dry cloth	/			Average track width (mm) excluding stereo width		0.979				
			Ball specifications					Standard deviation excluding stereo width measurement		0.14				
			Material	Stainless steel	/									
			Geometry	Ball	/									
			Diameter	6	mm									
			Tribometer test parameters											
			Applied load	5	N									
			Wear track radius	2	mm									
			Sliding distance	150	m									
			Linear speed	12.57	cm/s									

Table C.24: Pin-on-disc screening wear test results for copper coated solid ABS test samples - Load variation.

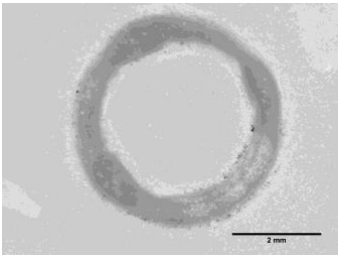
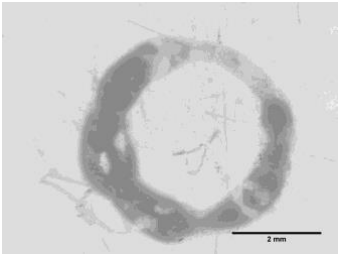
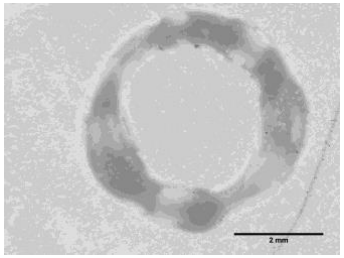
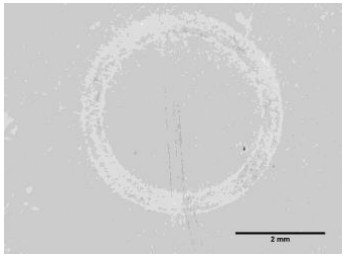
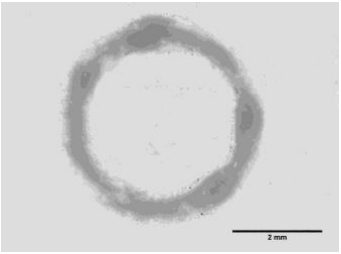
Load Variation	D	Cu(1)ABS	**Acquisition Parameters**		**Units**	**0.415**	0.034	Metallurgical Microscope (high magnification)	Width 1 (mm)	0.59541	7.10E-02	**3.55E-04**	Coating worn through. Coating debris on side of wear tracks. Coating debris on ball. No observable ball wear.	
			Acquisition Rate	30	Hz				Width 2 (mm)	0.45802				
			Test Duration	13.26	min				Width 3 (mm)	0.74000				
			Tribological Environment						Width 4 (mm)	0.55667				
			Sample temperature	24	°C			Stereoscopic Microscopy (Low magnification)	Circular outer area	17.764				
			Humidity	53	%				Circular outer radius	2.378				
			Disc specification						Circular inner area	8.762				
			Coating	Copper	/				Circular inner radius	1.67				
			Substrate	Solid ABS	/				Track width	0.708				
			Cleaning	Dry cloth	/			Average track width (mm) excluding stereo width		0.588				
			Ball specifications					Standard deviation excluding stereo width measurement		0.12				
			Material	Stainless steel	/									
			Geometry	Ball	/									
			Diameter	6	mm									
			Tribometer test parameters											
			Applied load	2	N									
			Wear track radius	2	mm									
			Sliding distance	100	m									
			Linear speed	12.57	cm/s									
	E	Cu(1)ABS	**Acquisition Parameters**		**Units**	**0.32**	0.02	Metallurgical Microscope (high magnification)	Width 1 (mm)	0.51439	1.18E-01	**2.36E-04**	Uneven wear track pattern. Coating worn through over the majority of the wear track. Debris observed on side of wear track.	
			Acquisition Rate	30	Hz				Width 2 (mm)	0.48333				
			Test Duration	13.26	min				Width 3 (mm)	0.74694				
			Tribological Environment						Width 4 (mm)	1.043				
			Sample temperature	25	°C			Stereoscopic Microscopy (Low magnification)	Circular outer area	17.613				
			Humidity	44	%				Circular outer radius	2.368				
			Disc specification						Circular inner area	7.642				
			Coating	Copper	/				Circular inner radius	1.56				
			Substrate	Solid ABS	/				Track width	0.808				
			Cleaning	Dry cloth	/			Average track width (mm) excluding stereo width		0.697				
			Ball specifications					Standard deviation excluding stereo width measurement		0.26				
			Material	Stainless steel	/									
			Geometry	Ball	/									
			Diameter	6	mm									
			Tribometer test parameters											
			Applied load	5	N									
			Wear track radius	2	mm									
			Sliding distance	100	m									
			Linear speed	12.57	cm/s									
	F	Cu(1)ABS	**Acquisition Parameters**		**Units**	**0.291**	0.014	Metallurgical Microscope (high magnification)	Width 1 (mm)	0.95488	2.16E-01	**3.08E-04**	Coating worn through. Coating debris on side of wear tracks. Coating debris on ball. No significant ball wear.	
			Acquisition Rate	30	Hz				Width 2 (mm)	0.93826				
			Test Duration	13.26	min				Width 3 (mm)	0.90939				
			Tribological Environment						Width 4 (mm)	0.60722				
			Sample temperature	24	°C			Stereoscopic Microscopy (Low magnification)	Circular outer area	18.777				
			Humidity	53	%				Circular outer radius	2.445				
			Disc specification						Circular inner area	8.031				
			Coating	Copper	/				Circular inner radius	1.599				
			Substrate	Solid ABS	/				Track width	0.846				
			Cleaning	Dry cloth	/			Average track width (mm) excluding stereo width		0.852				
			Ball specifications					Standard deviation excluding stereo width measurement		0.16				
			Material	Stainless steel	/									
			Geometry	Ball	/									
			Diameter	6	mm									
			Tribometer test parameters											
			Applied load	7	N									
			Wear track radius	2	mm									
			Sliding distance	100	m									
			Linear speed	12.57	cm/s									

Table C.25: Pin-on-disc screening wear test results for copper coated solid ABS test samples - Parametric combinations.

Combinations													
	G	Cu(1)ABS	**Acquisition Parameters**		**Units**	**0.494**	0.063	Metallurgical Microscope (high magnification)	Width 1 (mm)	0.3702	1.89E-02	**6.28E-04**	Coating partially worn. Consistent, even wear track. No debris on ball. No ball wear.	
			Acquisition Rate	30	Hz				Width 2 (mm)	0.38675				
			Test Duration	1.99	min				Width 3 (mm)	0.36668				
			Tribological Environment						Width 4 (mm)	0.3878				
			Sample temperature	24	°C			Stereoscopic Microscopy (Low magnification)	Circular outer area	15.435				
			Humidity	53	%				Circular outer radius	2.217				
			Disc specification						Circular inner area	10.205				
			Coating	Copper	/				Circular inner radius	1.802				
			Substrate	Solid ABS	/				Track width	0.415				
			Cleaning	Dry cloth	/			Average track width (mm) excluding stereo width		0.378				
			Ball specifications					Standard deviation excluding stereo width measurement		0.01				
			Material	Stainless steel	/									
			Geometry	Ball	/									
			Diameter	6	mm									
			Tribometer test parameters											
			Applied load	2	N									
			Wear track radius	2	mm									
			Sliding distance	15	m									
			Linear speed	12.57	cm/s									
	H	Cu(1)ABS	**Acquisition Parameters**		**Units**	**0.482**	0.04	Metallurgical Microscope (high magnification)	Width 1 (mm)	0.49696	4.21E-02	**4.21E-04**	Coating worn through with coating debris on the side of the wear tracks. Coating debris on ball. No significant ball wear.	
			Acquisition Rate	30	Hz				Width 2 (mm)	0.52186				
			Test Duration	6.63	min				Width 3 (mm)	0.48371				
			Tribological Environment						Width 4 (mm)	0.47231				
			Sample temperature	24	°C			Stereoscopic Microscopy (Low magnification)	Circular outer area	16.297				
			Humidity	53	%				Circular outer radius	2.278				
			Disc specification						Circular inner area	9.008				
			Coating	Copper	/				Circular inner radius	1.693				
			Substrate	Solid ABS	/				Track width	0.585				
			Cleaning	Dry cloth	/			Average track width (mm) excluding stereo width		0.494				
			Ball specifications					Standard deviation excluding stereo width measurement		0.02				
			Material	Stainless steel	/									
			Geometry	Ball	/									
			Diameter	6	mm									
			Tribometer test parameters											
			Applied load	2	N									
			Wear track radius	2	mm									
			Sliding distance	50	m									
			Linear speed	12.57	cm/s									

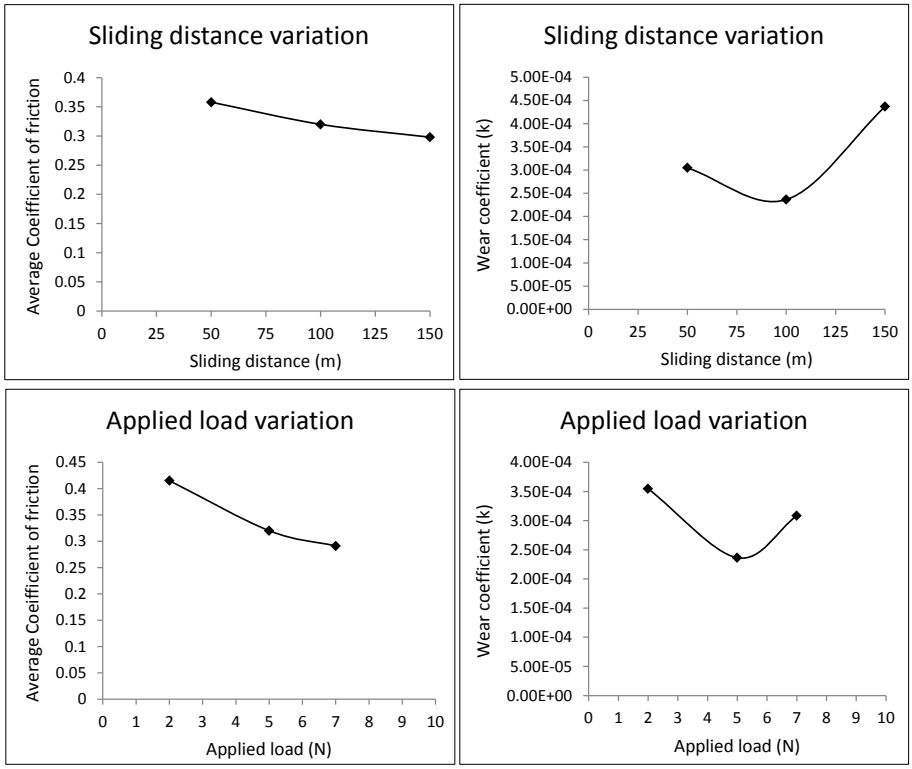


Figure C.1: Screening wear test parameter variations of friction and wear.

Table C.26: Combined surface wear test results for cold spray coatings and associated substrates.

Test sample	Average coefficient of friction (μ)		Average disc wear (mm^3)	Average wear coefficient of disc (k) [mm^3/N·m]	Average ball wear (mm^3)	Average wear coefficient of ball (k) [mm^3/N·m]
	Value	Std. dev.				
Copper coated solid ABS	0.442	0.040	0.066	4.40E-04	NSBW[1]	NSBW
Copper coated 3D printed ABS	0.509	0.048	0.195	1.30E-03	NSBW	NSBW
Copper coated PEEK	0.481	0.040	0.078	5.20E-04	NSBW	NSBW
Polished copper coated PEEK	0.452	0.059	0.037	2.47E-04	NSBW	NSBW
Copper coated vertically oriented 3D printed ABS	0.500	0.051	0.303	2.02E-03	NSBW	NSBW
Zinc coated 3D printed ABS	0.544	0.057	0.430	2.87E-03	NSBW	NSBW
Zinc coated solid ABS	0.413	0.047	0.253	1.69E-03	NSBW	NSBW
Zinc coated PC	0.505	0.066	0.272	1.81E-03	NSBW	NSBW
50% w/w copper-zinc coated 3D printed ABS	0.475	0.035	0.344	2.29E-03	NSBW	NSBW
Copper coated copper	0.334	0.036	0.201	1.34E-03	NSBW	NSBW
Copper metal	0.707	0.231	0.145	9.67E-04	2.00E-03	1.06E-05
Stainless steel	0.807	0.220	0.009	6.00E-05	2.00E-03	1.67E-05
3D printed ABS (hor.)	0.367	0.108	0.092	6.13E-04	NSBW	NSBW
3D printed ABS (vert.)	0.397	0.093	0.136	9.07E-04	NSBW	NSBW
Solid ABS	0.271	0.089	0.136	9.07E-04	NSBW	NSBW
Polycarbonate	0.518	0.134	0.296	1.97E-03	NSBW	NSBW
PEEK	0.245	0.057	0.007	4.67E-05	NSBW	NSBW

[1] NSBW - No Significant Ball Wear

Wear test data validation

According to the wear test procedure followed (ASTM G99) for the results to be considered experimentally valid and suitably precise it was stipulated that the coefficient of variation be less than 20% (see the surface wear test procedure). Table C.27 summarises the validation calculations, using the wear of copper coated 3D printed ABS and the corresponding control of 3D printed ABS. Both the coated and uncoated samples comply with the standard's guideline and therefore the calculated wear data may be considered suitably precise and ultimately experimentally valid.

Table C.27: Summary of wear test validation data using copper coated 3D printed ABS and uncoated 3D printed ABS as reference test samples.

	Disc volume loss			
	Disc volume loss (mm^3)	Average disc volume loss (mm^3)	Std. dev.	Coefficient of variation (%)
Copper coated 3D printed ABS	0.221 0.151 0.214	0.195	0.039	20
3D printed ABS	0.090 0.097 0.089	0.092	0.004	4

Appendix D Antimicrobial Susceptibility Test Data

Appendix D contains the sub-procedures, tabulated result data and additional information relating to the antimicrobial susceptibility testing. The following is included:

- Equipment and consumables Page 419
- Agar plating Page 419
- Pathogen datasheets Page 420
- Test sample naming convention Page 429
- Preparing the inoculate Page 430
- Streak test method - SOP Page 430
- Diffusion assay - SOP Page 431
- Dry contact test procedure - SOP Page 432
- Dry contact test data processing Page 434
- Diffusion assay - Standard coatings and pathogens Page 437
- Dry touch-contact test - Standard coatings and pathogens Page 440
- Diffusion assay - Silver additives Page 444
- Dry touch-contact test - Silver additives Page 446
- Dry touch-contact test - Resistant pathogens Page 449
- Pilot prototype testing Page 452

Equipment and consumables

- Tryptone Soya agar (TSA) (Laboratory Specialities)
- Tryptone Soya broth (TSB) (Laboratory Specialities)
- Sterile glass bottles (1 litre and 500 ml)
- Distilled water
- Micro-scale (mg)
- 90 mm disposable Petri dishes (MK Labs)
- Glass bottom examination trays
- Disposable L-shaped spreaders (MK Labs)
- Sterile forceps
- Glass McCartney bottles
- Micro-pipette, with disposable pipette tips
- Laminar flow unit
- Incubator
- Refrigerator
- Glass test tubes
- Vortex mixer
- Bunsen burner
- Sterile loop
- Light box

Agar plating

The agar plating procedure for antimicrobial assays is given below.

1. Prepare Tryptone Soya agar (TSA) solution.
    1.1. Sterilise all working surfaces.
    1.2. Suspend 40g of TSA (CM0131) in 1 litre of purified water.
    1.3. Shake until dissolved.
    1.4. Autoclave at 121 °C for 30 min.
2. Pour agar plates.
    2.1. Aseptically pour a fixed volume of autoclaved TSA solution into the test plates (petri dishes or trays).
    2.2. Allow agar to set before use.

Pathogen datasheets

Source: ATCC in partnership with LGC Standards

Reference: [225]

ATCC

Product Sheet

Staphylococcus aureus subsp. aureus (ATCC® 25923™)

Please read this FIRST

Storage Temp.
Frozen: -80°C or colder
Freeze-Dried: 2°C to 8°C
Live Culture: See Propagation Section

Biosafety Level
2

Intended Use

This product is intended for research use only. It is not intended for any animal or human therapeutic or diagnostic use.

Citation of Strain

If use of this culture results in a scientific publication, it should be cited in that manuscript in the following manner: *Staphylococcus aureus subsp. aureus* (ATCC® 25923™)

American Type Culture Collection
PO Box 1549
Manassas, VA 20108 USA
www.atcc.org

800.638.6597 or 703.365.2700
Fax: 703.365.2750
Email: Tech@atcc.org

Or contact your local distributor

Description

Designation: Seattle 1945
Deposited Name: *Staphylococcus aureus* Rosenbach
Product Description: Quality control strain for the CAMP test, assay of wood smoke concentrate, evaluation of Mueller-Hinton agar, examination of dairy products, media testing, CLSI disk diffusion, and for Abbott, API, and Autobac products.

Propagation

Medium
ATCC® Medium 18: Trypticase Soy Agar/Broth

Growth Conditions
Temperature: 37°C
Atmosphere: Aerobic

Propagation Procedure

1. Open vial according to enclosed instructions.
2. Using a single tube of #18 broth (5 to 6 mL), withdraw approximately 0.5 to 1.0 mL with a Pasteur or 1.0 mL pipette. Rehydrate the entire pellet.
3. Aseptically transfer this aliquot back into the broth tube. Mix well.
4. Use several drops of the suspension to inoculate a #18 agar slant and/or plate.
5. Incubate the tubes and plate at 37°C for 24 hours.

Notes

It is advisable to transfer from agar to agar to maintain MIC values.

Several GenBank accessions are available for this item:

1. Nucleotide (GenBank) : AF053568 Staphylococcus aureus ATCC 25923 heat shock protein 60 gene, partial cds.
2. Nucleotide (GenBank) : AX110511 Sequence 1244 from Patent WO0123604.
3. Nucleotide (GenBank) : AX110995 Sequence 1728 from Patent WO0123604.
4. Nucleotide (GenBank) : U02910 *Staphylococcus aureus* ATCC 25923 16S rRNA gene, partial sequence.
5. Nucleotide (GenBank) : U39769 *Staphylococcus aureus* 16S-23S ribosomal RNA spacer region.
6. Nucleotide (GenBank) : Z16422 *S. aureus* dfrB gene for dihydrofolate reductase.
7. Nucleotide (GenBank) : AB047239 *Staphylococcus aureus* DNA, complete structure of cassette chromosome(SCC)-like element, strain:ATCC 25923.

Additional information on this culture is available on the ATCC® web site at www.atcc.org.

References

References and other information relating to this product are available online at www.atcc.org.

Biosafety Level: 2

Appropriate safety procedures should always be used with this material. Laboratory safety is discussed in the current publication of the *Biosafety in Microbiological and Biomedical Laboratories* from the U.S. Department of Health and Human Services Centers for Disease Control and Prevention and National Institutes for Health.

ATCC Warranty

ATCC® products are warranted for 30 days from the date of shipment, and this warranty is valid only if the product is stored and handled according to the information included on this product information sheet. If the ATCC® product is a living cell or microorganism, ATCC lists the media formulation that has been found to be effective for this product. While other, unspecified media may also produce satisfactory results, a change in media or the absence of an additive from the ATCC recommended media may affect recovery, growth and/or function of this product. If an alternative medium formulation is used, the ATCC warranty for viability is no longer valid.

Source: ATCC in partnership with LGC Standards

Reference: [226]

ATCC

Product Sheet

Pseudomonas aeruginosa (ATCC® 27853™)

Please read this FIRST

Storage Temp.
Frozen: -80°C or colder
Freeze-Dried: 2°C to 8°C
Live Culture: See Propagation Section

Biosafety Level
2

Intended Use

This product is intended for research use only. It is not intended for any animal or human therapeutic or diagnostic use.

Citation of Strain

If use of this culture results in a scientific publication, it should be cited in that manuscript in the following manner: *Pseudomonas aeruginosa* (ATCC® 27853™)

American Type Culture Collection
PO Box 1549
Manassas, VA 20108 USA
www.atcc.org

800.638.6597 or 703.365.2700
Fax: 703.365.2750
Email: Tech@atcc.org

Or contact your local distributor

Description

Designation: Boston 41501
Deposited Name: *Pseudomonas aeruginosa* (Schroeter) Migula
Product Description: Used in media and susceptibility testing, evaluation of Mueller-Hinton Agar, and as a quality control strain for Abbott, API, Autobac, BBL, bioMerieux Vitek, Micro-Media, MicroScan™, Roche Diagnostics, and Sensititre products.

Propagation

Medium
ATCC® Medium 18: Trypticase Soy Agar/Broth

Growth Conditions
Temperature: 37°C
Atmosphere: Aerobic

Propagation Procedure

1. Open vial according to enclosed instructions.
2. Using a single tube of #18 broth (5 to 6 mL), withdraw approximately 0.5 to 1.0 mL with a Pasteur or 1.0 mL pipette. Rehydrate the entire pellet.
3. Aseptically transfer this aliquot back into the broth tube. Mix well.
4. Use several drops of the suspension to inoculate a #18 agar slant and/or plate.
5. Incubate the tubes and plate at 37°C for 24 hours.

Notes

Two colony types may be observed. They have been individually characterized and found to be identical. The predominant type is erose, rough, low convex, and approximately 2 mm in diameter. The secondary type is entire, glistening, smooth, and small. This strain produces both fluorescein and pyocyanin pigments. To prevent the proliferation of the second colony type, avoid passing this strain through broth for transfers. It is recommended to wash a slant with phosphate buffer and use that to inoculate further agar plates and/or agar flasks if needed.

Purified genomic DNA of this strain is available as ATCC ® 27853D-5™. Certified Reference Material of this strain is available as ATCC® CRM-27853™.

Several Genbank accessions are available for this item:

1. Nucleotide (GenBank) : AB037545 Pseudomonas aeruginosa gene for 16S ribosomal RNA, strain:ATCC 27853.
2. Nucleotide (GenBank) : AF094719 Pseudomonas aeruginosa strain ATCC 27853 16S ribosomal RNA gene, partial sequence.
3. Nucleotide (GenBank) : M63957 Pseudomonas aeruginosa heat shock protein (groES and groEL) genes, complete cds.
4. Nucleotide (GenBank) : U07832 Pseudomonas aeruginosa helicase I (helA) gene, partial cds.
5. Nucleotide (GenBank) : U64101 Pseudomonas aeruginosa heat shock protein (groesEL) gene, partial cds.
6. Nucleotide (GenBank) : U67855 Pseudomonas aeruginosa UDP-3-O-acyl-GlcNAc deacetylase (lpxC) gene, complete cds.
7. Nucleotide (GenBank) : X65933 P. aeruginosa pa-1L gene for PA-I galactophilic lectin.

Additional information on this culture is available on the ATCC® web site at www.atcc.org.

References

References and other information relating to this product are available online at www.atcc.org.

Biosafety Level: 2

Appropriate safety procedures should always be used with this material. Laboratory safety is discussed in the current publication of the *Biosafety in Microbiological and Biomedical Laboratories* from the U.S. Department of Health and Human Services Centers for Disease Control and Prevention and National Institutes for Health.

ATCC Warranty

Source: ATCC in partnership with LGC Standards

Reference: [227]

ATCC

Product Sheet

Candida albicans (ATCC® 10231™)

Please read this FIRST

Storage Temp.
Frozen: -80°C or colder
Freeze-Dried: 2°C to 8°C
Live Culture: See Propagation Section

Biosafety Level
1

Intended Use

This product is intended for research use only. It is not intended for any animal or human therapeutic or diagnostic use.

Citation of Strain

If use of this culture results in a scientific publication, it should be cited in that manuscript in the following manner: *Candida albicans* (ATCC® 10231™)

American Type Culture Collection
PO Box 1549
Manassas, VA 20108 USA
www.atcc.org

800.638.6597 or 703.365.2700
Fax: 703.365.2750
Email: Tech@atcc.org

Or contact your local distributor

Description

Strain Designation: 3147 [CBS 6431, CCY 29-3-106, CIP 48.72, DSM 1386, IFO 1594, NCPF 3179, NCYC 1363, NIH 3147, VTT C-85161]
Deposited Name: *Candida albicans* (Robin) Berkhout
Antigenic Properties: Serotype A
Product Description: An ampoule containing viable cells (may include spores and mycelia) suspended in cryoprotectant.

Propagation

The information recommended in this section is to assist users in obtaining living culture(s) for their studies. The recommendation does not imply that the conditions or procedures provided below are optimum. Experienced researchers may initiate the growth of a culture in their own way.

ATCC® Medium 200: YM agar or YM broth
ATCC® Medium 28: Emmons' modification of Sabouraud's agar
ATCC® Medium 1245: YEPD

Growth Conditions
Temperature: 24°C to 26°C
Atmosphere: Typical aerobic

Recommended Procedure
For **freeze-dry (lyophilized) ampoules:**

1. Open an ampoule according to enclosed instructions.
2. From a single test tube of **sterile distilled water** (5 to 6 mL), withdraw approximately 0.5 to 1.0 mL with a sterile pipette and apply directly to the pellet. Stir to form a suspension.
3. Aseptically transfer the suspension back into the test tube of sterile distilled water.
4. Let the test tube sit at room temperature (25°C) undisturbed **for at least 2 hours**; longer (e.g., overnight) rehydration might increase viability of some fungi.
5. Mix the suspension well. Use several drops (or make dilutions if desired) to inoculate recommended solid or liquid medium. Include a control that receives no inoculum.
6. Incubate the inoculum at the propagation conditions recommended.
7. Inspect for growth of the inoculum/strain regularly. The sign of viability is noticeable typically after 1-2 days of incubation. However, the time necessary for significant growth will vary from strain to strain.

Colony and Cell Morphology: On YEPD agar after 2 days at 25°C, colonies are cream-colored, shiny, and smooth. Older colonies show filaments-like structure at the margin and may have ridges or folders. Cells are ovoid (3.0-6.0 x 4.0-8.0 µm), budding, mostly singly and rarely clustered in young culture. Cells will elongate and form chain-like branched pseudohyphae in older culture.

Notes

This strain is recommended by ATCC for use in the tests described in ASTM Standard Test Method E979-91 where only the taxon is specified; For sterility testing, not more than five passages from the ATCC culture should be used; Purified genomic DNA of this strain is available as ATCC 10231D-5™.
Additional, updated information on this product may be available on the ATCC® web site at www.atcc.org.

DNA Sequence

18S ribosomal RNA gene, partial sequence; internal transcribed spacer 1, 5.8S ribosomal RNA gene, and internal transcribed spacer 2, complete sequence; and 26S ribosomal RNA gene, partial sequence
GGTTTCCGTAGGTGAACCTGCGGAAGGATCATTACTGATTTGCTTAATTGCACCACATGTGTTTTTCTTT
GAAACAAACTTGCTTTGGCGGTGGGCCCAGCCTGCCGCCAGAGGTCTAAACTTACAACCAATTTTTTAT
CAACTTGTCACACCAGATTATTACTAATAGTCAAAACTTTCAACAACGGATCTCTTGGTTCTCGCATCGA
TGAAGAACGCAGCGAAATGCGATACGTAATATGAATTGCAGATATTCGTGAATCATCGAATCTTTGAA
CGCACATTGCGCCCTCTGGTATTCCGGAGGGCATGCCTGTTTGAGCGTCGTTTCTCCCTCAAACCGCTGG
GTTTGGTGTTGAGCAATACGACTTGGGTTTGCTTGAAAGACGGTAGTGGTAAGGCGGGATCGCTTTGA
CAATGGCTTAGGTCTAACCAAAAACATTGCTTGCGGCGGTAACGTCCACCACGTATATCTTCAAACTTT
GACCTCAAATCAGGTAGGACTACCCGCTGAACTTAAGCATATCAATAA

D1D2 region of the 26S ribosomal RNA gene
ATATCAATAAGCGGAGGAAAAGAAACCAACAGGGATTGCCTCAGTAGCGGCGAGTGAAGCGGCAAA

Source: ATCC in partnership with LGC Standards

Reference: [228]

ATCC

Product Sheet

Klebsiella pneumoniae subsp. pneumoniae (ATCC® 13887™)

Please read this FIRST

Biosafety Level
2

Intended Use

This product is intended for research use only. It is not intended for any animal or human therapeutic or diagnostic use.

Citation of Strain

If use of this culture results in a scientific publication, it should be cited in that manuscript in the following manner: *Klebsiella pneumoniae subsp. pneumoniae* (ATCC® 13887™)

American Type Culture Collection
PO Box 1549
Manassas, VA 20108 USA
www.atcc.org

800.638.6597 or 703.365.2700
Fax: 703.365.2750
Email: Tech@atcc.org

Or contact your local distributor

Description

Designation: NCTC 9496 [NCDC 421-68, NCDC 4610-53]
Deposited Name: *Klebsiella edwardsii* subsp. *atlantae* Cowan et al.

Propagation

Medium
ATCC® Medium 3: Nutrient agar or nutrient broth

Growth Conditions
Temperature: 37.0°C

Propagation Procedure
1. Open vial according to enclosed instructions.
2. From a single tube of #3 broth (5 to 6 ml), withdraw approximately 0.5 to 1.0 ml with a Pasteur or 1.0 ml pipette and use to rehydrate the entire pellet.
3. Aseptically transfer the rehydrated pellet back into the broth tube. Mix well.
4. Use several drops of this suspension to inoculate an additional broth tube, an agar slant and/or plate.
5. Incubate the tubes and plate at 37°C for 24 hours.

Notes

Colonies on #3 plates are entire, glistening, smooth, opaque, mucoid, and gray.
Additional information on this culture is available on the ATCC web site at www.atcc.org.

References

References and other information relating to this product are available online at www.atcc.org.

Biosafety Level: 2

Appropriate safety procedures should always be used with this material. Laboratory safety is discussed in the current publication of the *Biosafety in Microbiological and Biomedical Laboratories* from the U.S. Department of Health and Human Services Centers for Disease Control and Prevention and National Institutes for Health.

ATCC Warranty

ATCC® products are warranted for 30 days from the date of shipment, and this warranty is valid only if the product is stored and handled according to the information included on this product information sheet. If the ATCC® product is a living cell or microorganism, ATCC lists the media formulation that has been found to be effective for this product. While other, unspecified media may also produce satisfactory results, a change in media or the absence of an additive from the ATCC recommended media may affect recovery, growth and/or function of this product. If an alternative medium formulation is used, the ATCC warranty for viability is no longer valid.

Disclaimers

This product is intended for laboratory research purposes only. It is not intended for use in humans.
While ATCC uses reasonable efforts to include accurate and up-to-date information on this product sheet, ATCC makes no warranties or representations as to its accuracy. Citations from scientific literature and patents are provided for informational purposes only. ATCC does not warrant that such information has been confirmed to be accurate.
This product is sent with the condition that you are responsible for its safe storage, handling, and use. ATCC is not liable for any damages or injuries arising from receipt and/or use of this product. While reasonable effort is made to insure authenticity and reliability of materials on deposit, ATCC is not liable for damages arising from the misidentification or misrepresentation of such materials.
Please see the enclosed Material Transfer Agreement (MTA) for further details regarding the use of this product. The MTA is also available on our Web site at www.atcc.org

Additional information on this culture is available on the ATCC web site at www.atcc.org.
© ATCC 2013. All rights reserved. ATCC is a registered trademark of the American Type Culture Collection. [01/14]

Source: ATCC in partnership with LGC Standards

Reference: [229]

ATCC

Product Sheet

Enterococcus faecalis (ATCC® 29212™)

Please read this FIRST

Storage Temp.
Frozen: -80°C or colder
Freeze-Dried: 2°C to 8°C
Live Culture: See Propagation Section

Biosafety Level
2

Intended Use

This product is intended for research use only. It is not intended for any animal or human therapeutic or diagnostic use.

Citation of Strain

If use of this culture results in a scientific publication, it should be cited in that manuscript in the following manner: *Enterococcus faecalis* (ATCC® 29212™)

American Type Culture Collection
PO Box 1549
Manassas, VA 20108 USA
www.atcc.org

800.638.6597 or 703.365.2700
Fax: 703.365.2750
Email: Tech@atcc.org

Or contact your local distributor

Description

Designation: [Portland]
Deposited Name: *Streptococcus faecalis* Andrewes and Horder
Product Description: Used in media testing, susceptibility testing, and as a CLSI quality control strain. Used as a quality control strain for BD, bioMérieux VITEK, RapID, MicroScan, and Sensititre products.

Propagation

Medium
ATCC® Medium 44: Brain Heart Infusion Agar/Broth
ATCC® Medium 260: Trypticase soy agar/broth with defibrinated sheep blood

Growth Conditions
Temperature: 37°C
Atmosphere: Aerobic

Propagation Procedure
1. Open vial according to enclosed instructions or visit www.atcc.org for instructions.
2. Rehydrate the entire pellet with approximately 0.5 mL of #44 broth. Aseptically transfer the entire contents to a 5-6 mL tube of #44 broth. Additional test tubes can be inoculated by transferring 0.5 mL of the primary broth tube to these secondary tubes.
3. Use several drops of the primary broth tube to inoculate a #260 plate and/or #260 agar slant.
4. Incubate at 37°C for 24 hours.

Notes

Additional information on this culture is available on the ATCC® web site at www.atcc.org.

References

References and other information relating to this product are available online at www.atcc.org.

Biosafety Level: 2

Appropriate safety procedures should always be used with this material. Laboratory safety is discussed in the current publication of the *Biosafety in Microbiological and Biomedical Laboratories* from the U.S. Department of Health and Human Services Centers for Disease Control and Prevention and National Institutes for Health.

ATCC Warranty

ATCC® products are warranted for 30 days from the date of shipment, and this warranty is valid only if the product is stored and handled according to the information included on this product information sheet. If the ATCC® product is a living cell or microorganism, ATCC lists the media formulation that has been found to be effective for this product. While other, unspecified media may also produce satisfactory results, a change in media or the absence of an additive from the ATCC recommended media may affect recovery, growth and/or function of this product. If an alternative medium formulation is used, the ATCC warranty for viability is no longer valid.

Disclaimers

This product is intended for laboratory research purposes only. It is not intended for use in humans.
While ATCC uses reasonable efforts to include accurate and up-to-date information on this product sheet, ATCC makes no warranties or representations as to its accuracy. Citations from scientific literature and patents are provided for informational purposes only. ATCC does not warrant that such information has been confirmed to be accurate.
This product is sent with the condition that you are responsible for its safe storage, handling, and use. ATCC is not liable for any damages or injuries arising from receipt and/or use of this product. While reasonable effort is made to insure authenticity and reliability of materials on deposit, ATCC is not liable for damages arising from the misidentification or misrepresentation of such materials.

Please see the enclosed Material Transfer Agreement (MTA) for further details regarding the use of this product. The MTA is also available on our Web site at www.atcc.org

Source: ATCC in partnership with LGC Standards

Reference: [230]

ATCC

Product Sheet

Staphylococcus aureus subsp. aureus (ATCC® 33592™)

Please read this FIRST

Storage Temp.
Frozen: -80°C or colder
Freeze-Dried: 2°C to 8°C
Live Culture: See Propagation Section

Biosafety Level
2

Intended Use

This product is intended for research use only. It is not intended for any animal or human therapeutic or diagnostic use.

Citation of Strain

If use of this culture results in a scientific publication, it should be cited in that manuscript in the following manner: *Staphylococcus aureus subsp. aureus* (ATCC® 33592™)

American Type Culture Collection
PO Box 1549
Manassas, VA 20108 USA
www.atcc.org

800.638.6597 or 703.365.2700
Fax: 703.365.2750
Email: Tech@atcc.org

Or contact your local distributor

Description

Designation: 1063
Deposited Name: *Staphylococcus aureus* subsp. *aureus* Rosenbach
Genotype: *pvl* negative
Product Description: Gentamicin- and methicillin-resistant.

Propagation

Medium
ATCC® Medium 3: Nutrient agar or nutrient broth

Growth Conditions
Temperature: 37°C
Atmosphere: Aerobic

Propagation Procedure

1. Open vial according to enclosed instructions.
2. Using a single tube of #3 broth (5 to 6 mL), withdraw approximately 0.5 to 1.0 mL with a Pasteur or 1.0 mL pipette. Rehydrate the entire pellet.
3. Aseptically transfer this aliquot back into the broth tube. Mix well.
4. Use several drops of the suspension to inoculate a #3 agar slant and/or plate.
5. Incubate the tubes and plate at 37°C for 24 hours.

Notes

Additional information on this culture is available on the ATCC® web site at www.atcc.org.

References

References and other information relating to this product are available online at www.atcc.org.

Biosafety Level: 2

Appropriate safety procedures should always be used with this material. Laboratory safety is discussed in the current publication of the *Biosafety in Microbiological and Biomedical Laboratories* from the U.S. Department of Health and Human Services Centers for Disease Control and Prevention and National Institutes for Health.

ATCC Warranty

ATCC® products are warranted for 30 days from the date of shipment, and this warranty is valid only if the product is stored and handled according to the information included on this product information sheet. If the ATCC® product is a living cell or microorganism, ATCC lists the media formulation that has been found to be effective for this product. While other, unspecified media may also produce satisfactory results, a change in media or the absence of an additive from the ATCC recommended media may affect recovery, growth and/or function of this product. If an alternative medium formulation is used, the ATCC warranty for viability is no longer valid.

Disclaimers

This product is intended for laboratory research purposes only. It is not intended for use in humans.
While ATCC uses reasonable efforts to include accurate and up-to-date information on this product sheet, ATCC makes no warranties or representations as to its accuracy. Citations from scientific literature and patents are provided for informational purposes only. ATCC does not warrant that such information has been confirmed to be accurate.
This product is sent with the condition that you are responsible for its safe storage, handling, and use. ATCC is not liable for any damages or injuries arising from receipt and/or use of this product. While reasonable effort is made to insure authenticity and reliability of materials on deposit, ATCC is not liable for damages arising from the misidentification or misrepresentation of such materials.

Please see the enclosed Material Transfer Agreement (MTA) for further details regarding the use of this product. The MTA is also available on our Web site at www.atcc.org

Source: BacDive Strain Identifier

Reference: [231]

Pseudomonas aeruginosa

Strain identifier

BacDive ID:	24356	**DOI:**	10.13145/bacdive24356.20180622.3
Type strain:	no	**Designation:**	9664
Culture col. no.:	DSM 46316, IMET 11035		

Sections

Name and taxonomic classification

Morphology and physiology

Culture and growth conditions

Application and interaction

References

Name and taxonomic classification

Ref.: 21105	**Domain**	Bacteria
Ref.: 21105	**Phylum**	Proteobacteria
Ref.: 21105	**Class**	Gammaproteobacteria
Ref.: 21105	**Order**	Pseudomonadales
Ref.: 21105	**Family**	Pseudomonadaceae
Ref.: 21105	**Genus**	Pseudomonas
Ref.: 21105	**Species**	Pseudomonas aeruginosa
Ref.: 21105	**Full Scientific Name**	Pseudomonas aeruginosa (Schroeter 1872) Migula 1900
Ref.: 21105	**Designation:**	9664
Ref.: 21105	**Type strain:**	no

Prokaryotic Nomenclature Up-to-date (PNU)

Ref.: 20215	**Domain**	Bacteria
Ref.: 20215	**Phylum**	Proteobacteria
Ref.: 20215	**Class**	Gammaproteobacteria
Ref.: 20215	Literature reference	Int. J. Syst. Evol. Microbiol. 55:2236
Ref.: 20215	**Family**	Pseudomonadaceae
Ref.: 20215	Literature reference	Int. J. Syst. Bacteriol. 30:237
Ref.: 20215	**Genus**	Pseudomonas
Ref.: 20215	Taxonomical status	genus (AL)
Ref.: 20215	Literature reference	Int. J. Syst. Bacteriol. 30:349 AL
Ref.: 20215	**Species**	Pseudomonas aeruginosa

Source: BacDive Strain Identifier

Reference: [231]

Pseudomonas aeruginosa

Ref.: 20215	Taxonomical status	species (AL)
Ref.: 20215	Literature reference	Int. J. Syst. Bacteriol. 30:349 AL
Ref.: 20215	**Full Scientific Name**	Pseudomonas aeruginosa (Schroeter 1872) Migula 1900

Morphology and physiology

Ref.: 21105 **API 20NE**

API ID	3703
NO3	+
TRP	-
GLU_Ferm	-
ADH (Arg)	+
URE	+/-
ESC	-
GEL	+
PNPG	-
GLU_Assim	+
ARA	-
MNE	-
MAN	+
NAG	-
MAL	-
GNT	+
CAP	+
ADI	+
MLT	+
CIT	+
PAC	-
OX	+

Ref.: 21105	**Decomposition/lysis**	ESBL

Culture and growth conditions

Ref.: 21105	**Culture medium**	ORGANIC MEDIUM 79 (DSMZ Medium 426), 30°C
Ref.: 21105	**Culture medium growth**	yes
Ref.: 21105	**Culture medium link**	https://www.dsmz.de/microorganisms/medium/pdf/DSMZ_Medium426.pdf

Source: BacDive Strain Identifier

Reference: [231]

Pseudomonas aeruginosa

	Temperatures	Kind of temperature	Temperature
Ref.: 21105		growth	30 °C

Ref.: 21105	**Temperature range**	mesophilic

Application and interaction

Ref.: 21105	**Pathogenicity (human)**	yes
Ref.: 21105	**Pathogenicity (animal)**	yes
Ref.: 21105	**Biosafety level**	2 Risk group (German classification)

Strain availability

Ref.: 21105	**Culture collection no.**	DSM 46316, IMET 11035
Ref.: 21105	**Strain history**	<- IMET <- U. Möllmann, 9664 <- W. Witte

Associated Passport(s) in StrainInfo

Ref.: 20218	340810 - http://www.straininfo.net/strains/340810
Ref.: 20218	340811 - http://www.straininfo.net/strains/340811

References

Ref.: 20215	D.Gleim, M.Kracht, N.Weiss et. al.: Prokaryotic Nomenclature Up-to-date - compilation of all names of Bacteria and Archaea, validly published according to the Bacteriological Code since 1. Jan. 1980, and validly published nomenclatural changes since.
Ref.: 20218	Verslyppe, B., De Smet, W., De Baets, B., De Vos, P., Dawyndt P. StrainInfo introduces electronic passports for microorganisms.. Syst Appl Microbiol. 37: 42-50 2014 (10.1016/j.syapm.2013.11.002, 24321274)
Ref.: 21105	Leibniz Institut DSMZ-Deutsche Sammlung von Mikroorganismen und Zellkulturen GmbH; Curators of the DSMZ; DSM 46316

*** These References are textmined**

back to top

Test sample naming convention

The names and reference numbers for cold spray test samples and their respective controls are tabulated in Table D.1, for the standard coatings, and Table D.2, for the silver additive coatings. The tables include the material description as well as the reference name, which was often used in the analyses. The copper cold spray coated copper test sample, while not representative of a polymer metallised coating type, performs the role of both test sample and associated control, for the purposes of this research.

Table D.1: Standard cold spray coatings and their controls.

	Material Description	Reference Name
Standard coatings	Copper coated 3D printed ABS	1 - Cu(1)3DABS
	Copper coated solid ABS	2 - Cu(1)ABS
	Copper coated PEEK	3 - Cu(1)PEEK
	Polished copper coated PEEK	4 - Cu(1)PEEK (polished)
	Copper coated vertically oriented 3D printed ABS	5 - Cu(1)VO3DABS
	Copper-Aluminium-Alumina coated 3D printed ABS	6 - Cu(2)3DABS
	Copper-Aluminium-Alumina coated solid ABS	7 - Cu(2)ABS
	Zinc coated 3D printed ABS	8 - Zn3DABS
	Zinc coated solid ABS	9 - ZnABS
	Zinc coated PC	10 - ZnPC
	75 wt% copper - 25 wt% zinc coated 3D printed ABS	11 - Cu(1)75Zn3DABS
	50% w/w copper-zinc coated 3D printed ABS	12 - Cu(1)50Zn3DABS
	75 wt% zinc - 25 wt% copper coated 3D printed ABS	13 - Zn75Cu(1)3DABS
	Copper coated copper	14 - Cu(1)-Cu
Silver additives	5 wt% silver - 95 wt% copper coated copper	15 - Ag5Cu(1)-Cu
	5 wt% silver - 95 wt% copper coated solid ABS	16 - Ag5Cu(1)ABS
	5 wt% silver - 95 wt% copper coated vertically oriented 3D printed ABS	17 - Ag5Cu(1)VO3DABS
	5 wt% silver - 95 wt% copper coated 3D printed ABS	18 - Ag5Cu(1)3DABS
	5 wt% silver - 47.5% w/w copper-zinc coated 3D printed ABS	19 - Ag5Cu(1)Zn3DABS
	5 wt% silver - 95 wt% zinc coated 3D printed ABS	20 - Ag5Zn3DABS
Control samples	Pure copper	C1 - Pure Copper
	Zinc coated/galvanised steel	C2 - Galvanised Steel
	Stainless steel	C3 - Stainless Steel
	3D printed ABS	C4 - 3DABS
	Vertically oriented 3D printed ABS	C5 - VO3DABS
	Solid ABS	C6 - ABS
	Solid polycarbonate	C7 - PC
	Solid polyetheretherketone	C8 - PEEK

Table D.2: Special cold spray coatings with a 5 wt% silver additive.

Material Description	Reference Name
5 wt% silver - 95 wt% copper coated copper	15 - Ag5Cu(1)-Cu
5 wt% silver - 95 wt% copper coated solid ABS	16 - Ag5Cu(1)ABS
5 wt% silver - 95 wt% copper coated vertically oriented 3D printed ABS	17 - Ag5Cu(1)VO3DABS
5 wt% silver - 95 wt% copper coated 3D printed ABS	18 - Ag5Cu(1)3DABS
5 wt% silver - 47.5% w/w copper-zinc coated 3D printed ABS	19 - Ag5Cu(1)Zn3DABS
5 wt% silver - 95 wt% zinc coated 3D printed ABS	20 - Ag5Zn3DABS

Preparing the inoculate

1. Prepare a 0.5 McFarland's culture dilution in Tryptone Soya broth (TSB).
2. Streak cultures to confirm culture purity and strain type.
3. Spread plate the culture to ensure sufficient concentration for the test being conducted. For example for a diffusion assay the incubated spread plate should produce a uniform and even microbial growth (carpeting the agar).

Streak test method - SOP

1. Heat loop in the flame of Bunsen burner.
2. Pass the neck of the inoculate test tube through the Bunsen burner flame.
3. Cool the loop in agar.
4. Dip the loop into the inoculate.
5. Make three uniform streaks of the inoculated loop over the agar.
6. Sterilize the loop in the flame of the Bunsen burner.
7. Turn petri dish 90° clockwise and streak three times across the end of previous streak lines.
8. Re-sterilize the loop as before.
9. Turn petri dish 90° clockwise and streak three times across the end of previous streak lines.

10. Turn petri dish 90° clockwise and streak a ribbon through last set of streak lines.

Diffusion assay - SOP

The following provides a standard operating procedure for the diffusion assays conducted in this research.

1. Prepare Tryptone Soya agar plates.
2. Prepare the culture inoculate.
3. Perform a streak test to validate culture viability and purity.
4. Sterilise all test samples.
    4.1. Dip samples in a 70% alcohol solution.
    4.2. Dry samples in an aseptic environment, preferably within a laminar flow unit.
5. Spread the inoculate evenly over the agar plate/petri dish.
    5.1. For a 90 mm Petri dish pipette 100 μl of inoculate.
    5.2. For a 250 x 250 mm glass bottomed tray pipette 0.5 ml of inoculate.
    5.3. Use a sterile L-shaped spreader to spread the aliquot of inoculate evenly over the agar. Avoid cross-contamination. Use a new spreader for each agar plate, even where the same culture is being used.
6. Place the test specimens onto the inoculated agar, coating side down.
    6.1. Map out sample placement, ensuring sufficient spacing between samples to prevent overlapping zones of inhibition.
    6.2. Place specimens with sterile forceps coating side down onto the prepared agar plates.
    6.3. Press down on samples to ensure uniform contact with inoculated agar surface.
7. Incubate the test plates.
    7.1. Refrigerate the plates for an hour, allowing for effective diffusion.
    7.2. Transfer plates to incubator and incubate for 16 - 24 hours at 37 °C for bacterial inoculates and 48 hours at 37 °C for fungal inoculates.
8. Measure and record the zones of inhibition.
    8.1. Remove the plates from the incubator.

8.2. Observe microbial growth under suitable lighting conditions (use of a light box may be required).

8.3. Measure the extent of the zones of inhibition (to the nearest 0.1 mm), as demonstrated by Figure D.1. A zone of inhibition measurement is taken from the sample/disc edge to the extent of inhibition. The average of four readings (m_1, m_2, m_3, m_4) represents the recorded zone of inhibition.

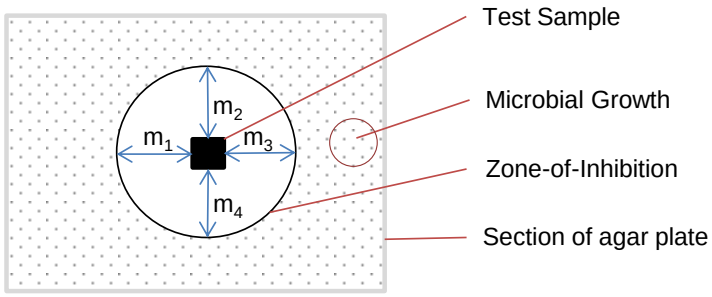


Figure D.1: Zone-of-inhibition measurement method.

9. Repeat the procedure for all coating-pathogen combinations.

10. Repeat the procedure using the raw feedstock powders as the antimicrobial discs.

10.1. Place an equal, small volume of powder directly only to inoculated agar as a small mound (with a diameter of approximately 5 mm).

Dry contact test procedure - SOP

The detailed Standard Operating Procedure for the dry contact tests, which simulate touch-contact activity, was based on time-kill assays.

Dry Contact Pre-test Preparation

1. Prepare agar plates in 90 mm disposable Petri dishes.

2. Prepare a saline solution.

2.1. Aseptically fill 35 McCartney bottles for every test sample type and culture type being tested, with 9.9 ml of the saline solution.

3. Prepare the test culture in TSB to an approximate concentration of 2 x 10^8 CFU/ml.

3.1. Use a turbidity test to achieve 0.5 McFarland Standard.

4. Sterilise test samples in 70% alcohol.

4.1. Ensure samples are completely dry before progressing to the next step.

Stage 1: Test Proceedings

5. Use a micro-pipette to spread 5 μl of culture over each sample.
6. Incubate samples at room temperature for 0.5, 5, 10, 15, 20, 60 and 180 minutes.
7. Aseptically transfer each sample after the elapsed time period to a saline filled McCartney bottle.
8. Vortex mix to remove any live cultures from the sample surface.
9. Dilute twice, in parallel, by a factor 1:100.
   9.1. Pipette 100 μl of solution from the neutralisation bottle (i.e. the first McCartney bottle) into McCartney bottles 1.1 and 1.2, as per Figure 3.8.
   9.2. Repeat dilution for bottles 2.1 and 2.2 after vortex mixing bottles 1.1 and 1.2.
10. Spread plate 100 μl of solution from both dilutions at each respective dilution level onto an agar plate.
    10.1. Pipette 100 μl onto each 90 mm agar plate.
    10.2. Spread the deposit evenly over entire agar surface using a sterile L-shaped spreader.
11. Repeat for each time period.
12. Incubate the agar plates.
    12.1. Bacterial test culture plates are to be incubated for 16 - 24 hrs. at 37°C.
    12.2. Fungal test culture plates are to be incubated for 48 hrs. at 37°C.

Stage Two: CFU Counts

13. After incubation all plates are inspected for growth and colony forming units quantified.
    13.1. OpenCFU, an open source colony counting software, was used in conjunction with verifying manual counts.
14. A Microsoft Excel template was developed to consolidate the test data and compute the geometric mean CFU/ml present at each respective time period[i]. The template coordinated data processing, graphing and detailed result analysis.
    14.1. Refer to the dry contact test data processing details which follow, for the sub-procedure and Microsoft Excel template.

[i]The geometric mean was used for averaging the quantified CFU/ml since colony forming units on an agar plate and, incidentally, within a broth follow a random distribution and therefore a Poisson distribution [188].

15. Apply linear regression modelling to the graphical data, in terms of an antimicrobial reduction rate (m_{ar}), which itself is expressed by Equation D.1. Where m_{ar} is the relative antimicrobial rate of a coating material compared to that of stainless steel's response (m_{ss}). The reduction rate of the test sample is given by m_{ts}. The antimicrobial rate has units of $\log_{10}$(CFU/ml)/min, from the use of a semi-log graph[ii]. A larger antimicrobial rate corresponds with a more antimicrobially active material, since the steeper the reduction gradient the faster the microbial reduction takes place.

$$m_{ar} = m_{ts} - m_{ss} \tag{D.1}$$

    15.1. The antimicrobial rate of the stainless steel samples, while not indicative of active antimicrobial ability from the metal, but rather was representative of system noise, which subsequently affects the antimicrobial rate. These noise factors include, but are not limited, to: plating stress, environmental conditions and volume loss during sample inoculation.

    15.2. The suitability of a regression model may be assessed by determining the coefficient of determination (R^2).

16. The antimicrobial rate (m_{ar}) was then used as a discriminating criterion for antimicrobial efficacy characterisation and later as part of the trend analysis against surface topographical properties.

    16.1. For trend analysis (Chapter 7), the average antimicrobial rate - neglecting any spurious microbial reduction effects and noise factors by subtracting the reduction rate observed for the neutral stainless steel control from this value - was compared to the roughness properties of the respective coatings.

Dry contact test data processing

The following methodology was devised for the analysis of quantified CFU counts as part of the dry contact antimicrobial susceptibility tests.

Table D.3 represents the Microsoft Excel data processing template devised. This includes the three dilutions (the first being the neutralisation stage). The average number of viable colony forming units was calculated per five micro-litres, corresponding with the volume of culture solution initially spread over the test sample surface, and per ml as a standard measure of microbial concentration. The dilution factors, plating volume and zero point reading are included. The zero point reading corresponds to a direct measure of the microbial concentration of 5 μls of culture solution.

[ii] The vertical axis representing the CFU/ml is presented in log form due to the scale and extent on antimicrobial reduction.

Table D.3: Microsoft Excel dry contact test data processing template for a single time period (30 sec).

Pathogen	30 Seconds											
Test Sample	1st Dilution		2nd Dilution				3rd Dilution				Average	Overall Average
	1/2000 (5µl)	CFU/5µl	1/100 (D1)			CFU/5µl	1/100 (D2)			CFU/5µl		
	D1	D1	D2.1	D2.2	$D2_{ave}$	$D2_{ave}$	D3.1	D3.2	$D3_{ave}$	$D3_{ave}$	CFU/5µl	CFU/ml
Test Sample 1												
Test Sample 2												
Test Sample 3												
Test Sample 4												
Test Sample 5												
Test Sample 6												
Test Sample 7												
Test Sample 8												
Test Sample 9												

The following steps and calculations are involved in the determination and interpretation of the resultant viable CFU/ml on each test sample surface after a given exposure time period.

Step 1 - Initial processing of results

1. Set up and define dilution factors

   1.1. Dilution ratio

$$\text{Dilution Ratio} = \frac{\text{Sampling Volume}}{\text{Diluent Volume} + \text{Sampling Volume}} \tag{D.2}$$

   1.2. Plating volume is the volume plated onto the agar plates for each dilution (100 μl).

   1.3. Dilution factor

$$\text{Dilution Factor} = \left(\frac{1}{\text{Plating Volume}} \times \frac{1}{\text{Dilution Ratio}}\right) \tag{D.3}$$

   1.4. Colony forming units per ml.

$$\frac{\text{CFU}}{\text{ml}} = \frac{\text{CFU}}{\text{plate}} \times \text{Dilution Factor} \tag{D.4}$$

2. Define and set up time periods (0.5, 5, 10, 15, 20, 60 and 180 minutes).

3. Define the zero point concentration.

4. Conduct test and populate the result table.

4.1. CFU quantification may be done by way of a manual count or using relevant image processing software (e.g. ImageJ, OpenCFU).

5. Compute the geometric mean CFU/ml.

5.1. When working with the geometric mean the handling of zero terms is important. In general zeros are ignored from calculations, yet if all values in a calculation are zero the geometric mean is set as zero.

5.2. The advantage of using the geometric mean, given by Equation D.5, is due to its handling of outliers. The geometric mean is seen to dampen out the response of outliers.

$$\text{Geometric mean} = 10^{\left(\frac{logx_1 + logx_2 + \cdots + logx_n}{n}\right)} \tag{D.5}$$

6. Flag any data discrepancies.

Step 2 - Data processing

Check, isolate and remove any data discrepancies, which may have been caused by minor contamination or experimental error.

Step 3 - Graphing and analysis

1. Plot sample efficacy trends against the test controls.

1.1. Include a semi-log graph to better represent microbial reduction trends.

2. Calculate the percent reduction (Red.%) for each respective time period with respect to the zero point concentration value.

3. Calculate the percentage reduction (Red.%) for each respective time period with respect to stainless steel's response.

4. Define each percent reduction in terms of log reduction, where:

1 log reduction = 90% reduction	No. of CFUs is 10 times smaller
2 log reduction = 99% reduction	No. of CFUs is 100 times smaller
3 log reduction = 99.9% reduction	No. of CFUs is 1000 times smaller
4 log reduction = 99.99% reduction	No. of CFUs is 10000 times smaller
5 log reduction = 99.999% reduction	No. of CFUs is 100000 times smaller
6 log reduction = 99.9999% reduction	No. of CFUs is 1000000 times smaller

5. Compute the average percentage reduction over all time periods for both the t=0 and stainless steel referenced calculations.

6. Using a linear regression analysis compute the gradient, which represents the microbial reduction rate (m), for the test sample (m_{ts}), the substrate control sample (m_{cs}) and the stainless steel control (m_{ss}).

Step 4 - Interpretation and material ranking

Ranking was based on three factors: firstly, the relative antimicrobial rate (mar); secondly, complete elimination and the respective time this was first achieved (within reason depending on result variance) and thirdly, the average percentage reduction after 15 min of direct exposure to the test pathogen.

Step 5 - Overall sample efficacy ranking

When test samples are tested against a number of pathogens an overall ranking may be beneficial. The ranking was based on each of the three ranking criteria as given in the order of priority.

Diffusion assay - Standard coatings and pathogens

Table D.4 and Table D.5 contain the test results for the diffusion assay of standard cold spray coatings against the standard pathogens.

Table D.4: Average zone of inhibition results from diffusion assays of standard coatings against standard pathogens.

Test sample	Test sample reference	Extent of inhibition [mm]				
		Gram-positive pathogens		Gram-negative pathogens		Yeast pathogen
		S. aureus (ATCC 25923)	*E. faecalis* (ATCC 29212)	*K. pneumoniae* (ATCC 13887)	*P. aeruginosa* (ATCC 27853)	*C. albicans* (ATCC 10231)
Copper coated 3D printed ABS	Cu(1)3DABS	0.35	2.05	0.00	0.13	0.00
Copper coated solid ABS	Cu(1)ABS	0.70	2.65	0.15	3.15	0.00
Copper coated PEEK	Cu(1)PEEK	1.10	2.55	0.30	1.50	0.00
Polished copper coated PEEK	Cu(1)PEEK (Polished)	0.55	3.90	0.25	2.65	0.00
Copper coated vertically oriented 3D printed ABS	Cu(1)VO3DABS	0.45	1.65	0.40	2.20	0.00
Copper-Aluminium-Alumina coated 3D printed ABS	Cu(2)3DABS	0.40	0.90	0.15	2.20	0.00
Copper-Aluminium-Alumina coated solid ABS	Cu(2)ABS	0.40	1.15	0.20	3.30	0.00
Zinc coated 3D printed ABS	Zn3DABS	4.25	1.15	0.75	3.20	0.00
Zinc coated solid ABS	ZnABS	3.70	1.2	0.75	2.65	0.00
Zinc coated PC	ZnPC	4.00	1.00	0.80	2.70	0.00
75 wt% copper - 25 wt% zinc coated 3D printed ABS	Cu(1)75Zn3DABS	3.95	1.00	0.80	4.25	0.00
50% w/w copper-zinc coated 3D printed ABS	Cu(1)50Zn3DABS	6.10	1.05	1.40	4.85	0.00
75 wt% zinc - 25 wt% copper coated 3D printed ABS	Zn75Cu(1)3DABS	4.00	0.70	0.40	3.00	0.00
Copper coated copper	Cu(1)-Cu	2.30	3.35	2.40	4.10	0.00
Pure copper	Pure Copper	0.25	1.05	0.25	0.40	0.00
Zinc coated/galvanised steel	Galvanised Steel	5.75	3.85	1.35	4.45	0.00
Stainless steel	Stainless Steel	0.00	1.25	0.60	0.00	0.00
3D printed ABS	3DABS	0.00	1.75	0.45	0.00	0.00
Vertically oriented 3D printed ABS	VO3DABS	0.00	2.50	0.35	1.00	0.00
Solid ABS	ABS	0.00	0.00	0.00	0.90	0.00
Solid polycarbonate	PC	0.00	0.00	0.40	0.00	0.00
Solid polyetheretherketone	PEEK	0.00	0.70	0.00	1.20	0.00
Ciprofloxacin	PCD	13.65	15.8	18.40	13.65	/
Nystatin		/	/	/	/	5.30

Table D.5: Diffusion assay efficacy ranking per culture and pathogen type - standard coatings.

Rank	*S. aureus* (ATCC 25923)		*E. faecalis* (ATCC 29212)		Gram-positive pathogens	*K. pneumoniae* (ATCC 13887)		*P. aeruginosa* (ATCC 27853)		Gram-negative pathogens	*C. albicans* (ATCC 10231)	
	Test Sample	ZOI [mm]	Test Sample	ZOI [mm]		Test Sample	ZOI [mm]	Test Sample	ZOI [mm]		Test Sample	ZOI [mm]
1	PCD	13.65	PCD	15.80	PCD	PCD	18.40	PCD	13.65	PCD	PCD	5.3
2	Cu(1)50Zn3DABS	6.10	Cu(1)PEEK (Polished)	3.90	Galvanised Steel	Cu(1)-Cu	2.40	Cu(1)50Zn3DABS	4.85	Cu(1)-Cu	Cu(1)3DABS	0
3	Galvanised Steel	5.75	Galvanised Steel	3.85	Cu(1)50Zn3DABS	Cu(1)50Zn3DABS	1.40	Galvanised Steel	4.45	Cu(1)50Zn3DABS	Cu(1)ABS	0
4	Zn3DABS	4.25	Cu(1)-Cu	3.35	Cu(1)-Cu	Galvanised Steel	1.35	Cu(1)75Zn3DABS	4.25	Galvanised Steel	Cu(1)PEEK	0
5	ZnPC	4.00	Cu(1)ABS	2.65	Zn3DABS	ZnPC	0.80	Cu(1)-Cu	4.10	Cu(1)75Zn3DABS	Cu(1)PEEK (Polished)	0
6	Zn75Cu(1)3DABS	4.00	Cu(1)PEEK	2.55	ZnPC	Cu(1)75Zn3DABS	0.80	Cu(2)ABS	3.30	Zn3DABS	Cu(1)VO3DABS	0
7	Cu(1)75Zn3DABS	3.95	VO3DABS	2.50	Cu(1)75Zn3DABS	Zn3DABS	0.75	Zn3DABS	3.20	Cu(2)ABS	Cu(2)3DABS	0
8	ZnABS	3.70	Cu(1)3DABS	2.05	ZnABS	ZnABS	0.75	Cu(1)ABS	3.15	ZnPC	Cu(2)ABS	0
9	Cu(1)-Cu	2.30	3DABS	1.75	Zn75Cu(1)3DABS	Stainless Steel	0.60	Zn75Cu(1)3DABS	3.00	ZnABS	Zn3DABS	0
10	Cu(1)PEEK	1.10	Cu(1)VO3DABS	1.65	Cu(1)PEEK (Polished)	3DABS	0.45	ZnPC	2.70	Zn75Cu(1)3DABS	ZnABS	0
11	Cu(1)ABS	0.70	Stainless Steel	1.25	Cu(1)PEEK	Cu(1)VO3DABS	0.40	Cu(1)PEEK (Polished)	2.65	Cu(1)ABS	ZnPC	0
12	Cu(1)PEEK (Polished)	0.55	ZnABS	1.20	Cu(1)ABS	Zn75Cu(1)3DABS	0.40	ZnABS	2.65	Cu(1)PEEK (Polished)	Cu(1)75Zn3DABS	0
13	Cu(1)VO3DABS	0.45	Cu(2)ABS	1.15	VO3DABS	PC	0.40	Cu(1)VO3DABS	2.20	Cu(1)VO3DABS	Cu(1)50Zn3DABS	0
14	Cu(2)3DABS	0.40	Zn3DABS	1.15	Cu(1)3DABS	VO3DABS	0.35	Cu(2)3DABS	2.20	Cu(2)3DABS	Zn75Cu(1)3DABS	0
15	Cu(2)ABS	0.40	Cu(1)50Zn3DABS	1.05	Cu(1)VO3DABS	Cu(1)PEEK	0.30	Cu(1)PEEK	1.50	Cu(1)PEEK	Cu(1)-Cu	0
16	Cu(1)3DABS	0.35	Pure Copper	1.05	3DABS	Cu(1)PEEK (Polished)	0.25	PEEK	1.20	VO3DABS	Pure Copper	0
17	Pure Copper	0.25	ZnPC	1.00	Cu(2)ABS	Pure Copper	0.25	VO3DABS	1.00	PEEK	Galvanised Steel	0
18	Stainless Steel	0.00	Cu(1)75Zn3DABS	1.00	Cu(2)3DABS	Cu(2)ABS	0.20	ABS	0.90	ABS	Stainless Steel	0
19	3DABS	0.00	Cu(2)3DABS	0.90	Pure Copper	Cu(1)ABS	0.15	Pure Copper	0.40	Pure Copper	3DABS	0
20	VO3DABS	0.00	Zn75Cu(1)3DABS	0.70	Stainless Steel	Cu(2)3DABS	0.15	Cu(1)3DABS	0.13	Stainless Steel	VO3DABS	0
21	ABS	0.00	PEEK	0.70	PEEK	Cu(1)3DABS	0.00	Stainless Steel	0.00	3DABS	ABS	0
22	PC	0.00	ABS	0.00	ABS	ABS	0.00	3DABS	0.00	PC	PC	0
23	PEEK	0.00	PC	0.00	PC	PEEK	0.00	PC	0.00	Cu(1)3DABS	PEEK	0

Dry touch-contact test - Standard coatings and pathogens

The following tables (Table D.6, Table D.7 and Table D.8) contain the colony forming unit counts (exponential form) for standard cold spray coatings and their respective controls against the three standard pathogens (*Staphylococcus aureus*, *Pseudomonas aeruginosa* and *Candida albicans*).

Table D.6: Dry contact test results of standard coatings against *Staphylococcus aureus* (ATCC 25923).

CFU/ml

Test sample	Contact period (minutes)								Pearson coefficient (R)	Coefficient of determination (R^2)
	0	0.5	5	10	15	20	60	180		
Copper coated 3D printed ABS	1.17E+08	1.25E+07	3.67E+07	4.00E+04	2.00E+04	0.00E+00	0.00E+00	0.00E+00	-0.652	0.425
Copper coated solid ABS	1.17E+08	1.11E+07	1.18E+06	4.00E+04	6.00E+04	0.00E+00	0.00E+00	0.00E+00	-0.568	0.323
Copper coated PEEK	1.17E+08	1.54E+07	1.94E+06	4.47E+05	7.27E+06	0.00E+00	0.00E+00	0.00E+00	-0.573	0.328
Polished copper coated PEEK	1.17E+08	8.54E+07	1.93E+07	8.00E+05	1.00E+05	4.20E+05	0.00E+00	0.00E+00	-0.552	0.305
Copper coated vertically oriented 3D printed ABS	1.17E+08	1.06E+07	5.45E+06	8.21E+06	0.00E+00	0.00E+00	0.00E+00	0.00E+00	-0.586	0.343
Copper-Aluminium-Alumina coated 3D printed ABS	1.17E+08	1.00E+08	2.68E+07	3.30E+06	4.40E+05	6.00E+06	4.00E+04	0.00E+00	-0.427	0.182
Copper-Aluminium-Alumina coated solid ABS	1.17E+08	3.04E+07	2.22E+07	4.60E+06	1.20E+06	1.94E+06	3.40E+05	2.00E+04	-0.362	0.131
Zinc coated 3D printed ABS	1.17E+08	2.34E+07	2.12E+07	8.64E+06	4.85E+06	4.88E+06	1.46E+06	2.92E+06	-0.343	0.118
Zinc coated solid ABS	1.17E+08	6.90E+07	6.32E+06	5.66E+06	9.47E+06	1.19E+07	5.65E+06	2.86E+06	-0.385	0.148
Zinc coated PC	1.17E+08	5.18E+07	4.70E+07	8.90E+06	1.10E+07	6.10E+06	1.00E+06	4.91E+06	-0.433	0.187
75 wt% copper - 25 wt% zinc coated 3D printed ABS	1.17E+08	1.81E+07	1.81E+07	3.61E+06	2.47E+06	2.60E+06	1.25E+06	4.00E+05	-0.327	0.107
50% w/w copper-zinc coated 3D printed ABS	1.17E+08	1.85E+07	1.29E+07	2.66E+06	1.13E+06	5.94E+06	5.40E+05	1.60E+05	-0.321	0.103
75 wt% zinc - 25 wt% copper coated 3D printed ABS	1.17E+08	1.90E+07	9.25E+06	8.41E+06	2.88E+06	7.61E+06	3.67E+06	1.84E+06	-0.315	0.099
Copper coated copper	1.17E+08	1.03E+08	0.00E+00	0.00E+00	0.00E+00	0.00E+00	0.00E+00	0.00E+00	-1.000	1.000
Pure copper	1.17E+08	1.95E+07	2.68E+07	3.79E+07	2.32E+07	3.77E+07	1.13E+07	3.10E+06	-0.474	0.225
Zinc coated/galvanised steel	1.17E+08	2.28E+07	3.39E+07	1.60E+07	2.27E+07	4.00E+06	1.29E+07	7.79E+06	-0.362	0.131
Stainless steel	1.17E+08	2.24E+07	2.80E+07	3.97E+07	1.81E+07	7.56E+07	3.44E+07	2.90E+07	-0.249	0.062
3D printed ABS	1.17E+08	2.59E+07	3.69E+07	2.52E+07	1.31E+07	4.02E+07	8.94E+06	3.31E+06	-0.469	0.220
Vertically oriented 3D printed ABS	1.17E+08	4.40E+07	1.70E+07	2.27E+07	1.49E+07	5.95E+06	1.14E+07	5.84E+06	-0.392	0.154
Solid ABS	1.17E+08	8.24E+07	5.14E+07	5.83E+07	7.20E+07	4.10E+07	1.55E+07	4.10E+07	-0.476	0.227
Solid polycarbonate	1.17E+08	1.89E+07	4.20E+07	1.50E+07	5.28E+06	1.67E+07	1.05E+07	1.50E+07	-0.293	0.086
Solid polyetheretherketone	1.17E+08	5.66E+07	6.75E+07	4.80E+07	4.58E+07	9.09E+07	2.76E+07	5.37E+07	-0.308	0.095

Table D.7: Dry contact test results of standard coatings against *Pseudomonas aeruginosa* (ATCC 27853).

CFU/ml

Test sample	Contact period (minutes)								Pearson coefficient (R)	Coefficient of determination (R^2)
	0	0.5	5	10	15	20	60	180		
Copper coated 3D printed ABS	1.38E+08	2.53E+08	1.15E+07	0.00E+00	0.00E+00	0.00E+00	0.00E+00	0.00E+00	-0.825	0.681
Copper coated solid ABS	1.38E+08	1.22E+07	5.40E+05	0.00E+00	0.00E+00	0.00E+00	0.00E+00	0.00E+00	-0.613	0.376
Copper coated PEEK	1.38E+08	1.98E+07	1.18E+07	0.00E+00	0.00E+00	0.00E+00	0.00E+00	0.00E+00	-0.655	0.429
Polished copper coated PEEK	1.38E+08	3.55E+07	1.03E+07	0.00E+00	0.00E+00	0.00E+00	0.00E+00	0.00E+00	-0.728	0.530
Copper coated vertically oriented 3D printed ABS	1.38E+08	3.58E+07	1.46E+07	4.00E+06	0.00E+00	0.00E+00	0.00E+00	0.00E+00	-0.710	0.504
Copper-Aluminium-Alumina coated 3D printed ABS	1.38E+08	1.67E+07	7.83E+06	0.00E+00	0.00E+00	4.00E+04	0.00E+00	0.00E+00	-0.638	0.407
Copper-Aluminium-Alumina coated solid ABS	1.38E+08	2.34E+07	7.28E+06	0.00E+00	0.00E+00	0.00E+00	0.00E+00	0.00E+00	-0.670	0.449
Zinc coated 3D printed ABS	1.38E+08	2.53E+08	2.33E+08	1.94E+07	3.68E+06	3.06E+06	9.40E+05	1.00E+05	-0.466	0.217
Zinc coated solid ABS	1.38E+08	1.30E+07	1.22E+07	1.58E+06	6.00E+05	1.80E+05	6.00E+04	0.00E+00	-0.289	0.084
Zinc coated PC	1.38E+08	1.08E+07	9.61E+06	6.28E+06	2.00E+04	0.00E+00	0.00E+00	0.00E+00	-0.579	0.335
75 wt% copper - 25 wt% zinc coated 3D printed ABS	1.38E+08	3.40E+08	6.60E+07	1.66E+07	1.38E+06	1.60E+06	4.00E+04	2.00E+04	-0.387	0.150
50% w/w copper-zinc coated 3D printed ABS	1.38E+08	9.64E+07	1.41E+08	3.30E+06	1.00E+05	2.20E+05	6.00E+04	0.00E+00	-0.461	0.213
75 wt% zinc - 25 wt% copper coated 3D printed ABS	1.38E+08	2.67E+08	1.20E+08	1.60E+07	2.70E+06	0.00E+00	2.80E+05	0.00E+00	-0.445	0.198
Copper coated copper	1.38E+08	4.28E+07	0.00E+00	0.00E+00	0.00E+00	0.00E+00	0.00E+00	0.00E+00	-0.797	0.635
Pure copper	1.38E+08	1.78E+08	2.20E+07	1.67E+08	5.40E+07	1.12E+07	2.42E+06	6.00E+04	-0.540	0.292
Zinc coated/galvanised steel	1.38E+08	2.28E+07	2.28E+07	8.03E+06	1.20E+07	3.41E+06	1.60E+05	0.00E+00	-0.357	0.127
Stainless steel	1.38E+08	4.79E+08	2.13E+08	1.49E+08	1.70E+08	1.30E+07	4.52E+06	3.08E+06	-0.534	0.285
3D printed ABS	1.38E+08	1.07E+07	9.34E+06	1.70E+07	1.48E+07	6.20E+05	4.40E+05	1.40E+05	-0.322	0.104
Vertically oriented 3D printed ABS	1.38E+08	8.94E+07	1.71E+07	3.26E+07	5.29E+06	1.46E+07	1.46E+06	2.00E+04	-0.463	0.214
Solid ABS	1.38E+08	1.85E+07	5.30E+06	1.30E+07	8.06E+06	4.10E+06	1.68E+06	2.36E+06	-0.304	0.092
Solid polycarbonate	1.38E+08	3.36E+07	1.71E+07	3.87E+07	7.98E+07	1.76E+07	1.12E+06	5.20E+05	-0.482	0.232
Solid polyetheretherketone	1.38E+08	1.26E+07	1.69E+07	1.30E+07	8.06E+06	6.88E+06	3.54E+06	9.60E+05	-0.325	0.106

Table D.8: Dry contact test results of standard coatings against *Candida albicans* (ATCC 10231).

Test sample	CFU/ml Contact period (minutes) 0	0.5	5	10	15	20	60	180	Pearson coefficient (R)	Coefficient of determination (R^2)
Copper coated 3D printed ABS	1.81E+06	1.23E+06	5.80E+05	0.00E+00	0.00E+00	0.00E+00	0.00E+00	0.00E+00	-0.957	0.916
Copper coated solid ABS	1.81E+06	1.00E+06	7.20E+05	0.00E+00	0.00E+00	0.00E+00	0.00E+00	2.00E+04	-0.916	0.839
Copper coated PEEK	1.81E+06	1.48E+06	8.60E+05	0.00E+00	0.00E+00	0.00E+00	0.00E+00	0.00E+00	-0.992	0.984
Polished copper coated PEEK	1.81E+06	1.87E+06	2.00E+06	0.00E+00	0.00E+00	0.00E+00	0.00E+00	0.00E+00	-0.834	0.696
Copper coated vertically oriented 3D printed ABS	1.81E+06	1.08E+06	1.13E+06	0.00E+00	1.80E+05	0.00E+00	0.00E+00	0.00E+00	-0.875	0.766
Copper-Aluminium-Alumina coated 3D printed ABS	1.81E+06	1.80E+06	1.89E+06	2.00E+06	0.00E+00	0.00E+00	0.00E+00	6.00E+04	-0.713	0.508
Copper-Aluminium-Alumina coated solid ABS	1.81E+06	1.25E+06	3.12E+06	1.23E+06	0.00E+00	0.00E+00	0.00E+00	0.00E+00	-0.576	0.332
Zinc coated 3D printed ABS	1.81E+06	1.17E+06	8.20E+05	4.00E+04	6.00E+04	0.00E+00	0.00E+00	0.00E+00	-0.891	0.794
Zinc coated solid ABS	1.81E+06	1.72E+06	6.40E+05	1.20E+05	2.00E+04	0.00E+00	0.00E+00	0.00E+00	-0.902	0.814
Zinc coated PC	1.81E+06	1.77E+06	2.32E+06	1.00E+05	0.00E+00	0.00E+00	0.00E+00	0.00E+00	-0.841	0.707
75 wt% copper - 25 wt% zinc coated 3D printed ABS	1.81E+06	1.15E+06	7.20E+05	0.00E+00	0.00E+00	0.00E+00	6.00E+04	0.00E+00	-0.949	0.901
50% w/w copper-zinc coated 3D printed ABS	1.81E+06	8.00E+05	8.72E+05	0.00E+00	0.00E+00	0.00E+00	0.00E+00	0.00E+00	-0.843	0.711
75 wt% zinc - 25 wt% copper coated 3D printed ABS	1.81E+06	1.44E+06	1.12E+06	0.00E+00	0.00E+00	2.00E+04	0.00E+00	0.00E+00	-0.972	0.945
Copper coated copper	1.81E+06	8.80E+05	3.00E+05	0.00E+00	0.00E+00	2.00E+04	0.00E+00	0.00E+00	-0.866	0.750
Pure copper	1.81E+06	1.54E+06	9.80E+05	2.60E+05	3.00E+05	/	0.00E+00	0.00E+00	-0.719	0.517
Zinc coated/galvanised steel	1.81E+06	1.47E+06	9.17E+05	1.10E+06	2.60E+05	1.20E+05	/	8.00E+06	0.945	0.893
Stainless steel	1.81E+06	1.02E+06	4.40E+05	2.40E+05	3.40E+05	1.00E+05	/	0.00E+00	-0.470	0.221
3D printed ABS	1.81E+06	6.40E+05	5.00E+05	1.52E+06	2.20E+05	5.60E+05	0.00E+00	2.00E+04	-0.542	0.294
Vertically oriented 3D printed ABS	1.81E+06	2.32E+06	1.15E+06	7.48E+05	4.40E+05	1.40E+05	2.00E+04	2.00E+04	-0.575	0.331
Solid ABS	1.81E+06	9.38E+05	1.28E+06	1.10E+06	3.00E+05	2.40E+05	2.00E+04	0.00E+00	-0.624	0.389
Solid polycarbonate	1.81E+06	1.15E+06	1.66E+06	9.59E+05	1.06E+06	9.59E+05	1.04E+06	2.00E+04	-0.845	0.714
Solid polyetheretherketone	1.81E+06	1.77E+06	1.54E+06	5.80E+05	1.08E+06	1.12E+06	4.00E+04	0.00E+00	-0.752	0.566

Diffusion assay - Silver additives

Table D.9 contains the diffusive assay results for cold spray coatings containing a 5 wt% silver additive when tested against the standard pathogens. Table D.10 provides a ranking of all test samples per culture and pathogen type for the silver additive test samples.

Table D.9: Average zone of inhibition results from diffusion assays of special, silver additive, coatings against standard pathogens.

Test sample	Test sample reference	Average Zone of Inhibition [mm]				
		S. aureus	*E. faecalis*	*P. aeruginosa*	*K. pneumoniae*	*C. albicans*
5 wt% silver - 95 wt% copper coated copper	Ag5Cu(1)-Cu	8.1	7.8	2.5	0.6	0
5 wt% silver - 95 wt% copper coated solid ABS	Ag5Cu(1)ABS	6	5.7	1.4	0	0
5 wt% silver - 95 wt% copper coated vertically oriented 3D printed ABS	Ag5Cu(1)VO3DABS	5.1	4.7	1.1	0	0
5 wt% silver - 95 wt% copper coated 3D printed ABS	Ag5Cu(1)3DABS	4.6	4	0.9	0	0
5 wt% silver - 47.5% w/w copper-zinc coated 3D printed ABS	Ag5Cu(1)Zn3DABS	0.9	1	1.2	0.5	0
5 wt% silver - 95 wt% zinc coated 3D printed ABS	Ag5Zn3DABS	1.2	0.3	0.9	1.2	0
Pure copper	Pure Copper	4.3	3.7	1.1	0	0
Solid ABS	ABS	0	0	0	0	0
Vertically oriented 3D printed ABS	VO3DABS	0	0	0	0	0
3D printed ABS	3DABS	0	0.8	0	0	0
Stainless steel	Stainless Steel	0	0	0	0	0
Ciprofloxacin	PCD	14.7	14	17	17.5	/
Nystatin		/	/	/	/	3.9

Table D.10: Efficacy ranking of culture and pathogen type for silver additive diffusion assay.

Rank	*S. aureus* (ATCC 25923)		*E. faecalis* (ATCC 29212)		Gram-positive pathogens	*K. pneumoniae* (ATCC 13887)		*P. aeruginosa* (ATCC 27853)		Gram-negative pathogens	*C. albicans* (ATCC 10231)	
	Test Sample	ZOI [mm]	Test Sample	ZOI [mm]		Test Sample	ZOI [mm]	Test Sample	ZOI [mm]		Test Sample	ZOI [mm]
1	PCD	14.70	PCD	14.00	PCD	PCD	17.50	PCD	17.00	PCD	PCD	3.9
2	Ag5Cu(1)-Cu	8.10	Ag5Cu(1)-Cu	7.80	Ag5Cu(1)-Cu	Ag5Zn3DABS	1.20	Ag5Cu(1)-Cu	2.50	Ag5Cu(1)-Cu	Ag5Cu(1)-Cu	0
3	Ag5Cu(1)ABS	6.00	Ag5Cu(1)ABS	5.70	Ag5Cu(1)ABS	Ag5Cu(1)-Cu	0.60	Ag5Cu(1)ABS	1.40	Ag5Zn3DABS	Ag5Cu(1)ABS	0
4	Ag5Cu(1)VO3DABS	5.10	Ag5Cu(1)VO3DABS	4.70	Ag5Cu(1)VO3DABS	Ag5Cu(1)Zn3DABS	0.50	Ag5Cu(1)Zn3DABS	1.20	Ag5Cu(1)Zn3DABS	Ag5Cu(1)VO3DABS	0
5	Ag5Cu(1)3DABS	4.60	Ag5Cu(1)3DABS	4.00	Ag5Cu(1)3DABS	Ag5Cu(1)ABS	0.00	Ag5Cu(1)VO3DABS	1.10	Ag5Cu(1)ABS	Ag5Cu(1)3DABS	0
6	Pure Copper	4.30	Pure Copper	3.70	Pure Copper	Ag5Cu(1)VO3DABS	0.00	Pure Copper	1.10	Ag5Cu(1)VO3DABS	Ag5Cu(1)Zn3DABS	0
7	Ag5Zn3DABS	1.20	Ag5Cu(1)Zn3DABS	1.00	Ag5Cu(1)Zn3DABS	Ag5Cu(1)3DABS	0.00	Ag5Cu(1)3DABS	0.90	Pure Copper	Ag5Zn3DABS	0
8	Ag5Cu(1)Zn3DABS	0.90	3DABS	0.80	Ag5Zn3DABS	Pure Copper	0.00	Ag5Zn3DABS	0.90	Ag5Cu(1)3DABS	Pure Copper	0
9	ABS	0.00	Ag5Zn3DABS	0.30	3DABS	ABS	0.00	ABS	0.00	ABS	ABS	0
10	VO3DABS	0.00	ABS	0.00	ABS	VO3DABS	0.00	VO3DABS	0.00	VO3DABS	VO3DABS	0
11	3DABS	0.00	VO3DABS	0.00	VO3DABS	3DABS	0.00	3DABS	0.00	3DABS	3DABS	0
12	Stainless Steel	0.00	Stainless Steel	0.00	Stainless Steel	Stainless Steel	0.00	Stainless Steel	0.00	Stainless Steel	Stainless Steel	0

Dry touch-contact test - Silver additives

The dry contact test results for the special coatings with a 5 wt% silver additive against the three standard pathogens are tabulated below in Table D.11 for *S. aureus*, Table D.12 for *P. aeruginosa* and Table D.13 for *C. albicans*.

Table D.11: Dry contact test results of special coatings against *Staphylococcus aureus* (ATCC 25923).

CFU/ml

Test sample	Contact period (minutes)									Pearson coefficient (R)	Coefficient of determination (R^2)
	0	0.5	2.5	5	10	15	20	60	180		
5 wt% silver - 95 wt% copper coated copper	2.33E+07	1.17E+07	6.39E+06	0.00E+00	0.00E+00	0.00E+00	0.00E+00	0.00E+00	0.00E+00	-0.906	0.821
5 wt% silver - 95 wt% copper coated solid ABS	2.33E+07	1.45E+07	1.17E+07	9.38E+06	2.00E+04	4.00E+04	8.00E+04	0.00E+00	0.00E+00	-0.611	0.373
5 wt% silver - 95 wt% copper coated vertically oriented 3D printed ABS	2.33E+07	1.18E+07	6.63E+06	3.73E+06	8.00E+04	2.00E+04	0.00E+00	0.00E+00	0.00E+00	-0.763	0.582
5 wt% silver - 95 wt% copper coated 3D printed ABS	2.33E+07	8.65E+06	1.20E+07	1.65E+07	1.08E+06	0.00E+00	2.00E+04	0.00E+00	0.00E+00	-0.595	0.354
5 wt% silver - 47.5% w/w copper-zinc coated 3D printed ABS	2.33E+07	1.53E+07	1.19E+07	9.23E+06	1.07E+07	1.96E+06	7.60E+05	8.80E+05	1.00E+05	-0.564	0.318
5 wt% silver - 95 wt% zinc coated 3D printed ABS	2.33E+07	1.69E+07	1.27E+07	9.49E+06	1.57E+06	1.30E+06	6.60E+05	3.00E+05	4.00E+04	-0.495	0.245
Pure copper	2.33E+07	1.37E+07	1.44E+07	1.52E+07	2.13E+07	1.45E+07	1.06E+07	1.43E+06	3.80E+05	-0.778	0.605
Stainless steel	2.33E+07	1.81E+07	1.89E+07	1.97E+07	2.11E+07	1.77E+07	7.12E+06	1.33E+07	4.71E+06	-0.765	0.585
3D printed ABS	2.33E+07	1.35E+07	9.64E+06	6.88E+06	1.11E+07	1.62E+07	8.91E+06	5.17E+06	7.85E+06	-0.390	0.152
Vertically oriented 3D printed ABS	2.33E+07	8.90E+06	9.31E+06	9.75E+06	1.07E+07	1.08E+07	1.97E+07	9.25E+06	1.46E+07	0.056	0.003
Solid ABS	2.33E+07	1.61E+07	1.32E+07	1.08E+07	1.59E+07	1.15E+07	1.18E+07	9.01E+06	1.28E+07	-0.276	0.076

Table D.12: Dry contact test results of special coatings against *Pseudomonas aeruginosa* (ATCC 27853).

CFU/ml

Test sample	Contact period (minutes)									Pearson coefficient (R)	Coefficient of determination (R^2)
	0	0.5	2.5	5	10	15	20	60	180		
5 wt% silver - 95 wt% copper coated copper	2.30E+07	1.17E+07	4.02E+06	0.00E+00	0.00E+00	0.00E+00	0.00E+00	0.00E+00	0.00E+00	-0.892	0.796
5 wt% silver - 95 wt% copper coated solid ABS	2.30E+07	2.50E+07	2.00E+07	1.60E+07	0.00E+00	8.00E+04	0.00E+00	0.00E+00	0.00E+00	-0.925	0.856
5 wt% silver - 95 wt% copper coated vertically oriented 3D printed ABS	2.30E+07	1.17E+07	1.04E+07	9.20E+06	0.00E+00	0.00E+00	0.00E+00	0.00E+00	0.00E+00	-0.878	0.771
5 wt% silver - 95 wt% copper coated 3D printed ABS	2.30E+07	1.11E+07	7.18E+06	4.63E+06	0.00E+00	0.00E+00	0.00E+00	0.00E+00	0.00E+00	-0.834	0.696
5 wt% silver - 47.5% w/w copper-zinc coated 3D printed ABS	2.30E+07	1.58E+07	1.60E+07	1.61E+07	1.80E+05	1.40E+05	2.60E+05	0.00E+00	2.00E+04	-0.492	0.242
5 wt% silver - 95 wt% zinc coated 3D printed ABS	2.30E+07	1.39E+07	1.04E+07	7.75E+06	3.40E+05	1.40E+05	3.80E+05	4.00E+04	0.00E+00	-0.451	0.203
Pure copper	2.30E+07	1.75E+07	1.69E+07	1.63E+07	2.07E+07	1.06E+07	9.58E+06	2.80E+05	1.00E+05	-0.779	0.607
Stainless steel	2.30E+07	1.01E+07	1.09E+07	1.18E+07	9.24E+06	1.06E+06	5.34E+06	1.28E+06	1.20E+06	-0.548	0.300
3D printed ABS	2.30E+07	1.70E+07	1.29E+07	9.82E+06	6.32E+06	1.84E+07	2.14E+06	1.32E+06	1.02E+06	-0.596	0.355
Vertically oriented 3D printed ABS	2.30E+07	1.88E+07	2.20E+07	2.57E+07	1.16E+07	2.24E+07	1.78E+07	2.28E+06	8.00E+05	-0.801	0.642
Solid ABS	2.30E+07	9.72E+06	7.87E+06	6.37E+06	7.47E+06	1.73E+07	7.16E+06	1.80E+06	1.12E+06	-0.556	0.309

Table D.13: Dry contact test results of special coatings against *Candida albicans* (ATCC 10231).

CFU/ml

Test sample	Contact period (minutes)									Pearson coefficient (R)	Coefficient of determination (R^2)
	0	0.5	2.5	5	10	15	20	60	180		
5 wt% silver - 95 wt% copper coated copper	4.61E+06	3.13E+06	4.41E+06	6.21E+06	7.27E+04	0.00E+00	7.27E+04	7.27E+04	0.00E+00	-0.472	0.223
5 wt% silver - 95 wt% copper coated solid ABS	4.61E+06	4.13E+06	3.12E+06	2.36E+06	0.00E+00	0.00E+00	0.00E+00	0.00E+00	0.00E+00	-0.996	0.992
5 wt% silver - 95 wt% copper coated vertically oriented 3D printed ABS	4.61E+06	3.31E+06	4.06E+06	4.99E+06	2.65E+06	1.16E+06	0.00E+00	0.00E+00	0.00E+00	-0.904	0.817
5 wt% silver - 95 wt% copper coated 3D printed ABS	4.61E+06	5.54E+06	5.12E+06	4.74E+06	3.19E+06	0.00E+00	0.00E+00	0.00E+00	0.00E+00	-0.929	0.863
5 wt% silver - 47.5% w/w copper-zinc coated 3D printed ABS	4.61E+06	2.98E+06	4.10E+06	5.63E+06	3.53E+06	0.00E+00	0.00E+00	0.00E+00	0.00E+00	-0.691	0.477
5 wt% silver - 95 wt% zinc coated 3D printed ABS	4.61E+06	3.60E+06	3.54E+06	3.49E+06	2.09E+06	7.27E+04	0.00E+00	0.00E+00	0.00E+00	-0.968	0.937
Pure copper	4.61E+06	3.35E+06	3.05E+06	2.77E+06	3.51E+06	3.53E+06	3.64E+04	5.45E+05	0.00E+00	-0.688	0.473
Stainless steel	4.61E+06	3.45E+06	4.30E+06	5.37E+06	4.84E+06	1.96E+06	3.76E+06	2.57E+06	1.45E+05	-0.829	0.687
3D printed ABS	4.61E+06	3.04E+06	3.98E+06	5.22E+06	2.75E+06	3.02E+06	1.02E+06	5.82E+05	7.27E+04	-0.727	0.529
Vertically oriented 3D printed ABS	4.61E+06	2.80E+06	2.92E+06	3.05E+06	2.22E+06	3.06E+06	7.18E+06	6.91E+05	7.27E+04	-0.593	0.352
Solid ABS	4.61E+06	5.23E+06	3.32E+06	2.11E+06	3.88E+06	2.89E+06	2.62E+06	8.91E+05	1.45E+05	-0.78	0.608

Dry touch-contact test - Resistant pathogens

The results for the dry contact tests for selected coatings against the resistant pathogens are given in the following tables: Table D.14 for those tested against GMRSA, Table D.15 for those against the reference *P. aeruginosa* strain and Table D.16 for those against the clinically resistant *C. albicans* strain.

Table D.14: Dry contact test results against Gentamicin-methicillin-resistant *S. aureus* (GMRSA) (ATCC 33592).

CFU/ml

Test sample	Contact period (minutes)									Pearson coefficient (R)	Coefficient of determination (R^2)
	0	0.5	2.5	5	10	15	20	60	180		
5 wt% silver - 95 wt% copper coated copper	2.60E+07	2.73E+06	1.37E+06	0.00E+00	0.00E+00	0.00E+00	0.00E+00	0.00E+00	0.00E+00	-0.657	0.432
50% w/w copper-zinc coated 3D printed ABS	2.60E+07	7.36E+06	3.88E+06	2.05E+06	1.76E+06	2.40E+05	2.40E+05	3.60E+05	3.00E+05	-0.321	0.103
Copper coated copper	2.60E+07	3.83E+06	4.79E+05	6.00E+04	0.00E+00	0.00E+00	0.00E+00	0.00E+00	0.00E+00	-0.576	0.332
Copper coated solid ABS	2.60E+07	3.38E+06	2.38E+06	1.68E+06	0.00E+00	0.00E+00	0.00E+00	0.00E+00	0.00E+00	-0.588	0.346
Copper coated 3D printed ABS	2.60E+07	2.66E+06	1.87E+06	1.31E+06	0.00E+00	0.00E+00	0.00E+00	0.00E+00	0.00E+00	-0.567	0.321
Pure copper	2.60E+07	3.80E+06	5.31E+06	7.43E+06	3.76E+06	5.15E+06	2.62E+06	2.34E+06	2.42E+06	-0.321	0.103
Stainless steel	2.60E+07	6.91E+06	6.61E+06	6.33E+06	7.71E+06	5.23E+06	4.10E+06	4.46E+06	4.31E+06	-0.311	0.097
3D printed ABS	2.60E+07	7.00E+06	7.31E+06	7.63E+06	3.57E+06	4.03E+06	4.68E+06	4.67E+06	3.70E+06	-0.314	0.099
Solid ABS	2.60E+07	4.91E+06	4.96E+06	5.02E+06	7.96E+06	5.43E+06	3.22E+06	1.90E+06	1.30E+06	-0.390	0.152

Table D.15: Dry contact test results against reference *P. aeruginosa* (RPA)(DSM 46316).

CFU/ml

Test sample	Contact period (minutes)									Pearson coefficient (R)	Coefficient of determination (R^2)
	0	0.5	2.5	5	10	15	20	60	180		
5 wt% silver - 95 wt% copper coated copper	7.73E+07	1.92E+07	9.60E+06	0.00E+00	0.00E+00	0.00E+00	0.00E+00	0.00E+00	0.00E+00	-0.754	0.568516
50% w/w copper-zinc coated 3D printed ABS	7.73E+07	1.78E+07	1.90E+07	2.03E+07	4.06E+06	9.13E+06	3.51E+06	8.44E+06	6.80E+05	-0.382	0.145924
Copper coated copper	7.73E+07	2.71E+07	1.36E+07	0.00E+00	0.00E+00	0.00E+00	0.00E+00	0.00E+00	0.00E+00	-0.819	0.670761
Copper coated solid ABS	7.73E+07	1.84E+07	7.96E+06	3.44E+06	0.00E+00	2.00E+04	2.00E+04	6.00E+04	0.00E+00	-0.292	0.085264
Copper coated 3D printed ABS	7.73E+07	3.69E+07	9.64E+06	2.52E+06	6.60E+05	0.00E+00	2.00E+04	6.00E+04	4.00E+04	-0.328	0.107584
Pure copper	7.73E+07	5.33E+07	3.73E+07	2.61E+07	3.03E+07	2.90E+06	1.15E+07	1.02E+07	7.65E+06	-0.485	0.235225
Stainless steel	7.73E+07	2.88E+07	2.85E+07	2.83E+07	5.00E+07	9.95E+06	1.41E+07	9.46E+06	1.57E+07	-0.386	0.148996
3D printed ABS	7.73E+07	4.84E+07	2.71E+07	1.52E+07	3.84E+07	1.30E+07	1.13E+07	1.49E+07	7.34E+06	-0.471	0.221841
Solid ABS	7.73E+07	2.10E+07	1.94E+07	1.79E+07	1.31E+07	6.66E+06	1.05E+07	6.58E+06	1.49E+07	-0.239	0.057121

Table D.16: Dry contact test results against clinically resistant *C. albicans* (CRCA) (Ref. No. 4122).

CFU/ml

Test sample	Contact period (minutes)									Pearson coefficient (R)	Coefficient of determination (R^2)
	0	0.5	2.5	5	10	15	20	60	180		
5 wt% silver - 95 wt% copper coated copper	2.00E+06	1.42E+06	7.10E+05	0.00E+00	0.00E+00	0.00E+00	0.00E+00	0.00E+00	0.00E+00	-0.977	0.955
50% w/w copper-zinc coated 3D printed ABS	2.00E+06	1.67E+06	1.28E+06	9.82E+05	0.00E+00	0.00E+00	0.00E+00	0.00E+00	0.00E+00	-0.99	0.980
Copper coated copper	2.00E+06	1.09E+06	4.87E+05	2.18E+05	0.00E+00	0.00E+00	0.00E+00	0.00E+00	0.00E+00	-0.822	0.676
Copper coated solid ABS	2.00E+06	1.13E+06	1.18E+06	1.24E+06	0.00E+00	0.00E+00	0.00E+00	0.00E+00	0.00E+00	-0.879	0.773
Copper coated 3D printed ABS	2.00E+06	1.13E+06	1.16E+06	1.20E+06	0.00E+00	0.00E+00	0.00E+00	0.00E+00	0.00E+00	-0.884	0.78
Pure copper	2.00E+06	8.73E+05	1.38E+06	2.18E+06	2.38E+06	9.09E+05	3.64E+04	0.00E+00	0.00E+00	-0.659	0.434
Stainless steel	2.00E+06	2.47E+06	1.95E+06	1.54E+06	2.21E+06	2.55E+05	0.00E+00	0.00E+00	0.00E+00	-0.871	0.759
3D printed ABS	2.00E+06	1.45E+06	1.47E+06	1.49E+06	1.99E+06	2.36E+06	7.27E+04	0.00E+00	0.00E+00	-0.695	0.483
Solid ABS	2.00E+06	1.05E+06	1.32E+06	1.67E+06	8.00E+05	7.27E+04	0.00E+00	0.00E+00	0.00E+00	-0.888	0.789

Pilot prototype testing

Table D.17 contains the autoclave sterilisation effects on diffusive activity for copper and zinc cold spray coatings.

Table D.17: Average zone of inhibition sizes for cold spray coatings undergoing two sterilisation techniques: alcohol dip and autoclave sterilisation.

Test samples		Average zone of inhibition size [mm]					
		S aureus		*E faecalis*		*K pneumoniae*	
		Autoclaved	Alcohol dipped	Autoclaved	Alcohol dipped	Autoclaved	Alcohol dipped
Copper coated polymers	Copper coated 3D printed ABS	0	0.7	1.4	2.7	0	0
	Copper coated solid ABS	0	1.4	3.2	2.1	0	0.3
	Copper coated PEEK	0.6	1.6	3.5	1.6	0.3	0.3
	Polished copper coated PEEK	0	1.1	3.9	/	0.5	0
	Copper coated vertically oriented 3D printed ABS	0	0.9	1.6	1.7	0.8	0
Zinc coated polymers	Zinc coated 3D printed ABS	4.3	4.2	0.9	1.4	1	0.5
	Zinc coated solid ABS	3.4	4	2.4	0	1	0.5
	Zinc coated PC	3.1	4.9	1.5	0.5	1.1	0.5
50% w/w copper-zinc coated 3D printed ABS		7.4	4.8	0.6	1.5	1.8	1

Table D.18 contains the autoclave sterilisation effect data for touch-contact activity of copper and zinc cold spray coatings.

Table D.19 contains the complete set of results from the antimicrobial Smartphone cover longitudinal study conducted at the University of the Witwatersrand, Johannesburg, South Africa.

Table D.18: Autoclave sterilisation effects on touch-contact antimicrobial activity for cold spray coated 3D printed ABS polymers. (CFU/ml).

Test sample		CFU/ml							
		Contact period (minutes)							
Material Description	Reference Name	0	0.5	5	10	15	20	60	180
Copper coated 3D printed ABS*	Cu(1)3DABS*	1.17E+08	8.60E+07	3.60E+07	2.20E+05	0.00E+00	1.00E+07	4.80E+05	4.00E+04
Zinc coated solid ABS*	ZnABS*	1.17E+08	1.56E+08	3.70E+07	4.84E+07	5.48E+06	1.47E+07	4.20E+06	6.32E+06
50% w/w copper-zinc coated 3D printed ABS*	Cu(1)50Zn3DABS*	1.17E+08	3.00E+08	2.00E+07	4.88E+06	6.86E+06	1.00E+07	3.05E+06	2.46E+06
Stainless steel*	Stainless Steel*	1.17E+08	3.60E+07	2.00E+07	2.38E+07	1.26E+08	1.00E+08	1.81E+08	1.60E+08

*Autoclave sterilisation

Table D.19: Quantified viable bacterial and fungal colony forming units over a three week longitudinal study of a copper and zinc coated 3D printed ABS smartphone cover, used in a microbiology laboratory environment.

Week One

Day	Bacterial CFUs (37°C 24 hours)					Fungal CFUs (25°C five days)				
	Active Coating: Cover	Control: Inside Cover	Control: Back of Phone	Control: Phone Screen	Average Control	Active Coating: Cover	Control: Inside Cover	Control: Back of Phone	Control: Phone Screen	Average Control
Monday	9	19	3	6	9	0	4	5	1	3
Tuesday	0	0	73	0	24	1	17	6	1	8
Wednesday	0	1	1	9	4	5	12	1	0	4
Thursday	9	6	2	19	9	15	5	0	101	35
Friday	1	1	2	29	11	1	5	1	2	3
Average	4	5	16	13	11	4	9	3	21	11

Week Two

Day	Bacterial CFUs (37°C 24 hours)					Fungal CFUs (25°C five days)				
	Active Coating: Cover	Control: Inside Cover	Control: Back of Phone	Control: Phone Screen	Average Control	Active Coating: Cover	Control: Inside Cover	Control: Back of Phone	Control: Phone Screen	Average Control
Monday	14	6	0	1	2	7	5	2	0	2
Tuesday	1	15	3	0	6	0	29	51	4	28
Wednesday	1	5	18	18	14	0	5	5	2	4
Thursday	3	1	0	32	11	0	1	4	1	2
Friday	0	2	1	1	1	3	3	2	3	3
Average	4	6	4	10	7	2	9	13	2	8

Week Three

Day	Bacterial CFUs (37°C 24 hours)					Fungal CFUs (25°C five days)				
	Active Coating: Cover	Control: Inside Cover	Control: Back of Phone	Control: Phone Screen	Average Control	Active Coating: Cover	Control: Inside Cover	Control: Back of Phone	Control: Phone Screen	Average Control
Monday	2	18	40	0	19	0	5	6	5	5
Tuesday	2	0	0	1	0	1	4	0	2	2
Wednesday	11	/	47	9	28	2	52	16	16	28
Thursday	0	0	0	0	0	0	3	6	0	3
Friday	1	7	8	1	5	0	3	4	1	3
Average	3	6	19	2	10	1	13	6	5	8

Appendix E Coating Combinations

Table E.1 contains all cold spray coating combinations that were explored in this research; from the theoretical coatings, to the experimental optimisation coatings and finally those coatings evaluated for their innate antimicrobial efficacy. These coatings represent the development of successful cold spray polymer metallisation across a wide and diverse range of coating-substrate combinations, including the integration of the additive manufacturing techniques of cold spray and 3D printing.

Table E.1: Cold spray coating naming convention for theoretical, experimental and antimicrobial susceptibility tests.

Theoretical Coatings		Experimental Optimisation Coatings		Antimicrobial Susceptibility Test Coatings	
Coating	Substrate	Coating	Substrate	Coating	Substrate
Copper	ABS	Copper	3D Printed ABS (hor.* and vert.*)	Copper	3D Printed ABS (hor. and vert.)
	Polycarbonate		ABS		ABS
	PEEK		Polycarbonate		PEEK
Nickel	ABS		PEEK		PEEK (polished coatings)
	Polycarbonate	Cu-Al-Al_2O_3	3D Printed ABS (hor.)		Copper
	PEEK		ABS	Cu-Al-Al_2O_3	3D Printed ABS (hor.)
Zinc	ABS		Polycarbonate		ABS
	Polycarbonate	75 wt% Cu - 25 wt% Zn	3D Printed ABS (hor.)	Zinc	3D Printed ABS (hor.)
	PEEK	50% (w/w) Cu-Zn	3D Printed ABS (hor.)		ABS
Tin	ABS	75 wt% Zn - 25 wt% Cu	3D Printed ABS (hor.)		Polycarbonate
	Polycarbonate	Zinc	3D Printed ABS (hor.)	75 wt% Cu - 25 wt% Zn	3D Printed ABS (hor.)
	PEEK		ABS	50% (w/w) Cu-Zn	3D Printed ABS (hor.)
Aluminium	ABS		Polycarbonate	75 wt% Zn - 25 wt% Cu	3D Printed ABS (hor.)
	Polycarbonate			5 wt% Ag - 95 wt% Cu	Copper
	PEEK				3D Printed ABS (hor. And vert.)
					ABS
				5 wt% Ag - 47.5% (w/w) Cu-Zn	3D Printed ABS (hor.)
				5 wt% Ag - 95 wt% Zn	3D Printed ABS (hor.)

* hor. = horizontal print orientation, vert. = vertical print orientation

Appendix F Research Consolidation

Appendix F contains the the research data required for the effective evaluation of the design and development of cold spray coatings on polymer substrates for the mitigation of nosocomial infections through the control and prevention of touch-contact surface contamination. The following is included:

- Surface wear and topography correlation analysis Page 457
- Substrate roughness and particle depth-of-penetration Page 458
- Targeted particle depth-of-penetration - Revised Page 459
- Theoretical particle depth-of-penetration - Revised Page 460

Surface wear and topography correlation analysis

Table F.1: Surface topography effects of ABS polymer substrates against wear properties for cold spray zinc coatings.

	Zinc coating			
Substrate	Roughness		μ	k [mm^3/N·m]
ABS	Ra	6.27		
	Rs	0.07	0.413	1.69E-03
	Rsk	0.5		
3D printed ABS (H)	Ra	4.98		
	Rs	0.05	0.544	2.87E-03
	Rsk	-0.1		

Table F.2: Surface topography effects on wear properties from polished and unpolished copper cold spray coatings on PEEK substrates.

	PEEK Substrate			
Coating	Roughness		μ	k [mm^3/N·m]
Copper	Ra	3.93		
	Rs	0.06	0.481	5.20E-04
	Rsk	0.28		
Copper polished	Ra	2.94		
	Rs	0.06	0.452	2.47E-04
	Rsk	-0.55		

Table F.3: Overall data for surface wear and topographical effects correlation.

Test samples	Surface roughness properties					Wear properties		
	Ra [μm]	Rz [μm]	Rsm [mm]	Rs [mm]	Rsk	μ	V_{disc} [mm^3]	k_{disc}
Copper coated solid ABS	1.04	7.85	0.05	0.03	0.04	0.442	0.066	4.40E-04
Copper coated 3D printed ABS	3.61	11.36	0.08	0.05	0.33	0.509	0.195	1.30E-03
Copper coated PEEK	3.93	29.82	0.09	0.06	0.28	0.481	0.078	5.20E-04
Polished copper coated PEEK	2.94	18.64	0.08	0.06	-0.55	0.452	0.037	2.47E-04
Copper coated vertically oriented 3D printed ABS	6.09	17.86	0.06	0.04	-0.04	0.5	0.303	2.02E-03
Zinc coated 3D printed ABS	4.98	18.02	0.07	0.05	-0.1	0.544	0.43	2.87E-03
Zinc coated solid ABS	6.27	43.43	0.11	0.07	0.5	0.413	0.253	1.69E-03
Zinc coated PC	7.01	46.71	0.13	0.07	0.24	0.505	0.272	1.81E-03
50% w/w copper-zinc coated 3D printed ABS	5.16	14.78	0.07	0.03	0.14	0.475	0.344	2.29E-03
Pure copper	0.19	1.11	0.08	0.04	-0.4	0.707	0.145	9.67E-04
Stainless steel	0.11	0.86	0.01	0.01	-1.24	0.807	0.009	6.00E-05
3D printed ABS	4.26	5.18	0.02	0.03	0.24	0.367	0.092	6.13E-04
Vertically oriented 3D printed ABS	7.36	17.01	0.02	0	-0.02	0.397	0.136	9.07E-04
Solid ABS	0.41	1.19	0.18	0.03	0.84	0.271	0.136	9.07E-04
Solid polycarbonate	0.01	0.07	0.08	0.01	2.69	0.518	0.296	1.97E-03
Solid polyetheretherketone	0.87	5.76	0.14	0.06	-1.69	0.245	0.007	4.67E-05

Table F.4: Pearson correlation coefficients (R) for surface wear and topographical effects correlation analysis.

Coated substrates			Substrates			Coatings and Substrates		
Pearson correlation coefficient (R)		Strength of linear correlation	Pearson correlation coefficient (R)		Strength of linear correlation	Pearson correlation coefficient (R)		Strength of linear correlation
Variables	R		Variables	R		Variables	R	
Ra-μ	0.25	weak	Ra-μ	-0.33	weak	Ra-μ	-0.18	weak
Rz-μ	-0.18	weak	Rz-μ	-0.37	weak	Rz-μ	-0.10	weak
Rsm-μ	-0.08	weak	Rsm-μ	-0.55	moderate	Rsm-μ	-0.49	weak
Rs-μ	-0.09	weak	Rs-μ	-0.37	weak	Rs-μ	-0.21	weak
Rsk-μ	-0.12	weak	Rsk-μ	-0.10	weak	Rsk-μ	-0.10	weak
Ra-k_{disc}	0.7	moderate	Ra-k_{disc}	-0.04	weak	Ra-k_{disc}	0.48	weak
Rz-k_{disc}	0.12	weak	Rz-k_{disc}	-0.14	weak	Rz-k_{disc}	0.32	weak
Rsm-k_{disc}	0.07	weak	Rsm-k_{disc}	0.08	weak	Rsm-k_{disc}	0.09	weak
Rs-k_{disc}	-0.11	weak	Rs-k_{disc}	-0.41	weak	Rs-k_{disc}	0.08	weak
Rsk-k_{disc}	0.21	weak	Rsk-k_{disc}	0.94	strong	Rsk-k_{disc}	0.49	weak

Substrate roughness and particle depth-of-penetration

The following tables explore the effects of substrate surface topography on the ideal particle depth-of-penetration for the case of cold spray metallisation of polymers.

Table F.5: Pearson correlation analysis for identifying linear trends between substrate surface topographical effects and particle depth-of-penetration using copper coatings on various ABS polymer substrates as a test case.

Normalised particle depth of penetration (X/D)		
Pearson correlation coefficient (R)		Strength of linear correlation
Variables	R	
Ra-ZOI	0.77	moderate
Rz-ZOI	0.87	strong
Rsm-ZOI	-0.34	weak
Rs-ZOI	-0.16	weak
Rsk-ZOI	-0.78	moderate

Table F.6: Pearson correlation analysis for identifying linear trends between substrate surface topographical effects and particle depth-of-penetration for copper coated polymer substrates.

Normalised particle depth of penetration (X/D)		
Pearson correlation coefficient (r)		Strength of linear correlation
Variables	R	
Ra-M_{ar}	0.59	moderate
Rz-M_{ar}	-0.19	weak
Rsm-M_{ar}	-0.60	moderate
Rs-M_{ar}	-0.51	moderate
Rsk-M_{ar}	-0.83	strong

Table F.7: Pearson correlation analysis for identifying linear trends between substrate surface topographical effects and particle depth-of-penetration for zinc coated polymer substrates.

Normalised particle depth of penetration (X/D)		
Pearson correlation coefficient (R)		Strength of linear correlation
Variables	R	
Ra-M_{ar}	0.50	moderate
Rz-M_{ar}	-0.27	weak
Rsm-M_{ar}	0.37	weak
Rs-M_{ar}	0.28	weak
Rsk-M_{ar}	0.71	moderate

Targeted particle depth-of-penetration - Revised

In order to re-derive a targeted particle depth-of-penetration model data from optimum experimental polymer coatings were compiled, as given in Table F.8. The table includes published literature findings, yet this data was excluded from the re-derived model since the data related specifically to hard-on-hard copper cold spray, and was therefore deemed irrelevant.

A similar process was followed as was used in the first model derivation, whereby relationships were graphed and a suitable analytical expression derived giving an equation for the general trend. This process is depicted in Figure F.1.

The empirical model was then formulated as given in the main document and expressed in terms of Equation 7.1.

Table F.8: Depth of penetration, substrate surface roughness and coating-substrate ratios of density, Young's Modulus and ultimate tensile strength for the optimum cold spray coatings.

	Optimum test samples	Ideal depth of penetration (X/D)	Substrate surface roughness (Ra)	Density ratio (ρ_p/ρ_s)	Youngs Modulus ratio (E_p/E_s)	Ultimate tensile strength ratio (UTS_p/UTS_s)
Experimental data (polymer metallisation)	Copper coated 3D printed ABS	0.57	4.26	/	50.00	6.36
	Copper coated solid ABS	0.81	0.41	8.62	64.71	6.56
	Copper coated PEEK	0.28	0.87	6.68	27.50	2.14
	Copper coated vertically oriented 3D printed ABS	2.01	7.36	/	/	/
	Zinc coated 3D printed ABS	1.29	/	/	43.9	3.76
	Zinc coated solid ABS	0.92	/	6.83	56.76	3.88
	Zinc coated PC	0.96	0.01	5.97	43.86	1.80
Literature data (hard-on-hard) Not included in analysis	Copper coated stainless steel [117,192]	0.15	/	1.12	0.52	0.408
	Copper coated Al7050 [153]	0.60	/	3.17	1.53	0.401
	Copper coated Aluminium [153]	1.15	/	3.32	1.59	1.909

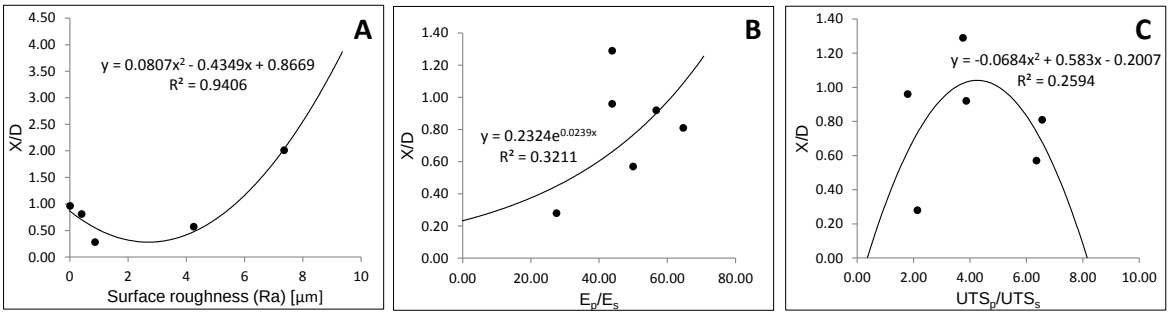


Figure F.1: Trends between cold spray particle depth-of-penetration and the associated system property of (A) surface roughness and the particle and substrate material properties of (B) Young's Modulus and (C) ultimate tensile strength.

Theoretical particle depth-of-penetration - Revised

Coming full circle the proceeding tests and analysis, which were important in seeing the development of cold spray polymer metallisation for antimicrobial surface coating applications, were integral to the re-derived theoretical particle depth-of-penetration model. The key model adjustments, based on the development of a target scaling factor (η) to be integrated into the aforementioned theoretical model are tabulated and graphed in Table F.9 and Figure F.2, respectively.

Table F.9: Cold spray particle and substrate material density ratios and target scaling factors for normalised particle depth-of-penetration for various copper and zinc polymer metallised coatings.

	Copper coated 3D printed ABS	Copper coated ABS	Copper coated PEEK	Zinc coated 3D printed ABS	Zinc coated ABS	Zinc coated PC
Density ratio	8.615	8.615	6.892	6.827	6.827	5.966
Target scaling factor*	0.322	0.458	0.318	0.733	0.523	0.793

*Ratio between the experimentally optimum normalised depth of penetration (X/D_{actual}) and the normalised depth of penetration predicted by Model 1 depth of penetration model (X/D_{model})

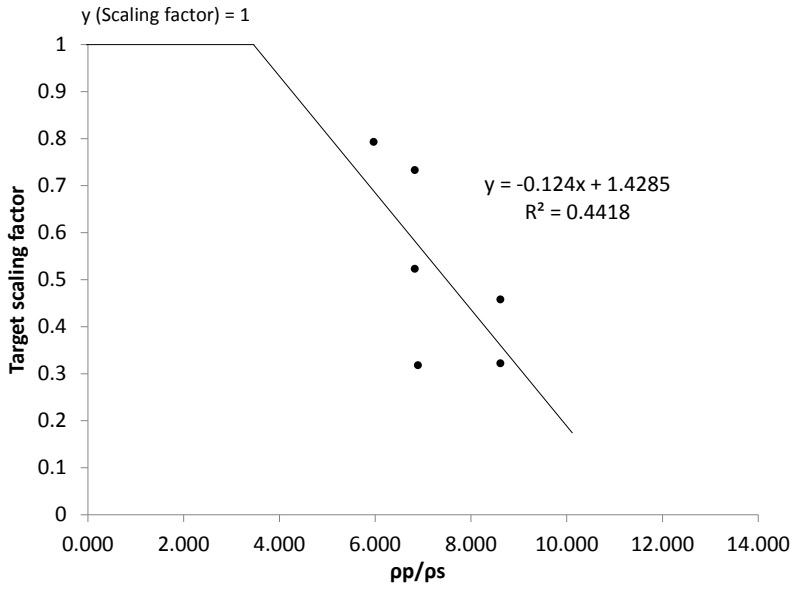


Figure F.2: Piecewise graph of powder-substrate density ratio vs target scaling factor for optimum particle depth of penetration of cold spray polymer metallisation.